

**1998**

**Technical**

**Digest Series**

**Volume 4**

# Integrated Photonics Research

## Technical Digest

**DISTRIBUTION STATEMENT A**  
Approved for Public Release  
Distribution Unlimited

**March 30–April 1, 1998**

**Victoria Conference Centre**  
Victoria, British Columbia, Canada

**Conference Edition**

*Sponsored by*  
**Optical Society of America**

*In cooperation with*

**European Conference on Integrated Optics (ECIO)**

*Technical Cosponsor*

**IEEE/Lasers and Electro-Optics Society**

QC QUALITY INSPECTED 4

**20000626 038**

**OSA**  
Optical Society of America

## 1998 OSA Technical Digest Series

**Vol. 1 VISION SCIENCE AND  
ITS APPLICATIONS**

Santa Fe, New Mexico

February 6, 1998

List Price \$92 Member Price \$60

**Vol. 2 OPTICAL FIBER COMMUNICATION  
CONFERENCE (OFC)**

San Jose, California

February 22, 1998

List Price \$92 Member Price \$60

**Vol. 3 LASER APPLICATIONS TO  
CHEMICAL AND ENVIRONMENTAL  
ANALYSIS**

Orlando, Florida

March 9, 1998

List Price \$75 Member Price \$48

**Vol. 4 INTEGRATED PHOTONICS  
RESEARCH**

Victoria, British Columbia, Canada

March 29, 1998

List Price \$92 Member Price \$60

**Vol. 5 NONLINEAR GUIDED WAVES  
AND THEIR APPLICATIONS**

Victoria, British Columbia, Canada

March 29, 1998

List Price \$75 Member Price \$48

**Vol. 6 CONFERENCE ON LASERS AND  
ELECTRO-OPTICS (CLEO)**

San Francisco, California

May 3, 1998

List Price \$92 Member Price \$60

**Vol. 7 INTERNATIONAL QUANTUM  
ELECTRONICS CONFERENCE  
(IQEC)**

San Francisco, California

May 3, 1998

List Price \$92 Member Price \$60

**Vol. 8 OPTICAL DATA STORAGE**

Aspen, Colorado

May 10, 1998

List Price \$75 Member Price \$48

More to come, including:

**DIFFRACTIVE OPTICS AND  
MICRO-OPTICS**

Kailua-Kona, Hawaii

June 8, 1998

List Price \$75 Member Price \$48

**SIGNAL RECOVERY AND  
SYNTHESIS**

Kailua-Kona, Hawaii

June 8, 1998

List Price \$66 Member Price \$43

# REPORT DOCUMENTATION PAGE

AFRL-SR-BL-TR-00-

Public reporting burden for this collection of information is estimated to average 1 hour per response, including gathering and maintaining the data needed, and completing and reviewing the collection of information, collection of information, including suggestions for reducing this burden, to Washington Headquarters Service, Davis Highway, Suite 1204, Arlington, VA 22202-4302, and to the Office of Management and Budget,

1 sources,  
act of this  
Jefferson  
3.

0242

1. AGENCY USE ONLY (Leave blank)		2. REPORT DATE		3. R 01 Feb 98 to 31 Oct 98 Final	
4. TITLE AND SUBTITLE ORGANIZATION OF THE 1998PHOTONIC SCIENCE TOPICAL MEETINGS				5. FUNDING NUMBERS 61102F 2301/AS	
6. AUTHOR(S) Dr Fantone					
7. PERFORMING ORGANIZATION NAME(S) AND ADDRESS(ES) Optical Society of America 2010 Massachusetts Ave NW Washington, DC 20036				8. PERFORMING ORGANIZATION REPORT NUMBER	
9. SPONSORING/MONITORING AGENCY NAME(S) AND ADDRESS(ES) AFOSR/NE 801 North Randolph Street Rm 732 Arlington, VA 22203-1977				10. SPONSORING/MONITORING AGENCY REPORT NUMBER  F49620-98-1-0220	
11. SUPPLEMENTARY NOTES					
12a. DISTRIBUTION AVAILABILITY STATEMENT APPROVAL FOR PUBLIC RELEASE; DISTRIBUTION UNLIMITED				12b. DISTRIBUTION CODE	
13. ABSTRACT (Maximum 200 words)  The topical meetings technical program and the list of attendees demonstrates the international scope of the present effort in this technology. Finally, are pleased to thank the following organizations for their generous financial support of the meeting.  ALL INFORMATION CONTAINED HEREIN IS UNCLASSIFIED EXCEPT WHERE SHOWN OTHERWISE DATE OF TRANSMITTAL TO DTIC THIS TECHNICAL REPORT HAS BEEN REVIEWED AND IS APPROVED FOR PUBLIC RELEASE DATE 1996-12. DISTRIBUTION IS UNLIMITED					
14. SUBJECT TERMS				15. NUMBER OF PAGES	
				16. PRICE CODE	
17. SECURITY CLASSIFICATION OF REPORT UNCLASSIFIED		18. SECURITY CLASSIFICATION OF THIS PAGE UNCLASSIFIED		19. SECURITY CLASSIFICATION OF ABSTRACT UNCLASSIFIED	
				20. LIMITATION OF ABSTRACT UL	

# Integrated Photonics Research

Conference Edition

**Technical  
Digest**

*Collocated with*

**The Workshop on Novel Solitons and Nonlinear Periodic  
Structures**

**Nonlinear Guided Waves and Their Applications**

**March 30–April 1, 1998**

**Victoria Conference Centre  
Victoria, British Columbia, Canada**

**1998 OSA Technical Digest Series  
Volume 4**

*In cooperation with the*  
**European Conference on Integrated Optics (ECIO)**

*Technical Cosponsor*  
**IEEE/Lasers and Electro-Optics Society**

*Sponsored by*  
**Optical Society of America**  
2010 Massachusetts Avenue, NW  
Washington, DC 20036-1023

**OSA.**

AIR FORCE OFFICE OF SCIENTIFIC  
RESEARCH (AFOSR)  
NOTICE OF TRANSMITTAL TO DTIC. THIS  
TECHNICAL REPORT HAS BEEN REVIEWED  
AND IS APPROVED FOR PUBLIC RELEASE  
IWA AFR 190-12. DISTRIBUTION IS  
UNLIMITED.  
YONNE MASON  
STINFO PROGRAM MANAGER

**DTIC QUALITY INSPECTED 4**

Articles in this publication may be cited in other publications. To facilitate access to the original publication source, the following form for the citation is suggested:

Name of Author(s), "Title of Paper," in Integrated Photonics Research, Vol. 4, OSA  
Technical Digest Series (Optical Society of America, Washington DC, 1998), pp. xx-xx.

#### Optical Society of America

##### ISBN

Conference Edition	1-55752-535-8
Postconference Edition	1-55752-536-6
1998 Technical Digest Series	1-55752-521-8

##### Library of Congress Catalogue Card Number

Conference Edition	97-81335
Postconference Edition	97-81336

Copyright © 1998, Optical Society of America

Individual readers of this digest and libraries acting for them are permitted to make fair use of the material in it, such as to copy an article for use in teaching or research, without payment of fee, provided that such copies are not sold. Copying for sale is subject to payment of copying fees. The code 1-55752-521-8/98/\$15.00 gives the per-article copying fee for each copy of the article made beyond the free copying permitted under Sections 107 and 108 of the U.S. Copyright Law. The fee should be paid through the Copyright Clearance Center, Inc., 21 Congress Street, Salem, MA 01970.

Permission is granted to quote excerpts from articles in this digest in scientific works with the customary acknowledgment of the source, including the author's name and the name of the digest, page, year, and name of the Society. Reproduction of figures and tables is likewise permitted in other articles and books provided that the same information is printed with them and notification is given to the Optical Society of America. In addition, the Optical Society may require that permission also be obtained from one of the authors. Address inquiries and notices to Director of Publications, Optical Society of America, 2010 Massachusetts Avenue, NW, Washington, DC 20036-1023. In the case of articles whose authors are employees of the United States Government or its contractors or grantees, the Optical Society of America recognizes the right of the United States Government to retain a nonexclusive, royalty free license to use the author's copyrighted article for United States Government purposes.

Printed in the U.S.A.

# Contents

<b>Agenda of Sessions</b>	iv
<b>IPR Abstracts</b>	ix
<b>Workshop on Novel Solitons and Nonlinear Periodic Structures Abstracts</b>	xxiv
<b>Nonlinear Guided Waves and Their Applications Abstracts</b>	xxviii
<b>IMA</b> Plenary Session	1
<b>IMB</b> Beam Propagation Methods	7
<b>IMC</b> Waveguide Materials and Devices	23
<b>IMD</b> WDM I	39
<b>IME</b> Vectorial Simulations	55
<b>IMF</b> Novel Fabrication Techniques	75
<b>IMG</b> WDM II/ Filters	89
<b>IMH</b> Poster Session	105
<b>ITuA</b> Photonic Nanostructures I	173
<b>ITuB</b> Lasers I	185
<b>ITuC</b> Photonic Packaging I	205
<b>ITuD</b> Photonic Nanostructures II	217
<b>ITuE</b> Modulators/Switches	233
<b>ITuF</b> Photonic Packaging II	249
<b>ITuG</b> Quantum Wells I: Carrier Transport in Quantum Well Devices	267
<b>ITuH</b> Silicon Based Optoelectronic Technology	281
<b>ITuI</b> Electrooptic Materials and Devices	297
<b>ITuJ</b> Quantum Wells II: Heterojunction Engineering, Optical Gain and Electroabsorption	317
<b>ITuK</b> Novel Silicon Based Structures	333
<b>ITuL</b> Polymer Based Devices	349
<b>IWA</b> Device Simulations I	359
<b>IWB</b> Lasers II: WDM/VCSELS	379
<b>IWC</b> Device Simulations II	395
<b>IWD</b> Multimode Optical Interconnects	411
<b>Key to Authors and Presiders</b>	428

# Agenda of Sessions

**Sunday, March 29, 1998**

	Salon A	Salon B	Salon C	Saanich	Esquimalt	Oak Bay
Registration	8:00am–6:00pm, 2nd Floor Lobby					
Early Morning					8:45am–10:30am WSA, Temporal Solitons 1	
Morning Break						Coffee Break
Late Morning					11:00am–12:30pm WSB, Temporal Solitons 2	
Lunch Break					12:30pm–2:00pm NSNPS Lunch Break	
Early Afternoon					2:00pm–4:00pm WSC, Novel Solitons	
Afternoon Break						4:00pm–4:30pm Coffee Break
Late Afternoon					4:30pm–6:30pm WSD, Spatial Solitons 1	
Evening	Welcome Reception & Pub Crawl					

**Monday, March 30, 1998**

	Salon A	Salon B	Salon C	Saanich	Esquimalt	Oak Bay
Registration	7:00am–5:00pm, 2nd Floor Lobby					
Early Morning		8:00am–10:30am IMA, Plenary Session			8:30am–10:30am WMA, Nonlinear Periodic Structures 1	
Morning Break	10:30am–11:00am Morning Coffee Break & Exhibits					
Late Morning		11:00am–12:30pm IMB, Beam Propagation Methods	11:00am–12:15pm IMC, Waveguide Materials & Devices	11:00am–12:30pm IMD, WDM 1	11:00am–1:00pm WMB, Nonlinear Periodic Structures 2	
Lunch Break		12:30pm–2:00pm IPR Lunch Break			1:00pm–2:00pm NSNPS Lunch Break	
Early Afternoon		2:00pm–3:30pm IME, Vectorial Simulations	2:00pm–3:30pm IMF, Novel Fabrication Techniques	2:00pm–3:30pm IMG, WDM 2/ Filters		2:00pm–3:30pm WMC, Poster Session

# Monday, March 30, 1998 (continued)

	Salon A	Salon B	Salon C	Saanich	Esquimalt	Oak Bay
Afternoon Break	3:30pm-4:00pm IPR Coffee Break and Exhibits					
Late Afternoon	4:00pm-6:00pm IMH, Poster Session				3:30pm-6:00pm WMD, Spatial Solitons 2	
	6:00pm-7:30pm IPR Conference Reception Crystal Ballroom, Empress Hotel				6:00pm-7:30pm NSNPS Dinner Break	
Evening					7:30pm-9:30pm WME, Panel Discussion	

# Tuesday, March 31, 1998

	Salon A	Salon B	Salon C	Saanich	Esquimalt	Oak Bay
Registration	8:00am-6:00pm, 2nd Floor Lobby					
Early Morning		8:30am-10:00am ITuA, Photonic Nanostructures 1	8:30am-10:00am ITuB, Lasers 1	8:30am-10:00am ITuC, Photonic Packaging 1		
Morning Break	10:00am-10:30am Coffee Break and Exhibits					
Late Morning		10:30am-12:00m ITuD, Photonic Nanostructures 2	10:30am-12:00m ITuE, Modulators/ Switches	10:30am-12:00m ITuF, Photonic Packaging 2		
Lunch Break	12:00m-1:30pm IPR Lunch Break					
Early Afternoon		1:30pm-3:00pm ITuG, Quantum Wells 1: Carrier Transport in Quantum Well Devices	1:30pm-3:00pm ITuH, Silicon Based Optoelectronic Technology	1:30pm-3:00pm ITuI, Electrooptic Materials and Devices		
Afternoon Break	3:00pm-3:30pm Coffee Break and Exhibits					
Late Afternoon		3:30pm-5:00pm ITuJ, Quantum Wells 2: Heterojunction Engineering, Optical Gain and Electroabsorption	3:30pm-4:45pm ITuK, Novel Silicon Based Structures	3:30pm-4:30pm ITuL, Polymer Based Devices		
	5:00pm, IPR Postdeadline Paper Session					

### Wednesday, April 1, 1998

	Salon A	Salon B	Salon C	Saanich	Esquimalt	Oak Bay
Registration	8:00am-6:00pm, 2nd Floor Lobby					
Early Morning		8:30am-10:00am IWA, Device Simulations 1	8:30am-10:00am IWB, Lasers 2: WDM/VCSELS	8:15am-8:30am Introduction  8:30am-10:00am NWA, New and Weird Soliton Effects		
Morning Break	10:00am-10:30am Coffee Break and Exhibits					
Late Morning		10:30am-11:45am IWC, Device Simulations 2	10:30am-12:00m IWD, Multimode Optical Interconnects	10:30am-12:00m NWB, Nonlinear Waveguides		
Lunch Break	12:00m-1:30pm Lunch Break					
Early Afternoon				1:30pm-3:00pm NWC, Dispersion Managed Solitons		
Afternoon Break	3:00pm-3:30pm Coffee Break and Exhibits					
Late Afternoon				3:30pm-4:30pm NWD, Frequency Mixing in Waveguides		
				4:30pm-6:30pm NWE, Poster Session 1		

### Thursday, April 2, 1998

	Salon A	Salon B	Salon C	Saanich	Esquimalt	Oak Bay
Registration	8:00am-6:00pm, 2nd Floor Lobby					
Early Morning				8:30am-10:00am NThA, Temporal Propagation Effects 1		
Morning Break				10:00am-10:30am Coffee Break		
Late Morning				10:30am-12:00m NThB, Semiconductor Nonlinearities		
Lunch Break				12:00m-1:30pm Lunch Break		

# Thursday, April 2, 1998 (continued)

	Salon A	Salon B	Salon C	Saanich	Esquimalt	Oak Bay
Early Afternoon				1:30pm-3:00pm NThC, Photorefractive and Kerr Solitons		
Afternoon Break				3:00pm-3:30pm Coffee Break		
Late Afternoon				3:30pm-4:30pm NThD, WDM Soliton Systems		
Evening					4:30pm-6:30pm NThE, Poster Session 2	
				6:30pm-7:30pm Conference Reception Crystal Ballroom, The Empress Hotel		

# Friday, April 3, 1998

	Salon A	Salon B	Salon C	Saanich	Esquimalt	Oak Bay
Registration	8:00am-6:00pm, 2nd Floor Lobby					
Early Morning				8:30am-10:15am NEA, Second- Order Processes and Materials		
Morning Break				10:15am-10:45am Coffee Break		
Late Morning				10:45am-12:00pm NFB, Postdeadline Paper Session		
Lunch Break				12:00pm-1:30pm Lunch Break		
Early Afternoon				1:30pm-3:00pm NFC, Temporal Propagation Effects 2		
Afternoon Break				3:00pm-3:30pm Coffee Break		
Late Afternoon				3:30pm-5:00pm NFD, Non-Kerr and Quadratic Solitons  5:00pm-5:15pm Closing Remarks		

# Integrated Photonics Research '98

March 30–April 1, 1998

## IPR Advisory Committee

David Yevick, Chair, *Queen's University, Canada*  
Anand Gopinath, *University of Minnesota, USA*  
Steven Korotky, *Lucent Technologies, USA*  
Curtis Menyuk, *University of Maryland, USA*  
Meint Smit, *Technical University of Delft, The Netherlands*  
David A. Smith, *Case Western Reserve University, USA*

## IPR '98 Technical Program Committee Members

### General Chair:

Robert Deri, *Lawrence Livermore National Lab., USA*

### Program Co-Chairs:

Nadir Dagli, *University of California Santa Barbara, USA*  
Jane E. Zucker, *Lucent Technologies, Bell Labs, USA*

### Asia/Pacific Liaison Committee:

Shunji Seki, Chair, *NTT, Japan*  
Edwin Y.B. Pun, *City University of Hong Kong*  
Rodney S. Tucker, *University of Melbourne, Australia*

### Europe Liaison Committee:

K. Alan Shore, Chair, *University of Wales, UK*  
Meint Smit, *Technical University of Delft, Netherlands*  
K. Petermann, *Technische University Berlin, Germany*

### OSA Technical Council Representative:

Terry Smith, *3M Company, USA*

## Technical Program Subcommittees

### Category I. Compound semiconductor photonic devices

Julian Soole, Chair, *Tellium, USA*  
Niraj Agrawal, *Heinrich Hertz Institut, Germany*  
Martin Amersfoort, *BBV Design BV, The Netherlands*  
Roel Baets, *University of Gent, Belgium*  
S. Chandrasekhar, *Bell Labs, Lucent Technologies, USA*  
Richard De La Rue, *University of Glasgow, UK*  
Gregory A. Magel, *Texas Instruments, USA*  
Kunishige Oe, *NTT Opto-electronics Laboratories, Japan*  
Claude Rolland, *Nortel Technology, Canada*  
Jean-Francois Vinchant, *Alcatel Optronics, France*  
Robert Walker, *GEC-Marconi Materials Technology, UK*

### Category II. Dielectric waveguides and photonic devices

Leon McCaughan, Chair, *University of Wisconsin-Madison, USA*  
Martin M. Fejer, *Stanford University, USA*  
Fred Heismann, *Bell Labs, Lucent Technologies, USA*  
Martin Hempstead, *University of Southampton, UK*  
Janet Jackel, *Bellcore, USA*  
Bahram Jalali, *University of California Los Angeles, USA*  
Yasuo Kokubun, *Yokohama National University, Japan*  
William J. Minford, *Bell Labs, Lucent Technologies, USA*  
Ed J. Murphy, *Bell Labs, Lucent Technologies, USA*  
Yutaka Ohmori, *Osaka University, Japan*  
Ramu Ramaswamy, *University of Florida, USA*  
Wolfgang Sohler, *Universitat-GH Paderborn, Germany*  
Richard A. Soref, *Rome Laboratory, USA*  
David Weidman, *Corning Inc., USA*

### Category III. Modeling, numerical simulation, and theory

Sujeet Chaudhuri, Chair, *University of Waterloo, Canada*  
Shunji Seki, *NTT Multimedia Systems Department, Japan*  
K. Alan Shore, *University of Wales, UK*  
S.L. Chuang, *University of Illinois, USA*  
Joe Donnelly, *MIT Lincoln Labs, USA*  
G.R. Hadley, *Sandia National Labs., USA*  
Y. Nakano, *University of Tokyo, Japan*  
Eoin O'Reilly, *University of Surrey, UK*  
K. Petermann, *Technische University Berlin, Germany*  
B. Tromborg, *Tele Denmark Research, Denmark*  
C.M. Weinert, *Heinrich Hertz Institute, Germany*  
John M. Zavada, *US Army Research Office, USA*  
R.W. Ziolkowski, *University of Arizona, USA*

### Category IV. Photonic manufacturing, packaging and prototyping

Lewis Aronson, Chair, *Hewlett Packard, USA*  
Philip J. Anthony, *Bell Labs, Lucent Technologies, USA*  
Ian R. Croston, *Integrated Optical Components, UK*  
Paul O. Haugsjaa, *GTE Laboratories, USA*  
Mark Lowry, *Lawrence Livermore National Lab., USA*  
Mary Hibbs-Brenner, *Honeywell Technology Center, USA*  
Nan-Marie Jokerst, *Georgia Institute of Technology, USA*  
Peter Krusius, *Cornell University, USA*  
Chip Mueller, *AMP Inc., USA*  
Hyun-Kuk Shin, *Samsung Electronics Co., Ltd., Korea*  
Laura Ann Weller-Brophy, *Corning, Inc., USA and Applications Contact*  
Norihide Yamada, *Hewlett-Packard Laboratories, Japan*

# Agenda

■ **Monday**  
■ **March 30, 1998**

---

## Salon B&C

---

8:00am–10:30am

### IMA ■ Plenary Session

Robert J. Deri, *Lawrence Livermore National Laboratories, USA, Presider*

8:15am (Plenary)

**IMA1 ■ Planar lightwave circuits: penetration into real telecom markets**, Masao Kawachi, *NTT Science and Core Technology Laboratory Group, Japan*. Low-loss integrated silica waveguides with well-defined core geometry are used to form a variety of planar lightwave circuits (PLCs) for optical branching, filtering, switching and hybrid optoelectronic integration. This talk reviews the recent progress in silica-based PLC technologies which are now penetrating real telecom markets through application in optical access networks and dense WDM systems. (p. 2)

9:00am (Plenary)

**IMA2 ■ Indium phosphide photonic waveguide devices and their fiber pigtailing**, Hans Melchior, *Swiss Federal Institute of Technology, Switzerland*. Indium phosphide photonic waveguide devices, including laser-diodes, semiconductor optical amplifiers, modulators, switches and wavelength converters evolve in fiber optical communications. While high performance leads to minimization of their optically active areas, efficient coupling to optical fibers and fiber-arrays demands monolithic beam expanders and automatic chip-to-fiber alignment techniques. (p. 3)

9:45am (Plenary)

**IMA3 ■ Commercialization timescales for photonic integration**, Philip J. Anthony, *Lucent Technologies, USA*. The speed of the future commercialization of integrated photonic devices can be predicted by the rate of introduction of other new technologies, both in optoelectronics and in other fields. (p. 4)

---

## Salon A

---

10:30am–11:00am

**Morning Coffee Break & Exhibits**

---

## Salon B

---

11:00am–12:30pm

### IMB ■ Beam Propagation Methods

G. Ronald Hadley, *Sandia National Laboratories, USA, Presider*

11:00am (Invited)

**IMB1 ■ Beam propagation method for simulation of optical waveguides: theory, algorithm and application**, Wei-Ping Huang, Chenglin Xu, Kang Li, S.K. Chaudhuri, *Univ. Waterloo, Canada*. Recent development in the beam propagation method (BPM) for simulation of optical waveguides is reviewed. Important issues on theoretical and practical aspects of this powerful method are discussed. (p. 8)

11:30am

**IMB2 ■ Beam propagation method benchmark test: symmetrical coupler and gain-loss waveguide**, H.-P. Nolting, M. Gravert, *Heinrich-Hertz Institut, Germany*; H.J.W.M. Hoekstra, R. Stoffer, G.J.M. Krijnen, *Univ. Twente, The Netherlands*; C. Sibilio, M. de Minicis, *Univ. Degli Studi Di Roma, Italy*; R. Pregla, O. Conradi, *Fernuniversität, Hagen, Germany*. Two new benchmark tests for BPM algorithms have been used to investigate different interface conditions for an arbitrary positioned waveguide on a BPM-grid. (p. 11)

11:45am

**IMB3 ■ A novel beam propagation algorithm for three-dimensional tapers**, P. Sewell, S. Sujecki, T.M. Benson, P.C. Kendall, *Univ. Nottingham, U.K.* Numerical noise in beam propagation simulations of three-dimensional optical tapers arising from nonphysical staircasing is eliminated by use of tapered and oblique coordinate systems. (p. 14)

12:00m

**IMB4 ■ Beam propagation method using local oblique coordinate systems**, Yih-Peng Chiou, Hung-chun Chang, *National Taiwan Univ.* A novel beam propagation method derived in local oblique coordinate system is proposed to accurately investigate z-dependent structures without taking staircase approximation. (p. 17)

12:15pm

**IMB5 ■ Bi-directional beam propagation method based on full-wave analysis**, Chenglin Xu, Kang Li, Wei-Ping Huang, *Univ. Waterloo, Canada*; Wayne Lui, Kiyoyuki Yokoyama, *NTT Opto-electronics Laboratories, Japan*. The new bi-directional BPM overcomes the conventional plane wave or local guided wave approximations. It applies to waveguides with arbitrary longitudinal discontinuities. (p. 20)

12:30pm–2:00pm

Lunch Break

---

## Salon C

---

11:00am–12:15pm

### IMC ■ Waveguide Materials & Devices

David L. Weidman, *Optical Components Tech., USA, Presider*

11:00am

**IMC1 ■ Formation of Bragg gratings on thin films prepared by sol-gel and sputtering processes**, Junji Nishii, *Osaka National Research Institute, Japan*; Noboru Tohge, Gaoyang Zhao, *Kinki Univ., Japan*. Bragg gratings could be printed on thin films prepared by sol-gel and sputtering methods by irradiation with ultraviolet laser. The characteristics of the gratings are discussed. (p. 24)

11:15am

**IMC2 ■ Luminescence and gain in co-sputtered  $\text{Al}_2\text{O}_3$  erbium-doped waveguides**, Klein L. Johnson, Anand Gopinath, William Berglund, Ben Ellerbusch, *Univ. Minnesota, USA*; Carol Ford, Randy Ramberg, Lance Vreze, *Honeywell Military Avionics Division, USA*. Luminescence and lifetime data is presented for Er-doped  $\text{Al}_2\text{O}_3$  planar waveguide amplifiers fabricated on Si substrates by co-sputtering. (p. 27)

11:30am

**IMC3 ■ Birefringent oxidized porous silicon-based optical waveguides**, Yu. N. Korkishko, V.A. Fedorov, S.A. Gavrilov, *Moscow Institute of Electronic Technology, Russia*; V.V. Karavanskii, *Russian Academy of Science*. We have found that integrated optical waveguides based on oxidized porous silicon have a relatively large birefringence. As a result, the modes of both polarizations are supported. The origin of observed phenomenon is discussed. (p. 30)

11:45am

**IMC4 ■ Fabrication of planar and channel waveguides on As-S-(Se) chalcogenide glasses for integrated optical devices**, K. Le Foulgoc, J.-F. Viens, A. Villeneuve, *Univ. Laval, Canada*; K. Richardson, T. Cardinal, *Univ. Central Florida, USA*. Preparation process of infrared sulfide chalcogenide glasses waveguides are presented. Integrated optical devices such as photoinduced waveguides and directional couplers are investigated. (p. 33)

12:00m

**IMC5 ■ Photoinduced index-tapered channel waveguides in chalcogenide glasses for guided mode-size conversion**, Siddharth Ramachandran, Stephen G. Bishop, *Univ. Illinois, USA*. Enhanced photosensitivity in rapid thermally annealed chalcogenide glasses is used to demonstrate an index-tapered channel waveguide for on-chip spot-size conversion applications. Mode dimension changes by a factor of 2.6 over an 8-mm length are demonstrated. (p. 36)

12:30pm–2:00pm

Lunch Break

---

## Saanich

---

11:00am–12:30pm

### IMD ■ WDM I

Julian B. Soole, *Tellium, Inc., USA, Presider*

11:00am (Invited)

**IMD1 ■ Integrated optical devices for WDM networks**, Y. Yoshikuni, *NTT Opto-electronics Laboratories, Japan*. Recent progress in the WDM networks accelerates developments of integrated optical devices. This presentation reviews recent progress in developments of the monolithic and the hybrid integrated optical devices. (p. 40)

11:30am (Invited)

**IMD2 ■ Channel monitoring in WDM networks: a systems perspective**, Gabriela Livescu, *Lucent Technologies, Bell Labs, USA*. Optical channel monitoring in a WDM system implies measurement of wavelength, power and optical signal-to-noise ratio of all channels. This information can be used for control of network elements, and for network maintenance and performance monitoring. I shall discuss a variety of devices applicable to optical monitoring, and useful in control, maintenance and provisioning of lightwave systems. (p. 43)

12:00m

**IMD3 ■ Box-like broadband filters using chirped waveguides**, S.T. Chu, W. Pan, S. Sato, T. Maeda, Y. Kokubun, *Kanagawa Academy of Science & Technology, Japan*; B. Little, *Massachusetts Institute of Technology, USA*; T. Kato, *Yokohama National Univ., Japan*. The design of fabrication-insensitive broadband filters with ideal spectral response by tapering the width of the waveguides is presented. (p. 46)

12:15pm

**IMD4 ■ Integrated DBR laser-EA modulators for WDM applications**, P. Legay, A. Ramdane, D. Delprat, A. Ougazzaden, Y. Sorel, M. Morvan, *France Télécom/CNET, France*. The integration scheme of DBR laser-EA modulators has been optimized in order to achieve a 10 Gb/s transmission on 75 km of dispersive fiber for four 80 GHz spaced channels. (p. 49)

12:30pm

**IMD5 ■ Sampled grating DBR lasers with integrated wavelength monitoring**, Beck Mason, Olga Lavrova, Greg A. Fish, Steve P. DenBaars, Larry A. Coldren, *Univ. California Santa Barbara, USA*. We report on a sampled grating DBR laser with an integrated wavelength monitor. The monitor consists of a two mode interference waveguide with a Y-branch that acts as a wavelength dependent splitter with two output detectors. (p. 52)

12:45pm–2:00pm

Lunch Break

---

## Salon B

---

2:00pm–3:30pm

### IME ■ Vectorial Simulations

Wei Ping Huang, *University of Waterloo, Canada, Presider*

2:00pm

**IME1 ■ Techniques of improving the imaginary-distance full-vectorial BPM based on Yee's Mesh**, Junji Yamauchi, Naofumi Morohashi, Hisamatsu Nakano, *Hosei Univ., Japan*. High-order formulas are applied to the analysis of a graded-index waveguide. A rib waveguide is analyzed with use of the interface condition based on Ampere's law. (p. 56)

2:15pm

**IME2 ■ Efficient multistep methods using a nonuniform grid**, Jun Shibayama, Kenji Matsubara, Minoru Sekiguchi, Junji Yamauchi, Hisamatsu Nakano, *Hosei Univ., Japan*. The Douglas scheme generalized for a nonuniform grid is applied to the multistep method for wide-angle beam propagation analysis. (p. 59)

2:30pm

**IME3 ■ Finite-elements semivectorial beam propagation method for nonlinear integrated optical devices**, A. Cucinotta, S. Selleri, L. Vincetti, *Univ. Parma, Italy*. A semivectorial beam propagation method based on finite elements for nonlinear waveguides is presented. Because of its semivectorial nature, the approach accounts for polarization effects and highlights the limits of scalar formulations. (p. 62)

2:45pm

**IME4 ■ Vectorial beam propagation method based on mixed elements**, D. Schulz, C. Glingener, E. Voges, *Univ. Dortmund, Germany*; M. Bludszweit, *Technische Univ. Hamburg-Harburg, Germany*. An efficient mixed element beam propagation method for 3D simulations is presented for integrated optic devices allowing energy conservation when assuming metallic walls and lossless media. (p. 65)

3:00pm

**IME5 ■ Field singularities in full-vectorial optical waveguide analysis**, Chenglin Xu, Wei-Ping Huang, *Univ. Waterloo, Canada*; Kiyoyuki Yokoyama, Wayne W. Lui, *NTT Opto-electronics Laboratories, Japan*. Field singularities at corners of rectangular dielectric waveguides are notoriously difficult to model, let alone characterize accurately. An algorithm is proposed to circumvent such difficulties. (p. 68)

3:15pm

**IME6 ■ Design and analysis of optical polarizers incorporating MQW waveguides**, M. Rajarajan, B.M.A. Rahman, K.T.V. Grattan, *City Univ., U.K.* A novel approach has been demonstrated in the design of an optical polarizer that uses nonidentical coupled optical waveguides with 2-D confinement. (p. 71)

---

## Salon A

---

3:30pm–4:00pm

Coffee Break and Exhibits

---

## Salon C

---

2:00pm–3:30pm

### IMF ■ Novel Fabrication Techniques

Claude Rolland, *Bell Northern Research Ltd., Canada, Presider*

2:00pm (Invited)

**IMF1 ■ Fused optoelectronic devices**, John Bowers, Near Margalit, Alexis Black, Aaron Hawkins, Bin Liu, Ali Shakouri, Patrick Abraham, Evelyn Hu, *Univ. California Santa Barbara, USA*. The integration of optical components with electrical components is critically important and the integration problems can be solved with wafer fusion. The wafer fusion technique also allows the demonstration of new devices with improved performance. Three dimensional integration is possible with multiple bonded substrates which can ease the problems of multilayer optical interconnects. (p. 76)

2:30pm

**IMF2 ■ Substrate-removed optical waveguides in GaAs/AlGaAs epitaxial layers embedded in benzocyclobutene**, Steven R. Sakamoto, Cem Ozturk, Young Tae Byun, Jack Ko, Nadir Dagli, *Univ. California Santa Barbara, USA*. Optical waveguides fabricated in GaAs/AlGaAs epitaxial layers are removed from GaAs substrates and bonded to transfer substrates by use of benzocyclobutene with no degradation in optical loss. (p. 79)

2:45pm

**IMF3 ■ High performance photoelastic semiconductor laser and electroabsorption waveguide modulator**, W.X. Chen, Q.Z. Liu, L.S. Yu, N.Y. Li, Q.J. Xing, J.T. Zhu, G.L. Li, P.K.L. Yu, S.S. Lau, C.W. Tu, *Univ. California San Diego, USA*; H.P. Zappe, *Paul Scherrer Institute, Switzerland*. High-performance planar InGaAsP/InP electroabsorption waveguide modulator and separate-confinement single-quantum-well GaAs/AlGaAs lasers are fabricated with use of thin-film WNi photoelastic stressors for waveguiding and ion-implantation for isolation. (p. 82)

3:00pm (Invited)

**IMF4 ■ Pick-and-place multi-wafer bonding of photonic devices on Si**, D. Crouse, Z.H. Zhu, Yu-Hwa Lo, *Cornell Univ., USA*; H. Hou, *Sandia National Labs, USA*. The technology of single wafer bonding and pick-and-place multi-wafer bonding will be discussed. The former has been used to make various optoelectronic devices and create new templates for heteroepitaxial growth. The latter was designed for optoelectronic integration, particularly large scale, Si-based OEICs. (p. 85)

---

## Salon A

---

3:30pm–4:00pm

Coffee Break and Exhibits

---

## Saanich

---

2:00pm–3:30pm

**IMG ■ WDM II/Filters**

Janet Lehr Jackel, *Bellcore, USA, Presider*

2:00pm

**IMG1 ■ Wavelength filters based on low-loss polymer waveguides and high-index polymer gratings**, Min-Cheol Oh, Myung-Hyun Lee, Joo-Heon Ahn, Hyung-Jong Lee, Seon-Gyu Han, *Electronics and Telecommunications Research Institute, Korea*. Based on low-loss polymer waveguides and high-refractive-index polymer gratings, Bragg reflection wavelength filters are demonstrated with 30 dB reflectivity, 0.6 nm bandwidth, and 3.7 dB insertion loss. (p. 90)

2:15pm

**IMG2 ■ Temperature-independent optical filter at 1.55  $\mu\text{m}$  wavelength using a silica-based athermal waveguide**, Yasuo Kokubun, Shigeru Yoneda, Shinnosuke Matsuura, *Yokohama National Univ., Japan*. We realized a temperature-independent optical filter at 1.55  $\mu\text{m}$  wavelength using a silica-based athermal waveguide in which optical path length is independent of temperature. (p. 93)

2:30pm (Invited)

**IMG3 ■ Tunable add/drop filters using  $\text{LiNbO}_3$** , Minoru Seino, *Fujitsu Laboratories Ltd., Japan*. A thin-film loaded-type SAW guide is used in the AOTF. It realizes a low x-talk, narrow FWHM and low loss characteristics enough for the ADM. (p. 96)

3:00pm

**IMG4 ■ Planar waveguide grating optical spectrum analyzer**, C.K. Madsen, J. Wagener, T.A. Strasser, M.A. Milbrodt, E.J. Laskowski, J. DeMarco, *Bell Labs, Lucent Technologies, USA*. An optical spectrum analyzer is demonstrated with a FWHM of 0.15 nm and bandwidth of 7.8 nm by use of a UV-induced grating in a planar waveguide. (p. 99)

3:15pm

**IMG5 ■ Planar waveguide add/drop filter employing a mode-converting grating in an adiabatic coupler**, C.K. Madsen, T.A. Strasser, M.A. Milbrodt, C.H. Henry, A.J. Bruce, J. DeMarco, *Bell Labs, Lucent Technologies, USA*. A new planar waveguide add/drop filter is demonstrated with a drop loss of 0.5 dB, FWHM = 0.35 nm, and transmission isolation of 15 dB. (p. 102)

---

## Salon A

---

3:30pm–4:00pm

Coffee Break and Exhibits

---

## Salon A/Lobby

---

4:00pm–6:00pm

**IMH ■ Poster Session**

**IMH1 ■ Analysis and design of rib waveguide**

**spotsizes transformers**, P. Sewell, T.M. Benson, P.C. Kendall, *Univ. Nottingham, U.K.* An extended spectral index method efficiently analyzes the guided modes of waveguide spotsizes transformers where a tapered small rib waveguide couples vertically into a large spot rib. (p. 106)

**IMH2 ■ Nonlinear Helmholtz equation resolution**

**through the finite element method**, A. Cucinotta, S. Selleri, L. Vincetti, *Univ. Parma, Italy*. A fast and accurate full-FEM-based propagation method that directly implements the nonlinear Helmholtz equation is presented. The analysis of spatial soliton evolution confirms phenomena not described in the frame of the slowly varying envelope approximation. (p. 109)

**IMH3 ■ Mechanism of ultrafast pulse generation in a symmetric three-section DFB semiconductor laser,** Byoung-Sung Kim, Youngchul Chung, *Kwangwoon Univ., Korea*; Kyoung-Hyun Park, Sun-Ho Kim, *Korea Institute of Science and Technology*. The modified large-signal time-domain model is used to clarify the mechanism of ultrafast pulse generation resulting from the mode beating in a symmetric three-section DFB semiconductor laser. (p. 112)

**IMH4 ■ Accurate analysis of bending losses in rectangular optical waveguides,** M.G. Mirkov, B.G. Bagley, R.T. Deck, *Univ. Toledo, USA*. An accurate method for the calculation of bending losses in optical waveguides is presented, and the results are compared with the results of other methods. (p. 115)

**IMH5 ■ Interdiffused AlGaAs/GaAsP quantum well lasers,** K.S. Chan, *City Univ. Hong Kong*; Michael C.Y. Chan, *Univ. Hong Kong*. The optical gain of various interdiffused  $\text{GaAs}_{1-\gamma}\text{Al}_{0.33}\text{Ga}_{0.67}\text{As}$  quantum well structures are calculated numerically and found to depend on the interdiffusion processes. (p. 118)

**IMH6 ■ A numerical study of spatially controlled impurity-free vacancy-enhanced quantum well intermixing,** Y.H. Wong, K.S. Chan, E.Y.B. Pun, A.H.P. Ho, P.S. Chung, *City Univ. Hong Kong*; J.H. Marsh, *Univ. Glasgow, U.K.* The spatial control of impurity-free vacancy-enhanced quantum well intermixing using  $\text{SiO}_2$  capping layer with  $\text{SrF}_2$  as the mask is studied numerically. (p. 121)

**IMH7 ■ New design procedure for large-input/output-number multimode interference couplers and application to WDM routers,** J.Z. Huang, R. Scarmozzino, R.M. Osgood, Jr., *Columbia Univ., USA*. A new design procedure for  $N \times N$  MMI couplers with large  $N$  is accomplished through phase-error optimization; a low-crosstalk  $8 \times 8$  MMI router design is demonstrated. (p. 124)

**IMH8 ■ Design optimization of a notched Y-branch  $\text{Ti:LiNbO}_3$  Mach-Zehnder interferometric intensity modulator,** G. Peng, G.L. Yip, F.Y. Gan, P. Noutios, *McGill Univ., Canada*. The design optimization of a notched Y-branch  $\text{Ti:LiNbO}_3$  Mach-Zehnder interferometric intensity modulator has been performed, yielding an extinction ratio above 20 dB at a bandwidth of 80 GHz. (p. 127)

**IMH9 ■ Master-slave configuration for VCSEL synchronization,** P.S. Spencer, K.A. Shore, *Univ. Wales, U.K.*; C.R. Mirasso, *Univ. Illes Balears, Spain*; P. Colet, *CSIC-UIB, Spain*. It is demonstrated numerically that synchronization of optically coupled chaotic VCSELs can be effected in a robust manner, thus enabling application in optical data encryption. (p. 130)

**IMH10 ■ An integrated CAD package for rapid design and analysis of optoelectronic components,** Peter S. Weitzman, *Concepts ETI, Inc., USA*. Work has commenced on the development of a comprehensive CAD package for optoelectronic integrated circuits. The software will contain optical solvers, electrical models, and layout. (p. 133)

**IMH11 ■ Vectorial electromagnetic model for the accurate analysis of finite length surface-relief structures of high complexity,** Kim Dridi, Anders Bjarklev, *Technical Univ. Denmark*. The finite difference time domain method is applied for accurate analysis of the optical behavior of finite, periodic surface-relief gratings in planar dielectric waveguides. (p. 136)

**IMH12 ■ MoL-eigenmode analysis with precise resolution by enhanced generalized line algorithm,** Reinhold Pregla, *Fern Univ., Germany*. A new eigenmode algorithm with precise results based on the MoL is proposed and substantiated. The algorithm uses discretization lines in different and mutually perpendicular directions. (p. 139)

**IMH13 ■ A hybrid analysis method for Er-doped planar devices,** A. Shooshtari, *Ecole Polytechnique de Montreal, Canada*; S. Safavi-Naeini, *Univ. Waterloo, Canada*. A new analysis method based on a combination of the beam propagation method and the rate equations for active planar devices is presented. (p. 142)

**IMH14 ■ Influence of laser linewidth on optical fiber transmission: modeling and measurement,** C.M. Weinert, C. Caspar, H.-M. Foisel, B. Strebel, *Heinrich-Hertz-Institut, Germany*. Enlarged laser linewidths exhibit increasing penalties for transmission over standard fibers. The linewidth is modeled and the simulation of signal degradation is compared with experiment. (p. 145)

**IMH15 ■ Paper withdrawn.**

**IMH16 ■ Analysis and design of high power DFB lasers with reduced longitudinal spatial hole burning,** Jing-Yi Wang, Michael Cada, *Dalhousie Univ. Polytechnic, Canada*; Toshihiko Makino, *Nortel Technology Inc., Canada*. A set of nonlinear coupled-power equations is derived for high-power DFB lasers and is used to design coupling profiles that eliminate spatial hole burning. (p. 149)

**IMH17 ■ Modeling a distributed spatial filter low-noise semiconductor optical amplifier,** R.P. Ratowsky, S. Dijaili, J.S. Kallman, M.D. Feit, J. Walker, W. Goward, M. Lowry, *Lawrence Livermore National Laboratory, USA*. We show, using a beam propagation technique, how periodic spatial filtering can reduce amplified spontaneous emission noise in a semiconductor optical amplifier. (p. 152)

**IMH18 ■ Optimizing a multi-wavelength laser design using an expert-system-based approach**, D. Van Thourhout, T. Van Caenegem, R. Baets, *Univ. Gent, Belgium*. Today's CAD tools are limited when developing complex PICs. Expert-system-based design tools could be an improvement. This is illustrated for a multi-wavelength laser. (p. 155)

**IMH19 ■ Buried waveguides in a 1.5  $\mu\text{m}$  InGaAs/InGaAsP structure fabricated by ion-induced quantum well intermixing**, J.E. Haysom, J.H. He, P.J. Poole, Emil S. Koteles, A. Delage, Y. Feng, S. Charbonneau, *National Research Council Canada*. Using selective area implantation-induced quantum well intermixing, we have fabricated buried waveguides in a 1.52  $\mu\text{m}$  InGaAs/InGaAsP laser structure. Near-field mode profiles demonstrate guiding over a wavelength range of 1.50  $\mu\text{m}$  to 1.59  $\mu\text{m}$ . (p. 158)

**IMH20 ■ Four-channel wavelength demultiplexing multiple quantum well photodetectors for 850 nm optical local area networks**, K.W. Goossen, R. Leibenguth, *Lucent Technologies, Bell Labs., USA*. We demonstrate an in-line stacked n-i(MQW)-p-i(MQW)-n-i(MQW)-p-i(MQW)-n photodiode that demultiplexes wavelengths at 810, 825, 840, and 855 nm, for use in optical local area networks. (p. 161)

**IMH21 ■ All-optical wavelength converter based on coupled semiconductor optical amplifiers**, Byongjin Ma, Yoshiaki Nakano, Kunio Tada, *Univ. Tokyo, Japan*. We propose a novel wavelength converter consisting of an active directional coupler. Operation mechanism and several features are presented through a numerical analysis. (p. 164)

**IMH22 ■ Proposal of spectrum sliced multi-wavelength light sources using integrated high power superluminescent diodes**, F. Koyama, S. Mori, *Tokyo Institute of Technology, Japan*. A spectrum-sliced multi-wavelength light source using a high power tapered superluminescent diode (SLD) is proposed. A tapered SLD exhibits a potential of high power exceeding several hundreds mW. We also discuss a possibility of producing "nearly coherent light" from sliced incoherent light using saturated semiconductor optical amplifiers. (p. 167)

**IMH23 ■ Application of synthetic aperture techniques to arrayed-waveguide grating passband control**, M.C. Parker, F. Farjady, *Fujitsu Telecommunications Europe Ltd. Research, U.K.*; S.D. Walker, *Univ. Essex, U.K.* We describe a novel synthetic aperture technique based on a series of polynomial-profiled electrodes to control arrayed-waveguide grating characteristics, such as passband width and tuning. (p. 170)

---

## Crystal Ballroom, Empress Hotel

---

6:00pm–7:30pm  
Conference Reception

■ Tuesday  
■ March 31, 1998

---

**Salon B**

---

8:30am–10:00am

**ITuA ■ Photonic Nanostructures I**

B.E. Little, *Massachusetts Institute of Technology, USA* and  
R.W. Ziolkowski, *University of Arizona, USA, Presiders*

8:30am (Invited)

**ITuA1 ■ Advances in photonic crystals and devices,**

J.D. Joannopoulos, *MIT, USA*. During the last few years a new class of materials has emerged, called photonic crystals, which provide capabilities along new dimensions for the control and manipulation of light. A photonic crystal affects the properties of light in much the same way that a semiconductor affects the properties of electrons. Consequently, photons in photonic crystals can have band-gaps, localized defect-states, surface-states, etc. This new ability to mold and guide light leads naturally to many novel applications of these materials as microphotonic devices and device components. An introductory survey including recent exciting developments in the field of photonic crystals is presented. (p. 174)

9:00am

**ITuA2 ■ FDTD modeling of photonic nanometer-sized power splitters and switches,** Richard W. Ziolkowski, *Univ. Arizona, USA*. Nanometer PBG waveguide structures that act as power splitters (Y-junctions) and switches (Y-junctions with a defect) have been modeled with a full-wave, vector Maxwell equation FDTD simulator. (p. 175)

9:15am (Invited)

**ITuA3 ■ Fabrication processes for 3D periodic nanostructures and photonic crystals,** Shojiro Kawakami, *Tohoku Univ., Japan*. We review process technologies for 3D periodic nanostructures and photonic crystals. We then propose layer-by-layer deposition by bias sputtering, and demonstrate its usefulness. The mechanism of stationary pattern formation is elucidated. (p. 178)

9:45am

**ITuA4 ■ Membrane microresonator lasers with 2-D photonic bandgap crystal mirrors for compact in-plane optics,** B. D'Urso, O. Painter, A. Yariv, A. Scherer, *Caltech, USA*. We have microfabricated 2-D photonic bandgap structures in a thin slab of dielectric material to define reflectors and high-Q microresonators. (p. 181)

---

**Salon A**

---

10:00am–10:30am

Coffee Break & Exhibits

---

**Salon C**

---

8:30am–10:00am

**ITuB ■ Lasers I**

Jean Francois Vinchant, *Alcatel Optronics, France, Presider*

8:30am

**ITuB1 ■ Single transverse mode active MMI**

**InGaAsP/InP laser diode,** Kiichi Hamamoto, Emilio Gini, Christoph Holtmann, Hans Melchior, *Swiss Federal Institute of Technology, Switzerland*. A novel laser diode structure incorporating active multi-mode interferometers realized in InGaAsP/InP achieves up to 90% higher single lobe and fiber coupled outputs at 1.3  $\mu\text{m}$ . (p. 186)

8:45am

**ITuB2 ■ Integrated amplifier/multi-mode interference coupler laser for high optical power in a single-mode waveguide,** F. Camacho, C.J. Hamilton, A.C. Bryce, J.H. Marsh, *Univ. Glasgow, U.K.* By quantum-well intermixing, four amplifiers have been integrated with a passive MMI coupler and output waveguide. The device has a threshold current of 120 mA, and generates over 180 mW of optical power. (p. 189)

9:00am

**ITuB3 ■ Efficient InP-based integrable spot-size converter,** J. Stulemeijer, M.K. Smit, F.H. Groen, *Delft Univ. Technology, The Netherlands*; A.F. Bakker, *BBV Software BV, The Netherlands*; I. Moerman, *Univ. Gent-IMEC, Belgium*. An InP-based spot-size converter has been realized in a relatively simple technology, showing less than 3 dB coupling loss to a cleaved fiber for TE polarized light. (p. 192)

9:15am

**ITuB4 ■ High power InGaAsP laser diodes with circular beam profile,** Heonsu Jeon, Atul Mathur, Mehrdad Ziari, *SDL Inc., USA*. We report high power 1.55  $\mu\text{m}$  InGaAsP laser diodes integrated with vertically tapered mode transformer providing the beam divergence angles of  $12^\circ \times 14^\circ$  at FWHM with the maximum output power over 130 mW. (p. 195)

9:30am (Invited)

**ITuB5 ■ Overview of integrated semiconductor multiwavelength lasers,** C.R. Doerr, *Bell Labs, Lucent Technologies, USA*. We discuss and compare two types of semiconductor transmitters consisting of multiple lasers and an integrated combiner/multiplexer: those with the lasers combined extra-cavity and those with the lasers combined intra-cavity. (p. 198)

10:00am

**ITuB6 ■ Monolithic integration of a quantum well laser and an optical amplifier using an asymmetric twin-waveguide structure**, P.V. Studenkov, M.R. Gokhale, J.C. Dries, S.R. Forrest, *Princeton Univ., USA*. A novel, asymmetric twin-waveguide structure is used for monolithic integration of a 1.55  $\mu\text{m}$  wavelength InGaAsP/InP multiple quantum well laser and a traveling-wave optical amplifiers. (p. 201)

---

## Salon A

---

10:15am–10:30am

Coffee Break & Exhibits

---

## Saanich

---

8:30am–10:00am

### ITuC ■ Photonic Packaging I

Nan Marie Jokerst, *Georgia Institute of Technology, USA, Presider*

8:30am (Invited)

**ITuC1 ■ Manufacturing technology of VCSEL modules**, Jun-Young Kim, *Samsung Electron-Mechanics Co. Ltd., Korea*. No abstract available. (p. 206)

9:00am (Invited)

**ITuC2 ■ Overview of MEMS technology for packaging optoelectronic components**, Ming C. Wu, *Univ. California Los Angeles, USA*. The emerging MEMS technology has opened up many new possibilities for packaging optoelectronic components. We will review the current state of the art of the MEMS technology, and describe examples of optoelectronic packaging. (p. 207)

9:30am

**ITuC3 ■ Hybrid  $4 \times 4$  optical matrix switch module on silica-based planar lightwave circuit by self-align multiple chip bonding technique**, J. Sasaki, H. Hatakeyama, T. Tamanuki, M. Yamaguchi, N. Kitamura, T. Shimoda, M. Kitamura, T. Kato, M. Itoh, S. Kitamura, *NEC Corp., Japan*. We developed a  $4 \times 4$  gate matrix switch by hybridly integrating spot size converter integrated semiconductor optical amplifier gate arrays and optical fibers on a Si platform with silica waveguides, employing the newly developed self-align multiple chip assembly technique. (p. 210)

9:45am

**ITuC4 ■ New promising technological approach for optoelectronic hybridization**, P. Mottier, Cl. Massit, G. Parat, G. Grand, *CEA-LETI, France*. A cost-effective technique for achievement of hybrid optoelectronics units is proposed. Compared with the previous ones, it offers relaxed alignment tolerances and high versatility. (p. 213)

---

## Salon A

---

10:00am–10:30am

Coffee Break & Exhibits

---

## Salon B

---

10:30am–12:00m

### ITuD ■ Photonic Nanostructures II

B.E. Little, *Massachusetts Institute of Technology, USA* and R.W. Ziolkowski, *University of Arizona, USA, Presiders*

10:30am (Invited)

**ITuD1 ■ Meso-optoelectronic devices and applications**, A.F.J. Levi, *Univ. Southern California, USA*. This talk presents a case for developing meso-optic technology based on its potential to enhance the capabilities of otherwise all-electronic systems. (p. 218)

11:00am

### ITuD2 ■ Photonic bandgap membrane

**microresonator**, O. Painter, R. Lee, A. Yariv, A. Scherer, *California Institute of Technology, USA*; J. O'Brien, *Univ. Southern California, USA*. We have designed and fabricated an optical microcavity formed from a defect in a two-dimensionally patterned, half-wavelength-thick, InGaAs/InGaAsP multi-quantum well membrane. (p. 221)

11:15am

**ITuD3 ■ Dynamic analysis of lasing microcavities**, Ira B. Schwartz, Ioana Triandaf, *Naval Research Laboratory, USA*. Dynamics and active control of light dumping of lasing microcavities are analyzed theoretically. Mean escape times for light dumping are controlled via cavity boundary perturbations. (p. 224)

11:30am

**ITuD4 ■ FDTD analysis and comparison of circular and elongated ring designs for waveguide-coupled microcavity ring resonators**, S.C. Hagness, D. Rafizadeh, S.T. Ho, A. Taflov, *Northwestern Univ., USA*. Using FDTD models of integrated microcavity ring resonators, we investigate geometries such as the racetrack resonator that allow wider coupling gaps between the ring and adjacent waveguides, easing fabrication requirements. (p. 227)

11:45am

### ITuD5 ■ Noise characteristics of two-polarization microcavity semiconductor lasers

G.P. Bava, P. Debernardi, *Politecnico di Torino, Italy*. Noise properties of semiconductor microcavity post lasers are studied for the realistic case of two quasi-degenerate modes. The model is based on quantum mechanical equations and Langevin noise forces. (p. 230)

12:00m–1:30pm

Lunch Break

---

## Salon C

---

10:30am–12:00m

### ITuE ■ Modulators/Switches

S. Chandrasekhar, *Lucent Technologies, USA, Presider*

10:30am (Invited)

**ITuE1 ■ Optical processing with electroabsorption modulators**, F. Devaux, *Alcatel Alsthom Recherche, France*; A. Carenco, *France Telecom*. Specific characteristics of electroabsorption (EA) modulators allow unique processing functions. We consider multiple EA modulators in series for coding, pulse generation and demultiplexing, and in parallel for single-side-band (SSB) conversion, duobinary coding and filtering. (p. 234)

11:00am

**ITuE2 ■ Low-loss and efficient InAsP/GaN MQW electroabsorption waveguide modulators for analog fiber-optic links**, K.K. Loi, X.B. Mei, J.H. Hodiak, C.W. Tu, W.S.C. Chang, *Univ. California San Diego, USA*. The microwave performance of electroabsorption modulators was characterized and a 5 dB fiber-to-fiber insertion loss, 23 GHz electrical bandwidth, and -26 dB RF link gain have been achieved. (p. 237)

11:15am

**ITuE3 ■ A compact integrated phasor-based optical crossconnect on InP**, C.G.P. Herben, C.G.M. Vreeburg, D.H.P. Maat, X.J.M. Leijtens, Y.S. Oei, F.H. Groen, M.K. Smit, *Delft Univ. Technology, The Netherlands*; J.J.G.M. van der Tol, *KPN-Research, The Netherlands*; P. Demeester, *Univ. Gent, Belgium*. We report the first InP-based integrated optical crossconnect. The device can crossconnect signals at four wavelengths independently from two input fibers to two output fibers. (p. 240)

11:30am

**ITuE4 ■ InGaAsP/InP scaleable, photonic crossconnects using optically amplified suppressed modal interference switch arrays**, Gregory A. Fish, Larry A. Coldren, Steven P. DenBaars, *Univ. California Santa Barbara, USA*. A novel, compact  $1 \times 2$  optical switch incorporating two unique switches with an integrated curved amplifier is demonstrated as a basic building block for scaleable, lossless photonic crossconnects. (p. 243)

11:45am

**ITuE5 ■ Polarization-independent InP-based switch with relaxed fabrication tolerances**, D.H.P. Maat, C.G.P. Herben, M.K. Smit, F.H. Groen, H. van Brug, H.J. Frankena, *Delft Univ. Technology, The Netherlands*; I. Moerman, *Univ. Gent-IMEC, Belgium*. A polarization-independent MZI switch is presented in which the fabrication tolerances are relaxed by use of double, orthogonal phase-shifting sections. (p. 246)

12:00m–1:30pm

Lunch Break

---

## Saanich

---

10:30am–12:00m

### ITuF ■ Photonic Packaging II

Robert J. Deri, *Lawrence Livermore National Laboratories, USA, Presider*

10:30am (Invited)

**ITuF1 ■ Molded plastic optics in fiber optic transceivers**, Ching-Long Jiang, *AMP Inc., USA*. Molded plastic optics have been widely used in fiber optic transceivers. In this talk, salient features of the molded plastic optics will be presented. (p. 250)

11:00am

**ITuF2 ■ Flip-chip GaN LED with highly reflective Ag p-contact**, You Kondoh, Satoshi Watanabe, Yawara Kaneko, Shigeru Nakagawa, Norihide Yamada, *Hewlett-Packard Laboratories, Japan*. A new flip-chip technique that uses a highly reflective Ag p-contact was developed for blue GaN LEDs, which is twice as bright as top-emitting GaN LEDs. (p. 253)

11:15am

**ITuF3 ■ Nonperipheral epilayer cleaving of GaAs for hybrid device applications**, J. Fujita, M. Levy, R.M. Osgood, Jr., *Columbia Univ., USA*. A new technique for nonperipheral epilayer cleaving is described, demonstrated, and optically characterized. An on-chip polarizer with >20 dB extinction ratio has been demonstrated. (p. 256)

11:30am

**ITuF4 ■ Alignment-tolerant smart pixel bi-directional optoelectronic links using co-located emitters and detectors**, Jeffrey Cross, Mikkel A. Thomas, Nan Marie Jokerst, *Georgia Institute of Technology, USA*. We report optimization of packaging alignment tolerance for fabricating low-cost free-space bi-directional optoelectronic links with co-located emitters and detectors. (p. 260)

11:45am

**ITuF5 ■ Single-mode stability of Fabry-Pérot taper-lasers with external fiber Bragg gratings**, E. Rönneberg, G. Vollrath, B. Hübner, Ch. Gréus, H. Burkhard, *Deutsche Telekom AG, Germany*. We have theoretically and experimentally investigated the effect of variation of the resonator phase on the single-mode stability of Fabry-Pérot taper-lasers with external fiber Bragg gratings. (p. 263)

12:00m–1:30pm

Lunch Break

---

## Salon B

---

1:30pm–3:00pm

### ITuG ■ Quantum Wells I: Carrier Transport in Quantum Well Devices

Shun-Lien Chuang, *University of Illinois Urbana-Champaign, USA, Presider*

1:30pm (Invited)

**ITuG1 ■ Simulation of nonlinear gain and the modulation of quantum well laser diodes**, Karl Hess, Matt Grupen, *Univ. Illinois-Urbana, USA*. We present a simulator (MINILASE II) for quantum well laser diodes that includes the effects of capture and hot electron as well as hot phonon effects. Comparison with experimental results shows the predictive power of the simulator. (p. 268)

2:00pm

**ITuG2 ■ Carrier transport effects in the frequency modulation response of quantum well lasers**, Luis Pesquera, N. Mustafa, *Instituto de Fisica de Cantabria, Spain*; I. Esquivias, *Univ. Politecnica de Madrid, Spain*. We show that carrier transport has a significant effect in the FM response of QW lasers as a result of the contribution of the unconfined carriers. (p. 271)

2:15pm

**ITuG3 ■ Optical gain enhancement in InP-based quantum-well lasers with *n*-doped separate confinement heterostructure layers**, Shunji Seki, Kiyoyuki Yokoyama, *NTT Opto-electronics Laboratories, Japan*. We demonstrate that *n*-type doping in separate confinement heterostructure layers exerts a significant effect on optical gain over a wide range of temperature in InP-based quantum-well lasers. (p. 274)

2:30pm (Invited)

**ITuG4 ■ Direct measurement of capture and escape rates in quantum well active layers**, Kerry Vahala, Roberto Paiella, Guido Hunziker, *California Institute of Technology, USA*; Uzi Koren, *Lucent Technologies, USA*. Results from two measurement techniques that provide frequency domain response functions (1 GHz to several 100 GHz) for carrier capture and interwell equilibration are presented. (p. 277)

---

## Salon A

---

3:00pm–3:30pm

Coffee Break and Exhibits

---

## Salon C

---

1:30pm–3:00pm

### ITuH ■ Silicon Based Optoelectronic Technology

Richard A. Soref, *Rome Laboratory, AFRL/SNHC, USA, Presider*

1:30pm

**ITuH1 ■ Fabrication and characterization of a 1-to-48 fanout H-tree structure for clock signal distribution system**, Linghui Wu, Bipin Bihari, Jianhua Gan, Ray T. Chen, *Univ. Texas-Austin, USA*; Suning Tang, *Radiant Research Inc., USA*; Randy Wickman, *Cray Research Inc., USA*. Fabrication and characterization of a low-loss 1-to-48 fanout H-tree structure for high-performance optical clock-signal distribution systems using cascaded 3-dB curved 1-to-2 splitters are presented. (p. 282)

1:45pm

**ITuH2 ■ Waveguide-fed SiGe avalanche pin photodetector grown on SOI substrate with 0.2 A/W external responsivity at 1.3  $\mu$ m**, T. Yoshimoto, S. Thomas, K.L. Wang, B. Jalali, *Univ. California Los Angeles, USA*. We demonstrate a SiGe avalanche photodetector grown on a silicon-on-insulator (SOI) passive waveguide. The thick SOI waveguide couples the light from an optical fiber into the SiGe detector with strain-limited thin absorption region. The detector exhibits low dark current, sharp breakdown and an external responsivity of 0.2 A/W at 1.3  $\mu$ m. (p. 285)

2:00pm (Invited)

**ITuH3 ■ Gbit/s Integrated Si/InGaAs telecommunication photodetectors**, Barry Levine, *Bell Labs, Lucent Technologies, USA*. High-performance 1550-nm PIN and avalanche photodiodes have been fabricated by direct bonding of III-V and Si wafers. These detectors show 100% internal quantum efficiency, RC-limited 21 GHz response and less than 100 pA dark current at 4V bias. (p. 289)

2:30pm

**ITuH4 ■ Silicon-on-insulator waveguide Bragg gratings**, Jolyon Tidmarsh, John Drake, *Bookham Technology Ltd., U.K.* Successful narrow line-width operation of silicon waveguide Bragg gratings to select wavelengths in the 1550 nm range illustrates potential for successful registration of ITUT channels. (p. 290)

2:45pm

**ITuH5 ■ Amorphous silicon light modulators for I.R. fiber optic digital communications**, G. Cocorullo, F.G. Della Corte, I. Rendina, *Consiglio Nazionale delle Ricerche, Italy*; R. De Rosa, A. Rubino, E. Terzini, *Ente per le Nuove Tecnologie, Italy*. A light modulator based on a low loss amorphous silicon rib-like waveguide is presented. The prototype shows a switching frequency of 600 kHz. (p. 293)

---

## Salon A

---

3:00pm–3:30pm

### Coffee Break and Exhibits

---

## Saanich

---

1:30pm–3:00pm

### ITul ■ Electrooptic Materials and Devices

William Minford, *Lucent Technologies/Bell Labs, USA, Presider*

1:30pm

**ITul1 ■ Influence of phase state of  $\text{Li}_{1-x}\text{H}_x\text{NbO}_3$  waveguiding layer on rate of copper exchange and photorefractivity**, S.M. Kostitskii, *Kemerovo State Univ., Russia*; Y.N. Korkishko, V.A. Fedorov, *Moscow Institute of Electronics Technology, Russia*. The copper exchange of waveguides, containing the different  $\text{Li}_{1-x}\text{H}_x\text{NbO}_3$  phases, is investigated. The significant increase of holographic sensitivity, depending on phase state, is observed because of the copper exchange. (p. 298)

1:45pm

**ITul2 ■ Evolution of crystal phases and refractive index profiles in X-cut annealed proton-exchanged  $\text{LiTaO}_3$** , David B. Maring, Robert F. Tavlykaev, Ramu V. Ramaswamy, *Univ. Florida, USA*; Yuri N. Korkishko, *Moscow Institute of Electronic Technology, Russia*; John M. Zavada, *U.S. Army Research Office, USA*. A complete phase diagram for annealed proton exchanged  $\text{LiTaO}_3$  is presented, for the first time. The evolution of index profiles with annealing, as well as temporal stability, are characterized. (p. 301)

2:00pm

**ITul3 ■ Integrated optical  $\text{Ti:Er:LiNbO}_3$  DBR laser with fixed photorefractive grating**, Hubertus Suche, Ch. Becker, A. Greiner, Th. Oesselke, A. Pape, W. Sohler, *Univ.-GH Paderborn, Germany*. For the first time, we believe, an integrated optical DBR laser with fixed photorefractive grating in  $\text{LiNbO}_3$  has been realized. Sample preparation, grating fabrication, and laser characteristics for emission at  $\lambda = 1531.7$  nm are reported. (p. 304)

2:15pm

**ITul4 ■ Drive voltage reduction in Mach-Zehnder electrooptic modulators using systems approach**, Nadir Dagli, *Univ. California Santa Barbara, USA*. A system behaving just like the Mach-Zehnder electrooptic modulators it contains but with significantly reduced drive voltage and identical frequency response was proposed and analyzed. (p. 307)

2:30pm

**ITul5 ■ 10-GHz modelocked  $\text{Ti:Er:LiNbO}_3$  waveguide laser**, R. Wessel, A. Greiner, W. Qiu, H. Suche, W. Sohler, *Univ.-GH Paderborn, Germany*. Modelocked laser operation with a stabilized, packaged, and diode-pumped  $\text{Ti:Er:LiNbO}_3$  waveguide laser has been demonstrated at 1561 nm (TE) and 1575 nm (TM) wavelength with 14% slope efficiency. Pulse widths of <10 ps at 10-GHz pulse repetition rate have been measured. (p. 310)

2:45pm

**ITul6 ■ Fabrication of new abrupt waveguide bends in lithium niobate**, Tzyy-Jiann Wang, Pei-Kuen Wei, Way-Seen Wang, *National Taiwan Univ.* A new abrupt waveguide bend in lithium niobate with proton-exchanged micro-prism is fabricated for the first time, we believe, and a great improvement of bend loss is obtained. (p. 313)

---

## Salon A

---

3:00pm–3:30pm

### Coffee Break and Exhibits

---

## Salon B

---

3:30pm–5:00pm

### ITuJ ■ Quantum Wells II: Heterojunction Engineering, Optical Gain and Electroabsorption

Joseph P. Donnelly, *MIT Lincoln Laboratory, USA, Presider*

3:30pm

**ITuJ1 ■ InGaAs/InAlAs asymmetric triple coupled quantum well for blue-chirp electroabsorption optical modulators**, Masaki Kato, Kunio Tada, Yoshiaki Nakano, *Univ. Tokyo, Japan*. We present a lattice-matched ternary InGaAs/InAlAs asymmetric triple coupled quantum well with which blue-chirp electroabsorption optical modulators with low insertion loss are obtainable. (p. 318)

3:45pm

**ITuJ2 ■ MQW waveguide electroabsorption modulators on InGaAsP with absorption edge merging**, A. Ahland, D. Schulz, E. Voges, *Univ. Dortmund, Germany*. An optimized InGaAsP based MQW modulator with low chirp is proposed. The TE absorption is enhanced by field-induced heavy and light hole absorption merging. (p. 321)

4:00pm

**ITuJ3 ■ Design of polarization insensitive semiconductor optical amplifiers at 1300 nm**, Sangin Kim, WoonJo Cho, Xiaobo Zhang, Mark Hopkinson, Anand Gopinath, *Univ. Minnesota, USA*. Semiconductor optical amplifiers at 1300 nm have been built in AlInGaAs, with tensile strain in the wells to equalize the gain of both polarizations. (p. 324)

4:15pm

**ITuJ4 ■ Many-body optical gain of wurtzite InGaN quantum-well lasers**, Seoung-Hwan Park, Shun-Lien Chuang, *Univ. Illinois-Urbana-Champaign, USA*. Theoretical results on the optical gain of wurtzite InGaN QW lasers taking into account the many-body effects are presented and they agree very well with experimental data. (p. 327)

4:30pm (Invited)

**ITuJ5 ■ Wavefunction engineering: optimizing heterostructure design**, L.R. Ram-Mohan, *WPI, USA*; J.R. Meyer, *Naval Research Laboratory, USA*. Computational tools permit wavefunction engineering of optical properties of semiconductor heterostructures with complex geometries, e.g., the Interband Cascade Laser, and allow optimizing specific physical properties. (p. 330)

---

## Salon C

---

3:30pm–4:45pm

### ITuK ■ Novel Silicon Based Structures

Gregory A. Magel, *Texas Instruments Inc., USA, Presider*

3:30pm (Invited)

**ITuK1 ■ Si-based nanostructures for optoelectronics**, Kang L. Wang, *Univ. California Los Angeles, USA*. The talk will address the current status and opportunities of Si-based nanostructures for optoelectronic applications. Si-based nanostructures can now be prepared by several methods for sizes down to as small as a few nanometers. We will review different growth modes as well as the control of strain for improving the optical properties. Device applications of Si-based quantum dots, with emphasis on light emission will also be discussed. (p. 334)

4:00pm

**ITuK2 ■ Enhancement of propagation characteristics in all-silicon waveguide by ion implantation**, Giuseppe Cocorullo, Francesco G. Della Corte, Mario Iodice, Ivo Rendina, *IRECE, Italy*; Pasqualina M. Sarro, *Tu Delft, The Netherlands*. A 7.0 dB/cm propagation loss improvement and higher confinement are achieved by ion implantation in all-silicon waveguides matched to fiber size. Simulations for optimized structures predict 4.0 dB/cm attenuation. (p. 339)

4:15pm

**ITuK3 ■ Bistable Si-micromachined fiber switches**, M. Hoffmann, P. Kopka, T. Groß, E. Voges, *Univ. Dortmund, Germany*. A bistable single-mode fiber optical  $1 \times 2$  switch based on silicon-micromechanics has been fabricated. The input fibers is switched and fixed in a V-groove clamp by use of thermal actuators. (p. 342)

4:30pm

**ITuK4 ■ Polarization insensitive vycor-based optical waveguide for planar lightwave circuits on silicon substrate fabricated by aerosol flame deposition**, Hyang Gon Jeong, Yong Tae Lee, Young Yun Chun, Jong Ha Moon, Hyung Jong Lee, *Chonnam National University, South Korea*. (p. 345)

---

## Saanich

---

3:30pm–4:30pm

### ITuL ■ Polymer Based Devices

Lewis Aronson, *Hewlett Packard, USA, Presider*

3:30pm

**ITuL1 ■ 3D directional coupler device with nine channels in three layers**, Th. Hennig, Ch. Wächter, W. Karthe, A. Bräuer, *Fraunhofer Institut für Angewandte Optik und Feinmechanik Jena, Germany*; Ch. Véron, *Friedrich-Schiller Univ. Jena, Germany*; H. Wolter, *Fraunhofer Institute for Silicate Research Würzburg, Germany*. Numerical and experimental results of investigating a compact monomode powersplitter with a three-dimensional layout are presented. We show that the chosen configuration is advantageous with respect to production tolerances. (p. 350)

3:45pm (Invited)

**ITuL2 ■ Polymeric optical space switches**, Norbert Keil, Huihai Yao, Crispin Zawadzki, *Heinrich-Hertz-Institut, Germany*. The research and development of polymeric optical space switches, including interferometric and digital type switches, are reviewed. These switches will find wide applications in telecommunications, CATV, LAN and in sensor and measurement techniques. (p. 353)

4:15pm

**ITuL3 ■ Organic light-emitting diodes for integrated optics**, Yutaka Ohmori, Katsumi Yoshino, *Osaka Univ., Japan*. Organic light-emitting diodes integrated with plastic waveguides have been proposed and their optical and electrical characteristics discussed. (p. 356)

■ **Wednesday**  
■ **April 1, 1998**

---

**Salon B**

---

8:30am–10:00am

**IWA ■ Device Simulations I**

K. Alan Shore, *University of Wales, U.K., Presider*

8:30am

**IWA1 ■ Design and simulation of phased-array wavelength router with flat response using Fourier optics concept**, Youngchul Chung, Namhoon Kim, Kwangwoon Univ., Korea. A new design of passband-flattened phased-array wavelength router based on Fourier optics concept is presented. The wavefront shaping is accomplished through proper removal of waveguide sections and the resulting wavelength router shows the desired performances. (p. 360)

8:45am

**IWA2 ■ Improved extinction ratio in ultrashort directional couplers using asymmetric structures**, Boo-Gyoun Kim, Ali Shakouri, Bin Liu, John E. Bowers, Univ. California–Santa Barbara, USA. The asymmetry required to realize ultrashort directional couplers (10–200  $\mu\text{m}$ ) with high extinction ratio (>30 dB) is analyzed. The application to fused vertical couplers are discussed. (p. 363)

9:00am

**IWA3 ■ Amplification of strong picosecond optical pulses in semiconductor optical amplifiers**, J.M. Tang, K.A. Shore, Univ. Wales, U.K. It is shown that both two-photon absorption and ultrafast nonlinear refraction effects play important roles in the amplification of picosecond optical pulses in SOAs. (p. 366)

9:15am

**IWA4 ■ Application of a hybrid implicit-explicit FDTD scheme to nonlinear distributed Bragg resonators**, Vien Van, Sujeet K. Chaudhuri, Univ. Waterloo, Canada. A hybrid finite-difference time-domain scheme employing both explicit and implicit time discretizations is presented, with application to nonlinear distributed Bragg resonators. (p. 369)

9:30am

**IWA5 ■ Efficient analysis of nonsymmetric periodic optical devices**, Stefan F. Helfert, Fern Univ., Germany. The combination of Floquet's theorem with an impedance transfer results in a very efficient and stable algorithm for analysis of nonsymmetric periodic structures. (p. 372)

9:45am

**IWA6 ■ Mode engineering in periodically segmented waveguides**, D. Ortega, J.M. Aldariz, J.S. Aitchison, Univ. Glasgow, U.K. We report on the fabrication and testing of  $\text{Ti:LiNbO}_3$  periodically segmented waveguides and the use of a 3D finite difference beam propagation method to simulate the evolution of the optical field. (p. 375)

---

**Salon A**

---

10:00am–10:30am

**Coffee Break and Exhibits**

---

**Salon C**

---

8:30am–10:00am

**IWB ■ Lasers II: WDM/VCSELS**

Richard M. DeLaRue, *University of Glasgow, U.K., Presider*

8:30am

**IWB1 ■ Vertical-cavity surface-emitting lasers with spatially adjustable DBR reflectivity to enable free-space photonic repeaters**, Aaron E. Bond, P. Daniel Dapkus, Univ. Southern California, USA. By use of selective oxidation of AlAs, high performance top and bottom emitting VCSELS were fabricated from the same epitaxial structure to enable complex free-space optical interconnects. (p. 380)

8:45am

**IWB2 ■ First demonstration of highly TM reflective and highly polarization-selective diffraction gratings for long-wavelength VCSELS**, S. Goeman, S. Boons, B. Dhoedt, K. Vandeputte, K. Caekebeke, R. Baets, P. Van Daele, Univ. Ghent-IMEC, Belgium. We present experimental results on surface relief gratings in GaAs and InP with high reflectivity (>85%) and polarization selectivity to normal incidence. The potential for polarization stabilization with a reduced mirror complexity for long-wavelength VCSELS is discussed. (p. 383)

9:00am

**IWB3 ■ Compact semiconductor lasers with photonic microstructure mirrors and oxide apertures**, Thomas F. Krauss, Axel Scherer, California Institute of Technology, USA; John S. Roberts, Sheffield Univ., U.K.; Richard M. De La Rue, Communications Research Lab, Japan. We demonstrate the combination of selective oxidation and photonic microstructure mirrors, which have already shown reflectivities near 100%, as an enabling technology for ultracompact light-emitting devices. (p. 386)

9:15am

**IWB4 ■ Simultaneous time-window gating and wavelength conversion using an injection-locked Fabry–Periot laser diode**, L.Y. Chan, H.K. Tsang, S.P. Yam, C. Shu, *The Chinese University of Hong Kong*. An all-optical time-window gating device has been implemented using a dual-wavelength injection-locked Fabry–Periot laser diode. Demultiplexing of a 2 GHz pulse train with simultaneous wavelength conversion was successfully demonstrated. (p. 389)

9:30am (Invited)

**IWB5 ■ Semiconductor integrated devices for all-optical wavelength conversion**, S.J.B. Yoo, *Bellcore, USA*. This talk reviews semiconductor wavelength conversion techniques and examines the advantages and disadvantages of each technique in light of all-optical network applications. After a brief introduction of the network issues and a remark on the O/E/O conversion method, we will discuss all-optical wavelength converters, which fall into two categories: optical gating (e.g. cross-gain and cross-phase modulation) and wavemixing (e.g. four-wave mixing and difference-frequency-mixing). (p. 392)

---

## Salon A

---

10:00am–10:30am

Coffee Break and Exhibits

---

## Salon B

---

10:30am–11:45am

**IWC ■ Device Simulations II**

Anand Gopinath, *University of Minnesota, USA, Presider*

10:30am

**IWC1 ■ Modeling of normal and backward integrated electroabsorption modulator and laser**, A. Hsu, W. Fang, S.L. Chuang, *Univ. Illinois–Urbana-Champaign, USA*. A theoretical comparison of the spectrum and longitudinal photon density profiles for a normal EML and an integrated wavelength-tunable laser, or backward EML, is presented. (p. 396)

10:45am

**IWC2 ■ Calculations of highly nondegenerate four-wave mixing characteristics of  $\lambda/4$ -shifted DFB lasers**, Jacques W.D. Chi, Jean Le Bihan, *Ecole Nationale d'Ingénieurs de Brest, France*; K. Alan Shore, *Univ. Wales, U.K.* An analysis of wavelength conversion using highly nondegenerate four wave mixing in  $\lambda/4$ -shifted DFB lasers predicts conversion efficiency  $\geq 20$  dB for probe-pump detuning  $\sim 2$  THz. (p. 399)

11:00am

**IWC3 ■ Numerical investigation of leaky mode coupling in VCSELs**, G. Ronald Hadley, *Sandia National Laboratories, USA*. We investigate various aspects of leaky mode coupling behavior in VCSELs using a 2D finite difference model to simulate two coupled pixels. Phase-locking is shown to occur in a manner consistent with previous simple models. (p. 402)

11:15am

**IWC4 ■ Noise properties and selection of transverse modes in external cavity vertical-cavity surface-emitting lasers**, Angel Valle, L. Pesquera, *Instituto de Física de Cantabria, Spain*; J. Dellunde, *Univ. Barcelona, Spain*; K.A. Shore, *Univ. Wales, U.K.* Low mode partition noise of solitary multi-mode vertical cavity lasers is maintained with optical feedback. Multiple reflections affect mode selection depending on feedback delay. (p. 405)

11:30am

**IWC5 ■ Simulation of scattering and reflection problems via solution of the 2D Helmholtz equation**, Frank Schmidt, *Konrad-Zuse-Zentrum, Germany*. A finite-element method to solve general scalar reflection problems is developed. This includes the construction of a new type of discrete transparent boundary conditions. (p. 408)

12:00m–1:30pm

Lunch Break

---

## Salon C

---

10:30am–12:00m

**IWD ■ Multimode Optical Interconnects**

Lewis B. Aronson, *Hewlett-Packard, USA, Presider*

10:30am (Invited)

**IWD1 ■ VCSEL devices and packaging for fiber optic transceivers**, Michael S. Lebby, *Motorola, USA*. This paper will detail OPTOBUS™ packaging as well as two approaches to discrete VCSEL packaging that are commercially competitive: the flip-chip and the angled TO-can. (p. 412)

11:00am

**IWD2 ■ Optical interface issues in VCSEL-based multimode fiber-optic interconnects**, D. Haritos, K. Giboney, A. Yuen, P. Rosenberg, B. Lemoff, L. Aronson, L. Buckman, J. Straznicky, K. Wu, D. Dolfi, *Hewlett-Packard Laboratories, USA*. A key component of affordable fiberoptic links is the optical interface coupling light between fiber and optoelectronics. Critical issues and tradeoffs will be discussed. (p. 416)

11:15am

**IWD3 ■ Simple fabrication of WDM filters for byte-wide, multimode cable interconnects**, R.J. Deri, S. Gemelos, H.E. Garrett, R.E. Haigh, B.D. Henderer, J.D. Walker, M.E. Lowry, *Lawrence Livermore National Laboratory, USA*. We demonstrate a simple approach to fabricate add/drop WDM filters for byte-wide multimode fiber ribbon cable with low loss (1.0 dB) and small footprint. **(p. 419)**

11:30am

**IWD4 ■ Four-channel multimode wavelength division demultiplexer based on photopolymer volume holographic gratings and substrate-guided waves**, Charles C. Zhou, Sean Sutton, Ray T. Chen, *Univ. Texas–Austin, USA*; Boyd V. Hunter, Paul Dempewolf, *LightPath Technologies Inc., USA*. We report a multimode four-channel integrated wavelength division demultiplexer operating at 750, 780, 810, and 840 nm. Surface-normal configuration is realized with use of volume holographic gratings and substrate-guided waves. **(p. 422)**

11:45am

**IWD5 ■ A planarized two-dimensional multi-wavelength routing network with 1-to-many cascaded fanouts**, Jian Liu, Ray T. Chen, *Univ. Texas–Austin*. A planarized two-dimensional wavelength-division demultiplexing device is demonstrated to separate and distribute optical signals having 760, 790, and 820 nm by integrating stacked input holograms and 1-to-many cascaded output holograms on a waveguiding plate. **(p. 425)**

# Workshop on Novel Solitons and Nonlinear Periodic Structures

March 29–30, 1998

## Abstracts and Schedule

■ Sunday  
■ March 29, 1998

---

### Esquimalt

---

8:45am–10:30am

#### **WSA ■ Temporal Solitons 1**

Benjamin Eggleton, *Bell Labs, Lucent Technologies, USA*,  
*Presider*

8:45am

#### **Introduction**

William Torruellas, *Washington State University, USA*,  
*General Chair*  
Benjamin Eggleton, *Bell Labs, Lucent Technologies, USA*

9:00am (Keynote)

**WSA1 ■ Massive WDM with solitons: the challenge and the golden opportunity**, Linn F. Mollenauer, *Bell Labs, Lucent Technologies, USA*. Systems developers are now beginning to demand total transmission capacities of many hundreds of Gbit/s on a single fiber, robust and error-free over very great distances. Many real world problems, such as polarization-mode-dispersion, polarization-dependent loss, and those associated with the required wide wavelength bands, make this a most daunting challenge. To meet it, there is no one magic bullet. Rather, one must combine the very best of dispersion-managed solitons, passive optical regeneration, and the latest in advanced fiber designs.

10:00am (Invited)

**WSA2 ■ Wavelength division multiplexed (WDM) solitons: four wave mixing and collision induced timing jitter**, Mark J. Ablowitz, *Univ. Colorado, Boulder, USA*. Wavelength division multiplexed (WDM) soliton communication offers a number of practical advantages. However at the same time there are associated potential technological difficulties. Analytical results will be outlined regarding two important issues: i) resonance between four wave mixing (FWM) and amplifier spacing and ii) collision induced timing jitter due to soliton interactions in the presence of filters and dispersion management.

---

### Oak Bay

---

10:30am–11:00am  
**Coffee Break**

---

### Esquimalt

---

11:00am–12:30pm

#### **WSB ■ Temporal Solitons 2**

Alejandro B. Aceves, *University of New Mexico, USA*,  
*Presider*

11:00am (Invited)

**WSB1 ■ Remarkable properties of dispersion managed solitons**, N.J. Doran, W. Forystiak, J.H.B. Nijhof, A. Niculae, *Aston Univ., U.K.* Dispersion managed solitons are shown to have remarkable properties related to the map strength which allows soliton propagation in the normal, as well as the anomalous, dispersion region.

11:30am (Invited)

**WSB2 ■ Optimal launching of solitons in wavelength-division-multiplexed dispersion-managed optical fibers**, Tian-Shiang Yang, William L. Kath, *Northwestern Univ., USA*. The performance of data transmission in optical fibers can be significantly improved by varying the group-velocity dispersion periodically with distance, a technique known as dispersion management. We use averaging methods to analyze pulse propagation in such systems, and derive expressions for the launch points in wavelength-division-multiplexed systems which minimize the radiative shedding of energy.

12:00m (Invited)

**WSB3 ■ Chirped nonlinear pulse propagation in a periodically dispersion compensated system**, Yuji Kodama, *Osaka Univ., Japan*. There exists a quasi-stationary pulse in an optical transmission line having periodic dispersion compensation. The width and chirp of the pulse oscillate with the period of the dispersion compensation. The average behavior of the pulse can be described by the nonlinear Schrödinger equation with a nontrapping quadratic potential. Using this equation, we theoretically explain several new features of the pulse.

12:30pm–2:00pm  
**Lunch Break**

---

## Esquilmalt

---

2:00pm–4:00pm

### WSC ■ Novel Solitons

Falk Lederer, *Friedrich Schiller University of Jena, Germany, Presider*

2:00pm (Invited)

**WSC1 ■ Polarization domain wall solitons with counterpropagating beams in optical fibers**, G. Millot, S. Pitois, S. Wabnitz, *Université de Bourgogne, France*. In analogy with magnetic materials, cross-polarization interaction between counterpropagating beams in fibers leads to topologically stable domain wall solitons. First experimental observations confirm this prediction.

2:30pm (Invited)

**WSC2 ■ Solitons in systems with gain and loss**, N.N. Akhmediev, *Australian National Univ.* I consider solitons generated by passively mode-locked lasers, taking into account slow and fast parts of the semiconductor saturable absorber response. Despite the fact that lumped effects are present in the laser, it can be modeled as a distributed system in certain conditions. Solitons in these systems have a number of unusual properties.

3:00pm (Invited)

**WSC3 ■ Ultrafast time-division-multiplexed networks integrating all-optical access nodes and soliton technologies**, Mohammed N. Islam, *Univ. Michigan, USA*. This talk will present the motivation and goals of ultra-high-speed TDM networks as well as critical technologies that will be required. In particular, key enabling technologies required for reading the address on an information packet at speeds of 100 Gbit/s will be reviewed. Technology challenges exist in all-optical switching, compact diode-pumped short pulse lasers, high-speed synchronization and short pulse propagation in fibers. The materials challenge centers on the need for high-nonlinearity materials that can be fabricated into guided-wave structures. Our experiments on all-optical switching use low-birefringent nonlinear optical loop mirrors. We use passively-modelocked short pulse erbium-doped fiber lasers as the optical power supplies, and we synchronize two lasers using a novel acousto-optic modulator/grating scheme and a phase-lock loop. Finally, we will report our progress on integrating the lasers, logic gates, synchronization circuits and propagation for rudimentary system demonstrations of header processing at network nodes or add/drop multiplexers.

3:30pm (Invited)

**WSC4 ■ What is the polarization of that soliton?**, Yaron Silberberg, Yaniv Barad, *Weizmann Institute of Science, Israel*. We shall discuss the possible polarization states of optical solitons, and report experiments on temporal soliton polarization evolution in various environments.

---

## Oak Bay

---

4:00pm–4:30pm

### Coffee Break

---

## Esquilmalt

---

4:30pm–6:30pm

### WSD ■ Spatial Solitons 1

Alain Barthelemy, *University of Limoges, France, Presider*

4:30pm (Invited)

**WSD1 ■ Photorefractive spatial solitons**, Mordechai Segev, *Princeton Univ., USA*. We present an overview on spatial solitons in photorefractive materials along with recent results on 3D collisions of interacting solitons and self-trapping of incoherent bright and dark light beams.

5:00pm (Invited)

**WSD2 ■ All we know about 'real solitons'**, Yuri Kivshar, *Australian National Univ.* I am going to review a number of common properties of solitary waves of nonintegrable systems (solitons of real physical models) comparing them with the results for integrable systems. Unlike a common belief that 'real solitons' are all different, I will try to show that, similar to 'integrable solitons', solitary waves of nonintegrable models (e.g., the generalized NLS equation, two- and three-wave parametric solitons in  $\chi^{(2)}$  materials, vectorial solitons, etc.) do possess many common features. This includes stability, evolution of unstable states and switching, internal modes, collisions, etc.

5:30pm (Invited)

**WSD3 ■ 1D solitary waves due to cascaded second-order nonlinearities**, Roland Schiek, *Technical Univ. Muechen, Germany*. We report on our experiments with (in 1 dimension) self-trapped optical waves in lithium niobate film waveguides. The formation, steering and interaction of solitary waves were investigated.

6:00pm (Invited)

**WSD4 ■ Self-localization in nonlinear waveguide arrays**, J. S. Aitchison, R. Morandotti, *Univ. Glasgow, U.K.*; H. Eisenberg, Y. Barad, Y. Silberberg, *The Weizmann Institute of Science, Israel*. In this presentation we will describe our experimental results on nonlinear waveguide arrays fabricated in AlGaAs and operated in the half-band gap spectral region. We observe evidence of self-localization and will present results on both strong and weakly coupled waveguide arrays. The conditions for the observation of discrete spatial solitons will also be discussed.

■ **Monday**  
■ **March 30, 1998**

---

## **Esquilmalt**

---

**8:30am–10:30am**

**WMA ■ Nonlinear Periodic Structures 1**

John Sipe, *University of Toronto, Canada, Presider*

**8:30am (Invited)**

**WMA1 ■ Nonlinear effects in fiber gratings: switching, solitons and other surprises,**

Martijn de Sterke, *Univ. Sydney, Australia*. The nonlinear optics of periodic media is now a blossoming field, with contributions coming from theory and experiments. Here I review some of the history of this area, and point to possible future developments.

**9:00am (Invited)**

**WMA2 ■ Bragg soliton experiments,** R.E. Slusher, B.J. Eggleton, *Bell Labs, Lucent Technologies, USA*. Bragg solitons were observed for the first time in 1995 in uniform fiber gratings. These experiments revealed that at high intensities, the combination of the strong dispersion provided by the Bragg grating, along with the third order nonlinear response give rise to pulse compression and pulse retardation. Indeed it was confirmed by numerical simulation that we had observed the formation and propagation of solitons that propagate at velocities substantially less than the speed of light. In this talk we discuss our recent experiments studying soliton propagation and soliton dynamics in novel fiber grating structures and highly nonlinear materials. The phenomena of modulational instabilities has been observed in apodized gratings in good agreement with numerical simulations and a simple analytical model based on the nonlinear Schroedinger equation. We have also explored various schemes for slowing soliton pulses to a fraction of the speed of light using chirped gratings as well as using defect states to "trap" solitons. Initial experiments on soliton-soliton interactions will also be described along with simulations that show behavior for the symmetric and anti-symmetric cases that are remarkably similar to solitons in normal fiber. Initial results on pulse propagation in highly nonlinear chalcogenide fiber gratings will also be described.

**9:30am (Invited)**

**WMA3 ■ Nonlinear switching using Bragg gratings,** N.G.R. Broderick, D. Taverner, D.J. Richardson, M. Ibsen, R.I. Laming, *Univ. Southampton, U.K.* We report on the construction of three different kinds of nonlinear switches involving nonlinear fiber Bragg gratings. Two switches involve gap soliton formation while the last relies on cross-phase modulation and is based on the optical pushbroom.

**10:00am (Invited)**

**WMA4 ■ Parametric gap solitons,** Stefano Trillo, *Fondazione Ugo Bordon, Italy*. An overview of recent studies on gap solitons sustained via parametric three-photon conversion in Bragg structures will be carried out. This will be made on the basis of recent theoretical achievements including existence and classification of solutions, their stability and excitability, and finally outlining the open problems and directions.

---

## **Salon A**

---

**10:30am–11:00am**

**Morning Coffee Break and Exhibits**

---

## **Esquilmalt**

---

**11:00am–1:00pm**

**WMB ■ Nonlinear Periodic Structures II**

Herbert G. Winful, *University of Michigan, USA, Presider*

**11:00am (Invited)**

**WMB1 ■ All-optical switching with chirped gratings in semiconductor optical amplifiers,** Govind P. Agrawal, Drew Maywar, *Univ. Rochester, USA*. Bragg gratings in a semiconductor optical amplifier allow access to the nonlinear effects at much lower powers compared with those needed for fiber gratings. The response time of the gain-induced nonlinearity (~100 ps) is fast enough to be useful for all-optical switches operating at power levels below 1 mW. In this talk, we discuss the physical mechanism behind such devices and consider how chirped gratings can be used to improve the switching characteristics.

**11:30am (Invited)**

**WMB2 ■ Spontaneous emission and nonlinear effects in photonic band-gap materials,** Ishella S. Fogel, Jon M. Bendickson, Michael D. Tocci, Mark J. Bloemer, Michael Scalora, Charles M. Bowden, Jonathan P. Dowling, *U.S. Army Aviation and Missile Command, USA*. We summarize and review our theoretical and experimental work on spontaneous emission and nonlinear effects in one-dimensional, photonic band-gap (PBG) structures; including second-harmonic generation, optical limiting and switching, and spontaneous emission control.

12:00pm (Invited)

**WMB3 ■ Nonlinear Bragg reflectors in semiconductor waveguides: what, how and why?**, Thomas G. Brown, *Univ. Rochester, USA*. Periodic structures with a semiconductor as the nonlinear medium were the first to demonstrate the optical switching behavior that had long been predicted to occur in nonlinear Bragg reflectors. We discuss the materials, fabrication, and waveguide design considerations which are important for providing efficient coupling of pulses into semiconductor periodic structures. Finally, we will discuss two classes of structures which raise interesting possibilities for gap-soliton experiments: 1) Higher-order gratings which (for planar waveguides) allow direct excitation by radiation modes; and 2) Structures which allow control over both the amplitude and phase of the coupling coefficient.

12:30pm (Invited)

**WMB4 ■ Multi-dimensional parametric solitons in photonic bandgaps**, Peter Drummond, *Univ. Queensland, Australia*. We analyze novel soliton behavior in coupled periodic structures with a  $\chi^{(2)}$  nonlinearity, via a coupled mode Hamiltonian. Starting from the mode structure of a Bragg grating, we are able to reduce this problem to the travelling-wave  $\chi^{(2)}$  problem with solitons in one, two or three dimensions. The analytic results are numerically checked for stability via the full coupled equations.

1:00pm–2:00pm

**Lunch Break**

---

## Oak Bay Room

---

2:00pm–3:30pm

**WMC ■ Poster Session**

---

## Esquimalt

---

3:30pm–6:00pm

**WMD ■ Spatial Solitons 2**

Alex A. Zozulya, *University of Colorado, USA, Presider*

3:30pm (Invited)

**WMD1 ■ Cavity spatial solitons**, L.A. Lugiato, F. Prati, L. Spinelli, G. Tissoni, *Univ. di Milano, Italy*; M. Brambilla, *Politecnico di Bari, Italy*. We discuss a novel kind of spatial solitons that are obtained by shining short and narrow laser pulses in a nonlinear material contained in an optical cavity driven by a coherent field. We illustrate how they interact, how they can be controlled, arranged in arrays and utilized for purposes of information processing.

4:00pm (Invited)

**WMD2 ■ Transverse instabilities in nonlinear optics and atomoptics**, Mark Saffman, *Risø National Laboratory, Denmark*. Modulational instabilities of both plane waves and localized solitary solutions lead to the formation of complex spatial structures. These instabilities limit single

spatial mode energy transfer in nonlinear media, yet are also useful as a means of generating sophisticated waveguide topologies. I will discuss aspects of convective transverse instabilities in photorefractive, and atomoptical interactions.

4:30pm (Invited)

**WMD3 ■ Optical vortex propagation dynamics**, Grover A. Swartzlander, Jr., *Worcester Polytechnic Institute, USA*. Optical vortices are robust topological features of a wave that remain intact in both linear and nonlinear optical materials. In self-defocusing media they form dark solitons which resemble graded index optical fibers. These structures may be used not only to guide light, but, owing to their propagation dynamics, may also be used to form dynamic waveguides with variable guiding properties and reconfigurable positioning. We will describe our experimental and numerical investigations of the propagation dynamics of optical vortices in linear and nonlinear media, and describe our efforts to form nonlinear guided wave modulators, logic gates, and active interconnects.

5:00pm (Invited)

**WMD4 ■ Interaction of spatial photorefractive solitons**, W. Krolikowski, B. Luther-Davies, *Australian National Univ.*; M. Saffman, *Risø National Laboratory, Denmark*; M. Belic, A. Stepken, *Darmstadt Univ. Technology, Germany*. We present results of numerical and experimental investigations of interaction of 3D spatial solitons in photorefractive media with anisotropic nonlocal nonlinear response. We show that collision of photorefractive screening soliton may result in soliton annihilation, fusion, or birth. We also demonstrate that photorefractive nonlinearity leads to anomalous interaction of incoherent solitons which may experience both attractive or repulsive force depending on their mutual location and separation.

5:30pm (Invited)

**WMD5 ■ Spatio-temporal solitons for optical switching**, Kelvin Wagner, Steve Blair, Kishore Yellampalle, Robert McLeod, *Univ. Colorado, Boulder, USA*. The asymmetric spatial dragging interaction of initially overlapping orthogonally polarized 1+1 dimensional spatial, 2+1 D and 3+1 D spatio-temporal optical solitons, in a saturating nonlinear optical medium will be shown to be capable of achieving high speed, parallel, phase insensitive, cascable, high contrast, logic operations with gain.

6:00pm–7:30pm

**Dinner Break**

---

## Esquimalt

---

7:30pm–9:30pm

**WME ■ Panel Discussion: A Shared Vision of Novel Solitons and Nonlinear Periodic Structures**

Gaetano Assanto, *Terza University of Rome, Italy, Presider*

# Nonlinear Guided Waves & Their Applications

## Abstracts and Schedule

■ **Wednesday**  
■ **April 1, 1998**

---

### Saanich Room

---

8:15am–8:30am

#### Opening Remarks

Martin Fejer, *Stanford University, USA*

---

### Saanich Room

---

8:30am–10:00am

#### NWA ■ New and Weird Soliton Effects

Stefano Trillo, *Fondazione Ugo Bordonì, Italy, Presider*

8:30am (Invited)

**NWA1 ■ Optical bullet-holes**, William J. Firth, *Univ. Strathclyde, U.K.* Stable two-dimensional soliton-like states occur in many nonlinear optical cavity configurations. Their physics and potential applications will be reviewed.

9:00am

**NWA2 ■ Observation of multi-hump multi-mode self-trapped beams**, Matthew Mitchell, Mordechai Segev, *Princeton Univ., USA*; Demetrios N. Christodoulides, *Lehigh Univ., USA*. We present the first observation of multi-hump multi-mode self-trapped beams in nature. Double and triple humped spatial profiles are found by incoherently populating two modes of the beams' self-induced waveguide.

9:15am

**NWA3 ■ Oscillating cavity solitons with a saturable defocusing nonlinearity**, Dirk Michaelis, Ulf Peschel, Falk Lederer, *Friedrich-Schiller-Univ. Jena, Germany*. We show for the first time, to our knowledge, that cavity solitons may undergo a Hopf bifurcation that leads to pronounced self oscillations.

9:30am

**NWA4 ■ Beam control and switching in nonlinear meso-optical structures**, David S. Citrin, Steven Tomsovic, William E. Torruellas, *Washington State Univ., USA*. The presence of cross-phase modulation coupling a strong pump and a trapped intracavity field prevents the appearance of spatial chaos in an otherwise chaotic mesoscopic cavity.

9:45am

**NWA5 ■ Self-organization, motion and decay of vectorial dichromatic cavity solitons**, U. Peschel, D. Michelis, C. Etrich, F. Lederer, *Friedrich-Schiller-Univ. Jena, Germany*. We demonstrate that symmetry breaking in intracavity vectorial second harmonic generation leads to the formation of new types of resting and moving cavity solitons.

---

### Salon A

---

10:00am–10:30am

#### Coffee Break and Exhibits

---

### Saanich Room

---

10:30am–12:00m

#### NWB ■ Nonlinear Waveguides

J. Stewart Aitchison, *University of Glasgow, U.K., Presider*

10:30am (Invited)

**NWB1 ■ Ultrafast all-optical waveguide devices based on bandgap resonant nonlinearities**, Patrick LiKam Wa, *CREOL, Univ. Central Florida, USA*. Carrier induced nonlinearities in semiconductor multiple quantum wells have been utilized to achieve ultrafast optical gating in waveguide devices. A temporal switching window of 9ps has been demonstrated.

11:00am

**NWB2 ■ All-optical buffers via localization of two-color quadratic gap solitons**, Gaetano Assanto, *Terzo Univ. Rome, Italy*; Claudio Conti, Stefano Trillo, *Fondazione Ugo Bordonì, Italy*. Bragg localization of two-color gap solitons can be achieved in frequency-doubling media. Self-trapped states are "stored" via collision of counterpropagating pulses, and probed by another pulse.

11:15am

**NWB3 ■ All-optical switching using modal interference resulting from the cascaded nonlinearity**, Y. Baek, G. Assanto, R. Schiek, G.I. Stegeman, *Univ. Central Florida, USA*. The inversion of the output beam position from a single lithium niobate channel waveguide was observed as a result of the modal interference condition change caused by the cascaded nonlinearity.

11:30am

**NWB4 ■ Optical Bloch oscillations and solitons in nonlinear arrays with linearly varying wave number**, U. Peschel, F. Lederer, *Friedrich-Schiller-Univ. Jena, Germany*; T. Pertsch, *Fraunhofer-Institut, Germany*. In a waveguide array with linear variation of the propagation constant soliton multistability, nonlinearly induced energy transport and symmetry breaking resulting from discreteness are identified.

11:45am

**NWB5 ■ Self-writing channel waveguides in  $As_2S_3$  thin films by two-photon absorption**, Chiara Meneghini, Alain Villeneuve, *Univ. Laval, Canada*. Self-writing of channel waveguides in  $As_2S_3$  thin films, by two-photon absorption of femtosecond pulses near 800 nm, is presented.

12:00m–1:30pm

**Lunch Break**

---

### Saanich Room

---

1:30pm–3:00pm

**NWC ■ Dispersion Managed Solitons**

Alexei N. Pilipetskii, *TYCO Submarine Systems Laboratories, USA, Presider*

1:30pm (Invited)

**NWC1 ■ Dispersion-managed soliton systems**, Gary M. Carter, John M. Jacob, *Univ. Maryland–Baltimore County, USA*. We present experimental evidence and modeling that indicate pulse dynamics and communication performance are closely coupled by in-line optical filters in dispersion-managed soliton systems.

2:00pm

**NWC2 ■ Dispersion management in optical fiber links: a differential equation for the eigenmode(s)**, C. Paré, P.-A. Bélanger, *Univ. Laval, Canada*. An ordinary differential equation for the stationary chirped pulse propagating in a dispersion-managed system is derived and solved. We discuss the existence of higher-order solutions and the possible implications for optical communications.

2:15pm

**NWC3 ■ Analysis of stabilizing effect of filters in dispersion-managed soliton systems**, Masayuki Matsumoto, *Osaka Univ., Japan*. Effects of guiding filters on dispersion-managed solitons is theoretically analyzed. It is shown that the strength of stabilization of pulse energy decreases as the strength of the management is increased.

2:30pm

**NWC4 ■ Conditions for stationary pulse propagation in the strong dispersion management regime**, T.I. Lakoba, D.J. Kaup, *Clarkson Univ., USA*; J. Yang, *Univ. Vermont, USA*; B.A. Malomed, *Tel Aviv Univ., Israel*. Analytical conditions for stationary propagation of a Gaussian pulse in a strongly dispersion-managed fiber are obtained and verified numerically. Both the lossless fiber and that with losses and periodic amplification are considered.

2:45pm

**NWC5 ■ Dispersion-managed solitons with average normal dispersion**, Stephen G. Evangelides Jr., *Tyco Submarine Systems Ltd. Laboratories, USA*; J. Nathan Kutz, *Hong Kong Polytechnic Univ.* Using a variational approach, we demonstrate that dispersion-managed solitons can exist even when the path average dispersion is in the normal regime.

---

### Salon A

---

3:00pm–3:30pm

**Coffee Break & Exhibits**

---

### Saanich Room

---

3:30pm–4:30pm

**NWD ■ Frequency Mixing in Waveguides**

Martin M. Fejer, *Stanford University, USA, Presider*

3:30pm (Invited)

**NWD1 ■ Wavelength conversion by difference-frequency-generation for telecommunications applications**, S.J. B. Yoo, *Bellcore, USA*. This paper reviews difference-frequency-generation (DFG) in light of all-optical network applications. Compared to other wavelength conversion techniques, DFG offers a number of unique advantages including strict transparency to signal formats, simultaneous multi-channel conversion, and chirp reversal. Recent results obtained on DFG in an AlGaAs waveguide show polarization independent simultaneous conversion of 2.5 and 10 Gb/s signals.

4:00pm

**NWD2 ■ Efficient generation of Infrared light in  $LiNbO_3$  waveguides with integrated coupling structures**, M.H. Chou, M.A. Arbore, M.M. Fejer, *Stanford Univ., USA*; A. Galvanauskas, D. Harter, *IMRA America Inc., USA*. We report generation and wavelength conversion of infrared light by difference frequency mixing and optical parametric generation in periodically poled  $LiNbO_3$  waveguides. Integrated coupling structures were used for efficient launching of the input light.

4:15pm

**NWD3 ■ Third harmonic generation of Nd:YAG laser light in periodically poled LiNbO<sub>3</sub> waveguide,** K. Kintaka, M. Fujimura, T. Suhara, H. Nishihara, *Osaka Univ., Japan*. We demonstrate a LiNbO<sub>3</sub> waveguide device with cascading a quasi-phase-matched second-harmonic generation part and a quasi-phase-matched sum-frequency generation part, and achieved 355 nm light generation.

---

## Oak Bay and Esquimalt Rooms

---

4:30pm–6:30pm

### NWE ■ Poster Session I

**NWE1 ■ Dispersion management in optical fiber links: self-consistent solution for the RMS pulse parameters,** P.-A. Bélanger, C. Paré, *Univ. Laval, Canada*. Self-consistent solutions and propagation laws for the RMS characteristics of the stationary pulse of a dispersion-managed system are derived from invariance relations of the nonlinear Schrödinger equation and second-order moment theory.

**NWE2 ■ Conjugate solitons in optical fibers,** Stefan Wabnitz, *Univ. Bourgogne, France*; J. Soto-Crespo, *Instituto de Optica, Spain*. A new class of two-color stable coupled solitary waves is found, which represents the optimal frequency conversion of an ultrashort soliton pulse.

**NWE3 ■ Soliton propagation in the vicinity of a two-photon resonance,** J. Hickmann, J.M. de Oliveira, Solange B. Cavalcanti, *Univ. Federal de Alagoas, Brazil*. We investigate the effects of frequency dispersion of the nonlinear susceptibility associated with two-photon resonance, obtaining the necessary conditions for a solitary wave solution, even in the presence of a self-steepening term.

**NWE4 ■ Higher-order quasi-solitons of an adapted dispersion profile,** C. Paré, *Univ. Laval, Canada*. It is argued that the dispersion profile adapted to the so-called “quasi-soliton” introduced by Kumar and Hasegawa can also support higher-order modes sharing the same propagation law.

**NWE5 ■ Nonlinear guided soliton pulse trains in lossy optical fibers,** M.V. Guerreiro das Neves, J.A.M. Brandão Faria, *IST, Portugal*. A numerical simulation procedure aiming at the analysis of soliton pulse train propagation in nonlinear lossy fibers is presented. The simulation, based on the SSFM, is applied to a train of three soliton pulses, showing that strong interaction among pulses may occur even when an amplitude diversity strategy is employed.

**NWE6 ■ Robust solitary waves in fiber transmission lines with semiconductor optical amplifiers,** M. Göllés, I.M. Uzunov, F. Lederer, *Freidrich-Schiller-Univ. Jena, Germany*. A family of stationary solutions in a fiber transmission line with semiconductor optical amplifiers was identified. They are robust against fluctuations of the input amplitude.

**NWE7 ■ Bright and dark pulses in fiber lasers and optical transmission lines,** Adrian Ankiewicz, Nail Akhmediev, *Australian National Univ.*; J.M. Soto-Crespo, *Instituto de Optica, Spain*. We present a segment energy balance method for obtaining exact solutions of the complex Ginzburg-Landau equation. The method allows us to analyze various types of solutions.

**NWE8 ■ Periodically conjugated solitons in dispersion-managed optical fiber,** Jaime Piña, Bryan Abueva, Christopher G. Goedde, *DePaul Univ., USA*; William L. Kath, *Northwestern Univ., USA*. The averaged evolution equation for very short solitons in dispersion-managed fiber with periodic optical phase conjugation is derived and compared with numerical simulations.

**NWE9 ■ Modulational instability in a communication link exploiting a negative nonlinearity for compensation of self-phase modulation,** C. Paré, A. Villeneuve, S. Larochelle, *Univ. Laval, Canada*. We show that the use of a medium exhibiting a negative nonlinearity for the compensation of nonlinear effects incurred along an optical communication line may induce a sideband instability.

**NWE10 ■ 40 Gbit/s soliton transmission over standard fiber with dispersion management,** Donald Govan, W. Forysiak, N.J. Doran, *Aston Univ., U.K.* Use of a novel dispersion map has been shown to allow the propagation of soliton-like pulses over more than 2000 km of standard fiber at 40 Gbit/s.

**NWE11 ■ Propagation of light beam in sillenite crystal with a square-wave applied field,** Stanislav M. Shandarov, Nadezhda I. Nazhestkina, Oleg V. Kobozev, Rudolf V. Litvinov, *State Univ. Control Systems and Radioelectronics, Russia*; Yuri F. Kargin, Vladimir V. Volkov, *Institute of General and Chemistry of Russian Science, Russia*. We consider a one-dimensional space-charge field induced in sillenite crystal with an applied square-wave electric field during propagation of a light beam and report on the experimental investigation of the self-bending of light beam in Bi<sub>12</sub>TiO<sub>20</sub> crystal.

**NWE12 ■ Geometric control of harmonic generation,** Gregory Luther, *Northwestern Univ., USA*; M.S. Alber, *Univ. Notre Dame, USA*; J.E. Marsden, *California Institute of Technology, USA*; J.M. Robbins, *Hewlett-Packard Labs., USA*. Analogs of the Poincaré sphere are introduced to analyze control strategies for harmonic generation.

**NWE13 ■ Continuous-wave measurement of the fiber nonlinear index**, D. Monzon, A.N. Starodumov, Yu.O. Barmenkov, I. Torres, *Centro de Investigaciones en Optica, Mexico*. A method for measuring the fiber nonlinear refractive index is demonstrated. A cw optical source and direct intensity measurements permits one to avoid errors caused by fiber dispersion and uncertainty of spectral peak difference measurements for pulse-based methods.

**NWE14 ■ Packet networks using all-optical bit serial processing**, K.J. Blow, A. Poustie, R.J. Manning, *BT Laboratories, U.K.* The design of a subsystem of an optical packet receiver is used to illustrate the application of bit serial processing in ultrafast data networks.

**NWE15 ■ Generation of spatial solitons from guided modes of nonlinear waveguides**, R.W. Micallef, Y.S. Kivshar, J.D. Love, *Australian National Univ.*; D. Burak, R. Binder, *Univ. Arizona, USA*. The nonlinear modes of a slab waveguide may be used to generate single solitons waves, bound states of two solitons, or two repelling solitons.

**NWE16 ■ Spatial control of pulses in quadratic nonlinear materials**, R. Cerioni, C. Sibilio, M. Bertolotti, *Univ. Roma, Italy*; J. Dekker, *Univ. Twente, The Netherlands*. A numerical study of the propagation of intense beams in a quadratic nonlinear material is presented, when a second harmonic amplification process occurs. Sinusoidal spatial amplitude modulation of the input fields is shown to be able to control the splitting of the propagating beams and their stability.

**NWE17 ■ Generalized higher-order nonlinear evolution equation for multi-dimensional spatio-temporal propagation**, Steve Blair, Kelvin Wagner, *Univ. Colorado, USA*. A nonlinear wave equation is presented that describes propagation with large spatial and temporal frequency bandwidths. Stabilized spatiotemporal solitary wave propagation is also shown.

**NWE18 ■ Theory of mixed-polarization spatial solitons in anisotropic cubic media**, David Hutchings, J.M. Arnold, *Univ. Glasgow, U.K.*; D.F. Parker, *Univ. Edinburgh, U.K.* The polarization dynamics of spatial solitons in anisotropic, cubic non-Kleinmann media (e.g., AlGaAs at the half-bandgap) are addressed. The consideration of plane-wave stationary solutions and their stability helps explain the numerical results for the spatial soliton case.

**NWE19 ■ Nonparaxiality stabilizes three-dimensional soliton beams in Kerr media**, A.P. Sheppard, *Australian National Univ.*; M. Haelterman, *Univ. Libre de Bruxelles, Belgium*. Considering the nonparaxial wave equation, we show, on the basis of simple physical arguments, that three-dimensional soliton beams in Kerr media are stable.

**NWE20 ■ Self-focusing and solitary waves in bulk media with quadratic and cubic nonlinearity**, Ole Bang, *Australian Photonics Cooperative Research Centre*; Yuri S. Kivshar, Alexander V. Buryak, *Australian Defence Force Academy*; Alfredo De Rossi, Stefano Trillo, *Fondazione Ugo Bordon, Italy*. We find the existence and stability regimes and dynamical properties of bright solitary waves in bulk media with quadratic and cubic nonlinearities.

**NWE21 ■ Efficient birefringence phase-matched blue light second-harmonic generation in KNbO<sub>3</sub> ridge waveguides**, Tomas Pliska, Daniel Fluck, Peter Günter, Emilio Gini, Hans Melchior, *Swiss Federal Institute of Technology, Switzerland*; Lutz Beckers, Arne Eckau, Christoph Buchal, *Forschungszentrum, Germany*. Ridged channel waveguides in KNbO<sub>3</sub> were fabricated with use of a new technique involving He<sup>+</sup> ion implantation and Ar<sup>+</sup> ion sputtering. A continuous-wave second-harmonic power of 14 mW at 438 nm was obtained with an in-coupled fundamental power of 340 mW.

**NWE22 ■ Flip-flop operation based on symmetry breaking in vectorial intracavity second harmonic generation**, Falk Lederer, Ulf Peschel, Christoph Etrich, *Friedrich-Schiller-Univ. Jena, Germany*. We show that beyond a certain input amplitude symmetry breaking occurs in vectorial intracavity second harmonic generation. This effect can be exploited for flip-flop operation.

■ Thursday  
■ April 2, 1998

---

## Saanich Room

---

8:30am–10:00am

### NThA ■ Temporal Propagation Effects I

Nail Akhmediev, *University of Canberra, Australia, Presider*

8:30am

**NThA1 ■ Average dark soliton dynamics in periodically dispersion-compensated fiber transmission systems**, Yijiang Chen, *Australian National Univ.*; Javid Atai, *Univ. Sydney, Australia*. We examine propagation of dark solitons in periodically dispersion-compensated (PDC) fiber transmission systems. Distinctive features of the dark soliton in PDC transmission systems are reported and are compared with the bright soliton.

8:45am

**NThA2 ■ Dark soliton train generation in a birefringent fiber**, Stefan Wabnitz, G. Millot, E. Seve, *Univ. Bourgogne, France*; M. Haelterman, *Univ. Bruxelles, Belgium*. Experiments show that modulational polarization instability in a normally dispersive low-birefringence optical fiber leads to ultrashort dark soliton-like trains with THz repetition rates.

9:00am

**NThA3 ■ Modulational instabilities in a nonlinear all-fiber cavity**, S. Coen, M. Haelterman, Ph. Emplit, *Univ. Libre de Bruxelles, Belgium*. We show theoretically and experimentally that modulational instability plays an essential role in the dynamics of a nonlinear fiber cavity even in the normal dispersion regime.

9:15am

**NThA4 ■ Gain characteristics in birefringent fiber optical parametric amplifiers**, T. Sylvestre, H. Maillotte, E. Lantz, *Univ. Franche-comté, France*. A characteristic bell-shaped gain curve versus the pump power for parametric amplification in birefringent fibers is experimentally demonstrated, as a result of intensity-dependent phase-matching conditions and nonphase-matched waves.

9:30am

**NThA5 ■ Stability criterion and multistability of Kerr-like gap solitons**, Alfredo De Rossi, Claudio Conti, Stefano Trillo, *Fondazione Ugo Bordoni, Italy*. We derive a stability criterion for gap solitons, which predicts stability in fibers, whereas a defocusing self-phase modulation leads to multistability, wobbling, and decay of gap solitons.

9:45am

**NThA6 ■ Mixing of a laser beam and a spectrum of light in a birefringent optical fiber**, Kin Seng Chiang, Kar Pong Lor, Yuk Tak Chow, *City Univ. Hong Kong*. We demonstrate that a laser beam and a spectrum of light can mix in a birefringent optical fiber to generate a distinct frequency-shifted beam.

---

## Lower Lobby

---

10:00am–10:30am

Coffee Break

---

## Saanich Room

---

10:30am–12:00m

### NThB ■ Semiconductor Nonlinearities

Alain Villeneuve, *University of Laval, Canada, Presider*

10:30am (Invited)

**NThB1 ■ Switching in low-temperature-grown InGaAs MQWs**, Ryo Takahashi, *NTT Opto-electronics Laboratories, Japan*. A 250-fs all-optical switch is demonstrated with use of low-temperature-grown InGaAs MQWs. It has many possible applications, such as to demultiplexers, repeaters, and samplers.

11:00am

**NThB2 ■ Effect of two-photon absorption nonlinearity on short pulse propagation in semiconductor optical amplifiers at transparency**, J.M. Tang, K.A. Shore, *Univ. Wales, U.K.* We show that the effects of two-photon absorption and ultrafast nonlinear refraction are essential for describing experimental results on the propagation of strong picosecond optical pulses in semiconductor optical amplifiers at the transparency point.

11:15am

**NThB3 ■ All-optical regenerative memory with full read/write capability**, A.J. Poustie, A.E. Kelly, K.J. Blow, R.J. Manning, *BT Laboratories, U.K.* We demonstrate an all-optical regenerative memory with the capability to write and read-out optical pulses at any time slot in an optical fiber delay line.

11:30am (Invited)

**NThB4 ■ Vertical waveguiding in etched semiconductor nonlinear microcavities**, Jean-Louis Oudar, Thomas Rivera, *France Telecom-CNET, France*. Vertical waveguiding in monolithic bistable microcavities improves the device efficiency, by avoiding the diffraction losses of planar structures. Scaling of optical loss with microresonator diameter is discussed.

12:00m–1:30pm

Lunch Break

---

## Saanich Room

---

1:30pm–3:00pm

### **NThC ■ Photorefractive and Kerr Solitons**

Mordechai Segev, *Princeton University, USA, Presider*

1:30pm (Invited)

#### **NThC1 ■ Self-trapped optical beams in semiconductors**

M. Chauvet, S.A. Hawkins, G.J. Salamo, *Univ. Arkansas, USA*; M. Segev, *Princeton Univ., USA*; D.F. Bliss, G. Bryant, *U.S. Air Force, Rome Laboratory, USA*. We discuss experimental evidence for trapping of one and two-dimensional beams by the photorefractive effect in InP:Fe. In addition, we report on the collision between two trapped beams. Results are different than those found in insulators.

2:00pm

#### **NThC2 ■ Generation and propagation of stable periodic arrays of soliton stripes in a bulk Kerr liquid**

Hervé Maillotte, Régis Grasser, *Univ. Franche-Comté, France*. Stable periodic arrays of Kerr soliton stripes are generated within bulk carbon disulfide and propagate through the medium by controlling modulation instability with Bragg diffraction.

2:15pm

#### **NThC3 ■ Anomalous interaction of spatial solitons in photorefractive media**

Wieslaw Królikowski, Barry Luther-Davies, *Australian National Univ.*; Mark Saffman, *Risø National Laboratory, Denmark*; Cornelia Denz, *Darmstadt Univ. Technology, Germany*. We investigate the interaction of mutually incoherent spatial solitons in photorefractive media with anisotropic nonlocal nonlinear response. We show that the photorefractive nonlinearity leads to an anomalous interaction between solitons. Theoretical and experimental results reveal that an incoherent soliton pair may experience both attractive and repulsive forces, depending on their mutual separation.

2:30pm

#### **NThC4 ■ Incoherent dark quasi-solitons in biased photorefractive media**

Tamer H. Coskun, Demetrios N. Christodoulides, *Lehigh Univ., USA*; Matthew Mitchell, Zhigang Chen, Mordechai Segev, *Princeton Univ., USA*. We show that incoherent dark solitons are possible in biased photorefractive crystals. Their coherence properties are also affected by the self-trapping process.

2:45pm

#### **NThC5 ■ Self-trapping of dark incoherent light beams**

Zhigang Chen, Matthew Mitchell, Mordechai Segev, *Princeton Univ., USA*; Tamer H. Coskun, Demetrios N. Christodoulides, *Lehigh Univ., USA*. We report, we believe, the first observation of self-trapping of dark incoherent beams (dark stripes and vortices) in nonlinear media, or the first observation of self-trapping of dark incoherent wavepackets in nature.

---

## Lower Lobby

---

3:00pm–3:30pm

### **Coffee Break**

## Saanich Room

3:30pm–4:30pm

### **NThD ■ WDM Soliton Systems**

Pavel V. Mamyshev, *Bell Labs/Lucent Technologies, USA, Presider*

3:30pm (Invited)

#### **NThD1 ■ Massive WDM with solitons**

Linn F. Mollenauer, P.V. Mamyshev, *Bell Labs, Lucent Technologies, USA*. To meet the present demands of system builders, we are attempting to develop massive (many hundreds of Gbit/s total capacity) WDM at per-channel rates of 10 Gbit/s or higher, robust and error-free over trans-oceanic distances. We believe that this can be done only by combining the very best version of dispersion-managed solitons, sliding-frequency filters, and fibers with improved (low-slope) dispersion characteristics. Experimental results will be reviewed.

4:00pm

#### **NThD2 ■ Collision-induced timing jitter in dispersion-managed soliton systems**

Mark J. Ablowitz, Gino Biondini, Sarbarish Chakravarty, Rudy L. Horne, *Univ. Colorado, USA*. Collision-induced timing jitter in a wavelength-division-multiplexed soliton system is studied with damping, amplification, filtering, and dispersion management.

4:15pm

#### **NThD3 ■ Soliton collisions in strong dispersion-managed WDM systems**

Anne Niculae, W. Forysiak, N.J. Doran, *Aston Univ., U.K.* A modified theory of soliton collisions in strongly dispersion-managed systems is presented. Ten-fold suppression of the residual frequency shift is obtained.

---

## Oak Bay and Esquimalt Rooms

---

4:30pm–6:30pm

### **NThE ■ Poster Session II**

#### **NThE1 ■ Waveguides induced by photorefractive screening solitons**

Ming-feng Shih, Zhigang Chen, Matthew Mitchell, Mordechai Segev, *Princeton Univ., USA*; Howard Lee, Robert S. Feigelson, Jeffrey P. Wilde, *Stanford Univ., USA*. Waveguides induced by 1D screening solitons are studied theoretically and experimentally. Bright-soliton-induced waveguides can be multimode, depending on soliton parameters, whereas dark-solitons-induced waveguides are single mode.

**NThE2 ■ Bright and dark discrete solitons in waveguide arrays with quadratic nonlinearity,** F. Lederer, S. Darmanyan, A. Kobayakov, *Friedrich-Schiller-Univ. Jena, Germany*. The existence and stability of bright and dark highly localized discrete modes in an array of waveguides with quadratic nonlinearities is analytically and numerically studied.

**NThE3 ■ Existence and stability of dark solitary waves in the presence of third-harmonic generation,** Rowland Sammut, A.V. Buryak, *Australian Defence Force Academy*; Y.S. Kivshar, *Australian National Univ.* We show that parametric coupling between the fundamental and third-harmonic frequencies in Kerr media may lead to either modulational instability or other instability mechanisms for dark spatial solitary waves.

**NThE4 ■ Stable dark and vortex parametric solitons due to competing nonlinearities,** Alexander Buryak, *Australian Defence Force Academy*; Tristram J. Alexander, Yuri S. Kivshar, *Australian National Univ.* We demonstrate how the influence of a weak Kerr effect in quadratic nonlinear media can eliminate parametric modulational instability of plane waves, leading to the existence of stable dark and vortex solitons.

**NThE5 ■ All-optical soliton switching in periodically poled lithium niobate,** E. Ibragimov, *Michigan Technological Univ., USA*. Effective soliton switching of a 1-ps 1.55- $\mu\text{m}$  pulse is predicted in a 12-mm crystal of periodically poled lithium niobate. Intensity of the control pulse is 55 MW/cm<sup>2</sup>.

**NThE6 ■ Vector cw and solitary wave interactions with mixed Type I-Type II second-harmonic generation,** A.D. Boardman, P. Bontemps, K. Xie, *Univ. Salford, U.K.*; D. Parker, *Univ. Edinburgh, U.K.* Vector equations appropriate to a mixed Type I-Type II second-harmonic generation are used to model polarization-controlled switching and solitary wave applications will be discussed.

**NThE7 ■ Semiconductor heterostructure bandstructure algorithms for the determination of nonlinear optical coefficients,** David Hutchings, J.M. Arnold, *Univ. Glasgow, U.K.* Semiconductor heterostructure bandstructure algorithms are developed for the computation of second- and third-order nonlinear optical coefficients. The influence of the upper conduction band, responsible for bulk second-order effects and anisotropy, is addressed.

**NThE8 ■ Stability of quasi-periodic solitary pulse trains in nonintegrable Hamiltonian wave systems,** J.M. Arnold, *Univ. Glasgow, U.K.* Interactions of solitary pulses in a nonlinear Hamiltonian wave system are examined with use of a Lagrangian perturbation theory, leading to a variant of the Complex Toda Lattice.

**NThE9 ■ Phase-locking and periodic evolution of solitons in passively modelocked fiber lasers with slow saturable absorber,** José M. Soto-Crespo, *Instituto de Optica, Spain*; Nail Akhmediev, *Australian National Univ.* We found that, in the laser system with birefringent fiber, four different branches of solitons can be generated including phase-locked soliton states.

**NThE10 ■ Soliton-like pulses generated by modelocked lasers with either slow or fast saturable absorber response,** N.N. Akhmediev, A. Ankiewicz, M.J. Lederer, B. Luther-Davies, *Australian National Univ.* We present a new exact solution for pulses generated by passively modelocked lasers, taking into account slow and fast parts of the saturable absorber response.

**NThE11 ■ Controlling chaos in a simple nonlinear fiber resonator,** S. Lynch, A.L. Steele, *Manchester Metropolitan Univ., U.K.* Control of instabilities in a nonlinear fiber resonator described by the Ikeda map is achieved by use of targeting and the Ott, Grebogi, and Yorke method.

**NThE12 ■ An experimental investigation of Stokes pulse energy noise in an optical fiber Raman generator,** David Baiocchi, Peng Her, Panagiotis Sidereas, John R. Thompson, *DePaul Univ., USA*. Statistical features of multi-order Raman generation are presented, including local noise minima, reshaping of pulse energy distributions, and statistical effects of the broad gain spectrum.

**NThE13 ■ The role of birefringence in modulation instability fiber ring resonators,** Alessandro Tonello, *Univ. Padova, Italy*. Modulation instability gain in fiber ring cavities could be strongly conditioned by intrinsic and induced birefringence. Through linear stability analysis, tunable parametric converters are investigated.

**NThE14 ■ Switching of short pulses in nonlinear directional couplers: effects resulting from the dispersion of the coupling coefficient,** Kin Seng Chiang, Ping Shum, *City Univ. Hong Kong*. We show with examples that a dispersive coupling coefficient can have significant effects on the switching dynamics of short pulses in a nonlinear directional coupler.

**NThE15 ■ Three-channel directional coupler with an optically induced grating,** Ewa Weinert-Raczka, *Technical Univ. Szczecin, Poland*. An asymmetric three-channel directional coupler with a thin optically induced grating as an all-optical switching and wavelength demultiplexing element with memory is analyzed.

**NThE16 ■ Influence of high probe power on multi-wave mixing characteristics of semiconductor lasers,** J.M. Tang, K.A. Shore, *Univ. Wales, U.K.* We demonstrate that pump depletion and carrier diffusion effects are important for the enhanced nonlinear mixing process in semiconductor lasers subject to high probe power.

**NThE17 ■ Active polarization converter in AlGaAs,** Marie Fontaine, *Univ. Québec à Hull, Canada*. The design of an AlGaAs active polarization converter operated at photon energies below the band gap has been optimized to allow efficient all-optical switching.

**NThE18 ■ Raman-effect-based optical switching in highly GeO<sub>2</sub>-doped fibers,** A.N. Stavodumov, Yu.O. Barmenkov, A. Martinez, I. Torres, *Centro de Investigaciones en Optica, Mexico*. A switching energy of about 1 pJ is predicted for an ultrafast switch based on Raman and Kerr effects in a Sagnac interferometer with highly GeO<sub>2</sub>-doped fibers. 35 dB gain and switching have been demonstrated experimentally with the switching power of 130 W.

---

**Crystal Ballroom, Empress Hotel**

---

**6:30pm–7:30pm**  
**Conference Reception**

■ Friday  
■ April 3, 1998

---

## Saanich Room

---

8:30am–10:15am

### NFA ■ Second-Order Processes and Materials

Pierre-Andre Belanger, *University of Laval, Canada, Presider*

8:30am (Invited)

**NFA1 ■ Experimental processing of light pulses with quadratic nonlinearity under type II phase-matched conditions**, Alain Barthelemy, *IRCOM, France*. Early experiments demonstrating the capability of nonlinear propagation in quadratic material for ultrafast processing of light signal such as, switching, phase modulation, phase conjugation, and transistor operation will be reported.

9:00am

**NFA2 ■ Nonlinear phase shift and all-optical switching in quasi-phase-matched quadratic media**, Andrey Kobayakov, Falk Lederer, *Friedrich-Schiller-Univ. Jena, Germany*; Ole Bang, Yuri S. Kivshar, *Australian National Univ.* We analytically study the influence of the induced cubic nonlinearity on the amplitude and phase modulation in quadratic QPM media and predict efficient all-optical switching.

9:15am

**NFA3 ■ Competing nonlinearities at the origin of temporal soliton formation in a femtosecond OPO**, William E. Torruellas, Pey-Shuan Jian, *Washington State Univ., USA*; Ulf Peschel, Cristoph Etrish, Falk Lederer, *Friedrich-Schiller-Univ., Germany*; Stefano Trillo, *Fondazione Ugo Bordon, Italy*; Marc Haelterman, *Univ. Libre de la Paix, Belgium*. Soliton-like pulse formation can be understood and modeled in repetitively pumped OPOs with competing second- and third-order nonlinear interactions.

9:30am

**NFA4 ■ Cascading of second-order processes in a type II phase-matched SHG crystal applied to modelocking of a cw Nd:YAG laser**, V. Couderc, O. Guy, L. Lefort, A. Barthélémy, *Institut de Recherche en Communications Optiques et Microondes, France*. Passive modelocking of a cw Nd:YAG laser using nonlinear polarization evolution resulting from cascading in a phasematched KTP crystal is demonstrated for the first time, we believe.

9:45am

**NFA5 ■ Measurement of the nonuniformity of the wave-vector mismatch in waveguides for second-harmonic generation**, R. Schiek, H. Fang, C.G. Treviño-Palacios, G.I. Stegeman, *Univ. Central Florida, USA*. An inverse Fourier transformation of the second-harmonic field tuning curve yields the nonuniform wave-vector distribution along a waveguide for second-harmonic generation.

10:00am

**NFA6 ■ The seeding and all-optical patterning of polymer materials**, J.-M. Nunzi, C. Fiorini, A.-C. Ettilé, *CEA/Saclay, France*. The nonlinear excitation of organic molecules in polymer matrices using dual-frequency beams permits the achievement of a large and permanent second-order nonlinearity. The practical case of polymer fibers is discussed.

---

## Lower Lobby

---

10:15am–10:45am

Coffee Break

---

## Saanich Room

---

10:45am–12:00m

### NFB ■ Postdeadline Paper Session

12:00m–1:30pm

Lunch Break

---

## Saanich Room

---

1:30pm–3:00pm

### NFC ■ Temporal Propagation Effects II

Stephen G. Evangelides, *Tyco Submarine Systems Ltd. Laboratories, USA, Presider*

1:30pm

**NFC1 ■ Stable multiple pulses in optical fibers with phase-sensitive amplification**, R.O. Moore, W.L. Kath, *Northwestern Univ., USA*; Ba. Sanstede, *Ohio State Univ., USA*; C.K.R.T. Jones, *Brown Univ., USA*; J.C. Alexander, *Univ. Maryland, USA*. We demonstrate stable multiple pulses with distinct, easily distinguished energies in an optical fiber storage loop where phase-sensitive amplification is used to compensate linear loss.

1:45pm

**NFC2 ■ Pulse-pulse interaction in systems with gain and loss**, N.N. Akhmediev, A. Ankiewicz, *Australian National Univ.*; J.M. Soto-Crespo, *Instituto de Optica, Spain*. We present novel stable solutions that are soliton pairs of the complex Ginzburg–Landau equation, and analyze them on the two-dimensional phase plane (“interaction plane”).

2:00pm

**NFC3 ■ Noise reduction of 20 Gbit/s pulse train using spectrally filtered optical solitons,** Masaki

Asobe, Akira Hirano, Yutaka Miyamoto, Kenji Sato, Kazuo Hagimoto, Yoshiaki Yamabayashi, *NTT Optical Network Systems Laboratories, Japan*. We demonstrate that the spectrally filtered soliton is effective in improving the signal-to-noise ratio of optical transmitters, repeaters, and receivers.

2:15pm

**NFC4 ■ Self- and cross-phase modulation of chirped pulses: spectral imaging of pulse temporal profile,**

L.K. Mouradian, *Yerevan State Univ., Armenia*; C. Froehly, F. Louradour, A. Barthelemy, *Institut de Recherche en Communications Optiques et Microondes, France*. A nonlinear-optic Fourier transformer is proposed and experimented for femtosecond pulse measurements. It reproduces in the frequency domain the temporal envelope of input signal.

2:30pm

**NFC5 ■ The effect of pump fluctuation in supercontinuum pulse generation,** Kunihiko Mori,

Hidehiko Takara, Satoki Kawanishi, *NTT Optical Network Systems Laboratories, Japan*. Noise amplification or suppression in the supercontinuum generation process is found to be dependent on the pump power and the observed wavelengths.

2:45pm

**NFC6 ■ 450 kW, all-fiber, picosecond chirped pulse amplification system based on a large mode area fiber Bragg grating compressor,** N.G.R. Broderick, D.J.

Richardson, D. Taverner, J.E. Caplen, L. Dong, M. Ibsen, *Univ. Southampton, U.K.* We report the amplification of picosecond pulses to microjoule energy levels and pulse peak powers in excess of 450 kW in an all-fiber chirped pulse amplification system based on novel large mode area fiber components.

---

**Lower Lobby**

---

3:00pm–3:30pm

**Coffee Break**

---

**Saanich Room**

---

3:30pm–5:00pm

**NFD ■ Non-Kerr and Quadratic Solitons**

David Richardson, *Southampton University, UK, Presider*

3:30pm (Invited)

**NFD1 ■ Non-Kerr spatial solitons,** Allan W. Snyder, *Australian National Univ.* Non-Kerr spatial solitons are the building blocks for virtual circuitry. I introduce novel findings from a unifying perspective, including those on incoherent solitons.

4:00pm

**NFD2 ■ One-dimensional quadratic walking solitons in lithium niobate planar waveguides,** Y. Baek, R.

Schiek, G.I. Stegeman, *Univ. Central Florida, USA*. The properties of one-dimensional quadratic walking solitons were investigated in planar lithium niobate waveguides near the Type I phase-matching condition for second harmonic generation.

4:15pm

**NFD3 ■ Two-dimensional quadratic solitons collision in KTP,** C. De Angelis, B. Costantini, *Univ. Padova, Italy*; B.

Bourliaguet, V. Kermene, A. Barthelemy, *Institut de Recherche en Communications Optiques et Microondes, France*. Numerical and experimental results show the possibility of elastic or inelastic collision of two-dimensional spatial solitons in KTP crystal depending on the collision angle.

4:30pm

**NFD4 ■ Scattering and spiraling of solitons in a bulk quadratic medium,** V.V. Steblina, Y.S. Kivshar, *Australian National Univ.*; A.V. Buryak, *Australian Defence Force Academy*. We analyze interactions of (2+1)-dimensional

parametric solitons and demonstrate nonplanar beam switching in a bulk quadratic medium. An analytical model predicting results of the soliton scattering is derived and verified by direct numerics.

4:45pm

**NFD5 ■ Transverse instabilities of higher-order spatial solitons in quadratic nonlinear media,** Dmitry

V. Skryabin, William J. Firth, *Univ. Strathclyde, U.K.* Stationary ring structures exist in  $\chi^{(2)}$  media. Most fragment: we calculate the daughter solitons' escape speed analytically. Surprisingly, some implode, preserving cylindrical symmetry.

---

**Saanich Room**

---

5:00pm–5:15pm

**Closing Remarks**

Keith Blow, *BT Systems, UK*

**Integrated Photonics Research**

# Plenary Session

**Monday, March 30, 1998**

**Robert J. Deri, Lawrence Livermore National Laboratory**  
President

**IMA**

**8:00am–10:30am**

Salon B&C

## **Planar lightwave circuits: Penetration into real telecom markets**

Masao Kawachi

NTT Science and Core Technology Laboratory Group  
Morinosato Wakamiya, Atsugi-shi, Kanagawa 243-01, Japan  
Phone: +81 462 40 5100 Fax: +81 462 70 2365  
e-mail: kawachi@will.brl.ntt.co.jp

Low-loss integrated silica waveguides with well-defined core geometry provide an efficient means of lightwave interaction and have been used to form a variety of planar lightwave circuits (PLCs) [1]. The time is now ripe for actual introduction of some of these PLCs into real telecom markets [2]. The first major stream is the use of integrated 1xN optical splitters for constructing passive double star (PDS) systems for optical access networks. In NTT's access networks, integrated arrays of wavelength-insensitive couplers (WINC) are also introduced as optical taps for monitoring optical fiber transmission lines in the field. The second major stream is the use of arrayed-waveguide grating (AWG) multiplexers for constructing dense wavelength-division multiplexing (WDM) systems with 8, 16, 32 or even more wavelength channels. Integrated thermooptic (TO) switches are also opening the door to the construction of more advanced WDM systems with optical add-drop multiplexing (ADM) or cross-connect (XC) functions.

Another important role of silica-based PLCs is to provide platforms for hybrid integration, where optoelectronic (OE) chips, such as laser diodes, detectors and OEICs, are integrated together with passive silica waveguides on silicon. Hybrid optical transceivers with a spot-size-converted laser diode on the PLC platform will bring about a cost reduction, making fiber-to-the-home (FTTH) a reality.

The deeper understanding of guided-wave optics and device packaging, gained through the commercialization of silica-based PLCs, will also be useful for the development of other material circuits, including polymer-on-silicon, silicon-on-insulator (SOI) and InP-based waveguides.

- [1] M. Kawachi, "Silica waveguides on silicon and their application to integrated-optic components", *Optical and Quantum Electronics*, Vol. 22 (1990) pp. 391-416.
- [2] *IEE Proc. Optoelectronics*, Vol. 143 No. 5 (1996), special issue on guided-wave optics on silicon.

## **Indium Phosphide Photonic Waveguide Devices and their Fiber Pigtailling**

Hans Melchior  
Institute of Quantum Electronics  
ETH-Honggerberg, HPT  
CH-8093 Zurich  
Switzerland  
Phone: ++41-1-633-2101  
Fax: ++41-1-633-1109  
[h.melchior@iqe.phys.ethz.ch](mailto:h.melchior@iqe.phys.ethz.ch)

Indium phosphide photonic waveguide devices, including laser-diodes, semiconductor optical amplifiers, modulators, switches and wavelength converters evolve in fiber optical communications. While high performance leads to minimization of their optically active areas, efficient coupling to optical fibers and fiber-arrays demands monolithic beam expanders and automatic chip-to-fiber alignment techniques.

## Commercialization Timescales for Photonic Integration

Philip J. Anthony

Lucent Technologies

Room 1E-302, 700 Mountain Avenue, Murray Hill NJ 07974

(908) 582-4091, fax (908) 582-4868, pja@lucent.com

Looking at the present scale of optical integration compared to the grand vision (Refs. 1-5) of a photonic version of electronic ICs, one finds that commercial photonic devices are trailing silicon devices by six orders of magnitude. There are a few limited functionality devices with hundreds of connections such as photonic switch arrays in polymer or lithium niobate waveguide technology, a few truly integrated components with a small number of elements such as circuits for fiber-optic gyroscopes, and several other two-component integration products such as electro-absorption-modulated lasers. The commercial acceptance of these initial devices should now begin to unleash an economical route to higher levels of integration. The doubling time for the scale of integration could become a relevant metric to track in the photonics industry.

The speed of the future commercialization of integrated photonic devices should be predictable based on the rate of introduction of other new technologies, both in photonics and in other fields. The economics of constructing a high-technology business (Ref. 6) are remarkably independent of the underlying technology. To start up a business with a yearly revenue level of a given magnitude, it takes roughly an initial investment of that same order of magnitude. With the overall photonics market (Ref. 7) of \$7B growing at  $\sim 20\%$  per year, a new integrated device will become a significant segment ( $> 1\%$ ) of the market only with an initial investment of many millions of dollars. The business can grow thereafter without further infusions of money only at a rate that is some small multiplier times its profitability level (generally  $\sim 10\text{-}20\%/yr$ ). With the rapid changes experienced in photonics technology, the risk for any such investment in a new technology is high, but is generally less for an established operation. Thus, extensions of existing technology and hybrid integration using previous investments are often less risky until an initial foray into integration is successful. Then the advantages of integration (size, cost, and complexity) can rapidly produce a sustainable advantage.

A review of earlier R&D in integrated photonics (Refs. 8-9) reveals only about a  $\sim 10\%$  success rate of reporting on work that subsequently followed a significant commercial path on 9-year and 4-year time scales, with a similar percentage that still shows obvious promise. One example of how it is often easier to commercialize a hybrid integration of a particular function than to push a full monolithic integration is exemplified by optical amplifiers. Work on semiconductor amplifiers was making slow but steady progress as an essential building block component for integrated photonic circuits, but was overtaken by fiber amplifiers. The separation of the amplifier functions into easily manufactured parts allowed immediate implementation of much higher performance amplifiers, overcoming obvious deficiencies in size, power, complexity, and presumed ultimate manufacturing cost.

Semiconductor lasers for telecommunications have successfully begun the first step of commercial integration – not as perhaps expected as a laser with a built-in monitor detector, but rather with a separate modulator. These electro-absorption-modulated lasers represent the fastest growing segment of the laser market due to their use in high-speed DWDM systems and now constitute more than 1 % of the photonics market.

Competing with electro-absorption-modulated lasers for high-speed DWDM transmission are lithium niobate modulators. Although the technology has been ready for commercialization for more than 15 years, it is only in the last few that lithium niobate modulators have achieved a significant share of the photonics market. A large fraction of the modulators are now produced incorporating the first stages of integration: phase modulators (to lessen the effects of fiber non-linearities) and attenuators.

Lithium niobate switch arrays, and similar polymer switch arrays, are finding use in optical networking systems. They are already sold as components with on the order of one hundred switches, which meets the needs of systems with only a few fibers and a few wavelengths. However, as the scale of optical networking continues to grow, the limits of the present switch technology will soon be reached. The challenge, therefore, is to innovate at a sufficient rate to expand the limits faster than the needs of commercial optical networks.

Silicon optical bench technology was developed specifically for photonic integration and has now achieved one of its goals with the acceptance of waveguide grating routers for DWDM systems. The extension of those systems in just three years from 8 to 16 to 80 channels was enabled by (but also fueled) the integration of silica waveguides on silicon. The small scale hybrid integration of lasers and detectors with silicon optical bench components for telecommunication access markets may soon fulfill the technology's other original goal.

Parallel-fiber-optic links offer a natural commercial outlet for arrays of lasers and photodetectors, perhaps integrated with driver and receiver electronics, but do not strictly integrate much on a photonic level.

The exponential advance of electronics technology as exemplified in the scale of transistor integration, in computer operations per second, and in LAN bandwidth is mirrored in the similar advance of bandwidth for telecommunications systems. If photonics technology can successfully build in additional functionality via integration, then the commercialization already begun should lead to similar doubling times for the scale of photonic integration.

#### References:

1. R. Shubert and J. H. Harris, "Optical surface waves on thin films and their application to integrated data processors," *IEEE Trans. Microwave Theory and Techniques* MTT-16 (12), 1048-1054 (1968).
2. S. E. Miller, *Integrated Optics: An Introduction*, "Bell System Tech. J." 48 (7), 2059-2069 (1969).

3. T. Tamir (ed.), Integrated Optics, 2<sup>nd</sup> edition, Topics in Applied Physics, Vol. 7, (Springer-Verlag, New York, 1979).
4. L. D. Hutcheson (ed.), Integrated Optical Circuits and Components, (Marcel Dekker, New York, 1987).
5. R. G. Hunsberger (ed.), Integrated Optics, 4<sup>th</sup> edition, (Springer-Verlag, New York, 1995).
6. G. D. Hutcheson and J. D. Hutcheson, "Technology and economics in the semiconductor industry," *Scientific American*, 54-62 (January 1996).
7. R. V. Steele, "The worldwide top fifty optoelectronics firms," *Laser Focus World*, 62-65 (December 1997).
8. M. R. Papuchon, A. Carencio, and D.B. Ostrowsky (eds.), 5<sup>th</sup> European Conference on Integrated Optics: ECIO'89, SPIE Vol. 1141 (SPIE, Bellingham WA, 1989).
9. Integrated Photonics Research, 1994 Technical Digest Series, Vol. 3 (Optical Society of America, Washington, DC, 1994).

**Integrated Photonics Research**

# **Beam Propagation Methods**

**Monday, March 30, 1998**

**G. Ronald Hadley, Sandia National Laboratories**  
Presider

**IMB**

**11:00am–12:30pm**

Salon B

# Beam Propagation Method For Simulation of Optical Waveguides:

## Theory, Algorithm and Application

Wei-Ping Huang, Chenglin Xu, Kang Li\*, S. K. Chaudhuri  
 Department of Electrical and Computer Engineering, University of Waterloo  
 Waterloo, Ontario N2L 3G1 Canada, Email: [wphuang@maxwell.uwaterloo.ca](mailto:wphuang@maxwell.uwaterloo.ca)

\*On leave from Dept. of Electronics, Shandong University, Shandong, P.R. China

Since the pioneer work of Feit and Fleck [1], the beam propagation method (BPM) has proved to be a powerful method for simulation of optical waveguides. Aside from the tremendous improvement in computing power, cost and accessibility, progress in theoretical formulations, numerical algorithms, as well as user-friendliness have advanced the capability of this numerical method and brought it into the design process of a wide range of guided-wave photonic devices. In this presentation, we will give a critical review about the recent progress in development of the beam propagation method for simulation of optical waveguides. In particular, we will discuss both theoretical and practical issues that are relevant to the applications of this method for computer-aided design of photonic devices and circuits.

### 1. Scalar and Vector formulations:

The scalar formulation based on the scalar Helmholtz equation is only an approximation to the electromagnetic fields and waves in optical waveguides, but self-consistent. The accuracy and scope of validity for the scalar formulations have been studied extensively in the context of circular fibers as well as planar waveguides [2,3]. To overcome the limitation of the scalar formulation, a number of semi-vector and full-vector formulations have been proposed and demonstrated in the beam propagation method [4,5]. Consequently, the polarization dependence and the hybrid nature of the electromagnetic fields are considered by the vector beam propagation method (VBPM); this is a definite advantage over the scalar BPM. On the other hand, however, the self-consistency and the scope of validity for these vectorial formulations are less clear as they are in most cases derived under certain approximations. For instance, the semi-vector formulations are based on either single transverse electric field component or single transverse magnetic field component, which have no apparent links with each other under the semi-vector approximation. Also, the accuracy and validity for the approximations made in the full-vector formulations based on the transverse electric or magnetic fields are yet to be investigated, especially in the case of wide-angle propagation [6]. Furthermore, it appears that there are inherent difficulties with the vectorial formulations due to the neglect of the backward propagating wave [7]. Recently, a new algorithm to solve the Maxwell's equations directly in frequency domain was proposed and demonstrated [8]. But questions still remain as to the viability of this approach for the full-vector wave simulation.

### 2. Paraxial, wide-angle and reflective algorithms

Methods such as the Taylor expansion [9], the Pade approximant [10], and Lancos reduction [11] have been proposed to solve the one-way wave equation or the Helmholtz equation. With these wide-angle algorithms, the critical dependence on the choice of the reference index is relaxed, accurate simulation for multi-mode and/or off-axis wave propagation can be simulated accurately. Furthermore, the wide-angle algorithms have been applied in the semi-vector [12] and the full-vector [13] BPM.

The one-way formulations are valid only if the index discontinuities or variation along the direction of wave propagation are small and/or do not constitute the Bragg conditions so that the reflected waves can be neglected. To overcome this limitation, several reflective algorithms have been proposed and developed:

- (1) the time-domain approach such as the finite-difference time-domain (FDTD) technique [14,15] and the slowly-varying temporal envelope (SVTE) method [16,17];
- (2) the frequency-domain approach such as the solution of Helmholtz equation [18];
- (3) the bi-directional BPM based on the mode-expansion [19], the split-step FFT [20], and the finite-difference [21,22] techniques.

The time-domain approach is straightforward, but time-consuming whereas the frequency-domain approach is more difficult to implement and potentially more efficient. If the reflections generated in the waveguides have short lifetime and do not lead to resonance, the bi-directional BPM is the most efficient. Another challenge for the reflective algorithm is that the reflection in optical waveguides is usually small, therefore high degree of accuracy is necessary. Given the fact that the current optical waveguides are relatively long relative to wavelength, it seems to be impractical to expect that the full-wave reflective algorithms can be applied to the simulation of the entire waveguides. For this reason, a combination of the one-way and the reflective algorithms might be a good approach. One such approach by combination of FDTD and BPM was demonstrated lately [23].

### 3. Novel numerical solution techniques:

A wide range of powerful techniques to solve the governing equations for the different formulations have been developed and reported [24]. For the sake of discussion, we may group the different approaches into the explicit and the implicit schemes. The explicit schemes are simple, efficient, conditionally stable/consistent and non-dissipative, whereas the implicit schemes are more complicated, perhaps less efficient, but unconditionally stable and dissipative. Recently, a novel BPM based on Douglas scheme has been demonstrated, which significantly improves the efficiency of the implicit scheme [25,26]. So far, this technique has only implemented for the scalar formulations and its extension to the vector formulations appears to be nontrivial and yet to be realized.

A disadvantage of the finite-difference method is its inherent rectangular mesh discretization, which is often not consistent with waveguide geometry such as bends, curves and tapers. To overcome this limitation, a number of conformal mapping and/or coordinate system transformation have been proposed and shown significant improvement [27-29]. It, however, remains a challenge to incorporate these schemes into the general-purpose BPM simulation tools to treat variety of complex waveguide structures.

### 4. Novel numerical boundary conditions

Numerical boundary conditions are key elements for numerical methods such as the BPMs. The most commonly used boundary condition is the transparent boundary condition (TBC) [30]. While the TBC is quite successful for the paraxial and lower-order wide-angle algorithms, it still

experiences difficulties with the wide-angle BPM. A novel boundary condition, namely, the perfect matched layer (PML) boundary condition originally introduced for the FDTD method [31], has been implemented for BPM [32]. In fact, the TBC and the PML can be combined to provide a highly effective numerical boundary condition in various BPM algorithms.

#### Reference:

- 1) M. D. Feit and J.A. Fleck Jr., *Appl. Opt.*, vol.17, pp.3990-3998, 1978.
- 2) W. Snyder and J. D. Love, *Optical Waveguide Theory*, Chapman & Hall, London, 1983.
- 3) Vassollo, *Optical Waveguide Concept*, Elsevier, Amsterdam, 1991.
- 4) W.-P.Huang, C.-L.Xu, S.T.Chu and S.K.Chaudhuri, *J. Lightwave Technol.*, vol.10, pp.295-305, 1992.
- 5) W.-P.Huang and C.-L.Xu, *IEEE J. Quantum. Electron.*, vol.29, pp.2639-2649, 1993.
- 6) Mansour, A. D. Capobianco, and C. Rosa, *J. Lightwave Technol.*, vol.14, pp.908-913, 1996.
- 7) Vassollo, *Electron. Lett.*, vol.33, pp.61-62, 1997.
- 8) T. Shintaku, *Opt. Lett.*, vol.21, 1996.
- 9) Y. Chung and N. Dagli, *IEEE Photon. Technol. Lett.*, vol.6, pp.540-542, 1994.
- 10) G. R. Hadley, *Opt. Lett.*, vol.17, pp.1426-1428, 1992.
- 11) R. Ratowsky and J. A. Fleck. Jr., *Opt. Lett.*, vol.16, pp.787-789, 1992.
- 12) W.-P.Huang, C.-L.Xu and S.K.Chaudhuri, *IEEE Photon. Technol. Lett.*, vol.3, pp.1117-1120, 1991.
- 13) F.Ma, C.L.Xu, W.-P.Huang, *IEEE Pro. J. Optoelectron.*, vol.143, pp.139-143, 1996.
- 14) S.T.Chu and S.K.Chaudhuri, *J. Lightwave Technol.*, vol.5, pp.2033-2038, 1989.
- 15) W.-P.Huang, S.T.Chu, A.Goss, and S.K.Chaudhuri, *IEEE Photon. Technol. Lett.*, vol.3, pp.524-526, 1991.
- 16) P.L.Liu and F.S.Choa, *IEEE Photon. Technol. Lett.*, vol.7, pp.890-892, 1995.
- 17) G.Jin, J.Harari, J.P.Vilcor and D.Decoster, *IEEE Photon. Technol. Lett.*, vol.9, pp.348-350, 1997.
- 18) G.R.Hadley, *Opt. Lett.*, vol.19, pp.84-86, 1994.
- 19) J.Willems, J.Haes, R.Baets, *Opt. Quantum. Electron.*, vol.27, pp.995-1007, 1995.
- 20) D.Yevick, W.Bardyszewski, B.Hermanson, and M.Glasner, *IEEE Photon. Technol. Lett.*, vol.3, pp.527-529, 1991.
- 21) Y. Chiou and H. Chang, *IEEE Photon. Technol. Lett.*, vol.9, pp.964-966, 1997.
- 22) C.L.Xu, K.Li, W.-P. Huang, W.Lui, K.Yokoyama, *IPR98*, submitted.
- 23) J. Yamauchi, Private communication.
- 24) W.-P. Huang (ed), *Methods for Modeling and Simulation of Guided-Wave Optoelectronic Devices: Part II Waves and Interactions*, EMW Publishing, Cambridge, 1995.
- 25) J. Yamauchi, J.Shibayama, H.Nakano, *IEEE Photon. Technol. Lett.*, vol.7, pp.661-663, 1995.
- 26) M.Rivera, *J. Lightwave Technol.*, vol.13, pp.233-238, 1995.
- 27) P.Sewell, T.M.Benson, T.Anada, P.C.Kenall, *J. Lightwave Technol.*, vol.15, pp.688-696, 1997.
- 28) C.-T.Lee, M.-L.Wu, J.-M.Hsu, *J. Lightwave Technol.*, vol.15, pp.2183-2189, 1997.
- 29) G.R.Hadley, *IEEE J. Quantum. Electron.*, vol.28, pp.363-370, 1992.
- 30) J.P.Berenger, *J. Computation. Phys.*, vol.114, pp.185-200, 1994.
- 31) W.-P.Huang, C.-L.Xu, W.Lui, and K.Yokoyama, *IEEE Photon. Technol. Lett.*, vol.8, pp.649-651, 1996.

# Beam-Propagation Method Benchmark Test: Symmetrical Coupler and Gain-Loss Waveguide

H.-P. Nolting\*, M. Gravert\*, H. J. W. M. Hoekstra#, R. Stoffer#, G. J. M. Krijnen#, C. Sibilis+, M. de Minicis+, R. Pregla&, O. Conradi&

(\*) Heinrich-Hertz Institut für Nachrichtentechnik Berlin GmbH, Einsteinufer 37, 10587 Berlin, Germany, +(4930) 31002 427 (nolting@hhi.de), (#) University of Twente, MESA Research Institute, Enschede, The Netherlands, (+) University Degli Studi Di Roma „La Sapienza“, Dipartimento Di Energetica, Via A. Scarpa, 00161 Roma, Italy, (&) Fernuniversität, Hagen, Germany

## Motivation

The Beam Propagation Method (BPM) is an established technique to simulate the propagation of the optical field in integrated optical circuits including optical waveguides composed of active (with gain) and lossy media. Members of the COST 240 project „Techniques for Modelling and Measuring Advanced Photonic Telecommunication Components“, Working Group 2, have been engaged in the past in the development and investigation of two benchmark tests for the accuracy of BPM algorithms<sup>1</sup>. This new BPM benchmark test is complementary to the two tests published earlier. It is focused on the discretization and the interface problem of BPMs especially for waveguides with gain or loss. For the first time, the accuracy of BPM calculations of couplers with and - for comparison - without an imaginary part of the refractive index are investigated. As done in the earlier benchmark test, we restrict the tests to two dimensional beam propagation, i.e. to beam propagation starting from a one dimensional cross section. In the earlier benchmark test we have discussed the strong influence of the choice of the right reference refractive index, the advantages of transparent boundary conditions and of wide angle BPMs. Here we will focus on the investigation of the accuracy of different discretization schemes, which have been developed for waveguide structures with abrupt transitions of the refractive index at arbitrary positions relative to the BPM-grid.

## Definition of the benchmark tests

As device under test for this benchmark test, two devices with well known accurate (numerical) solutions have been chosen. Two couplers will be compared: a passive symmetrical directional coupler (Sym DC) and a waveguide with a balance between loss and gain (GL WG), which are defined in Figure 1. In both cases the spectral behaviour can be calculated semi-analytical using well known eigenmode solvers<sup>1</sup>. We focus on the beatlength behaviour of both devices and compare the results of different BPM algorithms with the eigenmode solution.

- The calculation of the passive Sym DC is straightforward. Propagating an eigenmode of the input waveguide along the coupler structure leads to a beating of the coupler eigenmodes and the beatlength  $\Lambda$  can be determined. Here we investigate the accuracy of the calculation of the beatlength  $\Lambda$ .
- The dispersion diagram of the GL WG as a function of the imaginary part of the refractive index, which is a function of the loss or gain parameter  $\alpha$  has been investigated earlier<sup>2</sup>. The dispersion curves have a particular behavior at  $\alpha_1 = 2725,67 \text{ cm}^{-1}$ , where a second order mode appears, and  $\alpha_{\text{branch}} = 5226.3023 \text{ cm}^{-1}$ , which is a branching point for  $N_{\text{eff}}$  curves. For values of  $\alpha < \alpha_1$  the waveguide is *single-mode* and the mode propagates without loss or gain. In the interval  $\alpha_1 < \alpha \leq \alpha_{\text{branch}}$  the waveguide supports two complex but *lossless* modes with *real* effective refractive indices. Finally, for values of  $\alpha > \alpha_{\text{branch}}$ , the two modes have mutually complex-conjugate effective indices. Here we will focus on the beatlength behaviour in the region of  $\alpha_1 < \alpha \leq \alpha_{\text{branch}}$ , which can be used to extrapolate the branching point  $\alpha_{\text{branch}}$  from the zero of the  $1/\Lambda^2(\alpha)$ -plot.

## Influence of the discretization scheme on the accuracy

Fig. 2 shows the step function of the imaginary refractive index of the GL WG and its digital representation on the equidistant grid  $x_i$ . For such simple structure as the GL WG the grid can be chosen in an optimal configuration by putting the step function in the middle between two  $x_i$  values. This is not possible for a more sophisticated geometry like the Sym DC. Thus an uncertainty from  $w - dx/2 < w_x < w + dx/2$  is obvious. A more accurate result can be accomplished by decreasing the  $dx$  intervall. Because the window has to be kept constant, the number of discretization points and the calculation effort has to be increased. Therefore different methods are in use to get reasonably accuracy with a low number of discretization points. Among them there are: (i) adaptive mesh size<sup>1</sup>, (ii) different implementations of efficient boundary conditions<sup>1,3</sup> and (iii) rounding or smoothing the step refractive index. All these methods have the objective to introduce the precise position of the step function, which may be described by  $x_j + q \cdot dx$  with  $0 < q \leq 1$  (see Figure 2 (b)) into the algorithm.

We can divide the methods contributed to this investigation<sup>1</sup> in three classes: Fourier Transform BPM, FD BPM and eigenmode propagation methods like MoL and BEP. The results of Fourier Transform BPM are quite far away from the semi-analytic values. This can be attributed to the fact that FFT BPM is not very suitable for guides with large index differences. Results from FFT BPM are neglected here. Finite difference (3-point and 5 point FD Operator) BPM with third order SVEA correction Pade (3,3) and efficient interface conditions<sup>1</sup> have been used by University Twente. HHI has used FE/FD BPM with a rounding algorithm for the refractive index profile. Fundamentally, the MoL (used by U Hagen and U Roma) is an eigenmode propagation method. The difference to BEP is the discretization in lateral direction. Thus for large values of  $dx$ , we expect similar behaviour as in case of FD BPM. BPM with an adaptive mesh size is missing in this contribution. BEP results are dropped, because they are identical with the result of eigenmode solvers, which are used as a reference.

The methods to handle the interface conditions are all described in the literature<sup>1</sup> and will not repeated here. For better understanding the fundamental problems a very simple method will be described here. HHI prefers a rounding or smoothing

algorithm for the refractive index prior to the ordinary FD/FE BPM calculation (see Figure 2 (a)). Here the convolution-integral

$$\varepsilon(x_j) = \int_{x_j-dx}^{x_j+dx} g(\xi, x_j) \varepsilon(\xi) d\xi \quad \text{between the dielectric constant } \varepsilon = (n_{WG} + j \cdot n'')^2 \quad \text{and a cosin slit function}$$

$$g(\xi, x_j) = \frac{1}{2 \cdot dx} \left( 1 + \cos \left[ \pi \frac{\xi - x_j}{dx} \right] \right) \quad \text{with the width } 2dx \text{ (see Figure 2 (b)) is used.}$$

## Results and Discussion

Figure 3 shows the results for some methods studying the interface conditions for a moderate grid width of  $dx=50\text{nm}$ . To prove the influence on the accuracy, we have shifted the grid relative to the actual device in small steps (variation of  $q$  between zero and unity).

- In the case of *not* taking care of the exact position one gets wrong results. The symmetric coupler will be modelled as an asymmetric coupler with an asymmetry of  $\delta/\kappa = 1.7$  in the worst case. Using the quasi-analytic solution of the branching point of the gain-loss waveguide, we can estimate from the uncertainty interval the variation of the  $\alpha_{branch}$  value will range from 5060 to 5420.
- The usage of interface conditions leads to reasonably accurate results for the Sym DC, which are close to the exact value. But for the GL WG a variation of  $\Delta\alpha_{branch}$  in the order of  $\pm 10$  for the MoL (U Hagen) and (80 ... 92) for FE/FD BPM (HHI) has been found.

Figure 4 shows the behaviour for decreasing  $dx$ -values. All methods show a good convergence to the neighbourhood of the exact value for very low  $dx$  (number of grid points a few thousand). For moderate values of  $dx=50\text{nm}$  FD BPM with a 5-point operator shows superior accuracy for both devices. The rounding of the refractive index profile is useful for passive waveguide structures ( $dx=50\text{nm}$ ), but not for waveguides with an imaginary part of the refractive index. In any case, to be sure on the accuracy of a calculation the convergence behaviour has to be proved for low  $dx$ , as is demonstrated in Fig. 4. The best approximation can be extrapolated from those curves using a numerical fit for  $dx$  converge to zero.

## Conclusion

The accuracy of different BPM algorithms have been investigated with the help of two new benchmark tests based on a symmetrical directional coupler and a waveguide with a balance of gain and loss. In both cases the spectral behaviour can be calculated semi-analytically as a reference using well known eigenmode solvers. Important results are:

- Accurate BPM calculation for waveguides with an *imaginary part of the refractive index* need low grid values  $dx$  in the order of a few nm.
- Operators based on 5-point algorithms have a much higher accuracy then 3-point operators. This is true for both FD BPM and MOL.
- Algorithms which include an efficient interface handling like FD BPM from U Twente or MoL from U Hagen have higher precision for larger  $dx$ -values.
- To be shure on the accuracy of a calculation, the convergence behaviour has to be proofed for a series decreasing  $dx$ -values. The best approximation can be extrapolated from those curves using a numerical fit for  $dx$  converging to zero.

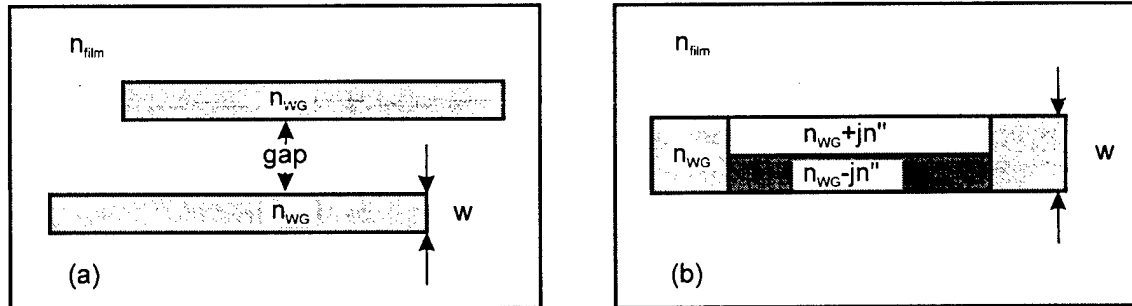


Fig. 1: Two devices are under test (a) symmetrical coupler and (b) the gain-loss waveguide. The refractive indices  $n_{WG}=3.252398$ ,  $n_{film}=3.169355$  and the wavelength  $\lambda=1,550 \mu\text{m}$  are common to both structures. In case of the passive symmetrical coupler (a) the widths are  $w=1,02555 \mu\text{m}$  and  $gap=1,555 \mu\text{m}$ . The gain-loss waveguide has a total width of  $w=1,000 \mu\text{m}$  and is composed of two layers with mutually complex conjugate refractive indices  $n''(\alpha) = \alpha \lambda / 4\pi$ . The imaginary parts vary in a very broad range: in terms of the power absorption (gain) coefficient  $\alpha$ , between zero and  $\pm 10^4 \text{ cm}^{-1}$ .

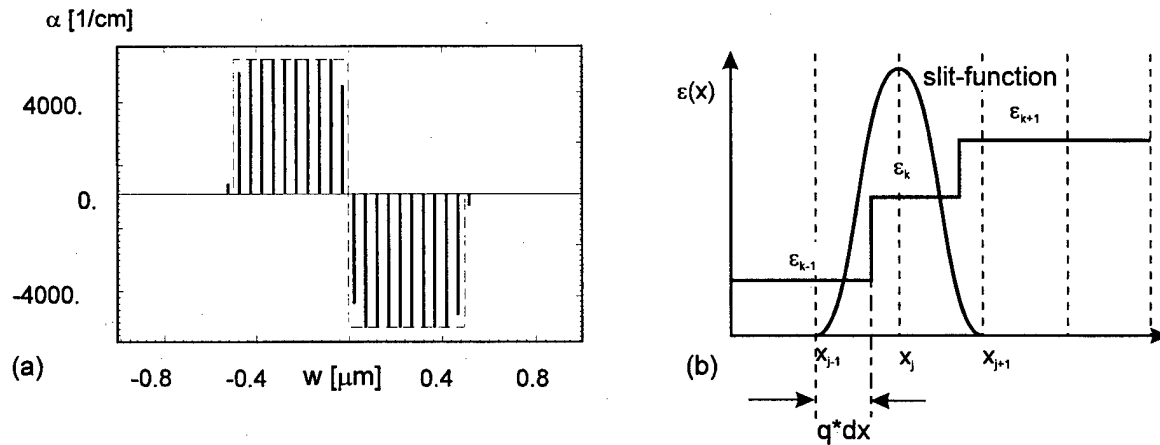


Fig. 2: Example of a discretization method. The original refractive index profile is shown in (a) as a dashed line. The straight lines of (a) shows the imaginary part of the gain-loss waveguide using a convolution with a slit function as is sketched in (b): used is a cosin-slit function for step-wise constant refractive index waveguides.

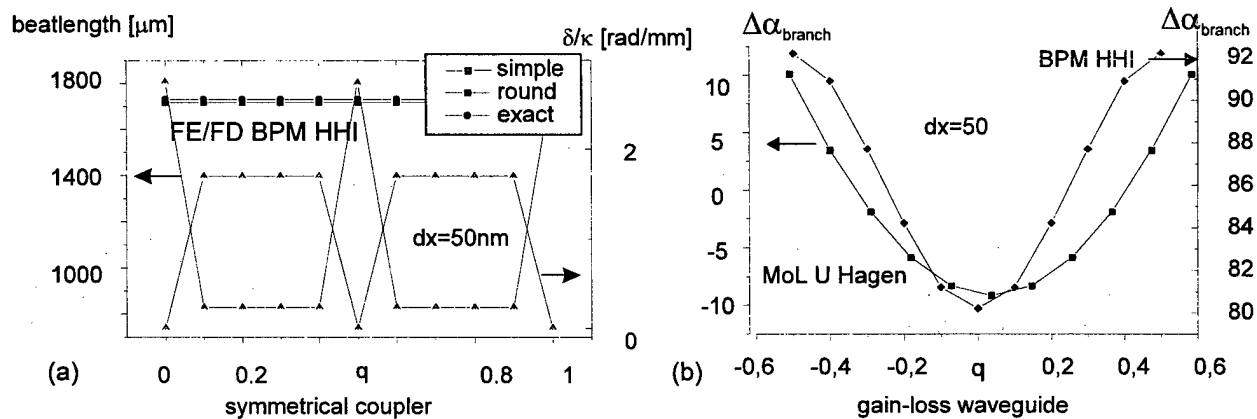


Fig. 3: Comparison of results for different relative positions between the test device and the grid (shift  $q$ ) for  $dx=50nm$ . (a) shows predominantly wrong results (asymmetrical instead of symmetrical coupler) for the simple BPM and fairly good coincidence with the exact value for rounded refractive index profile and MoL (not shown here). (b) shows strong variations of the  $\alpha_{branch}$  value as a function of  $q$ .

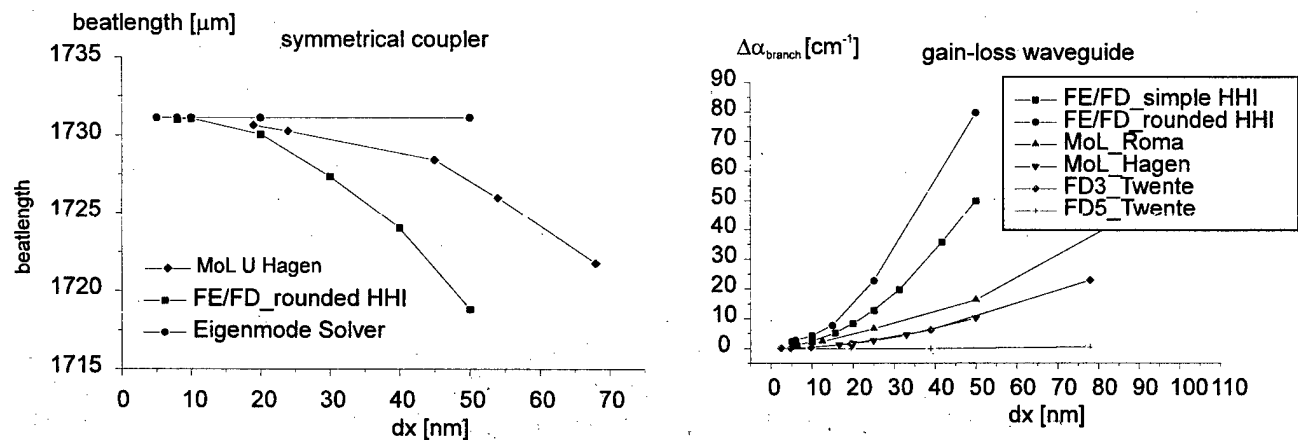


Fig. 4: Convergence behaviour for decreasing  $dx$ -values. All methods show a good convergence to the exact  $\alpha_{branch}$  value.

<sup>1</sup>H.-P. Nolting and R. März, "Results of Benchmark Tests for Different Numerical BPM Algorithms," *IEEE J. Lightwave Technology*, vol.13, No.2, pp.216–224, 1995

<sup>2</sup>H.-P. Nolting, M. Grawert, G. Sztefka and J. Ctyroky, "Wave propagation in a waveguide with a balance of gain and loss", IPR '96, Integrated Photonics Research '96, April 29 - May 2, 1996, Boston, Ma, USA, Technical Digest Series Vol 6, pp. 76-79

<sup>3</sup>S. Helfert, R. Pregla "Finite Difference Expressions for Arbitrarily Positioned Dielectric Steps in Waveguide Structures", *IEEE Journal of Lightwave Technology*, vol 14, No. 10, Oct. 96, pp. 2414–2421.

## A novel beam propagation algorithm for three dimensional tapers

P Sewell, S Sujecki, T M Benson and P C Kendall: Department of Electrical and Electronic Engineering, University of Nottingham, Nottingham NG7 2RD, UK.

### Introduction

Finite difference beam propagation methods (FD-BPM) have received considerable attention in recent years as one of the few viable ways of simulating the performance of a wide variety of complex optical structures, [1-3]. The disadvantages of BPM are its long calculation time and its nonphysical staircasing of tilted waveguides, curves and tapers. The latter problem necessitates the use of a fine mesh to avoid the resultant numerical "noise" becoming significant, especially when the staircasing occurs at a semiconductor-air interface. This noise not only compromises the accuracy of the simulation but, for the 3D case which usually relies upon iterative linear equation solvers, can also significantly increase the calculation time. This is because the number of iterations required to determine the field at the present propagation step from that of the previous one, depends upon the "smoothness" of the field evolution.

The present authors have previously demonstrated that the use of nonorthogonal coordinate systems chosen to avoid staircasing, yields significant improvements in performance over the conventional rectangular coordinate BPM. Substantial accuracy and calculation gains have been reported for a variety applications including, tilted waveguides, Y-junctions, curves and 2D tapers [4-7]. The present paper presents a novel algorithm for modelling fully 3D tapered waveguides that combines two nonorthogonal coordinate systems, the tapered and the oblique, in a manner that eliminates staircase approximations and thus numerical noise. Further features of the approach are that it overcomes the difficulty associated with the origin of the tapered coordinate system and is simple to interface with the conventional rectangular coordinate BPM, allowing the optimal system to be used for simulating each part of the structure.

### Theory

The application of the novel algorithm is illustrated by a scalar analysis of the 3D rib waveguide taper shown in figure 1. Figure 2 shows the combined tapered and oblique coordinate system used to describe the geometry of the taper, along with the conventional rectangular coordinates used to describe the input and output guides. Clearly the sidewalls of the rib are exactly modelled without staircasing. In the event that the rib width is tapered down to zero, it is clear that the tapered coordinates alone would be inadequate for representing the field, however, the inclusion of the oblique system overcomes this problem. It is noted that both the tapered and the oblique algorithms are simultaneously stepped forward on planes of constant  $z$ . Figure 3 shows the transverse coordinate variables. In the tapered system, the transverse coordinate variable is  $t$ , which is the tangent of the angle made by the coordinate line with the  $x=0$  axis.  $t_0$  indicates the coordinate line following the side of the taper which is also where the oblique coordinate system takes over. In the latter, the transverse coordinate lines are all parallel to the side of the taper and are characterised by the variable  $u$ , the distance from the taper side in the  $x$  direction. It is simple to show that the paraxial scalar wave equation in the nonorthogonal tapered and oblique systems can be expressed as;

$$\left[ \frac{\partial^2}{\partial z^2} - \frac{2t}{z} \frac{\partial^2}{\partial z \partial t} - 2j\beta \frac{\partial}{\partial z} + \frac{1}{z^2} \frac{\partial}{\partial t} (1+t^2) \frac{\partial}{\partial t} + \frac{\partial^2}{\partial y^2} + 2j\beta \frac{t}{z} \frac{\partial}{\partial t} + k^2 - \beta^2 \right] \psi(t, z) \quad (1)$$

$$\left[ \frac{\partial^2}{\partial z^2} - 2t_o \frac{\partial^2}{\partial z \partial u} - 2j\beta \cos(\theta_o) \frac{\partial}{\partial z} + (1+t_o^2) \frac{\partial^2}{\partial u^2} + \frac{\partial^2}{\partial y^2} + k^2 - \beta^2 \right] \psi(u, y, z) = 0 \quad (2)$$

respectively, where  $\beta$  is an imposed propagation constant chosen to allow the envelope  $\psi$  to be a slowly varying function of  $z$ . Both of these expressions are straightforward to discretise in both  $z$  and the transverse variable,  $t$  or  $u$ , producing a simple finite difference BPM algorithm.

At the interface between the two coordinate systems, it is necessary to interpolate and this is illustrated in figure 3. The directly sampled field values used in the algorithm are shown as solid points, but to evaluate the wave equation in the tapered coordinates at points lying along the line between the two systems, the field values at the empty points are required and these are found by simple linear interpolation. It is noted from figures 2 and 3 that these points always fall between the first two coordinate lines of the oblique system thus simplifying the interpolation.

To demonstrate how the novel algorithm eliminates numerical noise, a simple embossed rib taper has been simulated and the results compared to those from a conventional rectangular coordinate BPM algorithm. The rib is of height  $1\mu\text{m}$  and its width tapers from  $3\mu\text{m}$  to  $1\mu\text{m}$  over a distance of  $100\mu\text{m}$ . The rib and substrate indices are 3.44 and 3.40 and the wavelength is  $1.15\mu\text{m}$ . The mesh sizes,  $\Delta x$  and  $\Delta y$  at the start of the taper are both  $0.05\mu\text{m}$  and the propagation step size,  $\Delta z$ , is  $1\mu\text{m}$ . Figure 5 shows the field profile on the  $x$ - $z$  plane  $0.25\mu\text{m}$  under the base of the rib. Advantage has been taken of symmetry so that only half of the waveguide cross-section is modelled. It is clear that, whilst the two algorithms produce the same large scale field profiles, the profile obtained from the conventional algorithm is numerically very noisy, whereas as that from the novel algorithm is significantly less so. As the mesh size and step length are reduced, both sets of results converge. However, as illustrated, the novel algorithm converges much more rapidly and thus produces accurate results for less computational effort.

## References

1. W Huang, C Xu, S-T Chu and S K Chaudhuri, "The finite-difference vector beam propagation method; analysis and assessment," *IEEE Journal of Lightwave Tech.*, vol 10, 1997, pp 295-305.
2. Y Chung and N Dagli, "An assessment of finite difference beam propagation method", *IEEE J. Quantum Electron.*, vol 26, 1990, pp 1335-1339.
3. B Hermansson, D Yevick and P Danielson, "Propagating beam analysis of multimode waveguide tapers", *IEEE J. Quantum Electron.*, vol 19, 1983, pp 1246-1251
4. T Anada, T M Benson, P Sewell and P C Kendall, "Oblique wide angled beam propagation", Proc. OSA/IEEE Integrated Photonics Research Tech. Digest, Boston, 1996, pp 119-121.
5. P Sewell, T M Benson, P C Kendall and T Anada, "Tapered beam propagation", *Electronics letters*, vol. 32, no 11, 23rd May 96, pp 1025-6.
6. P. Sewell, T Anada, T M Benson and P C Kendall, "Non-standard propagation", *Microwave and Optical Technology Letters*, vol 13, no 1, pp 24-26, Sept 96.
7. P Sewell, T M Benson, T Anada and P C Kendall, "Bi-oblique propagation analysis of symmetric and asymmetric Y-junctions", *IEEE Journal of Lightwave Tech.*, vol 15, no 4, April 97, pp 688-696.

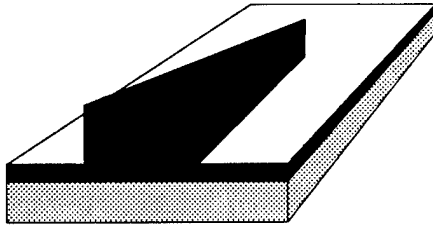


**Figure 1:** A typical 3D taper propagation problem

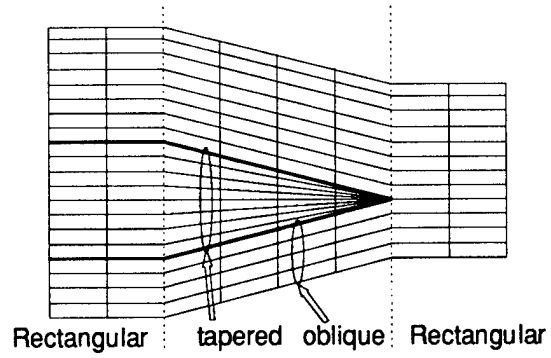


**Figure 2:** The nonorthogonal coordinates used to avoid staircasing

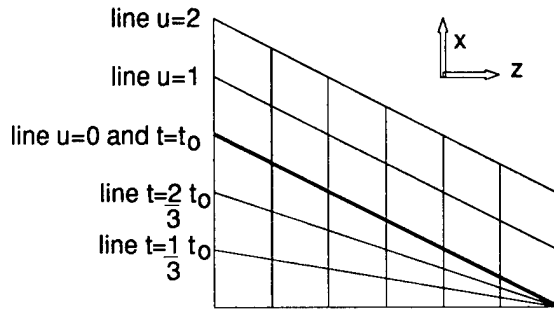


**Figure 3:** The tapered and oblique coordinate variables

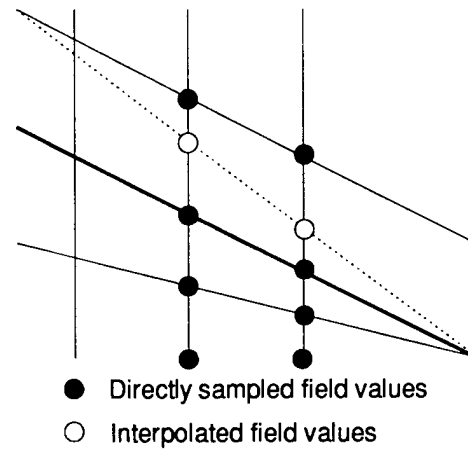
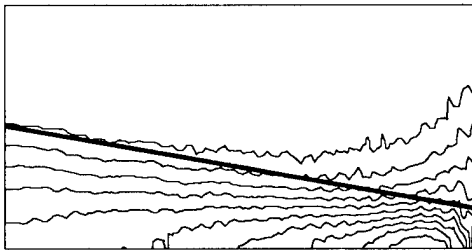
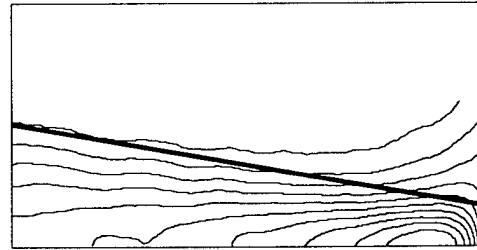


**Figure 4:** Interfacing the tapered and oblique coordinates



(a)



(b)

**Figure 5:** Field profiles in the x-z plane  $0.25\mu\text{m}$  under the base of an embossed rib taper. The details of the structure are given in text. a) conventional rectangular BPM b) the novel BPM.

# Beam Propagation Method Using Local Oblique Coordinate Systems

Yih-Peng Chiou and Hung-chun Chang

College of Electrical Engineering, National Taiwan University,

Taipei, Taiwan 106-17, Republic of China

Phone: +886-2-23635251 ext. 513 Fax: +886-2-23638247

E-mail: hcchang@cc.ee.ntu.edu.tw

## I. Introduction

The beam propagation method (BPM), originally derived from the scalar Helmholtz equation under the paraxial approximation, has been widely used in the investigation of optoelectronic waveguide devices. Later, vectorial and wide-angle formulations were developed. A comprehensive review can be found in [1].

To apply the most current BPMs, developed in the rectangular coordinate system (RCS), to the  $z$ -dependent structures, we need to make staircase approximation. Consequently, small meshes must be employed to minimize the discretization error, which requires large memory and much computation time. For some tilted waveguides with parallel interfaces, BPMs using an oblique coordinate system (OCS) were developed and they worked much better than the RCS-BPMs [2]–[4]. However, the applications of OCS-BPMs are restricted to structures with interfaces parallel to the axes of the OCS. They are thus not suitable to treat such frequently encountered structures as tapered waveguides.

To alleviate such restriction, we propose a BPM derived from the local oblique coordinate (LOC) system, which is called LOC-BPM. Instead of using a global OCS, a local OCS is defined for every sampled point and thereafter all local OCSs are combined into a global ensemble. Because the  $z$ -dependent interfaces are modelled separately by their corresponding local OCSs, this proposed method not only saves the numerical effort as previous OCS-BPMs in [2]–[4] do, but also is versatile in application to  $z$ -dependent structures. In particular, previous OCS-BPMs can be considered special cases of the LOC-BPM with all the tilted angles being the same, and the RCS-BPMs those with zero tilted angles. Moreover, the power conservation problem [5] of the current BPMs is prevented.

## II. Formulation

Considering an interface with titled angle  $\theta$  from the  $z$ -axis as shown in Fig. 1, we make a coordinate transformation defined by  $\xi = x - z \tan \theta$  and  $\zeta = z$  such that locally the refractive index  $n(x, z) = n(\xi)$ , and hence the staircase approximation is avoided. Under the slowly varying envelope approximation along the interface

$$E(x, z) = \Phi(x, z) \exp[-jk_0 \bar{n}(z \cos \theta + x \sin \theta)], \quad (1)$$

the Helmholtz equation becomes

$$\left\{ \frac{\partial^2}{\partial z^2} + \frac{\partial^2}{\partial x^2} - 2jk_0 \bar{n} \left( \cos \theta \frac{\partial}{\partial z} + \sin \theta \frac{\partial}{\partial x} \right) + k_0^2 [n^2(x, z) - \bar{n}^2] \right\} \Phi(x, z) = 0 \quad (2)$$

where  $k_0$  is the wavenumber in free space and  $\bar{n}$  is the reference refractive index. Making use of the coordinate transformation, (2) in the local OCS comes out to be

$$\left\{ \frac{\partial^2}{\partial \zeta^2} + \sec^2 \theta \frac{\partial^2}{\partial \xi^2} - 2jk_0 \bar{n} \cos \theta \frac{\partial}{\partial \zeta} - 2 \tan \theta \frac{\partial^2}{\partial \xi \partial \zeta} + k_0^2 [n^2(\xi) - \bar{n}^2] \right\} \Phi(\xi, \zeta) = 0. \quad (3)$$

Neglecting  $\partial^2 / \partial \zeta^2$  and taking the central difference scheme as in the RCS-BPMs, the field at the  $s$ -step,  $\Phi^s$ , is expressed in terms of that in the previous step as  $(M^s \Phi^s = M^{s-1} \Phi^{s-1})_L$ , where

$L$  denotes local. Since  $\Phi$ s are functions of local variables in their corresponding OCSs, they are combined through (1) into the global field  $E$ . An ensemble form  $(H^s E^s = H^{s-1} E^{s-1})_G$  similar to the RCS-BPMs is obtained, where  $G$  denotes global, and can be solved efficiently by such techniques as Thomas algorithm. As to the truncated boundary conditions, such algorithms as the TBC [6] and the PML [7] can be applied as in the RCS-BPMs. The wide-angle recurrence relation can also be derived from (3) similarly as in [8] or [9].

### III. Numerical Results

The BPMs using global OCS have been successfully applied to solve tilted waveguides with parallel interfaces in [2]–[4]. The undesirable mode mismatch loss using the OCS-BPMs can be even several order smaller than that using the RCS-BPMs. Besides, this spurious loss using the RCS-BPMs accumulates to significant amount, while that using the OCS-BPMs remains almost constant.

The widely used RCS-BPMs suffer from such an  $L^2$ -paradox [5] that the power conservation is usually taken as  $P_1 = \int |E|^2 dx$ .  $P_1$  may be used in  $z$ -invariant structures but we need a more accurate definition of power,  $P_0 = \text{Re} \int E^* \times H dx$ , in the  $z$ -dependent structures. To demonstrate the applicability of the LOC-BPM, we consider a normal mode in a curved slab waveguide with a sufficiently small curvature for a true adiabatic propagation without radiation leakage, as shown in Fig. 2. The accurate  $P_0(\theta)$  at any  $\theta$  for the normal mode should always be equal to  $P_0(z=0)$ , which would lead to  $P_1(\theta) = \sec\theta P_1(z=0) = P_0(z=0)/\beta \cos\theta$ , after propagating  $z = R \sin\theta$ , where  $\beta$  is the propagation constant of the fundamental mode and  $R$  is the radius of the curved waveguide.

Fig. 3 shows the calculated normalized power  $P_0(z)/P_0(z=0)$  using the RCS-BPM and the LOC-BPM, respectively, for a curved waveguide with radius  $R = 1$  cm, wavelength  $\lambda = 1.55 \mu\text{m}$ , waveguide width  $D = 2 \mu\text{m}$ , core refractive index  $n_{\text{core}} = 1.55$ , and cladding refractive index  $n_{\text{clad}} = 1.52$ , under the fundamental mode incidence. The calculated power using the LOC-BPM remains almost constant and the small deviation ( $< 10^{-4}$ ) is mainly due to the mismatch between the analytical and discretized normal modes. Although the RCS-BPM satisfies the nonphysical  $L^2$  conservation, it gives physical power which decreases with  $\cos\theta$  as the field propagates.

Fig. 4 shows the calculated field distribution as a function of the transverse distance using the LOC-BPM after propagating  $z = R \sin(60^\circ)$ . The cross correlation between the calculated and analytical fields is 0.9999, and not only the field intensities but also the phases are almost indistinguishable. Our calculations for similar structures with different parameters also yield excellent results.

### IV. Conclusion

An efficient BPM has been derived based on local oblique coordinate system to treat  $z$ -dependent structures. The staircase approximation is prevented so that more accurate results have been obtained. Since the refractive index interfaces can be arbitrary and are not necessarily parallel, the application regime of this proposed method is more general. The present method has been numerically validated by examining power conservation of the guided mode in a curved waveguide.

### References

1. D. Yevick, "A guide to field propagation techniques for guided-wave optics," *Optic. Quantum Electron.* **26**, S185 (1994).
2. J. Yamamuchi, J. Shibayama, and H. Nakano, "Propagating beam analysis based on the implicit finite-difference method using the oblique coordinate system," *OSA/IEEE Integr. Photon. Res. Tech. Dig.*, 19 (1994).

3. P. Sewell, T. Anada, T. M. Benson, and P. C. Kendall, "Nonstandard beam propagation," *Microwave Opt. Tech. Lett.* **13**, 24 (1996).
4. —, "Bi-oblique propagation analysis of symmetric and asymmetric Y-junctions," *IEEE J. Lightwave Technol.* **13**, 688 (1997).
5. C. Vassallo, "Limitations of the wide-angle beam propagation method in the nonuniform systems," *J. Opt. Soc. Am. A*, **13**, 761 (1996).
6. G. R. Hadley, "Transparent boundary condition for the beam propagation method," *IEEE J. Quantum Electron.* **28**, 363 (1992).
7. J. P. Berenger, "A perfectly matched layer for the absorption of electromagnetic waves," *J. Comp. Phys.* **114**, 185 (1994).
8. G. R. Hadley, "Wide-angle beam propagation using Padé approximant operators," *Opt. Lett.* **17**, 1426 (1992).
9. Y. P. Chiou and H. C. Chang, "An efficient wide-angle beam propagation method," *IOOC-ECOC97*, **2**, 220 (1997).

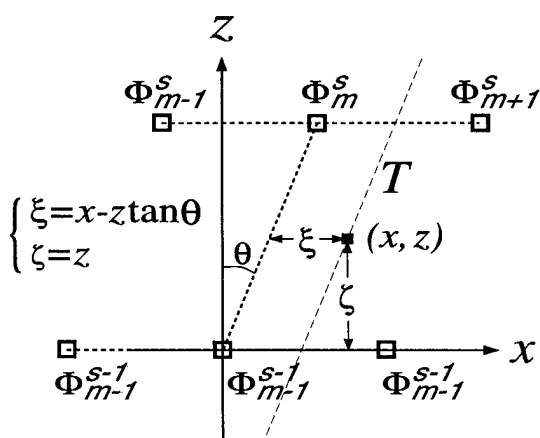
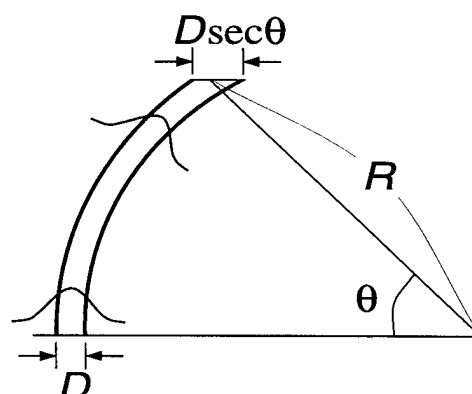

 Fig. 1 Sampled points near the interface  $T$ .


Fig. 2 A sketch of the curved waveguide.

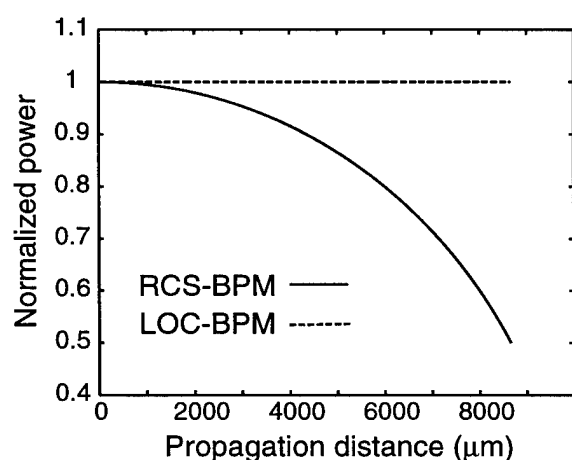
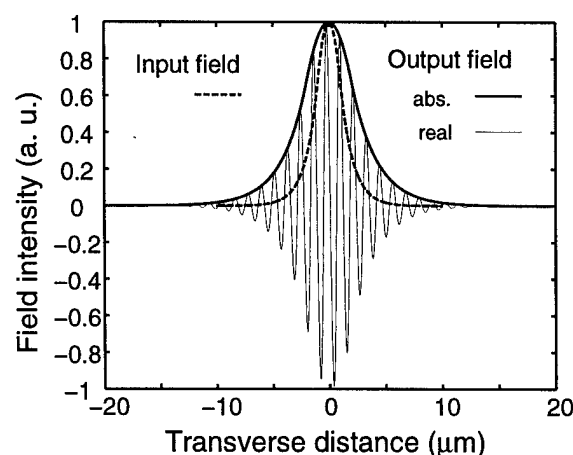


Fig. 3 Normalized power variation as the guided mode propagates along the curved waveguide. Solid and dashed curves are obtained using the RCS-BPM and the LOC-BPM, respectively.


 Fig. 4 Field distributions of the guided mode after propagating  $z = R \sin 60^\circ$ . Thick and thin solid curves are the field intensity amplitude and its corresponding real part, respectively.

# Bi-Directional Beam Propagation Method Based on Full-Wave Analysis

Chenglin Xu<sup>1</sup>, Kang Li<sup>3</sup>, Weiping Huang<sup>1</sup>, Wayne Lui<sup>2</sup>, Kiyoyuki Yokoyama<sup>2</sup>

<sup>1</sup>Dept. of Electrical and Computer Engineering, University of Waterloo  
Waterloo, Ontario N2L 3G1 Canada, Email: [chenglin@maxwell.uwaterloo.ca](mailto:chenglin@maxwell.uwaterloo.ca)

<sup>2</sup>NTT Opto-electronics Laboratories, 3-1 Morinosato, Wakamiya, Atsugi, Kanagawa, Japan

<sup>3</sup>On leave from Dept. of Electronics Engineering, Shandong University, Shandong, P.R. China

Beam propagation method (BPM) has been one of the most popular methods for simulation of electromagnetic wave propagation in optical waveguides. Despite the tremendous improvement in the past few years, the BPM traces the wave propagation in one direction only. Hence the backward reflections at the discontinuities along the waveguides are ignored. For many waveguide structures, this may be a valid approximation, for the reflections are usually small and not cumulative. As the optical waveguide structures become more complex and more photonic components are integrated, the need for accurate modeling of reflections will become more acute. In fact, there has been great effort in the past decade on development of bi-directional BPM, which can simulate both forward and backward wave propagation [1-3]. While simulation of bi-directional wave propagation does not seem to constitute a great challenge, the calculation of reflection does. In the reported work, the reflection was calculated by approximating the guided wave as either plane wave within whole Fourier spectrum range [1], or local plane waves[3], or local guided waves[2] within each homogeneous transverse segment. These methods may be sufficient for weakly guiding waveguides. However, for strongly guiding waveguides with considerable refractive index difference, the homogeneous treatment is not sufficient since fields interacting at the interface between homogenous segments can not be ignored.

In this paper, we propose a novel bi-directional BPM which takes into account the full wave effects at the index discontinuities. It applies to waveguides with arbitrary longitudinal discontinuities.

Let us start from the Holmholtz equation

$$\frac{\partial^2 \psi}{\partial z^2} + P\psi = 0$$

where  $\psi$  in the context of this report stands for  $E_y$  field for TE wave and  $H_y$  for TM wave.

$P\psi = \frac{\partial^2 \psi}{\partial x^2} + n^2 k_0^2 \psi$  is the operator. The solution to above equation is straightforward and can be expressed as

$$\psi(z) = \psi^+(0) \exp(-jz\sqrt{P}) + \psi^-(0) \exp(+jz\sqrt{P})$$

where  $\psi^+(0)$  and  $\psi^-(0)$  are forward and backward field at the junction shown in Figure 1. By matching the boundary conditions, we obtain the transmission and reflection matrices for TE and TM waves, respectively [4].

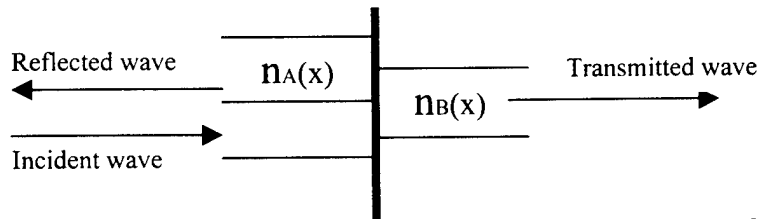


Figure.1. A dielectric junction with arbitrary transverse refractive index profiles

$$[R]_{TE} = \frac{E_A^-}{E_A^+} = \frac{\sqrt{P_A} - \sqrt{P_B}}{\sqrt{P_A} + \sqrt{P_B}} \quad [T]_{TE} = \frac{E_B^+}{E_A^+} = \frac{2\sqrt{P_A}}{\sqrt{P_A} + \sqrt{P_B}}$$

$$[R]_{TM} = \frac{H_A^-}{H_A^+} = \frac{\frac{1}{n_A^2}\sqrt{P_A} - \frac{1}{n_B^2}\sqrt{P_B}}{\frac{1}{n_A^2}\sqrt{P_A} + \frac{1}{n_B^2}\sqrt{P_B}} \quad [T]_{TM} = \frac{H_B^+}{H_A^+} = \frac{\frac{2}{n_A^2}\sqrt{P_A}}{\frac{1}{n_A^2}\sqrt{P_A} + \frac{1}{n_B^2}\sqrt{P_B}}$$

There are different ways to approximate the “square root” operators in the above equations. For instance, we can use the Taylor expansion in which  $\sqrt{P}$  is expanded at a reference point  $n_0 k_0$  such that

$$\sqrt{P} = \sqrt{n_0^2 k_0^2 + (P - n_0^2 k_0^2)} \approx n_0 k_0 + \frac{1}{2n_0 k_0} (P - n_0^2 k_0^2) + \frac{1}{8n_0^3 k_0^3} (P - n_0^2 k_0^2)^2 + ..$$

where  $n_0$  is the reference refractive index.

On the other hand,  $\sqrt{P}$  can also be expanded by Pade approximation [4]. Similar to the Taylor expansion, the Pade expands  $\sqrt{P}$  around a reference point  $n_0 k_0$  as

$$\sqrt{P} \approx n_0 k_0 + jF^m$$

where

$$F^{m+1} = \frac{P - n_0^2 k_0^2}{j2n_0 k_0 - F^m}$$

with  $F^0 = 0$ .

As examples, we apply the new bi-directional BPM, which combines above techniques with the wide-angle vector BPM [5], to a waveguide junction problem as shown in Figure 2. The forward, backward, and total waves are shown separately. The standing wave pattern formed by forward and backward wave interference is clearly observed.

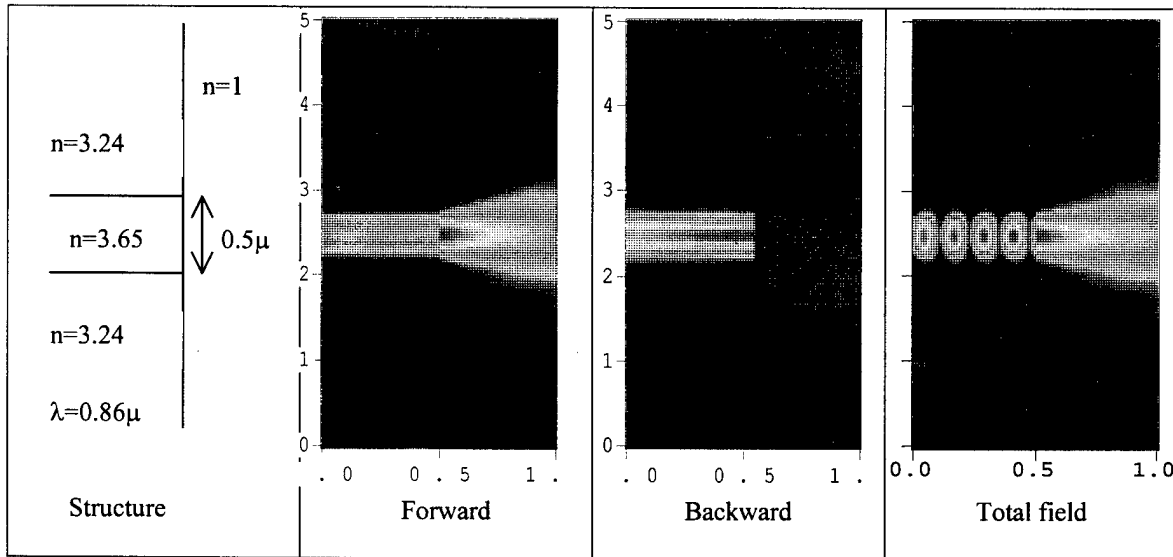


Figure 2a typical junction problem and the simulation results.

As another example, a tapered waveguide structure with continuous reflection is also simulated and the results are shown in Figure 3.

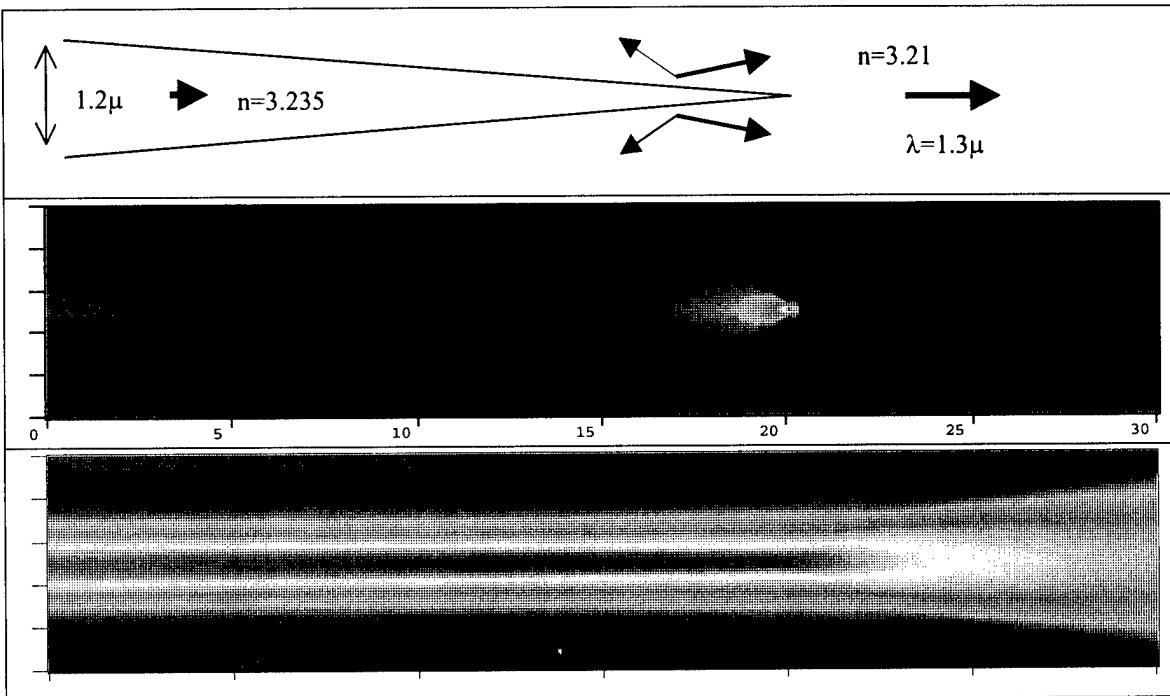


Figure.3. Taper waveguide structure and simulation results (reflected field and total field)

It is observed that the backward reflection is small, but occurs continuously along the waveguide.

In conclusion, a novel bi-directional beam propagation method based on full-wave analysis have been developed and presented. It accounts for the full-wave effects in calculation of reflections generated at discontinuities of arbitrary configurations and therefore more accurate than the conventional plane wave or local guided wave approximation. In comparison with other full-wave approaches such as the FDTD method, the bi-directional BPM is more efficient and can be readily incorporated into the existing BPM to simulate of optically large waveguide structures.

### References

1. P. Kaczmarek and P. E. Lagasse, "Bidirectional beam propagation method," *Electronics Lett.*, Vol. 24, pp.675-676, 1988.
2. D. Yevick, W. Bardyszewski, B. Hermanson, and M. Glasner, "Split-operator electric field reflection techniques," *IEEE Photonics Tech. Lett.*, Vol. 3, pp. 527-529, 1991.
3. Y. Chung and N. Dagli, "A non-iterative bidirectional beam propagation method," IPR'92, paper WE4-1, New Orleans.
4. Y. Chiou and H. Chang, "Analysis of optical waveguide discontinuities using Pade approximants," *IEEE Photonics Tech. Lett.*, Vol. 9, pp. 964-966, 1997.
5. W. P. Huang and C. L. Xu, "A Wide Angle Vector Beam Propagation Method," *IEEE Photon. Tech. Lett.*, Vol. 4, pp. 1118-1120, October 1992.

**Integrated Photonics Research**

# Waveguide Materials and Devices

**Monday, March 30, 1998**

**David L. Weidman, Optical Components Tech.**  
Presider

**IMC**  
**11:00am–12:15pm**  
Salon C

## Formation of Bragg gratings upon thin films prepared by sol-gel and sputtering processes

Junji Nishii

Osaka National Research Institute, AIST

1-8-31 Midorigaoka, Ikeda, Osaka 563, Japan

tel:+81-727-51-9543, fax:+81-727-51-9627, e-mail:jnishii@onri.go.jp

Noboru Tohge and Gaoyang Zhao

Faculty of Science and Technology, Kinki University

3-4-1 Kowakae, Higashi-Osaka, Osaka 577, Japan

Diffraction elements are attractive for integrated optical circuits with functions of filter, wavelength division, focusing, etc. Such elements can be obtained not only by machining but by optical processing. For example, photon induced refractive index change in optical fiber is useful for the preparation of permanent Bragg gratings[1,2,], which produced splendid progress in subscriber loops of fiber network. The dominant origin of the photosensitivity of fiber is the formation of color centers by ultraviolet laser irradiation[3,4]. On the other hand, we investigated the photosensitivity of thin films prepared by sol-gel[5] and sputtering[6] methods for the preparation of diffraction elements. The present paper describes the preparation and characteristics of Bragg gratings printed upon these thin films by excimer laser irradiation.

The first candidate was the chemically modified  $\text{Al}_2\text{O}_3$  gel films derived from aluminum tri-sec-butoxide( $\text{Al}(\text{O-sec-Bu})_3$ ) modified with benzoylacetone (BzAcH)[5]. The preparation of the starting solution was carried out in a  $\text{N}_2$  atmosphere. The second thin films were formed by a  $\text{GeO}_2$ - $\text{SiO}_2$  binary glass system, which were prepared by a conventional rf-sputtering method. Thin films deposited upon Si substrates were exposed to ultraviolet photons emitted from excimer laser through a silica phase mask(1.06  $\mu\text{m}$  pitch, QPS Tech.) at room temperature.

It has been reported that the  $\text{Al}_2\text{O}_3$  gel film exhibits an absorption peak at 325nm due to the  $\pi - \pi^*$  transition of the chelete ring, and the breaching of this band is required for the polymerization of the film[4]. XeF laser(351 nm) was used as the light source for the

bleaching. Figure 1 shows the SEM image of the  $\text{Al}_2\text{O}_3$  thin film grating after irradiation through the mask followed by the leaching in  $\text{HNO}_3$ -acetone solution. It is apparent that the grating having same pitch with the phase mask was formed, which was stable after heat treatment at  $400^\circ\text{C}$  for 1h. Diffraction efficiencies(first-order diffraction power/input power) of this grating before and after leaching were estimated as 0.3 and 24.2 %, respectively.

Previously we found out an ultraviolet(uv) light induced large volume expansion in  $\text{GeO}_2$ - $\text{SiO}_2$  thin glass films prepared by a conventional rf-sputtering[5]. Positive sinusoidal wave pattern could be printed by irradiation with KrF(248 nm) or ArF(193 nm) laser pulses upon these films. Figure 2 shows the AFM image of the as-printed Bragg grating upon Si substrate after irradiation with 1200 ArF laser pulses( $40\text{mJ}/\text{cm}^2$ ).



Fig.1, SEM image of the  $\text{Al}_2\text{O}_3$  grating prepared by sol-gel process.

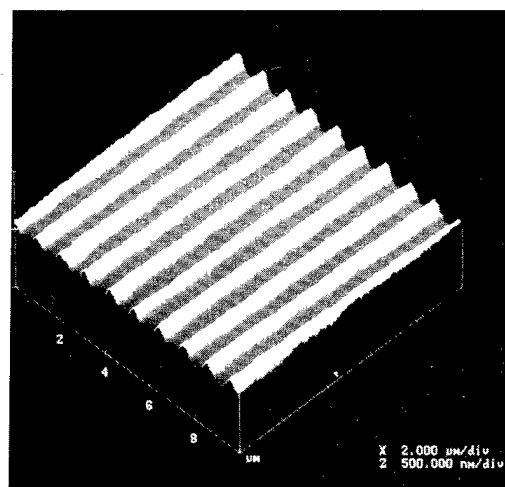


Fig.2, AFM image of the  $\text{GeO}_2$ - $\text{SiO}_2$  grating prepared by sputtering method.

Furthermore, the irradiated area, i.e., the volume expanded area, was quickly leached by a HF solution, and the negative pattern was remained. Figure 3 shows an example of the change in the pattern before and after etching. Figure 4 shows the relationship between the etching time and the diffracted power of He-Ne laser beam(633 nm). The diffraction efficiency was as high as 1 % for as-printed grating, and increased to 8.3 % after 100 sec of

etching.

Diffraction efficiency of Bragg gratings printed upon sol-gel thin films was much higher than that for sputtering thin films, which was closely related with the photo-sensitivity of the films. Both of these gratings exhibited excellent thermal, mechanical and chemical stability in air. It was easy to print the gratings quickly upon any materials. Therefore, these gratings should be useful for the micro-diffractive optics.

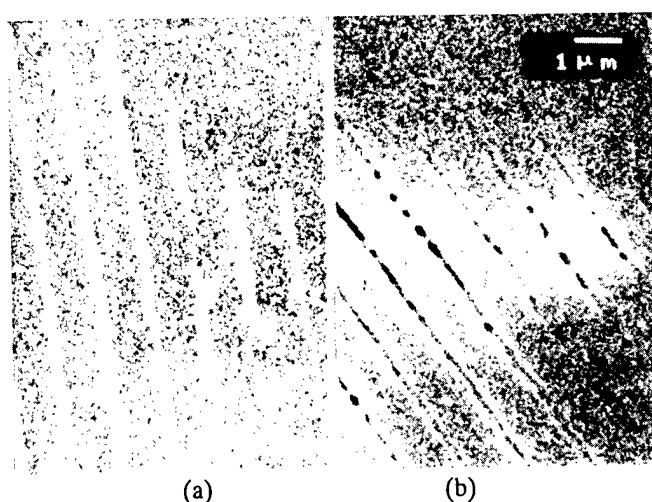


Fig.3, Surfaces of  $\text{GeO}_2\text{-SiO}_2$  gratings (a) before and (b) after etching by 0.01% HF solution.

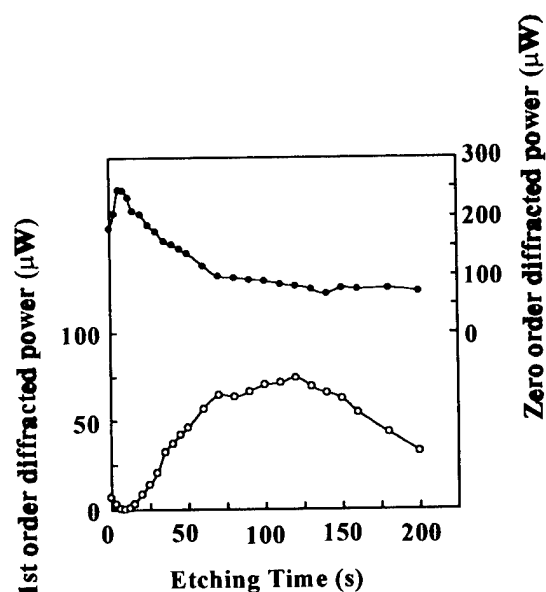


Fig.4, Relationship between etching time and diffraction efficiency of  $\text{GeO}_2\text{-SiO}_2$  grating.

## References

- [1] K.O.Hill, Y.Fujii, D.C.Johnson and B.S.Kawasaki, Appl. Phys. Lett. 62(1993)1035.
- [2] F.Bilodeau, D.C.Johnson, S.Theriault, B.Malo, J.Albert and K.O.Hill, IEEE Photon. Tech. Lett., 7(1995)388.
- [3] J.Nishii, N.Kitamura, H.Yamanaka, H.Hosono and H.Kawazoe, Opt. Lett. 20(1995)1184.
- [4] J.Nishii, K.Fukumi, H.Yamanaka, H.Hosono and H.Kawazoe, Phys. Rev. B52(1995)1161.
- [5] G.Zhao and N.Tohge, Kobunshi Ronbunshu, 53(1996)253.
- [6] J.Nishii, H.Yamanaka, H.Hosono and H.Kawazoe, Appl. Phys. Lett., 64(1993)282.

## Luminescence and Gain in Co-Sputtered $\text{Al}_2\text{O}_3$ Erbium-Doped Waveguides

Klein L. Johnson, Anand Gopinath, William Berglund and  
University of Minnesota Dept. of Electrical Engineering  
4-174 EE/CSCI Bldg. 200 Union ST SE  
Minneapolis, MN 55455  
Phone: (612) 625-3054

Carol Ford, Randy Ramberg, and Lance Vreze  
Honeywell Military Avionics Division  
200 Stinson Ave. SE  
Minneapolis, MN 55455  
Phone: (612) 5203

### Introduction

Rare earth doping of planar waveguides may potentially yield very compact optical amplifiers, lasers, and amplified spontaneous emission light sources, as well as zero insertion loss waveguide routers, splitters, and multiplexers. Among the most developed to date are  $\text{Er}^{3+}$  doped devices which emit at around 1530nm and can be pumped efficiently at 980 or 1480 nm. Interest in these devices has inspired a great deal of research into Erbium-doped thin film and bulk materials. Presently, active devices have been fabricated from silica-based [1], crystalline  $\text{LiNbO}_3$  [2], and sputtered  $\text{Al}_2\text{O}_3$  dielectric films[3], to name just a few. Typically, incorporation of the Erbium is accomplished through ion implantation, indiffusion, or by sputtering from preconstituted targets. While ion implantation provides good control of the dopant profile, a high temperature ( $\sim 800^\circ\text{C}$ ) anneal is required to activate the Erbium ions and remove the damage to the host material caused by the high energy ion bombardment. Diffusion also is a high temperature process, and may require in excess of 100 hours to achieve several microns penetration into the host material. Sputtering from preconstituted targets provides excellent compositional control, yet can be expensive as a new target is required for each experimental run.

We have developed a process with which to deposit truly amorphous  $\text{Al}_2\text{O}_3$  films suitable for the fabrication of waveguides with very low bulk scatter losses.  $\text{Al}_2\text{O}_3$  has a structure very similar to  $\text{Er}_2\text{O}_3$ , suggesting that high Er doping levels may be possible in this material without the onset of clustering effects.[3] As an alternative to the above processes, we have developed a process for the fabrication of Er-doped  $\text{Al}_2\text{O}_3$  waveguides which involves the co-deposition of the Erbium atoms by simultaneous sputtering along with the host material. This method has shown to provide excellent control over compositional parameters, and a high degree of optical activity in the deposited films.

### Experimental

In order to investigate the luminescence properties of the doped  $\text{Al}_2\text{O}_3$  films, we fabricated  $\text{SiO}_2$  stripe loaded channel waveguides with the doped  $\text{Al}_2\text{O}_3$  films comprising the guide region. Samples for analysis were prepared in the form of a typical slab waveguide geometry. Initially, a 3.0 micron  $\text{SiO}_2$  buffer layer with a refractive index of 1.49@6328A was

sputtered on a 4" silicon substrate. Erbium and Erbium/Ytterbium doped thin films of  $\text{Al}_2\text{O}_3$  (refr.index=1.8) were then deposited by co-sputtering using annular targets to a thickness of 0.6 microns to form the waveguide core region, followed by a 1.0 micron  $\text{SiO}_2$  cap layer. Control of Erbium concentration is achieved by variation of target size and position. Stripe-loaded waveguides were then formed by etching 5.0 micron wide lines in the top  $\text{SiO}_2$  by  $\text{CF}_4$  RIE through a 75 nm Cr mask. Finite-difference modeling has shown this configuration to be single mode at 1500nm, while marginally supporting a second-order mode at 980nm.

## Results

A series of runs were performed utilizing Er alone, along with samples co-doped with Yb to improve pump utilization and emission bandwidth. The doping levels ranged from 0.05 to 0.1 a.t.% for the Er and were held constant at 0.2 a.t.% for the Yb. Luminescence and lifetime data was collected by endfire coupling light from a 100mW 974nm semiconductor laser diode pump into the cleaved end-facets of the waveguides and observing the emitted light by coupling into a 1-meter scanning monochromator equipped with a InGaAs photodetector.

A typical luminescence spectra is shown in Fig.1, corresponding to an Er concentration of 0.1 a.t.% as verified from RBS data. A 500C post deposition bake step has shown to improve the observed radiative lifetimes. Figure 2 shows the lifetime data for the investigated compositions, indicating a 40% increase over the unbaked data. The relatively short 4 mSec lifetimes observed do not quite compare with the 6-10mSec lifetimes previously observed in  $\text{Al}_2\text{O}_3$  [3] and the 10-12mSec lifetimes typical of silica-based hosts.[4] However, initial indications suggest that this can be improved through refinement of the deposition and bakeout procedures.

We have also observed amplifying behavior in these waveguides by coupling a ~1500nm signal from an external cavity tunable diode laser into one facet while backward pumping the sample from the other end with the pump laser. We have measured in excess of 1.0dB/cm internal gain at  $\lambda=1530\text{nm}$  for 20mW launched pump power. Further data on the amplifying behavior, lifetime studies, and absorption/emission cross sections will be presented.

## Conclusions

Simultaneous co-sputtering has been shown to be a possible means for the economical fabrication of Erbium-doped waveguide devices based on  $\text{Al}_2\text{O}_3$ , and can easily be extended to other host materials. Lifetime studies have shown that further improvements can be made, possibly making this technology comparable to silica based materials.

## References

- [1] J. Shmulovich, et al., *Optical Fiber Communication*, 1996 OSA Tech. Digest Series, pp.250-51.
- [2] W. Sohler, *Integrated Photonics Research*, Vol. 7, 1995 OSA Tech. Digest Series, pp.212-14.
- [3] G. N. van den Hoven, et al., *J. Appl. Phys.*, Vol. 79, No. 3, pp.1258-66, 1996.
- [4] E. Desurvire, "Erbium-Doped Fiber Amplifiers: Principles and applications", John Wiley & Sons, Inc., New York, 1994.

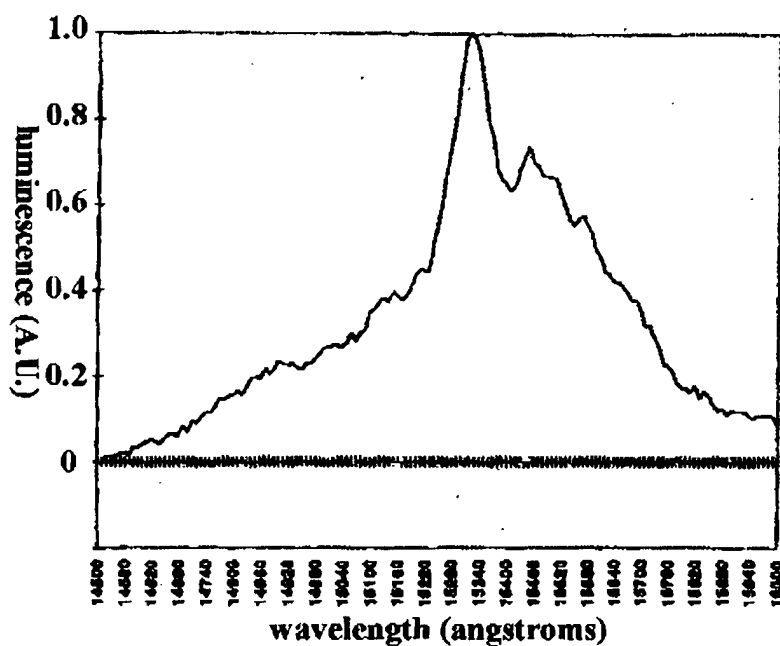


Figure 1. Luminescence of  $\text{Al}_2\text{O}_3$  waveguide with 0.1 a.t.% Er doping pumped at 974 nm.

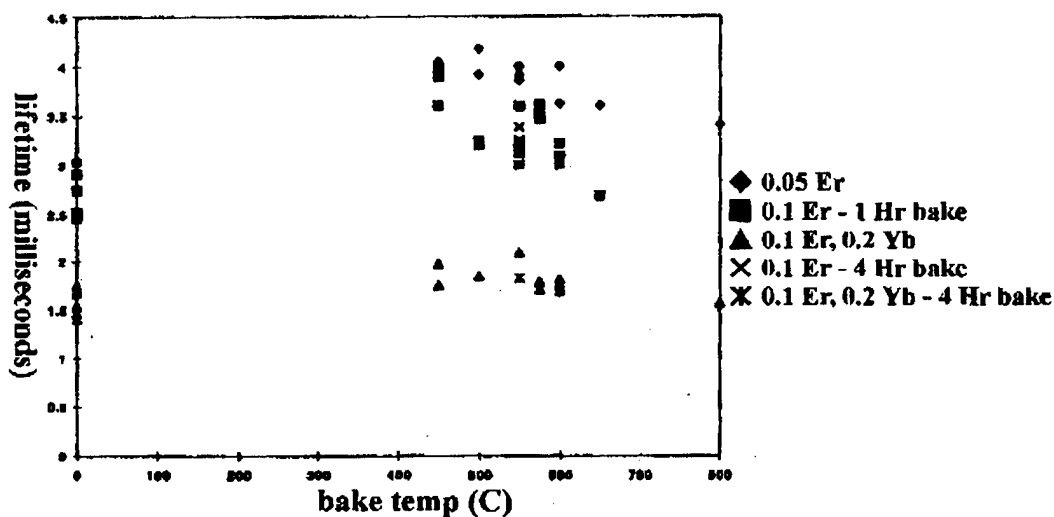


Figure 2 under various baking Observed radiative lifetimes of Er and Er/Yb doped  $\text{Al}_2\text{O}_3$  waveguides conditions.

## BIREFRINGENT OXIDIZED POROUS SILICON BASED OPTICAL WAVEGUIDES

**Yu.N.Korkishko, V.A.Fedorov, S.A.Gavrilov**

Moscow Institute of Electronic Technology (Technical University)  
103460, Moscow, Zelenograd, Russia

**V.V.Karavanskii**

General Physics Institute, Russian Academy of Science, Leninskii prospect, 47,  
Russia

### Abstract

We have found that integrated optical waveguides based on oxidized porous silicon have a relatively large birefringence. As a result, the modes of both polarizations are supported. The origin of observed phenomenon is discussed.

### 1. Introduction

Since the demonstration that porous silicon (PS) has effective luminescence in the visible range [1], the old idea of electronics and optics integration using silicon technology has received a strong impetus. Routing, splitting and modulation of optical signals between a porous silicon light emitter and other integrated optical circuits components will require the use of optical waveguide interconnects which are designed for use at the emitter wavelength. It is possible to fabricate waveguide structures utilising porous silicon [2,3] or oxidized porous silicon multilayers [3,4], since variations in the porosity, and therefore the refractive index, can be easily obtained by changing the electrochemical anodisation parameters. Such a structures consist of a low porosity waveguiding layer placed on higher porosity lower cladding layers.

The photoluminescence of porous Si has been shown to exhibit pronounced polarization effect (see review [5]), however, in our knowledge, birefringent pure or oxidized porous silicon optical waveguides have not been reported yet.

### 3. Sample preparation and characterization

Porous silicon films are produced by the anodisation of silicon wafers in an aqueous solution of hydrofluoric acid with current densities below those used for electropolishing. The resulting material contains a network of pores of dimensions around 10 nm and still retains the single crystal character of the original wafer. Because of its high internal surface area, porous silicon is highly reactive at relevant temperatures and exposure to wet oxygen at 900-1000°C rapidly produces a bulk oxide with dielectric properties comparable with conventionally produced silicon oxide [6]. Double layer planar waveguides were formed by electrochemically anodising (111)-orientated p-type silicon (0.03  $\Omega$  cm) in an electrolyte mixture composed of 48% hydrofluoric acid and ethanol (1:2). Current densities were controlled and switched automatically, between 10 mA·cm<sup>-2</sup> and 50 mA·cm<sup>-2</sup>, the anodisation times being chosen to give the layer thicknesses required. The resulting double-layer porous silicon structures consisted of 62% porosity upper layer and 75% porosity deeper layer. After that, the samples were heated in an oxidising atmosphere to 900°C for 1 h. The resulting

double-layer silicon oxide structures consisted of waveguide layer and lower cladding layer which provides an optical isolation of the waveguide layer from the silicon substrate because of its lower density.

In order to find mode effective indices, we measured excitation angles of dark  $m$ -lines of modes with one prism coupler setup at the 633 nm wavelength. The refractive index profiles in the waveguides were reconstructed by the IWKB technique proposed by White and Heidrich [7] and improved by Dikaev et al. [8]. The calculation procedure proposed by Chiang [9] has also been used. The refractive index profile was determined as the average between ones obtained by using these two methods.

#### 4. Results and discussions

Planar waveguiding was observed at  $\lambda=0.63$   $\mu\text{m}$  in all of the oxidized porous silicon structures. The waveguides supported the modes of both polarizations. The relatively large difference between effective indices of TE and TM modes points to that the waveguides used are birefringent. From measured refractive indices for TE and TM modes the ordinary and extraordinary refractive index profiles were reconstructed according methods [8,9]. Fig.1 shows the ordinary (in the direction perpendicular to the surface plane) and extraordinary (in the direction lies in surface plane) refractive index profiles for waveguides with different porosity. One can see, that at the surface the ordinary index is higher on 0.01 than extraordinary index and birefringence decreases with depth. The specific feature is that extraordinary profiles show a long tail, which stretches for a couple of microns to lower cladding layer. Such effect does not observe for ordinary refractive index profiles.

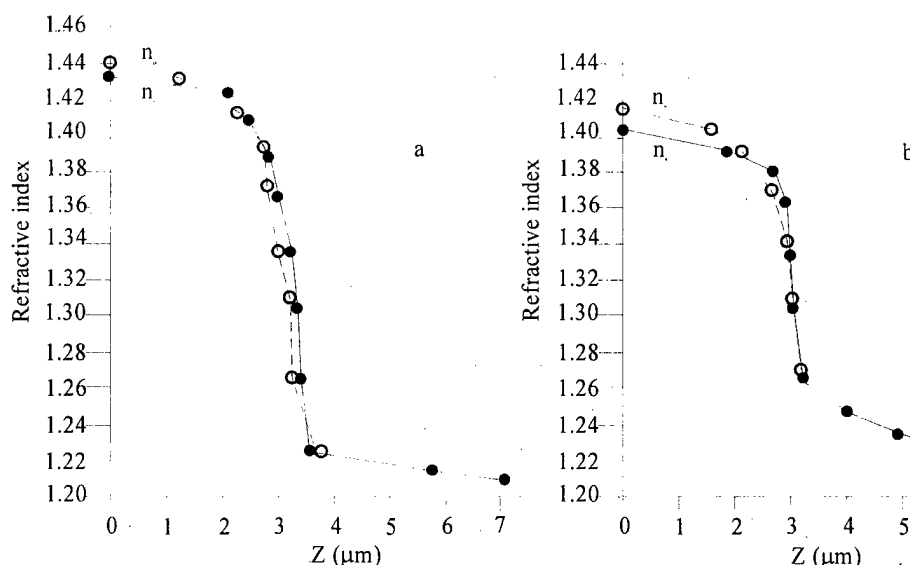


Fig.1. Ordinary (open circles, dashed lines) and extraordinary (closed circles, solid lines) refractive index profiles in oxidized porous silicon oxide waveguides prepared under different electrochemically anodising conditions and then heated in an oxidising atmosphere to 900°C for 1 h.

a) 10  $\text{mA}\cdot\text{cm}^{-2}$  for 250 sec. followed by 50  $\text{mA}\cdot\text{cm}^{-2}$  for 50 sec.

b) 25  $\text{mA}\cdot\text{cm}^{-2}$  for 100 sec. followed by 50  $\text{mA}\cdot\text{cm}^{-2}$  for 50 sec

One possible reason of observed phenomenon is that the lower cladding layer has a small gradient of porosity,  $\rho$ , and the sensitivity of extraordinary index to changing of  $\rho$ , is larger than this sensitivity for ordinary index, i.e.  $\frac{\partial n_e}{\partial \rho} > \frac{\partial n_o}{\partial \rho}$ . As a result, the ordinary refractive index gradient in the lower cladding layer is smaller than that needed to exit the TE modes (cut-off conditions). In contrast, the TM modes are exited in this region.

The birefringency in oxidized porous silicon could be induced by stresses appeared due to large surface energy. However, putting of samples in vapours of water, alcohol, and acetone does not change the ordinary and extraordinary index profiles. Besides that, annealing in vacuum at 900°C during 1 h also does not effect on birefringence. Therefore, we can make a conclusion that adsorption and desorption processes do not effect on birefringence of oxidized porous silicon waveguides. One should find the reason of that in the anisotropy of oxidized porous silicon media.

The effective refractive index of porous silicon has been calculated by the Bruggeman effective medium approximation [10]. However, this approach did not take into account the possible anisotropy of porous silicon. Evidently, that the anisotropy depends on orientation of silicon plate used. This can explain why Loni et al. [3] reported that oxidized porous silicon waveguides formed on (100)-orientated silicon plate were polarization independent.

It was obtained, that after keeping of waveguides for 2 hour in water at room temperature, the waveguides becomes polarization independent. In this case, the water fills the voids and because the refractive index of water ( $n=1.33$ ) is much more close to one of bulk silicon oxide ( $n=1.46$ ) than air ( $n=1$ ), the anisotropy of water filled structure decreases.

Unfortunately, we were not able to characterize the porous silicon waveguides, due to the absorptive nature of the remaining silicon at short wavelengths. This experiments will be performed at IR wavelengths in near future.

## References

- [1] L.T.Canham, Appl.Phys.Lett., **57** (1990) 1046.
- [2] M.G.Berger, C.Dieker, M.Thonissen, L.Vescan, H.Luth, H.Munder, W.Theiss, M.Wernke, and P.Grosse, J.Phys. D:Appl.Phys., **27** (1994) 1333.
- [3] A.Loni, L.T.Canham, M.G.Berger, R.Arens-Fischer, H.Munder, H.Luth, H.F.Arrand, T.M.Benson, Thin Solid Films, **276** (1996) 143.
- [4] V.P.Bondarenko, A.M.Dorofeev, and N.M.Kazuchits, Proc. 7th Eur. Conf. on Integrated Optics, April 3-6, 1995, Delft, The Netherlands.
- [5] A.G.Cullis, L.T.Canham, and P.D.J.Calcott, J.Appl.Phys., **82** (1997) 909.
- [6] T. Unagami, Jap.J.Appl.Phys., **7** (1980) 231.
- [7] J.M.White and P.F.Heidrich, Appl.Opt., **15**, (1976) 151.
- [8] Y.M. Dikaev, Yu.A. Kopylov, and I.M. Kotelyanskii, Simple method to determine the index profiles in graded waveguides, *Kvantovaya Elektronika*, **8** (1981) 378.
- [9] K.S.Chiang, *IEEE J. Lightwave Techn.*, **3** (1985) 385.
- [10] C.Pickering, M.I.J.Beale, D.J.Pearson, R.Greef, J.Phys.C: Solid State Phys., **17** (1984) 6535.

## FABRICATION OF PLANAR AND CHANNEL WAVEGUIDES ON As-S-(Se) CHALCOGENIDE GLASSES FOR INTEGRATED OPTICAL DEVICES

K. Le Foulgoc, J-F. Viens, A. Villeneuve

Centre d'Optique, Photonique et Laser (COPL), Université Laval,  
Cité Universitaire, Pavillon A.-Vachon, Québec, Canada, G1K 7P4  
Tel. : 1-418-656-3568 Fax : 1-418-656-2623, e-mail : klefoulg@phy.ulaval.ca

K. Richardson, T. Cardinal  
CREOL, University of Central Florida, Orlando, USA 32826

In the field of integrated optics, passive or active microdevices such as power splitters and lasers are of major interest. Chalcogenide glasses (ChG) are excellent candidates for infrared guiding configuration because of their wide optical transmission range, their potentially low losses in the telecommunication band, and their attractive properties as host materials for active rare-earth ions (Pr, Nd, Dy, Er...). These glasses have emerged as an outstanding class of materials for fiber laser sources and amplifiers [1], for all-optical switches [2], and for sensing applications. Because of the guiding and confinement similarities with optical fibers, planar waveguides are a promising technology for realizing compact devices. Glassy compositions  $\text{As}_2\text{S}_3$  and  $\text{As}_{24}\text{S}_{38}\text{Se}_{38}$  (doped with rare-earth or not) have been selected for the realization of integrated optical waveguides because of their large glass forming regions. These highly photosensitive materials also exhibit unique characteristics such as a large linear and nonlinear index of refraction, a wide transparency in infrared (0.6 - 12  $\mu\text{m}$ ) and a low-phonon energy [4].

To fabricate planar waveguide, we have chosen a thermal evaporation technique for our ChG thin films deposition, although other techniques such as sputtering have also been used by other groups [5]. The realization of integrated optical devices requires the confinement of the light in both transverse directions. Therefore, we have developed the capability to fabricate channel waveguides. To define the channels in the As-S-(Se) chalcogenide glasses films, three techniques have been used; a photolithographic process, the use of the strong photosensitivity of ChG, and finally He ion implantation. In this paper, we will present our results on the first two methods.

The As-S-(Se) films were deposited by a conventional evaporation technique onto unheated  $\text{SiO}_2/\text{Si}$  wafers. The thermal oxide is present to optically isolate the ChG waveguides from the higher index silicon wafer. The growth rate and thickness of these films were controlled by a quartz crystal thickness monitor. The evaporation rate was in the order of 3.5 nm/sec. A multilayer planar waveguide is obtained by depositing successive As-S and As-S-Se layers. The chalcogenide films are then annealed at about 130°C for several hours in order to improve the mechanical and optical properties. The adhesion and stability of deposited chalcogenide films strongly depend on the surface preparation and on the successive handling of the films. The films are resistant to the 3M Scotch tape test MIL-C-14804 and have survived over time. The films are somewhat sensitive to certain chemical environment, to mechanical abrasion and stress, thermal shock and to aging. Therefore, a careful packaging of the device will be necessary. The optical quality and surface uniformity of deposited films were monitored using optical microscopy and a Dektak profilometer. The wafers are then cleaved to the desired length in order to obtain high quality facets for efficient endfire coupling as can be seen in Figure 1.

In order to create a channel waveguide, we used the standard photolithographic process commonly employed in microelectronic device fabrication. The usual steps involved in photolithography (spincoating of the photoresist, baking, UV exposure through an amplitude mask, developing and etching of the glass) have been carefully and completely characterized. We have chosen what we believe to be the optimal conditions. Our early results were not all executed in a clean room environment, and we feel that our new clean room facility will greatly improve our

process. Straight channel waveguides, 1 to 10  $\mu\text{m}$  wide were fabricated and tested. Although the 1  $\mu\text{m}$  guides were more lossy, they propagated light over a few cm's, indicating the quality of our process.

A new result is shown in figure 2 which represents a frontview photograph of a multilayer  $\text{As}_{24}\text{S}_{38}\text{Se}_{38}/\text{As}_2\text{S}_3$  channel waveguide, obtained by the above process. We distinguish clearly the 1.25  $\mu\text{m}$  thick  $\text{As}_{24}\text{S}_{38}\text{Se}_{38}$  glass core and the 1.3  $\mu\text{m}$  thick  $\text{As}_2\text{S}_3$  claddings. The spacing between the lines is about 6  $\mu\text{m}$  and the  $\text{As}_2\text{S}_3$  cladding has been developed until it reaches 1.3  $\mu\text{m}$ . This picture represents an optical multilayer directional coupler.

In order to maintain a good reproducibility of the waveguides properties, control over all of the process parameters is required. The propagation losses in ChG waveguides were measured at different wavelengths (800, 1000, 1300, 1500 nm), and a minimum loss of less than 1dB/cm has been achieved above  $\lambda=1.3 \mu\text{m}$  for a single layer,  $\text{As}_2\text{S}_3$  planar waveguide. The As-S-Se waveguides exhibit generally higher losses, especially at shorter wavelengths. Unannealed waveguides show propagation losses twice the measured values.

The ChG glasses also exhibit a high photosensitivity in the visible spectral range. Photostructural changes (refractive index variation, photodarkening, photoexpansion) are induced by exposing the glassy material to near band-gap light [5,6]. Also, a 3-D channel waveguide can be easily formed in a ChG film by optical beam writing using a CW Ar ion laser (10mW) beam exposure at 514 nm. The structure of a multilayer waveguide is represented in Figure 3. The lateral dimension of waveguide varies from several mm to a cm whereas the ChG thin films have typically a 1-3  $\mu\text{m}$  thickness. The light's signal is preferentially propagated in the As-S-Se films because of their high refractive index ( $n\sim 2.47$ ). This structure ensures the vertical confinement of laser beam in different levels of the waveguide. For our experiment, we have used a multilayer structure composed of 2  $\mu\text{m}$  thick  $\text{As}_{24}\text{S}_{38}\text{Se}_{38}$  cores and 3  $\mu\text{m}$  thick  $\text{As}_2\text{S}_3$  cladding. The laser beam profile is stretched with a cylindrical telescope to cast a very thin line of light on the ChG films. Figure 4 shows the endview output of double core planar waveguide before and after 150 second Ar laser beam exposure. The light at the  $\lambda=1.3 \mu\text{m}$  is confined laterally by 25  $\mu\text{m}$  in the exposed As-S-Se core regions. The propagation loss in this waveguide has been measured at about 2 dB/cm at 1.3  $\mu\text{m}$  and is at 0.9 dB/cm in a  $\text{As}_2\text{S}_3$  photoinduced channel waveguide. The topview picture of a waveguide shown in figure 5, indicates the coupling behavior of the light between the two photoinduced cores. This photoinduced phenomenon has created a vertical directional coupler.

In conclusion, a technology has been developed to produce integrated optic components in chalcogenide glasses. The fabrication of planar/channel ChG glass waveguides and the optical characterization performed, has been reported. The photosensitive effects in As-S-(Se) glass thin films have also been investigated and this study has allowed the fabrication of photoinduced double core waveguides and vertical directional couplers. These new microcircuits have been inscribed on multilayer glass structures by writing laser beam exposure. This new generation of ChG waveguides suggests a field of research in the development compact integrated devices with optical routing in 3-D space.

## References

- [1] Y. Oshini, A. Mori, T. Kanamori, K. Fujira, S. Sudo, Appl. Phys. Lett., **65**, 13-15, (1994)
- [2] M. Asobe, T. Kanamori, K. Kubodera, IEEE J. Quantum Electronics, **29**, 2325-2333, (1993)
- [3] D. Pruss, Materials Science Forum, Vols.**32-33**, 321-330, (1988)
- [4] K. Richardson, J.M. McKinley, B. Lawrence, A. Villeneuve accepted, J. Opt. Materials (August 1997)
- [5] S. Ramachandran, S.G. Bishop, J.P. Guo, D.J. Brady, IEEE Phot.Tech.Lett., Vol.**8**, No.8 (1996)
- [6] A. Zakery, P.J.S Owen, A.E. Owen, J.Non Cryst. Sol., 198-200 (1996) 769-773

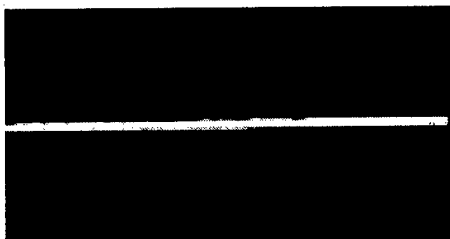


Figure 1 : Endview output of a 1.5  $\mu\text{m}$  thick  $\text{As}_2\text{S}_3$  planar waveguide, showing efficient endfire coupling.

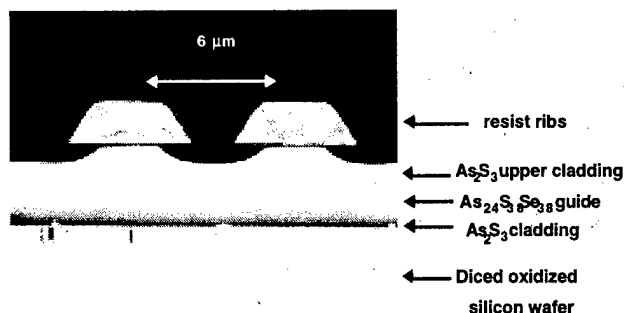


Figure 2 : SEM frontview microphotography of a multilayer ChG directional coupler (with a  $\text{As}_{24}\text{S}_{38}\text{Se}_{38}$  glass core of 1.25  $\mu\text{m}$  thickness and a  $\text{As}_2\text{S}_3$  cladding at 1.3  $\mu\text{m}$ ).

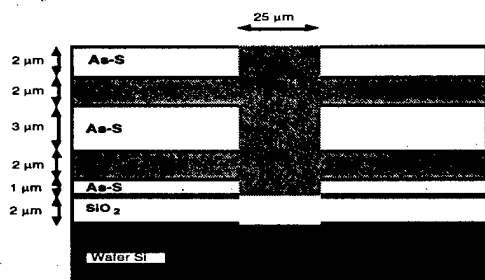


Figure 3 : Structure of a multilayer ChG glass waveguide, showing the successive  $\text{As}_2\text{S}_3/\text{As}_{24}\text{S}_{38}\text{Se}_{38}$  thin film

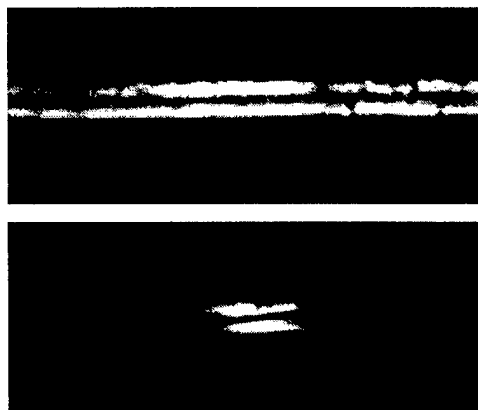


Figure 4 : Endview output of a photoinduced double core planar waveguide, before (top) and after (bottom) the 150 sec 10mW Ar laser exposure (500mJ/mm<sup>2</sup> at 514nm).

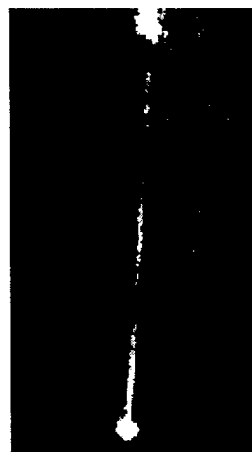


Figure 5 : Topview of the photoinduced double core ChG waveguide, showing the vertical coupling process between the two cores at 1300nm.. The light is injected at bottom, and the guide's length is 12 mm. A difference of refractive index of 0.025 is obtained between the core and the cladding.

## Photoinduced index-tapered channel waveguides in chalcogenide glasses for guided mode-size conversion.

S. Ramachandran and S.G. Bishop

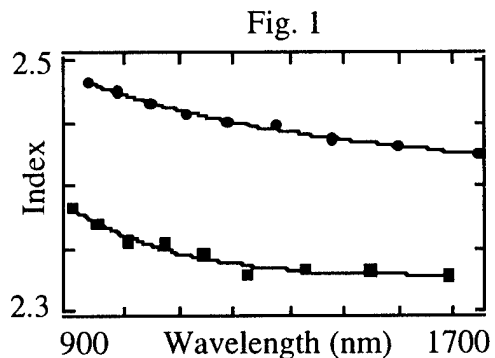
(217) 244-0834 (voice), (217) 244-6375 (fax), [sid-r@uiuc.edu](mailto:sid-r@uiuc.edu)

*Center for Optoelectronic Science and Technology, Microelectronics Laboratory,  
Department of Electrical and Computer Engineering, University of Illinois,  
Urbana, IL 61801*

Optical elements for photonic integrated circuits (PIC) can be directly recorded in chalcogenide glasses by photodarkening<sup>1</sup>, which is a photoinduced red shift of the optical absorption edge and is accompanied by an increase in the index of refraction in the transparent spectral range below the absorption edge. Recently, we reported<sup>2</sup> the use of rapid thermal annealing (RTA) on deposited films of  $\text{Ge}_{10}\text{As}_{40}\text{Se}_{25}\text{S}_{25}$  glasses, to yield photoinduced index changes as high as 5% ( $\Delta n \sim 0.11$ ) upon illumination with 488 nm light from an Argon ion laser. In this paper, we use the large dynamic range of index changes possible in these films, to demonstrate an index tapered waveguide, whose guided mode size changes along the direction of propagation. The fabrication procedure involved a simple exposure, eliminating the need for multi-step etching and developing processes common in defining tapers, and spot size conversions by a factor of 2.6 were achieved within an 8 mm propagation distance. The ease of fabrication, and the ability to sputter these glasses on any semiconductor substrate, makes this technology attractive for monolithic integration of tapers with semiconductor laser diodes, for efficient chip-to-fiber coupling.

One micron thick chalcogenide glass films were sputtered on glass slides and RTAed to characterize the photodarkening properties. The fringe contrasts resulting from transmission measurements are used to compute the index of refraction as a function of wavelength in the transparent region. Index measurements shown in Fig. 1 reveal that the index change between as-deposited and annealed films is as high as 5%.

Chalcogenide glass films for the tapered waveguide devices were sputtered on films of  $\text{SiN}_x$  pre-deposited on Si wafers. The PECVD deposited  $\text{SiN}_x$  film has a refractive index of 2.04 in the 1500 nm range and serves as the bottom cladding layer separating the higher index Si substrate from the chalcogenide glass films ( $\text{Ge}_{10}\text{As}_{40}\text{Se}_{25}\text{S}_{25}$  glass:  $n \sim 2.3$  to 2.5, depending on dosage of photoinducing light). Spatially filtered and collimated Argon laser light at 488 nm was used for patterning the devices. A neutral density filter with linearly varying density was placed in



the beam path and the samples were exposed through a mask with  $2\text{ }\mu\text{m}$  wide lines, yielding an intensity profile that varies monotonically, along the length of the sample. The resulting waveguides were excited by end-fire coupling  $1566\text{ nm}$  light from a diode laser and the output facets were imaged on to an infra-red Vidicon camera with a  $40\times$  microscope objective. Mode profiles at various longitudinal positions along the waveguide were measured by the cut-back technique.

Fig. 2

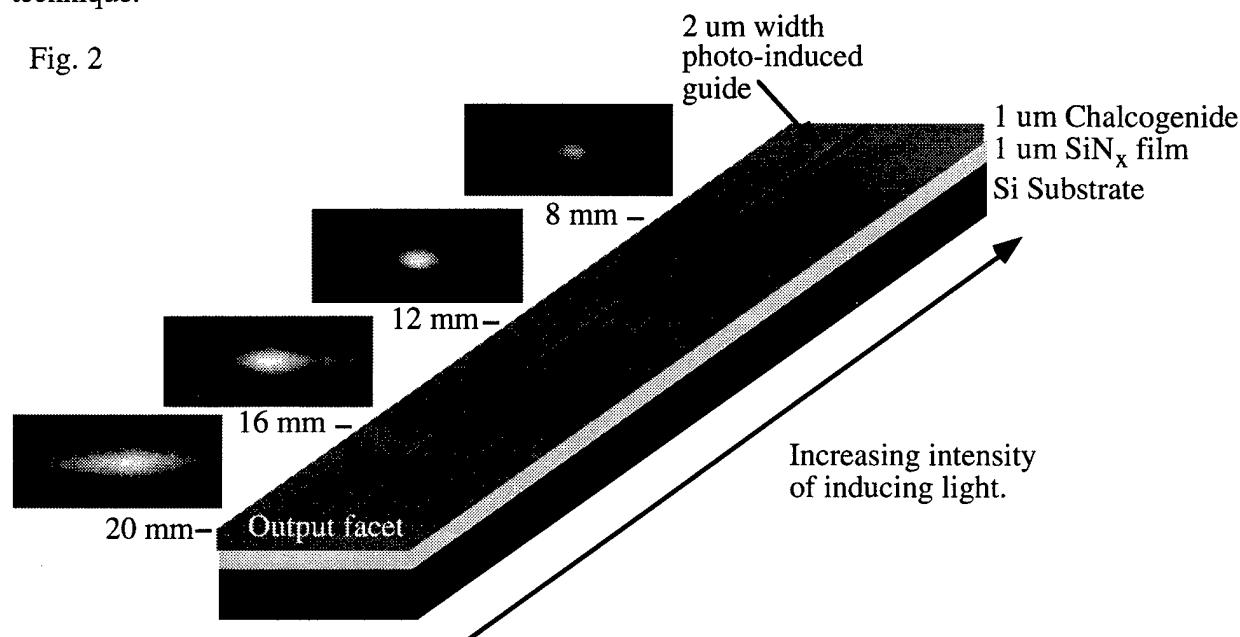


Figure 2 (above) shows a schematic of the photoinduced waveguide, and the mode profiles at different longitudinal positions along a  $20\text{ mm}$  long  $\times 2\text{ }\mu\text{m}$  wide  $\times 1\text{ }\mu\text{m}$  thick waveguide. The dosage of inducing light was constant at  $846\text{ J/cm}^2$  for  $4\text{ mm}$  from the input end and thereafter, monotonically decreased to  $233\text{ J/cm}^2$  by the output end. The near field images of the guided mode shown in Fig. 1 clearly indicate that the mode size increases as the mode propagates away from the input facet. Fig. 3 is a plot of the mode profiles shown in Fig. 2. The different mode profiles in this figure are labeled by the distance away from the input facet ( $0\text{ mm}$ ), at which they were obtained. The larger modes (low confinement), away from the input facet, appear to have side-lobes and features not characteristic of single mode operation. In addition to the photoinduced channel waveguides, the unexposed film forms a slab waveguide, and modes from the two guides overlap, giving rise to the spurious side-lobes.

Fig. 3

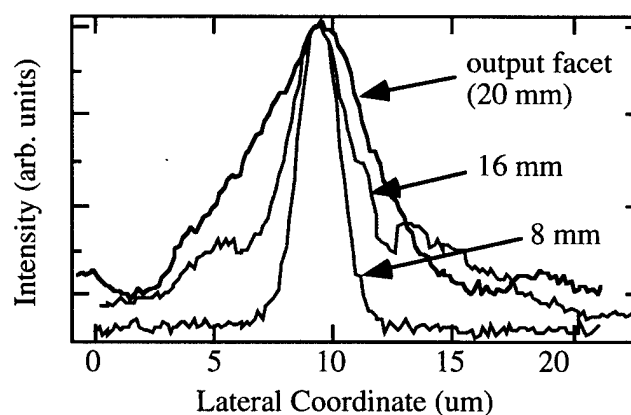
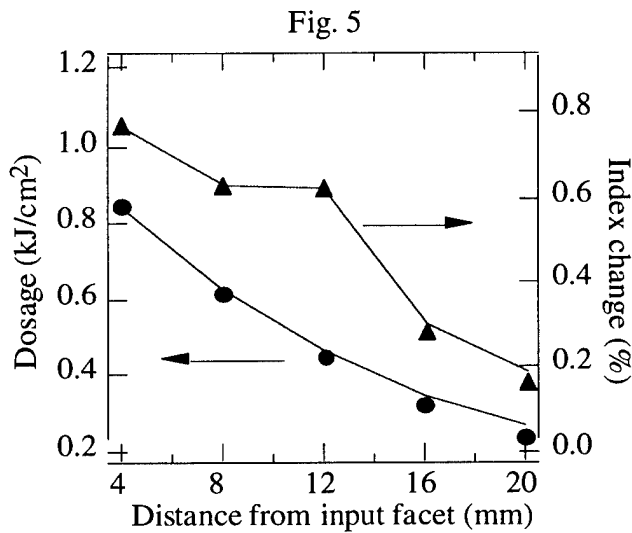
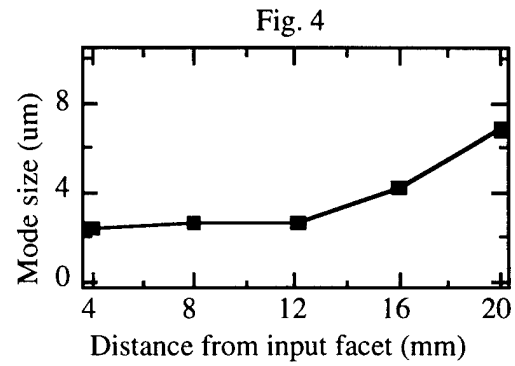


Figure 4 is a plot of the lateral mode size ( $1/e$  width) versus distance from the input facet, for the aforementioned guide. The most dramatic change in the mode size occurs for less confined modes, away from the input facet. The lateral mode size changes from  $2.61\text{ }\mu\text{m}$ , 12 mm away from the input facet, to  $6.82\text{ }\mu\text{m}$  farthest away from the input facet (20 mm), translating to a spot-size conversion by a factor of 2.6 within a distance of 8 mm. Over the entire device length of 16 mm, the mode size changes by a factor of 3. The index contrast at different positions along the waveguide was extracted from the measured



mode sizes using the effective index approximation. Figure 5 plots the longitudinal variation of the calculated index change for this guide. Also plotted in Fig. 5, is the dosage distribution along the waveguide. The dramatic change in mode sizes in the 12-20 mm region shown in Fig. 4, is also reproduced in the corresponding index variation, and we conclude that the photodarkening process exhibits the highest sensitivity for doses lesser than  $450\text{ J}/\text{cm}^2$ . Since at low index contrast levels, the width of the waveguide also plays

an important role in determining the mode-size, even larger longitudinal variations should be possible for smaller widths of the photoinduced region. All devices reported here had a film thickness of one  $\mu\text{m}$ , which is lesser than the skin-depth of the inducing light. Thicker films will lead to a gradient index distribution in the vertical dimension, allowing the same principle to define 2-D tapers.

This work is supported by DARPA under the Center for Optoelectronic Science and Technology (Grant #MDA972-94-1-0004) Program.

## References

1. Y. Utsugi and Y. Mizumisha, *Jpn. J. Appl. Phys.* **31**, Pt. 1, 3922 (1992).
2. S. Ramachandran and S.G. Bishop, "Rapid thermal annealing of chalcogenide glasses for photodarkened waveguide and grating applications", *OSA Fall Topical Meetings on Bragg Gratings, Photosensitivity, and Poling in Glass Fibers and Waveguides.*, OSA Technical Digest **17**, 194 (1997).

**Integrated Photonics Research**

# WDM I

**Monday, March 30, 1998**

**Julian B. Soole, Tellium, Inc.**  
Presider

**IMD**  
**11:00am-12:30pm**  
Saanich Room

# Integrated optical devices for WDM networks

Y. Yoshikuni

NTT Opto-electronics Laboratories

3-1 Morinosato-wakamiya, Atsugi-shi, Kanagawa, 243-01 Japan

Phone: +81 462 40 2857, Facsimile: +81 462 40 4302, E-mail: yosikuni@aecl.ntt.jp

## **1. Introduction**

Integrated optics are key technologies for developing compact and low-cost optical devices needed to realize WDM networks. Many devices have been made using monolithic and hybrid integrated optics with a view toward applying them to WDM networks in the future. This presentation reviews the recent progress of monolithic and hybrid integrated optics in device applications.

## **2. Hybrid Integrated Devices**

The recent development of the semiconductor spot-size converter has significantly increased the possibility of hybrid integration. The integrated spot-size converter enables us to obtain efficient light coupling between semiconductor devices and a silica-based waveguide and to make various hybrid integrated circuits without the need for precise alignment. Figure 1 shows a hybrid integration of a four-channel semiconductor optical amplifier (SOA) with a silica-based planar lightwave circuit (PLC) <sup>1</sup>. The SOA has a nearly square ( $0.4\ \mu\text{m}$  by  $0.6\ \mu\text{m}$ ) active layer that obtains low polarization dependence of less than 1 dB <sup>2</sup>. The fiber-to-fiber gain characteristics shown in Fig. 2 are uniform for all four devices. The SOA provides high-speed gate operation as well as optical gain, and enables us to make various integrated circuits. Figure 3 shows a high-speed wavelength selector containing a 4-channel SS-SOA gate module and an 8x8 PLC arrayed waveguide grating (AWG). The input signal was demultiplexed by the PLC-AWG and then selected by the SOA gate. The output waveform in the figure shows rise- and fall-time of less than 1 ns, which is suitable for high-speed optical switching. Figure 4 shows the bit error rate (BER) of signals after passing through the wavelength selector. There was no power penalty due to electrical and optical interference, even when the other channels were randomly driven.

## **3. Monolithic Integrated Devices**

Semiconductor AWGs are promising candidates for optical filters in monolithic integrated devices. Although InP-based AWGs have attractive features such as small chip size and easy integration with other devices, their drawback is large polarization dependence. Recently polarization-insensitive semiconductor AWGs have been fabricated with deep ridge waveguides. The composition, thickness, and width of the waveguides are carefully designed to make the refractive index polarization insensitive, as shown in Fig. 5. This waveguide structure was utilized to make polarization-insensitive 8-channel AWGs with a cross-talk of -30 dB in a very

small chip size (2.4 mm by 3.0 mm)<sup>3</sup>. The small bending radius of the waveguides also enables fabrication of large-scale InP-based AWGs. Figure 6 shows a photograph of a 64-channel arrayed waveguide grating with channel spacing of 50 GHz<sup>4</sup>. It contains 64 input/output waveguides and 232 arrayed waveguides in a chip size of only 3.6 mm by 7.0 mm. Figure 7 shows the wavelength dependence of the AWG. The transmission spectra for all 64 output channels are overlapped. Fiber-to-fiber transmission of -14.4 dB and cross-talk of less than -20 dB have been obtained. The polarization dependence of the peak frequency is less than 10 GHz, as shown in Fig. 7(b)

## 5. Conclusion

Recent progress in integrated optical devices for use in WDM networks is reviewed. The development of semiconductor optical amplifiers integrated with a spot-size converter (SS-SOA) eliminates loss limitation in hybrid integration and enables us to make various devices with hybrid integration. Progress in InP-based AWGs enables to make compact, polarization-insensitive optical filters on InP substrates. These filters will be integrated with various semiconductor devices, such as photo-detectors, optical amplifiers, and semiconductor lasers.

<sup>1</sup> T. Ito et al., "Ultra-wide-band high-speed wavelength selector using a hybrid integrated gate module: a 4-channel SS-SOA gate array on PLC platform," IOOC/ECOC '87, post deadline papers, pp. 53-56, 1997.

<sup>2</sup> N. Yoshimoto et al., "Four-channel polarization-insensitive SOA array integrated with butt-jointed spot-size converters," Electron. Lett., vol. 33, pp. 2045-2046, 1997.

<sup>3</sup> M. Kohtoku et al., "Polarization-Independent InP Arrayed Waveguide Grating Filter using Deep Ridge Waveguide Structure," CLEO Pacific Rim' 97, FN4.

<sup>4</sup> M. Kohtoku et al., "InP-based 64-channel arrayed waveguide grating with 50-GHz channel spacing and up to -20 dB crosstalk," Electron. Lett., vol. 33, pp. 1786-1787, 1997.

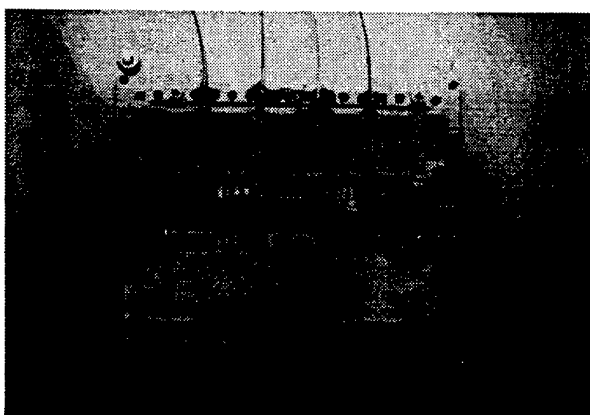


Fig. 1. Photograph of gate module: a 4-channel SS-SOA on PLC platform.

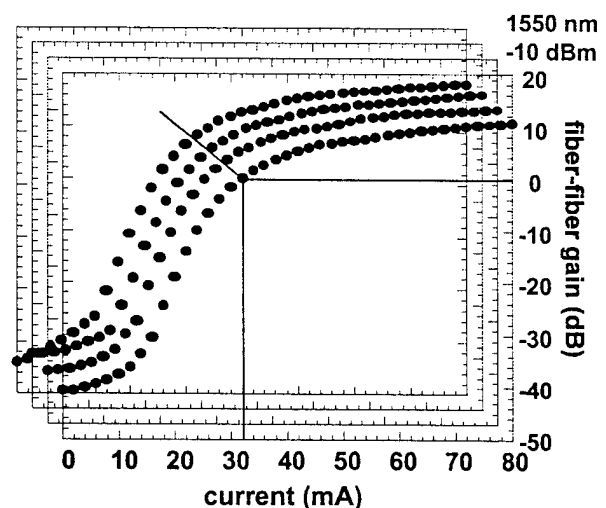


Fig. 2. Gain characteristics of a 4-channel gate module.

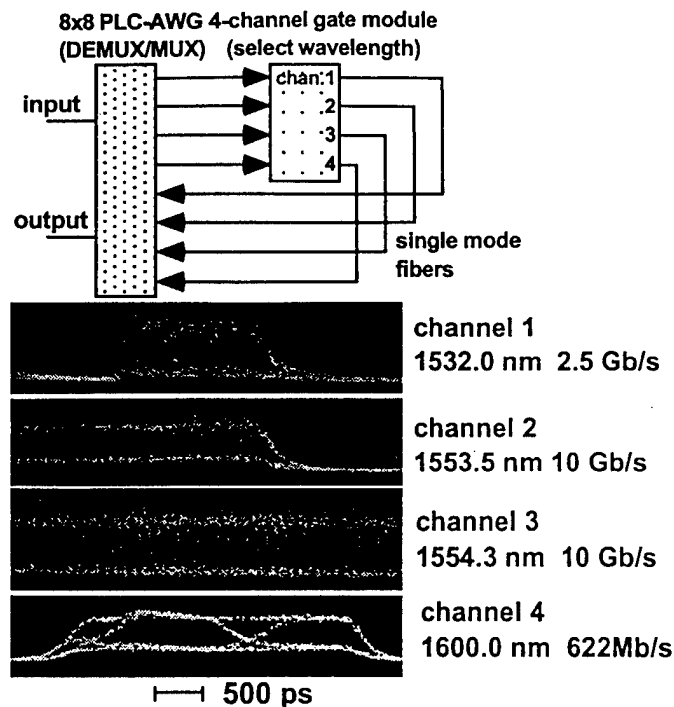


Fig. 3. Dynamic response of an ultra-wide band wavelength selector using a 4-channel gate module and PLC-AWG.

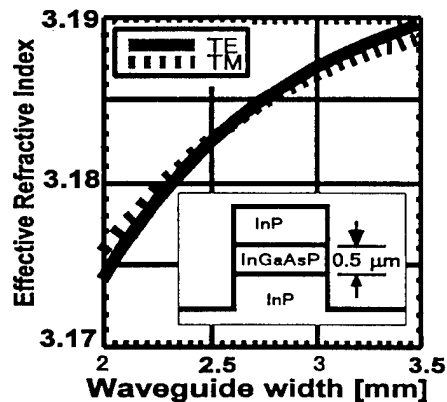
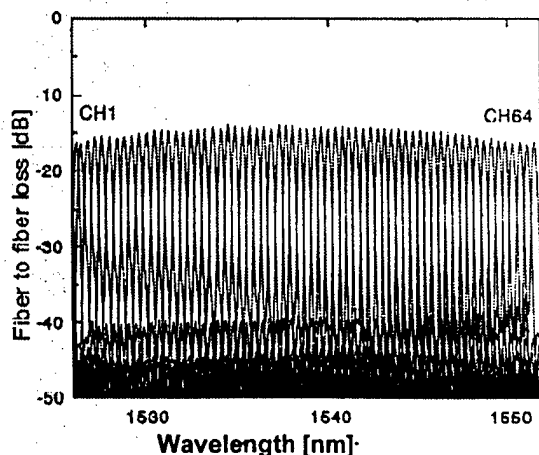
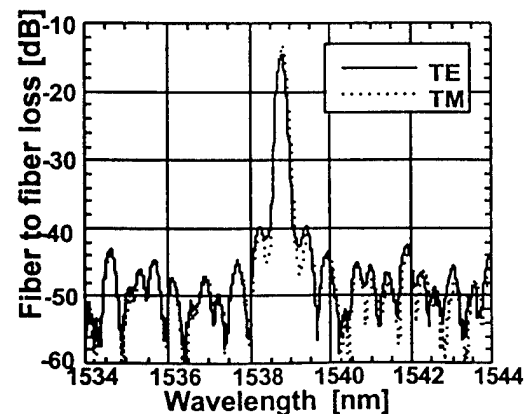


Fig. 5. Calculated refractive index for TE and TM modes as a function of waveguide width.



(a) Transmission spectrum for all 64-channels



(b) Transmission spectrum of central output port

Fig. 7. Transmission spectrum of the 64-channel arrayed waveguide grating.

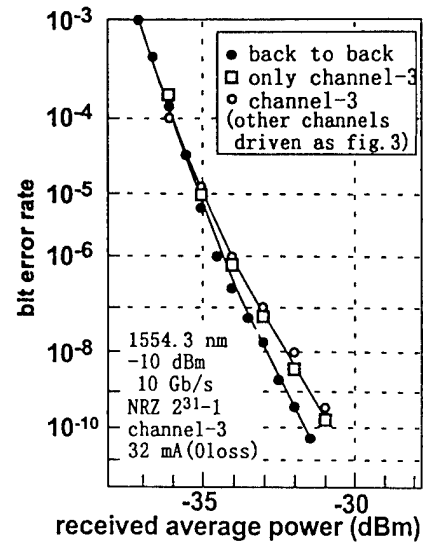


Fig. 4. Bit error rate of the ultra-wide band wavelength selector.

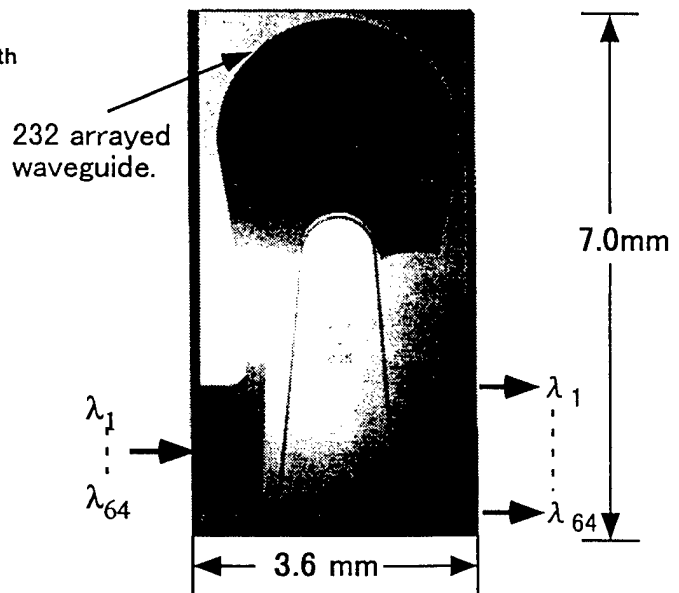


Fig. 6. Photograph of the InP-based 64 channel arrayed waveguide grating

## Channel monitoring in WDM networks: a systems perspective

Gabriela Livescu

Lucent Technologies, Holmdel, NJ 07733

Phone: (732) 949-3207 Fax: (732) 834-5420 E-mail: gabi@lucent.com

### Abstract

Optical Channel Monitoring in a WDM system implies measurement of wavelength, power, and optical signal-to-noise ratio of all channels. This information can be used for control of network elements, network maintenance, and performance monitoring. I shall discuss a variety of devices applicable to optical monitoring, and useful in the control, maintenance, and provisioning of lightwave systems.

### 1. Introduction

Wavelength Division Multiplexing (WDM) networks are becoming increasingly complex as the number of wavelengths (channels) on a single fiber increases, channels are added and dropped at various sites, and/or exchanged between two or more optical networks. Operation of *optical* networks will require functions in the *optical layer* dedicated to the transport infrastructure [1], with *performance monitoring* and *failure isolation* features that are at least as good as those provided by today's SONET (Synchronous Optical Networks) [2]. These features must be built into the most critical network elements. We will concentrate here on one key performance monitoring feature: optical channel monitoring.

### 2. Optical networks and SONET connections

An example optical network with 10 sites is illustrated in Fig.1(a). It interconnects various network elements, such as terminals and switches. The lines connecting the sites carry different numbers of channels, for example 16 between sites 1,2,8,7, and 80 between sites 1,2,3,6, etc. Channels are added and dropped at some of the sites; other sites may have cross-connects to direct channels to different parts of the network. The two-sided arrows between the sites are bi-directional optical lines, carrying the optical signals originating at terminals. Fig.1(b) illustrates one such line. At the terminals, information bearing electrical signals (data) from the customer premises are built (time multiplexed) into SONET frames. A SONET frame contains two parts: the payload (data), and the overhead (system related information, such as performance monitoring and system maintenance messages). The electrical SONET frame is then converted into an optical signal of wavelength  $\lambda$ . In a WDM system, the different channels  $\lambda_i$  originating at terminals "i" are optically multiplexed and launched into the transmission fiber. At the receiving end, the WDM signal is spectrally separated and directed to the corresponding SONET terminals, where the optical signal is detected and the electrical SONET frame is disassembled, to retrieve the transmitted payload and overhead.

In SONET terminology, the connection between the point at which a frame is assembled in the *electrical* signal, and the point at which it is disassembled, is called a path. A line is the connection between the point where the frame bearing *optical* signal is first generated, and the point where it is last detected. Thus a line consists of transmitter lasers, transmission medium (fiber), repeaters, and receivers. A portion of the line in which the signal stays optical is a section, and the equipment delimiting a section is called network element. The overhead part of the SONET frame contains path, line, and section related information, which is read and written at the network elements terminating the path, line, and section. The overhead is used for network management functions, such as network configuration, fault management, performance monitoring, billing and security. The SONET transport protocol allows for highly reliable networks, which form the basis for the explosion of information exchange we have seen in the last few years.

Before the advent of the optical amplifier, repeater sites were regenerators, performing an optical-to-electrical (O/E) and electrical-to-optical (E/O) conversion. The repeater sites were thus separated by SONET sections. The overhead was read and re-created at every repeater site, and the only non-monitored part of the transmission system was the fiber, or the optical layer. The management of the network and network elements was done via the overhead, entirely in the electrical layer.

The optical amplifier and WDM systems changed all that: the repeaters are now part of the *optical layer*, and so are wavelength multiplexers, optical add/drop sites, and optical crossconnects. More and more of

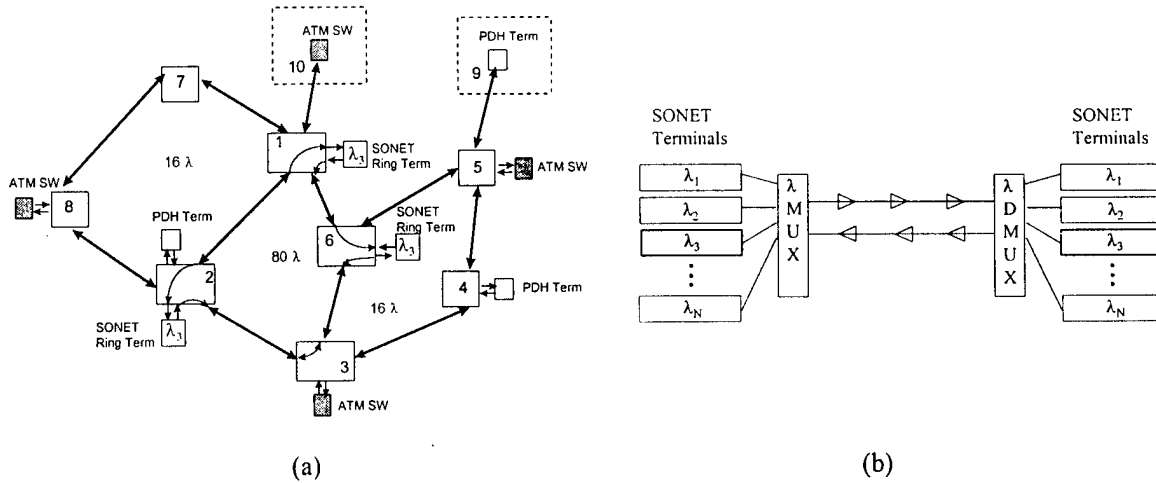


Fig. 1. (a) An example optical network. The double-arrows are point-to-point *optical line* connections, carrying various numbers of channels, with different channels directed to different sites. For example, a SONET ring at wavelength  $\lambda_3$  connects sites 1, 2 and 6. (b) A typical bi-directional *optical line* connection.

the optical network is transparent, bit rate and format independent. This is good news for bandwidth and speed, but it requires a completely new approach to network management. To achieve network management capabilities in WDM systems, an additional channel, the supervisory (telemetry) channel, is used. It undergoes an O/E and E/O conversion at every network element, acquiring and transmitting system monitoring and maintenance information. Some of the key parameters to be acquired and monitored in an optical network [2] are per channel power and optical signal-to-noise ratio (OSNR). Such parameters need to be known and controlled to avoid power loss in single channels, or to determine the gain spectrum of the optical amplifier, or to equalize channel powers after add/drop multiplexers, etc. This information must often be acquired at points in the system where many or all channels are simultaneously present, and must be delivered on a per channel basis. Thus, an optical monitoring unit must be capable to spectrally separate and analyze the channels: it should be an optical spectrum analyzer. Such a unit could be built into the most critical network elements, such as the optical amplifier, the add-drop, or the optical crossconnect. An optical monitor must have a spectral range covering all the channels, a spectral resolution compatible with the smallest channel spacing in the system, and provide accurate wavelength and power measurement, independent of polarization. To be useful for field applications, it must be mechanically and thermally stable, and its size and cost must be small.

### 3. Optical Monitoring Devices

There are a variety of approaches to this device, which must perform two functions: dispersion and detection of light. They can be classified in two basic categories: (i) scanning dispersion element followed by a single detector, and (ii) fixed dispersion element, followed by an array of detectors. A scanning Fabry-Perot (FP) filter can be used as the scanning dispersion element in the first category. For today's applications with large numbers (many tens) of closely spaced channels (50-100GHz), this apparently simple approach imposes tough requirements on the filters. Commercially available bulk glass or fiber FP filters can achieve a spectral resolution of 0.07nm (<10GHz), and a power accuracy of  $\pm 0.5$ dB.

In the second category, a fixed dispersive element, such as a dispersion grating or a waveguide router, can be followed by an array of detectors. This approach, which imposes difficult requirements on both elements of the monitor, has been pursued by different groups and significant results have been reported recently. For example, a monitor composed of a blazed and chirped fiber Bragg grating followed by a 256 element detector array was recently demonstrated by Wagener et al [3] of Lucent Technologies. A schematic description is shown in Fig.2(a). Over its spectral range, this compact device showed a performance equivalent to a single pass optical spectrum analyzer, with 0.1nm (12.5GHz) resolution and a power accuracy of  $\pm 0.5$ dBm. The spectral range and resolution are determined by the fiber grating and the number of pixels in the detector array: a spectral range of 32nm was recently achieved with a 256 pixel array. Fig.2(b) shows a spectrum obtained with this monitor. The spacing between the 26 channels

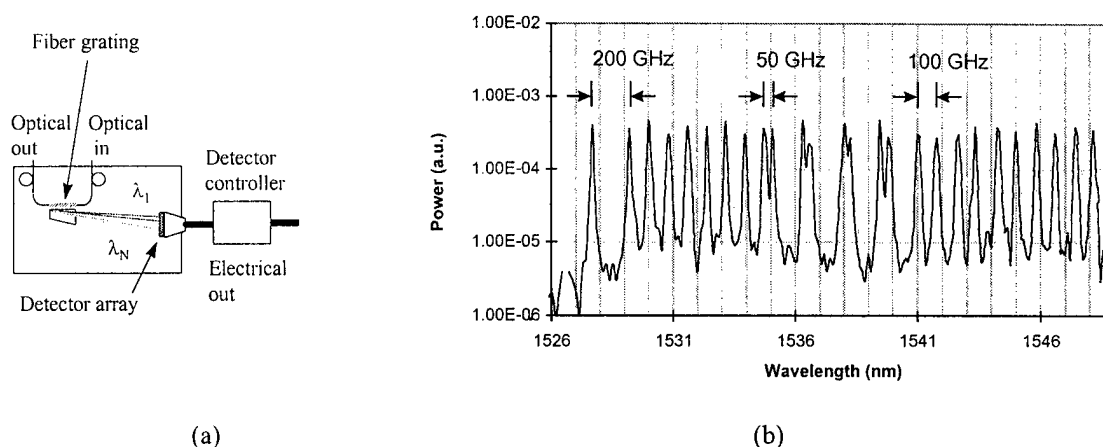


Fig.2. (a) Schematic description of fiber grating spectrometer. (b) Example spectrum, measured with this spectrometer: 26 channels are shown, with separations varying from 200GHz to 25GHz.

shown here ranges between 25GHz and 200GHz. The spectral resolution of 0.12nm (15GHz) allowed for peak-to-valley ratios of about 20dB, 17dB and 10dB for channels spaced by 200GHz, 100GHz and 50GHz respectively. Such a device can be used in a dense WDM system to identify channels, to monitor the number of channels, the power-per-channel and the gain spectrum. For single channel OSNR measurements, a better spectral resolution would be required.

Other examples of this type of monitor were demonstrated: a bulk diffraction grating followed by a 256 element p-i-n photodiode array [4], used to control the power of 8 channels entering an Add/Drop node; a waveguide router with 18 arms followed by a 36 pixel detector array [5], used to control wavelength of 8 lasers acting as regenerators in an optical crossconnect with wavelength conversion; a similar device was used to perform network fault detection in an optical crossconnect [6].

Another approach, which may also be included in this category, proposed by Lucent's Giles [7] and Nelson [8], is based on mapping of wavelength into time delay by using group-velocity dispersion in fiber. In this method, the multi- $\lambda$  input is passed through a series of fiber gratings, which temporally separate the different  $\lambda$ 's, and the channels can be identified by their time delays upon reaching the detector. The identification of the channels can be done either by asynchronously modulating them at a low duty cycle [7], or by using data correlation to determine the time shift of the channels [8].

#### 4. Conclusions

We presented here some of the optical channel monitoring devices that have been reported recently. The results so far indicate that one or more of these devices may very soon demonstrate the capabilities and the reliability required for deployment in today's transmission systems.

#### Acknowledgments

For their contributions to this work, the author is indebted to the following colleagues at Lucent Technologies: in Holmdel, to D. Al Salameh, for insightful comments on optical networks, N. Denkin, for his invaluable help in understanding optical monitors and transmission system circuit packs, M. Zirngibl, for providing access to the multi-channel optical system, and to Stan Lumish, for his support and encouragement; in Murray Hill, to J. Wagener and C. Koeppen, for generously providing the broadband fiber grating spectrometer and the software running it.

#### References

1. C. Fan and J.P. Kunz, in "Optical Fiber Telecommunications", ed. I.P. Kaminow and T. Koch, (Academic Press, 1997), vol. IIIA, p. 265-301
2. L. Yu, Proceedings of NFOEC 1997, Vol.2, p.109.
3. J. L. Wagener et al., Proceedings of ECOC '97, Vol.5, p. 65.
4. K. Otsuka et al., Proceedings of ECOC '97, Vol.2, p.147.
5. M. Teshima et al., Proceedings of ECOC '97, Vol.3, p.59.
6. H. Takeshita et al, Proceedings of ECOC '97, Vol.3, p.335
7. R. Giles, submitted to IEEE Photon. Technol. Lett., 1998.
8. L. Nelson et al., submitted to IEEE Photon. Technol. Lett., 1998.

## Box-like broadband filters using chirped waveguides

S. T. Chu<sup>1</sup>, W. Pan<sup>1</sup>, B. Little<sup>2</sup>, S. Sato<sup>1</sup>, T. Maeda<sup>1,3</sup>,  
T. Kato<sup>3</sup>, and Y. Kokubun<sup>1,3</sup>

<sup>1</sup> Kanagawa Academy of Sci. & Tech. 3D Microphotonics Project 3-2-1 Sakato, Takatsu-ku Kawasaki, Japan 213	<sup>2</sup> Massachusetts Inst. of Tech. Research Lab. of Electronics Cambridge MA 02139 U.S.A.	<sup>3</sup> Yokohama Nat'l Univ. Dept. Elect. & Comp. Eng. 79-5 Tokiwadai, Hodogaya Yokohama, Japan 240
--	---	---

### Summary

In the subscriber WDM system, filters are needed to separate wavelengths at the two channels of 1.3 and 1.55  $\mu m$ . These filters should be broadband enough so that they can provide the required tolerance for the source lasing spectrum. Ideal wavelength filters using adiabatic coupling was suggested in [1]. The response of these filters are characterized as being boxlike: flat, unity transmission over a range of wavelengths within the passband, infinite rejection outside the passband, and a sharp roll-off between these two regions. These devices are similar to directional coupler filters. In the conventional couplers, power transfer between waveguides varies periodically along their length. In addition, the degree of power transfer is governed by the synchronism between the two guided modes.

In the proposed structure, as shown in Figure 1, the width of one of the waveguides is linearly chirped in the direction of propagation. Depending on the degree of chirping and the length of the device, each wavelength within a range will now be synchronous at some coupler position. Power transfer now becomes monotonic over the device length. With the judicious choice of structure parameters, the spectral response become box-like, with a flat passband and very low sidelobes. The details of the chirp and coupling strength profiles do not need to be precisely controlled, however, and are indeed relatively insensitive to variations. Some of the required conditions on the minimum device length and chirp have been set out in Reference [1].

Figure 2 shows qualitatively the preferred coupling strength and detuning along the length of the waveguides. The detuning or chirp varies linearly, while the coupling strength is constant over the device length and tapers off smoothly towards the ends. The detuning curve shown is

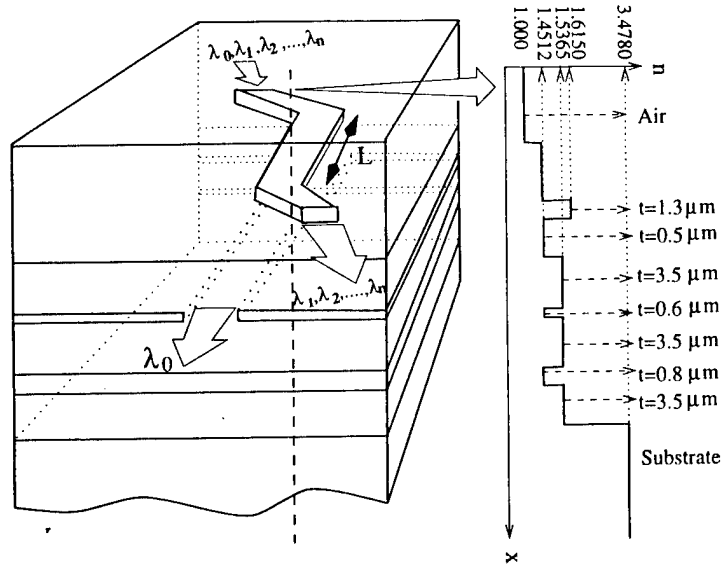
at a single wavelength. The change of wavelength shifts this curve vertically, so that the synchronous point ( $\Delta\beta(\lambda, z) = 0$ ) falls at a different position along the device. Such characteristics can be realized by the arrangement depicted in Figure 1.

Figure 1 schematically depicts the device of the current study. It consists of a pair of waveguides coupled vertically [2]. In this arrangement, the bottom waveguide is either an ARROW or conventional channel guide, while the top is a channel guide. The width of one of the guides is varied linearly. The dispersion characteristic of the ARROW is relatively flat. Thus for broadband operation, the width of the ARROW guide must be varied considerably to achieve a similar chirp of the propagation constant compared to the conventional guide. This feature allows more precise control of the degree of chirping and the bandwidth.

Typical spectral responses for various degree of waveguide chirp (the change of waveguide width) are depicted in Figure 3. These simulations were carried out using the exact modes [3] of the individual waveguides, and using coupled mode theory to determine the power transfer characteristics. The waveguide parameters used in these simulations are listed in Figure 1 with the width of the channel waveguide fixed at  $1.30\ \mu\text{m}$  while the width of the ARROW waveguide was tapered linearly. For the first set of examples shown in Figure 3, the coupling length  $L$  of each device is kept fixed at  $30\ \text{mm}$ , while the degree of waveguide chirp is varied from 5, 4, and  $3\ \mu\text{m}$  and the FWHM of the responses are 32.7, 25.3, and  $18.3\ \text{nm}$ , respectively. These curves demonstrate that the degree of chirp alone determine the desired bandwidth. We are currently fabricating the proposed filter to verify the above analysis.

## REFERENCES

- [1] B. E. Little, "Ideal wavelength filters using semiadiabatic coupling," *Opt. Lett.*, **21**, pp. 1424-1426, 1996.
- [2] S. T. Chu, W. Pan, S. Sato, T. Maeda, B. Little, and Y. Kokubun, "Reduction of Filter Sidelobe Level by an X-crossing Vertical Coupled ARROW Filter," *IEEE Photon. Technol. Lett.*, *accepted to be published*.
- [3] C.L. Xu, W. P. Huang, M. S. Stern, and S. K. Chaudhuri, "Full-vectorial mode calculation by finite difference method," *IEE Pro-Optoelectron.*, **141**, pp. 281-286, 1994.



**Figure 1:** The ARROW-type vertical coupler filter.

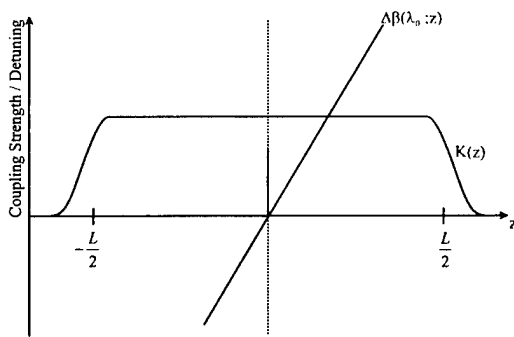


**Figure 2:** General description of waveguide interaction  $\kappa(z)$ .

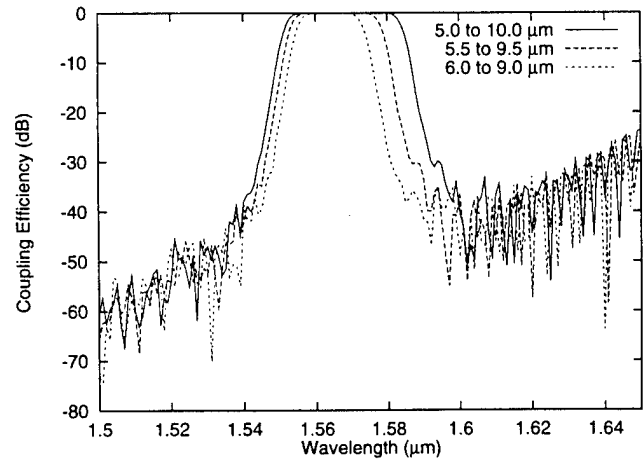


**Figure 3:** Typical box-like filter responses.

## Integrated DBR laser - EA modulators for WDM applications

P. Legay, A. Ramdane, D. Delprat, A. Ougazzaden, Y. Sorel\*, M. Morvan\*

France Télécom / CNET / DTD / Laboratoire de Bagneux, 196 Av. H. Ravera,  
92225 Bagneux Cedex, France  
Tel : 33 1 42 31 77 18  
Fax : 33 1 42 53 76 32  
e-mail : philippe.legay@cnet.francetelecom.fr

\* France Télécom / CNET / DTD / 2 Avenue Pierre Marzin, 22307 Lannion Cedex, France

° Now at Corning SA, 7 bis Avenue de Valvins, 77210 Avon, France

### INTRODUCTION

Multigigabit wavelength division multiplexed (WDM) transmission systems are based on distributed feedback lasers (DFB) with external or integrated modulators as transmitters. Precise combs of wavelengths are used in these applications, which implies stringent requirements for their achievement in a reproducible manner. The ability to use tunable sources with integrated modulators is hence very attractive for such systems. Indeed, DBR lasers bring flexibility for wavelength allocation to a precise value. Moreover, wavelength tuning may be put to advantage as in e.g. network reconfiguration at the emitter for security purposes.

We used MOCVD Selective Area Growth (SAG) to achieve the laser-modulator monolithic integration. In a previous paper [1], it had been shown that a major issue in DBR laser-EA modulator integration was related to the achievement of adequate output power on the Bragg (and modulator) side of the device, while keeping a sufficiently high side mode suppression ratio (SMSR). The multiple quantum well (MQW) structure was hence subsequently modified to overcome this problem. Here are presented components with optimized characteristics. The interest for WDM systems is furthermore highlighted with transmission experiments at 10 Gb/s over 75 km of standard single mode dispersive fiber on the four channels of an integrated device.

### DEVICE DESIGN AND FABRICATION

From the previous results, we modified the laser structure by decreasing the number of quantum wells and lowering the coupling coefficient strength in order to increase the output power.

The three sections of the DBR laser / EA modulator are defined using SAG of InGaAsP wells and barriers. A SiNx mask has been designed to adjust the material photoluminescence peak values at 1.55, 1.5 and 1.45  $\mu\text{m}$  respectively in the laser, modulator and Bragg grating sections. Another mask configuration has also been tested for which the wavelength of the Bragg grating and the modulator sections are kept the same. The Bragg grating period was adjusted for a 50 nm wavelength detuning between the laser and the modulator, for optimized chirping behaviour. A 2  $\mu\text{m}$  width ridge technology was achieved in the three sections, yielding small modulator capacitance compatible with 10 Gb/s operation. Finally, an antireflection coating was deposited on the modulator facet. Figure 1 shows a view of the integrated component after the technology.

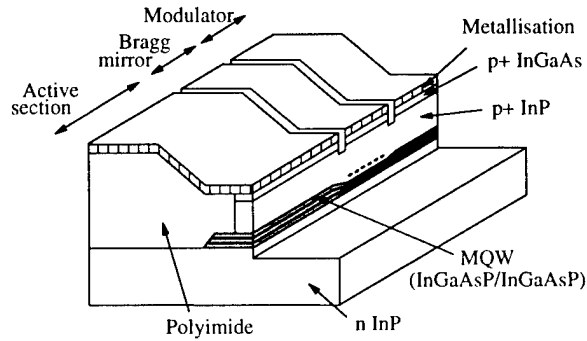


**Figure 1 :** Schematic viewgraph of the integrated device

## DEVICE PERFORMANCES

The DBR ridge lasers exhibit threshold current of about 30 mA and the coupled output power into the fiber ranges from 0 to -5 dBm for  $I \sim 100$  mA. On the same wafer, two lasing wavelengths of 1.43  $\mu\text{m}$  and 1.53  $\mu\text{m}$  are obtained, depending on the mask configuration used for SAG. The tuning of the laser is obtained by current injection into the Bragg section (Figure 2). The typical tuning range we measured is 3.2 nm with 4 or 5 channels with a side mode suppression ratio higher than 35 dB for all channels. This result confirms that the KL coefficient is well adjusted for a good trade-off between increased output power and single mode state of the laser.

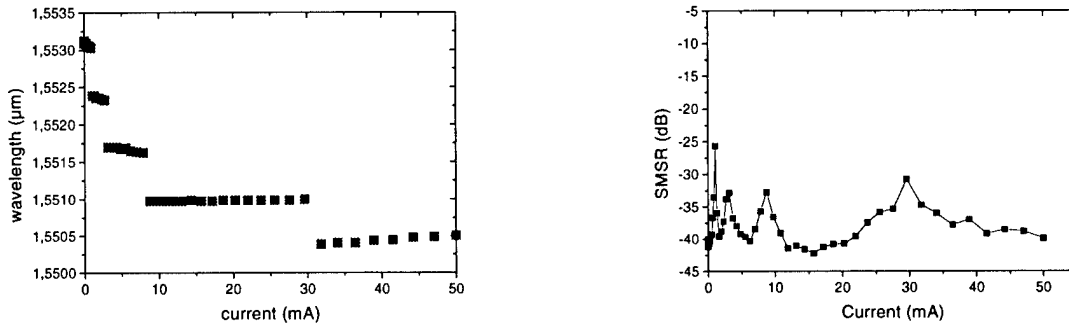


**Figure 2 :** Left curve : tunability of the DBR laser. Right curve : SMSR on all the tuning range

We also checked the fine tuning of the wavelength with the temperature for two adjacent channels spaced by 90 GHz (Figure 3). When the temperature increases, the wavelength shifts to higher values with the expected rate of 0.1 nm/°C. This demonstrates that we can adjust the wavelength to a precise allocated value within a 0.05 nm ( $\sim 5$  GHz) tolerance for the whole tuning range.

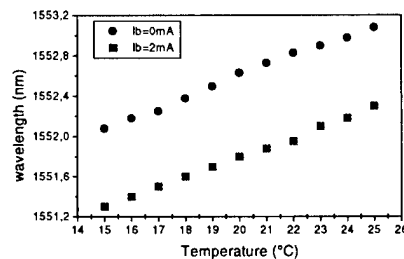


**Figure 3 :** Fine tuning of the wavelength with the temperature for two adjacent channels of the DBR laser

The modulation characteristics are presented in Figure 4 for the 4 channels of a DBR laser. For all the channels the extinction ratio is higher than 10 dB for a 2V swing.

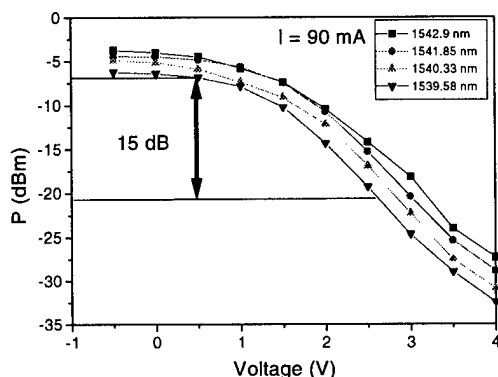


**Figure 4 :** Output power of an integrated device versus reverse voltage applied to the modulator for the different wavelengths of the laser.

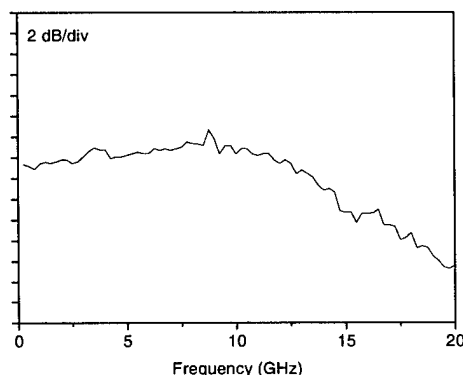


**Figure 5 :** HF response of an integrated DBR laser-modulator.

The small signal modulation shows a bandwidth of 15 GHz (Figure 5), compatible with transmission experiments at 10 Gb/s.

Finally, transmission was performed at 10 Gb/s for the four channels of the DBR laser over 75 km of standard G652 fiber. Previous transmission experiments using the same kind of device were reported at 2.5 Gb/s [2]. From the bit error rate (BER) measurements, we determined a penalty lower than 2 dB for all the channels. This implies very small chirping characteristics of the light source. Detailed results will be presented at the conference.

## CONCLUSION

DBR laser - EA modulator monolithic integration has been investigated with SAG. The adjustment of the structure leads to the fabrication of integrated components with high coupled output power, with a tuning range  $>3$  nm and with good static and dynamical modulation characteristics. These transmitters were used to perform, to our knowledge for the first time, transmission at 10 Gb/s over 75 km of standard fiber on four channels of the DBR lasers.

## References

- [1] D Delprat, A Ramdane, L Silvestre, A Ougazzaden, F Delorme, and S Slemphes  
IEEE Photonics Technology Letters, vol. 9, pp 898-900, 1997
- [2] K C Reichmann, P D Magill, U Koren, B I Miller, M Young, M Newkirk, and D Chien  
IEEE Photonics Technology Letters, vol. 5, pp 1098-1100, 1993

### Sampled grating DBR lasers with integrated wavelength monitoring

Beck Mason, Olga Lavrova, Greg A. Fish, Steve P. DenBaars, Larry A. Coldren  
Electrical and Computer Engineering Department, University of California Santa Barbara

Sampled Grating DBR lasers, and other devices which achieve wide range tunability through the use of Vernier effect tuning, show great promise for implementation in WDM communication systems [1]. One limitation of these devices is the complicated tuning mechanism which they employ. Since the channel spacing in dense WDM networks requires precise control of the lasing wavelength it is essential to employ some form of wavelength monitoring and feedback for the device. Some techniques rely on externally monitoring the output power and wavelength of the laser [2]. In order to reduce the system complexity and provide for local feedback and control, it is desirable to have an integrated wavelength and power monitor for the device capable of tracking the wavelength of the laser over the entire tuning range. The concept of using a filter with a wavelength dependant response for this task has been well established [3]. Typically the light is split into a reference and a filtered component, and the ratio between these is used to determine the filter transmission and, thus the wavelength. In more advanced versions, a device such as an overcoupled coupler with a wavelength dependent splitting ratio, is used to eliminate the filter element.

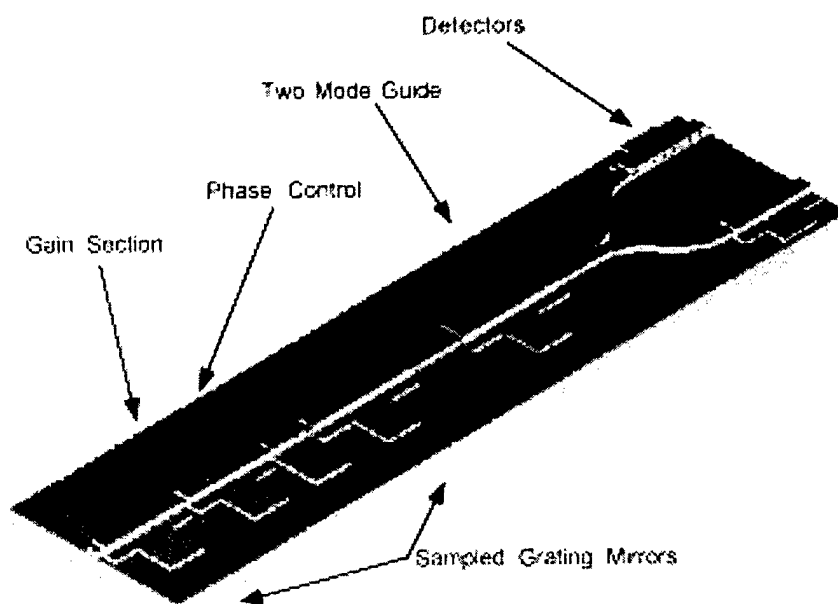


Figure 1. Device Schematic

In this device we have integrated the wavelength dependent splitter and two detectors onto the back end of a SGDBR laser Fig. 1. This results in a compact and efficient wavelength and power monitor. The wavelength dependent splitter consists of a two mode interference waveguide (TMI) terminated in a Y branch splitter with a waveguide detector in each branch. The structure is analogous to a zero gap coupler with an extremely long coupling length. The light from the

back mirror of the laser is launched into the TMI waveguide asymmetrically so as to excite the two lowest order lateral modes of the guide. The light propagates along the guide and is split into two output waveguides at the Y branch with a ratio that is dependent on the modal interference pattern. The difference in propagation constant for the two modes leads to a characteristic beat length for the modal interference. When the TMI section is made long enough that multiple beat lengths occur within it, there is a strong wavelength dependence in the splitting ratio. For this device, the TMI guide was  $1400\mu\text{m}$  long with a  $400\mu\text{m}$  Y branch and  $300\mu\text{m}$  long detectors. The laser employed a ridge waveguide  $3\mu\text{m}$  wide with front mirror, back mirror, gain and phase sections that were  $500, 650, 100$ , and  $550\mu\text{m}$  in length respectively. The total length of the device is  $4.2\text{mm}$ . The wavelength response of the splitter was analyzed using a beam propagation method simulation. The results from this indicate a sinusoidally varying wavelength dependence for the output current from the two detectors which has a range of  $100\text{nm}$  Fig. 3. By normalizing the detector currents it is possible to remove the power dependence and derive a wavelength reference signal from the device.

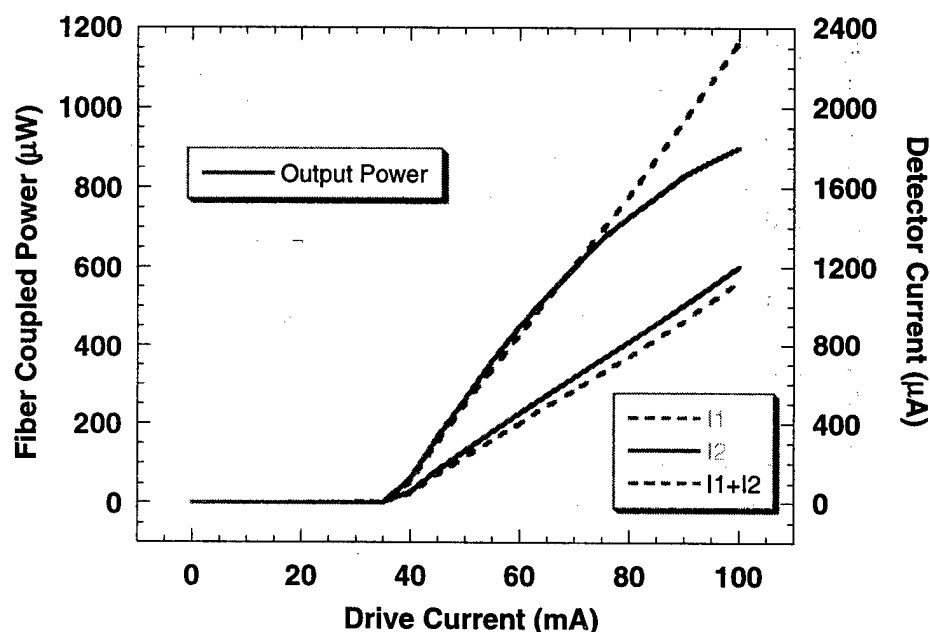


Figure 2. L-I curve and detector currents for integrated device.

The integrated device was easy to fabricate since the fabrication procedure used the same processing steps required for the regular ridge waveguide SGDBR laser. The base structure was grown by MOCVD with a  $4000\text{\AA}$  thick  $1.4Q$  waveguide, and four  $1\%$  compressively strained offset quantum wells. The active passive junctions were formed by a combination of selective wet etching steps. The gratings were patterned using a holographic exposure over openings defined in a  $\text{SiNx}$  mask and then transferred into the waveguide with a methane, hydrogen, argon (MHA) reactive ion etcher (RIE). The mask was stripped off and a  $1.9\mu\text{m}$  thick InP cap layer with an InGaAs contact layer were regrown over the structure. The ridge waveguides were

etched in another MHA RIE step and a short selective wet chemical etch was used to provide a uniform etch depth and remove any damage from the dry etch.

The integrated device was tested with a reverse bias of 2V on the detectors. The fiber coupled output power and the monitor currents for the device are shown in Fig. 2. The deviation from linearity for the output power is a result of the shift in the laser mode with respect to the front mirror peak as the current in the active region is increased. The wavelength is locked to the rear mirror peak so monitor shows a linear increase in detector current above threshold. The laser was tuned by injecting current into the front and back mirrors while maintaining a constant drive current in the gain region. The response for the wavelength monitor in the integrated device and the corresponding laser spectra are shown in Fig. 3a,b. In this plot the expected sinusoidal response is overlaid on the measured detector currents for the four different wavelengths. Currently the characterization of the integrated device is limited by the tuning range of the SGDBR laser which was much lower than anticipated.

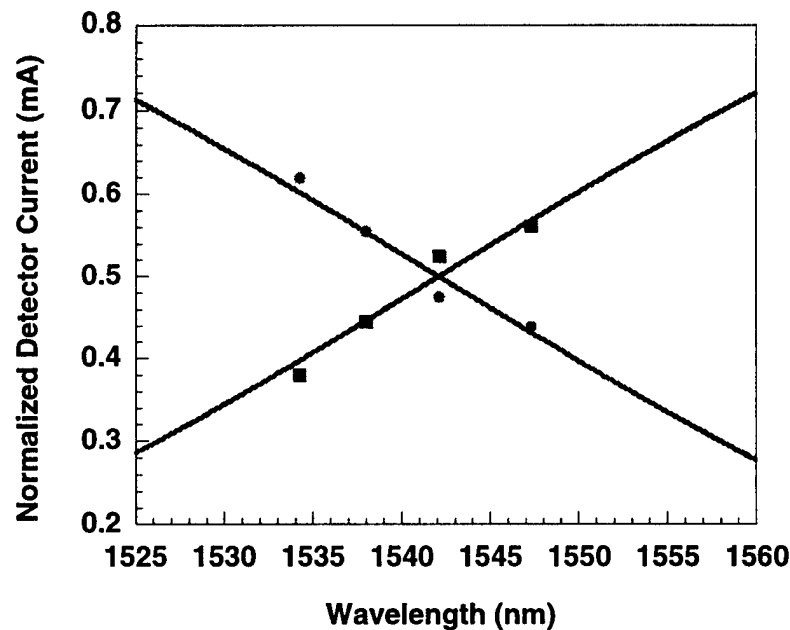


Figure 3. Detector currents at four different laser wavelengths overlaid with calculated response curves

#### References:

- [1] Jayaraman, V.; Chuang, Z.-M.; Coldren, L.A., "Theory, design, and performance of extended tuning range semiconductor lasers with sampled gratings.", *IEEE J. of Q. Elect.*, June 1993, vol.29, (no.6):1824-34.
- [2] Ishii, H.; Kano, F.; Yoshikuni, Y., "Wavelength stabilization of a superstructure-grating DBR laser for WDM networks.", 23 European Conference on Optical Communications IOOC-COC97 No.448, London, UK: IEE, 1997. p. 103-6 vol.1.
- [3] Melle, S.M.; Liu, K.; Measures, R.M., "Practical fiber-optic Bragg grating strain gauge system.", *Applied Optics*, 1 July 1993, vol.32, (no.19):3601-9.

**Integrated Photonics Research**

# **Vectorial Simulations**

**Monday, March 30, 1998**

**Wei Ping Huang, University of Waterloo, Canada**  
Presider

**IME**

**2:00pm–3:30pm**

Salon B

# Techniques of improving the imaginary-distance full-vectorial BPM based on Yee's mesh

Junji Yamauchi, Naofumi Morohashi, and Hisamatsu Nakano

College of Engineering, Hosei University

3-7-2 Kajino-cho, Koganei, Tokyo 184 Japan

Phone: +81-423-87-6190, Fax: +81-423-87-6381, e-mail: junji@yma.ei.hosei.ac.jp

## 1 Introduction

Recently, Lee[1] has proposed the full-vectorial finite-difference beam-propagation method (FD-BPM) based on Yee's mesh[2]. Using the imaginary-distance procedure[3], he succeeded in developing the eigenmode solver. The use of Yee's mesh has the advantage that all  $E$ - and  $H$ -field components are simultaneously evaluated, and that the obtained eigenmode field is directly utilized for the time-domain Yee's algorithm, the so-called FD-TD method. It should be noted, however, that Lee employed the conventional second-order accurate scheme. Furthermore, he did not describe the interface condition for a step-index waveguide in detail.

In this paper, we discuss techniques of improving the accuracy of Lee's method. High-order accurate schemes are applied to the analysis of a graded-index waveguide, and the increased accuracy is demonstrated. For the analysis of a step-index waveguide, the interface condition predominates the accuracy. After confirming the second-order accuracy in two-dimensional step-index waveguides, we analyze a rib waveguide using the index averaging technique based on Ampere's law. The effective index and the field profiles of major and minor components are presented and discussed.

## 2 Graded-index waveguides

We first consider a two-dimensional waveguide with a graded-index distribution expressed as  $n^2(x) = n_s^2 + 2n_s\Delta n/\cosh^2(2x/w)$ , where  $n_s = 2.1455$ ,  $\Delta n = 0.003$  and  $w = 5\mu m$ . In this case the accuracy is mainly determined by the finite-difference formula to be used. For the conventional FD methods using Yee's mesh, the second-order formula was used. In this section we employ the fourth- and sixth-order formulas in the transverse direction. These formulas can be derived as follows:

$$\frac{\partial\phi(x)}{\partial x} = \frac{9}{8} \frac{\phi(x + \Delta x/2) - \phi(x - \Delta x/2)}{\Delta x} - \frac{1}{24} \frac{\phi(x + 3\Delta x/2) - \phi(x - 3\Delta x/2)}{\Delta x} + O(\Delta x^4) \quad (1)$$

$$\begin{aligned} \frac{\partial\phi(x)}{\partial x} = & -\frac{75}{64} \frac{\phi(x + \Delta x/2) - \phi(x - \Delta x/2)}{\Delta x} + \frac{25}{384} \frac{\phi(x + 3\Delta x/2) - \phi(x - 3\Delta x/2)}{\Delta x} \\ & - \frac{3}{640} \frac{\phi(x + 5\Delta x/2) - \phi(x - 5\Delta x/2)}{\Delta x} + O(\Delta x^6) \end{aligned} \quad (2)$$

For the longitudinal direction, the conventional second-order formula is used.

Fig.1 shows the overlap-integral error between the numerical and exact fields of  $TE_0$  mode as a function of transverse mesh width  $\Delta x$ . A wavelength of  $\lambda = 1.3\mu m$  is used. The relation of  $\Delta z/\Delta x = 1/2$  is fixed[1], and the computational window dimension is taken to be  $2L_x = 120\mu m$ . A unit amplitude field is used as a starting field. It is found that the present schemes achieve high-order accuracies, while the conventional scheme exhibits second-order accuracy. It is interesting to note that the results obtained from the fourth-order scheme almost coincide with the data obtained using the FD-BPM based on the generalized Douglas scheme[4].

### 3 Step-index waveguides

For a step-index waveguide, the numerical results are severely affected by the interface condition imposed at the interface. In this section we first treat a two-dimensional waveguide whose refractive indices of the core and cladding are  $n_{co} = 3.512$  and  $n_{cl} = 3.17$ , respectively. The core width is taken to be  $2d \simeq 0.316\mu m$ , and the wavelength is chosen to be  $\lambda = 1.0\mu m$ , so that the normalized frequency is  $V = 1.5$ . The mesh width is taken to be  $\Delta z/\Delta x = 1/2$ . The computational window dimension is fixed to be  $2L_x \simeq 4.5\mu m$ .

Consideration is first given to the TE mode. Fig.2 shows the effective-index error of the fundamental mode as a function of transverse mesh width. Two curves are shown. One is the case in which the interface is placed on the  $E_y$  component and the refractive index at the interface is averaged by Ampere's law. The other is the case in which the interface is placed on the  $H_z$  component (no index-averaging technique is used). It is seen that the results using the former technique are slightly better than those in the latter one, indicating the second-order accuracy for each technique.

The corresponding result for the TM mode is presented in Fig.3, where two curves correspond to the cases in which the interface is placed on the  $E_z$  component, with or without using the averaging technique. The averaging technique again leads to the second-order accuracy, while the case without averaging results in the first-order accuracy.

Since the effectiveness of the averaging technique has been confirmed, we now analyze a rib waveguide as a classical benchmark. The waveguide configuration is specified in [5]. Note that the  $E_z$  component should be located at the corner of the waveguide, taking advantage of the tangential continuity across material interfaces. The computational dimensions are taken to be  $4.5 \times 8\mu m^2$ . The convergence behavior of the normalized effective-index  $B$  as a function of mesh width  $\Delta (= \Delta x = \Delta y)$  is shown in Fig.4. For comparison, the data obtained with the modal transverse resonance method (MTRM) [5][6] are also presented. Careful examination of Fig.4 reveals that the convergence rate is second order. It should be noted that the second-order accuracy cannot be readily achieved in the conventional full-vectorial BPM in which Yee's mesh is not employed.

Fig.5 illustrates the field profiles of major and minor components for the quasi-TM mode. It is worth mentioning that the field singularity at the corner is clearly observed in the minor component.

### 4 Conclusions

The imaginary-distance full-vectorial FD-BPM based on Yee's mesh has been improved. For a graded-index waveguide, the increased accuracy is achieved by high-order accurate schemes. For a step-index waveguide, the interface condition obtained from Ampere's law maintains the second-order accuracy even in a three-dimensional waveguide with corners. The present results clearly show the field profiles with discontinuities in major and minor components.

### 5 Acknowledgment

The authors would like to thank Dr. W. Lui of NTT for invaluable discussions on field singularity at the corner of a rib waveguide.

### References

- [1] S.M. Lee, Opt. Soc. Am. A, vol.13, no.7, pp.1369-1377, 1996.
- [2] K.S. Yee, IEEE Trans. Antennas Propag., vol.AP-14, no.3, pp.302-307, 1966.
- [3] D. Yevick and B. Hermansson, IEEE J. Quantum Electron., vol.25, no.2, pp.221-229, 1989.
- [4] J.Yamauchi et al., IEEE Photon. Tech. Lett., vol.9, no.1, pp.67-69, 1997.
- [5] C. Vassallo, Optical and Quantum Electron., vol.29, no.2, pp.95-114, 1997.
- [6] A.S. Sudbø, J. Europ. Opt. Soc. A, Pure Appl. Opt., vol.2, pp.211-233, 1993.

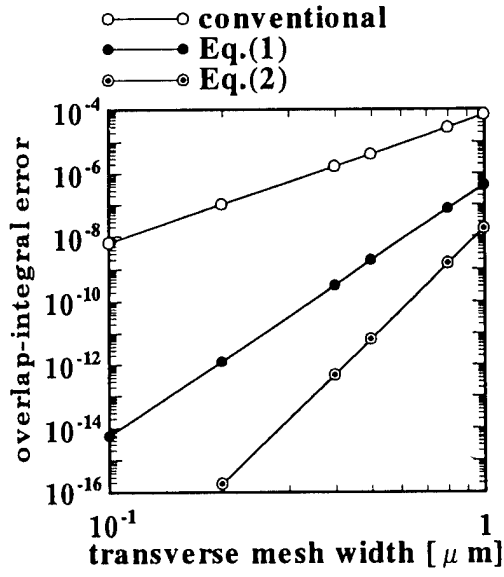


Fig.1 Overlap-integral error.

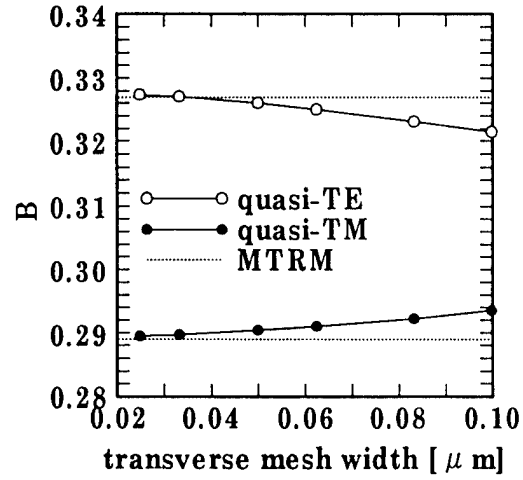


Fig.4 Convergence behavior of normalized effective index.

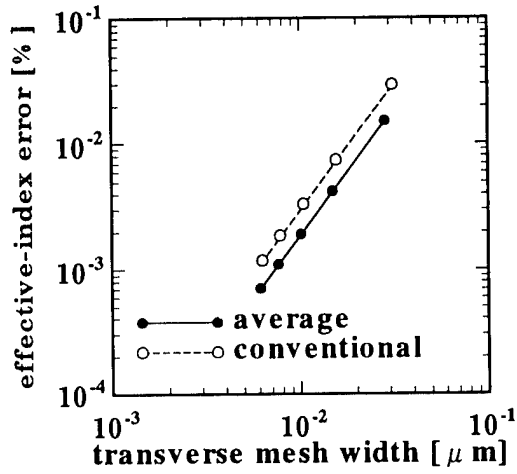
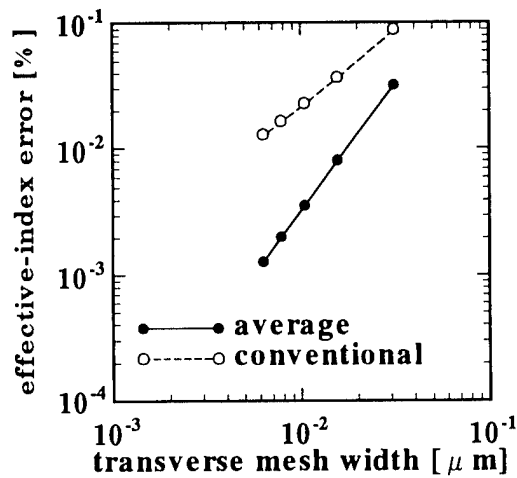
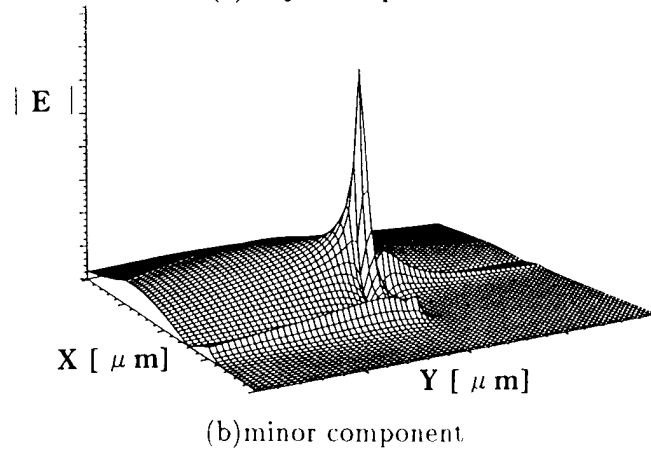
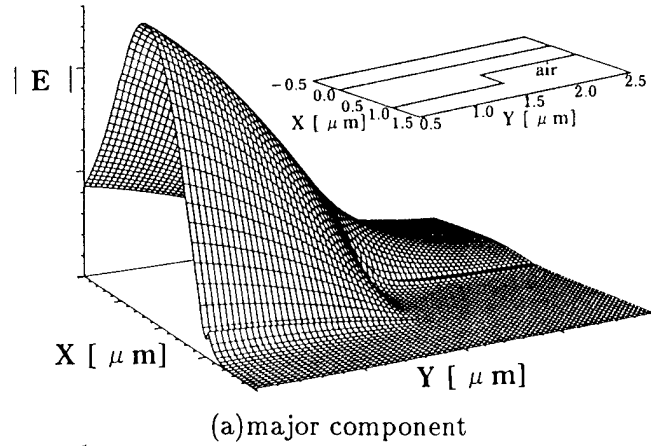
Fig.2 Effective-index error of  $TE_0$  mode.Fig.3 Effective-index error of  $TM_0$  mode.

Fig.5 Field profiles of a rib waveguide.

# EFFICIENT MULTISTEP METHODS USING A NONUNIFORM GRID

Jun SHIBAYAMA, Kenji MATSUBARA, Minoru SEKIGUCHI, Junji YAMAUCHI,  
and Hisamatsu NAKANO

College of Engineering, Hosei University

3-7-2, Kajino-cho, Koganei, Tokyo 184, Japan

Tel: +81-423-87-6190, Fax: +81-423-87-6381, e-mail: junji@yma.ei.hosei.ac.jp

## 1 Introduction

Wave propagation in an optical waveguide can efficiently be analyzed by the beam propagation method(BPM). However, in the analysis of wide-angle beam propagation, the accuracy is degraded due to the paraxial approximation. To overcome this problem, the multistep method has been developed[1]. The accuracy of the multistep method can be improved by the generalized Douglas(GD) scheme without increase in computational time[2].

A nonuniform grid contributes to enhancing the efficiency of BPM analysis. Recently, we have extended the GD scheme to a nonuniform grid[3], in which the truncation error is reduced to  $O(\Delta x)^4$ . The increased accuracy is maintained even when a grid growth factor is relatively large.

The purpose of this paper is to apply a highly accurate nonuniform scheme to the multistep method and demonstrate its effectiveness. We present two different methods. One is the computational space method (CSM), in which the GD scheme is employed after replacing a nonuniform grid in the physical space with a uniform one in the computational space[4]. The other is the physical space method (PSM), in which the GD scheme is applied to a nonuniform grid in the physical space[3]. As an application, taking advantage of the PSM, we introduce an adaptive grid[5]-[8] into the multistep method.

## 2 Nonuniform schemes for multistep method

For the CSM, a nonuniform grid in the physical space  $(x, z)$  is transformed to a uniform grid in the computational space  $(u, z)$  using a mapping function[4]

$$x = \alpha \tan(u) \quad (1)$$

where  $\alpha$  is a scaling parameter. To facilitate derivation of the finite-difference equation, the transformation of the field is also imposed[4]. After obtaining the scalar Helmholtz equation with the slowly varying envelope formalism, we employ the GD scheme in the computational space. On the other hand, for the PSM, the highly accurate scheme for a nonuniform grid[3] is directly applied to the second derivative in the physical space.

From the above-mentioned methodology, we can finally obtain the following finite-difference equations for the  $K$ -th partial step of an  $N$ -th order Padé propagator:

$$\begin{aligned} & \zeta_{i+1}^{m+K/N} E_{i+1}^{m+K/N} + \xi_i^{m+K/N} E_i^{m+K/N} + \eta_{i-1}^{m+K/N} E_{i-1}^{m+K/N} \\ & = \zeta_{i+1}^{m+(K-1)/N} E_{i+1}^{m+(K-1)/N} + \xi_i^{m+(K-1)/N} E_i^{m+(K-1)/N} + \eta_{i-1}^{m+(K-1)/N} E_{i-1}^{m+(K-1)/N} \end{aligned} \quad (2)$$

For the CSM

$$\zeta_i = \eta_i = \frac{1}{12} \frac{\alpha^2}{\cos^3(u_i)} + \Gamma_K \left( \frac{1}{\Delta u^2} + \frac{1}{12} \tau_i \right) \cos(u_i), \quad \xi_i = \frac{5}{6} \frac{\alpha^2}{\cos^3(u_i)} + \Gamma_K \left( -\frac{2}{\Delta u^2} + \frac{5}{6} \tau_i \right) \cos(u_i)$$

where

$$\tau_i = 1 + k^2(n_i^2 - n_0^2)\alpha^2 / \cos^4(u_i),$$

while for the PSM

$$\zeta_{i+1} = R_1 + \Gamma_K \left[ \frac{2}{r(r+1)\Delta x^2} + R_1 k^2 (n_{i+1}^2 - n_0^2) \right], \quad \xi_i = R_2 - \Gamma_K \left[ \frac{2}{r\Delta x^2} - R_2 k^2 (n_i^2 - n_0^2) \right]$$

$$\eta_{i-1} = R_3 + \Gamma_K \left[ \frac{2}{(r+1)\Delta x^2} + R_3 k^2 (n_{i-1}^2 - n_0^2) \right]$$

where

$$\Gamma_K = a_K : m + (K-1)/N$$

$$= a_K^* : m + K/N$$

and

$$R_1 = \frac{3r^2 - 3r + 1}{6r(r+1)}, \quad R_2 = \frac{-r^2 + 7r - 1}{6r}, \quad R_3 = \frac{r^2 - 3r + 3}{6(r+1)},$$

in which  $k$  is the free-space wavenumber,  $n$  is the index profile of the waveguide, and  $n_0$  is the reference index. The superscript  $m$  indicates position along the  $z$  axis and the  $a$ 's can be determined by the one-time solution of an  $N$ th-order complex algebraic equation.  $r$  represents the grid growth factor in the physical space.

Evidently, Eq.(2) is solvable using the standard techniques, such as Thomas algorithm. The CSM can be easily implemented, since the transverse coordinate is discretized by a uniform grid. But the grid growth factor is limited due to the mapping function of Eq.(1). In contrast, the PSM has flexibility in the choice of the grid growth factor.

To confirm the accuracy, we analyze a symmetrical graded-index slab waveguide which is tilted at an angle of 45 degrees with respect to the  $z$  axis. The refractive index is  $n^2(x) = n_s^2 + 2n_s \Delta n / \cosh^2(2x/w)$ , where  $n_s = 2.1455$ ,  $\Delta n = 0.003$  and  $w = 5\mu m$ . The wavelength considered here is  $\lambda = 1.3\mu m$ . We treat the case in which the grid growth factor is determined by Eq.(1); the grid spacing becomes gradually coarse from the center of the computational window toward the edges.

Preliminary calculations show excellent agreement between the results in the CSM and the PSM. Therefore, we show only the results of the CSM. Figs.1(a) and (b) show the field distributions for the GD scheme and the conventional Crank-Nicholson(CN) scheme, respectively. The results are obtained at a propagation distance of  $100\mu m$ . It is found that the results for the GD scheme offer a substantial improvement in accuracy, when compared with those of the CN scheme.

### 3 Application to adaptive grid

As mentioned above, the PSM has the advantage of flexibility in the choice of the grid growth factor. Therefore, we introduce an adaptive grid[5]-[8] into the multistep method using the PSM. The waveguide considered here is the same as that in Fig.1 except that the tilt angle is varied from 0 to 50 degrees.

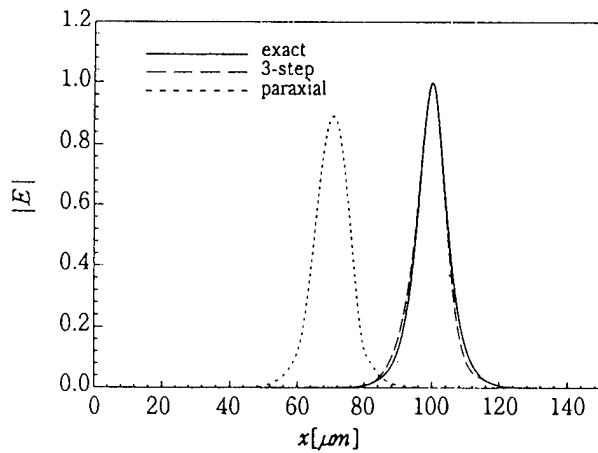
Fig.2 shows an example of the distribution of sampling points using an adaptive grid. The missing values between the sampling points are generated using a Lagrange's third-order interpolation technique. Fig.3 shows the coupling efficiency evaluated at a propagation distance of  $100\mu m$ . It is noteworthy that the multistep method with an adaptive grid can successfully achieve high accuracy regardless of a small number of sampling points. In the regular grid, 2000 sampling points are required to obtain the same accuracy as that for the adaptive grid.

### 4 Conclusions

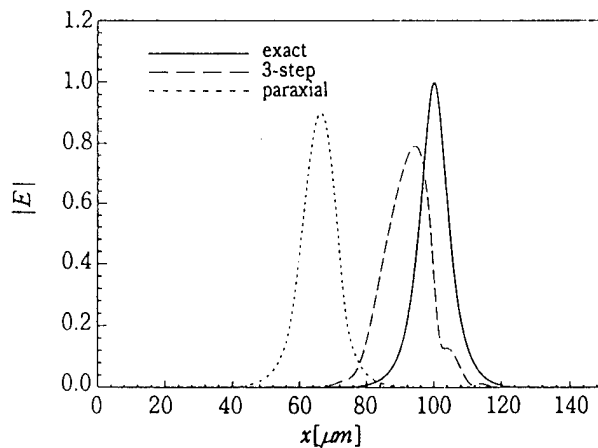
We have studied the applicability of highly accurate nonuniform schemes to the multistep method and presented two methods. The computational space method using a mapping technique is easy to implement, while in this method, the grid growth factor is subject to the mapping function. In contrast, the physical space method is more flexible in the choice of the grid growth factor. The numerical accuracy is confirmed by the analysis of wide-angle beam propagation. As an application, an adaptive grid is introduced into the physical space method.

## References

- [1] G. R. Hadley, Opt. Lett., vol.17, pp.1743-1745, 1992.
- [2] J. Yamauchi et al., IEEE Photon. Technol. Lett., vol.8, pp.1361-1363, 1996.
- [3] J. Yamauchi et al., IEEE Photon. Technol. Lett., vol.9, pp.67-69, 1997.
- [4] F. Ladouceur, Opt. Lett., vol.21, pp.4-5, 1996.
- [5] M. Artiglia et al., Electron. Lett., vol.27, no.5, pp.474-475, 1991.
- [6] F. Schmidt, J. Lightwave Technol., vol.11, pp.1425-1434, 1993.
- [7] M. Koshiba and Y. Tsuji, IEEE Photon. Technol. Lett., vol.8, pp.1208-1210, 1996.
- [8] C. Massini et al., Opt. and Quantum Electron., vol.27, pp.915-959, 1995.



(a) GD scheme



(b) CN scheme

Fig.1. Field distributions for TE<sub>0</sub> mode:  
(a) Generalized Douglas scheme and  
(b) Crank-Nicholson scheme.

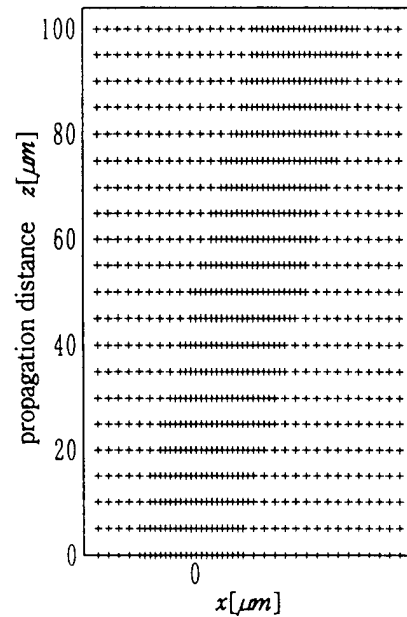


Fig.2. Distribution of sampling points.

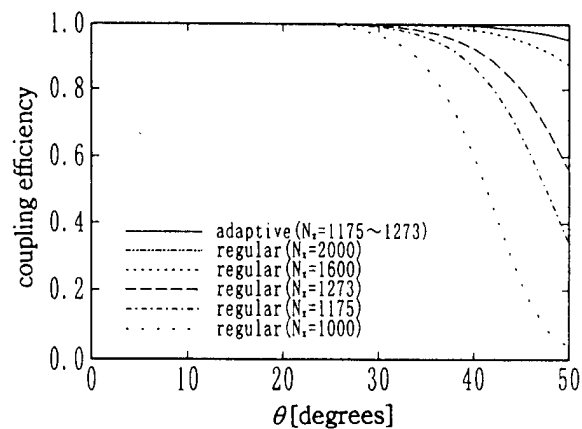


Fig.3. Coupling efficiency for TE<sub>0</sub> mode  
as a function of tilt angle  $\theta$   
(three-step method with the GD scheme).

# Finite-elements semivectorial beam propagation method for nonlinear integrated optical devices

A. Cucinotta, S. Selleri, L. Vincetti

Dipartimento di Ingegneria dell'Informazione, Parma University

Viale delle Scienze I-43100 Parma, Italy.

Fax: + 39 521 905758; Tel: + 39 521 905765

Email: selleri@pccampi3.tlc.unipr.it

## Introduction

The Beam Propagation Method (BPM) is a widespread technique to study the properties of various guided wave optic structures. In the last years many BPM formulations solving the scalar wave equation for nonlinear medium have been developed [1]-[4]. In three dimensional waveguides, due to the field confinement in both the transverse directions, the waves are true hybrid and the behavior of the different polarization (quasi-TE and quasi-TM waves) can significantly change especially when strongly guiding waveguides or strongly nonlinear index variations are considered. As a consequence, scalar formulations, as unable to describe the vectorial properties of the electromagnetic field, are not suitable for the analysis of this kind of structures.

Recently a full-vectorial BPM based on Finite Elements (FEs) has been presented [5] and extended to anisotropic [6] and  $z$ -varying [7] structures. In this work a semivectorial formulation has been derived from [5] and applied the analysis of nonlinear devices. Semivectorial formulations are simpler and faster than vectorial approaches still able nevertheless to distinguish the field polarizations. Moreover the FEs allows an accurate description of nonlinear and non homogeneous media. In particular the use of second order shape functions permits to describe the variation of the medium characteristics within each element of the grid [8], [9]. This way, together with a non uniform distribution of nodal points, a considerable reduction of computational time and requirement can be obtained. Numerical results show the performance of the proposed semivectorial FE-BPM and highlight the limits of scalar approaches.

## Formulation

Consider the curl-curl equation in term of the magnetic field  $\overline{\mathcal{H}}$ :

$$\overline{\nabla} \times (\epsilon_r^{-1} \overline{\nabla} \times \overline{\mathcal{H}}) - k_0^2 \overline{\mathcal{H}} = 0; \quad (1)$$

here  $k_0$  is the wavenumber in the vacuum and  $\epsilon_r(x, y, z) = \epsilon_{rlin}(x, y, z) + \alpha |\overline{\mathcal{E}}(x, y, z)|^2$  the nonlinear relative permittivity;  $\alpha$  is the nonlinear Kerr coefficient and  $\overline{\mathcal{E}}$  the electric field. By expressing  $\overline{\mathcal{H}}(x, y, z) = \overline{H}(x, y, z)e^{-j\beta z}$ , with  $\beta$  a phase factor and  $z$  the propagation direction, by introducing the magnetic field divergence equation and by applying the standard Galerkin method to (1) it yields [5]:

$$\begin{aligned} 2j\beta \int_{\Omega} \epsilon_r^{-1} \frac{\partial H_x}{\partial z} N_j d\Omega &= \int_{\Omega} \epsilon_r^{-1} \frac{\partial H_y}{\partial x} \frac{\partial N_j}{\partial y} d\Omega - \int_{\Omega} \epsilon_r^{-1} \frac{\partial H_x}{\partial y} \frac{\partial N_j}{\partial x} d\Omega \\ + \int_{\Omega} \epsilon_r^{-1} \frac{\partial}{\partial x} (j\beta H_z - \frac{\partial H_z}{\partial z}) N_j d\Omega &+ k_0^2 \int_{\Omega} H_x N_j d\Omega - \beta^2 \int_{\Omega} \epsilon_r^{-1} H_x N_j d\Omega; \quad (2) \\ 2j\beta \int_{\Omega} \epsilon_r^{-1} \frac{\partial H_y}{\partial z} N_j d\Omega &= + \int_{\Omega} \epsilon_r^{-1} \frac{\partial H_x}{\partial y} \frac{\partial N_j}{\partial x} d\Omega - \int_{\Omega} \epsilon_r^{-1} \frac{\partial H_y}{\partial x} \frac{\partial N_j}{\partial y} d\Omega \end{aligned}$$

$$+ \int_{\Omega} \epsilon_r^{-1} \frac{\partial}{\partial y} (j\beta H_z - \frac{\partial H_z}{\partial z}) N_j d\Omega + k_0^2 \int_{\Omega} H_y N_j d\Omega - \beta^2 \int_{\Omega} \epsilon_r^{-1} H_y N_j d\Omega; \quad (3)$$

$N_j(x, y)$  are the weight functions with  $j = 1 \dots n$ , with  $n$  the number of points of the element  $\Omega$ . In (2) and (3) slowly variations of the refractive index along  $z$  has been supposed. Notice that in the equations (2) and (3) the first three terms of the right hand-side allow to describe the vectorial behaviour of the field [5]. By neglecting the coupling terms

$$\int_{\Omega} \epsilon_r^{-1} \frac{\partial H_y}{\partial x} \frac{\partial N_j}{\partial y} d\Omega \quad \text{and} \quad \int_{\Omega} \epsilon_r^{-1} \frac{\partial H_x}{\partial y} \frac{\partial N_j}{\partial x} d\Omega$$

in (2) and (3) respectively and using again the magnetic field divergence equation two decoupled differential equations can be obtained:

$$[J_A] \frac{d\{H_A\}(z)}{dz} = [K_A] \{H_A\}(z), \quad (4)$$

$$[J_B] \frac{d\{H_B\}(z)}{dz} = [K_B] \{H_B\}(z) \quad (5)$$

where

$$\{H_A\}(z) = \begin{pmatrix} \{H_x\}(z) \\ \{H_z\}(z) \end{pmatrix}, \quad \{H_B\}(z) = \begin{pmatrix} \{H_y\}(z) \\ \{H_z\}(z) \end{pmatrix}$$

with  $[J_A]$ ,  $[J_B]$ ,  $[K_A]$  and  $[K_B]$  four sparse matrices of order  $2N \times 2N$  being  $N$  the number of nodal points of the whole cross-section.  $\{H_x\}(z)$ ,  $\{H_y\}(z)$  and  $\{H_z\}(z)$  are the vectors of the magnetic field components on the grid points. Notice that in this formulation the transverse components depend on the longitudinal one also if the medium characteristics are independent from  $z$  [5]. Equations (4) and (5) are used to describe the quasi-TM and the quasi-TE waves evolution respectively.

## Numerical results

The performances of the proposed formulation are illustrated by modelling the quasi-TE polarization propagation in 3-D directional couplers with nonlinear cores. In these devices the field confinement in the launching core depends on the power level of the input field. If this power is greater than a threshold value, the field focuses within the core up to the extent of inhibiting the coupling effect [10].

First a weakly guiding coupler with  $n_{co} = 1.518$  and  $n_{cl} = 1.51$  is analyzed at the wavelength  $\lambda = 1.532 \mu m$  [4]. In this condition the scalar approaches provide an acceptable description of the field evolution. For the linear case, by exciting the structure with the fundamental mode of the single waveguide, the coupling lengths are  $L_{sv} = 1355 \mu m$  and  $L_s = 1319 \mu m$  for the semivectorial and the scalar formulation respectively. Conversely by exciting the coupler with the sum of even and odd supermodes having effective indices  $n_{eff1} = 1.51071$  and  $n_{eff2} = 1.51014$  respectively, the results are  $L_{sv} = 1348 \mu m$  and  $L_s = 1343 \mu m$  which are in very good agreement with  $L = \lambda / (2|n_{eff1} - n_{eff2}|) = 1344 \mu m$ . For the nonlinear case, with the fundamental mode of the single guide as launching condition, the threshold power is about  $1.3 mW$  for both the formulations and [4] as well. Notice that triangular elements with second order shape functions have been considered. Their use allows the nonlinear index to vary within each element of the grid, resulting in a very accurate description of the index variation [9]. As a consequence less than 800 nodal points have been sufficient

to obtain grid independence results. In [4] 1470 points have been used to analyze the same device.

As a second example a directional coupler made by two rectangular  $2\mu\text{m} \times 1\mu\text{m}$  straight waveguide of nonlinear Kerr type material with  $\alpha = 3.1 \cdot 10^{-13} \text{m}^2/\text{V}^2$  is considered. The distance between the two core centers is  $4\mu\text{m}$  and the indices are  $n_{co} = 1.6$ ,  $n_{cl} = 1.51$  respectively. The cross-section has been divided into 480 second order triangles with 969 points. The device is excited with the fundamental mode of the single waveguide at  $\lambda = 1.532\mu\text{m}$ . Fig. 1 shows for the semivectorial polarization the power, normalized to its input value, computed on half numerical window along the propagation direction. The threshold power obtained is  $0.25\text{mW}$ . In Fig. 2 the results of the semivectorial and the scalar formulations are compared and the different behaviour of the two approaches can be clearly observed. In particular notice that at the threshold power level defined by the semivectorial formulation, a commutation still occurs with the scalar one.

In conclusion a semivectorial BPM based on finite element method has been presented. The use of the shape functions to describe the index variation within each triangle has allowed to reduce the computational efforts. The limits of scalar approximations have been pointed out by analyzing nonlinear directional couplers.

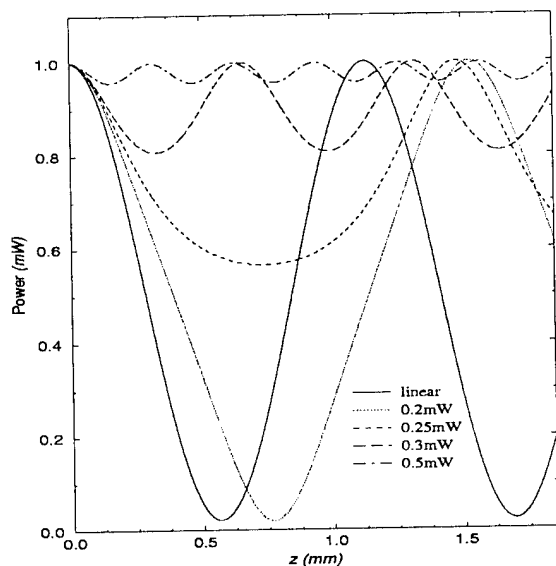


Figure 1: semivectorial result.

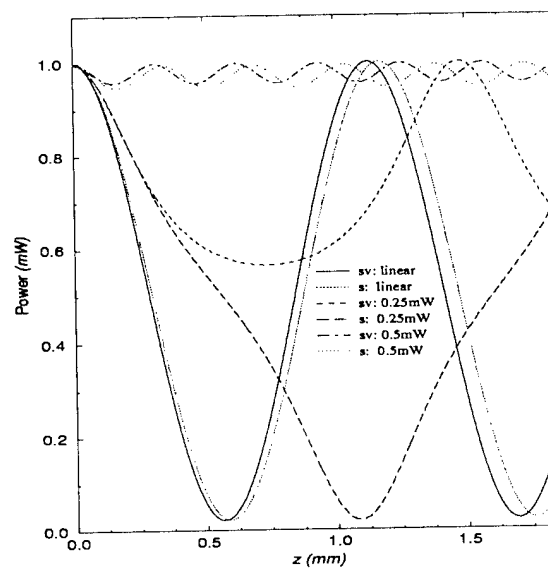


Figure 2: scalar (s) and semivectorial (sv) results.

## References

- [1] K. Hayata, A. Misawa and M. Koshiba, J. Opt. Soc. Am. B **7**, 1772 (1990).
- [2] H.E. Hernandez-Figueroa, J. Opt. Soc. Am. B **11**, 798 (1994).
- [3] F. Gonther, A. Henault, S. Lacroix, R. Black, J. Bures, J. Opt. Soc. Am. B **8**, 416 (1991).
- [4] H.E. Hernandez-Figueroa, Phot. Tech. Lett. **9**, 351 (1997).
- [5] E. Montanari, S. Selleri, L. Vincetti and M. Zoboli, Phot. Tech. Lett. **9**, 1244 (1997).
- [6] A. Cucinotta, E. Montanari, S. Selleri, L. Vincetti and M. Zoboli, ICEAA 97 Int. Conf. Electromagnetics in Advanced Applications, Sept. 15-18 1997, Torino, Italy.
- [7] E. Montanari, S. Selleri, L. Vincetti and M. Zoboli, submitted to J. Lightwave Technology.
- [8] K. Hayata, M. Nagai, M. Koshiba, IEEE Microwave Theory Tech. **36**, 1207 (1988).
- [9] S. Selleri and M. Zoboli, IEEE Microwave Theory Tech. **43**, 887 (1995).
- [10] S. M. Jensen, IEEE Microwave Theory Tech. **30**, 1568 (1982).

## VECTORIAL BEAM PROPAGATION METHOD BASED ON MIXED ELEMENTS

D. Schulz<sup>1</sup>, C. Glingener<sup>1</sup>, M. Bludszuweit<sup>2</sup>, E. Voges<sup>1</sup>

<sup>1</sup>Lehrstuhl für Hochfrequenztechnik, Universität Dortmund, D-44227 Dortmund, Germany

Phone: +49 231 755-3909, Fax: +49 231 755-4631

e-mail: schulz@hft.e-technik.uni-dortmund.de

<sup>2</sup>Arbeitsbereich Halbleitertechnologie, Technische Universität Hamburg-Harburg,  
D-21073 Hamburg, Germany

**Abstract:** An efficient mixed element beam propagation method for 3D-simulations is presented for integrated optic devices allowing energy conservation when assuming metallic walls and lossless media.

**Introduction:** Beam propagation methods (BPM) are at present the most versatile techniques to investigate integrated optical waveguide devices. Most methods are based on finite difference approximations of the lateral discretization operator under consideration of boundary conditions at dielectric interfaces except the scalar approach [1-3]. Unfortunately, the eigenvalue spectrum of vectorial discretization schemes contain complex eigenvalues as the FD-matrices are non-hermitian. It has been proved that these approaches lead to unphysical gain if an arbitrary field is assumed [4]. This non-unitarity is a serious and general problem of finite difference techniques. An approach has been undertaken previously to overcome this serious limitation [5]. An alternating direction implicit method has been introduced to reduce the effect of unphysical gain, but the described effect cannot be circumvented. Furthermore, in FD-approximations the description of interface conditions is inadequate, because truncated Taylor series are applied, and spurious solutions occur within vectorial formulations. For this reason vectorial FD beam propagation methods lead to erroneous results especially when polarization effects are investigated.

Common finite element (FE) approaches utilize nodal elements and have been successfully demonstrated for the simulation slab (2D-) waveguides [6-8]. Unfortunately, they cannot be applied to 3D-waveguides due to the nature of nodal elements as they do not prevent spurious solutions. The introduction of edge elements [9] for transverse components and nodal elements for axial components of the electrical or either magnetic field leads to a unitary 3D-propagation schemes as we will show. This combination of edge and nodal elements is called a mixed element approach. A full vectorial simulation of 3D-waveguide structures becomes possible, because spurious modes can be prevented and boundary conditions at interfaces are correctly described. In addition to that waveguides with reentrant corners, geometries containing lossy media, dielectric and magnetic materials can be analyzed simultaneously [10]. The ability to model reentrant corners is important for the correct description of the polarization behavior.

**3D-Finite Element Discretization:** We consider a planar optical waveguide with an index distribution  $n(x,y,z)$ , where  $x$ ,  $y$  and  $z$  are the transverse directions and propagation (axial) direction respectively. We analyze isotropic waveguides with and a step index distribution is assumed. The whole cross section is divided into linear triangular elements. A Galerkin procedure based on Maxwell's equations results in the following mixed element formulation for the electric field allowing a propagation along the  $z$ -direction:

$$[A] \frac{\partial}{\partial z} \begin{Bmatrix} \Phi_t \\ \Phi_z \end{Bmatrix} + \frac{j}{2k_0 n_0} [A] \frac{\partial^2}{\partial z^2} \begin{Bmatrix} \Phi_t \\ \Phi_z \end{Bmatrix} = \frac{j}{2k_0 n_0} [B] \begin{Bmatrix} \Phi_t \\ \Phi_z \end{Bmatrix} \quad (1)$$

$\Phi_t$  and  $\Phi_z$  are vectors containing the discretized transverse and axial field components.  $k_0$  is the propagation constant in free space and  $n_0$  is the reference index. The envelope function concept for the element vectors as well as the second derivative  $\Phi_z' = j d\Phi_z/dz$  have been introduced. A common feature of both system matrices  $[A]$  and  $[B]$  is, that they are hermitian and sparse. A matter of prime importance is, that for this formulation unconditional stability can be proved theoretically in contrast to a propagation scheme based on mixed elements, which has already been presented in [11].

**Propagation Scheme:** Applying the well known Padé approximants concept [12], we formally rewrite eq. (1) resulting in the following recurrence relation with

$$\frac{j}{2k_0 n_0} \frac{\partial}{\partial z} \bigg|_n = \frac{\frac{1}{4k_0^2 n_0^2} [A]^{-1} [B]}{1 + \frac{j}{2k_0 n_0} \frac{\partial}{\partial z} \bigg|_{n-1}} \quad (2)$$

The iterative determination of the approximated operator requires an initial operator, which is the operator of the Fresnel-equation. In propagation (axial) direction a finite difference approximation is utilized. With respect to numerical stability we choose a Crank Nicolson scheme, which is unconditionally stable. The transparent boundary condition (TBC) is applied. Assuming lossless media and a lateral enclosure by perfectly reflecting walls, the eigenvalue spectrum of each operator exclusively contains real eigenvalues. For this reason general stability and the existence of a unitary propagation operator can be proved by induction.

With regard to the accuracy we note that all accuracy investigations presented in [12] with regard to different wide angle approximations are also valid for the proposed method. The lateral discretization accuracy of the mixed element approach can be improved by choosing higher approximations such as quadratic elements. This aspect has been investigated previously [13].

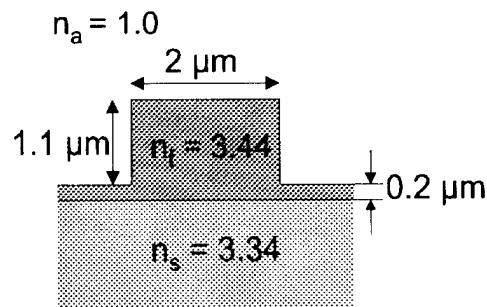


Fig. 1: Waveguide structure

**Examples:** The example involves the simulation of a Y-junction, which has been studied by several authors. This Y-junction has a shape function of the waveguide center lines according to  $x(z) = \pm(1 - \cos(\pi z / 40 \mu m))$  for  $0 \mu m < z < 40 \mu m$ , and a constant  $4 \mu m$  center to center waveguide separation for  $z > 40 \mu m$ . The waveguide profile corresponds to the structure in Fig. 1. The waveguide has a rib height  $h = 2 \mu m$ , width  $w = 3 \mu m$  and a slab height  $t = 1 \mu m$ , a refractive

index  $n_f = 3.44$  in the guiding layer,  $n_s = 3.34$  in the substrate and  $n_a = 1.0$  in the superstrate. This example is simulated using the first order Padé approximation, and the propagation step is  $dz = 0.025 \mu m$  taking regard of the strong index variation along the  $z$ -direction. The

calculation is performed at  $1.55\text{ }\mu\text{m}$  wavelength. The BPM calculation is advantageously performed by using a  $10\text{ }\mu\text{m} \times 6\text{ }\mu\text{m}$  calculation window. It is uniformly discretized with grid spacings  $dx=dy=0.1\text{ }\mu\text{m}$ . A uniform discretization is chosen because a non-equidistant discretization creates radiation modes. The excitation field at  $z=0$  is the fundamental HE-mode of the waveguide. In Fig. 2a) the field components  $E_y$ ,  $E_z$  and  $H_z$  of the initial field distribution are shown as well as the field distribution for these components at the end of the Y-junction. It is obvious from this Fig. 2b) that the eigenmode reaches the stable state very slowly. A stabilization towards the guided mode in each arm of the Y-junction occurs beyond  $z=100\text{ }\mu\text{m}$ . Moreover the coupling between the dominant component ( $E_y$ -component) and the non-dominant component ( $E_z$ -component) at the edges can be seen.

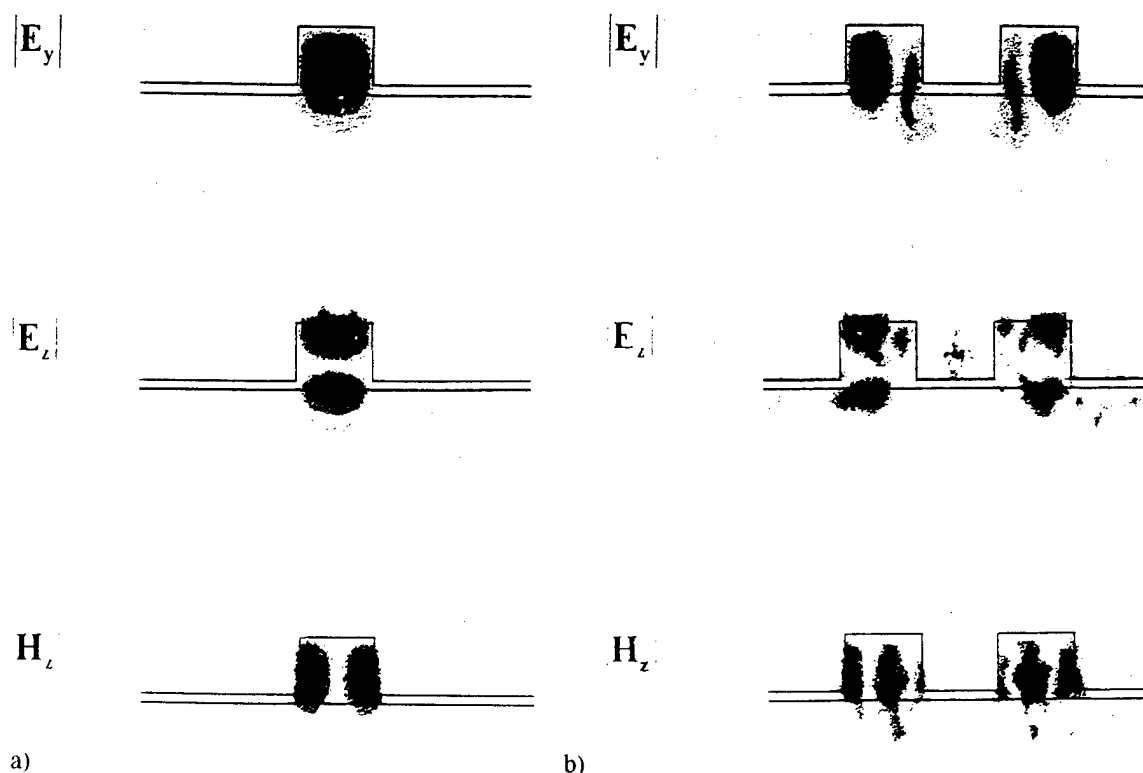


Fig. 2: Field distribution at  $z=0$  and at the output of the Y-junction

#### References:

- [1] W. Huang and S.-T. Chu, *J. Lightwave Technol.*, vol. 10, no. 3, pp. 295-305, 1992
- [2] E. Kriezis et al, *IEEE Trans. Magnetics*, vol. 33, no. 2, pp. 1540-1543, 1997
- [3] D. Li et al, *Optical and Quantum Electron.*, vol. 29, pp. 312-322, 1997
- [4] D. Yevick, *Optical and Quantum Electron.*, vol. 26, pp. 185-197, 1994
- [5] D. Yevick et al, *IEEE Photon. Technol. Lett.*, vol. 7, no. 6, pp. 658-660, 1995
- [6] Y. Tsuji and M. Koshiba, *J. Lightwave Technol.*, vol. 14, no. 2, pp. 217-222, 1996
- [7] I. B. Koch et al, *Electron. Lett.*, vol. 25, no. 8, pp. 514-516, 1989
- [8] Y. Tsuji et al, *IEEE Trans. Magnetics*, vol. 33, pp. 1544-1547, 1997
- [9] M. Koshiba et al, *IEEE Trans. Microwave Theory and Techn.*, vol. 40, pp. 371-377, 1992
- [10] B. M. Dillon et al, *IEEE Trans. Microwave Theory and Techn.*, vol. 42, pp. 308-316, 1994
- [11] D. Schulz et al, *Proc. ECIO '97*, Stockholm, Sweden, pp.226-229, 1997
- [12] G. R. Hadley, *Opt. Lett.*, vol. 17, pp. 1426-1428, 1992
- [13] M. Koshiba et al, *J. Lightwave Technol.*, vol. 12, pp. 595-502, 1994

## Field Singularities in Full-Vectorial Optical Waveguide Analysis

Wayne W. Lui, Chenglin Xu<sup>1</sup>, Wei-Ping Huang<sup>1</sup> and Kiyoyuki Yokoyama

NTT Opto-electronics Laboratories, 3-1 Morinosato, Wakamiya, Atsugi, Kanagawa, Japan.

<sup>1</sup>Dept. of Electrical and Computer Engineering, Univ. of Waterloo, Waterloo, Ontario, Canada.

E-mail address: waynelui @ aecl . ntt . co . jp

Field singularities are manifestations of the vector nature of electromagnetic waves (see Fig.1), which occur at corners of rectangular dielectric waveguides [1] such as those found in OEIC. Although well-known among microwave device designers, their significances have been acknowledged only recently within the optoelectronics community, for example, when vector properties are found responsible for polarization conversion of optical field in bending waveguides [2]. What has also been recognized, on the other hand, are difficulties with modal field analysis if these field singularities are to be modelled and resolved accurately [3]. In this paper, an algorithm is proposed to circumvent such difficulties.

Due to the highly localized nature of field singularities at corner regions of rectangular waveguides, it is sufficient to confine our attention to only the neighborhood of each corner region that is within a distance small compared to the wavelength of interest [1]. Within this neighborhood, moreover, since the spatial variation of the field singularity is expected to be much larger than the temporal variation due to wave propagation, the field can be considered quasi-static. In other words, in the vicinity of a corner, the  $\vec{E}$ -field can be expressed — within the quasi-static approximation — as the gradient of a potential function  $\psi$  such that it obeys the following Laplace's equation:

$$\nabla \cdot (n^2 \nabla \psi) = 0 \quad (1)$$

If the waveguide is  $z$ -invariant, solution of (1) in cylindrical coordinates  $(r, \phi)$  is well-known [1,4]:

$$\psi(r, \phi) = A r^v \cos[v(\phi + \phi_0)] \quad (2)$$

where  $A$ ,  $v$  and  $\phi_0$  are constants to be determined.

In particular, consider the right-angle corner as shown in Fig.2. Let the origin be right at the corner, and assume that the potential distribution  $\psi$  is *symmetrical* with respect to the  $\phi = 0$  axis (conventionally called the first symmetry). By imposing boundary conditions along the material interface such that continuity of (i) the potential function  $\psi$  and (ii) the normal  $\vec{D}$ -field component  $D_\phi$  are maintained,  $v = v_1$  is found to be:

$$v_1 = \frac{4}{\pi} \tan^{-1} \left[ \frac{n_1^2 + 3n_2^2}{3n_1^2 + n_2^2} \right]^{1/2} \quad (3a)$$

In cases where the potential distribution  $\psi$  is *anti-symmetrical* with respect to the  $\phi = 0$  axis (conventionally called the second symmetry),  $v = v_2$  is given by:

$$v_2 = \frac{4}{\pi} \tan^{-1} \left[ \frac{n_2^2 + 3n_1^2}{3n_2^2 + n_1^2} \right]^{1/2} = 2 - v_1 \quad (3b)$$

$\vec{E}$ -field components parallel to the  $x$ - and  $y$ -axes as shown in Fig.2 can be obtained by straightforward differentiation of the potential function  $\psi$  along the appropriate direction. When this is done, it is found that both  $E_x$  and  $E_y$  have the following property:

$$E_{x,y}(r, \phi = \text{constant}) \propto r^{v-1} \quad (4)$$

regardless of the value of  $\alpha$ . Field singularity may occur at the corner, in view of (4), when  $v < 1$ . This is possible in case of the first symmetry if  $n_1 > n_2$ ; and in case of the second symmetry,  $n_2 > n_1$ .

Equation (4) is the basis of the algorithm that we propose in this work. In the following, modal analysis similar to the finite-difference method as described in [5] is employed. Consider the case of Fig.3 in which the corner region of an optical waveguide and grid lines in the vicinity are shown. For simplicity, let the grid lines be uniformly spaced, and that each of the material interfaces lie in between two adjacent grid lines. Assuming that the grid spacing is much smaller than the operating wavelength, according to (4),

$$\frac{E_x(i, j)}{E_x(i+1, j+1)} = \frac{E_x(i, j-1)}{E_x(i+1, j-2)} = \frac{E_x(i-1, j-1)}{E_x(i-2, j-2)} = \frac{E_x(i-1, j)}{E_x(i-2, j+1)} = 3^{1-\nu} \quad (5)$$

where the value of  $\nu$  is determined by the symmetry under consideration. These relationships are valid also for  $E_y$  at the same grid points.

Unlike in [5], in our method the field components are not directly solved at grid points which are immediate to corners such as those marked by circles in Fig.3. In the discretization scheme when field values at these grid points are called for, they are provided indirectly via (5). For instance, at the grid point  $(i+1, j)$  the following finite-difference approximation is obtained:

$$\begin{aligned} \frac{\partial^2}{\partial x^2} E_x(i+1, j) &\approx \frac{1}{\Delta x^2} \left[ E_x(i, j) - 2E_x(i+1, j) + E_x(i+2, j) \right] \\ &= \frac{1}{\Delta x^2} \left[ 3^{1-\nu} E_x(i+1, j+1) - 2E_x(i+1, j) + E_x(i+2, j) \right] \end{aligned} \quad (6)$$

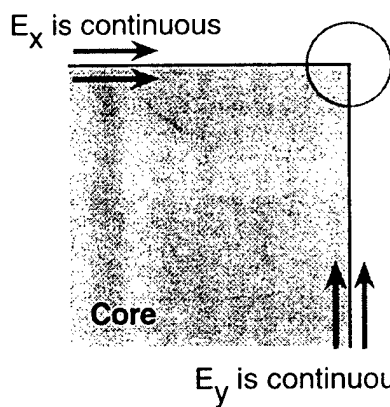
At grid points outside of the corner region, discretization of the wave equations follows the same procedure as described in [5].

A finite difference full-vectorial mode solver based on the above algorithm has been developed. As an illustration, the same simple square waveguide as discussed in [3], which is shown in Fig.4, has been analysed. The calculated  $E_x$  and  $E_y$  profiles are shown in Fig.5, where profiles along cross-sections indicated by broken lines are also plotted. Notice that although  $E_x$  is continuous along the  $y$ -direction, it is not so at the material interface along the  $x$ -direction. Moreover in the  $E_y$  profile, field singularities at corners are clearly shown. Important features of the field profiles in a simple square dielectric waveguide due to vector properties of optical field are found to be correctly resolved, demonstrating the versatility of the algorithm and the full-vectorial mode solver developed in this work.

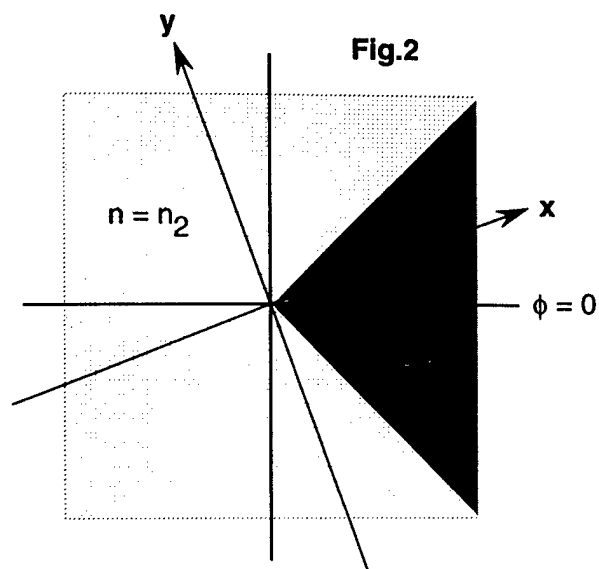
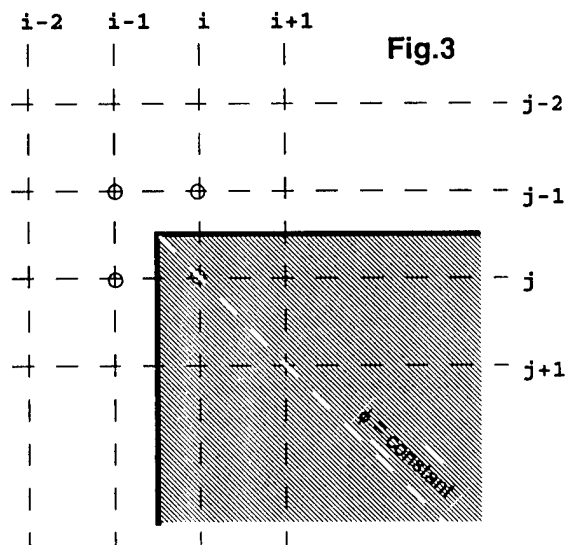
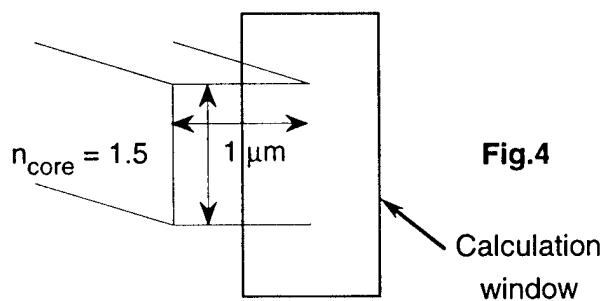
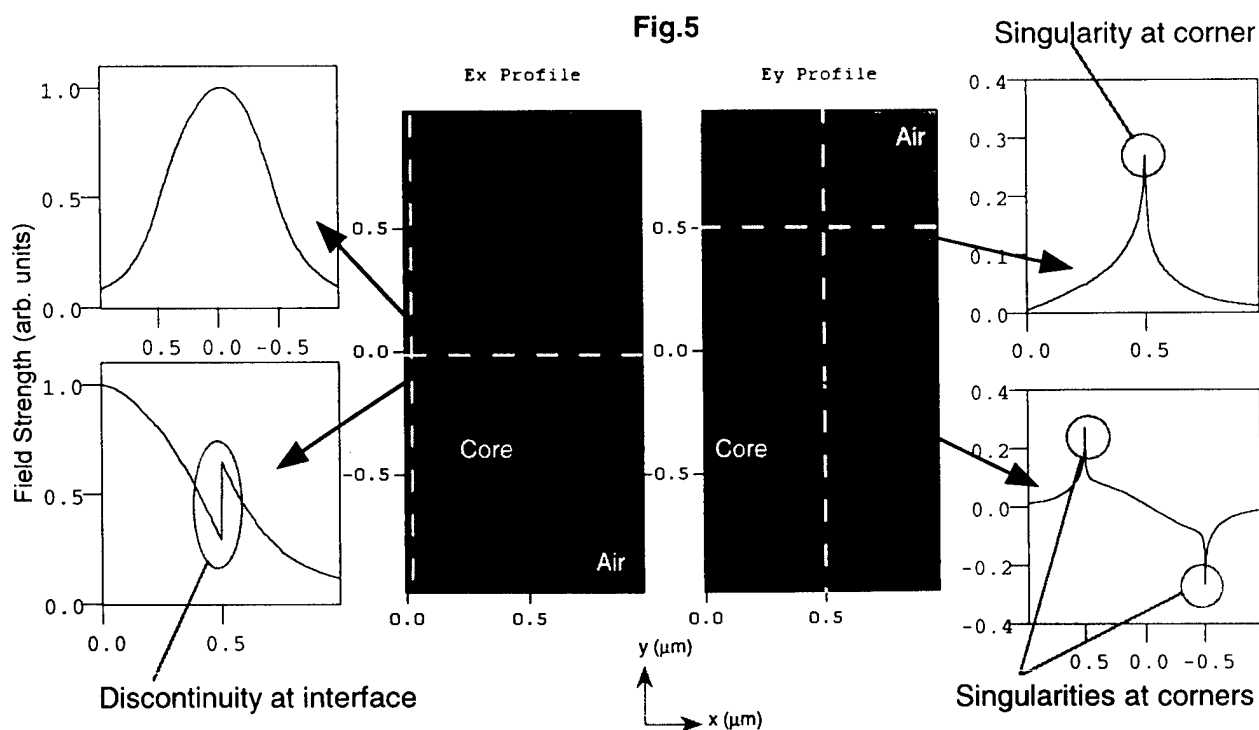
It is planned to incorporate the algorithm developed here into a full-vectorial BPM. When available, more realistic and precise modelling of devices such as polarization rotators will be possible. Further details of this work will be discussed at the presentation.

## References

- [1] J. Van Bladel, *Singular Electromagnetic Fields and Sources*, Chapter 4, IEEE/OUP Series on Electromagnetic Wave Theory, Oxford University Press, (1995), and references therein.
- [2] W. Lui, et al, "Modeling and design of bending waveguide based semiconductor polarization rotators," *IEEE Photonics Technology Letters*, vol.9, no.10, pp.1379-81, (1997).
- [3] A.S. Sudbø, "Why are accurate computations of mode fields in rectangular dielectric waveguides difficult?" *IEEE Journal of Lightwave Technology*, vol.10, no.4, pp.418-419, (1992).
- [4] K.J. Binns and P.J. Lawrenson, *Analysis and Computation of Electric and Magnetic Field Problems (2nd Ed.)*, Chapter 4, Pergamon Press, (1973).
- [5] C.L. Xu, et al, "Full-vectorial mode calculations by finite difference method," *IEE Proceedings of Optoelectronics*, vol.141, no.5, pp.281-6, (1994).

**Fig.1**

Tangential field components along interfaces are continuous, but they may not be so simultaneously at the corner. Field singularity may occur there.

**Fig.2****Fig.3****Fig.4**

# Design and Analysis of Optical Polarizers Incorporating MQW Waveguides

M. Rajarajan, B.M.A. Rahman, and K.T.V. Grattan

Department of Electrical, Electronic and Information Engineering

City University

Northampton Square, London EC1V 0HB, U.K.

Tel : +44-171-477-8123, Fax : +44-171-477-8568, Email : B.M.A.Rahman@city.ac.uk

## 1.0 Introduction

Polarization-sensitive devices are important for many applications, e.g., in a polarization-diversity coherent optical detection schemes, in multiplexing, in polarization shift keying and in polarization-independent wavelength filters. Asymmetric Y-branches on LiNbO<sub>3</sub> have been reported in which the effective indices were electro-optically controlled [1]. Monolithic integration requires polarization splitters in InP and/or GaAs-based devices, since only these semiconductors permit the realization of lasers, detectors, the associated electronics and waveguide components for the near infrared wavelength regions. Polarization splitters have been studied by various researchers using a range of different operating principles. Those based on metal-clad directional couplers in InGaAsP/InP have been demonstrated [2,3], and a tunable TE/TM splitter, based on a Mach-Zehnder interferometer, with an electro-optic switch, has been constructed [4]. The other techniques used include an anisotropic overlay [5] and a short section of proton exchanged waveguide [6]. The analysis methods used to understand them can be classified into either analytical and numerical methods, where analytical methods are only accurate for one-dimensional structures. However, most practical guided-wave devices must be considered as two-dimensional and thus for the accurate design and characterization of these devices, a rigorous numerical tool is often the most viable solution. The powerful and versatile Finite Element (FE) and the Least Squares Boundary Residual (LSBR) methods have been employed in this work to calculate the modal properties and the excited modal coefficients respectively in such systems.

## 2.0 Results of Analysis

Although a simple directional coupler shows a polarization-dependent performance, however, the use of its TE/TM extinction is not sufficient in the design of an effective optical polarizer. It is also known that multiple quantum well (MQW) regions show a different equivalent index for two polarizations, but however, this difference of equivalent indices is not also sufficient to enable the design of an optical polarizer incorporating two identical MQW waveguide cores. In this work, two nonidentical waveguides, with only one incorporating a MQW region, is used in the design of an optical polarizer. To do so, the vector **H**-field based finite element method (FEM) is used to find an accurate modal solution for coupled optical waveguide structures. However, due to the many layers involved in the MQW region, the concept of using the equivalent index for the MQW can be an acceptable approach to reduce computational costs. Since the equivalent index concept has thus far been derived [7] or numerically verified [8] for planar structures, in this work, a similar concept is rigorously tested for a 2-dimensional structure, using the vector **H**-field FE formulation. In this work, the lower guide, *b*, is a MQW guide compressing nine periods. Initially a single waveguide incorporating a InGaAsP well and a InP barrier layer completely covered by a InP region is considered for characterization. The thickness of the well (*H<sub>w</sub>*) and of the barrier (*H<sub>b</sub>*) are 20nm and the corresponding refractive indices were 3.4636 and 3.17174 respectively. The width of the waveguide was taken as 4μm and the operating wavelength as 1.52μm. For computational efficiency, a two-fold symmetry (thus considering only one-quarter of the structure) has been modelled. By using a total of 4800 first order elements, by representing the actual MQW region exactly, the effective index, (*n<sub>e</sub>*=β/*k<sub>0</sub>*), and propagation constant for the waveguide was calculated to be 3.20804 for the quasi-TE and 3.19955 for the quasi-TM polarized fundamental modes. To proceed, the entire MQW region has been replaced by a homogeneous region with its equivalent index, calculated by using the equations [7] below in the model

$$n_{TE} = \frac{n_w^2 H_w + n_b^2 H_b}{H_w + H_b} \quad \text{and} \quad \frac{1}{(n_{TM})^2} = \frac{\frac{H_w}{n_w^2} + \frac{H_b}{n_b^2}}{H_w + H_b}$$

and previously these equations have been verified numerically for planar waveguides [8].

In this example, following these equations, the equivalent index for the TE and TM polarizations were calculated as 3.3201 and 3.3080 respectively. When these equivalent indices were used to replace the MQW region, the modal solutions generated by the FEM yielded effective indices ( $n_e$ ) 3.21067 for the TE polarization and 3.20175 for the TM polarization which clearly shows an overestimate for both the polarizations. Next, the equivalent indices for the two polarizations are adjusted to obtain the same modal solutions as were obtained for the true MQW structure and the correct effective index values were found to be 3.3141 and 3.3013 respectively. It has been observed that the simple planar approximation used previously [7] overestimates the value obtained by rigorous numerical simulation for the MQW structures with 2-dimensional confinement.

A schematic of the directional coupler with nonidentical guides simulated in this study is illustrated in Figure 1, showing two guides  $a$  and  $b$  separated by a distance,  $S$ . In this design the top waveguide is fabricated from bulk  $\text{In}_{1-x}\text{Ga}_x\text{As}_y\text{P}_{1-y}$  material and by adjusting the molar fractions, the refractive index of the top guide can be made equal to 3.3141 for both the TE and TM polarizations. On the other hand, the lower waveguide, being a MQW region, “sees” an equivalent index for the TE and the TM polarizations of 3.3141 and 3.3013 respectively.

The vector FEM is used to find the modal solutions of the coupled structure. Fig. 2 shows the variation of the coupling length with the changing separation,  $S$ , between the guides. The coupling length axis is plotted in semi-log scale to reveal the exponential variation of the coupling length for the TE polarization (solid line) with the increasing separation. However the coupling length for the TM polarization (dashed line), initially increases exponentially with  $S$ , but asymptotically reaches a maximum value with the further increase of the separation. At higher separations the guides are isolated and with the waveguides being nonidentical, the propagation constant difference does not change with increasing separation. Thus the coupling length remains constant. From Fig. 2, a relationship can be derived such that a distance of twice the coupling length for the TM polarization equals the coupling length of the TE. In this case, when the separation between the waveguides was  $1.495\mu\text{m}$ , the coupling length of the TM polarization was  $110\mu\text{m}$  and that for the TE coupling length was  $220\mu\text{m}$ . Therefore by choosing a directional coupler section of  $220\mu\text{m}$ , an effective TE/TM polarizer can be designed. For the TE polarization, the waveguide parameters were designed such that the two waveguides were identical and the two supermodes were completely symmetrical or antisymmetrical. The height and width of the top guide was  $0.36\mu\text{m}$  and  $4\mu\text{m}$  respectively. On the other hand, for the even-like TM supermode (not shown here) most of the power is in guide  $a$  and there is little power in guide  $b$ , because the guides are nonidentical for the TM polarization. Next, using the field profiles and the propagation constants generated by employing the vector  $\mathbf{H}$ -field finite element method, the LSBR approach can be used to calculate the excited modal coefficients and from these parameters the composite field profiles at various  $z$  locations. It is assumed that the power is launched into the top waveguide,  $a$ , at the beginning of the directional coupler section. Figure 3a shows the composite field at one coupling length for the TM polarization. It can be noticed from this figure that only a fraction of the input power has transferred to the adjacent lower guide at one coupling length. As the power in the supermodes is not equally distributed for both the even and the odd supermodes, there is incomplete power transfer at the coupling length for the TM case. Figure 3b shows the composite field profile at twice the TM coupling length, i.e. at  $220\mu\text{m}$ . It can be seen from this figure that all of the power previously coupled to the lower guide,  $b$ , has now been transferred back to the top guide,  $a$ . However, for the TE polarization (not shown here), there will be complete power transfer from guide  $a$  to guide  $b$  at its coupling length, which is  $220\mu\text{m}$ .

Figure 4 shows the variation of the waveguide power along the axial direction for the TE and the TM polarizations. As can be seen from this figure, at  $z=0\mu\text{m}$  for both the TE and TM polarization, most of the power is in guide  $a$  and there is almost zero power in guide  $b$ . However, at  $z=220\mu\text{m}$  most of the TE power is in guide  $b$  and most of the TM power is in guide  $a$ . Therefore by carefully selecting the device parameter a passive TE/TM polarizer can be designed by incorporating the MQW region, without introducing surface plasmon modes, which are inherently lossy.

### 3.0 Summary

For the first time to the authors knowledge an appropriate model of MQW based polarizer with two-dimensional confinement has been discussed. The approximate equations to calculate the equivalent indices for the TE and the TM polarizations have shown to be inaccurate for the analysis of two-dimensional structures. The importance of the FE and the LSBR numerical schemes has also been demonstrated, in the design of optical polarizers, and appropriate supporting results given on these structures.

#### 4.0 References

- (1) Y.P. Liao, R.C. Lu, C.H. Yang, and W.S. Wang, "Passive Ni:LiNbO<sub>3</sub> Polarization splitter at 1.3 $\mu$ m wavelength," *Electron. Lett.*, Vol. 32, pp. 1003-1005, 1996.
- (2) P. Albrecht, M. Hamacher, H. Heidrich, D. Hoffmann, H.P. Nolting and C.M. Weinert, "TE/TM Mode Splitter on InGaAsP/InP," *IEEE Photon. Technol. Lett.*, Vol. 2, pp. 114-115, 1990.
- (3) M. Rajarajan, C. Themistos, B.M.A. Rahman, and K.T.V. Grattan, "Characterization of metal-clad TE/TM mode splitters using the finite element method," *J. Lightwave. Technol.*, Dec. 1997.
- (4) M. H. Hu, J.Z. Haug, R. Scarmozzino, M. Levy, and R.M. Osgood, "Tunable Mach-Zehnder polarization splitter using height-tapered Y-branches," *IEEE Photon. Technol. Lett.*, Vol. 9, pp. 773-775, 1997.
- (5) S. Uehara, T. Izawa, and H. Nakagome, "Optical waveguide polarizer," *Appl. Opt.*, Vol.13, pp. 1753-1757, 1974.
- (6) P. G. Suchoski, T.K. Findakly, and F.J. Leonberger, "Low-loss high-extinction polarizers fabricated in LiNbO<sub>3</sub> by proton exchange," *Opt. Lett.*, Vol. 13, pp. 172-174, 1988.
- (7) G. M. Alman, L.A. Molter, H. Shen, and M. Dutta, "Refractive Index Approximations from Linear Perturbation Theory for Planar MQW Waveguides," *J. Lightwave Technol.*, Vol. 28, pp. 650-657, 1992.
- (8) B.M.A. Rahman, Y. Liu, and K.T.V. Grattan, "Finite-Element Modelling of One- and Two-Dimensional MQW Semiconductor Optical Waveguides," *IEEE Photon. Technol. Lett.*, Vol. 5, pp. 928-931, 1993.

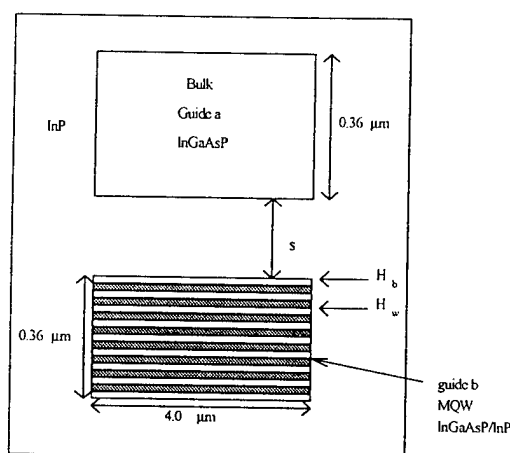


Fig. 1 A schematic of the directional coupler with non-identical guides

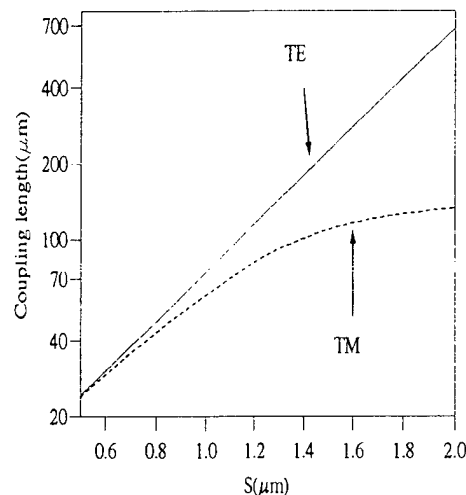


Fig. 2 Variation of the coupling length with the guide separation,  $S$ .

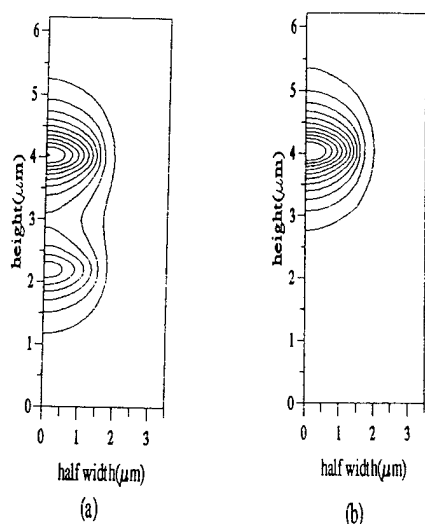


Fig. 3 (a) Composite field profile at a distance  $L_c$   
(b) Composite field profile at a distance  $= 2 L_c$

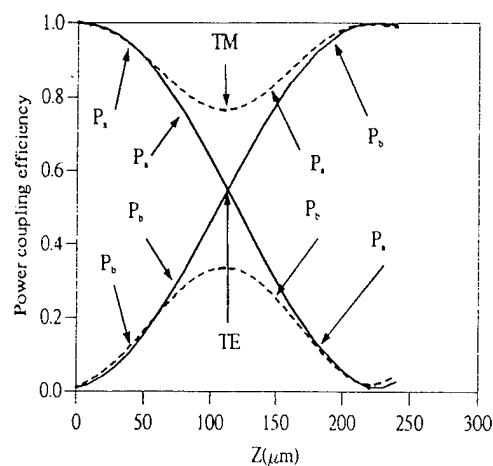


Fig. 4 Power transfer efficiency with the device length.



**Integrated Photonics Research**

# **Novel Fabrication Techniques**

**Monday, March 30, 1998**

**Claude Rolland, Bell Northern Research, Ltd., Canada**  
President

**IMF**

**2:00pm–3:30pm**

Salon C

## Fused Optoelectronic Devices

John Bowers, Near Margalit, Alexis Black, Aaron Hawkins, Bin Liu,  
Ali Shakouri, Patrick Abraham, Evelyn Hu

Department of Electrical and Computer Engineering  
University of California at Santa Barbara  
Santa Barbara CA, 93106

Semiconductor optoelectronic components such as lasers and detectors have revolutionized fiber optic communication. The efficiency and compact nature of such devices has allowed them to be incorporated into a wide variety of systems. Improvements in the epitaxial growth of devices have allowed for a wide range of material systems to be used to create ever more creative device designs. However, one fundamental constraint limiting the design of semiconductor components has been lattice matching within the structure. Non-lattice matched growth past a certain critical thickness results in strain relief by defect formation, degrading crystal quality. To overcome this barrier one can use the relatively new technique of wafer fusion to break the condition of lattice matching throughout a structure[1]. Using wafer fusion one can combine two materials not necessarily of the same lattice constant, without degrading the crystal quality away from the interface. Materials such as GaAs, InP, and Si can be combined into a single device. Each section of a device can be optimized using the material best suited for its function.

Although there may be many specifics to each fusion system the basic process goes as follows. Two epitaxial surface are taken and cleaned/passivated such that there are minimal contaminants on the surface. Then the two epitaxial surfaces are placed together in intimate contact, usually under pressure. One then heats up the wafers to near the growth temperature of one of the materials so that atomic redistribution can occur at the surface. Pressure is applied so that the voids are filled in during the fusion process. At the end of some period of time the wafer are cooled down at which point the two wafers are strongly bonded. To access the epitaxial region between the two substrates one of the substrates is removed to an etch stop layer. At the completion of this process, one has essentially transferred the epi from one substrate onto the epi from another substrate regardless of lattice constant. The defects arising from the mismatch in lattice constant are edge defects localized at the junction. We have demonstrated with low-temperature PL studies of quantum wells near the fused junction that the defects are localized to within 50 nm of the junction.

The relief of the lattice match design constraint has allowed for the creation of new high performance optoelectronic devices. One good example of such integration is the double-fused long wavelength vertical cavity laser. InP based vertical cavity lasers suffer from poor index difference from their natural InP/InGaAsP mirror system. This mirror system suffers from too much loss and too high a thermal impedance to operate to high temperatures in continuous wave operation. For this reason VCLs with the InP/InGaAsP mirror system have not operated above room temperature cw. On the other hand GaAs based VCLs have the GaAs/AlGaAs mirror system which allows for very high

performance operation[2]. In addition using lateral oxidation for current constriction has further improved the operation of such devices. In the double-fused VCL one can use the advantages of GaAs/AlGaAs mirrors along with a high performance InP/InGaAsP active region. In this way one can get the best of both worlds. Figure 1 shows a schematic of the double-fused laterally-oxidized 1.5  $\mu\text{m}$  VCL. This structure operates to 65°C cw operation, 30 °C higher than any structure not using wafer fusion[3].

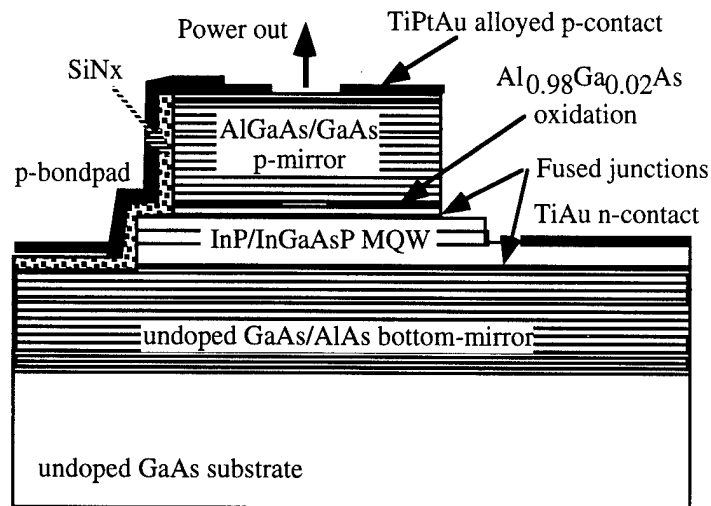


Figure 1- Long-wavelength vertical cavity laser operating to 65°C cw

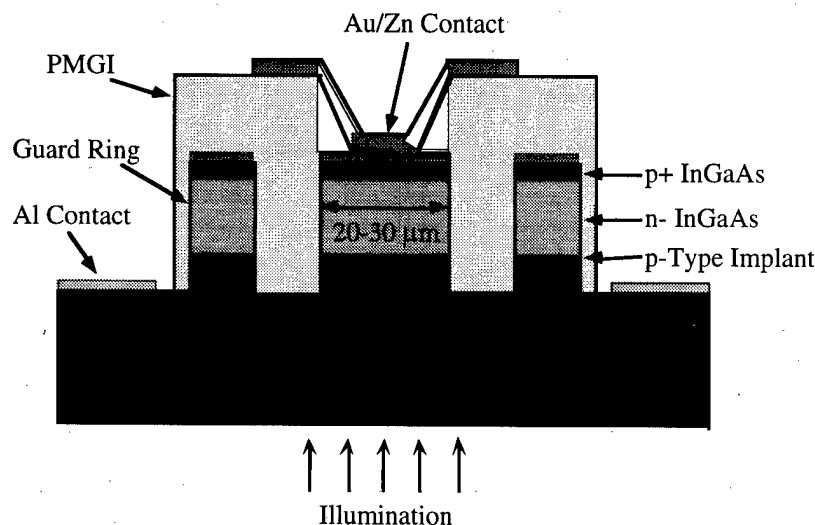


Figure 2- Fused avalanche photodiode for high gain-bandwidth product

Another good example of using fusion for the optimization of each layer is the InGaAs/Si avalanche photodetector. Si is a very good material for avalanche multiplication due to its large difference between hole ionization and electron ionization. This large difference means less noise and higher gain from avalanche photodetectors using Si versus InGaAs. The problem arises is that Si does not absorb light in the communication wavelengths of 1.3  $\mu\text{m}$  and 1.55  $\mu\text{m}$ . To overcome this problem, we have used wafer fusion to make a device with both InGaAs and Si. The InGaAs acts as the absorption layer

and the Si acts as the multiplication layer. This type of structure is known as a SAM APD (Separate Absorption and Multiplication photodetector). Figure 2 shows the structure for such a device. We have recently reported on a record gain bandwidth product from such a structure of 300 GHz[4].

In addition to integration of dissimilar materials wafer fusion can also be used to create structures that would normally be impossible to fabricate. Wafer fusion allows one to fabricate waveguides that can cross each other. This may enable optical switches to be fabricated that may scale to very large number of ports. An example of two ridge waveguides fused together is shown in Figure 3. One can have a very strong interaction between the waveguides as the two are co-linear, but one can also separate the two waveguides into different directions. In effect fusion allows for the equivalent of interconnects in integrated circuits for waveguide optics. With multiple fusion steps one can eventually incorporate 3-D structures into waveguide devices.

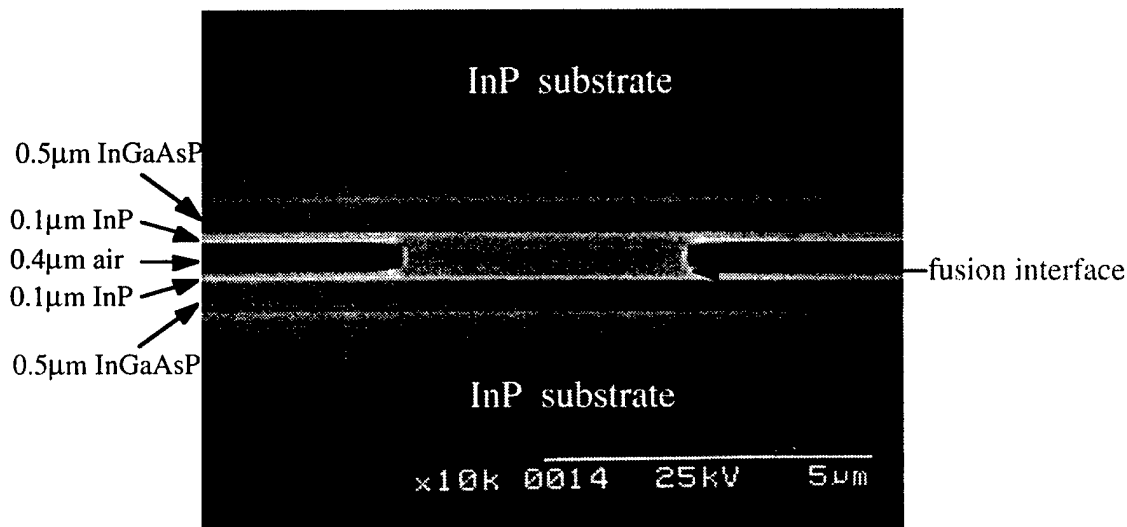


Figure 3 - Stain etched SEM picture of a fused vertical coupler

## References

- [1] R.J. Ram, J.J. Dudley, J.E. Bowers, L. Yang, K. Carey, S.J. Rosner, K. Nauka: "GaAs to InP wafer fusion.", *Journal of Applied Physics*, 15 Sept. 1995, vol.78, (no.6):4227-37.
- [2] R. Jager, M. Grabherr, C. Jung, R. Michalzik, G. Reiner, B. Weigl, K.J. Ebeling: "57% wallplug efficiency oxide-confined 850 nm wavelength GaAs VCSELs.", *Electronics Letters*, 13 Feb. 1997, vol.33, (no.4):330-1.
- [3] N.M. Margalit, J. Piprek, S. Zhang, D.I. Babic, K. Streubel, R.P. Mirin, J.R. Wesselmann, J.E. Bowers: "64 degrees C continuous-wave operation of 1.5-μm vertical-cavity laser.", *IEEE Journal of Selected Topics in Quantum Electronics*, April 1997, vol.3, (no.2):359-65.
- [4] A.R. Hawkins, Wu Weishu, P. Abraham, K. Streubel, J.E. Bowers: "High gain-bandwidth-product silicon heterointerface photodetector.", *Applied Physics Letters*, 20 Jan. 1997, vol.70, (no.3):303-5.

## Substrate-Removed (SURE) Optical Waveguides in GaAs/AlGaAs Epitaxial Layers Embedded in Benzocyclobutene (BCB)

Steven R. Sakamoto, Cem Ozturk, Young Tae Byun, Jack Ko, Nadir Dagli\*

Department of Electrical and Computer Engineering

University of California

Santa Barbara, CA 93106

\*Phone: (805) 893 - 4847 Fax: (805) 893 - 3262 e-mail: dagli@ece.ucsb.edu

### Introduction

Effective integrated optoelectronic devices made from III-IV semiconductors require low loss optical waveguides. Functionality for these devices is provided by the epitaxial layer. The presence of the substrate in compound semiconductors hinders the performance of high speed devices such as modulators [1] and photodetectors [2], since semiconductor substrates have high relative dielectric constants, and high microwave sheet and thermal resistances. The elimination of the substrate would relieve these drawbacks while enabling new advantages, such as being able to couple semiconductor epi layers with organic polymer waveguides and patterning and processing both sides of an epi layer. Hence, novel low propagation loss, low cost, easily fiber coupled polymer waveguides can be combined with the superior electro-optic properties of semiconductor waveguides. Here we investigate the characteristics of high performance optical waveguides removed from their substrates and bonded onto transfer substrates using an organic polymer.

### Waveguide Fabrication

First an unintentionally doped epitaxial layer was designed for optical waveguiding at 1.55 $\mu\text{m}$  and grown by molecular beam epitaxy (MBE). An AlAs etch stop layer between the bottom cladding and substrate was added to aid in the subsequent removal of the growth substrate. Two separate samples were cleaved from this wafer. The first sample was used for the novel substrate-removed (SURE) waveguides, and the other was used for the control waveguides.

On both epi layers, straight 4 $\mu\text{m}$  wide singlemode waveguides were patterned with standard photolithography and wet etched 5,000 $\text{\AA}$  using a 10:1 1M citric acid:H<sub>2</sub>O<sub>2</sub> solution. At this point the fabrication of the control sample was completed. It was then cleaved, mounted, and measured. A schematic of the control sample is given in Figure 1(b).

To continue with the fabrication of the SURE waveguides, a mechanical grade semi-insulating (S.I.) - GaAs transfer substrate was prepared by spinning AP-8000 adhesion promoter and 9 $\mu\text{m}$  of Cyclotene 3022-57, which is a form of benzocyclobutene (BCB) [3]. This polymer is known to produce easily fiber pigtailed, high quality optical waveguides [4]. The device, was also coated with adhesion promoter and then embedded, guides/epi down, into the BCB. To ensure that a quality facet could later be cleaved, the sample was roughly aligned to the edges of the transfer substrate. A full cure was performed in a nitrogen purged oven. We noted with past runs that the BCB would become less viscous at curing temperatures, allowing the samples to move on top of the transfer substrate. For this reason, the samples were deliberately set at an angle ( $\sim 10^\circ$ ) during the cure so as to allow the edge of the epi grown structure to align to the edge of the transfer substrate. The liquid tension near the edge prevented the sample from falling off the edge of the transfer substrate.

To remove the growth substrate from the epi layer, a GaAs substrate wet spray etch was performed. This consisted of a 30:1 mixture of H<sub>2</sub>O<sub>2</sub>:NH<sub>4</sub>OH sprayed as a fine mist onto the growth substrate. This left a BCB layer sandwiched between the thin epi layer structure and the underlying transfer substrate. The remaining exposed epi layer was very smooth and uniform, in

spite of being on top of BCB (e.g., no cracks or bubbles were seen). The planarity of the epi was good enough for another lithography.

Finally, optical-quality facets were made by cleaving. This was done by nicking the corner of the transfer substrate with a sharp blade, then by applying pressure to allow the cleave to propagate both laterally and vertically through the BCB and the epi layer. The sample was then mounted and measured. A schematic of the SURE waveguides is shown in Figure 1(a).

## Experimental results

Despite cleaving through a  $\sim 500$   $\mu\text{m}$  thick substrate, 9  $\mu\text{m}$  of BCB polymer, and the epi layer, good quality facets shown in Figure 2 were obtained. To measure the waveguide/material loss, the Fabry-Perot resonance technique was utilized. In our case, we varied the temperature of a 1.55  $\mu\text{m}$  distributed-feedback (DFB) laser through an external thermoelectric temperature controller. The TE polarized light was focused with a microscope objective through a collimating lens and onto the detector of an infrared camera. Voltage signals linearly proportional to the output intensities were fed from a video analyzer into a digitizing oscilloscope.

Eleven waveguides with a length of 9 mm were measured on the control sample. Measured propagation loss values varied from 0.87 dB/cm to 1.96 dB/cm for TE polarized input. The average propagation loss for the control waveguides was 1.46 dB/cm. The length of the SURE waveguides was 8 mm. The TE propagation loss for nine such waveguides ranged from 1.46 dB/cm to 1.87 dB/cm. The average TE propagation loss for this case was 1.58 dB/cm. On average the loss of the SURE waveguides was 0.12 dB/cm higher than the control waveguides which was very close to the standard deviation of the measured values. Indeed, some waveguides in the substrate removed sample had propagation losses lower than the regular waveguides in the control sample. This shows that the propagation loss increase due to this novel process was marginal.

## Conclusions

We have successfully demonstrated the feasibility of substrate removal and bonding the remaining epilayer on transfer substrates using BCB in the fabrication of optoelectronic devices in the GaAs/AlGaAs material system. In particular, optical waveguides fabricated in epilayers removed from substrates and embedded in BCB had an average propagation loss of 1.58 dB/cm at 1.55  $\mu\text{m}$  for TE polarization. This was only on average 0.12 dB/cm greater than control guides fabricated on GaAs substrates with air as the top cladding. The substrate removal process produced a smooth epi layer on which fine line lithography was possible. This demonstrates the feasibility of processing both sides of an epilayer. Optical quality cleaved facets were also produced by aligning the crystal axis of the growth and transfer substrates during bonding. Presently we are utilizing this novel process to fabricate low voltage, high speed electro-optic modulators.

## Acknowledgment

This work was supported by DARPA grant MDA 972-94-1-0002 and AFOSR grant F19628-97-C-0069.

## References

- [1]. R. Spickermann, S. R. Sakamoto, M. G. Peters and N. Dagli, "GaAs/AlGaAs Traveling Wave Electro-optic Modulator with an Electrical Bandwidth  $> 40$  GHz," *Electronics Letters*, Vol. 32, No. 12, pp. 1095-1096, 6 June 1996.
- [2]. A. R. Hawkins, T. E. Reynolds, D. R. England, D. I. Babic, M. J. Mondry, K. Struebel, and J. E. Bowers, "Silicon Heterointerface Photodetector," *Applied Physics Letters*, Vol. 68, No. 26, pp. 26-28, 24 June 1996.
- [3]. Form No: 296-01211-493NP&M, Dow Plastics, The Dow Chemical Company, 2040 Dow Center, Midland MI 48674.
- [4]. C. F. Kane and R. R. Krchnavek, "Benzocyclobutene Optical Waveguides," *IEEE Photonics Technology Letters*, Vol. 7, No. 5, pp. 535-537, May 1995.

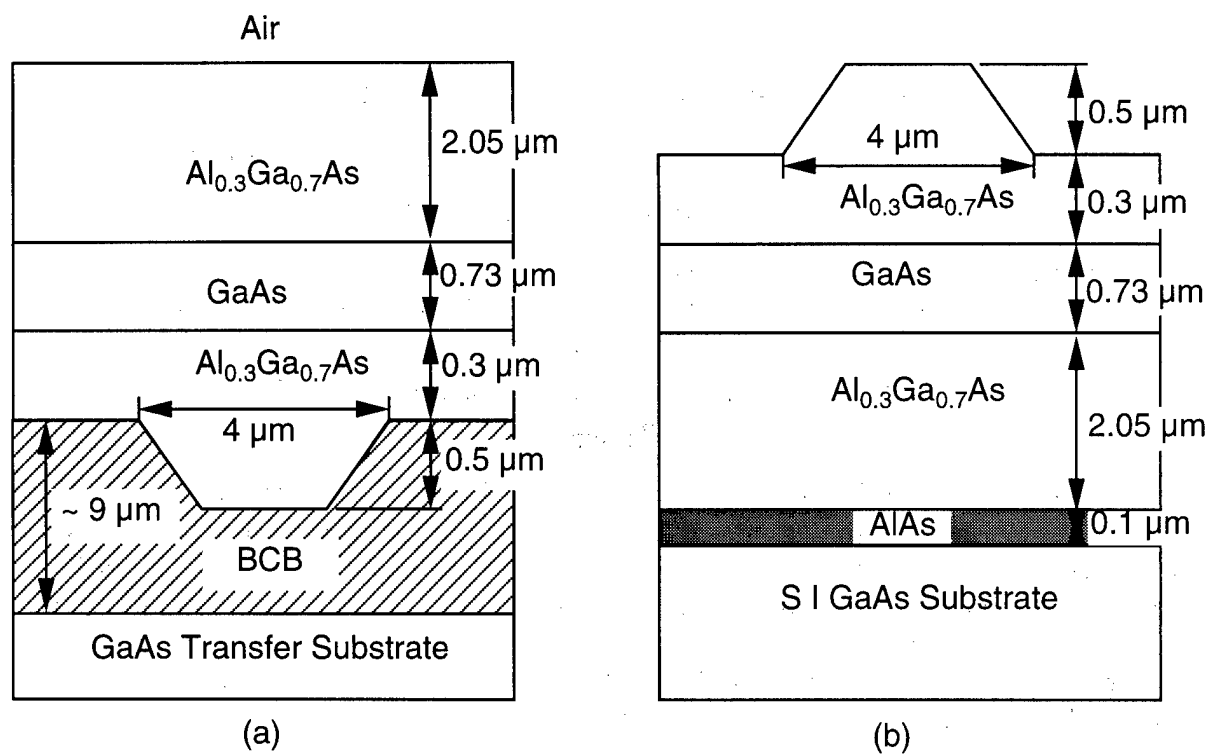


Figure 1 (a) Schematic cross sectional profile of the SURE waveguide, (b) conventional rib waveguide.

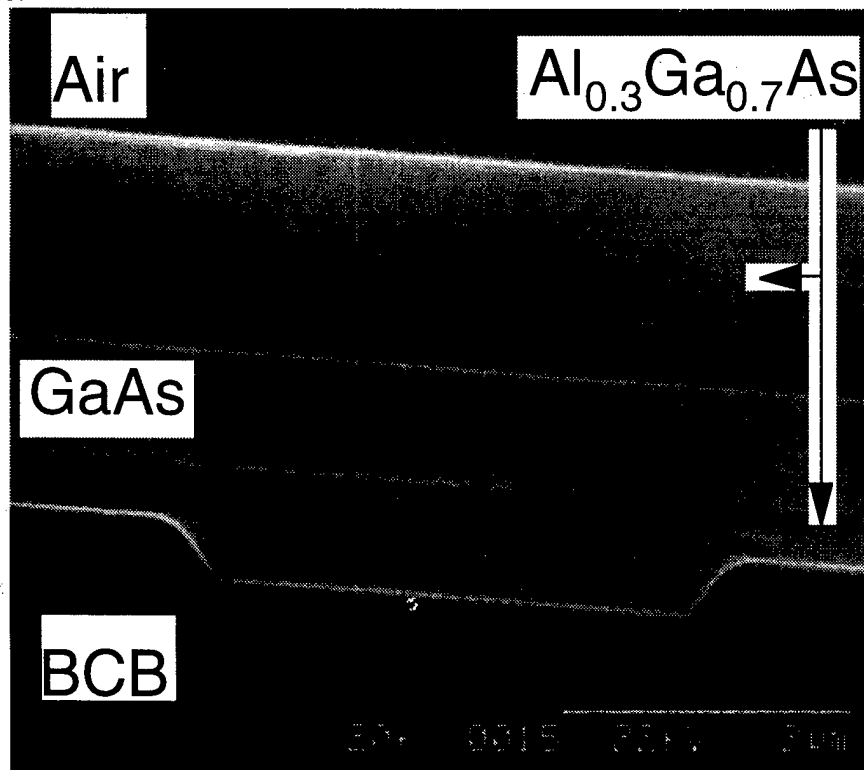


Figure 2. SEM photograph of a cleaved facet of a waveguide in a substrate removed GaAs/AlGaAs epitaxial layer embedded in BCB.

## High performance photoelastic semiconductor laser and electroabsorption waveguide modulator

W. X. Chen, Q. Z. Liu, L. S. Yu, N. Y. Li, Q. J. Xing, J. T. Zhu, G. L. Li, C. W. Tu,  
H. P. Zappe<sup>[1]</sup>, P. K. L. Yu, and S. S. Lau

Department of Electrical and Computer Engineering, University of California at San  
Diego, La Jolla, CA 92093-0407. Telephone: 619-534-6180;  
fax: 619-534 0556; email: wxchen@ece.ucsd.edu

[1] at Paul Scherrer Institute, 8048 Zurich, Switzerland

### Summary

Index-guided buried-heterostructure lasers offer good features such as stable lateral modes, reduced waveguide width and reduced threshold current. However, these advantages are usually obtained through the use of complicated processing and/or regrowth techniques, especially for lasers with planar structures. For instance, in a conventional fabrication of such lasers one would use an etching step to form ridges or grooves in the as-grown epitaxial layers, and then form the current-blocking and waveguide layers around the laser active region in a second growth process. Not only is the regrowth a difficult, low-yield process, it frequently results in non-planar surfaces, making integration of waveguides, transistors, and other devices with these lasers a difficult task.

At the University of California at San Diego, we have demonstrated that, by employing photoelastic effect with thermally stable and controllable metal stressor stripes for optical waveguiding, low propagation loss (on the order of 1 dB/cm or less) has been achieved in both InP and GaAs based planar waveguides<sup>[1]</sup>. We primarily focused on the study of stressors based on Ni and WNi stripes. The Ni-window stripes based on tensile stresses of the Ni-film (or Ni-compounds) on InP (InGaAs) or GaAs surface have resulted in low-loss waveguides (~ 1 dB/cm). On the other hand, WNi-stripes based on compressive stresses of relatively inert WNi layers stripes have resulted in waveguides with a strong lateral modal confinement and with a moderately low loss. The WNi waveguiding persists up to high temperatures (> 500 °C). We recently employed these techniques in the fabrication of high performance planar laser.

Previously Kirkby et al.<sup>[2]</sup> have investigated the photoelastic waveguiding effect induced by oxide stressor stripes on GaAs/AlGaAs semiconductor heterostructures. In their work the oxide films were compressive, and openings in the oxide films were needed for injecting current into a 20-μm wide stripe. They found that photoelastic waveguiding present in these 20-μm wide stripe-geometry lasers was essential in determining the good (kink-free) light/current (L-I) characteristics.

In our work, narrow (a few μm) stripe lasers are investigated to reduce the threshold currents in planar stripe-geometry lasers. More importantly, thin-film metal stressors are favored because they can also serve as ohmic contacts for current injection. Here we report the first demonstration of photoelastic lasers in a configuration where the compressively (rather than tensilely) stressed WNi stripe (a few μm in width) is used to

induce lateral light confinement and to inject current. Ion implantation is used for lateral electrical isolation and consequently the entire device structure is planar.

*Experimental:* The laser samples were grown on n-GaAs (100) substrates by low pressure organometallic vapor phase epitaxy. The separate-confinement GaAs/AlGaAs heterostructure contains a single quantum well in the active region. Fig. 1 depicts the schematic cross section view of the laser. The 12 nm thick GaAs quantum well is cladded between two 194 nm thick  $\text{Al}_{0.3}\text{Ga}_{0.2}\text{As}$  core layers. For some of the laser samples, a 100 nm thick carbon-doped  $\text{p}^{++}$ -GaAs layer (doping about  $1 \times 10^{20} \text{ cm}^{-3}$ ) was regrown at the top by chemical beam epitaxy (CBE) to improve ohmic contacts.

The processing of the lasers is as follows. A photoresist lift-off technique was used to form stripes that are 5  $\mu\text{m}$  wide and 200  $\mu\text{m}$  apart. WNi stressor stripes of  $\sim 100$  nm in thickness were deposited by rf sputtering, followed by deposition of the ion implantation mask, consisting of Hf (6 nm) and Au (600 nm), by e-beam evaporation. Sputtering was carried out using a source power of 250 watts, an argon pressure of 15 mTorr, and the sample under a bias of - 220V with respect to the ground. After the lift-off, the samples were annealed at 490  $^{\circ}\text{C}$  for 30 minutes to form ohmic contacts between the WNi layer and the top  $\text{p}^{+}$ -GaAs (or  $\text{p}^{++}$ -GaAs) contacting layer. Multiple-energy He<sup>+</sup> implantation was then performed at room temperature using ion doses of  $2.4 \times 10^{13} \text{ cm}^{-2}$  (80 keV),  $2 \times 10^{13} \text{ cm}^{-2}$  (120 keV),  $6 \times 10^{13} \text{ cm}^{-2}$  (180 keV) to ensure a uniform damage profile through most of the  $\text{p-Al}_{0.8}\text{Ga}_{0.2}\text{As}$  upper cladding layer for device isolation. After implantation, the top surface  $\text{p}^{+}$ -GaAs layer outside the stressor stripe was chemically removed by a selective etching solution of citric acid and hydrogen peroxide (5:1 ratio), with the Au/Hf/WNi stripes as the etching mask. The samples were then lapped down to about 100  $\mu\text{m}$  in thickness from the backside and loaded into an e-beam evaporator. A multilayer of Pd(10 nm)/Ge(44 nm)/Au(100 nm) was evaporated onto the back side of the samples followed by thermal annealing at 250  $^{\circ}\text{C}$  for 1 hour to form ohmic contact to the n-GaAs substrate.<sup>[3]</sup> Finally the samples were cleaved into devices of various lengths for characterization.

*Results:* After implantation and removal of the surface  $\text{p}^{++}$  and/or  $\text{p}^{+}$  layer by selective chemical etching, the resistance between neighboring laser diodes increases by at least 5 orders of magnitude. Typical I-V curve between neighboring p stripes of lasers (about 400  $\mu\text{m}$  long and 200  $\mu\text{m}$  apart) shows more than 1 M $\Omega$  isolation. It clearly demonstrates the effectiveness of device isolation by helium implantation.

The laser bars with different lengths were put onto a probe station for L-I and I-V measurements. The laser samples were p-side up for probing individually. The output light from one end-facet of the lasers was measured by a Si photodiode. Emission wavelength of these lasers is about 825 nm as measured by an HP70951A optical spectrum analyzer. For lasers with a stripe geometry of 178  $\mu\text{m}$  by 5  $\mu\text{m}$ , a threshold current of 29 mA is obtained under cw operation at room temperature. The turn-on voltage of the laser is about 1.5 V, and the series resistance is about 5 ohm. The threshold current density,  $J_{th}$ , is about 3.7 kA/cm<sup>2</sup>. The differential quantum efficiency from both facets is about 43%.

In Fig. 2, we have plotted the differential quantum efficiency,  $\eta_d$ , versus the laser length. From this figure, an internal quantum efficiency,  $\eta_i$ , of 75 % and an  $\alpha_i$  of about 40 cm<sup>-1</sup> are obtained.

Similar planar processes, involving both photoelastic WNi stressor and He-implantation, have been used in the fabrication of the InGaAsP/InP Franz-Keldysh effect electroabsorption waveguide modulators. The parasitic contact pad capacitance is minimized through use of polyimide. Efficient optical modulations are observed for both TE and TM polarized light at 1.3  $\mu\text{m}$ . The C-V measurement of the  $\sim 200 \mu\text{m}$  long and 4  $\mu\text{m}$  wide waveguide gives a capacitance of 0.3 pF at -1.0 V, which corresponds to a 3-dB bandwidth over 10 GHz.

#### References:

1. L. S. Yu, Z. F. Guan, W. Xia, Q. Z. Liu, F. Deng, S. A. Pappert, P. K. L. Yu, S. S. Lau, L. T. Florez, J. P. Harbison, Appl. Phys. Lett., **62**, 2944-2946 (1993).
2. P. A. Kirkby, P. R. Selway, L. D. Westbrook, J. Appl. Phys. **50**, 4567 (1979).
3. L. C. Wang, P. H. Hao, B. J. Wu, Appl. Phys. Lett. **67**, 509 (1995).

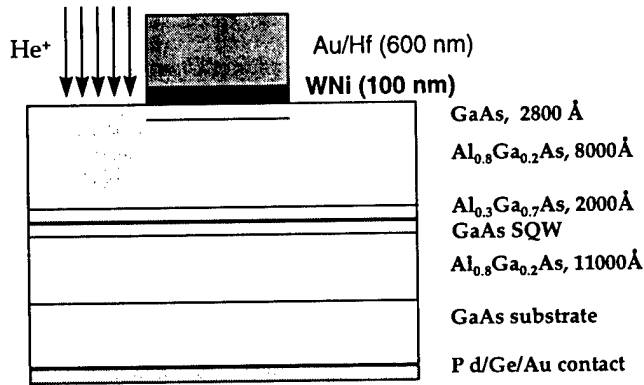


Fig. 1. Schematic cross-section of the photoelastic laser.

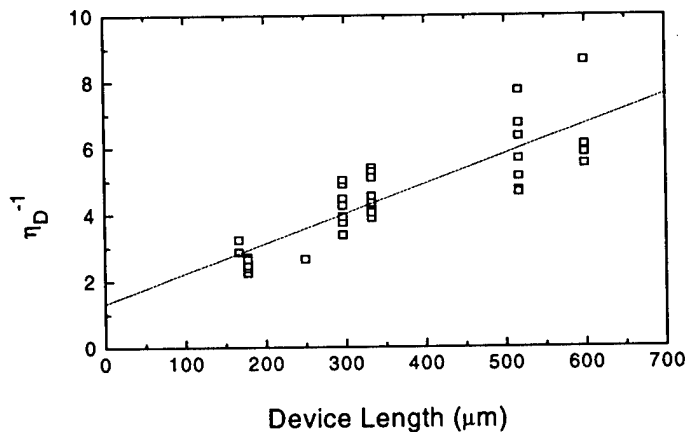


Fig. 2 Reciprocal differential efficiency versus length of the lasers. A linear fit is shown.

## Pick-and-place multi-wafer bonding of photonic devices on Si

D. Crouse, Z. H. Zhu <sup>a)</sup>, Y.H. Lo,  
School of Electrical Engineering, Cornell University, Ithaca, NY 14853  
H. Hou  
Sandia National Laboratories, Albuquerque, NM 87185

There has recently been great strides in device integration using wafer bonding. The various photonic devices that have emerged that incorporate wafer-bonding in their fabrication are visible light emitting diodes (LED's)<sup>1</sup>, 1.3 and 1.5  $\mu\text{m}$  vertical-cavity surface-emitting-lasers (VCSEL's)<sup>2,3</sup>, integrated 1.3  $\mu\text{m}$  InP-InGaAsP-Si edge emitting lasers<sup>4</sup>, and integrated InGaAs-Si avalanche photodetectors (APD's)<sup>5</sup>. All of these devices however, were fabricated using a single piece of epi-grown wafer to a host substrate. Recently we have demonstrated the first use of pick-and-place technology by simultaneously direct bonding nine 1.3  $\mu\text{m}$  InP strain-compensated multi-quantum-well (MQW) wafers, each  $2 \times 2 \text{ mm}^2$ , to a  $1 \times 1 \text{ cm}^2$  GaAs substrate<sup>6</sup>. This pick-and-place process has been extended by using Si as the host wafer instead of GaAs and by further device processing on the individual chips resulting in photonic devices being placed at specific locations on the Si substrate. This technology is desirable since it resolves the wafer size mismatch between small III-V based photonic structures and the Si substrate wafer. The ability to fabricate certain electronic components on the Si host wafer that can withstand the mild bonding conditions of 560 °C coupled with the ability to perform multiple bonding procedures using different III-V epi-grown optical structures for various functions will allow for the fabrication of increasingly complex OEIC's.

The pin structure was fabricated by MOCVD. First a InP buffer layer was grown on the InP substrate. Following the buffer layer was first a 400 nm InGaAs etch stop layer, then a 400 nm n+ type InP layer, a 200 nm n-type InP layer, a 2.2  $\mu\text{m}$  InGaAs intrinsic layer, a 20 nm p-type InP layer and finally a 1.0  $\mu\text{m}$  quaternary InGaAsP layer.

The wafer bonded array was fabricated by first cleaving nine pin chips, each  $2 \times 2 \text{ mm}^2$ . Then the nine pin chips along with the Si substrate were thoroughly cleaned with acetone, isopropanol, and D.I. water followed by a HF dip to remove the native oxide. The nine chips were placed with the p-type InP epitaxial layer in contact with the Si substrate. After alignment, moderate pressure was applied to promote Van-der Waal bonding. The sample was then annealed in a  $\text{H}_2$  atmosphere at 560 °C for 45 min. The device at this stage is shown in Fig. 1. The bonding strength was adequate enough to withstand the many subsequent processing procedures needed to fabricate the pin photodetectors. Following the annealing, the InP substrate was removed using 3 HCl: 1  $\text{H}_2\text{O}$ . The InGaAs etch stop layer was then removed by 1  $\text{H}_2\text{SO}_4$ : 8  $\text{H}_2\text{O}$ : 8  $\text{H}_2\text{O}_2$ . Then the deposition of n-contacts and p-contacts was performed on the n+-type InP layer and the backside of the Si substrate respectively. Finally, the mesa geometry was fabricated by an additional photolithography process followed by a 1  $\text{H}_2\text{SO}_4$ : 8  $\text{H}_2\text{O}$ : 8  $\text{H}_2\text{O}_2$  etch of the InGaAs intrinsic region resulting in pin devices shown in Fig. 1.

Following the fabrication, I-V measurements were performed resulting in an average dark current of ~5 nA at 5 volts reverse bias. The dark current was significantly greater than expected due to the incomplete etch of the intrinsic InGaAs layer, yet concerns about undercut during the InGaAs etch caused us to be conservative in the duration of this etching process.

In conclusion, for the first time, photonic devices have been fabricated on specific locations of a Si wafer using pick-and-place technology. This allows for the further development of device integration which will facilitate the fabrication of OEIC's.



Fig. 1

A scanning electron micrograph of the pick-and-place array showing alignment before substrate removal and device processing.

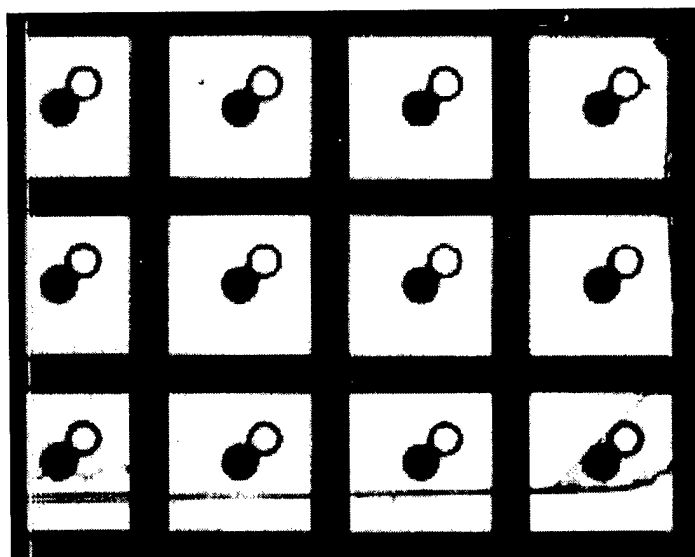


Fig. 2

A photograph of the final pin optical components fabricated on the  $2 \times 2 \text{ mm}^2$  chips. Almost the entire chip is bonded well resulting in numerous optical components even approaching the very edge of the  $2 \times 2 \text{ mm}^2$  chips

## References

- <sup>1</sup>F. A. Kish, F. M. Steranka, D. C. DeFever, D. A. Vanderwater, K. G. Park, C. P. Kuo, T. D. Osentowski, M. J. Peanasky, J. G. Yu, R. M. Fletcher, D. A. Streigerwald, M. G. Crawford, and V. M. Robbins, *Appl. Phys. Lett.* 64, 2839 (1994).
- <sup>2</sup>D. Babic, K. Streubel, R. P. Mirin, N. M. Margalit, J. E. Bowers, E. L. Hu, D. E. Mars, L. Yang, and K. Carey, *IEEE Photon. Technol. Lett.*, 7, 1225 (1995).
- <sup>3</sup>Y. Qian, Z. H. Zhu, Y. H. Lo, H. Q. Hou, M. C. Wang, and W. Lin, *IEEE Photon Technol. Lett.*, 9, 8 (1997).
- <sup>4</sup>Hiroshi Wada, and Takeshi Kamijoh, *IEEE J. Sel. Topic. Quantum Electron.* 3, 937 (1997).
- <sup>5</sup>A. R. Hawkins, T. E. Reynolds, D. R. England, D. I. Babic, M. J. Mondry, K. Streubel, and J. E. Bowers, *Appl. Phys. Lett.* 68, 3692 (1996).
- <sup>6</sup>Z. H. Zhu, Y. C. Zhou, D. Crouse, and Y. H. Lo, Submitted to *Appl. Phys. Lett.*, (1998).



**Integrated Photonics Research**

# **WDM II/ Filters**

**Monday, March 30, 1998**

**Janet Lehr Jackel, Belcore**  
Presider

**IMG**  
**2:00pm–3:30pm**  
Saanich Room

# Wavelength filters based on low-loss polymer waveguides and high-index polymer gratings

*Min-Cheol Oh, Myung-Hyun Lee, Joo-Heon Ahn, Hyung-Jong Lee,  
and Seon-Gyu Han*

*Photonic Switching Section*

*Electronics and Telecommunications Research Institute*

*161 Kajong-dong, Yusong, Taejeon, 305-350, Korea*

*(Tel) +82-42-860-5706, (Fax) +82-42-860-6858, (e-mail) mcoh@mail.etri.re.kr*

## I. Introduction

Wavelength filters are essential components for the optical signal processing systems based on wavelength division multiplexing in order to select one wavelength carrying a desired signal. Bragg reflectors imprinted in a photosensitive optical fiber by exposing the UV through a phase mask have been actively investigated because of the easy process and the excellent performances like narrow bandwidths and low insertion losses [1]. The phase mask technology was also applied to the silica waveguide devices and the semiconductor materials, then the Bragg gratings were integrated with other devices so as to demonstrate wavelength division multiplexers [2]. This technology provides very efficient way for the large-volume production. In this work, we apply the phase mask technology to polymer waveguide devices in order to fabricate polymeric gratings.

Recently, a low propagation loss around 1.55  $\mu\text{m}$  wavelength have been demonstrated in the polymeric optical waveguide devices [3]. They have a potential to be integrated with an electro-optic waveguide devices, which have been also actively investigated to demonstrate very wide modulation bandwidths [4] and low driving voltages [5].

The grating structures have been fabricated on polymer waveguides by using holographic setups, and e-beam direct writings [6]. For the grating layers, they used non-polymeric materials such as spin-on-glass and silicon nitride in order to avoid the complexity of the multi-layer polymer processing. However, in this work, a polymer material with a high refractive index is exploited for the grating layer so that the design flexibility of the device structure is improved. The grating pattern is produced by using a phase mask technology based on an incoherent light source attached in a usual mask aligner instead of a laser with a long coherence length. Therefore, the polymer gratings can be precisely aligned to the waveguide structures and be produced uniformly over the entire exposure area of the mask aligner. The polymer gratings are integrated with low-loss polymer rib waveguides in order to demonstrate wavelength filters. For the low-loss polymer waveguides operating around 1.55  $\mu\text{m}$  wavelength, we use a fluorinated polymer material which is developed by ourselves.

## II. Device Design and Fabrication

In order to investigate the polymer waveguide Bragg reflector, we have tried various polymer materials and selected the appropriate polymers with good optical and mechanical properties. Figure 1 shows the device structure, and the polymer materials for each layer is denoted. The polymer used for the waveguide core layer is fluorinated poly(arylene ethers) (FPAE) bearing crosslinkable ethynyl groups at the end of the chain. The crosslinkable FPAE is designed and synthesized by ourselves. It has lots of fluorine compound instead of hydrogen which causes high absorption losses around the 1.55  $\mu\text{m}$  wavelength due to the vibration absorption overtone of C-H bonds. In the FPAE, 60 % of C-H bonds are substituted by C-F bonds, then the absorption loss of the polymer is decreased. Details about the structure of the crosslinkable FPAE will be reported elsewhere.

For the grating layer, a polymer with a high refractive index is required so as to induce the large effective index difference in the Bragg reflector with a thin grating layer. The thinner grating relaxes the

fabrication difficulty. A phenol-formaldehyde polymer, Resole is found to be used as the high index grating layer. At the 1.55  $\mu\text{m}$  wavelength, the refractive index of Resole is 1.65, which is much higher than that of the FPAE, 1.51. Hence, by using a thin grating layer less than 200 nm, we can achieve the sufficient refractive index modulation  $\Delta n$  over 0.001.

Over the FPAE core layer, we fabricate grating patterns by using a phase mask. For the phase mask grating fabrication, a coherent light source like the Excimer laser have been usually used. However, an incident light source like Hg-lamp can also be used [7]. Because the Hg-lamp was usually incorporated in a mask aligner, we can use the light source as well as the alignment capability. A polarizer and an I-line filter transmitting 365 nm light are inserted in the mask aligner. Over the core layer, a diluted photoresist AZ5214 from Hoechst is coated to be about 200 nm on the FPAE core layer. After aligning and contacting the sample to the phase mask, the light is exposed normally to the mask. Because of the short coherence length of the Hg lamp, the contact should be strong enough in order to produce the grating pattern by the interference of the diffracted light from the phase mask. After development, we can observe a bright rainbow pattern all over the exposed area of 10 x 10 mm<sup>2</sup>.

The grating pattern made of photoresist is transferred to the FPAE core layer by the O<sub>2</sub> reactive ion etching (RIE). Over the grating patterns, the high index polymer Resole is spin-coated and baked at 150 °C for 10 min. and then 250 °C for 1 hour. The Resole fills up the grating grooves inscribed in the FPAE, then the Resole grating is formed as the thickness change. Over the Resole grating, the straight rib waveguide is defined by a photolithography and an O<sub>2</sub> RIE. Figure 3 shows the scanning electron microscopy (SEM) photography of the channel waveguide and the gratings. Because the Resole can not planarize the grating grooves completely, the Bragg gratings are still visible after the Resole coating. As the upper cladding layer, the PFCB is coated and baked to be 3.5  $\mu\text{m}$  thickness. The PFCB is provided by DOW chemical [8], and it has excellent optical and mechanical properties [9]. Finally the device is cleaved for the light coupling.

### III. Measurement results

In order to measure the Bragg reflections of the device, we used a tunable laser operating around 1.5  $\mu\text{m}$ . Single mode fibers were aligned at the two ends of the polymer waveguides. For the devices with different waveguide widths, the transmission spectra were measured as shown at Fig. 2. The reflectivity at the Bragg wavelength is about 30 dB for the grating length of about 9 mm. Based on a reflectivity calculation of multilayer dielectric stacks, it corresponds to the grating index modulation  $\Delta n$  of about 0.0007. In the measured transmissions, it is shown that the Bragg reflection wavelength is shifted to the longer wavelength for the wider waveguide because of the increase of the effective index. Moreover, for the wider waveguides, the reflectivity and the bandwidth are increased.

For the detection of the reflected signal from the channel waveguide, a circulator was connected between the device and the light source as shown at the inset of the Figure 3. From the port 3 of the circulator we can take the reflected signal. An index matching gel was used to decrease the Fresnel reflection from the end-face of the device and the connected fibers. Figure 3 shows the spectrum of the reflected signal. The 3-dB bandwidth of the device was about 0.6 nm, and the insertion loss was 3.7 dB. The propagation loss of the FPAE waveguide was determined by the cut-back method to be less than 0.7 dB/cm. Then, the device has 1.4 dB of the propagation loss for the propagation length of about 2 cm. The end-face scattering loss, the misalignment loss and the mode-mismatch loss are responsible for the remained 2.3 dB loss. The Bragg reflectors are going to be integrated with other waveguide devices like thermo-optic modulators in order to exploit various polymeric WDM devices.

### References

- [1] K. O. Hill et al., *Appl. Phys. Lett.*, Vol. 62, No. 10, pp. 1035-1037, 1993.
- [2] Y. Hibino et al., *IEEE Photon. Technol. Lett.*, Vol. 8, No. 1, pp. 84-86, 1996.
- [3] L. Eldada et al., *Organic Thin Films for Photonics Applications*, WA2, Long beach, California, 1997.

- [4] D. Chen et al., *Organic Thin Films for Photonics Applications*, FC1, Long beach, California, 1997.
- [5] M.-C. Oh et al., *IEEE Photon. Technol. Lett.*, Vol. 9, No. 9, pp. 1232-1234, 1997.
- [6] S. Aramaki et al., *J. Lightwave Technol.*, Vol. 11, No. 7, pp. 1189-1195, 1993.
- [7] J.-M. Verdiell et al., *IEEE Photon. Technol. Lett.*, Vol. 5, No. 6, pp. 619-621, 1993.
- [8] D. A. Babb et al., *J. Polymer Science: Part A: Polymer Chemistry*, Vol. 31, 3465-3477, 1993.
- [9] G. Fischbeck et al., *Electron. Lett.*, Vol. 33, No. 6, pp. 518-519, 1997.

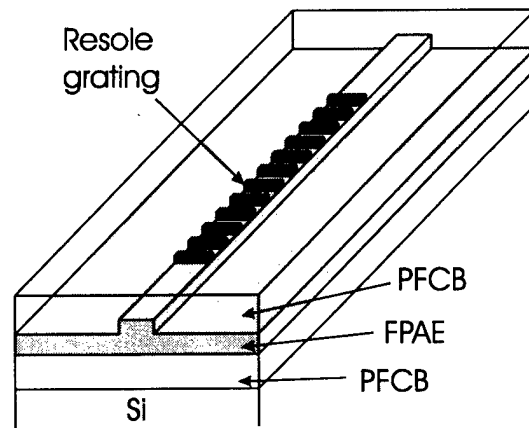


**Fig. 1.** Schematic diagram of the polymeric wavelength filter. Two kinds of fluorinated polymers, FPAE and PFCB are used for the core and cladding layers, respectively, and the grating is made of a high-index polymer, Resole.

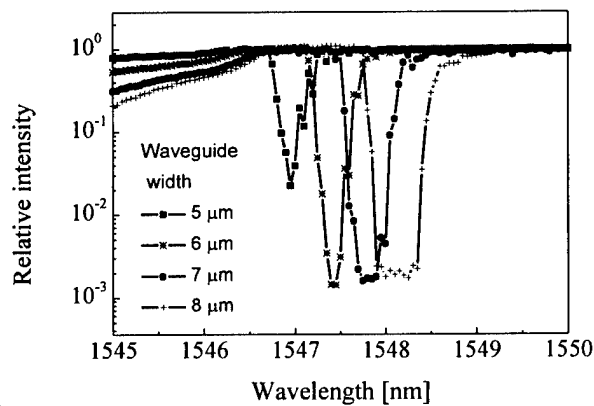


**Fig. 2.** Transmission spectra of the polymeric wavelength filters with different waveguide widths from 5  $\mu\text{m}$  to 8  $\mu\text{m}$ .

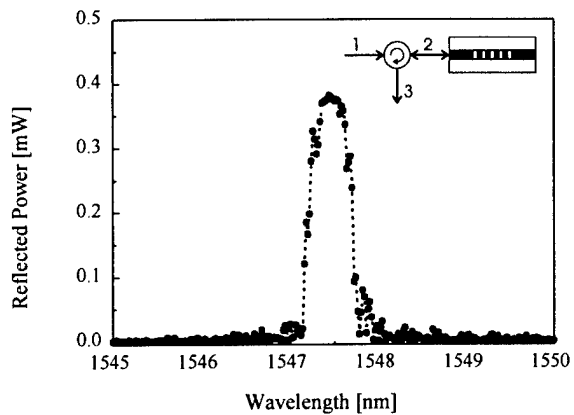


**Fig. 3.** Reflected power spectrum of the polymeric wavelength filters with the waveguide width of 6  $\mu\text{m}$  for the input power of 1 mW.

# Temperature-independent optical filter at 1.55 $\mu$ m wavelength using a silica-based athermal waveguide

Yasuo Kokubun<sup>1), 2)</sup>, Shigeru Yoneda<sup>1)</sup> and Shinnosuke Matsuura<sup>1)</sup>

1) Yokohama National University, Dept. of Electrical & Computer Eng.  
79-5 Tokiwadai, Hodogayaku, Yokohama, 240 Japan

2) Kanagawa Academy of Science and Technology  
3-2-1 Sakato, Takatsuku, Kawasaki, 213 Japan

The elimination of the temperature dependence of wavelength demultiplexer is essential to the practical use of dense WDM systems. In this report, we successfully realized a temperature-independent optical narrowband filter at 1.55 $\mu$ m wavelength, using a silica based athermal waveguide. This technology can be widely applied to most kinds of wavelength filters based on silica waveguide.

The temperature dependence of the central wavelength of narrowband optical filters is a serious and outstanding problem, because it reaches as large as 0.01nm/K for silica-based waveguide filters and 0.08nm/K for semiconductor-based waveguide filters. Since the temperature dependence is caused by the temperature dependence of optical path length which forms the resonator, the authors have proposed an athermal waveguide<sup>[1]</sup> in which the optical path length is independent of ambient temperature. The authors have realized the athermal waveguide first at 0.633 $\mu$ m wavelength<sup>[1], [2]</sup> and next a temperature-independent narrowband filter<sup>[3]</sup> at 1.3 $\mu$ m wavelength using the same technology. However, since the waveguide structure was a ridge-loaded channel waveguide composed of compound glass core(C7059 glass) and a polymer overcladding(PMMA) and the lateral optical confinement was weak, another type of athermal waveguide which can be widely applied to silica-based waveguides has been required. To solve this problem, the authors developed first a silica-based athermal waveguide at 1.55 $\mu$ m wavelength, which has a square cross-section and is compatible to PLC.

The temperature dependence of the central wavelength of filters is expressed by

$$\frac{d\lambda_0}{dT} = \left( \frac{1}{L} \frac{dS}{dT} \right) \frac{\lambda_0}{n_{eq}} \quad (1)$$

where  $\lambda_0$  is the central wavelength,  $L$  is the length,  $n_{eq}$  is the equivalent index of the waveguide, and  $S$  is the optical path length defined by  $S = n_{eq} \cdot L$ . The temperature coefficient of optical path length  $\frac{1}{L} \frac{dS}{dT}$  in an optical waveguide formed on a substrate is derived as

$$\frac{1}{L} \frac{dS}{dT} = n_{eq} \alpha_{sub} + \frac{dn_{eq}}{dT} \quad (2)$$

where  $\alpha_{sub}$  is the thermal expansion coefficient of the substrate<sup>[1]</sup>. An athermal waveguide is defined as a waveguide for which Eq.(2) equates to zero<sup>[2]</sup>. Since most of optical materials have positive values of  $\alpha_{sub}$  and  $\frac{dn}{dT}$ , the athermal waveguide requires a special material which has a negative value of  $\frac{dn}{dT}$  to realize  $\frac{dn_{eq}}{dT} < 0$ .

In the previous athermal waveguide<sup>[1]-[3]</sup>, PMMA(Poly-Methyl-Methacrylate) was used for the material of ridge-loaded layer with the negative value of  $\frac{dn}{dT}$ . However, since the refractive index of PMMA( $n=1.481$  @ $\lambda=1.55\mu$ m) is higher than the silica-based waveguide

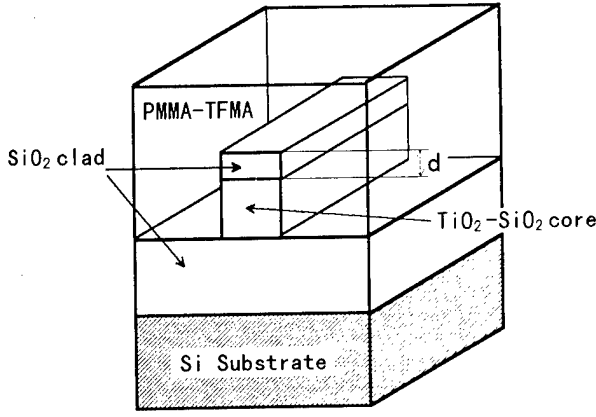


Fig.1: Rectangular silica-based athermal waveguide.

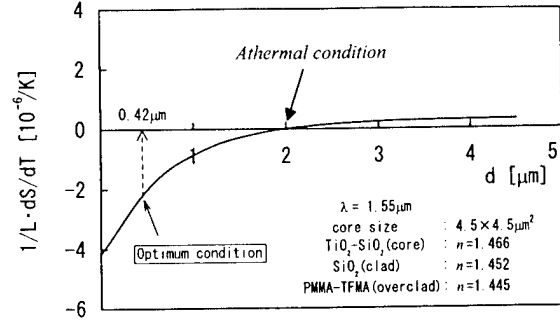


Fig.2: calculated  $\frac{1}{L} \frac{dS}{dT}$  vs.  $d$

materials ( $n=1.45\text{--}1.47$  @  $\lambda=1.55\mu\text{m}$ ), we developed a new copolymer for the overcladding material using TFMA (Tri-Fluoroethyl-Methacrylate) and PMMA. The refractive index is 1.445 at  $1.55\mu\text{m}$  wavelength. Using this material, a three-dimensional athermal waveguide with rectangular core shown in Fig.1 was designed. The core and the lower cladding are  $\text{TiO}_2\text{-SiO}_2$  ( $\text{TiO}_2$  5 wt.%  $n=1.466$  @  $\lambda=1.55\mu\text{m}$ ) and  $\text{SiO}_2$  ( $n=1.452$  @  $\lambda=1.55\mu\text{m}$ ), respectively, formed on a Si substrate. The upper-loaded cladding and overcladding are  $\text{SiO}_2$  and PMMA-TFMA copolymer, respectively. The core size is  $4.5 \times 4.5 \mu\text{m}^2$ . The upper-loaded  $\text{SiO}_2$  cladding layer is introduced to control the value of  $\frac{1}{L} \frac{dS}{dT}$  of the waveguide.

Since the values of  $\frac{dn}{dT}$  of these materials at  $1.55\mu\text{m}$  wavelength have not been known, we measured  $\frac{dn}{dT}$  of those films formed on a Si substrate using a Mach-Zehnder interferometer. The measured values of  $\frac{dn}{dT}$  of  $\text{SiO}_2$  and PMMA-TFMA are  $7.93 \times 10^{-6}/\text{K}$  and  $-143.9 \times 10^{-6}/\text{K}$ , respectively. The value of  $\frac{dn}{dT}$  of  $\text{TiO}_2\text{-SiO}_2$  was assumed to be the same as that of  $\text{SiO}_2$  because the mole fraction of  $\text{TiO}_2$  is very small (5%). Using these measured data and  $\alpha_{\text{sub}} = 2.63 \times 10^{-6}/\text{K}$  for Si, we designed the three dimensional athermal waveguide at  $1.55\mu\text{m}$  wavelength by a scalar finite element method. Fig.2 shows the value of  $\frac{1}{L} \frac{dS}{dT}$  vs the thickness of the upper-loaded layer  $d$ . Since the confinement factor of polymer layer decreases with the increase of temperature due to its negative value of  $\frac{dn}{dT}$ , we optimally designed  $d=0.42\mu\text{m}$ <sup>[3]</sup>. Then  $\frac{1}{L} \frac{dS}{dT}$  is slightly negative at the vicinity of room temperature and increases to positive at higher temperature as shown by the dotted line in Fig.3.

Using this silica-based athermal waveguide, we fabricated a ring resonator with the radius of 2.5mm. The theoretical values of the free spectrum range (FSR) and the finess are 0.11nm and 4.1, respectively. The propagation loss including the bending loss was assumed to be 1.0dB/cm in this calculation.

Fig.3 shows the measured filtering characteristic of fabricated ring resonator. The measured FSR and the finess were 0.11nm and 5.4, respectively. The discrepancy of finess between the measured and theoretical values seems to be attributed the lower propagation loss ( $\approx 0.2\text{dB/cm}$ ) than the assumed value.

Next, we measured the temperature dependence of the central wavelength by changing the temperature of the ring resonator. The measured values are plotted by ■ in Fig. 4.

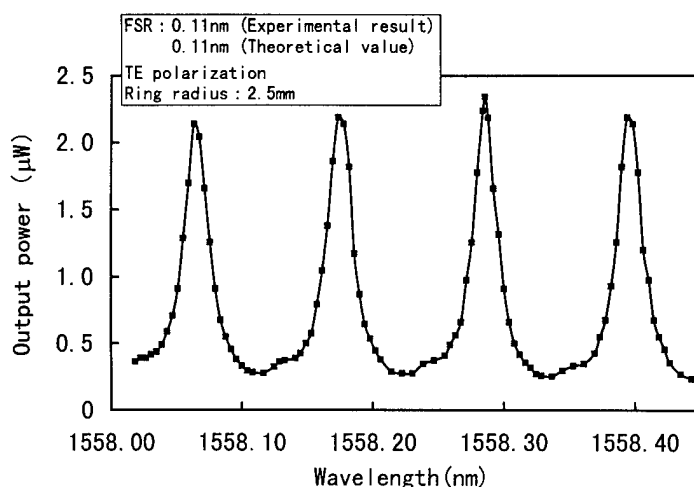


Fig.3: Measured filtering characteristic of ring resonator.

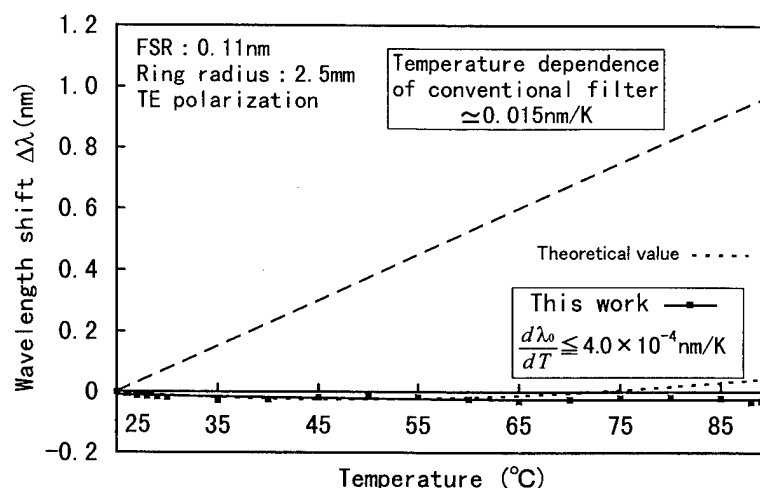


Fig.4: Central wavelength of ring resonator vs. temperature.

From this figure, we successfully decreased the temperature coefficient of central wavelength to 3% of that of  $\text{SiO}_2$  and 0.3% of that of semiconductor waveguide filters, in the temperature range of 25°C to 90°C.

Since the athermal waveguide eliminates the temperature dependence of optical path length, this technique is applicable to not only ring resonators but also most of filters, in contrast to the temperature independent AWG filter reported recently<sup>[4]</sup> which is applicable to only multi-path interferometers like AWG and suffers diffraction loss.

## References

- [1]Y. Kokubun, F. Funato and M. Takizawa: *Photon. Tech. Lett.*, **vol.5**, 1297-1300 (1993)
- [2]Y. Kokubun, M. Takizawa and S. Taga: *Electron. Lett.*, **vol.30**, pp.1223-1224 (1994)
- [3]Y.Kokubun, S.Yoneda, and H.Tanaka: *IEICE Trans. Electron.*, **vol.E80-C**, pp.632-639 (1997)
- [4]Y.Inoue, A.Kaneko, F.Hanawa, H.Takahashi, K.Hattori, and S.Sumida: *Electron. Lett.*, **vol.33**, pp.1945-1947 (1997)

# Tunable add/drop filters using $\text{LiNbO}_3$

M. Seino

Fujitsu Laboratories Ltd.  
10-1 Morinosato-Wakamiya, Atsugi 243-0197, Japan

## Abstract

Acousto-optical tunable filters (AOTFs) have the potential to be used in many advanced WDM systems. The wavelength add/drop multiplexing (ADM) system is one of the basic systems for wavelength division multiplexing (WDM) networks.

A TE/TM mode conversion type of AOTF in  $\text{LiNbO}_3$  can enable ADM on a single chip and has been developed in earnest <sup>(1), (2), (3)</sup>.

ADM systems require tunable filtering, narrow channel spacing, low cross-talk suppression, multi-wavelength filtering, low driving power, and a low insertion loss.

There remain some problems to be solved, however, before AOTFs can be commercially practical for ADM.

The most serious of these problems are to achieve a narrow bandwidth with a low side lobe, to decrease the driving power, and to prevent acousto-optical interactions between simultaneously applied signals.

The AOTF consists of polarizing beam splitters, straight optical waveguides for TE/TM mode conversion, a SAW guide, a transducer, and SAW absorbers. In this paper, I would like to discuss how to resolve these problems from the component level.

## 1. Film-loaded SAW Guides

There are several methods to propagate a SAW along an optical waveguide. A curved IDT is a very simple method, but makes it difficult to obtain a variety of SAW distributions for apodization and required a large-width IDT. Ti-deep diffused waveguides are used to design specific SAW distributions. However, this requires a complicated SAW waveguide circuit, a large waveguide width and a long processing time.

We tried to use Si-dioxide film for a SAW waveguide, which is a common material in  $\text{Ti:LiNbO}_3$  devices. Figure 1 is a schematic diagram of Si-dioxide loaded film. Figure 2 shows the measured TE/TM mode conversion efficiency for different samples at 10  $\mu\text{m}$ -spaced optical-waveguide positions. The film width is 140  $\mu\text{m}$  and its thickness is 0.4  $\mu\text{m}$ . The distribution takes a fundamental mode. The drive power at the center is 4.3 mw, which is 10% larger than a Ti-deep-diffused-type SAW guide of the same width and length ( $\Delta v = -0.3\%$ ). The SAW decay was measured to be below the measurement limits when changing the SAW absorber position for a sample interaction length of 30 mm. We confirmed that Si-dioxide loaded film has the necessary characteristics for  $\text{Ti:LiNbO}_3$  TE/TM mode conversion type devices. SAW confinement increases with the film thickness and by employing a metal-oxide dopant such as InSn-oxide. These waveguides propagate fundamental-mode SAW for a film width of 40 to 200  $\mu\text{m}$ . A narrow SAW waveguide decreases the tuning power and enables device integration.

Figure 3 shows the intersected SAW guide against the optical waveguide. The film is made of Si-oxide doped with 60 wt% InSn. The width is 120  $\mu\text{m}$ , the thickness is 0.4  $\mu\text{m}$ , and the intersecting angle is  $0.45^\circ$ . The filter characteristics are shown in Figure 4. The sidelobe suppression is 24 dB and the filter bandwidth is 1.4  $\mu\text{m}$ . This construction is more simple and compact than the Ti-deep diffused one.

These apodized low cross-talk filters decrease the influence of acousto-optical interactions.

These results suggest that the film-loaded SAW guide can help resolve the serious problems of AOTF for ADM.

## 2. Polarizing Beam Splitter (PBS)

The PBS is crucial for making polarization diversity constructions. Our PBS structure is shown in Figure 5. Its operation is based on two-mode interference in a zero gap coupler for TE and TM modes, respectively. To obtain a high splitting ratio while minimizing excess loss in the PBS, various parameters (such as the index profile, the length and shape of the central section, and branching angle,  $\theta$ ) should be optimized. Figure 6 shows a results of determining the optimal waist width of the central section. The outcome is a 0.15 dB loss and a TE/TM mode splitting ratio of less than -30 dB for a wide wavelength range, as shown in Figure 7.

## 3. SAW transducer

A SAW transducer is made up of IDT electrodes. It is formed on a  $\text{LiNbO}_3$  substrate and causes absorption loss of light. Although the structure of a buffer layer can effectively reduce absorption loss, it also drastically decreases the efficiency of generating the SAW. Hence, we inserted a patterned  $\text{SiO}_2$  buffer layer only between the waveguide and the IDT. The buffer layer thickness is  $0.5\mu\text{m}$ . The subsequent absorption loss was found to be below measurement capabilities without any increase in driving power.

A low driving power is important for multi-wavelength filtering systems. The driving power of a transducer changes to SAW, ohmic loss, and reflected RF power caused by impedance mismatch. Usually, large impedance mismatches occur because of the capacitance of IDT electrodes. Therefore, the inductance is exploited to match impedances.

## 4. Optical Waveguides

The optical waveguides of AOTFs are fabricated in x-cut, y-propagating  $\text{LiNbO}_3$ . These waveguides have large bending and coupling losses caused by a mismatch in the mode field pattern between the waveguide and the optical fiber. We optimized the design and fabricating conditions and achieved a 2.4 dB fiber-to-fiber insertion loss with a 0.1 dB PDL. Low insertion loss filters make possible to construct tandem connections of filter. It realizes narrow bandwidth with low side lobe, low driving power, and low acousto-optical interaction filters.

## 5. Conclusion

We integrated a film-loaded SAW waveguide with a  $\text{Ti:LiNbO}_3$  TE/TM mode conversion filter. The SAW waveguide was made of Si-oxide and has a good characteristics. The intersecting construction between the SAW and the optical waveguide produced a good sidelobe suppression. The insertion loss was decreased to 2.4 dB by optimizing the structure and process conditions.

This innovation will enable tunable filters that are sufficient for use in practical ADM systems.

## References

- (1) T. Nakazawa et al., Technical Report of IEICE., Vol. OPE96-123, pp. 79-84, 1996, in Japanese.
- (2) S. Taniguchi et al., 2nd Optoelectronics & Communications Conference (OECC' 97) Technical Digest, July 1997, Seoul, Korea.
- (3) M. Seino et al., 1997 Digest of the IEEE/LEOS Summer Topical Meetings, Post-deadline paper, Montreal, Canada

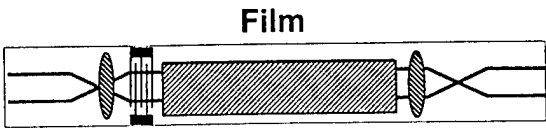


Fig. 1. Film-loaded SAW guide.

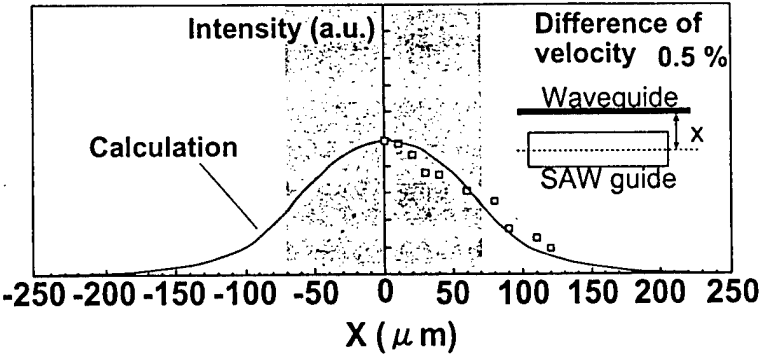


Fig. 2. Distribution of SAW intensity.

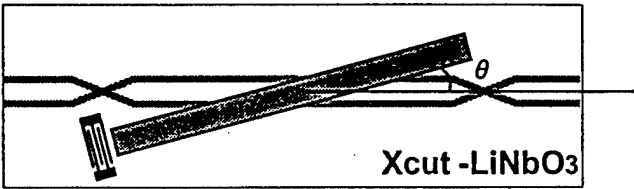


Fig. 3. Tilted SAW guide.

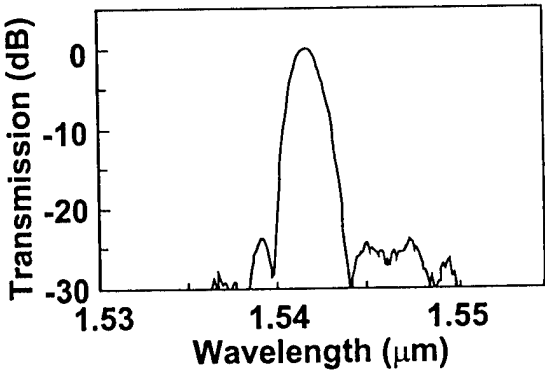


Fig. 4. Filtering characteristics.

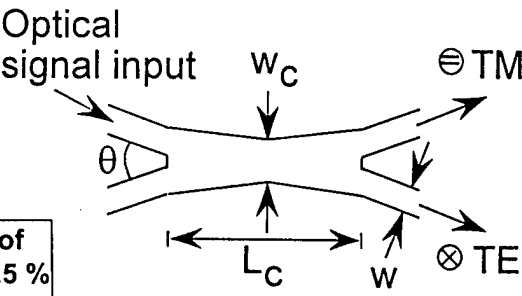


Fig. 5. PBS structure.

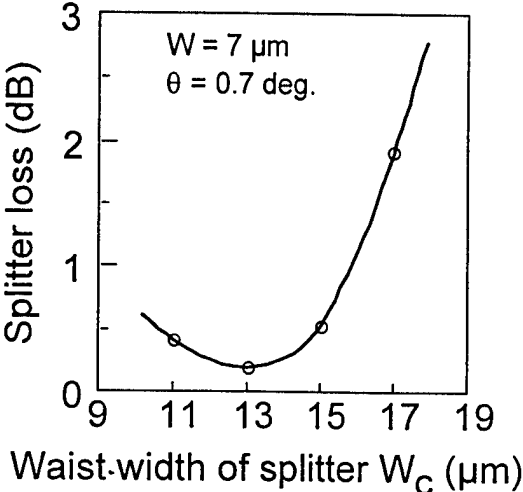


Fig. 6. Dependence of excess loss on waist width of PBS.

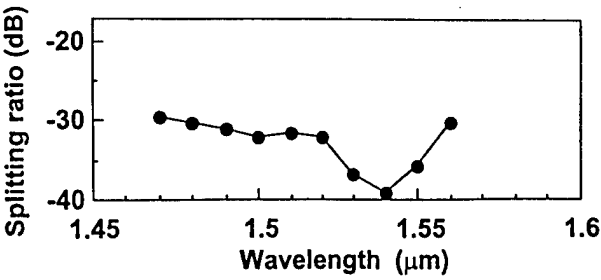


Fig. 7. PBS Splitting ratio.

## Planar Waveguide Grating Optical Spectrum Analyzer

C.K. Madsen, J. Wagener, T.A. Strasser, M.A. Milbrodt, E.J. Laskowski, and J. DeMarco  
 Bell Laboratories, Lucent Technologies, 600 Mountain Ave., Murray Hill, NJ 07974  
 Tel: (908) 582-6095, FAX: (908) 582-4868, email: cmadsen@lucent.com

Optical networking in WDM systems requires monitoring of each channel to provide information about its power and wavelength. Recently, a high resolution, grating-based spectrum analyzer tap was realized with an optical fiber [1]. The first experimental results on an integrate tap using tilted, chirped UV-induced gratings in a planar waveguide are presented in this paper.

Tilted gratings have been used to tap light out of an optical fiber [2]. When the grating is chirped, the light couples out at a different angle along the length of the grating and can be focused by an appropriate choice of the chirp [3,4]. The architecture for the planar waveguide implementation is shown in Fig. 1. Light is coupled into a singlemode waveguide which is offset from a rectangular slab region by 30  $\mu\text{m}$  to avoid evanescent coupling. The grating couples light out of the waveguide and into the slab where it remains guided in the vertical direction. A turning mirror reflects the light to obtain a double pass through the slab so that a larger focal distance can be used. A detector array collects the light near the focal point. The waveguides are made of phosphorous-doped silica with a core-to-cladding index of refraction difference of 0.6% on a silicon substrate. The chips are loaded with 2.5%  $\text{D}_2$  to increase their photosensitivity, and the grating is written using a chirped phase mask and 193 nm UV excimer laser source. The chirp is oriented so that the longest period is encountered first. This focuses the longest wavelength light at the shortest height along the detector array. The chip dimensions are 20 mm long by 10 mm high.

A 1 cm long grating was written with a tilt angle of  $4^\circ$  and a chirp of 1.75 nm/cm. A relatively large index change ( $\Delta n \sim 2 \times 10^{-3}$ ) was used resulting in a transmission loss for the waveguide of 10 dB at the peak of the radiation mode coupling spectrum. Measurements were made with a tunable laser source and TE polarization launched into the waveguide. The detector array, consisting of 256 elements on a 50  $\mu\text{m}$  pitch, was positioned 8 cm from the end of the chip. The shift in the position of the peak power with wavelength was used to calibrate the detector array response as a function of position. A wavelength dispersion of 1.6 mm/nm was calculated, corresponding to a visible bandwidth of 7.8 nm for this particular chirp and detector array size. By using a larger chirp, the focal length will be shorter, and the array can be positioned at the chip edge for easier packaging.

The results are shown in Fig. 2 for four different wavelengths, launched one at a time. The FWHM is 0.15 nm and the Full Width at 6 dB down is 0.20 nm. Each response is normalized to its peak power. The polarization dependence of this device is 0.25 nm. By summing the responses of three wavelengths, Fig. 3 shows that channels separated by 50 GHz are easily distinguished, having a 9 dB dip between them. Since the slab confines the light in the vertical direction and the grating chirp focuses it in the horizontal direction, the detector array is not power limited. A much weaker grating could be used, or a coupler with a small tap ratio could be used to sample the input signal.

An integrated optical spectrum analyzer was demonstrated with a high resolution capability. Since the dispersive and focusing elements are integrated and the vertical position of the detector array is not critical, a high reliability package can be made with the planar waveguide implementation.

#### References:

1. J. Wagener, T. Strasser, J. Pedrazzani, J. DeMarco, and D. DiGiovanni, "Fiber grating optical spectrum analyzer tap," ECOC, 1997, pp. 65-68, PD V.5.
2. G. Meltz, W. Morey, and W. Glenn, "In-fiber Bragg grating tap," Optical Fiber Conference, 1990, p. TuG1.
3. A. Katzir, A. Livanos, and A. Yariv, "Chirped-grating output couplers in dielectric waveguides," *Appl. Phys. Lett.*, vol. 30, no. 5, pp. 225-226, 1977.
4. G. Meltz, W.W. Morey, and A.L. Wilson, *U.S. Patent* 5,061,032, 1991.

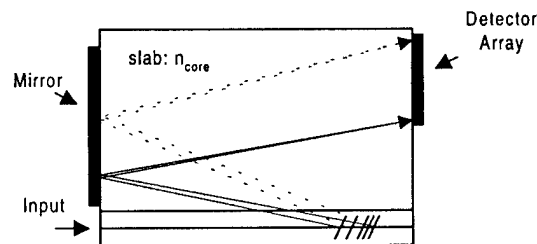


**Fig. 1. Planar waveguide grating optical spectrum analyzer.**

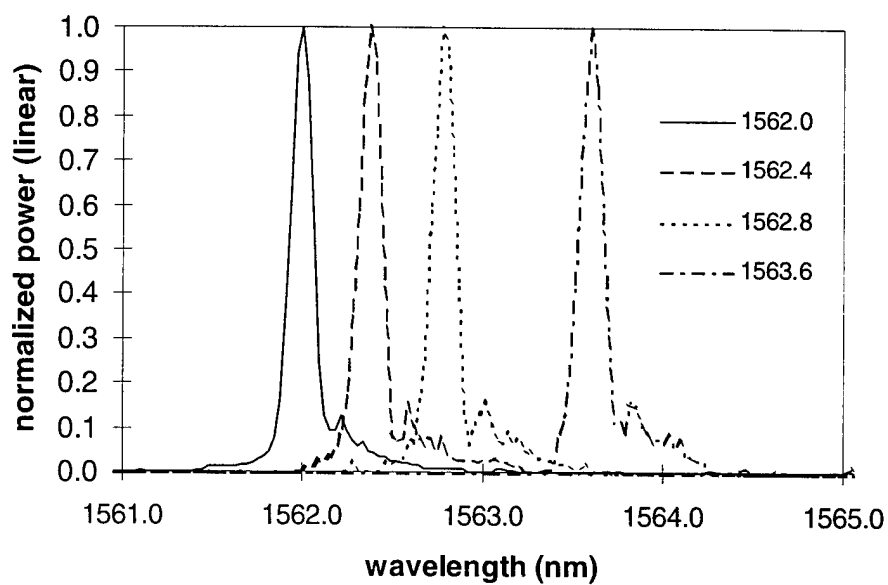


Fig. 2. Experimental results showing the response for several wavelengths.

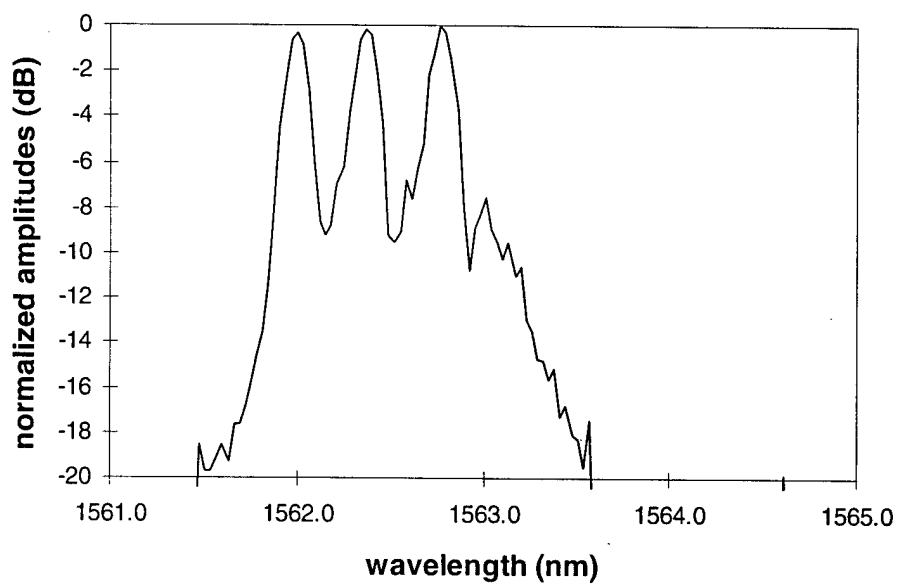


Fig. 3. Resolution of channels separated by 50 GHz.

## Planar Waveguide Add/Drop Filter Employing a Mode-Converting Grating in an Adiabatic Coupler

C.K. Madsen, T.A. Strasser, M.A. Milbrodt, C.H. Henry, A.J. Bruce, and J. DeMarco  
Bell Laboratories, Lucent Technologies, 600 Mountain Ave., Murray Hill, NJ 07974  
Tel: (908) 582-6095, FAX: (908) 582-4868, email: cmadsen@lucent.com

A new add/drop filter, consisting of an adiabatic coupler with a mode converting grating, is demonstrated in a planar waveguide for the first time in this paper. The use of reflective coupling from the input to an output port using adiabatic couplers was first proposed by [1]. An alternate configuration was recently demonstrated in tapered fibers [2]. The functionality is equivalent to a popular architecture for add/drop filters in planar waveguides based on a Mach-Zehnder Interferometer with identical Bragg gratings written in each arm [3]; however, the interferometric approach requires the fabrication of nearly perfect 3dB couplers and precise phase control between the arms to make a low loss device [4]. Other approaches such as gratings in directional couplers have been reported [5]; however, the coupling lengths are critical to achieving the desired performance. The advantage of the adiabatic coupler with a mode converter is that there are no critical length dimensions, coupling values, or phase relationships which must be maintained in order to achieve satisfactory device performance.

A planar waveguide adiabatic coupler is illustrated in Fig. 1. It functions as a null coupler [6] composed of two input and two output waveguides with different widths that are adiabatically tapered into and out of a symmetrical region which supports two modes [7]. A tilted Bragg grating is introduced in the symmetric section to couple between the forward traveling fundamental (even) and a reverse traveling first higher order (odd) mode. For the drop function, light is launched into the narrow input waveguide and excites the odd mode. At a wavelength which satisfies the Bragg condition, the odd mode is reflected into the even mode and exits through the wide waveguide. The Bragg condition is given by  $\frac{\lambda_{01}}{(n_0 + n_1)} = \Lambda$

where  $n_0$  and  $n_1$  are the effective indices for the fundamental and first higher order modes, respectively,  $\Lambda$  is the grating period, and  $\lambda_{01}$  is the Bragg wavelength. The coupling strength ( $\kappa$ ) depends on the overlap integral of the two fields and the tilted grating index profile. The tilt angle can be chosen to eliminate coupling of the fundamental mode to itself ( $\kappa_{00}=0$ ) or the first higher order mode to itself ( $\kappa_{11}=0$ ). The smallest angle of interest corresponds to  $\kappa_{11}=0$  and is assumed for Fig. 1.

A Ge-doped waveguide having a core-to-cladding index difference of 0.6% was used to demonstrate mode conversion in a planar waveguide adiabatic coupler. The waveguides were loaded with

2.5%  $D_2$  to increase their photosensitivity. A 1 cm long tilted grating with a fully apodized index profile was written using a phase mask and a 193 nm excimer laser source. Measurements were made using a broadband source followed by a polarizer as the input and an optical spectrum analyzer set at a 0.05 nm resolution on the output. The loss is referenced to a straight waveguide of the same length. The TM spectral responses are shown in Fig. 2 for a tilt angle of  $1.5^\circ$ . There are no transmission dips on the short wavelength side, so the odd-to-odd mode coupling is minimal. A stronger grating with the same tilt angle was written in a second coupler having slightly different adiabatic design parameters. The results are shown in Fig. 3. The loss for the drop channel is 0.5 dB, the transmission isolation is 15 dB, and the FWHM is 0.35 nm. The polarization dependent wavelength shift is 0.2 nm, and the residual reflection in the input port is 10 dB down.

The extinction ratio between the even and odd modes is 10 dB. Because a small fraction of light is carried in the even mode, reflections occur at wavelengths  $\lambda_{11}$  and  $\lambda_{10}$ , even if the tilt angle is perfect. A nonideal tilt angle produces reflections of varying strength at  $\lambda_{11}$ ,  $\lambda_{00}$ , and  $\lambda_{10}$ . The 0.6% core-to-cladding index difference limits the even and odd mode separation to  $\lambda_{00}-\lambda_{11} \sim 1.2$  nm; therefore, weak gratings are used to limit the reflection bandwidth and minimize interference between reflections resulting from the coupling of different modes. Adiabatic couplers with larger effective index differences between the even and odd modes will allow stronger gratings to be accommodated.

In summary, the planar waveguide adiabatic coupler with mode converting gratings offers a low loss add/drop device which is independent of critical lengths, coupling ratios and phase differences. Many gratings can be cascaded in the symmetrical region to drop one or several channels. With a larger index contrast and improvements in the extinction ratio, this device offers a promising alternative to interferometer based filters.

#### References:

1. C. Henry, R. Kazarinov, and Y. Shani, *U.S. Patent*, no. 5,093,876, 1992.
2. A. Kewitsch, G. Rakuljić, P. Willems, and A. Yariv, Bragg Gratings, Poling and Photosensitivity Conference. Williamsburg, VA, 1997, pp. 256-258.
3. R. Kashyap, J. Armitage, R. Wyatt, S. Davey, and D. Williams, *Electronics Lett.*, vol. 26, no. 11, 1990.
4. R. Kashyap, G. Maxwell, and B. Ainslie, *IEEE Photonics Technol. Lett.*, vol. 5, no. 2, pp. 191-194, 1993.
5. F. Bakhti, P. Sansonetti, C. Sinet, and L. Gasca, *Electron. Lett.*, vol. 33, no. 9, pp. 803-804, 1997.
6. T. Birks, S. Farwell, P.J. Russell, and C. Pannell, *Optics Lett.*, vol. 19, pp. 1964-1966, 1994.
7. R. Adar, C. Henry, R. Kazarinov, R. Kistler, and G. Weber, *J. of Lightw. Technol.*, vol. 10, no. 1, pp. 46-50, 1992.

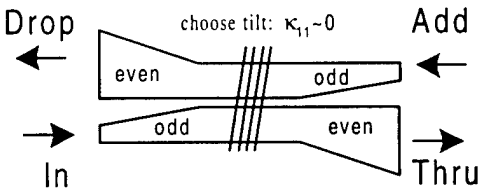


Fig. 1. Planar Waveguide Adiabatic Coupler with a Tilted, Mode Converting Grating

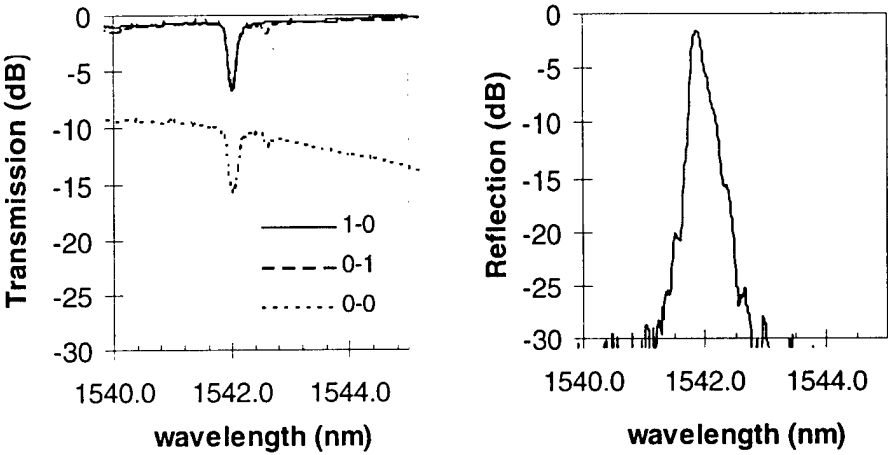


Fig. 2. Weak mode converting grating in an adiabatic coupler.

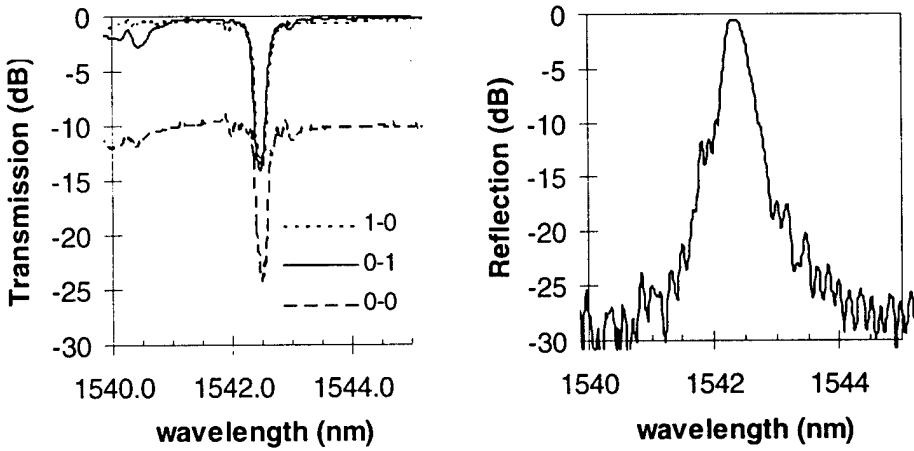


Fig. 3. Strong mode converting gratings in an adiabatic coupler.

**Integrated Photonics Research**

# Poster Session

**Monday, March 30, 1998**

**IMH**

**4:00pm–6:00pm**

Salon A

## Analysis and design of rib waveguide spotsize transformers

P Sewell, T M Benson and P C Kendall, Department of Electrical and Electronic Engineering, University of Nottingham, University Park, Nottingham NG7 2RD, U.K.

### Introduction

A key issue in the development of photonic integrated circuits in optical systems is the efficient coupling of semiconductor lasers, optical amplifiers and modulators to single mode optical fibers with typical core size 5-10  $\mu\text{m}$ . Mode spot size converters have been demonstrated [1-3] to improve coupling efficiency, relax positioning tolerances and improve long-term stability. The mode transformer typically has three sections, a tightly confined active device region, a tapered region in which the optical mode is progressively driven from the tightly guided region to a more loosely guided region and a passive output region. An accurate method which can simulate the behavior of such devices is important for design optimisation. Figure 1(a) shows the cross-sectional geometry of a version of this device recently proposed for microwave and millimeter optoelectronic integrated circuit modules [3]. This is the focus of the analysis undertaken in this paper. The relatively large dimensions of the device, particularly in the output region, do not lend themselves to efficient study using numerical techniques such as finite differences. Thus, in this paper, the semi-analytical Spectral Index Method [4-6], already proven to yield very reliable results for single and coupled rib waveguides, is extended to efficiently analyse this class of spot size converter, which vertically couples a tapered upper 'small spot' rib waveguide into a large spot rib.

### Theory

The geometry of the structure under consideration is shown in figure 1(a) where  $n_1 > n_2 > n_3$  and  $n_3$  is typically air. The Spectral Index Method approximates this structure by one with zero field boundaries placed at effective penetration depths as shown in figure 1(b). The effective penetration depths are  $\Delta_t = (\beta^2 - k_0^2)^{-1/2}$  and  $\Delta_b = (n_b/n_1)^2 \Delta_t$  on the boundaries to which the principal field component is normal and tangential respectively [5, p19]. Here  $k_0 = 2\pi/\lambda$ ,  $\lambda$  being the free-space wavelength, and  $\beta$  is the modal propagation constant.

Referring to figure 1(b) the Spectral Index Method proceeds in three stages by (1) finding a simple solution to the wave equation in the small rib region (ie for  $y < 0$ ), (2) finding an expression for the discrete Fourier transform of the solution in the region below the rib ( $y > 0$ ) and (3) using a variational boundary condition to join the two solutions together across the base of the small rib. In the Spectral Index analysis of single and coupled rib waveguides (see, for example [5]) stage (2) of the calculation requires that a response function of a multi-layered slab region to be evaluated. In the present case, however, evaluation of this response function is more involved since the presence of the large rib must be taken into account, including a small but important region of refractive index  $n_1$  and thickness equal to a penetration depth at the upper large rib-air interface. The approach given applies, with suitable modification, to the case where both the small and large rib structures as well as the substrate are multi-layered, however for clarity it shall be assumed here that they are not.

*Stage (1).* The guided mode field in the small rib region, usually designed to be mono-modal, is approximated by:

$$E_0(x, y) = \cos(s_1 x) \frac{\sin(\gamma_1(y + h_1'))}{\sin(\gamma_1 h_1')} , \quad s_1 = \frac{\pi}{2w_1'} \quad (1)$$

*Stage (2).* The field and its derivative with respect to  $y$  at the top and bottom of the large rib are expressed in terms of the local transverse solutions of the large rib:

$$E_1(x, 0) = \sum_{n=1}^N V_{1n} \cos(t_n x) , \quad E_2(x, h_2') = \sum_{n=1}^N V_{2n} \cos(t_n x) \quad (2)$$

$$\frac{dE_1}{dy}(x, 0) = \sum_{n=1}^N I_{1n} \cos(t_n x) , \quad \frac{dE_2}{dy}(x, h_2') = \sum_{n=1}^N I_{2n} \cos(t_n x) \quad (3)$$

The relationship between the expansion coefficients in these equations is presented most compactly in matrix form such that:

$$\begin{pmatrix} V_2 \\ I_2 \end{pmatrix} = \begin{pmatrix} A & B \\ C & D \end{pmatrix} \begin{pmatrix} V_1 \\ I_1 \end{pmatrix} \quad (4)$$

where, due the separable nature of the field solutions in the large rib, the sub-matrices  $A$ ,  $B$ ,  $C$  and  $D$  are diagonal and are found by cascading the ABCD matrices of the individual layers.  $V_2$  and  $I_2$  are also related by the response function of the multi-layered infinitely wide substrate region under the base of the rib i.e.  $I_2 = Y V_2$ . Using this, and (4) links  $V_1$  and  $I_1$  to produce the required response function as

$$(C - Y A) V_1 = (Y B - D) I_1 \quad (5)$$

Stage (3). Enforcing continuity of the field at  $y=0$  gives:

$$V_{1n} = \frac{s_1 \cos(t_n w_1')}{s_1^2 - t_n^2} \quad (6)$$

and the derivative of the field at  $y=0$  is then matched using the variational expression;

$$\int_0^\infty dx E_0^* \frac{dE_0}{dy} - E_1^* \frac{dE_1}{dy} = 0 , \quad \text{i.e. } Y_1 \cot(Y_1 h_1) - \left( \frac{w_2'}{w_1'} \right) Y_1 \quad (7)$$

where the superscript H indicates conjugate transpose.

In principle, the above theory is implemented by evaluating  $Y$ ,  $A$ ,  $B$ ,  $C$  and  $D$  and then solving (5) to yield  $I_1$  which is finally substituted into (7). The discrete values of the propagation constant,  $\beta$ , which satisfy this transcendental equation are the guided mode solutions of the structure. In practice, numerical difficulties can occur due to the weak coupling of the field at the base of the small rib to that at the base of the large rib by the higher order terms in (4). To overcome this problem, the concept of accessible modes is introduced, which recognises that the higher order terms remain localised to the interfaces at  $y=0$  and  $y=h_2'$ , and only a relatively few terms, the accessible modes, actually couple the two interfaces [7]. This procedure eliminates the numerical instabilities and typically the number of accessible modes need be no more than 10. As for the conventional Spectral Index Method the new method presented here runs on a small PC with modest memory requirements and requires only a few seconds of calculation time to produce modal propagation constant values and field profiles.

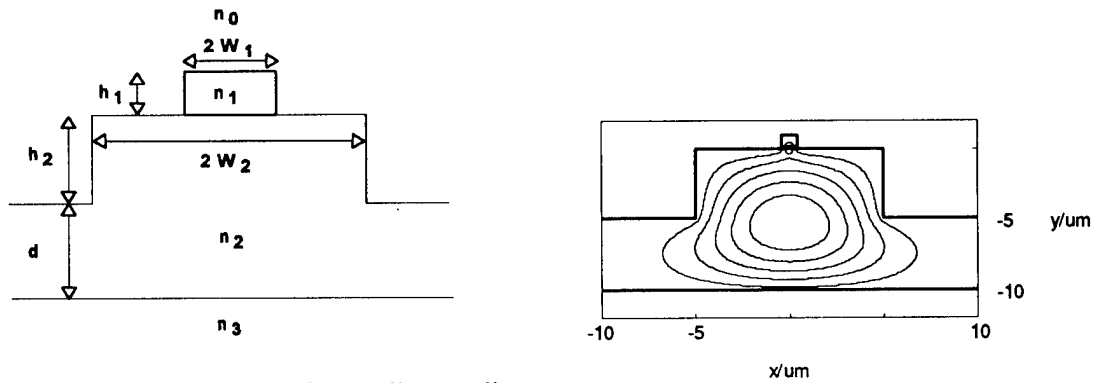
## Results

Figure 2 plots the modal index  $n_{\text{eff}} = (\beta/k_0)$  of the fundamental TE mode as a function of the small rib width  $W_1$  for a structure with  $h_1 = 1\mu\text{m}$ ,  $h_2 = 5\mu\text{m}$ ,  $d = 5\mu\text{m}$ ,  $w_2 = 5\mu\text{m}$ ,  $n_1 = 3.4092$ ,  $n_2 = 3.3592$  and  $n_3 = 3.3088$  at an operating wavelength of  $1.319\mu\text{m}$ . The figure clearly shows that the modal index changes rapidly over a narrow range of rib width, centered on  $5.8\mu\text{m}$  in this particular case. This emphasises the need for accurate design software. Figure 3(a-c) shows the corresponding field profiles for various  $W$  around the critical value of  $5.8\mu\text{m}$ . Further calculations show that higher order mode suppression is enhanced by suitable choice of the geometry.

## References

1. M DAGENAIS: Optoelectronic packaging: an enabling technology, *LEOS Newsletter*, 11(2), 3-11, April 1997.
2. G MULLER et al: Tapered InP/InGaAsP waveguide structure for efficient fiber-chip coupling, *Electron. Lett.*, 27, 1836-1838, 1991.
3. R E SMITH et al: Reduced coupling loss using a tapered-rib adiabatic-following fiber coupler, *IEEE Photonics Tech. Lett.*, 8, 1052-1054, 1996.

4. P C KENDALL et al: Spectral Index Method for rib waveguide analysis, *Electron. Lett.*, 25, 107-108, 1989.
5. P N ROBSON, P C KENDALL (ED), Rib waveguide theory by the Spectral Index Method, John Wiley and Sons Inc, 1990.
6. S V BURKE, The Spectral Index Method for semiconductor rib and ridge waveguides, *Progress in Electromagnetic Research, PIER* 10, 41-74, 1995.
7. D S JONES, *Methods in electromagnetic wave propagation*, Clarendon Press, Oxford, 1979, p311



**Figure 1a:** The small rib to large rib coupling structure

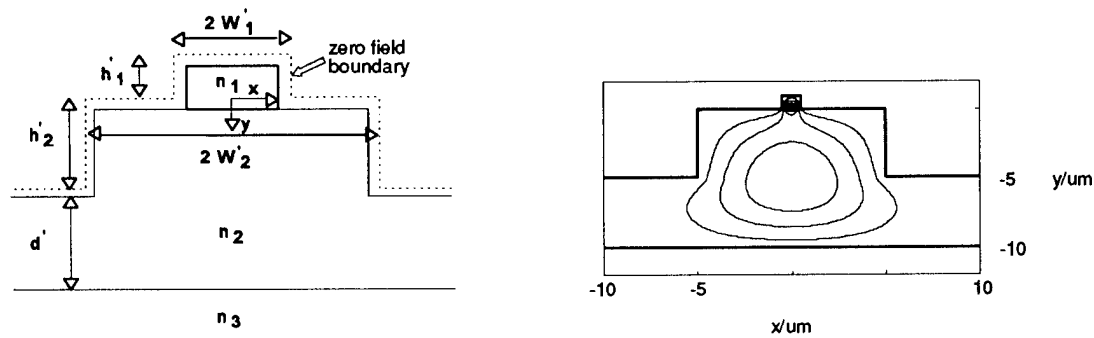


**Figure 1b:** The use of effective boundaries

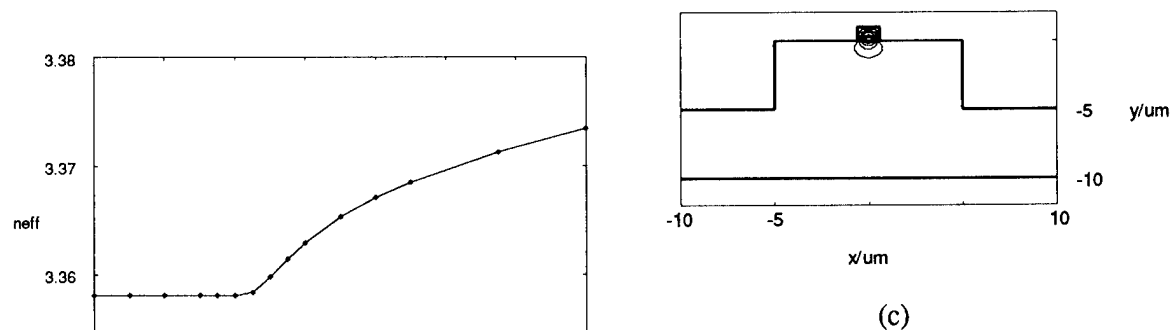


**Figure 2:** Modal index,  $n_{eff}$ , for the structure described in the text.

**Figure 3:** Field profile of the structure described in the text for: (a)  $w_1=0.6\mu\text{m}$ ; (b)  $w_1=0.5\mu\text{m}$ ; (c)  $w_1=0.4\mu\text{m}$

# Nonlinear Helmholtz equation resolution through the finite element method

A. Cucinotta, S. Selleri, L. Vincetti

Dipartimento di Ingegneria dell'Informazione, Parma University

Viale delle Scienze I-43100 Parma, Italy.

Fax: + 39 521 905758; Tel: + 39 521 905765

Email: selleri@pccampi3.tlc.unipr.it

## Introduction

In the last decades the propagation of light beams, first in cubic and more recently in quadratic nonlinear media, has been object of intense investigation. Since the first studies, great efforts have been devoted to the spatial Schrödinger and to the Fresnel nonlinear equations which have been frequently used, under opportune conditions, to analitically [1] and numerically [2], [3] describe electromagnetic wave evolution. These parabolic equations, in armonic regime, derive from the Helmholtz equation through the slowing varying envelope approximation (SVEA) that strongly limits their validity and accuracy [4], [5]. For this reason, non paraxial formulations have been developed, for example by generalizing the nonlinear Schrödinger equation (NLSE) [6] or by implementing wide-angle beam propagation algorithms. In the latter case, the Padé approximants have been widely used [7], [8] although their formalism can become very complicated. To the aim, also the Helmholtz equation has been directly solved through a finite difference based marching method [9] or through an highly time consuming algorithm involving the evaluation of a square root operator via matrix diagonalization procedure [10]. Further interesting approaches have been proposed [5], [11]; by directly solving the Maxwell's equations in the time domain these methods avoid any simplifying assumption, at the expense of very high computational time and requirements.

In this work a simple non-paraxial and nonlinear propagation method completely based on the finite elements (FEs) is presented. The method directly solves the nonlinear Helmholtz equation without introducing any approximation and fully takes advantage by the use of the FEs which have been applied both for the transverse discretization and for the longitudinal propagation. In particular the high sparsity of the system matrix, the efficient non-uniform nodal distribution, the usage of adaptive techniques and the FE transparent boundary conditions drastically reduce the computational efforts resulting in a very fast as well as accurate tool. Furthermore the FEs allow to deal with any kind of nonlinearities, index steps and anisotropies [12], as well as with loss or gain media. Moreover notice that, as the FE shape functions allow the medium characteristics to vary within each mesh element, the considered discretized structure is always described with a very high degree of accuracy [13]. In the following the method is presented and applied to the propagation analysis of spatial solitons. The examples here reported intend to highlight the importance of deriving formulations without approximations, as the SVEA one, and propose the present method as a fast, versatile and accurate tool in order to perform a reliable analysis of all optical devices.

## The finite element based approach

Consider the scalar Helmholtz equation for the electric field transverse component  $\mathcal{E}$ :

$$\frac{\partial^2 \mathcal{E}}{\partial x^2} + \frac{\partial^2 \mathcal{E}}{\partial y^2} + \frac{\partial^2 \mathcal{E}}{\partial z^2} + k_0^2 n^2 \mathcal{E} = 0 \quad (1)$$

where  $k_0$  is the wavenumber and  $n$  the nonlinear refractive index. By expressing  $\mathcal{E}(x, y, z) = E(x, y, z)e^{-j\beta z}$ , with  $\beta$  a phase factor and  $z$  the propagation direction, by dividing the transverse cross-section into second order elements and by expanding the field envelope through the FE shape functions  $N_i$ ,  $E(x, y, z) = \sum_i N_i(x, y)E_i$  the application of the standard Galerkin method to (1) yields:

$$[B] \frac{d^2 \{E\}(z)}{dz^2} - 2j\beta [B] \frac{d \{E\}(z)}{dz} + [k_0^2 [M] - \beta^2 [B] - [A]] \cdot \{E\}(z) = 0 \quad (2)$$

where  $[A]$  and  $[M]$  are matrices related respectively to the discretization of the operator  $\nabla_t^2$  and of the nonlinear refractive index and  $[B]$  is a matrix which contains the inner products of the shape functions  $N_i$ . The unknown vector  $\{E\}(z)$  can be further expanded along  $z$  in terms of new shape functions  $M_i(z)$ ; by considering two steps  $\Delta z$  it yields  $\{E\}(z) = M_{n-1}\{E\}_{n-1} + M_n\{E\}_n + M_{n+1}\{E\}_{n+1}$  where the subscripts indicate the considered cross-section along the propagation direction. The substitution into (2) and a further application of the Galerkin method along  $z$  yields:

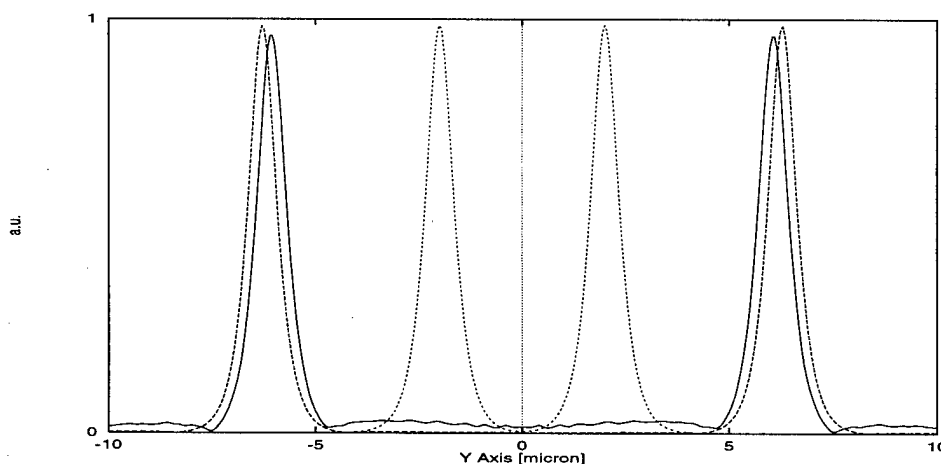
$$[P] \{E\}_{n+1} = [Q] \{E\}_n - [R] \{E\}_{n-1} \quad (3)$$

which provides the unknown field  $\{E\}_{n+1}$  as a function of the known fields on the two previous sections. The matrices  $[P]$ ,  $[Q]$  and  $[R]$  contain combinations of the matrices  $[A]$ ,  $[B]$  and  $[M]$  according to the shape and weight functions chosen during the Galerkin procedure. Considering second order  $M_i$  and the sum of two Dirac functions on the  $n-1$  and  $n+1$  sections as the weight, equation (3) represents a two steps recursive formula whose stability, in the case of linear media, is assured for  $\Delta z \geq 1/\beta$  [14]. In these conditions, for the nonlinear case, the matrices  $[P]$  and  $[R]$  depend on the field, respectively on the  $n+1$  and  $n-1$  sections. An iterative procedure is thus necessary to evaluate  $[P]$  at each propagation step. The application of (3) to the nonlinear case is then justified by observing that the iterative process actually solve, at each propagation step, a sequence of local linear problems.

## Numerical results

The capability of the proposed FE beam propagation method is demonstrated by describing soliton evolution and interactions in 2-D structures with Kerr materials. After having tested the proposed approach by simulating the evolution of the fundamental soliton, also for strongly non-paraxial propagations, the evolution of high order and two in-phase solitons have been considered. In these cases, the FE non-paraxial method confirms the periodic behaviors predicted by the SVEA based approaches but the related oscillation lengths which turn out to be longer especially when the ratio between the beam width  $w$  and wavelength  $\lambda$  in the material is close or less than unity. Consider, for example, two  $2\mu m$  separated in-phase solitons with  $w = 0.65\mu m$  launched at  $\lambda = 1.3\mu m$ , in a medium with relative permittivity  $\epsilon_{nl} = \epsilon_{lin} + \alpha|E|^2$  being  $\epsilon_{lin} = 6.0516$  and  $\alpha = 2 \cdot 10^{-20} m^2/V^2$  the nonlinear Kerr coefficient. The solitons periodically coalesce into a single pulse with an interaction length equal to  $32.5\mu m$  for the non-paraxial propagation method instead of  $29.5\mu m$  provided by a SVEA beam propagation method or by the NLSE theory [15]. Notice that these differences have already been pointed out through high time consuming FDTD approaches [5], [11]. Conversely for a  $100\mu m$  propagation with  $\Delta z = 0.1\mu m$  and 201 nodal points on the transverse cross-section the above results have been obtained in one minute on a personal computer at  $200 MHz$ .

An even more critical difference in the behavior of paraxial and non-paraxial approaches can be observed by launching two beams one against the other. By decreasing the ratio between  $w$  and  $\lambda$  down to values close and even less than unity, the two approaches provide solutions that can differ both in position and shape. For example, the figure reports two input beams (dotted line) launched forming an angle of  $15^\circ$  with the propagation direction, being  $w = 0.3\mu\text{m}$  and  $\lambda = 1.3\mu\text{m}$ . The ability of the non-paraxial propagator to account for the radiation field generated by the collision of the two beams allows to describe the waves after  $30\mu\text{m}$  propagation (solid line) with lower powers and different shapes. The paraxial solutions (dashed line) still present the same peak powers as the input beams and their positions slightly differ from the non-paraxial ones. Notice again that the computational time for this simulation was about half a minute being  $\Delta z = 0.1\mu\text{m}$  and 401 the number of the cross-section nodal points. In conclusion a propagation algorithm that directly implements the nonlinear Helmholtz equation has been presented. It is based on the FE method which has been applied both on the transverse cross-section and the longitudinal direction. It takes full advantages by the FE potentialities thus resulting in a very fast, versatile and accurate tool. The obtained non-paraxial algorithm allows to highlight the limits of the SVEA.



## References

- [1] V.E. Zakharov, V.V. Sobolev and V.S. Synach, *Sov. Phys. JEPT* **33**, 77 (1971).
- [2] K. Hayata, A. Misawa and M. Koshiba, *J. Opt. Soc. Am. B* **7**, 1772 (1990).
- [3] E. Montanari, S. Selleri, L. Vincetti and M. Zoboli, *Phot. Tech. Lett.* **9**, 1244 (1997).
- [4] N. Akhmediev, A. Ankiewicz and J.M. Soto-Crespo, *Opt. Lett.* **18**, 411 (1993).
- [5] R.M. Joseph and A. Taflove, *IEEE Phot. Tech. Lett.* **6**, 1251 (1994).
- [6] B. Crosignani, P. Di Porto and A. Yariv, *Opt. Lett.* **22**, 778 (1997).
- [7] G.R. Hadley, *Opt. Lett.* **17**, 1426 (1992).
- [8] O. Mitomi and K. Kasaya, *Electron. Lett.* **33**, 1461 (1997).
- [9] H.E. Hernandez-Figueroa, *Electron. Lett.* **30**, 352 (1994).
- [10] L. Thylen and C.M. Lee, *J. Opt. Soc. Am. A* **9**, 142 (1992).
- [11] G. Bellanca, R. Semprini and P. Bassi, *Opt. Quant. Electron.* **29**, 233 (1997).
- [12] A. Cucinotta, E. Montanari, S. Selleri, L. Vincetti and M. Zoboli, *ICEAA 97 Int. Conf. Electromagnetics in Advanced Applications*, Sept. 15-18 1997, Torino, Italy.
- [13] S. Selleri and M. Zoboli, *IEEE Microwave Theory Tech.* **43**, 887 (1995).
- [14] H.E. Hernandez-Figueroa, *J. Light. Tech.* **12**, 644 (1994).
- [15] J.S. Aitchison, A.M. Weiner, Y. Silberberg, D.E. Leaird, M.K. Oliver, J.L. Jackel and P.W.E. Smith, *Opt. Lett.* **16**, 15 (1991).

## Mechanism of ultrafast pulse generation in a symmetric three-section DFB semiconductor laser

Byoung-Sung Kim, Youngchul Chung, Kyoung-Hyun Park\*, and Sun-Ho Kim\*

Dept. of Electronic Communications Eng., School of Electronics Eng.  
Kwangwoon University, 447-1 Wolgye-Dong Nowon-Ku, Seoul, Korea 139-701  
TEL) +82-2-940-5138 FAX) +82-2-941-7855  
e-mail) ychung@daisy.kwangwoon.ac.kr

\* Photonics Research Center,  
Korea Institute of Science and Technology, Seoul, Korea 136-791

**Abstract** : The modified large-signal time-domain model is used to clarify the mechanism of ultrafast pulse generation due to the mode-beating in a symmetric three-section DFB semiconductor laser.

The pulse train can be used as the clock source and/or the clock recovery device in the optical time division multiplexing communication system[1], and is attractive as a optical source of the fiber-radio system, particularly in millimeter-wave region[2]. It is reported that the dynamic instability due to the high pumping of the carriers can result in the self-pulsation which is limited to 5 GHz[3,4] and DFB lasers with two or more than electrodes can self-pulsate due to the negative differential gain effect[1,5]. And also it is reported that mode-beating is the promising principle to generate self-pulsation above 100 GHz in multi-section devices[6].

In this paper, the mechanism of the pulse generation due to mode-beating in multi-section DFB lasers is clarified using the modified large-signal time-domain model. This model is based on the reference[7]. But, the detuning factor, which depends on the refractive index change due to the carrier injection, can cause the improper result in the numerical calculation, in the situation that multiple currents are injected into the electrodes simultaneously. To remove the possibility of the numerical error, the following time-stepped equations are used.

$$F(z + \Delta z, t + \Delta t) = [(g - \alpha)\Delta z]F(z, t) + e^{-i\delta\Delta z}F(z, t) + ix\Delta zR(z, t) \quad (1a)$$

$$R(z - \Delta z, t + \Delta t) = [(g - \alpha)\Delta z]R(z, t) + e^{-i\delta\Delta z}R(z, t) + ix\Delta zF(z, t) \quad (1b)$$

The equation (1) and the photon-carrier rate equation should be solved self-consistently. The multi-section DFB laser consists of three parts, which are partitioned by the electrode for current injection(Fig. 1). The longitudinal length of each section is 200  $\mu\text{m}$ , and the total length of the device is 600  $\mu\text{m}$ . The device parameters are as follows ; differential gain  $2.5 \times 10^{-16} \text{ cm}^{-2}$ , confinement factor 0.3, waveguide width 2  $\mu\text{m}$ , thickness of the active layer 0.2  $\mu\text{m}$ , transparency carrier density  $1.8 \times 10^{18} \text{ cm}^{-3}$ , linewidth enhancement factor 5, waveguide loss

$40\text{ cm}^{-1}$ , group refractive index 4, carrier lifetime 10 ns, gain saturation coefficient  $3 \times 10^{-17}\text{ cm}^3$ , and  $\kappa L$  3. The operating center wavelength is 1550 nm. And the facet reflectivities are assumed to be anti-reflection coated.

Figure 2 shows the transmission spectra of the multi-section DFB laser, which are calculated by the modified time-domain model (equation 1). The gain is assumed to be  $5\text{ cm}^{-1}$  along the whole device, but each section has the different detuning factor from each other. The  $\delta_{\text{side}}$  values in the figure is the detuning factor of the side sections. When the detuning factor is 0, the transmission spectrum is the same as the uniform grating DFB lasers. As  $\delta_{\text{side}}$  increases, the transmission spectrum translates its form into that of the chirped-grating DFB lasers showing the single-mode operation with high mode-suppression ratio. In the case that  $\delta_{\text{side}}$  is large, the side-modes of the DFB laser cavity become resonant. These modes make the stable pulse train in the form of mode-locking without mode-competition, of which the principle is similar to that of the mode-locking in compound cavity semiconductor lasers[8]. The factors that can make the detuning factor large are the high current injection into the side electrodes and the inheritant spatial hole burning.

Figure 3 shows the optical outputs and their frequency spectra. Figure 3(a) shows the optical output which shows the single-mode operation with the mode-suppression ratio more than 40 dB, indicated in the inset of the figure. The fluctuation in the optical power is due to the spontaneous emission noise in the cavity, and can be reduced by filtering out the noise components outside the signal frequency band. Shown in the inset of the figure 3(a), the weak side-mode is observed. As  $I_{\text{side}}$  increases, the weak side-mode gets resonant and becomes the strong one. Figure 3(b) shows the emission of the 83-GHz pulses due to the mode-beating. It can be seen that three modes oscillate and the weak mode in the figure 3(a) becomes the strongest one among the resonance modes. Pulse repetition rate does barely change for the change of the injection currents into the side electrodes, because the emission spectrum is almost constant during the side current variation.

In summary, the mechanism of the self-pulsation due to mode-beating in multi-section distributed feedback lasers is investigated using the modified large-signal time-domain model. The generated pulse train is very stable and fast in the form of the mode-locking without mode-competition, and is controlled by the injection currents.

- [1] Feiste, U. et al, IEEE Photon. Technol. Lett., vol. 6, no. 1, pp. 106-108, 1994.
- [2] Wake, D. et al, IEEE Trans. Microwave Theory Tech., vol. 43, no. 9, pp. 2270-2276, 1995.
- [3] Marcenac, D. D. et al, Electron. Lett., vol. 30, no. 14, pp. 1137-1138, 1994.
- [4] Lowery, A. J., Electron. Lett., vol. 29, no. 21, pp. 1852-1854, 1993.
- [5] Duan, G. H. et al, P., IEEE Photon. Technol. Lett., vol. 7, no. 3, pp. 278-280, 1995.
- [6] Sartorius, B. et al, IEEE J. Quantum Electron., vol. 33, no. 2, pp. 211-218, 1997.
- [7] Zhang, L. M. et al, IEEE J. Quantum Electron., vol. 30, no. 6, pp. 1389 - 1395, 1994.
- [8] Tager, A. A., IEEE Photon. Technol. Lett., vol. 6, pp. 164-166, 1994.

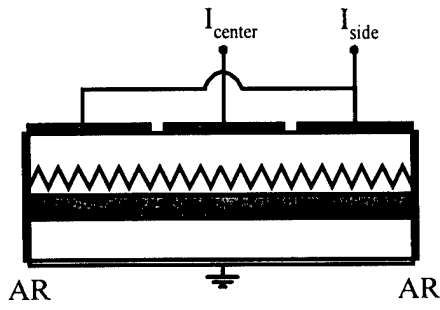


Fig. 1. Schematic drawing of the longitudinal cross section of the symmetric 3-section DFB laser

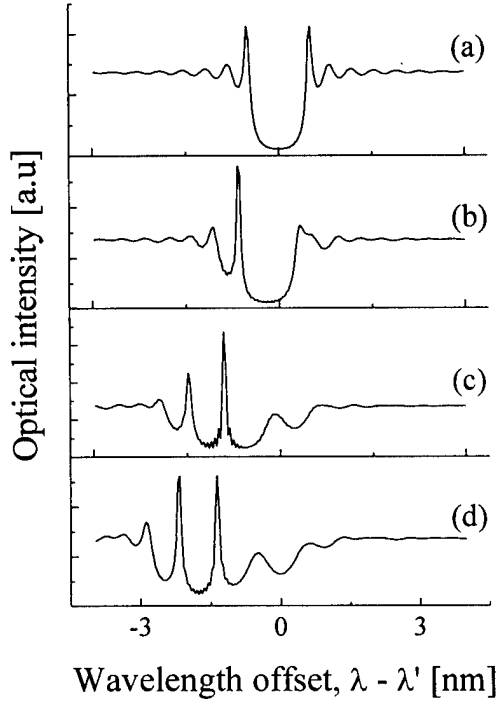
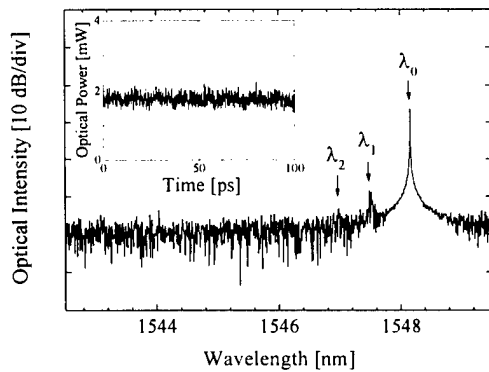
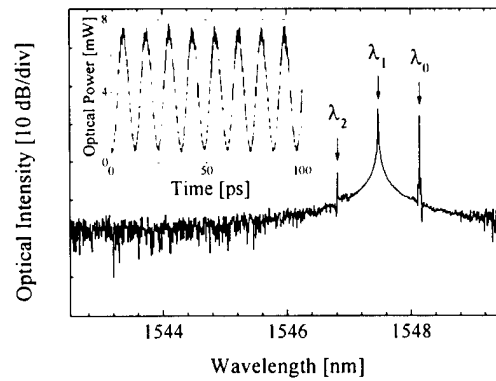


Fig. 2. The transmission spectra of the multi-section DFB laser, calculated by the large-signal time-domain model. Here,  $\lambda'$  is the operating center wavelength in the model and  $\delta_{\text{center}} = 0 \text{ cm}^{-1}$ .

(a)  $\delta_{\text{side}} = 0 \text{ cm}^{-1}$ , (b)  $\delta_{\text{side}} = 50 \text{ cm}^{-1}$ ,  
(c)  $\delta_{\text{side}} = 100 \text{ cm}^{-1}$ , (d)  $\delta_{\text{side}} = 150 \text{ cm}^{-1}$ .



(a)



(b)

Fig. 3. The output pulses (insets) and their spectra ( $\lambda_0 \approx 1548.1 \text{ nm}$ ,  $\lambda_1 \approx 1547.5 \text{ nm}$ ,  $\lambda_2 \approx 1546.9 \text{ nm}$ ). (a) when single-mode ( $I_{\text{side}} = 40 \text{ mA}$ ,  $I_{\text{center}} = 26 \text{ mA}$ ) (b) when the pulse is generated ( $I_{\text{side}} = 46 \text{ mA}$ ,  $I_{\text{center}} = 26 \text{ mA}$ )

## Accurate Analysis of Bending Losses in Rectangular Optical Waveguides

M.G.Mirkov, B.G.Bagley, R.T.Deck

*Department of Physics, University of Toledo, Toledo, Ohio 43606*

There are a large number of papers dedicated to the calculation of bending losses in optical waveguides under various approximations [1,2]. In this paper we show that one of the usual approximations is not necessary and that the analysis can be carried out more exactly.

We use a formalism for description of the bent rectangular structure similar to that in Refs.[2] and [3]. Specifically we separate the equation for the field in the waveguide in cylindrical coordinates, in terms of which the modification of the equation due to the curvature of the waveguide appears in the form of a space dependent dielectric function  $\epsilon_{\text{eff}}$ , which can be simulated by a multi-layered medium. Our method differs from that in Refs.[2] and [3] in that we determine the complex propagation constants  $\beta$  of the resultant leaky waveguide structure from the poles of the total reflection coefficient for the N Layers of the structure. In general the total reflection coefficient has the form

$$r_{123\dots N} = \frac{r_{12} + r_{23\dots N} e^{2ik_{\xi_2} d_2}}{1 + r_{12} r_{23\dots N} e^{2ik_{\xi_2} d_2}} \quad (1)$$

where  $r_{jl}$  represents the reflection coefficient at the single boundary separating media  $j$  and  $l$  and

$$k_{\xi_j} = \sqrt{\frac{\omega^2}{c^2} \epsilon_{\text{eff}}(\xi_j) - k_y^2 - \beta^2} \quad (2)$$

The equivalence between the poles of the quantity  $r_{123\dots N}$  and the propagation constants of the supermodes of the total waveguide structure allows the loss coefficient for the bent waveguide to be determined from the imaginary part of the values of  $\beta$  for which the absolute square of  $r_{123\dots N}$  approaches infinity  $|r_{123\dots N}(\beta)|^2 \rightarrow \infty$ .

The last equation is similar but not identical to Eq.(3) in [1] and Eq.(8) in [2]. In these latter references the real and imaginary parts of the pole values of  $\beta$  are respectively determined from the positions and half widths of the peaks in quantities analogous to  $|r_{123\dots N}(\beta)|^2$  plotted as a function of  $\text{Re}\beta$  under the assumption that the peaks are Lorentzian. Here we avoid the latter assumption and instead precisely determine the complex poles of the function  $|r_{123\dots N}(\beta_m)|^2$  by the

simplex method for determination of the maxima of a function of two variables. In this way the real and the imaginary parts of  $\beta_m$  are determined with a precision limited only by the computer accuracy.

In Fig.1 we show (as the solid line) our results for the loss coefficient, represented by the product of  $\text{Im}\beta$  and the width  $w$  of the waveguide channel, plotted as a function of the normalized bending radius  $(w/2\rho) \times 10^4$ .

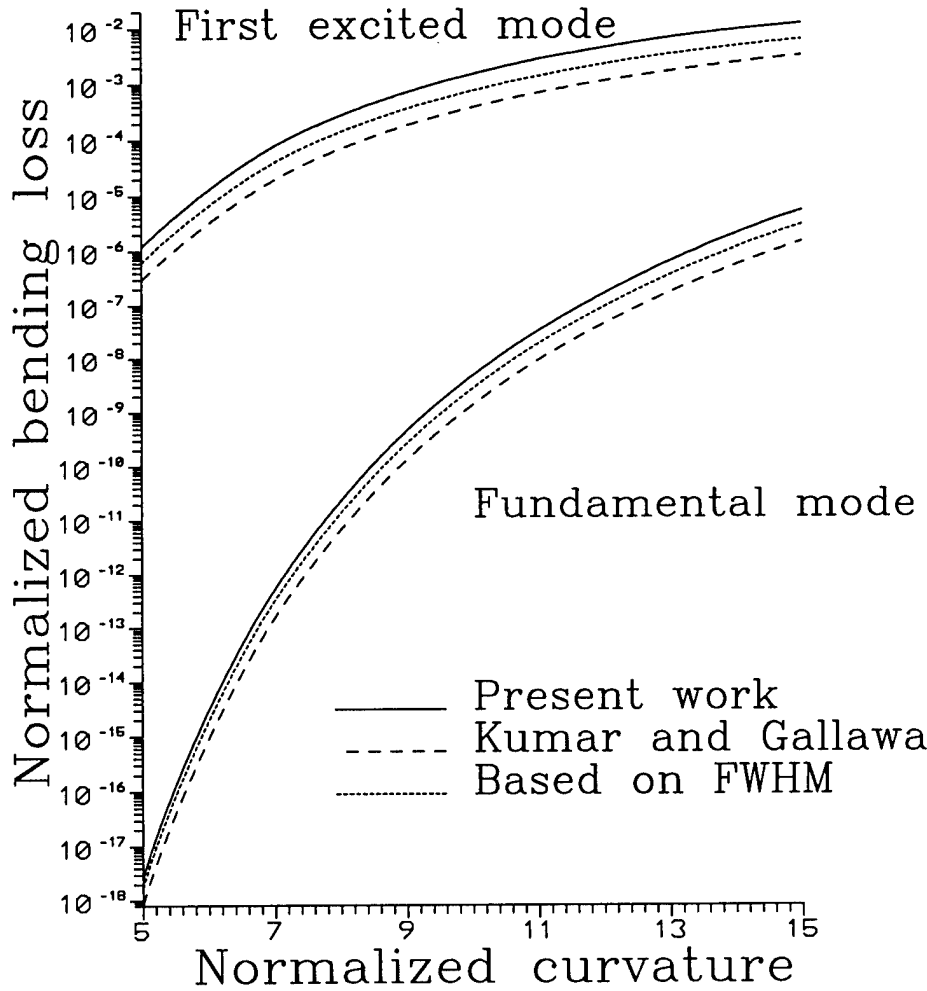


Fig. 1: Bending losses calculated by different methods.

The dotted and dashed lines in the same figure show the values of the corresponding quantity deduced from the half width of the "Lorentzian peaks" in  $\text{Im}\beta_{123..M}^2$  and in the analogous quantity in Ref.[3] respectively. It is significant that the loss coefficient obtained by the accurate method here can differ by more than 50% from that calculated in [3].

To further emphasize the difference between the present method and that based on the widths of the Lorentzian peaks, we show in Fig.2 the percentage difference between the exact value of  $\text{Im}\beta$  and the value deduced from the full width at half maximum (FWHM) of the peak in  $\text{Im}I_{23..N}^2$  plotted as a function of  $\text{Re}\beta$ .

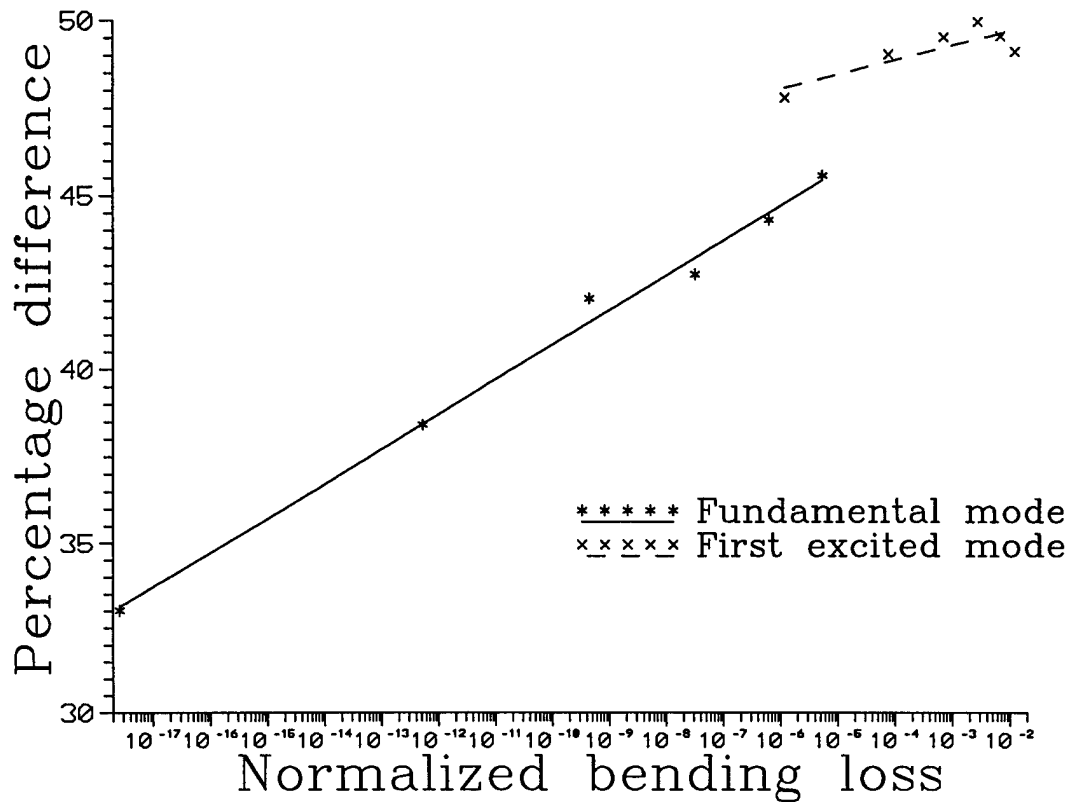


Fig. 2: Difference between the exact and approximate values for the bending loss.

Because of the significantly improved accuracy of the method of analysis introduced here, this method should be important for the estimate of bending losses in waveguiding structures that include curved channels.

1. M.R.Ramadas et al., Opt. Lett. **14**, 376-378 (1989)
2. K.Thyagarajan et al., Opt. Lett. **12**, 296-298 (1987)
3. Arun Kumar and R.L.Galawa, Opt. Lett **19**, 707-709 (1994)

## Interdiffused AlGaAs/GaAsP quantum well lasers

K.S.CHAN

City University of Hong Kong, Department of Physics and Materials Science, Kowloon,  
Hong Kong

MICHAEL C.Y.CHAN

University of Hong Kong, Department of Electrical & Electronic Engineering, Pokfulam,  
Hong Kong

Tel No: 27887814

Fax No: 27887830

E-mail: [apkschan@cityu.edu.hk](mailto:apkschan@cityu.edu.hk)

Several studies have reported that tensile strained QW lasers show improvement in performances including lower threshold currents, higher differential gains, and wider frequency modulation bandwidths as compared to the unstrained QW lasers [1,2]. In AlGaAs/GaAsP tensile strained QWs, the biaxial tensile strain shifts the light hole bands closer to the conduction band minimum than the heavy hole bands. Apart from tuning strain, interdiffusion of constituent atoms, the rates of which depend on lattice distortion, impurities, defects and the process temperatures, is a versatile technique to modify the bandstructure. Using this technique, the QW composition profiles, the confinement potentials and the optical properties can be modified as a result of the diffusion of constituent atoms. Three categories of intermixing of GaAsP/AlGaAs can occur for a quaternary based system: group-III only (GpIII) interdiffusion (Ga and Al), group-V only (GpV) interdiffusion (As and P), and both group-III and group-V (GpIII&V) sublattices diffusion. An interdiffusion of AlGaAs/GaAsP has been reported by Utpal et al with implantation of fluorine [3].

This paper presents a theoretical study of the effects of interdiffusion in a GaAsP/AlGaAs single QW structure. The effects of interdiffusion on the strains, the splitting of the HH and LH subbands and the optical gains of the QW laser are calculated based on a multi-band  $k \cdot p$  model including valance band-mixing. The optical gain spectra are calculated using the density matrix approach.

The group-III and group-V interdiffusion processes are modeled using the Fick's Law. The interdiffusion of the Al and Ga atoms is characterized by a diffusion length  $L_d^{III}$ , which is defined as  $L_d^{III} = \sqrt{(D^{III}t)}$ , where  $D^{III}$  is the diffusion coefficient of group-III atoms and  $t$  is the diffusion time. The interdiffusion of the As and P atoms is characterized in much the same way by the diffusion length  $L_d^V$ . The structure to be modeled consists of a layer of GaAsP sandwiched between two thick AlGaAs barriers. After intermixing, the Al and the P concentrations are described by

$$x_{Al}(z) = 1 - \frac{1-x_0}{2} \left[ \operatorname{erf}\left(\frac{L_z + 2z}{4L_d^{III}}\right) + \operatorname{erf}\left(\frac{L_z - 2z}{4L_d^{III}}\right) \right] \quad (1)$$

$$y_P(z) = \frac{y_0}{2} \left[ \operatorname{erf}\left(\frac{L_z + 2z}{4L_d^V}\right) + \operatorname{erf}\left(\frac{L_z - 2z}{4L_d^V}\right) \right] \quad (2)$$

where  $x_0$  is the as-grown Al content in the barrier,  $y_0$  is the as-grown P content in the well,  $L_z$  is the as-grown well width,  $z$  is the growth direction, and the QW is centered at  $z=0$ . In GpIII diffusion,  $L_d^V$  is set to be zero, while  $L_d^{III}$  equals zero in GpV diffusion.

A QW structure with a 60Å thick GaAsP well layer sandwiched between 1000Å thick  $\text{Al}_{0.33}\text{Ga}_{0.67}\text{As}$  barriers is considered in the present study. In our calculation, the P concentration in the as-grown quantum well,  $y_0$ , is set to be 0.08, 0.13 and 0.2. When  $y_0=0.08$ , heavy hole is the top valence subband; while  $y_0=0.2$ , light hole is the top valence subband. The heavy and light holes are degenerate at the zone centre when  $y_0=0.13$ .

To calculate the electron and hole wave functions in QW, we use the effective mass approximation. For most III-V semiconductors, it is a good approximation that the conduction and valence bands are decoupled. A parabolic band model and the Luttinger-Kohn Hamiltonian with strain components are used for the conduction and valence bands respectively. The envelope function scheme is adopted to describe the slowly varying (spatially extended) part of the wavefunction. The wavefunctions of the electron and hole subbands at the zone centre can be calculated separately by solving the one-dimensional Schrodinger equation. For valence band structure, it is necessary to diagonalize the Luttinger-Kohn Hamiltonian with appropriate confinement potentials for heavy and light holes. The hole envelope functions depend on  $k_{//}$  as a result of the mixing of the heavy and light hole bands. In this work, the effective Hamiltonian approach described in Chan [4] is used to solve the Luttinger-Kohn Hamiltonian to obtain the valence subband structure.

The optical gain spectra are calculated using the density matrix approach. The different well shapes obtained in different diffusion processes have very strong effects on the gain spectra. In figure 1, we plot the peak gain of the interdiffused QW lasers as a function of  $L_d$ . In GpIII diffusion, interdiffusion reduces the peak gain substantially in all three types of QWs. The peak gains are about zero when the  $L_d$  reaches the values of 15 to 20Å. This is due to the fact that the increase in Al concentration in the well layer due to diffusion reduces the confinement potential substantially. As the well becomes shallow, the quantum confinement of carriers is reduced which leads to reduction in gain. In GpV diffusion, the reduction in peak gain is not as much as in GpIII diffusion. The decreases in peak gain for all three wells are about 30% when  $L_d$  is increased from 0 to 5Å. When  $L_d$  is small, the effective barrier height is increased and the quantum confinement is increased. So the reduction in gain peak is mainly due to the change in effective mass of electron in the well. The out-diffusion of P atoms from the well increases the electron effective mass and hence reduce the gain. When  $L_d$  is greater than 5Å, the peak gain increases with  $L_d$ . This is due to the increase in the confinement potential and quantum confinement.

## REFERENCES

- [1] D.Sun, D.W.Treat, IEEE Phot. Tech. Lett. **8**, 13 (1996)
- [2] F. Agahi, K M Lau, H K.Choi, A Baliga and N. G. Anderson, IEEE Phot. Tech. Lett. **7**, 140 (1995)
- [3] Uptal Das, Steve Davis, Ramu V. Ramaswamy, Fred A. Stevie, Appl. Phys. Lett **60**, 210 (1992)
- [4] K.S.Chan, J. Phys. C **19**, L125 (1986)

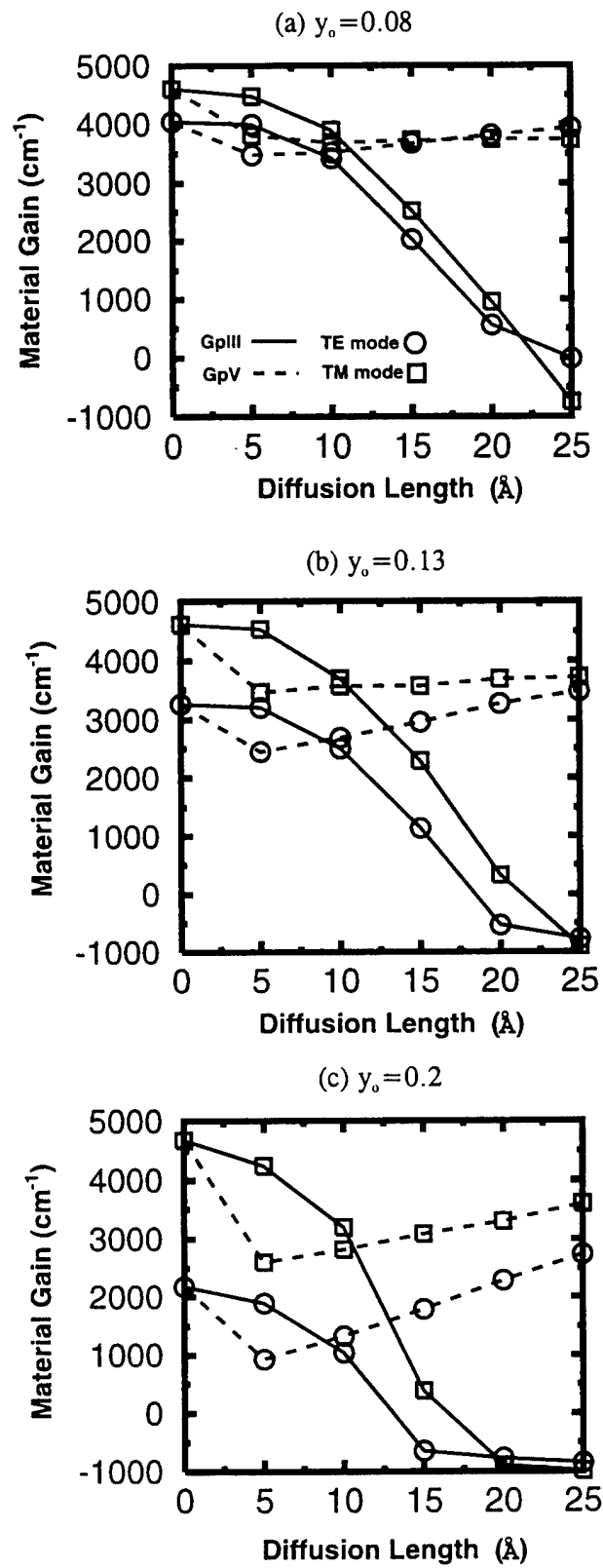


Fig. 1 Optical gain of interdiffused AlGaAs/GaAsP QW

# A Numerical Study of Spatially Controlled Impurity-Free Vacancy Enhanced Quantum Well Intermixing

Y. H. Wong, K. S. Chan, E. Y. B. Pun, A. H. P. Ho, and P. S. Chung  
Optoelectronics Research Centre  
City University of Hong Kong, Hong Kong

J. H. Marsh  
Department of Electronics and Electrical Engineering  
University of Glasgow, Scotland

Tel: (852) 27889907  
Fax: (852) 27887791  
E-mail: eeyhwong@cityu.edu.hk

The impurity-free vacancy disordering (IFVD) technique using  $\text{SiO}_2$  capping layer is widely used to integrate monolithically optoelectronic devices<sup>1,2,3</sup>. It is an efficient and promising technique for locally altering and controlling the bandgap and confinement potentials of a quantum well (QW). In a recent study<sup>2</sup>,  $\text{SrF}_2$  is used as a diffusion barrier to control spatially the degree of intermixing. The blue shift in the energy levels and the vacancy enhanced interdiffusion coefficients based on the spatially controlled QW intermixing have been reported<sup>1,2,3</sup>. However, no theoretical work has yet been reported on how the vacancy distribution in the QW is influenced by different  $\text{SrF}_2$  masking structures.

In this paper, we present the first numerical study of how Ga vacancy concentration is controlled by  $\text{SrF}_2$  masks. Our results are useful in understanding how vacancy concentration is controlled in the experiment<sup>2</sup>. The structure we study is shown in Fig.1. By varying the spacing,  $a$ , between the  $\text{SrF}_2$  stripes which prevents the out-diffusion of Ga atoms, different  $\text{SrF}_2$  coverage fractions (from 10% to 96%) are obtained. The 200nm  $\text{SiO}_2$  layer on the top allows the out-diffusion of Ga atoms. The amount of Ga vacancies is determined by the  $\text{SrF}_2$  coverage fraction. The enhancement of intermixing of the GaAs/AlGaAs QWs, located at a depth of  $1.7\mu\text{m}$  below the  $\text{SiO}_2$  layer, is caused by the increase in Ga vacancy concentration due to the out-diffusion of Ga atoms into  $\text{SiO}_2$  layer. The Ga vacancy diffusion is governed by the following two dimension diffusion equation,

$$\frac{\partial}{\partial t} C'_v = \frac{\partial}{\partial z} \left( D_v \frac{\partial}{\partial z} C'_v \right) + \frac{\partial}{\partial y} \left( D_v \frac{\partial}{\partial y} C'_v \right)$$

where  $C'_v$  is the normalized Ga vacancy concentration, and  $D_v$  is the vacancy diffusion coefficient<sup>4</sup>. The enhancement of Al diffusion rate due to vacancies is described by a diffusion coefficient which is proportional to  $C'_v$ ,  $D_{Al}(C'_v) = D_{Al,eq} C'_v$ , where  $D_{Al,eq}$  is the equilibrium Al diffusion coefficient. To solve the diffusion equation, the  $C'_v$  in the  $\text{SiO}_2$  layer should be known first. A set of values which fit the experimental results<sup>2,4</sup> obtained with 0%  $\text{SrF}_2$  coverage are listed in Table I. The value of the diffusion coefficient of vacancies depends on the material of the layer.

Fig. 2 shows how the normalized vacancy concentration,  $C'_v$ , at the QW depends on time,  $t$ . Two cases with different vacancy diffusion coefficients in  $\text{SiO}_2$  are considered here.

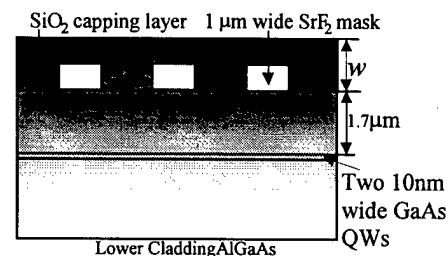


Fig.1 The structure of the sample

In case A (where the vacancy diffusion coefficient in SiO<sub>2</sub> and GaAs layers are of the same order of magnitude) the  $C_v'$  increases rapidly with time during the first 6 s, and then decreases gradually owing to the saturation of SiO<sub>2</sub> layer with Ga atoms. In case B (where the vacancy diffusion coefficient in the SiO<sub>2</sub> layer is very much smaller than that in GaAs) only the vacancies near the interface can diffuse into the QW.  $C_v'$  increases rapidly with time at the beginning and then slows down after 6 s.

The confinement profile of the vacancy enhanced interdiffused GaAs/AlGaAs QW is an error function profile characterized by an interdiffusion length. Fig. 3 shows the interdiffusion length against the square root of time,  $t^{1/2}$ , for different coverage fractions in case A. The effective interdiffusion coefficient,  $D_i$ , at different times is given by the slopes of the curves. It is interesting to note that, in case A, the interdiffusion length is approximately proportional to the square root of the time, which implies a constant  $D_i$  can be used to approximately characterized the intermixing process. Similar results have been obtained for case B. For case A with 0% SrF<sub>2</sub> coverage fraction,  $D_i$  is equal to  $1.4 \times 10^{-15}$  cm<sup>2</sup>/s, which is in good agreement with the experimental result<sup>1</sup>.

The energy shift due to the modification of the QW confinement profile as a function of the SrF<sub>2</sub> coverage fraction is shown in Fig. 4. The experimental results reported by Ooi *et al.*<sup>2</sup> are also shown for comparison. In both cases A and B, the energy shifts due to vacancy-enhanced diffusion have an approximate linear dependence on the coverage fraction, when the coverage fraction is less than 90%. In case B, only the vacancies near the SiO<sub>2</sub>/GaAs interface can diffuse into the QW, the energy shift is proportional to the area of SiO<sub>2</sub> in direct contact with the sample. In case A, the slope of the curve is not as steep as in case B, because the vacancy concentration is in fact proportional to the volume fraction of SiO<sub>2</sub> in the capping layer. The difference in energy shifts between 0% coverage and 66% coverage is about 22meV in case B, while in case A the difference is only 10meV. The difference in energy shift is a good measure of the effectiveness of the spatial control of intermixing. Hence, as a conclusion, the spatial control is more effective in case B. Nevertheless, the theoretical results is smaller than the experimental results obtained by Ooi *et al.*<sup>2</sup>. The discrepancy between theory and experiment is probably due to the effects of strains in the sample due to the difference in expansion coefficients of SiO<sub>2</sub>, SrF<sub>2</sub> and GaAs. The strains in the sample change the vacancy diffusion coefficients and hence the vacancy concentrations at the QW. This effect has been observed by Pepin *et al.*<sup>3</sup> and has been used to fabricate quantum wires.

#### References:

- <sup>1</sup>I. Gontijo, T. Kraues, J. H. Marsh, and R. M. De La Rue, IEEE J. Quantum Electron., Vol. **30**, 1189 (1994).
- <sup>2</sup>B. S. Ooi, S. G. Ayling, A. V. Bryce, J.H. Marsh, IEEE Photonics Tech. Lett., Vol. **7**, 994 (1995).
- <sup>3</sup>A. Pepin, C. Vieu, M. Schneider, G. Ben Assayag, F. R. Ladan, R. Planel, H. Launois, Y. Nissim, and M. Juhel, Appl. Phys. Lett. **69**, 61 (1996).
- <sup>4</sup>K. B. Kahen, D.L. Peterson, G. Rajeswaran, and D. J. Lawrence, Appl. Phys. Lett. **55**, 651 (1989).

Table I. Parameters used in the simulation.

Case	$D_v$ (cm <sup>2</sup> /s)	$D_{SiO_2}$ (cm <sup>2</sup> /s)	Thickness of SrF <sub>2</sub>	$C_v'$ in SiO <sub>2</sub> layer
A	$3 \times 10^{-9}$	$3D_v$	$0.5w$	1735
B	$3 \times 10^{-9}$	$5 \times 10^{-12}$	$0.5w$	3280

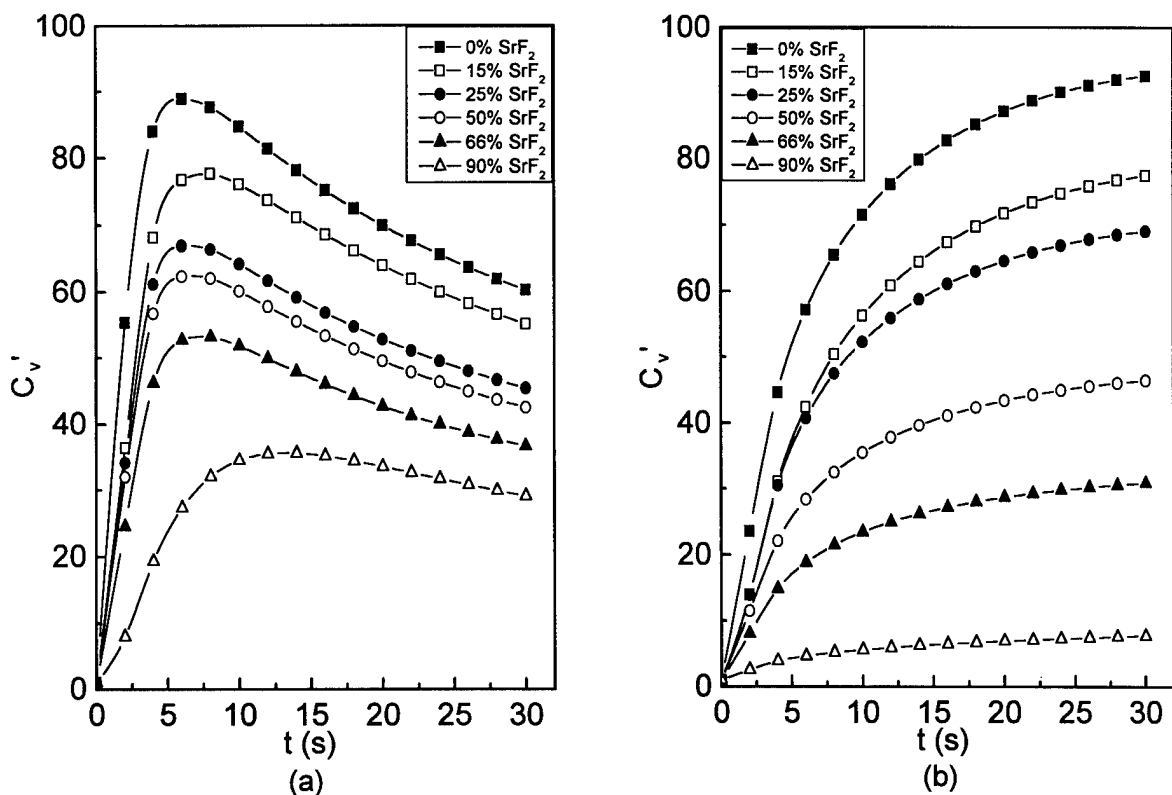


Fig. 2. Variation in normalized vacancy concentration  $C_v'$  as a function of annealing time,  $t$ , (a) for case A, (b) for case B.

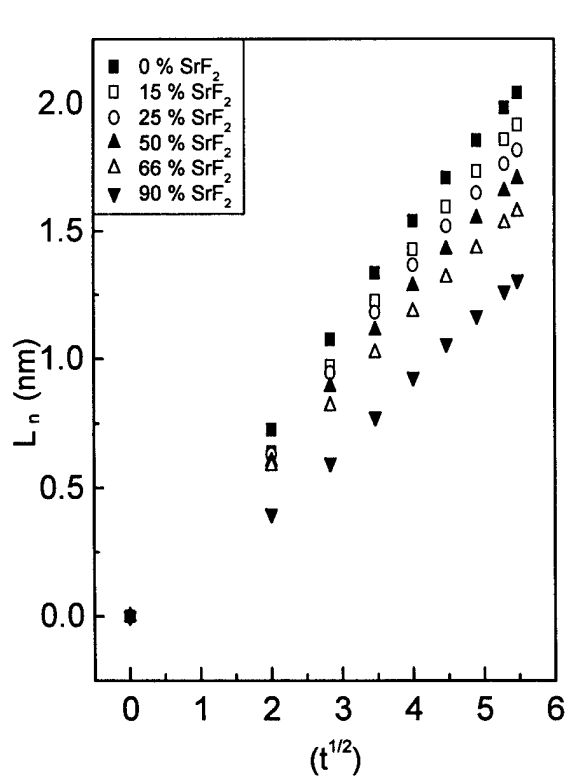


Fig. 3. Diffusion length  $L_n$  versus square root of annealing time for case A.

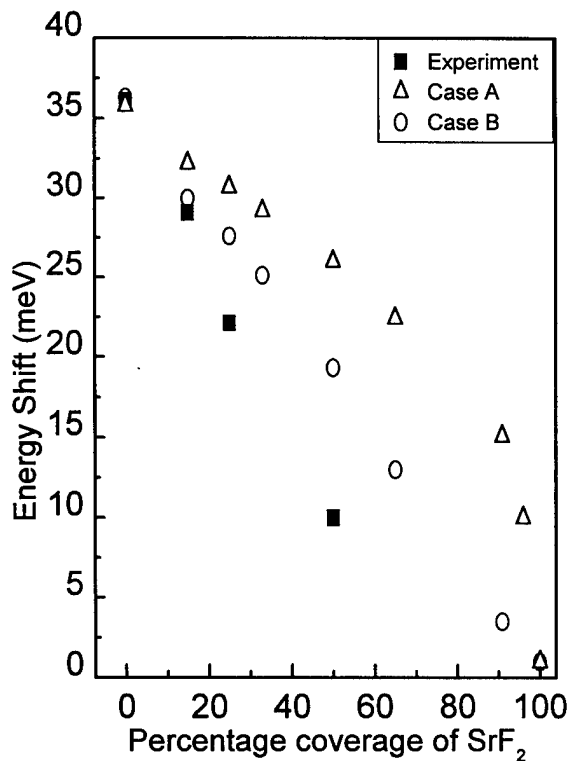


Fig. 4. Energy shift versus percentage coverage of SrF<sub>2</sub> for cases A and B.

## New Design Procedure for Large-Input/Output-Number Multimode Interference (MMI) Couplers and Application to WDM Routers

*J. Z. Huang, R. Scarmozzino and R. M. Osgood, Jr.*

*Microelectronics Sciences Laboratories, Columbia University, New York, NY 10027*

*Tel. (212) 854-8042 Fax (212) 860-6182 Email: johnny@cumsl.ctr.columbia.edu*

### INTRODUCTION

In recent years, multimode interference (MMI) devices, based on self-imaging principles, have been implemented for a variety of optical signal processing and routing functions in photonics integrated circuits [1]. Recently, these MMI devices have been used in phased-array wavelength routers since they have the potential advantages of low overall insertion loss, simplified device structure, and fabrication tolerance, compared to the use of conventional star-couplers. To date, 4x4 or 1x8 devices have been designed [2-3]. To design a NxN MMI-based wavelength router with a large number of input/output waveguides, i.e. for  $N \geq 8$  with the desired low crosstalk, a very high performance NxN MMI is required. However, the design complexity and corresponding solutions for NxN MMI couplers with large N have not been clearly investigated or addressed.

### PHASE ERROR ANALYSIS

In order to optimize the imaging performance of MMI devices, it is necessary to have an understanding of the phase errors which limit it [1]. Here we express this in a form which separates the two key issues, namely the effect of large mode number, and the effect of low index contrast; and subsequently investigate methods to improve performance for large N devices.

The general self-imaging principle for multimode waveguides is based on an ideal modal spectrum in which the spacing of the propagation constants has a specific relation with respect to the mode number [1]. This modal spectrum is:

$$\beta_0 - \beta_m = m(m+2)\pi / 3L_\pi, \quad \text{with } L_\pi = \pi / (\beta_0 - \beta_1) = 4n_f W_{e0}^2 / 3\lambda_0 \quad (1)$$

However, for an actual 2-D step-index waveguide with width W and core/cladding refractive indices  $n_f/n_c$ , the propagation constant  $\beta_m$  is represented exactly by:

$$\beta_m = k_0 n_f \sqrt{1 - \frac{k_{\perp m}^2}{k_0^2 n_f^2}} \quad \text{where } k_{\perp m} = (m+1)\pi / W_{em} \quad (2)$$

with  $k_0 = 2\pi / \lambda_0$ , and  $W_{em}$  representing the effective mode width for mode m. The ideal modal spectrum is recovered under two approximations: a) the square root term in (2) is expanded only to first order and b)  $W_{em}$  is assumed to be constant, equal to  $W_{e0}$ . The deviation of  $\beta_0 - \beta_m$  from the ideal behavior can be derived by considering the next term in each of the above approximations, yielding:

$$(\beta_0 - \beta_m)_{error} \approx \frac{k_{\perp m}^4}{(k_0 n_f)^3} \left[ \frac{1}{8} - \frac{n_f^2}{k_0 W (n_f^2 - n_c^2)^{3/2}} \right] \quad (3)$$

Finally, it is useful to express the above results in terms of the phase error,  $\Delta\phi_m$ , incurred by each mode at the N-fold imaging length ( $L = 3L_\pi / N$ ):

$$\Delta\phi_m \approx \frac{\pi}{N} \frac{\lambda^2 (m+1)^4}{2n_f^2 W^2} \left[ \frac{1}{8} - \frac{n_f^2}{k_0 W (n_f^2 - n_c^2)^{3/2}} \right] \quad (4)$$

## DESIGN IMPLICATIONS and OPTIMIZATION for LARGE N

We next consider the implication of the phase error in Eq. (4) in designing NxN MMI devices with large N, beginning with the case of high-index-contrast. In this case, only the first error term in (4) is significant since the Goos-Hähnchen effect associated with the second term is negligible. For an N-fold image,  $\sim 2N$  modes are generally required to obtain good imaging [1]. Thus to obtain a certain level of imaging performance,  $\Delta\phi_{2N}$  must be less than some allowable phase error  $\Delta\phi_{tol}$ . Combining this with (4) leads to the requirement that the waveguide width, W, must be proportional to  $N^{3/2}$ . Thus the required device length scales as  $N^2$ , and N is severely limited by acceptable device length.

In the case of low-index contrast, the second term in (4) must be considered, and is generally thought to degrade performance by introducing additional phase errors since for a low-index-contrast material system and small W, the second term dominates the first. However, for higher W, as required by large N, the second error term is comparable to the first. Furthermore, since the sign of the second term is opposite to the first, the two terms will compensate for each other. Thus we propose a new design approach for low-index contrast systems, namely to tailor  $\Delta n$  and W so as to nearly cancel the phase error in Eq. (4), yielding either better performance for a given device length, or shorter length for a given level of performance.

The above approach has been examined numerically. Consider, for example, two specific step-index multimode waveguides with  $W=40\text{ }\mu\text{m}$ ,  $n_f = 3.5$  and at  $\lambda = 1.55\text{ }\mu\text{m}$ ; the cladding indices  $n_c=1.0$  and  $n_c=3.44$  are used for the high- and low-index-contrast structure, respectively, and where the low-index-contrast system has been optimized through a choice of  $\Delta n$  so as to greatly reduce the phase error. The exact modal spectrum for each of these structures is calculated from the well-known dispersion equation for slab waveguides. The resulting phase errors at the theoretical imaging length for an 8x8 MMI coupler are shown in Fig. 1. For the high-index-contrast waveguide, the phase error deviates from zero for  $m \geq 13$ , while for the low-index-contrast one, the phase error stays near zero until  $m=25$ , and then increases due to higher-order error terms. Thus the number of modes which can accurately take part in imaging for this low-index-contrast system is essentially doubled over the number in the high-index system.

The effect of this reduction of phase error by using optimization of the index contrast on the imaging performance for the case of an 8x8 MMI coupler has been examined. An important additional design variable is the placement of the input waveguides, which must be optimized to meet the requirements of NxN imaging. To first order, this can be accomplished by evenly distributing the input waveguides with spacing  $W_{e0}/N$ .

The imaging of 8x8 MMI couplers designed in this manner was simulated by both mode propagation analysis (MPA) and the beam propagation method (BPM). The results for the high-index-contrast case showed that the power uniformity among the eight outputs was 0.47 dB, and the total insertion loss was 0.36 dB. For the optimized low-index-contrast case, the uniformity was 0.062 dB and the loss was 0.043 dB, demonstrating marked improvement compared to the high-index case. Further optimization of the waveguide placement, to be discussed in the talk, can achieve even better results.

It is important to note that wide-angle BPM was employed in the above calculations, and is critical since the paraxial BPM is equivalent to approximation a), and thus will artificially eliminate image degradation due to the first term in (4). This consideration will be elaborated in the talk.

## HIGH PERFORMANCE 8X8 WDM ROUTER DESIGN

An 8x8 MMI-based, phased-array wavelength router employing the above design concepts is considered next. Following [2], [3], based on the phase relationships of the inputs and outputs of NxN MMI couplers [1], the required delay lengths of the phased-array waveguides are determined so as to achieve the desired routing function, with minimal length and no waveguide crossing, and with a channel spacing of 1.6 nm. The spectral response of the router is then simulated by MPA and BPM for both the

high- and low-index-contrast design describe above. For the MMI router with the low-index-contrast structure (see Fig. 2), the center channel loss is less than 0.41 dB; the center channel crosstalk is better than 41 dB, and the 30dB crosstalk window is larger than 0.08 nm for all eight wavelength channels and each input waveguide. For the high-index device, the corresponding loss is 1.3 dB, the center crosstalk is only 30 dB, and for an 0.08 nm window the crosstalk is  $\sim 27$  dB. Thus a high-performance NxN MMI-based router with large N can be designed by the optimization procedure proposed in this paper.

## CONCLUSION

An explicit expression for phase error limiting performance in MMI couplers is presented in a useful form which separates the key factors determining performance. Based on this result, an optimization procedure for design of NxN MMI devices with large N is developed. By using a new phase error compensation scheme on low-index-contrast structures and optimizing the access waveguide positions, the design of a high-performance MMI coupler with large N is achieved. An 8x8 MMI-based wavelength router employing these concepts is simulated, and the result shows very low crosstalk. A 16x16 MMI-based router is being designed, and results will be presented at the conference.

## REFERENCES

- [1] L. B. Soldano and E. C. M. Pennings, "Optical multi-mode interference devices based on self-imaging: principles and applications," *J. Lightwave Technol.*, vol. 13, pp. 615-627, 1995.
- [2] C. van Dam, M. Amersfoort, G. ten Kate, F. van Ham, M. Smit, P. Besse, M. Bachmann, and H. Melchior, "Novel InP-based phased-array wavelength demultiplexer using a generalized MMI-MZI configuration," in *Proc. 7th Conf. Integrated Optics (ECIO '95), Delft, The Netherlands, 1995*, pp. 275-278.
- [3] L. O. Lierstuen and A. Sudbø, "8-Channel wavelength division multiplexer based on multimode interference couplers," *IEEE Photon. Technol. Lett.*, vol. 7, pp. 1034-1036, 1995.

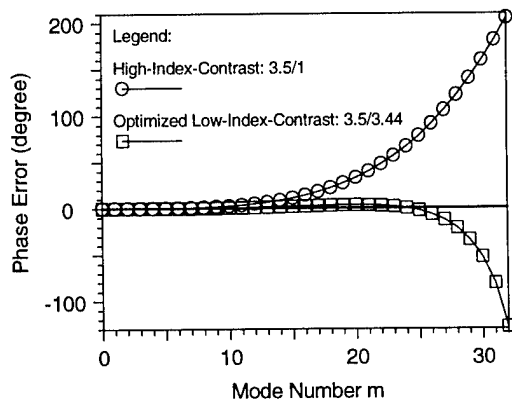


Fig. 1 Phase errors at imaging length for MMI with different index contrast ( $n_f/n_c$ ),  $W = 40 \mu\text{m}$ , and  $\lambda = 1.55 \mu\text{m}$ .

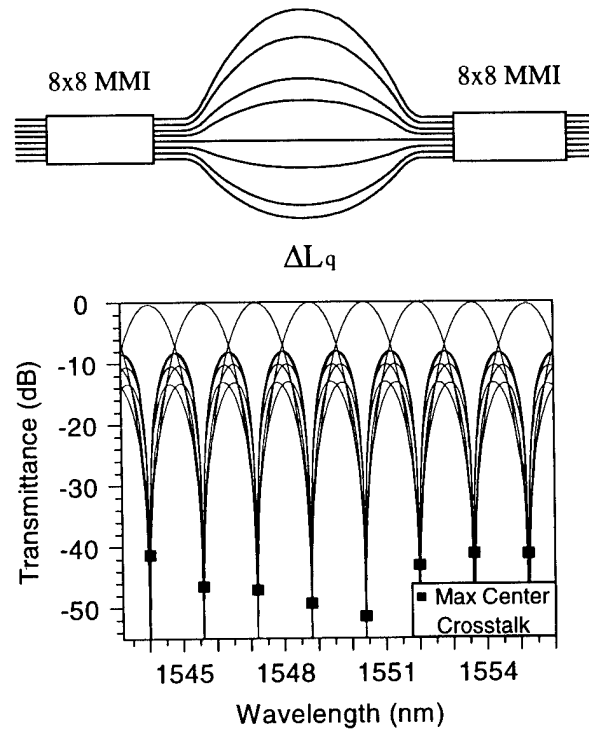


Fig. 2 Simulated spectral response for a 8x8 MMI-based router on optimized low-index-contrast structure.

# Design optimization of a notched Y-branch $Ti : LiNbO_3$ Mach-Zehnder interferometric intensity modulator

G. Peng, G.L. Yip, F.Y. Gan and P. Noutios  
 Guided-Wave Photonics Laboratory  
 Dept. of Electrical Engineering, McGill University  
 3480 University St., Montreal, PQ, Canada H3A 2A7  
 Phone: (514)398-7132, FAX: (514)398-4470  
 E-mail: yip@ee.lan.mcgill.ca

The Y-branch  $Ti : LiNbO_3$  Mach-Zehnder interferometric intensity modulator using coplanar wave-guide (CPW) traveling-wave electrodes is widely used because of its simplicity in structure, fabrication and low loss. A computer-aided numerical design of such a device consists of two parts: the design of the traveling-wave electrodes aiming at a low drive-voltage and a broad bandwidth, and the design of the Y-branch optical waveguide aiming at a minimum propagation loss and a maximum extinction ratio. Here, we report on the waveguide design part of this device (Z-cut substrate) using the effective-index method (EIM) [1] [2] and 2-D finite-difference beam propagation method (2D-FD-BPM) implemented with the transparent boundary condition (TBC) [3]. By incorporating the effects of the electrodes studied earlier [4], a design optimization for the whole device has been carried out.

The index profile of a titanium diffused channel waveguide can be expressed as  $n(x, y) = n_b + \Delta n g(x) f(y)$ , where  $\Delta n$ ,  $g(x)$  and  $f(y)$  can be experimentally determined. Under typical fabrication conditions,  $\Delta n$  is around 0.01, while  $g(x)$  can be fitted by a double error function and  $f(y)$  by simply a Gaussian distribution. Between the input and the active region, the waveguide consists of a taper and a branching region (see Fig. 1). Different expressions of  $g(x)$  must be used for these two regions to ensure continuity and thus accuracy (compared with [5]). In the effective-index modeling, we use the Runge-Kutta technique [6] to establish a lateral distribution of the effective index in the depth direction, from which the effective propagation constant and modal field distribution can be calculated. It has been found that the modal field of a  $6\mu m$  wide guide fits well with the near field distribution of a  $8\mu m$  fiber, and thus a low coupling loss between a fiber and the channel guide can be predicted.

With the initial reference index and modal field distribution obtained from the effective-index model, propagation losses corresponding to different branching angles ( $2\theta$ ) are obtained as well as the light intensity distribution pattern using the BPM method. By making use of the coherent coupling effect [7] of the radiation modes (as illustrated by Fig. 2), the propagation loss of a conventional sharp-bend Y-branch structure can be as low as 0.182 dB, with the length of the taper/branching region  $L_2 = 1000\mu m$  (full branching angle  $2\theta = 1.2^\circ$ ) and the length of the active region  $L_3 = 15100\mu m$ . This value of the length of the active region corresponds to an 80 GHz bandwidth when the thickness of the buffer layer is  $1.2\mu m$  and the thickness of the electrodes  $10\mu m$ , according to the electrode design (narrow center electrode, wide gap). The distance between the two parallel waveguide arms is chosen to be  $15\mu m$  which means a  $21\mu m$  center-to-center separation.

In order to further reduce the propagation loss, two modified Y-branches, namely the cosine-generated Y-branch and the notched Y-branch, have been design-tested because they involve

minimum fabrication and design complexities compared to some other structures. According to the computed results, for the weakly guided gradient index channel waveguide fabricated by titanium diffusion in lithium niobate, a cosine-generated Y-branch has a negative effect which brings about deterioration instead of improvement for the loss character (the taper/branching lengths studied range from 600 to 2000  $\mu m$ , or in terms of the full branching angle,  $2^\circ$  to  $0.6^\circ$ ). This is due to the constant rettiling of the wavefront in the wave path through the branching region which can cause an additional radiation loss. The idea of a notched branching structure was first brought up in [8]. In this paper, it is believed that it has been incorporated in the waveguide design of M-Z intensity modulators for the first time. The simple notched structure is shown in Fig. 3. There is only one degree of freedom because the bottom of the notch is fixed. By optimizing the width of the notch, loss reduction can be achieved. With a 1.5  $\mu m$  wide notch, the propagation loss can be reduced to 0.145 dB when  $L_2 = 1000\mu m$  and  $L_3 = 15080\mu m$ . The significance of coherent coupling effect of radiation modes has also been reduced which means a more relaxed mask fabrication tolerance. The wave propagation pattern inside such a notched structure is shown in Fig. 4.

To simulate the electrooptic effect of a M-Z interferometric modulator, it has been established [9] that the most computer-efficient and accurate method is to incorporate the spatially varying modulation field directly into the combination of EIM and 2D BPM. Here, the Fourier Series Method has been applied to compute the distribution of the electric field for a certain modulation voltage [4]. The modulation curve, the on-off voltage and the extinction ratio can be obtained by increasing the modulation voltage and evaluate the difference of the maximum and minimum loss in dB. Numerical results show that in order to get an ER greater than 20 dB, the center-to-center separation of the two waveguide arms has to be at least 21  $\mu m$ . Fig. 5 shows the cosine shape of modulation curve of the above mentioned optimized notched Y-branch structure. The minimum output power occurs at an applied voltage of 6.64-volt and the maximum achievable extinction ratio is 21.7 dB.

Details of computational techniques and the design optimization will be presented at the meeting.

## References

- [1] J. Albert and G. L. Yip, J. Lightwave Tech., **LT-6**, No.4, 552-563, (1988)
- [2] P. K. Mishra and A. Sharma, J. Lightwave Tech., **LT-4**, No.2, 204-211, (1986)
- [3] W. Huang, *et al.*, J. Lightwave Tech., **LT-10**, No.3, 295-305, (1992)
- [4] F. Y. Gan and G. L. Yip, submitted to Appl. Optics for publication, April, 1997
- [5] P. Danielsen, IEEE J. Quantum Electron., **QE-20**, No.9, 1093-97, (1984)
- [6] A. Ralston and H. Wilf, "Mathematical methods for digital computers", Vol.1, Wiley, 110-120, (1960)
- [7] D. Khalil and S. Tedjini, IEEE J. Quantum Electron., **QE-28**, No.5, 1236-38, (1992)
- [8] Z. Weissman, E. Marom and A. Hardy, Optics Letters, **14**, No.5, 293-295, (1989)
- [9] F. Chu and P. Liu, J. Lightwave Tech., **LT-8**, No.10, 1492-96, (1990)

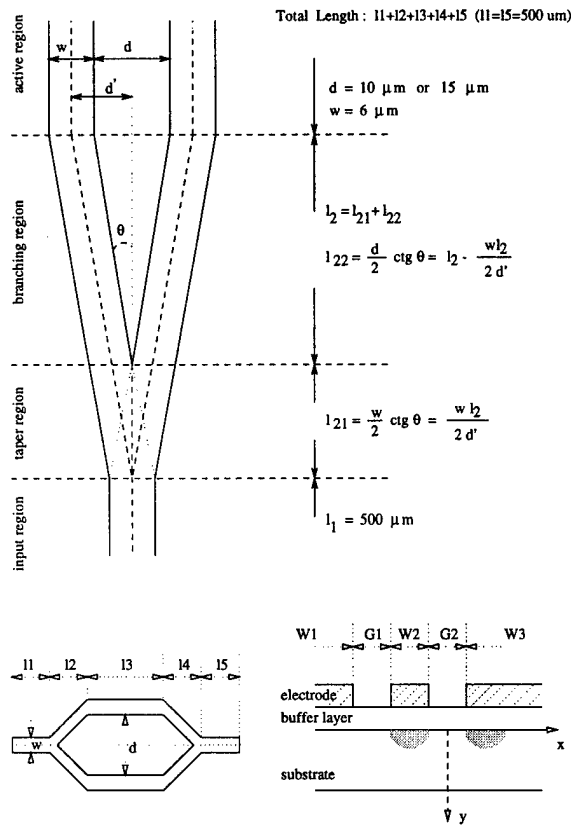


Figure 1: Schematic diagrams of the waveguide structure of a M-Z intensity modulator

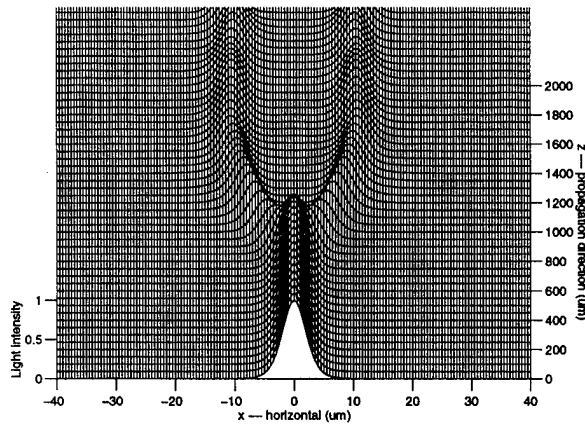


Figure 2: Field pattern at the first Y-branch of a conventional Y-branch structure with  $L_1=L_5=500 \mu\text{m}$ ,  $L_2=L_4=1000 \mu\text{m}$  ( $2\theta = 1.2^\circ$ ),  $L_3=15100 \mu\text{m}$ ,  $W=6 \mu\text{m}$  and  $d=15 \mu\text{m}$

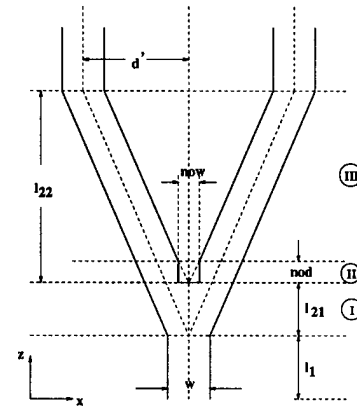


Figure 3: A notched Y-branch

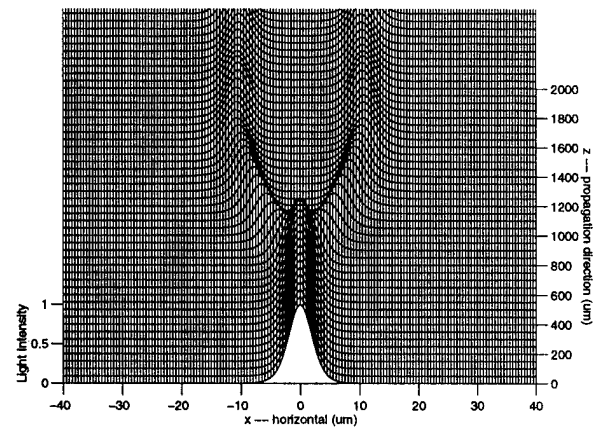


Figure 4: Field pattern at the first Y-branch of a notched structure with notch width  $1.5 \mu\text{m}$ ,  $L_2=1000 \mu\text{m}$  ( $2\theta = 1.2^\circ$ ) and  $L_3=15080 \mu\text{m}$

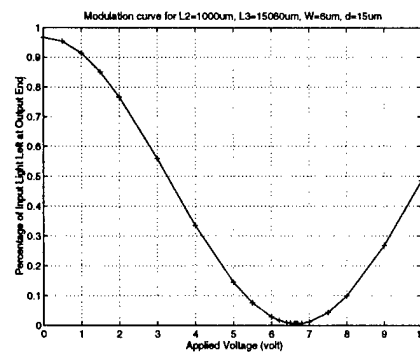


Figure 5: Modulation curve for a notched Y-branch structure of notch width  $1.5 \mu\text{m}$ ,  $L_2=1000 \mu\text{m}$ ,  $L_3=15080 \mu\text{m}$ ,  $W=6 \mu\text{m}$  and  $d=15 \mu\text{m}$

# Master-slave configuration for VCSEL synchronisation

P.S. Spencer<sup>1</sup>, C.R. Mirasso<sup>2</sup>, P. Colet<sup>3</sup> and K.A. Shore<sup>1</sup>

1- University of Wales, Bangor, School of Electronic Engineering and Computer Systems, BANGOR, LL57 1UT, Wales, UK

Phone: +44-1248-382618 fax: +44-1248-361429 e-mail: alan@sees.bangor.ac.uk

2- Departament de Física, Universitat de les Illes Balears,  
E-07071 Palma de Mallorca, Spain

Phone: 34-71-172783 fax: 34-71-173426 e-mail: claudio@hp1.uib.es

3- Instituto Mediterráneo de Estudios Avanzados, IMEDEA (CSIC-UIB),  
E-07071 Palma de Mallorca, Spain

Phone: 34-71-172537 fax: 34-71-173426 e-mail: pere@hp1.uib.es

## I. INTRODUCTION

The possibility of implementing secure optical communication systems based on chaotic data encryption has recently stimulated interest in controlling and synchronising chaotic dynamics in lasers [1] and, in particular, in semiconductor lasers [2-4] where chaos control techniques can also be used for ensuring immunity to coherence collapse [5]. It is known [6] that due to the similarity between photon lifetimes in edge-emitting laser diodes and VCSELs that, despite their high facet reflectivities, VCSELs are sensitive to optical feedback effects. Specifically, it has been shown recently using a travelling wave model [7] that VCSELs subject to strong optical feedback can exhibit chaotic dynamics over a wide range of operating currents [8]. The aim of the present contribution is to demonstrate, via numerical simulations, that synchronisation of VCSEL chaotic dynamics can be effected in a robust manner. This then opens the attractive option of using VCSELs as sources in chaotic optical receiver / transmitter modules.

## II. CONFIGURATION

Attention is given to the case of two identical VCSELs which are optically

coupled. It is supposed that optical isolation is arranged so that the output of one device (the master laser) can be used to influence that of the second laser (the slave laser) but not vice versa. Both lasers are taken to operate in a chaotic regime due to optical feedback from an external reflector. Even though the devices are identical their (chaotic) outputs would be different when the lasers operate independently. In this work it is shown that conditions for synchronising the chaotic outputs of the lasers can be readily identified.

The analysis has been undertaken using a modification of the travelling-wave approach [7,8] to account for the effect of the optical injection from the master laser on the slave laser dynamics. Attention is focussed on the influence of the laser drive current, the strength of the optical feedback and the master/ slave coupling on the synchronisation process. In particular attention will be given to the two cases of an external mirror having a low reflectivity 1 % or a high reflectivity of 50 %. Typical parameters for electrically driven VCSELs have been used in the calculations.

## III. RESULTS

To illustrate the effectiveness of the present scheme we show, in Figure 1, calculated photon numbers as a function of

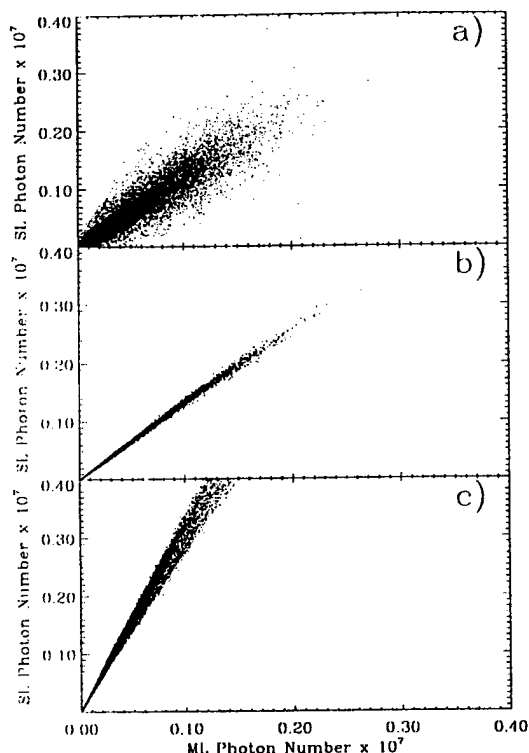


FIG. 1. Slave laser (SL) photon number vs. Master laser (ML) photon number for an optical coupling of a) 1 %; b) 2 % and c) 9 %.

increased coupling efficiency for master and slave lasers both biased at 4 times the stand-alone threshold current and both subjected to feedback from a high reflectivity mirror. In the case of very low coupling efficiency (1 %) (Figure 1 a) the correlation between the outputs of the master and slave lasers is rather poor. As the coupling is increased (2 %) towards an optimum range of values (Figure 1 b) the correlation is significantly improved and the lasers become synchronised. Further increase in the coupling efficiency (9 %) is seen to reduce the synchronisation (Figure 1 c). In the first case it is apparent that the signal from the master laser is too weak to effect the synchronisation whilst at the largest value the behaviour of the slave is too strongly affected by the master laser. As the light injected into the slave laser is increased it is expected that the output power of the slave will also increase. This is apparent

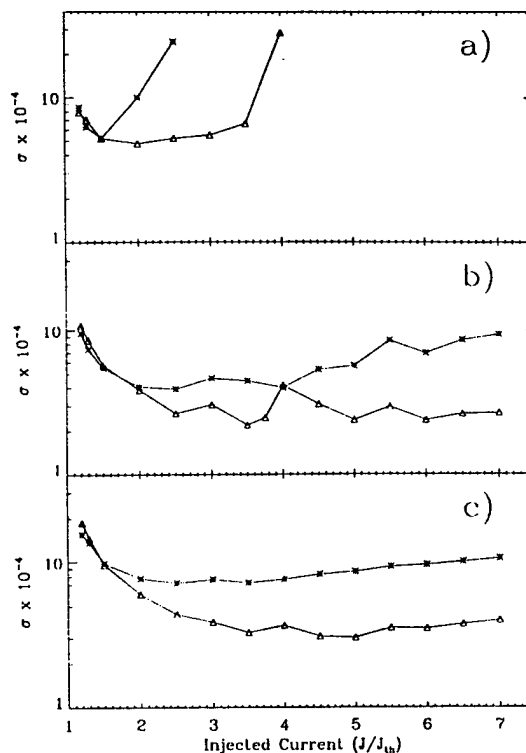


FIG. 2. Standard deviation  $\sigma$  from the least square fit vs. normalized injected current. Stars correspond to an external reflectivity of 50 % and triangles correspond to an external reflectivity of 1 %. Coupling efficiency a) 1 %, b) 2 % and c) 5 %.

in Figure 1 where it is seen that the average slope of the curve increases with the coupling efficiency. The same qualitative behaviour is observed for the case of low external reflectivity.

In order to characterise the success of the synchronisation procedure a least squares linear fit is made to the master and slave outputs shown in Figure 1. Then the standard deviation,  $\sigma$ , of the numerical data from the slope of that straight line is calculated. When synchronisation is effected  $\sigma$  should be very small. The result of such calculations is shown (using a logarithmic scale) in Figure 2. Here attention is given to the degree of synchronisation as a function of laser drive current for the cases of low and high external reflectivity and for a range of coupling coefficients in the optimum range identified from Figure 1. The results here demonstrate the existence of

a range of bias currents over which synchronisation can be achieved almost independent of the strength of the external feedback. (Figure 2 b). However, for coupling coefficients away from the optimum values the synchronisation is more effective for lower values of the external reflectivity (Figures 2 a and 2 c). Results will also be presented of a detailed examination of the dynamics of both lasers to provide further confirmation of the success of the synchronisation procedure.

#### ACKNOWLEDGEMENTS

This work was undertaken with support from the British Council / Ministerio de Educación y Cultura de España, Acciones Integradas OCCULT project. The work of P.S.Spencer and K.A.Shore was also supported by the UK EPSRC grant GR/K80136. The work of C.R. Mirasso was also supported by the project TIC97-0420 of the Comisión Interministerial de Ciencia y Tecnología CICYT (Spain).

<sup>a</sup> P.S.Spencer, Claudio R. Mirasso and K.A.Shore, "Strong optical feedback effects on the dynamics of VCSELs" IEEE Phot. Tech. Lett., submitted for publication.

---

<sup>1</sup> P.Colet and R.Roy, "Digital communication with synchronized chaotic lasers", Optics Letts. 19, 2056-2058, 1994.

<sup>2</sup> S.I.Turovets, J.Dellunde and K.A.Shore, "Selective excitation of periodic dynamics in external-cavity laser diodes", Electronics Letters 32, 42-43, 1996.

<sup>3</sup> Claudio R. Mirasso, Pere Colet and P.García-Fernández, "Synchronization of Chaotic Semiconductor Lasers: Application to Encoded Communications", IEEE Photonics Tech. Lett. 8, 299, 1996.

<sup>4</sup> V.Annovazzi-Lodi, S.Donati and A.Scire, "Synchronisation of chaotic injected-laser systems and its application to optical cryptography", IEEE J. Quant. Electron. 32, 953-959, 1996.

<sup>5</sup> J.Wieland, Claudio R. Mirasso and D.Lenstra, "Prevention of coherence collapse in diode lasers by dynamic targetting", Optics Lett. 22, 469-471, 1997.

<sup>6</sup> L.N.Langley and K.A.Shore, "The effect of optical feedback on noise properties of VCSELs", IEE Proc. Optoelectron. 144, 34-38, 1997.

<sup>7</sup> L.N.Langley, J.Mork and K.A.Shore, "Dynamics and noise properties of semiconductor lasers subject to strong optical feedback", Optics Letts. 19, 2137-2139, 1994.

## **An Integrated CAD Package for Rapid Design and Analysis of Optoelectronic Components**

**Peter S. Weitzman**

Concepts ETI, Incorporated

4 Billings Farm Road, White River Junction, Vermont 05001

Phone: (802) 296-2321, Fax: (802) 296-2325

e-mail: pweitzman@conceptseti.com

Computer Aided Design (CAD) tools have played a critical role in the spectacular advancements over the last three decades in the area of microelectronics. CAD tools for optical circuit design are in a far less advanced state than their microelectronic counterparts. Optical circuits and networks have shown exceptional promise for providing rapid, secure, and precise delivery of information. However, optoelectronics has not yet reached its potential, due in part to a lack of significant development and simulation tools.

A complete Optoelectronic CAD (OECAD) package would have the following elements:

1. Optical propagation models
2. Electrical circuit/field models
3. Electrical/optical interaction models
4. Empirical and quantum mechanical models of active device (laser and detector) performance
5. CAD capability for circuit layout
6. Thermal modeling capability
7. A graphical user interface linking the above items in an intuitive manner

A development effort creating the OECAD package incorporating the above elements is under way. Such an integrated package will support the goals of commercial high-speed communications industries by allowing substantially accelerated development of advanced optoelectronic components.

Some individual elements in the above list currently exist as commercial packages, and others exist as university research tools. Certainly in the electrical modeling and CAD areas some very mature products exist. Despite the existence of these codes, there is no available commercial CAD package for optoelectronics which combines all of the above-listed capabilities. When items 1-7 are integrated, the package will be invaluable to the designer who currently must run several different codes to analyze a device. The present optoelectronic designer relies on a disjointed combination of commercial layout and electrical packages and in most cases in-house "scratch" codes for optical modeling. Transferring data between these codes is a time-consuming process and can also lead to errors.

Figure 1 is a schematic representation of a typical optoelectronic (OE) circuit which cannot be designed using any commercial CAD package. It consists of two distributed feedback (DFB) lasers with two different resonance wavelengths on the same chip with waveguides and switches connecting them both to a single waveguide that is coupled to a fiber. A detector is present to monitor the power. The OE circuit depicted in Figure 1 would be used for wavelength division multiplexing (WDM), a promising technology for increasing information transport and processing.

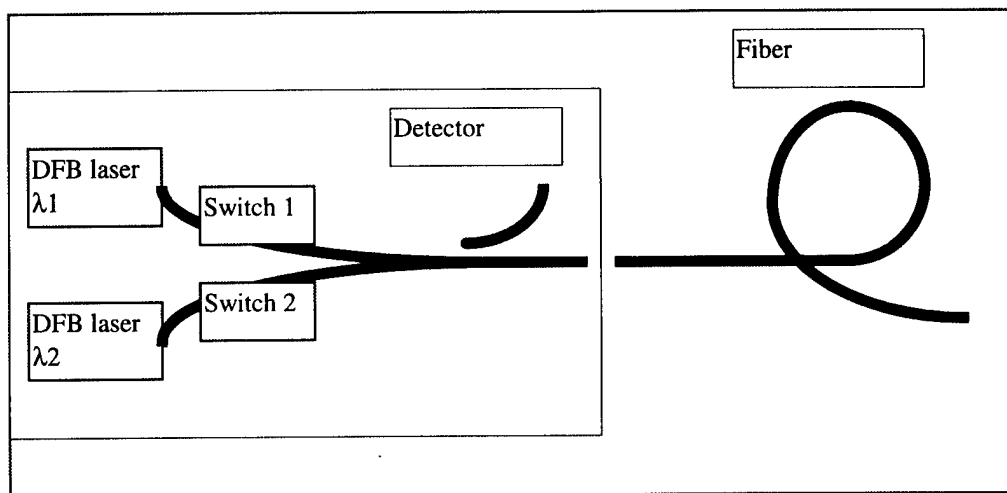


Figure 1. An optoelectronic circuit to be designed and modeled.

In order to minimize the semiconductor area taken up by the device in Fig. 1, the waveguides will need to be designed with the maximum curvature allowed within the constraints of optical confinement and limited crosstalk between channels. The use of Bezier-Bernstein polynomials will allow rapid generation of waveguide shapes with automatic constraints on slopes and curvatures. Bezier-Bernstein polynomials have been used in fluid dynamic design for 15 years. The transfer of this technology to the proposed OECAD package is a novel approach. Electrical modeling, thermal modeling, and CAD layout all exist as mature commercial packages. Through an object-oriented programming approach these can be linked to the OECAD package. The key element is the optical modeling and optical/electrical interactions which the remainder of this summary describes.

### Optical Modeling

Myriad numerical techniques have been developed to model the propagation of light in guided wave optical components. Of the existing methods, two techniques have emerged dominant in the area of integrated optical modeling. These are the Beam Propagation Method BPM [1,2] and the Finite Difference Time Domain FDTD [3] method. Both techniques solve Maxwell's equations, or an approximation to them, for optical fields. The BPM solves the paraxial wave equation where a direction of propagation is assumed which results in a parabolic equation, and where the optical field is propagated forward in space at each iteration. The FDTD technique can solve Maxwell's equations directly with a leapfrog technique, or as wave equations in hyperbolic form where an optical field is known at two points in time and propagated forward in time.

The BPM and FDTD techniques solve different classes of problems and are, therefore, complementary. The BPM is most useful when the refractive index changes slowly in the direction of propagation and reflections can be neglected. This is the case for waveguiding structures covering many optical wavelengths. The FDTD is used for the class of problems where strong wave interactions or reflections exist. Sharp bends, mirrors, semiconductor laser cavities, and the grating structures in distributed feedback (DFB) lasers all fall into this class of problems. The FDTD is performed in the time domain making it ideal for time-varying problems.

Many classes of optoelectronic devices will require modeling in an OECAD system. These include the basic building blocks of channel waveguides, fibers, laser diodes, and detectors, as well as fiber amplifiers and nonlinear optical devices, such as electro-optic modulators, and frequency doublers. Each of the different types of optoelectronic components can be modeled using Maxwell's equations, possibly

coupled to other equations describing gain, etc. A full vector solution to Maxwell's equations for all of the devices is possible using the FDTD method; however, it would be computationally inefficient to solve all problems with this level of complexity which is why the BPM is a useful algorithm. A circuit like the one displayed in Figure 1 will require the BPM for waveguide modeling and FDTD for laser modeling.

For the case of a strongly guiding waveguide where large refractive index changes exist in both the transverse dimensions, but not along the propagation direction, a vector BPM can be employed where two components of the electric field are significant and are coupled [4]. Wide angle BPM capabilities will be required in an OECAD package. In the interest of streamlining the design process, the scalar BPM should be employed when possible.

In the most general form, the FDTD technique solves the full vector Maxwell's equations in a heterogeneous medium. The combined equations are hyperbolic so that points in space separated by  $\Delta x > c\Delta t$  are decoupled in the solution. A leapfrog technique allows the two Maxwell curl equations to be integrated forward in time. This results in an algorithm which is simple to implement and extremely versatile [3]. The finite differencing is done in the time domain, in the spatial dimensions either finite elements or finite differences can be employed.

Time-dependent problems are handled with ease in this technique and steady-state solutions are obtained by stepping forward in time from an initial excitation until a steady state is reached. The BPM and FDTD can be linked by using BPM results as an initial excitation when the light reaches a region where the FDTD solver is required.

### **Optical/Electrical Interaction, Nonlinear Optical Device Modeling**

The source term in the BPM or FDTD allows a straightforward incorporation of a static electric field. With knowledge of applied electric fields and the nonlinear susceptibilities of the material, the electro-optic effect can be modeled. The source term in the BPM or FDTD can also incorporate coupling between optical wavelengths through second, third, or higher order nonlinear susceptibilities [1].

### **Active Device Models**

Active devices (lasers and detectors) will be handled in two ways. Empirical models for lasers and detectors must be available as components which can be inserted into the circuit. Likewise physical simulations must be present to model new devices or for detailed analysis.

### **References:**

- [1] P. S. Weitzman and U. Österberg, "A Modified Beam Propagation Method to Model Second Harmonic Generation in Optical Fibers," *IEEE J. Quantum Electronics*, Vol. 29, 1437 (1993).
- [2] P. S. Weitzman and U. Österberg, "A Modified Beam Propagation Method for Modeling Nonlinear Effects in Optical Fibers," OSA Integrated Photonics Research Conf., Mar. 1993, Palm Springs, CA.
- [3] S. T. Chu and S. K. Chaudhuri, "A Finite-Difference Time-Domain Method for the Design and Analysis of Guided Wave Optical Structures," *IEEE J. Lightwave Technology*, Vol. LT-7 pp. 2033-2038 (1989).
- [4] W. P. Huang, C. L. Xu and S. K. Chaudhuri, "A Finite-Difference Vector Beam Propagation Method for Three-Dimensional Waveguide Structures", *IEEE Photonics Technology Letters*, Vol. 4, No. 2, Feb. 1992.

# Vectorial electromagnetic model for the accurate analysis of finite length surface-relief structures of high complexity

Kim Dridi, and Anders Bjarklev, Dept. of Electromagnetic Systems,  
EMI, bldg 348, Technical University of Denmark, 2800 Lyngby, Denmark,  
Email: kd@emi.dtu.dk, Telephone: +45 45 88 38 14, Fax: +45 45 93 16 34

## Summary

### Introduction:

One of the interesting options in future optical sensor systems is the integration of the advantageous properties of optical waveguide systems for signal distribution and treatment, and the precise handling of the interaction between electromagnetic (optical) field and the medium that the sensor is designed to analyze. This implies a precise coupling between guided modes in the optical waveguides and radiating fields outside of these. An important element in this connection is the surface-relief grating [1,2,3], which for a practical system naturally has to be of finite length and may consist of complex geometries. However, at this point we have to face that models concerning finite diffractive optical structures with arbitrary material distributions are few and often inadequate for design optimization purposes requiring modest simulation times. A fact, which complicates this further, is that analysis and design of finite geometric structures of high complexity in the sub-wavelength range generally may not be performed to an acceptable accuracy by scalar analysis methods [4]. It is, therefore, necessary to develop multi-dimensional vectorial methods in order to study scattering phenomena, radiation, power-densities and -flows as well as polarization changes in near- and far-fields of the structures of interest. Since analytical approaches often are excluded due to structure complexity and/or very long analysis times, the attention must be directed towards numerical methods. Approaches such as the Moment method, the Finite Element method, and the Finite Difference Time Domain (FDTD) method [5,6,7,8] may be considered, but due to the complexity of the envisioned structures, the application of electromagnetic boundary conditions are difficult, making the first two methods least attractive. For this reason, the FDTD method was chosen, and the following presentation will demonstrate its applicability on analysis of surface-relief gratings with finite length.

### Theory:

A two-dimensional FDTD computational domain surrounding a diffractive region in a dielectric waveguide structure is illustrated in Figure 1. Square grid cells are used to map the environment where  $n_1$ ,  $n_2$ , and  $n_3$  denote the refractive index of air, film layer, and semi infinite substrate, respectively. The computational domain consists of a total field region, a scattered field region backed up by a Perfectly Matched Layer (PML), which in turn is terminated by second order generalized Trefethen-Halpern absorbing boundary conditions (THABC) [6]. In the PML region, outwards traveling electromagnetic fields are absorbed and attenuated, avoiding significant fictitious reflections into the center of the computational window. The THABC position, relative to the diffractive profile, and the PML thickness are optimized with that intention. The THABC perform the task of letting scattered radiating fields propagate outwards the computational domain, simulating the physical continuity. We make use of a fictitious transformation surface  $\Omega$  in free space, positioned at  $\mathbf{r}_\Omega$ , with unit normal vector  $\hat{\mathbf{n}}$ , where we place the auxiliary sources represented by the electric  $\mathbf{J} = \hat{\mathbf{n}} \times \mathbf{H}$ , and the magnetic  $\mathbf{M} = -\hat{\mathbf{n}} \times \mathbf{E}$  current densities, respectively. We define a free space Green function satisfying Maxwell's equations  $g(\mathbf{r}, \mathbf{r}_\Omega) = e^{-jk|\mathbf{r}-\mathbf{r}_\Omega|}/|\mathbf{r}-\mathbf{r}_\Omega|$  with  $k = 2\pi/\lambda$ ,  $\lambda$  being the free space wavelength,  $\omega = 2\pi/T$ ,  $j = \sqrt{-1}$ ,  $\epsilon_0$  and  $\mu_0$  as the permittivity and the permeability of air. The power density flow through the surface is found as  $\mathbf{P}_n = \frac{1}{T} \int_z \hat{\mathbf{n}} \cdot [\text{Re}(\mathbf{E}(t)) \times \text{Re}(\mathbf{H}(t))] dt dz$  where  $t$  is the time variable and  $T$  the oscillation period of the electromagnetic field. If the field observation point is placed at  $\mathbf{r}$ , its power intensity is then  $I = |\frac{1}{T} \int_T \text{Re}[\mathbf{E}(\mathbf{r})] \times \text{Re}[\mathbf{H}(\mathbf{r})] dt|$  where

$$\mathbf{E}(\mathbf{r}) = \int_{\Omega} [\mathbf{M}(\mathbf{r}_\Omega) \times \nabla_r g(\mathbf{r}, \mathbf{r}_\Omega) - \frac{1}{j\omega\epsilon_0} \nabla_r \times (\mathbf{J}(\mathbf{r}_\Omega) \times \nabla_r g(\mathbf{r}, \mathbf{r}_\Omega))] d\Omega \quad (1)$$

$$\mathbf{H}(\mathbf{r}) = \int_{\Omega} [-\mathbf{J}(\mathbf{r}_\Omega) \times \nabla_r g(\mathbf{r}, \mathbf{r}_\Omega) - \frac{1}{j\omega\mu_0} \nabla_r \times (\mathbf{M}(\mathbf{r}_\Omega) \times \nabla_r g(\mathbf{r}, \mathbf{r}_\Omega))] d\Omega \quad (2)$$

In solving the exact radiation integrals using the FDTD computed fields, we obtain near and farfield information. The farfield power intensity can be expressed as  $\mathbf{P}(\theta) = -\frac{1}{T} \int_T \text{Re}(E_\phi(t)) \text{Re}(H_\theta(t)) dt$  in a spherical coordinate system  $(r, \theta, \phi)$  corresponding to the cartesian one  $(x, y, z)$ .

### Results:

We present modeling results concerning finite periodic gratings in a perfect dielectric waveguide. Polymer materials are quite common as dielectrics and have been chosen for the simulations with  $n_2 = 1.58$  and  $n_3 = 1.47$ , while  $n_1 = 1$ . The film layer thickness has been chosen as  $d = 0.65\lambda$  in order to have a single mode traveling in the planar waveguide region, reducing the mode energy dispersion. The effective refractive index seen by the incident field is determined by solving a transcendental equation for the slab waveguide  $n_{eff} = 1.51312$ .

Theoretical, infinitely long, periodic surface-relief gratings have been studied in the 1980's with Coupled Wave theory [1,2] or Phase Matching Conditions [9] dictating how the fields are coupled out of the guide at diffraction angles satisfying

$$\sin \theta = \frac{1}{n_1} \left[ n_{eff} + \frac{\nu}{\Lambda} \right] \quad (3)$$

where  $\nu = 0, \pm 1, \dots$  and  $\Lambda$  as the grating period. One should bear in mind that equation (3) does not take into account the influence of the grating amplitude, nor the profile, nor its length. Figure 2 shows the main diffraction angles for maximal farfield power density as a function of the grating period, for several finite grating profiles (FDTD) and the ones from equation (3). We notice good agreement except for the wide angles above  $40^\circ$  and below  $-20^\circ$ . The difference is due to the infinite structure's narrow optical main beam and its ability to diffract more power into air, in every direction. The use of infinitely long structures in electromagnetic optical modeling and design does not give a realistic picture of the physics. Figure 3 shows the numerical farfield power radiation pattern of a sine profile surface-relief grating as a function of the grating length. The longer structures show narrower beams and the main diffraction angle is shifted to lower values as the farfield region of the structure moves farther away.

### Conclusions:

We have proposed and designed a vectorial electromagnetic model to accurately simulate the optical behavior of finite surface-relief gratings in dielectric waveguiding material. Numerical results show that the finite dimension of the structures have great importance for the accurate analysis of gratings. Further results on the exact properties of surface-relief gratings of finite length will be presented, including a detailed analysis of the influence of the surface profile. It will be demonstrated that the presented method provides a high power-conservation accuracy for moderate calculation times, which promises good prospects for future multidimensional models, enabling the handling of complex finite structures with arbitrary material distributions.

### References:

- [1] Gaylord and Moharam, "Analysis and applications of optical diffraction by gratings". Proceedings of the IEEE, 1985, page 894.
- [2] Moharam and Gaylord, "Diffraction analysis of dielectric surface-relief gratings". Optical Society of America, Oct. 1982, page 1385.
- [3] Nishihara, Ura, Suhara and Koyama, "An integrated-optic disk pickup device". Lightwave Technology, 1986, page 913.
- [4] Moharam, Pommert and Grann, "Limits of scalar diffraction theory for diffractive phase elements. Optical Society of America, 1994, page 1827.
- [5] K.S. Yee, "Numerical solution of initial boundary value problems involving Maxwells equations in isotropic media". IEEE Transactions on Antennas and Propagation, 1966, page 302.
- [6] Allen Taflove, "Computational Electrodynamics: the finite-difference time-domain method". Boston Mass: Artech House, 1995.
- [7] Zhang, Chu, Wu, Bi, Tiberio, Joseph, Taflove, Tu, Ho, "Nanofabrication of 1-D photonic bandgap structures along a photonic wire". IEEE Photonics Technology Letters, April, 1996, page 491.
- [8] Yang, "Finite difference analysis of 2-D photonic crystals". IEEE Trans. on Microwave Theory and Techniques, Dec 1996, page 2688.
- [9] Tamir T., "Beam and waveguide couplers". Integrated Optics, 1979, page 102.

Figure 1: FDTD two-dimensional computational grid surrounding a binary diffractive structure embedded in dielectric waveguiding material. The substrate, film layer and air have the refractive index  $n_3, n_2$  and  $n_1$  respectively.  $d$  is the film layer thickness in the region outside the grating region. The  $(x, y, z)$  coordinate system is used to define the geometric surface and in connection with the transformation surface, where we have secondary auxiliary electromagnetic sources. These are used in connection with exact radiation integrals. A transparent non physical rectangular box is used to verify energy conservation.  $\mathbf{n}$  is the normal vector of the transformation surface. We denote by  $P_d, P_{tr}, P_{rd}, P_{rb}$  the time averaged power intensity flows for the diffracted, transmitted, downwards and backwards reflected power, respectively.

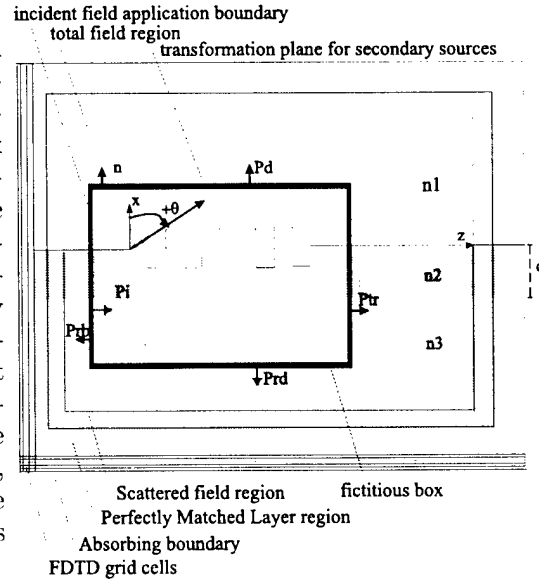


Figure 2: Farfield angle for maximal power density shown as a function of the grating period to free space wavelength ratio  $\Lambda/\lambda$  for different grating profiles. The amplitude to film layer thickness ratio  $A/d$  is 0.3 for the finite structures ( $10\lambda$  long). The refractive indices are  $n_1 = 1$ ,  $n_2 = 1.58$ ,  $n_3 = 47$ . The film layer to free space wavelength ratio  $d/\lambda$  is 0.65.

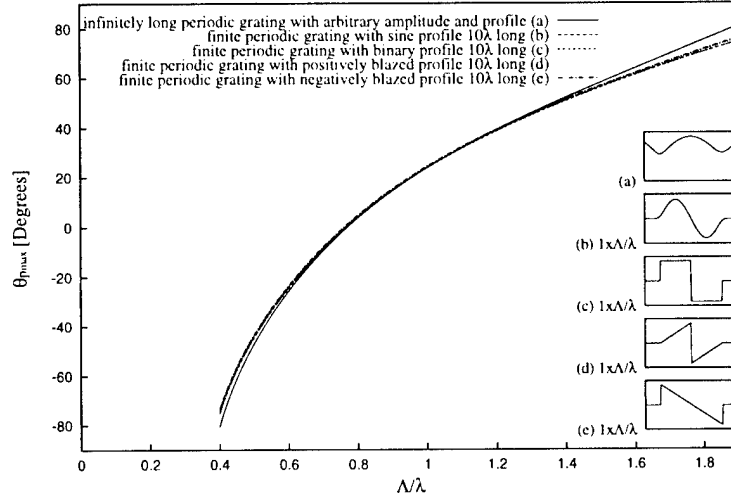
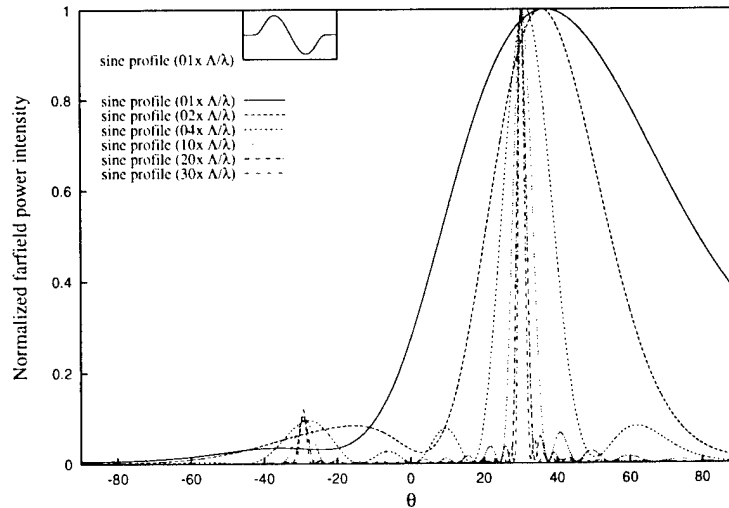


Figure 3: Normalized farfield power radiation pattern as a function of the farfield observation angle  $\theta$ , for surface-relief gratings with sine profiles of different lengths, in a two-layered dielectric slab waveguide. The grating period to free space wavelength ratio  $\Lambda/\lambda$  is 1. The grating amplitude to film layer thickness ratio  $A/\lambda$  is 0.3. The refractive indices are  $n_1 = 1$  for free space,  $n_2 = 1.58$  for the film layer and  $n_3 = 1.47$  for the semi infinite substrate. The film layer thickness to free space wavelength ratio  $d/\lambda$  is 0.65.



# MoL-eigenmode analysis with precise resolution by enhanced generalized line algorithm

Reinhold Pregla

Allgemeine und Theoretische Elektrotechnik, FernUniversität, D-58084 Hagen, Germany

Phone: +49 2331 987 1140

Fax: +49 2331 987 353

e-mail: R.Pregla@FernUni-Hagen.de

**Introduction:** Optical circuits consist mostly of multilayered waveguide structures. In general the layers are inhomogeneous. Usually the dimensions of the waveguide cross sections are small compared with the length of sections in the circuits. To describe the circuit behavior correctly it is necessary to determine the eigenmodes and especially the propagation constant precisely. In this contribution an adequate new procedure is described based on the Method of Lines (MoL) for precise computation of eigenmodes and propagation constant. In the MoL we discretize the field not completely but only as long as necessary. In the remaining direction the field dependence is calculated analytically. Fig. 1 shows an example of a rib waveguide cross section. The modal fields of this waveguide are concentrated in the rib and in the adjacent layers under it. This in turn requires a correct modeling of the fields in this part of the waveguide.

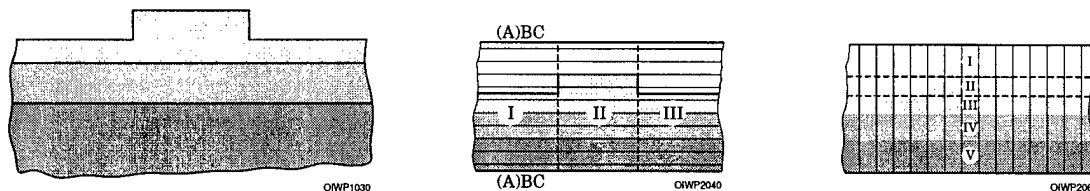


Fig. 1: Cross section of a rib waveguide and alternative discretization possibilities

Two ways of subdivision of the cross section for the purpose of analysis by the mode matching technique or by the Method of Lines (MoL) are shown in the right side of Fig. 1. In the first (second) case this subdivision is done by vertical lines and the discretization lines have horizontal (vertical) direction. Which type of subdivision and discretization has to be preferred cannot be recommended generally. A question arises why not to use subdivisions and discretization lines in both directions as shown in Fig. 2.

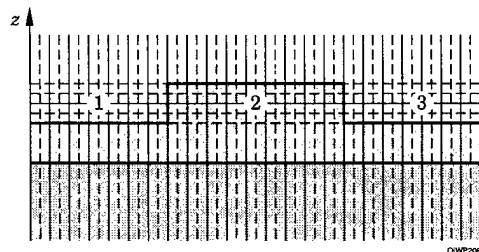


Fig. 2: Discretization with vertical and horizontal lines in some regions of the waveguide cross section in Fig. 1

To treat this problem especially in the layer with the rib we have now discretization lines in both directions. This in turn means the use of crossed discretization lines. In this way the fields can be determined more precisely. The other layers of the structure considered especially the film under the rib can also be discretized in this way. The crossed lines do not mean a 2D discretization. In the case considered the fields are composed of two parts from the two discretization line systems. The numbers of discretization lines in horizontal and vertical directions can be chosen separately.

Therefore, if necessary the number can be chosen large enough to obtain a high accuracy without increasing the numerical effort appreciably. In the regions with unidirectional discretization lines the field description is done as in [1].

**Basic theory:** The field description in the region with crossed lines can be done in the following way. Fig. 3 shows a general region R as e.g. region 2 in Fig. 2. In view of linearity of all materials and Maxwell equations, the following relation in matrix form between the tangential fields at the ports A, B, C and D

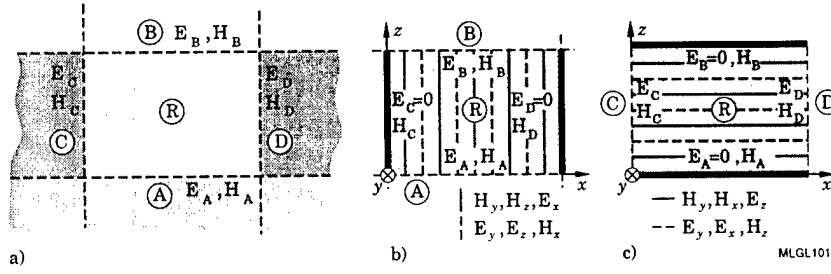


Fig. 3: Field calculation in a region R using crossed lines:

- a) general region R with definitions
- b) ports C and D short-circuited: analysis with vertical lines
- c) ports A and B short-circuited: analysis with horizontal lines

of the general region R holds

$$\begin{bmatrix} \mathbf{H}_A \\ -\mathbf{H}_B \\ \mathbf{H}_C \\ -\mathbf{H}_D \end{bmatrix} = \begin{bmatrix} \mathbf{y}_{AA} & \cdots & \mathbf{y}_{AD} \\ \vdots & & \vdots \\ \mathbf{y}_{DA} & \cdots & \mathbf{y}_{DD} \end{bmatrix} \begin{bmatrix} \mathbf{E}_A \\ \mathbf{E}_B \\ \mathbf{E}_C \\ \mathbf{E}_D \end{bmatrix} \quad (1)$$

$\mathbf{E}_U$  and  $\mathbf{H}_U$  ( $U = A, B, C, D$ ) are supervectors of the discretized tangential fields at port U. Each supervector consists of two vectors for the two tangential components. In more compact form we can write

$$\begin{bmatrix} \hat{\mathbf{H}}_{AB} \\ \hat{\mathbf{H}}_{CD} \end{bmatrix} = \begin{bmatrix} \mathbf{y}_{AB}^{AB} & \mathbf{y}_{AB}^{CD} \\ \mathbf{y}_{CD}^{AB} & \mathbf{y}_{CD}^{CD} \end{bmatrix} \begin{bmatrix} \hat{\mathbf{E}}_{AB} \\ \hat{\mathbf{E}}_{CD} \end{bmatrix} \quad \begin{aligned} \hat{\mathbf{H}}_{AB} &= [\mathbf{H}_A^t, -\mathbf{H}_B^t]^t & \hat{\mathbf{E}}_{AB} &= [\mathbf{E}_A^t, \mathbf{E}_B^t]^t \\ \hat{\mathbf{H}}_{CD} &= [\mathbf{H}_C^t, -\mathbf{H}_D^t]^t & \hat{\mathbf{E}}_{CD} &= [\mathbf{E}_C^t, \mathbf{E}_D^t]^t \end{aligned} \quad (2)$$

The admittance matrices can be calculated in the following way: By short-circuiting the ports C and D (using metallic walls) we obtain magnetic field parts at the ports A and B and even at ports C and D caused by the electric field  $\mathbf{E}_{AB}$ . All these field parts are determined using vertical discretization lines parallel to the metallic side walls. From these partial fields the matrices  $\mathbf{y}_{AB}^{AB}$  and  $\mathbf{y}_{CD}^{AB}$  are obtained. Similarly, short-circuiting ports A and B and using horizontal discretization lines we obtain the matrices  $\mathbf{y}_{AB}^{CD}$  and  $\mathbf{y}_{CD}^{CD}$ . For the regions with unidirectional discretization lines, analog equations as above can be written [1].

**Field equations:** In the following it will be described how in case of short circuiting the ports C and D the supermatrices  $\hat{\mathbf{y}}_{AB}^{AB}$  and  $\hat{\mathbf{y}}_{CD}^{AB}$  can be determined. Using the following definitions for the supervectors in transformed domain

$$\hat{\mathbf{H}} = \begin{bmatrix} -j\overline{\mathbf{H}}_y^t & \overline{\mathbf{H}}_x^t \end{bmatrix}^t \quad \hat{\mathbf{E}} = \begin{bmatrix} \overline{\mathbf{E}}_x^t & -j\overline{\mathbf{E}}_y^t \end{bmatrix}^t \quad (3)$$

the fields at ports A and B are related by [1]

$$\hat{\mathbf{H}}_{AB} = \begin{bmatrix} \hat{\mathbf{H}}_A \\ -\hat{\mathbf{H}}_B \end{bmatrix} = \begin{bmatrix} \overline{\mathbf{y}}_1 & \overline{\mathbf{y}}_2 \\ \overline{\mathbf{y}}_2 & \overline{\mathbf{y}}_1 \end{bmatrix} \begin{bmatrix} \hat{\mathbf{E}}_A \\ \hat{\mathbf{E}}_B \end{bmatrix} = \hat{\mathbf{y}}_{AB}^{AB} \hat{\mathbf{E}}_{AB} \quad (4)$$

where

$$\begin{aligned} \overline{\mathbf{y}}_1 &= \hat{\gamma} \mathbf{\Lambda} & \hat{\gamma} &= (\hat{\Gamma} \tanh(\hat{\Gamma} \bar{d}))^{-1} & \mathbf{\Lambda} &= \begin{bmatrix} \varepsilon_d \mathbf{I}_h & \tilde{\delta}^t \\ \tilde{\delta} & \varepsilon_r \mathbf{I}_e - \bar{\lambda}_e^2 \end{bmatrix} \\ \overline{\mathbf{y}}_2 &= -\hat{\alpha} \mathbf{\Lambda} & \hat{\alpha} &= (\hat{\Gamma} \sinh(\hat{\Gamma} \bar{d}))^{-1} \end{aligned} \quad (5)$$

$$\mathbf{T}_{e,h}^t \bar{\mathbf{D}}_{e,h}^t \bar{\mathbf{D}}_{e,h} \mathbf{T}_{e,h} = \bar{\lambda}_{e,h} \quad \bar{\delta} = \mathbf{T}_e^t \bar{\mathbf{D}}_h \mathbf{T}_h \quad \tilde{\delta} = \sqrt{\varepsilon_{re}} \bar{\delta} \quad (6)$$

$$\mathbf{I}_{e,h}^2 = \bar{\lambda}_{e,h}^2 - \varepsilon_d \mathbf{I}_{e,h} \quad \hat{\Gamma} = \text{diag}(\Gamma_h, \Gamma_e) \quad \varepsilon_d = \varepsilon_r - \varepsilon_{re} \quad (7)$$

$\bar{I}_{e,h}$  are identity matrices.  $\bar{D}_h(\bar{D}_e)$  is the first order difference operator for the field component  $\mathbf{H}_y(\mathbf{E}_y)$  for the line in vertical direction which has to fulfill Neumann (Dirichlet) boundary conditions. The magnetic field at ports C and D resulting from the above field can be described by the equations

$$\begin{bmatrix} -j\mathbf{H}_{yC} \\ j\mathbf{H}_{yD} \end{bmatrix} = \begin{bmatrix} \mathbf{V}_{CA}^n & \mathbf{V}_{CB}^n \\ \mathbf{V}_{DA}^n & \mathbf{V}_{DB}^n \end{bmatrix} \begin{bmatrix} -j\bar{\mathbf{H}}_{yA} \\ j\bar{\mathbf{H}}_{yB} \end{bmatrix} \quad \begin{bmatrix} \mathbf{H}_{zC} \\ -\mathbf{H}_{zD} \end{bmatrix} = \begin{bmatrix} \mathbf{V}_{CA}^d & \mathbf{V}_{CB}^d \\ \mathbf{V}_{DA}^d & \mathbf{V}_{DB}^d \end{bmatrix} \begin{bmatrix} \bar{\mathbf{H}}_{zA} \\ -\bar{\mathbf{H}}_{zB} \end{bmatrix} \quad (8)$$

with

$$\begin{aligned} \mathbf{V}_{CA} &= \mathbf{A}_A \mathbf{T}_C^d & \mathbf{V}_{CB} &= -\mathbf{A}_B \mathbf{T}_C^d \\ \mathbf{V}_{DA} &= -\mathbf{A}_A \mathbf{T}_D^d & \mathbf{V}_{DB} &= \mathbf{A}_B \mathbf{T}_D^d \end{aligned} \quad (9)$$

where the diagonal matrices  $\mathbf{T}_{C,D}^d$  are obtained from  $\mathbf{T}_h$  and are necessary for calculating the field values on the boundary. The full matrices  $\mathbf{A}_A$  and  $\mathbf{A}_B$  are given by following components

$$(\mathbf{A}_A)_{ik} = \sinh(\Gamma_{hk}(\bar{d}_{AB} - \bar{z}_i)) (\sinh(\Gamma_{hk}\bar{d}_{AB}))^{-1} \quad (10)$$

$$(\mathbf{A}_B)_{ik} = \sinh(\Gamma_{hk}\bar{z}_i) (\sinh(\Gamma_{hk}\bar{d}_{AB}))^{-1} \quad (11)$$

$\bar{d}_{AB} = k_0 d_{AB}$  is the distance between the ports A and B normalized with respect to free space wavenumber  $k_0$ . The positions  $z_i$  have to be taken on the places of the horizontal lines. They are different for the  $\mathbf{H}_y$  and  $\mathbf{H}_z$  vectors. The matrix  $\mathbf{y}_{CD}^{AB}$  is constructed from the two equation systems in (7) by replacing  $\bar{\mathbf{H}}_{yA,B}$  from eq. (4) and  $\bar{\mathbf{H}}_{zA,B}$  by

$$\bar{\mathbf{H}}_{zA,B} = \begin{bmatrix} -\sqrt{\epsilon_{re}} \mathbf{I}_h & \bar{\delta}^t \end{bmatrix} \hat{\mathbf{E}}_{A,B} \quad (12)$$

The whole analysis can now be performed as an impedance/admittance matching process [2].

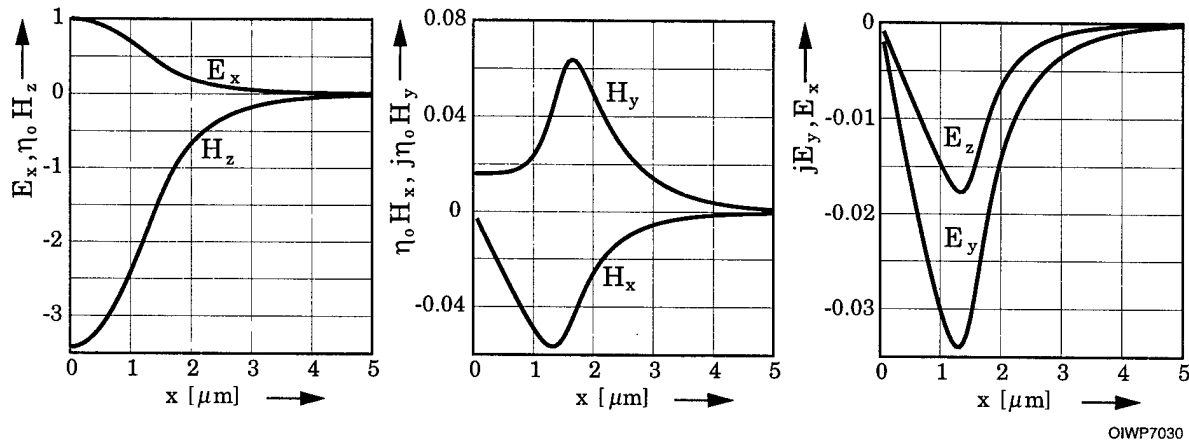


Fig. 4: Field distribution (normalized with respect to  $E_{x\max}$  of the fundamental TE mode in the center of the film layer of the benchmark test rib waveguide in [3] and  $t = 0.7$

**Numerical results:** The proposed algorithm is verified by numerical results for the rib waveguide of the benchmark test in [3] (see there TABLE 1). The normalized propagation constants differ slightly. Fig. 4 shows the distribution of the field components of fundamental quasi TE mode along the middle of the film layer demonstrating a highly accurate solution by the proposed method. Since the structure is symmetrical, only the right parts of all curves are shown.

## References

- [1] R. Pregla, "The Method of Lines for the Unified Analysis of Microstrip and Dielectric Waveguides", *Electromagnetics*, 15 (1995), pp. 441-456.
- [2] R. Pregla, "The Method of Lines as Generalized Transmission Line Technique for the Analysis of Multilayered Structures", *AEÜ*, Vol. 50, No. 5 (Sept. 1996), pp. 293-300.
- [3] C. Vassallo, "1993-1995 Optical mode solvers", *Optical and Quantum Electronics*, Vol. 29, No. 2 (Febr. 1997), pp. 95-114.

## A Hybrid Analysis Method for Er-doped Planar Devices

**A. Shooshtari**

Photonic Research Group, Ecole Polytechnique de Montreal, C.P. 6079, Succ. Centre-Ville, Montreal, Qc H3C 3A7, Canada  
Tel: (514)-340-4711, Fax: (514)-340-3218  
Email: shooshtari@email.phys.polymtl.ca

**S. Safavi-Naeini**

Department of Electrical and Computer Engineering, University of Waterloo, Waterloo, ON, N2L 3G1, Canada  
Tel: (519)-885-1211 X2822, Fax: (519)-746-3077  
Email: safavi@maxwell.uwaterloo.ca

### Introduction

Recently, Er<sup>3+</sup>-doped glass waveguide has been considered for fabrication of lossless or active devices. Planar lossless splitters at 1.5 μm, pumped at 980 nm were demonstrated in [1]. The existing analysis methods for Er-doped devices, such as the one presented in [2], are suitable only for straight channels. In this paper we present a new method based on a combination of the Beam Propagation Method (BPM) and the rate equations for the analysis of Er-doped planar devices.

### Outline of the method and the numerical results

*Complex Atomic Susceptibility* theory [3] is employed to derive an *equivalent* refractive index representing the effect of excited Er<sup>3+</sup>s. Let us consider an Er<sup>3+</sup>-doped optical device with the ordinary permittivity,  $\epsilon(x, y, z) = n^2(x, y, z)$ . Excited Er<sup>3+</sup> will modify the relative permittivity from  $\epsilon(x, y, z)$  to  $\epsilon_l^{eq} = \epsilon(x, y, z) + \bar{\epsilon}_l(x, y, z)$  for pump or signal wavelengths ( $l$  = pump or signal). The extra (active) term,  $\bar{\epsilon}_l$ , may have the positive (negative) imaginary part representing optical gain (loss):

$$\bar{\epsilon}_l(\omega, x, y, z) = \epsilon'_l + j\epsilon''_l, \quad \epsilon''_l = n(x, y, z) g_l / \omega_l \quad (1)$$

The parameter  $c$  represents the velocity of light in vacuum and  $\omega_l$  is the pump or the signal angular frequency. Optical gain,  $g_l$ , at the pump and signal wavelengths are given by :

$$g_{signal} = \sigma_{e21} N_2 - \sigma_{a12} N_1 \quad g_{pump} = \sigma_{e31} N_3 - \sigma_{a13} N_1 \quad (2)$$

where the parameters  $N_1$ ,  $N_2$ , and  $N_3$  are population densities in the ground state, metastable level and pump level (see Fig.1) respectively and  $\sigma_{eij}$  and  $\sigma_{aji}$  are the *emission* and *absorption* cross-sections between the  $i$  and  $j$  levels. Population densities,  $N_i(x, y, z)$ , depend on the intensity of the pump and the signal at  $(x, y, z)$  through the rate equations. Here we assume the Amplified Spontaneous Emissions (ASE) are much smaller than the pump and signal power and are neglected. The real part of relative permittivity,  $\epsilon'_l$ , although can be obtained by Kramers - Kronig relation, is very small compared with  $\epsilon$ , and is also omitted in the present analysis.

Based on  $\epsilon_l^{eq}$  we can formulate a *paraxial* scalar beam propagation equation for the main polarization component of the electric fields at the signal and pump wavelengths propagating along  $z$  [4]:

$$\frac{\partial}{\partial z} E_l(x, y, z) = -j \hat{\mathbf{H}}_l E_l, \quad \hat{\mathbf{H}}_l = \frac{1}{2n_0 k_l} \left[ \nabla_t^2 + k_l^2 (\epsilon_l^{eq} - n_0^2) \right], \quad l = \text{signal or pump} \quad (3)$$

where  $n_0$  is the reference refractive index and  $k_i$  is the wave-number in the vacuum at the signal and the pump wavelengths respectively. Assuming that the electric fields at the point  $z_0$  are known, we solve the rate equations for the population densities and obtain the equivalent relative permittivity,  $\bar{\epsilon}_1$ , at  $z_0$ . Then we proceed to calculate the electric field at  $z_0 + \Delta z$  by solving equation (3). This process continues along the device.

This method has been applied to several cases. The parameters of the glass shown in Table.1 and has been taken from [2]. We used a 2-dimensional ( $\partial/\partial y = 0$ ) finite difference method as in [4]. Therefore the pump and signal powers are expressed in terms of mW per unit length in y-direction. Channels are 2  $\mu\text{m}$  wide. The refractive indices of the core and cladding are 1.536 and 1.51 respectively. The signal and pump wavelengths are 1.531  $\mu\text{m}$  and 980 nm respectively. In all examples, the total device length is 9 mm, the input pump and signal powers are 10 mW /1  $\mu\text{m}$  and 10  $\mu\text{W}$  / 1  $\mu\text{m}$  y-direction respectively. The entire glass is uniformly doped with the erbium ions. The first example is a 9 mm straight ( 2-dimensional ) waveguide. Figure 2 shows the normalized intensity of the signal,  $|E_s(x,z)|^2$ , at several z-slices. The input signal power at  $z = 0$  has been assumed to be unity. As is shown in Fig. 2 the output signal power is 1.48 corresponding to a gain of 1.70 dB. A 9 mm splitter is chosen as the second example. The splitter structure is illustrated in Fig.3. The device is composed of two waveguides centered at  $\pm x$  where  $x$  is given by :

$x = R_t[1 - \cos(\pi z' / S_t)]/2$ . The parameters  $R_t$ ,  $S_t$ ,  $z'$  are shown in Fig. 3. Adding the output powers of the two branches we find that the total output from the device is about 1.61 times the input power.

Successful design of the planar active optical devices in Er-doped glass requires accurate analysis of the pump and the signal intensity profiles and radiation and scattering. The hybrid BPM method presented is a convenient tool for design and analysis of these types of optical devices.

## References

1. P. Camy, J.E. Roman, F.W. Willems, M. Hempstead, J.C. Van der Plaats, C. Prel, A.M.J. Koonen, J.S. Wilkinson, and C. Lermieux, "Ion exchanged planar loss-less splitter at 1.5  $\mu\text{m}$ ," *Electron. Lett.*, vol. 32, no.4, pp.321-323. 1996.
2. F. D. Pasquale and M. Zoboli, "Analysis of Erbium-doped waveguide amplifiers by a full-vectorial finite element method," *J. Lightwave Technol.*, vol. 11, no.10, pp.1565 -1574, May 1993.
3. Dessurvire, *Erbium Doped Fiber Amplifier*, J. Wiley & Sons Inc., New York 1994.
4. Y.Chung and N. Dagli, "Explicit finite difference beam propagation method: application to semiconductor rib waveguide Y- junction analysis," *Electron. Lett.* vol.26, no.11. pp.711-713, 1990.

Table.1 Parameters of the glass ,  $\text{Al}_2\text{O}_3 - \text{SiO}_2$  [4]

$\text{Er}^{3+}$ concentration, $N_{\text{OEr}}$	$1.0 \times 10^{+26} \text{ m}^{-3}$
$\text{Er}^{3+}$ emission cross section, $\sigma_{e21}$ ( 1.531 $\mu\text{m}$ )	$5.41 \times 10^{-25} \text{ m}^2$
$\text{Er}^{3+}$ absorption cross section, $\sigma_{a12}$ ( 1.531 $\mu\text{m}$ )	$5.36 \times 10^{-25} \text{ m}^2$
$\text{Er}^{3+}$ emission cross section, $\sigma_{e31}$ (980 nm )	0
$\text{Er}^{3+}$ absorption cross section, $\sigma_{a13}$ (980 nm )	$2.58 \times 10^{-25} \text{ m}^2$
$\text{Er}^{3+}$ emission life time, $\tau_{21}$	11 ms
$\text{Er}^{3+}$ non-radiative relaxation transition life time, $\tau_{32}$	1.0 ns

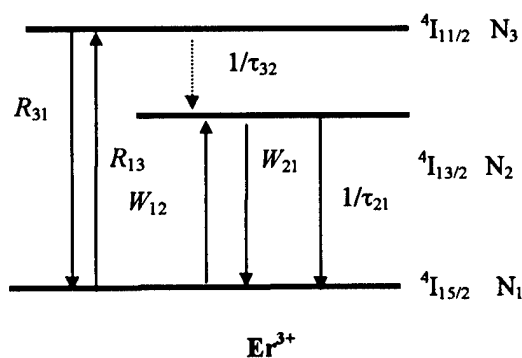


Fig.1. Energy level transitions for Erbium ions.

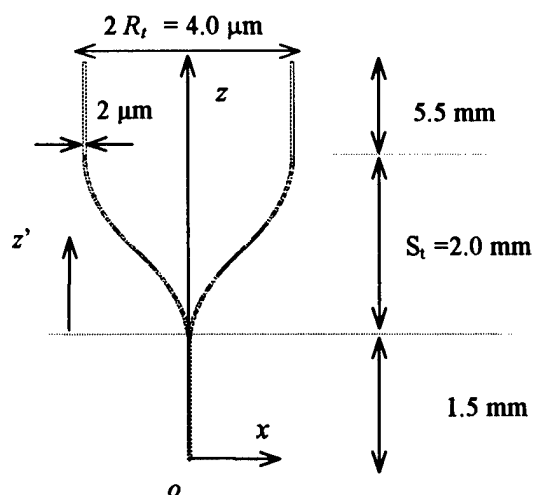


Fig. 3. An *Er* doped splitter with rectangular channel. The refractive index of the core and cladding are 1.536 and 1.51 respectively. The sizes are not in the same scale.

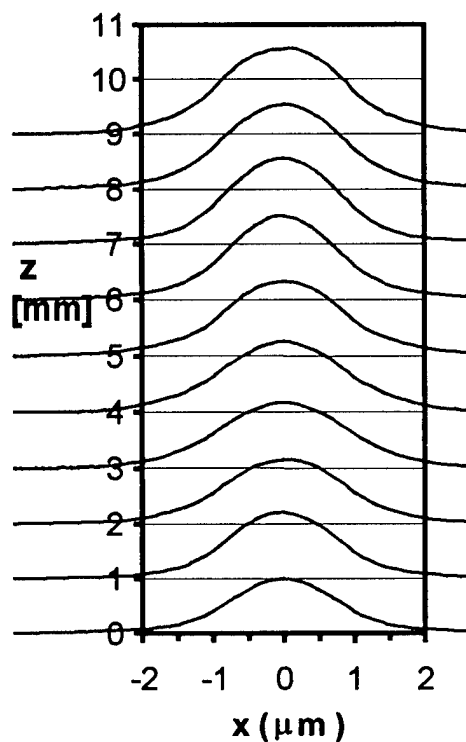


Fig. 2. The slices of signal intensity ( square of field ) in a 9 mm straight *Er*-doped waveguide.

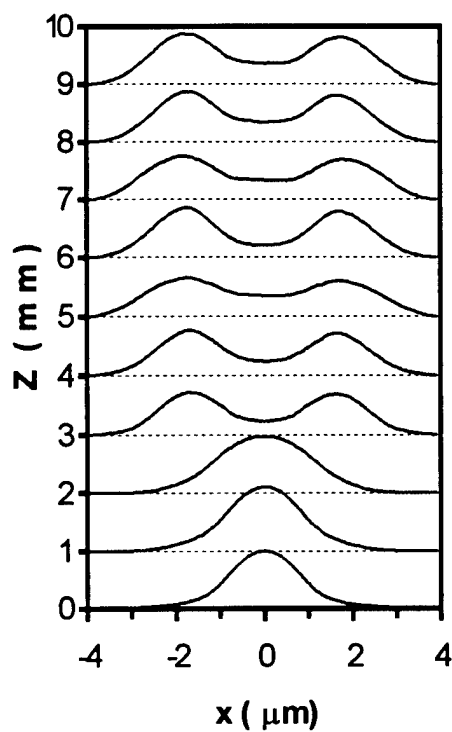


Fig.4. The slices of signal intensity ( square of field ) in a 9mm splitter. The dimensions of splitter are shown in Fig.3.

## Influence of laser linewidth on optical fiber transmission: modelling and measurement

C. M. Weinert, C. Caspar, H.-M. Foisel, B. Strebel

Heinrich-Hertz-Institut für Nachrichtentechnik Berlin GmbH  
Einsteinufer 37, D-10587 Berlin, Germany  
Tel. + 4930 31002 255/586, Fax. + 4930 31002 241

### Introduction

A topic of increasing importance for modelling is the investigation of the effects of components properties on optical signal transmission. To this aim, the isolated component has to be modelled as well as the complete fiber transmission line. For example, detailed knowledge of the optical transmitter properties is essential for the design of optical fiber links. We will here investigate the degradation of signal transmission by an enlarged laser linewidth. The phase noise [1] of a laser, observed as an enlarged linewidth is converted to intensity noise by fiber chromatic dispersion. In intensity modulated direct detected systems this phenomenon causes a signal to noise degradation [2] resulting in an additional limitation of optical transparency length.

In this work the penalty increase with the enhancement of transmitter laser linewidth is demonstrated in a 5Gb/s fiber loop experiments using different lasers. By numerical modelling of the linewidth effect on transmission, we show that the assumption of white Gaussian noise agrees qualitatively but not quantitatively with the measurements.

### Modelling of the laser linewidth

Following [1], the laser linewidth is modelled assuming that the variation of the electrical field  $E(t)$  due to random spontaneous emission:

$$\langle E(t)E(0) \rangle = |E(0)|^2 \exp(-|t|/t_c) \quad (1)$$

where  $t_c$  is the coherence time. The power spectrum of the laser is the Fourier transform of  $\langle E(t)E(0) \rangle$ . It is a Lorentzian and its full width at half maximum  $\Delta\nu$  is

$$\Delta\nu = (\pi t_c)^{-1} \quad (2)$$

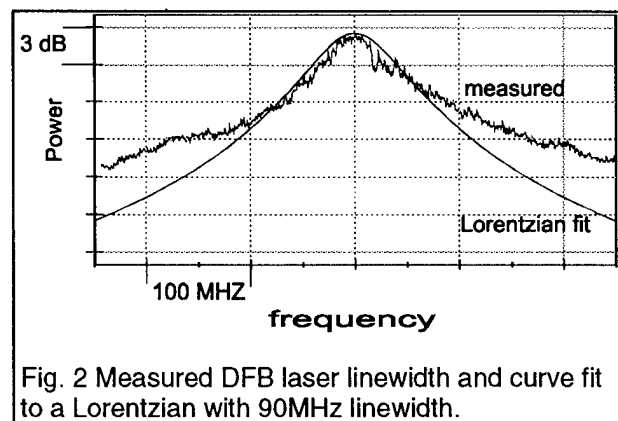


Fig. 2 Measured DFB laser linewidth and curve fit to a Lorentzian with 90MHz linewidth.

For Gaussian noise  $\Delta v$  is related to the variance of the phase noise  $\langle \Delta \Phi^2 \rangle / 2, 3/$  by:

$$\langle \Delta \Phi^2 \rangle = 2 \pi \Delta v t \quad (3)$$

where  $t$  are the sample points for the data signal. For the numerical simulation we use:

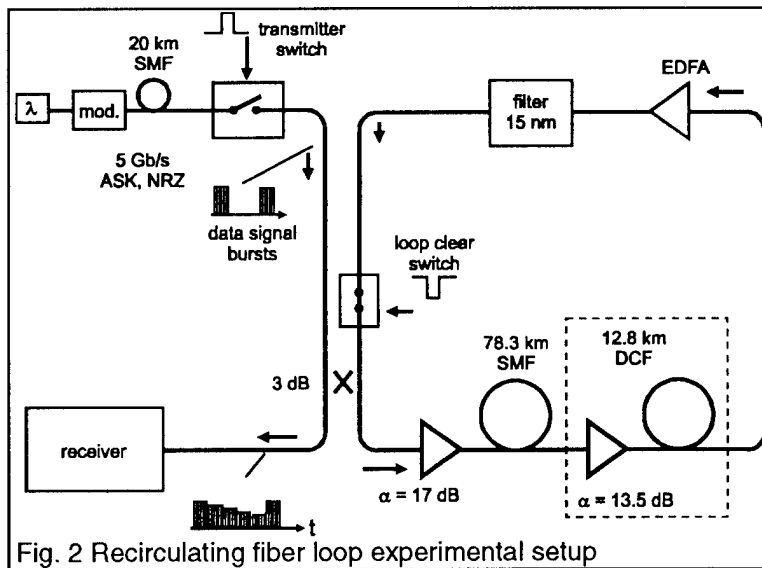
$$E(t) = (S(t))^{1/2} \exp(i \Delta \Phi) \quad (4)$$

where  $\Delta \Phi$  is a random variable with a variance given by equation (3).

In Fig. 1, we show the measured laser linewidth of a DFB laser together with the Lorentzian fit yielding a linewidth at half maximum of 90 MHz.

### Transmission experiment

Fig. 2 shows the experimental set up for a recirculating fiber loop experiment with a bit rate of 5Gb/s. The transmitter wavelength is 1551 nm. We have compared an external cavity laser with a linewidth of 0.1MHz, and a DFB laser with 90 MHz linewidth. The carrier wave is commonly external modulated by a PRBS signal, cut into signal bursts and sent into the fiber loop. The loop consists of 2 EDFAs, a 15nm filter and 78.3km standard single-mode fiber (SMF) with a dispersion of  $D = 17 \text{ ps}/(\text{nmkm})$ . The fiber input power amounted to 0dBm. For a comparison with compensated fiber trunks an additional dispersion compensating fiber (DCF) with 13.8km length and a further EDFA delivering a DCF input power of -2dBm could be inserted.



### Modelling of the fiber transmission

The transmission of this output wave over the SMF is calculated using the split step algorithm for the propagation equation including nonlinear effects and dispersion. First results of this calculations delivered much higher system penalties than found by experiment. In order to get an agreement between simulation and experiment for the bit error rate (Fig. 3) it was found, that only one fourth of the linewidth has to be inserted into the numerical phase noise description outlined above. This deviation

can be explained by the assumption, that the laser linewidth is only approximately Lorentzian and is only partially broadened by internal white noise. An advanced oscillator model would be necessary for a more exact description.

#### Transmission experiment

Fig. 3 shows measured and calculated bit error rates (BER) for the case of the dispersive standard SMF transmission for lasers with 0.1MHz and 90MHz linewidth. In agreement between measurement and theory we see a penalty increase due to enhanced linewidth in the standard SMF transmission (dashed and dashed-dotted lines). In order to prove that the signal degradation due to enlarged laser linewidth is induced by fiber dispersion, experiment and calculations were also done for the case of compensated chromatic dispersion. As seen from Fig.3 both measurement and simulation show that for this case the enlarged laser linewidth does not lead to an additional penalty (continuous and dotted lines). Thus, signal degradation due to laser phase noise can be avoided either by using lasers with narrow line widths or by using a dispersion compensated fiber trunk.

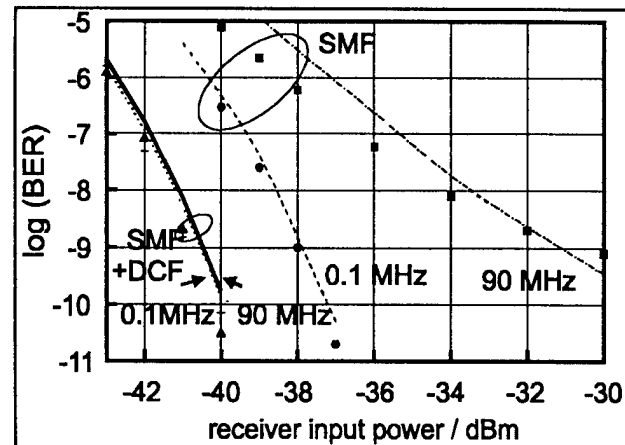


Fig. 3 Measured (symbols) and calculated (lines) BER for 5Gb/s single channel transmission over 313km of standard SMF and dispersion compensated SMF (+DCF) for lasers with 0.1MHz and 90MHz linewidths. Parameter: laser linewidth.

This work was performed under research contract with Deutsche Telekom AG.

#### References

- /1/ C. H. Henry, IEEE J. Quantum Electron., vol. QE-18, pp229-264, (1982)
- /2/ K. Petermann, J. Wang, Electron Lett, vol. 27, pp 2347-2348, (1991)
- /3/ A. Yariv, Optical Electronics, third edition, Holt, Reinehart and Winston, New York, (1985)

IMH15

Paper Withdrawn

## Analysis and Design of High Power DFB Lasers with Reduced Longitudinal Spatial Hole Burning

Jing-Yi Wang, Michael Cada

*Department of Electrical and Computer Engineering  
Dalhousie University Polytechnic, P.O.Box 1000, Halifax, N.S., B3J 2X4, Canada  
Tel: (902)420-7628, Fax: (902)420-7914, E-Mail: jwang@tuns.ca*

Toshihiko Makino

*Nortel Technology Inc., P.O. Box 3511, Station C,  
Ottawa, Ontario K1Y 4H7, Canada*

High power distributed feedback (DFB) lasers with stable single-longitudinal-mode operation are key components for long distance super-trunk fiber transmission links<sup>1</sup>. However, stability is not maintained at high optical power especially for devices with large coupling-length products due to the longitudinal spatial hole burning (SHB) of carrier density distribution resulting from a nonuniform optical power density distribution. Special laser structures with reduced SHB have been and are still being intensely investigated<sup>2,3,4</sup>, especially for high-power lasers<sup>5,6</sup>. In this communications, the coupled-power theory is employed to study high power DFB lasers. First, a set of nonlinear coupled-power equations for high power DFB lasers is derived. Second, a general condition for reduced SHB is obtained. This allows one to design novel high power DFB structures with the SHB completely eliminated.

For high power DFB lasers, a power-dependent refractive index should be considered, especially for active media such as GaAs, InGaAsP etc.. We start with the scalar wave equation for the electric field describing DFB lasers<sup>7</sup>. Assuming that the refractive index  $n(I)$  may be written as  $(n+n_2I)$ , the propagation constant  $k$  can then be determined from

$$k^2 = \frac{\omega^2}{c^2} \epsilon \left( 1 + 2 \frac{n_2}{n} I \right) - j\omega\mu\sigma, \quad (1)$$

where the same notation for parameters as in Ref. [7] is used.  $n_2$  is the optical nonlinear coefficient. In the following discussions, the index and gain coupling coefficients are denoted as  $\kappa_i$  and  $\kappa_g$ ;  $\alpha$  denotes the net mode gain per unit length;  $\delta_0$  ( $\delta_0 \approx \beta - \beta_0$ ) represents the Bragg deviation; the amplitudes of the forward and backward propagating waves are denoted as  $E^+(z)$  and  $E^-(z)$ . We assume in-phase or anti-phase relations between the index and gain coupling coefficients. This corresponds to practical cases. We introduce the power density variables  $I_t(z) = E^+(z)E^{+*}(z) + E^-(z)E^{-*}(z)$ ,  $I_d(z) = E^+(z)E^{+*}(z) - E^-(z)E^{-*}(z)$ , and  $I_c(z) = 2E^{+*}(z)E^-(z) \equiv I_{cr}(z) + jI_{ci}(z)$ , where  $I_t(z)$  describes the total photon power density along the cavity,  $I_d(z)$  is the net photon power density flux along the cavity, and  $I_c(z)$  is the power density of the mutual interaction along the cavity between the forward and backward waves due to coupling.  $I_c(z)$  describes the mutual interaction strength and phase relations between the forward and backward waves. Using the above new power density

variables, the DFB structure can be described by the following set of nonlinear coupled-power equations<sup>8</sup>:

$$\frac{dI_d(z)}{dz} = 2(\alpha L)I_i(z) \pm 2(\kappa_g L)I_{cr}(z) \quad (2)$$

$$\frac{dI_i(z)}{dz} = 2(\alpha L)I_d(z) - 2(\kappa_i L)I_{ci}(z) \quad (3)$$

$$\frac{dI_{cr}(z)}{dz} = 2(\delta L)I_{ci}(z) \mp 2(\kappa_g L)I_d(z) \quad (4)$$

$$\frac{dI_{ci}(z)}{dz} = -2(\delta L)I_{cr}(z) - 2(\kappa_i L)I_i(z). \quad (5)$$

Here all power densities are normalized with respect to  $I_s$  which is a normalizing quantity. The cavity longitudinal axis  $z$  is normalized with respect to the cavity length  $L$  and

$$(\delta L) = (\delta_0 L) + (\Theta L)I_i, \quad (\Theta L) = \frac{(\beta_0 L)n_2 I_s}{2\eta_0}. \quad (6)$$

The upper and lower signs in the above equations represent in-phase and anti-phase coupling, respectively. Eqs.(2-5) represent general coupled-power equations for high power DFB lasers and describe the power exchange between the forward and backward waves along the cavity due to coupling.

We note that a direct result of Eq.(3) is that the SHB can be completely eliminated if the following condition is satisfied

$$(\alpha L)I_d(z) = (\kappa_i L)I_{ci}(z). \quad (7)$$

This is a general condition eliminating the SHB irrespective of the boundary conditions. We have proposed, based on Eq.(7), some coupling profiles for reduced SHB in a DFB laser with a perfect AR-coating of the facets, and characterized main features of these lasers. Main results are summarized as follows:

- (1) The optical nonlinear effect must be considered in the design of high-power laser structures with reduced SHB (i.e., stable single-longitudinal-mode operation).
- (2) The complex-coupled DFB structures with a reduced SHB can be employed to reduce the threshold current compared with the index-coupled DFB structures with a reduced SHB.
- (3) A uniform power density results from the power exchange between the net photon power density flux and the power density of the mutual interaction. In fact, we can easily prove that  $I_d^2(z) + I_{cr}^2(z) + I_{ci}^2(z) = I$ . Here,  $I_i(z=0)$  was used as the normalizing quantity  $I_s$ . This is a general relation of the power exchange between the net photon power density flux and the power density of the mutual interaction necessary for elimination of the SHB in DFB lasers with a perfect AR-coating of the facets.
- (4) The phase difference between the forward and backward waves is locked along the cavity.

In conclusion, a set of nonlinear coupled-power equations for high power DFB laser diodes operating near the Bragg frequency has been derived. It is shown that these

equations lead in a straightforward way to a general condition for DFB lasers with eliminated SHB. For perfectly AR-coated facets, it is shown that a uniform power distribution results from the power exchange between the net photon power density flux and the power density of the mutual interaction of the forward and backward waves. Coupling profiles for reducing SHB have been designed.

M. Cada acknowledges support from Natural Sciences and Engineering Research Council (NSERC) and from Nortel Technology, Inc., both of Canada.

## References

1. Chen, J. Ungar, J. Iannelli, S. Oh, H. Liong and N. Bar-Chaim, "High power operation of InGaAsP/InP multi-quantum well DFB lasers at 1.55  $\mu\text{m}$  wavelength," *Electronics Letters*, Vol.32, No.10 (1996) 898.
2. Agrawal and A. H. Bobeck, "Modeling of distributed feedback semiconductor lasers with axially-varying parameters," *IEEE J. Quantum Electronics*, Vol. 24, No.12 (1988) 2407-2414.
3. Himura and A. Sugimura, "Linewidth reduction by coupled phase-shift distributed-feedback lasers," *Electron. Lett.*, Vol. 23, No. 19 (1987) 1014-1015.
4. Morthier and R. Baets, "Design of index-coupled DFB lasers with reduced longitudinal spatial hole burning," *J. Lightwave Tech.*, Vol. 9, No.10 (1991) 1305-1313.
5. F. Yu, C. W. Lo and E. H. Li, "High-power single-mode operation in DFB and FP lasers using diffused quantum-well structure," *IEEE J. Quantum Electronics*, Vol. 33, No.6 (1997) 999-1009.
6. C. -Y. Wang, Z. -M. Chuang, W. Lin, Y. -K. Tu and C. -T Lee, "Low-chirp and high-power 1.55- $\mu\text{m}$  strained-quantum-well complex-coupled DFB laser," *IEEE Photonics Technology Letters*, vol. 8, No. 3 (1996) 331-333.
7. Kogelnik and C. V. Shank, "Coupled-wave theory of distributed feedback lasers," *J. Appl. Phys.*, Vol. 43, No. 5 (1972) 2327-2335.
8. J. -Y. Wang, M. Cada and T. Makino, submitted to PTL.

## Modeling a distributed spatial filter low-noise semiconductor optical amplifier

R. P. Ratowsky, S. Dijaili, J. S. Kallman, M. D. Feit,  
J. Walker, W. Goward, and M. Lowry

University of California  
Lawrence Livermore National Laboratory  
Livermore, CA, 94550

A fundamental limit to the signal-to-noise ratio (SNR) obtainable in an optical amplifier is the amplified spontaneous emission (ASE) power couple into the signal mode. It has been realized since the invention of the laser that ASE noise can be minimized by appropriate spatial filtering of the laser output: Since the signal occupies a much smaller solid angle than the isotropic noise, the noise can be limited by simply limiting the angular aperture at the output [1].

Using a geometrical ray model for the noise, the ASE power in a bandwidth  $\Delta\nu$  into a solid angle  $\Delta\Omega$  can be calculated from the formula [1]

$$P_{ASE} = \mu (G - 1) A \frac{\Delta\Omega}{4\pi} h\nu \Delta\nu,$$

where  $\mu = N_2 / (N_2 - N_1)$  is the population inversion factor,  $G$  is the signal gain,  $\Delta\Omega$  is the solid angle subtended by the system aperture, and  $A$  is the aperture area. However, this expression assumes that the gain of the ASE is equal to the gain of the signal. For a single-mode high-gain amplifier, this is a valid assumption, since the appropriate gain is just that of the propagating mode. For the case of low gain, many non-orthogonal modes are present, and the SE emission into the all the modes contributes to the noise power in the signal. This leads to the so-called "excess noise" phenomenon, whereby longitudinally inhomogeneous gain gives the appearance of more than one noise photon per mode when extrapolated back to the source [2].

A design for a low-noise optical amplifier was recently proposed which exploits the multimode transient phase of propagation in a SOA [3]. In this design, the gain region is divided into a number of sections, with free-space diffraction regions between them (see Fig. 1). We call this geometry

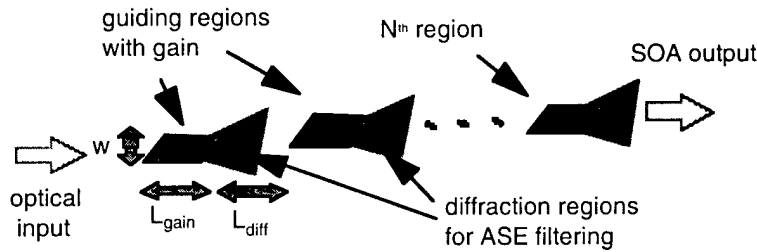


Fig. 1. Geometry of low-noise distributed spatial filter SOA

“distributed spatial filtering” (DSF). By keeping the gain-length product in each section small enough, the divergent ASE power is stripped before the single-mode state is reached and hence inhibits the ASE coupled into the signal mode. By distributing the spatial filtering using multiple sections, the stripping of the ASE occurs differentially for maximum effect.

To verify these ideas, we modeled the DSF low-noise SOA using a 2-dimensional FFT-based Beam Propagation Method, which solves a wide-angle paraxial wave equation. Spontaneous emission was treated as a randomly phased source throughout the laser. The amplitude of the SE was determined by demanding consistency between the paraxial equation and the radiation transport equation for the noise [4]. Observables such as field distributions and ASE power were calculated by ensemble average over realizations of the sources. Gain saturation was also included, although no detailed carrier dynamics was carried out.

In the following calculations we chose  $L_{\text{gain}} = L_{\text{diff}} = 50 \mu\text{m}$ ,  $w = 3.5 \mu\text{m}$ , and  $\lambda = 0.9 \mu\text{m}$ . The electric field intensity for a typical realization of the SE propagation is shown in Fig. 2. The diffraction of the ASE in the free-space regions is strikingly visible in this image.

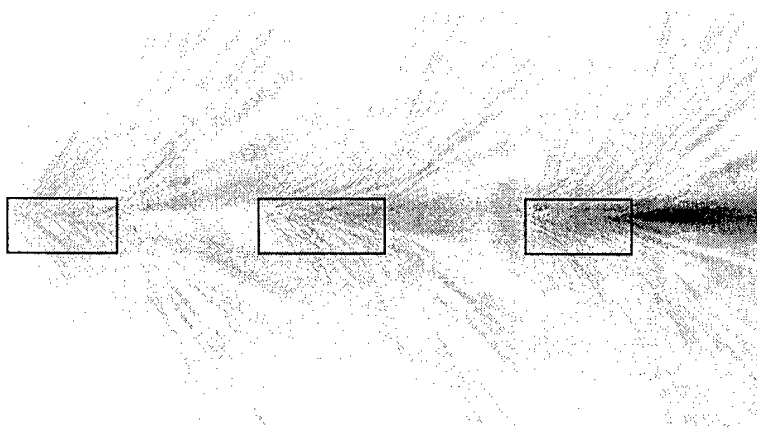


Fig. 2. Electric field intensity for three-stage DSF SOA

as mode selection due to propagation occurs, the multimode condition is lost. Next we look at the SNR (defined here as ratio of signal power to ASE power [1], valid for  $G \gg 1$ ). Fig. 4 shows that there is an optimal value of the gain for two stage spatial filtering, by showing the ratios of the SNR's, for 2-stage DSF compared with no DSF.

Finally, if we plot the ratio of signal power to ASE power as a function of the number of DSF stages (Fig. 5), we see a sharp, possibly exponential,

In Fig. 3, we compare the total ASE power as a function of the signal gain for a DSF SOA for 2 stages of filtering with a conventional SOA with the same gain-length product. We see that (1) there is a ~15 dB improvement in the ASE power for gains up to ~30 dB, and that (2) the improvement

increase. This apparently verifies the differential nature of the effect. As the number of stages increases further, we would expect to see the improvement saturate as mode selection occurs in the SOA. Work is currently underway to optimize and fabricate the DSF SOA.

This work was performed under the auspices of the U.S. Department of Energy under contract W-7405-ENG-48.

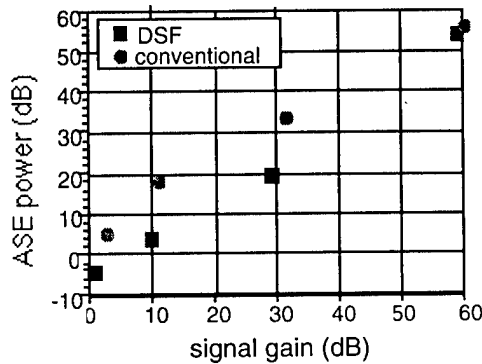


Fig. 3. ASE power vs. signal gain for a conventional and 2-stage DSF SOA

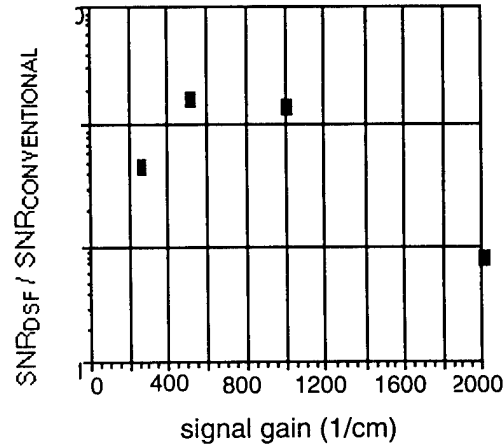


Fig. 4. Ratio of SNR's for 2-stage DSF to conventional SOA vs. signal gain

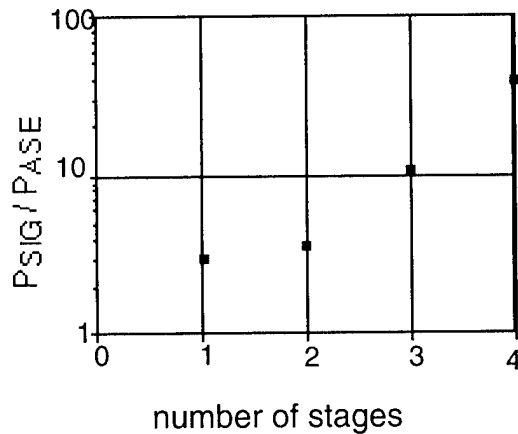


Fig. 5.  $P_{\text{SIG}}/P_{\text{ASE}}$  (SNR) growth with number of DSF SOA stages

#### References.

- [1] H. Kogelnik and A. Yariv, "Considerations of noise and schemes for its reduction in laser amplifiers", *Proc. IEEE* **52**, 165 (1964); A. Yariv, *Quantum Electronics*, John Wiley & Sons, New York, Chapter 21 (1989).
- [2] A. E. Siegman, "Excess spontaneous emission in non-Hermitian optical systems. I. Laser amplifiers," *Phys. Rev. A* **39**, 1253-1263 (1989); I. H. Deutsch, J. C. Garrison and E. M. Wright, "Excess noise in gain-guided amplifiers", *JOSA* **B8**, 1244 (1991).
- [3] S. P. Dijaili, F. G. Patterson, R. J. Deri, "Cross-talk free, low-noise optical amplifier, U. S. Patent Number 5,436,759 (1995).
- [4] M. D. Feit and J. A. Fleck, "Wave-optics description of laboratory soft x-ray lasers", *JOSA* **B7**, 2048 (1990).

## Optimising a multi-wavelength laser design using an expert system based approach

D. Van Thourhout, T. Van Caenegem, R. Baets

University of Gent, IMEC

St. Pietersnieuwstraat 41, B- 9000 Gent, Belgium

Tel + 32 9 2643324 Fax + 32 9 2643593 Email [driesvt@intec.rug.ac.be](mailto:driesvt@intec.rug.ac.be)

### Introduction

During the last few years relatively complex integrated optical circuits or Photonic Integrated Circuits (PICs) were demonstrated at laboratory level and a few, mainly passive, are commercially available now. However, the progress is slowed down by the complex technology required to integrate dissimilar devices, and the experimental trial-and-error process is costly and time consuming. Advanced design tools can have an important role to minimise this process. Although powerful simulation tools are available today, which can help to understand the experimental results and can reduce the number of experimental iteration steps, the situation is still far from ideal. Roughly speaking there are two problems and their solutions are rather incompatible. The first problem relates to accuracy, a various levels in the design. The device structure can be oversimplified (e.g. neglect of interface roughness) or inaccurately defined (e.g. inaccurate refractive index), the model can be simplified and also the numerical implementation may give rise to errors (e.g. grid size). The second problem relates to calculation time. Although the solution for the accuracy problem seems clear in the case of simple structures (use of more rigorous methods, better definition of applicability range, sensitivity studies to parameter uncertainties), calculation time becomes an issue for more complicated structures, built of many components. Furthermore when active devices are involved, the optical field modelling needs to be combined with the electrical and thermal modelling. Today it's not conceivable that rigorous electromagnetic solvers will become so time efficient that complex system calculation or extensive optimisation will become practical.

A possible solution is to move towards a knowledge driven tool, which contains, for a given PIC-technology, validated information for a range of basic waveguide elements. The knowledge base may contain information in different forms. It may be restricted to a library of well designed waveguide elements, it may be a table, containing data for a parametrised waveguide, or it may be a set of formulas and design rules, describing the behaviour of a component over the allowed parameter range. The information may be validated by experimental results or by rigorous calculation. In an advanced system, the database could also contain knowledge of a human expert. The other important part of the expert system is the inference engine: the analysis of a design is no longer carried out by field calculation as such but rather by intelligent combination and manipulation of previously obtained data. Based on the information held in the database, the global optimisation of a PIC or a sensitivity analysis are performed by a data flow oriented circuit simulation. Next to the knowledge base and the inference engine, a practical useful expert system will also require a (symbolic) circuit definition tool and an interface to a mask layout generator.

In this paper these ideas are illustrated by an example: the design of a multi-wavelength laser, where the challenge is to find the best waveguide design for both the active and the passive waveguide sections.

### Global optimisation of a multi-wavelength laser

We consider a multi-wavelength laser (MWL) that is realised by monolithic integration of amplifiers and a multiplexer in one cavity and in which a taper is used at the output facet to improve the coupling efficiency to fibre (*Figure 1a*). The integration is done by selective area growth: the layer stack, containing QW-layers, is grown in one time all over the wafer. Oxide stripes besides the amplifiers locally enhance the growth of the semiconductor material in the gap between the stripes (*Figure 1b*), resulting in a smaller effective bandgap of the QWs in the active region compared to the effective bandgap of the QWs in the planarly grown region. All waveguides are (dry) etched in one step and both active and passive waveguides are equally doped. The device should be optimised towards different goals: maximum differential efficiency to fibre, minimum threshold current, central wavelength within a certain range, minimum modulation bandwidth... Several primary design parameters have to be defined: material composition, layer thickness, number of QWs, waveguide width, device length, etch depth and doping level. These primary design parameters define others like the confinement factor in the QWs, the scattering and absorption loss, the minimum bend radius and the number of transversal modes. Some of the primary design parameters can be separately optimised for each device of the PIC (e.g. amplifier length and waveguide widths), others are constant over the wafer (e.g. etch depth) or are interdependent (due to the selective growth, the thickness of the layers in the active regions is one and a half time the thickness of the layers in the passive regions). The parametrised waveguide

is defined in Figure 1c and a database containing the following data for the structure is built: propagation constants, confinement factors in the QWs and in the doped cladding regions, integrated field strengths at the waveguide - air interfaces and lateral index contrast. From these parameters, it is easy to calculate other parameters such as the scattering and absorption loss of the waveguide and its minimum bend radius, using simple models. Afterwards these simple models were verified using rigorous calculation methods and experimental data.

The minimum bend radius is determined by choosing the radiation loss in the bends to be smaller than a certain value (typical  $\alpha_{rad} < 10^{-2} \text{ dB/90}^\circ$ ). In that case, the loss in the passive waveguides is restricted to scattering and absorption loss. The scattering loss is given by:

$$\alpha_{scat} = C \frac{E_s^2 \Delta n}{P} \quad (1)$$

$E_s$  being the field strength at the waveguide boundary,  $\Delta n$  the refractive index contrast and  $C$  an empirical constant, depending on the used etching process.  $C$  is determined by fitting experimental results to formula (1). The absorption loss is calculated as the sum of losses due to free carrier absorption in all fractions of the waveguide:

$$\alpha_{abs} = \sum \Gamma_{cl,i} \alpha_{dop,i} \quad (2)$$

The total length of the passive device is considered to be proportional with  $R_{min}$ , so the total loss in the passive part of the PIC is given by:

$$\alpha_{pass} = \zeta R_{min} (\alpha_{scat} + \alpha_{abs}) \quad (3)$$

$\zeta$  depends on the specific passive device and in this case we chose  $\zeta = 8$ . The important parameters in the active region are the confinement factor in the active layers, which is stored in our database and the material gain as function of current density. The latter was determined experimentally by fitting the function

$$J = J_0 \exp\left(\frac{g}{g_0} - 1\right)$$

proposed by Mc Ilroy [2], to experimental data. The threshold gain for the MWL is:

$$g_{th} = \frac{1}{\Gamma_{QW} L_u} \left( L_u \alpha_u + \alpha_{pass} + \frac{1}{2} \ln\left(\frac{1}{R_1 R_2}\right) \right)$$

Another parameter determining the performance of the laser is the series resistance  $R_s$ , which is inversely proportional with the doping level in the cladding layers [3]. Reducing the doping level will result in a lower absorption loss in the passive region but also in an increase of the series resistance  $R_s$ . To avoid thermal and modulation problems we want the series resistance  $R_s$  to be at most twice as high as in our standard laser structures. This determines the minimum doping level and, using (2), the minimum absorption loss in the waveguides.

After storing all this “knowledge” into a database, it is possible to use the latter to optimise the design of the MWL. We try to minimise the current  $I_{bias}$ , needed to obtain a certain power  $P_{out}$  into fibre:

$$I_{bias} = I_{th} + \xi \frac{1}{\eta_{ext}} \frac{e}{h\nu} P_{out}$$

$\xi$  being the coupling efficiency to fibre. This goal involves both threshold and internal efficiency. The optimisation process is illustrated by Figure 2. We limit the discussion here to the case where the width of the waveguides is constant ( $W=2\mu\text{m}$ ). Figure 2a shows the loss of the passive part, calculated using (3). As expected, this loss decreases for thicker guiding layers and greater etching depths. Since the optimal value for the confinement  $\Gamma_{cl}$  is located in the opposite corner (Figure 2b), it is clear that the minimum value for  $I_{bias}$  will be located somewhere in the centre of the investigated parameter space (Figure 2c). For an amplifier length of  $600\mu\text{m}$  and four quantum well layers, the optimal film layer thickness is  $800\text{nm}$  ( $530\text{nm}$  in the passive region) and the optimal etch depth is  $50\text{nm}$  ( $200\text{nm}$  in the passive region), resulting in a bias current of  $56\text{mA}$ . By repeating this optimisation for different values for the amplifier length, the optimal amplifier length can be calculated (Figure 2d).

### Conclusion

We built a database containing tables, formulas and rules. Using this knowledge base, we could optimise the design of a multi-wavelength laser. We believe such an expert system based approach can be a solution for the restrictions of the currently available CAD-tools with respect to calculation time and accuracy.

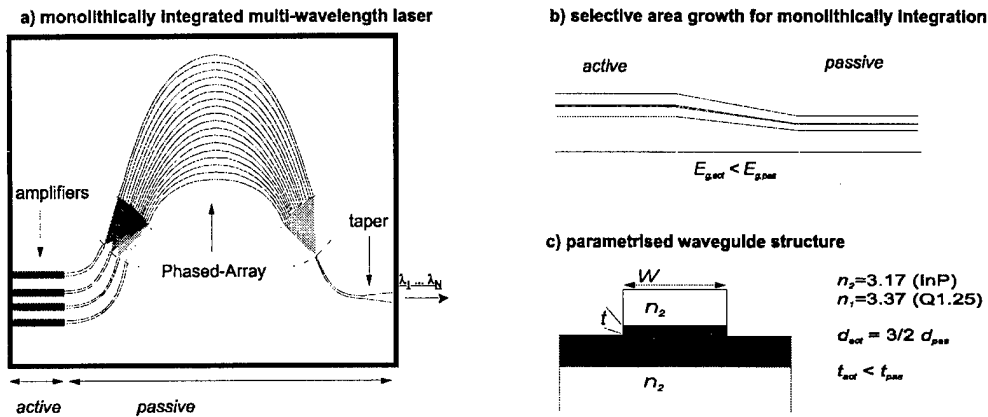


Figure 1 a) monolithically integrated multi-wavelength laser b) selective area growth c) parametrised waveguide: although the total etch depth is constant all over the wafer, it isn't constant due to the different layer thicknesses in active and passive regions.

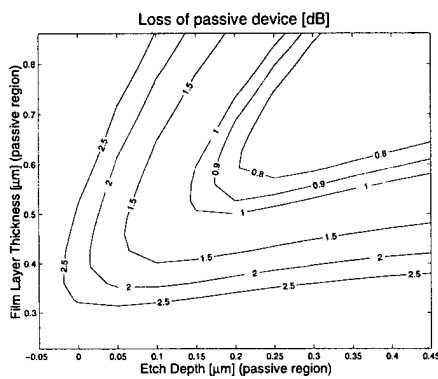
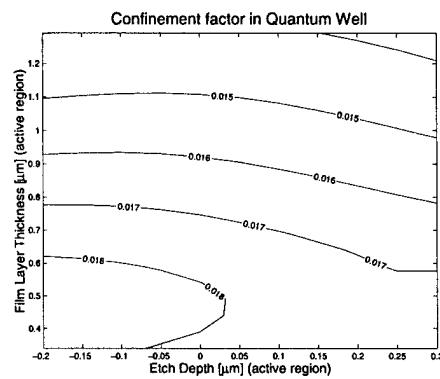


Figure 2 a) Total loss of passive device



b) Confinement factor  $\Gamma$  in active region

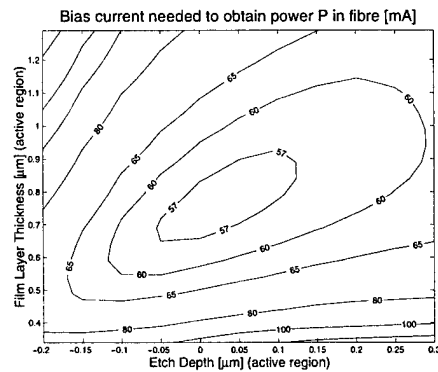
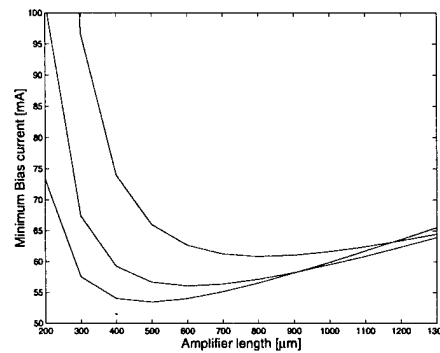


Figure 2 c)  $I_{bias}$  for 600 μm long laser with 4 QWs



d)  $I_{bias}$  for lasers with 3, 4 and 5 QWs

- [1] I. MOERMAN, T. VAN CAENEGEM, P. VAN DAELE, P. DEMEESTER, "MOVPE-based localised epitaxial growth techniques and its applications", IPRM '97 proceedings, Hyannis, MA.
- [2] P.W. MC ILROY, A. KUROBE, Y. UEMATSU, "Analysis and application of theoretical gain curves to the design of multi-quantum-well lasers", JQE, Vol. QE-21, No. 12, 1985, pp. 1958-1963.
- [3] G. MORTHIER, P. VANKWIKELBERGE, "Handbook of distributed Feedback Laser Diodes", Artech House 1997

DVT and TVC acknowledge the Flemish IWT for a doctoral grant. The ACTS project BLISS, partly funded by the European Union, is also acknowledged.

## Buried waveguides in a 1.5 $\mu$ m InGaAs/InGaAsP structure fabricated by ion-induced quantum well intermixing

J.E. Haysom\*, J.J. He, P.J. Poole, Emil S. Koteles, A. Delage, Y. Feng, and S. Charbonneau<sup>§</sup>

Institute for Microstructural Sciences, National Research Council Canada,

Montreal Road, Building M23A, Ottawa, Ontario, Canada K1A 0R6.

Ph: 613-993-7458 Fax: 613-952-8701 Email: joan.haysom@nrc.ca

\*also graduate student at University of Ottawa Department of Physics

<sup>§</sup> also Adjunct Professor at University of Ottawa Department of Physics

### Introduction

Quantum well intermixing (QWI) has been shown to be a powerful method for inducing post-growth modifications of the bandgap and optical properties of quantum well (QW) structures. The blueshift of the energy bandgap, which results from the intermixing process, also induces a decrease in the refractive index of the QWs<sup>1</sup>. This property has been used to create devices with lateral optical confinement, including waveguides<sup>2</sup> and index-guided lasers and modulators in GaAs/AlGaAs<sup>3,4,5</sup> and waveguides in InGaAs(P)/InP<sup>6,7,8</sup>. In this paper we buried waveguides (BWG) fabricated in an InGaAs/InGaAsP laser structure fabricated by the QWI process, and we evaluate the refractive index change,  $\Delta n$ , caused by QWI. We use high energy ion implantation of non-impurity species (phosphorous) to intermix the deep multi-quantum well structure without altering any electrical characteristics of the p-i-n structure<sup>9,10</sup>. To our knowledge, this is the first work of this nature on an InP-based laser structure. This technique is potentially useful for the integration of passive devices with active ones, and for the fabrication of index-guided buried-heterostructure lasers.

### Experiment

The structure used in this study was an MOCVD grown 1.52 $\mu$ m InGaAs/InGaAsP lattice matched laser structure. The active region consists of five 6nm In<sub>0.53</sub>Ga<sub>0.47</sub>As quantum wells surrounded by six 20nm In<sub>0.74</sub>Ga<sub>0.26</sub>As<sub>0.57</sub>P<sub>0.43</sub> barriers (all undoped), with another 50nm of doped quaternary above and below the active region<sup>11</sup>. The uppermost QW is situated 1.77 $\mu$ m below the surface. The sample was implanted with 1.0 MeV phosphorous ions to a dose of  $1.0 \times 10^{14}$  cm<sup>-2</sup> and annealed at 675°C for 180 seconds<sup>11</sup>. A patterned SiO<sub>2</sub> layer was used to mask selected areas during implantation, then removed before annealing. A blueshift of 40meV was observed between the photoluminescence peaks of implanted and masked regions (i.e. between the intermixed and as-grown regions).

The waveguides of this study consist of a narrow stripe of as-grown (non-intermixed) material, defined by SiO<sub>2</sub> implantation mask stripes, surrounded by implanted and intermixed regions. The difference in refractive index between as-grown and intermixed material results in index guiding. Large implanted and masked area, located elsewhere on the sample, were used to make slab waveguide (SWG) measurements of as-grown and intermixed material. The sample was cleaved to form a 1.0mm long Fabry-Perot cavity. Measurements were performed using a tunable (1.45 – 1.59 $\mu$ m) diode laser, modulated at 10kHz, and detected using a Ge detector and lock-in amplifier. Polarization-preserving fibers were used to couple light into the waveguides and to collect transmitted light; lenses at the fiber ends focused to a spot size of approximately 2  $\mu$ m.

### Results

Figure 1 shows the transmission spectra (which have been smoothed and normalized) for four different waveguides: intermixed and as-grown SWGs, and BWGs formed using 6.0 $\mu$ m and 4.5 $\mu$ m stripes. BWGs fabricated with narrower stripes had very low transmission intensities (similar to the intermixed SWG), as would be expected considering the very large degree of intermixing under narrower mask stripes. There are two important characteristics of the transmission spectra which are worth discussing. First, for the longer wavelengths, the transmission intensity of the BWGs decrease at a much faster rate than for the SWGs, indicative of a decrease in the BWGs ability to guide the light. Second, the bandedges of the TE and TM modes for the masked SWG do not coincide, as is expected for a QW structure, but they do coincide (to within 2-3 nm) in the case of the intermixed SWG. We attribute this to a build-up of tensile strain in the QW due to higher diffusion rates on the group V sublattice over the group III sublattice, as has been seen previously in this structure<sup>12</sup>. The tensile strain has shifted the heavy-hole and light-hole bands such that they overlap. The 4.5 $\mu$ m and 6.0 $\mu$ m BWGs exhibit a

reduced birefringence in comparison to the original material (the as-grown SWG). We postulate that with a larger degree of intermixing, such that TM bandedge is at shorter wavelengths than the TE bandedge in the "lateral cladding", it may be possible to achieve a polarization insensitive buried heterostructure.

The transmission spectra shown in Figure 1 have been smoothed for clarity, thus removing the high frequency Fabry-Perot interference fringes formed owing to multiple reflections at the cleaved facets. The intensity contrast of these Fabry-Perot fringes were used to calculate absorption losses and the refractive index<sup>13</sup>. For TE polarization and the 6.0µm BWG, the losses were found to be 180dB/cm at  $\lambda=1.52\mu\text{m}$  (the lasing wavelength of original material) but the values decreases to a minimum of 40dB/cm at  $\lambda=1.56\mu\text{m}$ . For the 4.5µm BWG, the losses were lower: 75dB/cm at  $\lambda=1.52\mu\text{m}$  with a minimum value of 30dB/cm at  $\lambda=1.55\mu\text{m}$ . The lower values for the 4.5µm BWG are expected since its bandedge has shifted further away from the as-grown bandedge. Here again, a larger degree of intermixing could be advantageous, allowing for reduced absorption losses at the as-grown wavelength.

The refractive index is calculated from the frequency of the Fabry-Perot fringes<sup>13</sup> and results are shown in Figure 2. The decrease in the refractive index due to QWI can be taken as the difference between the as-grown and intermixed SWGs measurements. This difference decreases at longer wavelengths, which results in weaker guiding as was seen in the transmission spectra. Between 1.58µm and 1.54µm we obtain values for  $\Delta n$  of 1.2 - 2.8% for TE, and 0.6 - 0.9% for TM. These values will increase at shorter wavelengths, but absorption losses will also increase. The effective refractive index of BWG structures lie in between the as-grown and intermixed SWG refractive indices, as expected. The narrower BWG is closer to the intermixed SWG due to a larger percentage of intermixing under a narrow mask.

To evaluate the modal behaviour, near field scans of the output beam are taken for different positions of the input beam. The 4.5µm BWG showed single mode guiding for  $\lambda=1.52\mu\text{m}$  and longer for both TE and TM polarizations (profiles for shorter wavelengths are not easily evaluated due to high absorption losses). The near field profiles for the 6.0µm BWG at  $\lambda=1.56\mu\text{m}$  indicate multimode

behaviour. The transition from multimode to single mode behaviour for this waveguide was found to occur at approximately 1.57µm, for both TE and TM modes.

## Conclusion

The highly selective nature of ion-induced QWI allows for the fabrication of narrow, index-guiding buried heterostructures, where refractive index differences are of the order of a few percent. In this paper, devices exhibited both single mode and multimode guiding, depending on the wavelength and guide width. A lower degree of intermixing should result in less confinement and therefore increase the window for single mode guiding. Alternately, a higher degree of intermixing could reduce the birefringence and the absorption losses at the expense of multimode behaviour.

The authors would like to thank R.D. Goldberg and I.V. Mitchell of the University of Western Ontario for the implantation.

- <sup>1</sup> Joseph Micallef, E. Herbert Li, Bernard L. Weiss, Appl. Phys. Lett. **62** (1993) 3164.
- <sup>2</sup> T. Wolf, C.L. Shieh, R. Engelmann, K. Alavi, J. Mantz, Appl. Phys. Lett. **55** (1989), 1412.
- <sup>3</sup> D.G. Deppe, N. Holonyak, J. Appl. Phys. **64** (1988) R93.
- <sup>4</sup> E. Kapon, N.G. Stoffel, E.A. Dobisz, R. Bhat, Appl. Phys. Lett. **52** (1988), 351.
- <sup>5</sup> S.I. Hansen, J.H. Marsh, J.S. Roberts, R. Gwilliam, Appl. Phys. Lett. **58** (1991) 1398.
- <sup>6</sup> S.A. Pappert, W. Xia, X.S. Jiang, Z.F. Guan, B. Zhu, Q.Z. Liu, L.S. Yu, A. R. Clawson, P.K.L. Yu, S.S. Lau, J. Appl. Phys. **75** (1994) 4352.
- <sup>7</sup> Y. Suzuki, H. Iwamura, T. Miyazawa, O. Mikama, Appl. Phys. Lett. **57** (1990) 2745.
- <sup>8</sup> J.E. Zucker, K.L. Jones, B. Tell, K. Brown-Groebeler, C.H. Joyner, B.I. Miller, M.G. Young, Electron. Lett. **28** (1992) 853.
- <sup>9</sup> S. Charbonneau, P.J. Poole, P.G. Piva, G.C. Aers, E. S. Koteles, M. Fallahi, J.-J. He, J.P. McCaffrey, M. Buchanan, M. Dion, R.D. Goldberg, and I.V. Mitchell, J. Appl. Phys. **78** (1995) 3697.
- <sup>10</sup> P.J. Poole, S. Charbonneau, M. Dion, G.C. Aers, M. Buchanan, R.D. Goldberg, and I.V. Mitchell, IEEE Photon. Technol. Lett. **8** (1996) 16.
- <sup>11</sup> J.E. Haysom, P.J. Poole, Y. Feng, Emil S. Koteles, J.J. He, S. Charbonneau, R.D. Goldberg, I.V. Mitchell, accepted for publication in J. Vac. Sci. Technol. A.
- <sup>12</sup> Emil S. Koteles, J.J. He, S. Charbonneau, P.J. Poole, G.C. Aers, Y. Feng, SPIE **2918** (1997) 184.
- <sup>13</sup> J.-J. He, Emil S. Koteles, M. Davis, P.J. Poole, M. Dion, Y. Feng, S. Charbonneau, P. Piva, M. Buchanan, R.D. Goldberg, I.V. Mitchell, Can. J. Phys. **74** (1996) S32.

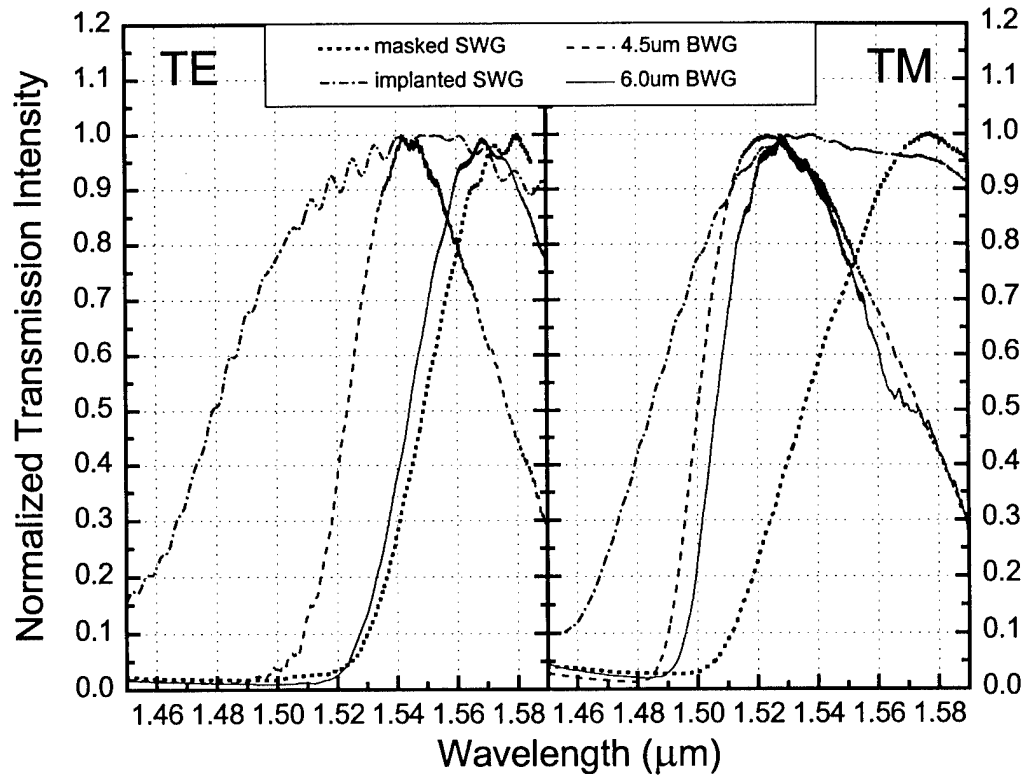


Figure 1: Transmission intensity as a function of wavelength for as-grown and intermixed slab waveguides (SWG), and for 4.5 $\mu\text{m}$  and 6.0 $\mu\text{m}$  wide buried waveguides(BWG).

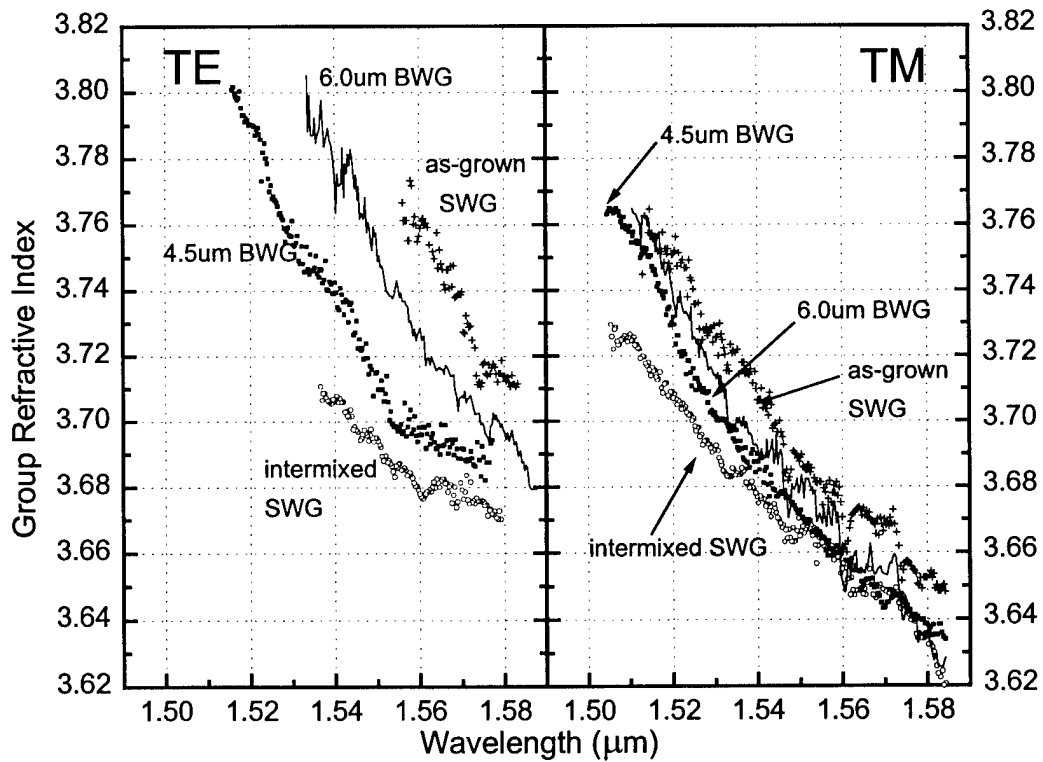


Figure 2 - The refractive index as a function of wavelength, as calculated from the frequency of the Fabry-Perot fringes in transmission measurements, for as-grown and intermixed slab waveguides (SWG), and for 4.5 $\mu\text{m}$  and 6.0 $\mu\text{m}$  wide buried waveguides(BWG).

# Four-channel wavelength demultiplexing multiple quantum well photodetectors for 850 nm optical local area networks

K.W. Goossen,<sup>1</sup> and R. Leibenguth<sup>2</sup>

*Lucent Technologies, Bell Laboratories, <sup>1</sup>4B-519 Crawfords Corner Rd, Holmdel NJ; <sup>2</sup>Murray Hill, NJ*

*(732) 949-6979 fax- (732) 949-2473 [goose@dnrc.bell-labs.com](mailto:goose@dnrc.bell-labs.com)*

The use of fiber optic communication is becoming widespread in high-speed local area networks. Optical fiber is already installed in a large fraction of building networks, and in the near future may extend to the desktop, with required data rates possibly  $> 1$  Gbit/sec. Particularly  $62.5 \mu\text{m}$  core multimode fiber constitutes 90 % of the installed base. As is plotted in Fig. 1, due to modal dispersion there is a bandwidth-distance limit to the use of multimode fiber, that prohibitively shortens the usable length as speeds increase beyond a gigabit/sec. Therefore, it may be desirable to use wavelength division multiplexing to increase the aggregate data rate of existing fiber. Very recently, a multiple VCSEL transmitter operating at 820, 835, 850 and 865 nm has been presented.<sup>1</sup> In [1], on the receiver side a complicated arrangement of filters packaged with waveguide splitters was used to demultiplex the signals. We present here an option that is simpler, and hence probably less expensive, a wavelength demultiplexing photodetector (WDM-PD).

The concept of a WDM-PD has existed for some time.<sup>2</sup> In [2], as here, the concept is to have several integrated photodetectors (i.e., n-i-p-i-...) with varying bandgaps in the optical path, and arrange them so that the optical signal passes through the larger bandgap photodetectors first. Thus, the lower band gap photodetectors are filtered by the higher bandgap photodetectors so that all the photodetectors receive in a different wavelength range. By tapping the appropriate

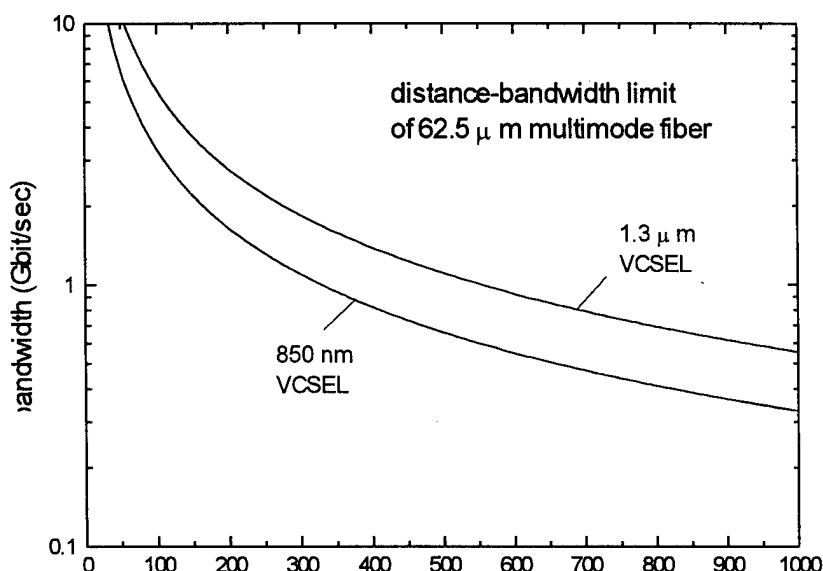


Fig. 1: Plot of the distance-bandwidth product of  $62.5 \mu\text{m}$  diameter multimode optical fiber, which constitutes 90 % of the imbedded base in customer premises.

	well width (Å)	number of wells
1 <sup>st</sup> (top) MQW	65	215
2 <sup>nd</sup> MQW	76	175
3 <sup>rd</sup> MQW	98	135
4 <sup>th</sup> (bottom) MQW	129	95

Table I: Sample parameters.

photodiode, a particular wavelength is selected. Such an arrangement is simpler than optical splitters since the device is packaged with a single optical fiber connection as for an ordinary photodiode. In [2], a two-wavelength WDM-PD was presented wherein the crystal growth technique was LPE and bulk materials were used, and hence the different wavelengths had to be separated by 150 nm. In [3] we showed use of molecular beam epitaxy and multiple quantum well material so that wavelengths may be as close as 15 nm. Here we extend this work to a four-channel device.

Our device is a n-i(MQW)-p-i(MQW)-n-i(MQW)-p-i(MQW)-n (substrate). The doped layers are 8000 Å  $\text{Al}_{0.11}\text{Ga}_{0.89}\text{As}$ , except the cap, which is 2000 Å with  $n^{++}$  100 Å GaAs at the surface. The MQW's are GaAs/AlAs, with the AlAs being 20 Å thick, and the number of wells and well thicknesses given in Table I. Four mesas are etched, each subsequent one being larger than the preceding, and separate contacts to each doped region placed on each mesa, using the substrate as the fifth contact.

Photocurrent spectra are taken for each diode by illuminating the area defined by the innermost mesa. The bottom MQW has a heavy-hole absorption peak at 854 nm, and as noted is low-pass filtered by the top MQW's whose heavy-hole excitons are at 842, 825 and 810 nm, from the bottom up, respectively. Note the design was for 855, 840, 825, and 810, which we slightly missed. Likewise, each photodiode is filtered by the ones above it so that they only detect in a narrow band. For signals with wavelengths at the exciton peaks, there is less than -12 dB of crosstalk between channels.

In conclusion, we have presented a four-wavelength demultiplexing photodiode utilizing multiple quantum well material so that for wavelengths as close as 15 nm there is less than -12 dB of crosstalk. The device may be packaged inexpensively as for ordinary photodetectors, and hence may find utility as a low-cost wavelength-division multiplexed local area network.

## REFERENCES

- [1] L.B. Aronson, B.E. Lemoff, L.A. Buckman, and D.W. Dolfi, "Low-cost multimode WDM for local area networks," postdeadline session of the 1997 Optical Fiber Communication conference..
- [2] J.C. Campbell, A.G. Dentai, T.P. Lee, and C.A. Burrus, "Improved two-wavelength demultiplexing InGaAsP photodetector," IEEE J. Quantum Electron. **QE-16**, 601 (1980).
- [3] K.W. Goossen and R. Leibenguth, "Wavelength demultiplexing multiple quantum well photodetectors operating of a medium spectral spacing," proceedings of the 1997 IEEE LEOS Annual Meeting, p. 200 (1997).

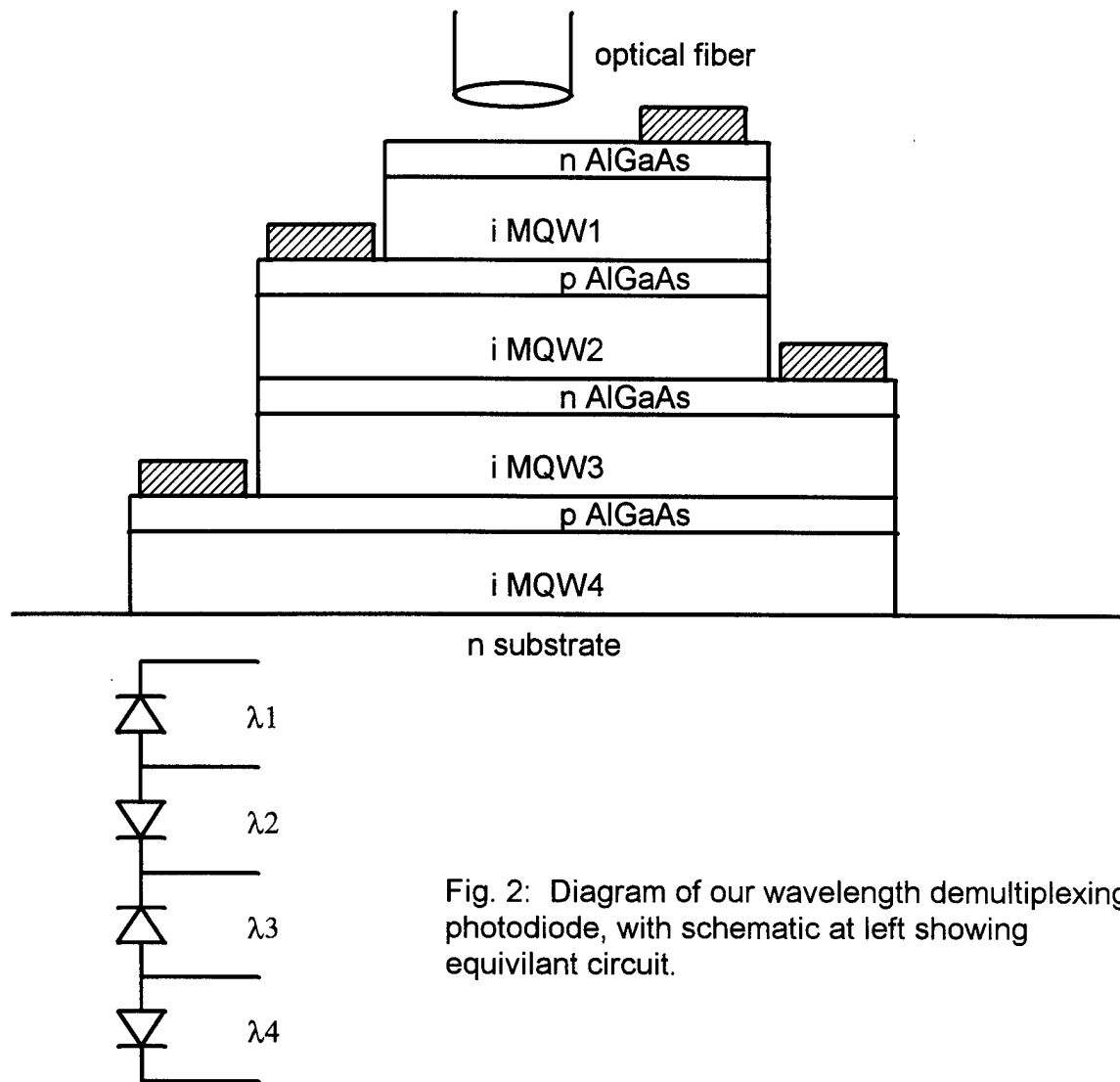


Fig. 2: Diagram of our wavelength demultiplexing photodiode, with schematic at left showing equivalent circuit.

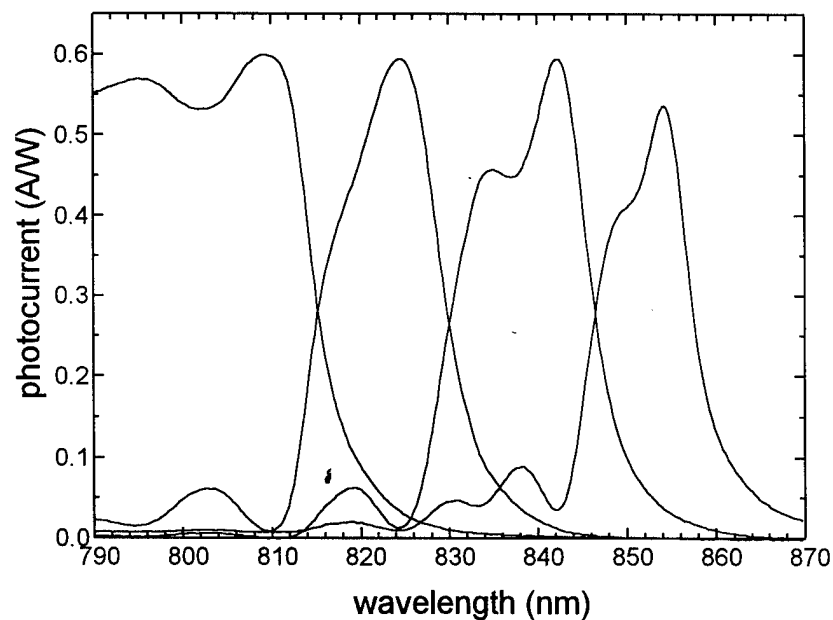


Fig. 3: Measured photocurrent spectra for each of the four photodiodes of our sample, showing less than -12 dB crosstalk at the center wavelength.

# All-Optical Wavelength Converter Based on Coupled Semiconductor Optical Amplifiers

*Byongjin Ma, Yoshiaki Nakano, and Kunio Tada*

Department of Electronic Engineering, The University of Tokyo

7-3-1 Hongo, Bunkyo-ku, Tokyo, 113-8656, Japan

Phone: +81-3-3812-2111 ext. 6753, Facsimile: +81-3-5802-3313

Internet: bjma@jungfrau.t.u-tokyo.ac.jp

## Introduction

It is no wonder that the introduction of optical wavelength division multiplexing (WDM) is now becoming a worldwide issue and is expected to meet the gigantic transmission capacity demand in future telecommunication networks. Wavelength conversion has been considered to be one of the key functions at cross-connects and switching nodes since it allows reuse of wavelengths, thus avoiding wavelength channel contention and giving larger flexibility to the systems [1]. Although there are several wavelength converters existing, problems such as insufficient conversion efficiency and critical operation condition have been preventing them from being widely deployed. In addition, compact device size and ease of fabrication may be the prerequisite parameters for more cost-effective systems. In this paper we describe another type of semiconductor wavelength converter with compact size and better conversion characteristics.

## Operation Principle

The newly proposed wavelength converter makes use of coupled active waveguides or coupled semiconductor optical amplifiers (SOAs), and has very simple structure as shown in Fig. 1. It is basically a directional coupler composed of not passive but active waveguides, in which the change in the carrier density caused by the external light injection results in changes in the real and imaginary parts of the refractive index,  $n'$  and  $n''$ .

The BPM (beam propagation method) simulation was carried out to understand the wavelength conversion operation. The parameters and their values used in the simulation are listed in Table I [2]. The antiguiding factor  $b$ , defined as the ratio of real part to imaginary part of the complex refractive index ( $n'/n''$ ), is known to have values between 0.5 and 6.2 [3]. Assumptions used in BPM simulations are as follows [2]:

1. two SOAs are completely symmetrical at the same injection currents,
2.  $\beta_1$  changes while  $\beta_2$  remains unchanged with input power, and
3. spatial distributions of  $\beta_1$  and  $\beta_2$  are ignored.

As shown in Fig. 2, when there is no input signal power ( $\lambda_{\text{pump}}$ ) entering, the optical modes of SOAs are completely coupled, namely,  $\beta_1 \doteq \beta_2$ , and the cross-state output takes its maximum value. As the input signal power increases, the optical modes become decoupled, namely,  $\beta_1 \neq \beta_2$ , and the cross-state output decreases significantly. On the contrary, the bar-state output becomes increased with the increase of input power. Therefore, both the polarity-inverted and polarity-noninverted output characteristics as well as wavelength conversion characteristics are obtainable simultaneously at the different output

ports, like in the case of the interferometric wavelength converters using cross-phase modulation (XPM) [4]. Over 20 dB output extinction ratio is expected at moderate input power. Furthermore, proper choice of input power level and range enlarges the extinction ratio at the output as compared to that at the input, thus giving rise to pulse-resaping functionality.

## Discussion

Our simulation so far assumed equal current injection to two SOAs for simple explanation of device operation. If asymmetric injection is incorporated, the adjustment and trimming of wavelength conversion characteristics would be possible, which are necessary to tolerate input signal uncertainties.

A filter should be placed at the output port in order to delete the input signal. This could be a serious problem since it makes system complex and costly. However, we are able to select other configurations in which there is no need of filter. One such configuration is to launch both the probe and pump signals into the upper SOA in Fig.1 but from opposite sides (probe from left hand side and signal from right hand side, for example). Then, only one signal (probe or pump signal) is detected at either end of the lower SOA.

## Conclusions

We proposed a novel wavelength converter. Besides its compact size, such advantages as moderate input power operation, pulse reshaping, and availability of both inverting and non-inverting outputs have been shown. Asymmetrical current injection and various input configurations may give us flexibility of operation.

This work was supported by the International Communications Foundation and the Mombusho Grant-in-Aid.

## References

- [1] S. L. Danielsen et al., Tech. Dig. of CLEO'97, paper CMF4.
- [2] J. M. Liu and C. Yeh, Appl. Phys. Lett. 50 (23), 8 June 1987.
- [3] K. Otsuka and H. Iwamura, IEEE J. Quantum Electron. 19, 1184, 1983.
- [4] B. Mikkelsen et al., Tech. Dig. of ITMPS'95, paper PWE1-1.

**Table I.** Parameters used in the BPM simulation

parameter	value
L ( length of waveguide )	1000 $\mu\text{m}$
W ( width of waveguide )	3 $\mu\text{m}$
G ( gap between waveguides )	3 $\mu\text{m}$
$n_{wg}$ ( refractive index of waveguide )	3.260
$n_{bg}$ ( refractive index of background )	3.255
$g_0$ ( unsaturated gain of SOA )	40 $\text{cm}^{-1}$
$\alpha$ ( distributed loss )	26 $\text{cm}^{-1}$
b ( antiguiding factor )	3
$I_s$ ( saturation input power )	7 mW

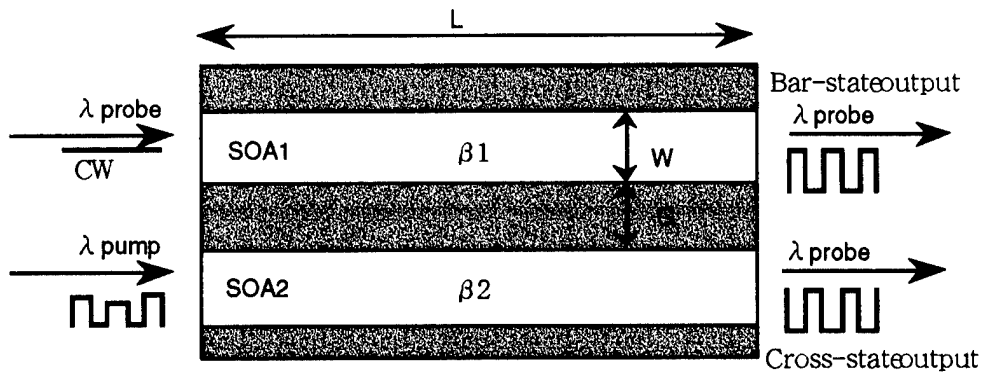


**Fig. 1.** Schematic top view of the proposed wavelength converter. Both SOAs are pumped with equal current (i.e.  $\beta_1 = \beta_2$  when no input optical power applied).

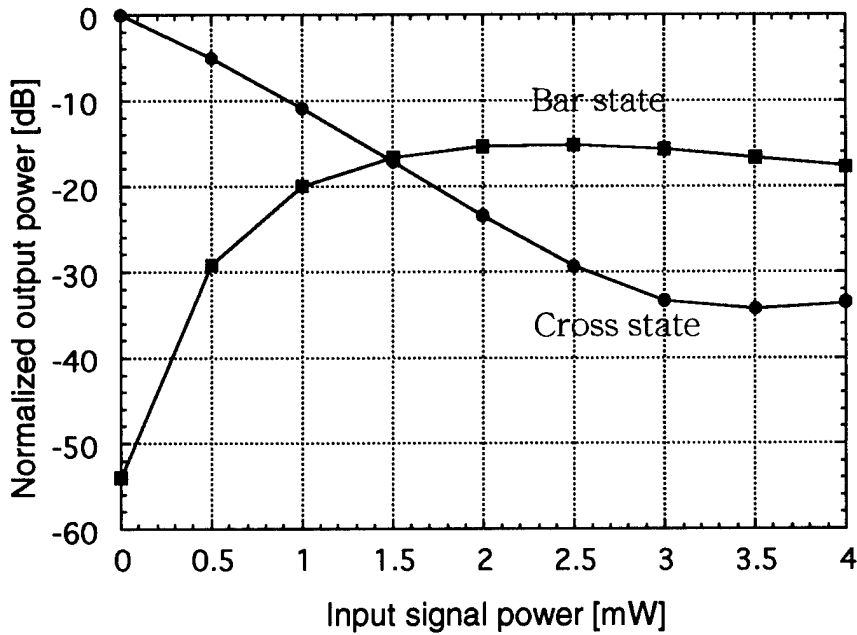


**Fig. 2.** Static output characteristics of the wavelength converter using coupled SOAs. CW input power ( $\lambda_{\text{probe}}$ ) is fixed at 1 mW and input signal power ( $\lambda_{\text{pump}}$ ) is varied from 0 to 4 mW. Both inverted (cross) and non-inverted (bar) wavelength conversions are achievable.

## Proposal of Spectrum Sliced Multi-wavelength Light Sources Using Integrated High Power Superluminescent Diodes

F. Koyama and S. Mori

Precision & Intelligence Laboratory, Tokyo Institute of Technology

4259 Nagatsuta, Midori-ku, Yokohama 226-8503, Japan

Tel: +81-45-924-5068, Fax: +81-45-921-0898, Email: koyama@pi.titech.ac.jp

### 1. Introduction

A multi-wavelength light source is one of key devices for future large scale wavelength division multiplexing (WDM) networks. Various kinds of multi-wavelength light sources have been proposed and demonstrated. A spectrum slicing technique using broadband light sources, such as light emitting diodes, super-luminescent diodes (SLDs), super-continuum generators and mode-locked semiconductor lasers<sup>1)-4)</sup>, is attractive especially for generating equally-spaced multi-wavelength light. The configuration of spectrum sliced light sources using incoherent light is simple, however, the drawback is a limited low power and a large excess intensity noise caused by a spontaneous emission beat noise.

In this study, we propose a novel integrated form of spectrum sliced multi-wavelength light source using a high power tapered SLD. Modeling and experiments on high power tapered SLDs are presented. Also, a novel technique of reducing the intensity noise of sliced light is proposed by using saturated semiconductor optical amplifiers (SOAs).

### 2. Spectrum Sliced Multi-wavelength Light Sources Using SLDs

The conceptional diagram of our spectrum sliced light source is shown in Fig. 1. A tapered active region superluminescent diode<sup>5), 6)</sup> is used to generate high power and wideband incoherent light. A high power amplified spontaneous emission is coupled into an arrayed waveguide grating (AWG) and is spectrally sliced. SOAs array may be used to reduce the intensity noise. An example of their one-chip integration form is schematically shown in Fig. 2.

### 3. Modeling and Experiment of High Power Superluminescent Diodes

We carried out the modeling and some experiments on a tapered active region SLD emitting at 1.5 $\mu$ m as shown in Fig. 3. The following traveling wave rate equations are used to model the tapered SLD.

$$\frac{\partial S_i}{\partial t} + v \frac{\partial S_i}{\partial z} = v(\xi G - \alpha)S_i + \frac{1}{2} \xi R_{\text{spont}} \frac{1}{L \cdot w_{\text{in}} \cdot d} \quad (1)$$

$$\frac{\partial N}{\partial t} = \frac{I}{eV_a} - \sum v(\xi G - \alpha)S_i - \frac{N}{\tau_s} - CN^3 \quad (2)$$

$S_i$  is the photon density,  $N$  is the carrier density,  $\xi$  is the optical confinement factor,  $G$  is the material gain,  $R_{\text{spont}}$  is the spontaneous emission rate,  $L$  is the length,  $w_i$  is the starting waveguide width of the taper,  $d$  is the total thickness of the active layer,  $\alpha$  is the absorption loss and  $C$  is the Auger coefficient. We assumed that a fundamental Gaussian beam propagates along with the tapered active region.

Figure 4 shows the calculated light output/current characteristics for various lengths of SLDs with a taper angle of 6°. We can expect a high output power over 1 W for SLDs with a few mm long active region. It is noted that the slope efficiency in the L/I is comparable to that of lasers by optimizing the device length.

We have fabricated tapered SLDs as shown in Fig. 5. The active region consists of strained Ga<sub>0.4</sub>In<sub>0.6</sub>As QWs (~6nm thick) with quaternary barriers, which is defined by a SiO<sub>2</sub> triangle window. The tapered angle is 6°. To eliminate facet reflections, the axis is tilted by 7°. The length of the SLD is typically 1.25 mm or more and the output width is 125 $\mu$ m. Figure 6 shows a typical L/I characteristic under pulsed condition. An output power of

600mW was obtained with a broad spectrum as wide as 30nm. The spectral profile can easily be controlled in the SLD. We already demonstrated a broad-band spectrum with a spectral width over 100nm by using non-uniform thickness quantum well stacks<sup>8)</sup>.

#### 4. Noise Reduction of Spectrum Sliced Light Sources by Nonlinear Amplification

The signal-to-noise ratio of the sliced incoherent light is simply expressed by  $B_{\text{opt}}/B_e$ , where  $B_e$  is the electrical bandwidth and  $B_{\text{opt}}$  is the optical spectral width. This means that the spectral width of sliced light can not be reduced for high bit rates, resulting in a significant limitation in a channel spacing. We propose a novel method to avoid this difficulty by using saturated SOAs. The saturation characteristic in semiconductor optical amplifiers will be helpful for reducing the excess intensity noise of spectrum-sliced light as shown in Fig. 7. Recently, a possibility of noise reduction of coherent light was presented by use of nonlinear amplification<sup>7)</sup>. We calculated the noise reduction of sliced light passing through saturated SOAs by using the traveling equations (1) and (2) with neglecting the spontaneous emission generated in the saturated SOA. We assumed cascading SOAs to enhance the nonlinear saturation effect. Figure 8 shows the noise power normalized to the wide-band noise power as a function of noise frequency for various number of cascading SOAs. A significant suppression effect of intensity noise can be expected by cascading saturated SOAs especially at a low frequency. Although the bandwidth for the noise reduction is limited by carrier lifetime, it would still be helpful for a few-Gbit/s systems.

#### 5. Conclusion

A spectrum-sliced multi-wavelength light source based on a high power tapered SLD is proposed. Experiments and modeling on SLDs show a potential of high power and high efficient SLDs. Also, nonlinear amplification may help us to generate "nearly coherent light" from sliced incoherent light. A single-chip large scale multi-wavelength light source can be expected using the proposed scheme.

#### Acknowledgments:

The author would like to acknowledge Prof. K. Iga of Tokyo Institute of Technology for his encouragement. This study was partly supported by Grant-in-Aid from the Ministry of Education, Science, Sports and Culture.

#### References

- 1) R.H. Reeve, A.R. Hunwicks, W. Zhao, S.G. Methley, L. Bickers and S. Hornung, *Electron. Lett.*, vol.24, pp.389-90, 1988.
- 2) S.S. Wagner and T.E. Chapuran, *Electron. Lett.*, 26, pp.696-697, 1990.
- 3) T. Morioka, H. Takara, S. Kawanishi, O. Kamatani, K. Takiguchi, K. Uchiyama, M. Saruwatari, H. Takahashi, M. Yamada, T. Kanamori and H. Ono, *OFC'96*, Post-deadline paper, PD21, 1996.
- 4) B. Glance, K.Y. Liou, U. Koren, E.C. Burrows, G. Raybon, C.A. Burrus, K. Dreyer and C. Doerr, *IEEE Photon. Tech. Lett.*, vol.8, pp.1241-1243, 1996.
- 5) J. N. Walpole, E.S. Kintzer, S. R. Chinn, C. A. Wang and L.J. Missagia, *Appl. Phys. Lett.*, vol.61, pp.740-742, 1992.
- 6) F. Koyama, K. Y. Liou, A. G. Dentai, T. Tanbun-ek and C. A. Burrus, *IEEE Photon. Tech. Lett.*, vol.5, pp.916-919, 1993.
- 7) M. Shtaiif and G. Eisenstein, *IEEE J. Quantum Electron.*, vol.32, pp.1801-1809, 1996.
- 8) F. Koyama, *LEOS'96*, TuY2, pp.333-334, 1997.

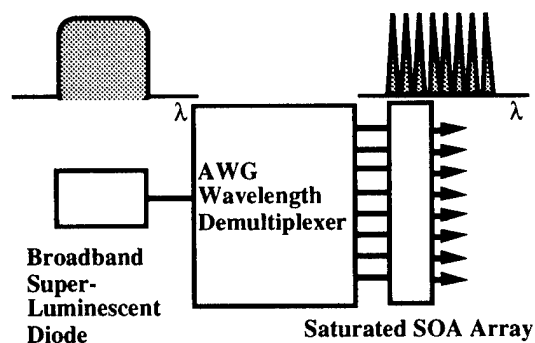


Fig. 1 Schematic of multi-wavelength light source using a high power SLD.

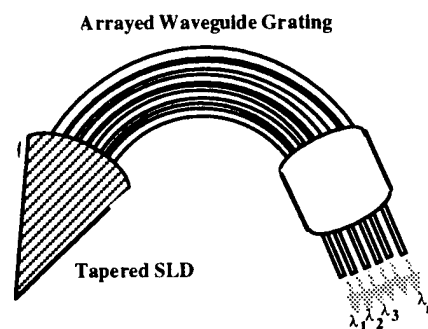


Fig. 2 Integrated multi-wavelength light source using a tapered SLD and AWG.

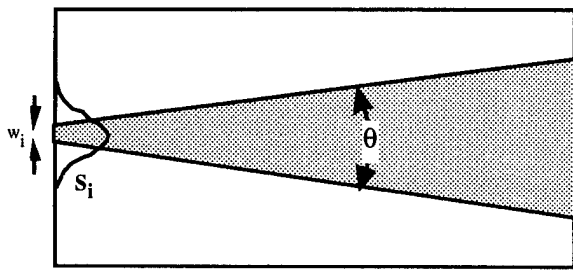


Fig. 3 Modeling structure of a tapered SLD.

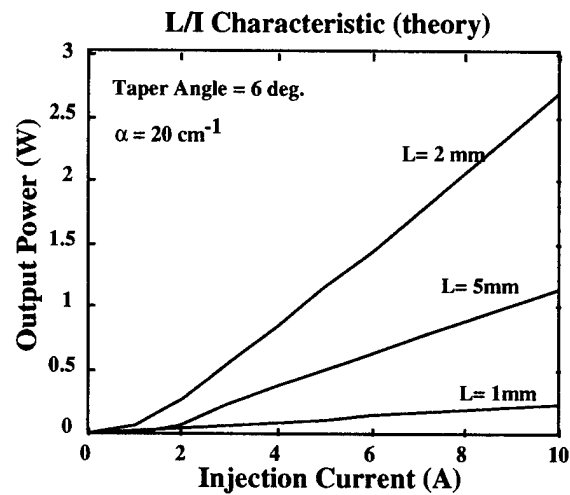


Fig. 4 Calculated L/I characteristics of a tapered SLD for various device lengths.

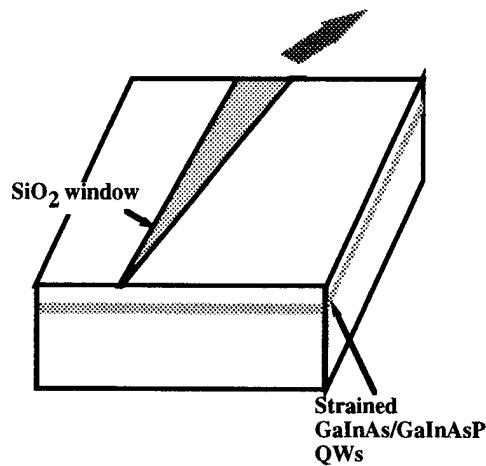
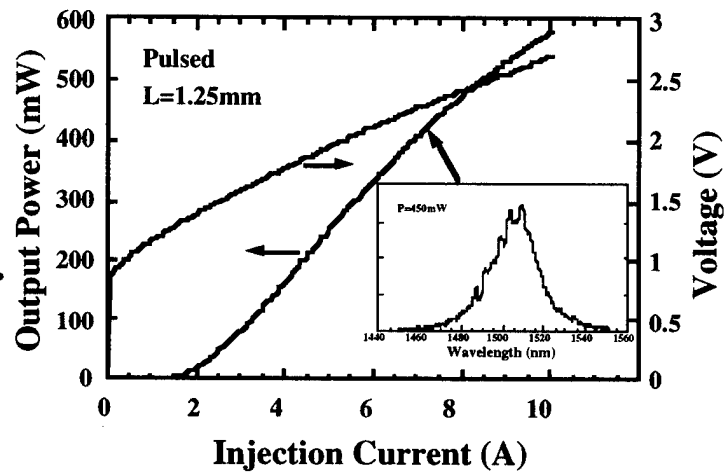
Fig. 5 Schematic of fabricated SLD emitting at 1.5  $\mu\text{m}$ .

Fig. 6 L/I characteristic and spectrum of a fabricated SLD with a taper active region.

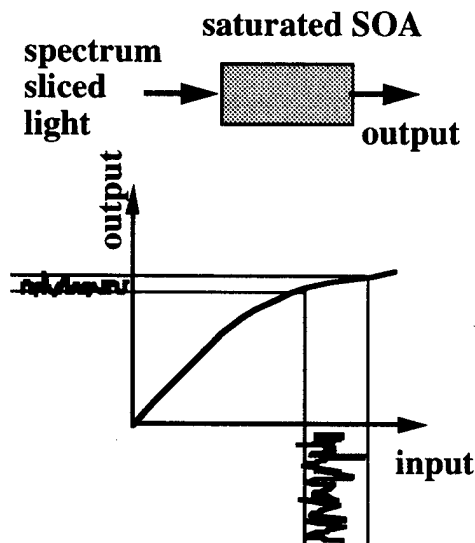


Fig. 7 Noise reduction of sliced light by using a saturated semiconductor optical amplifier.

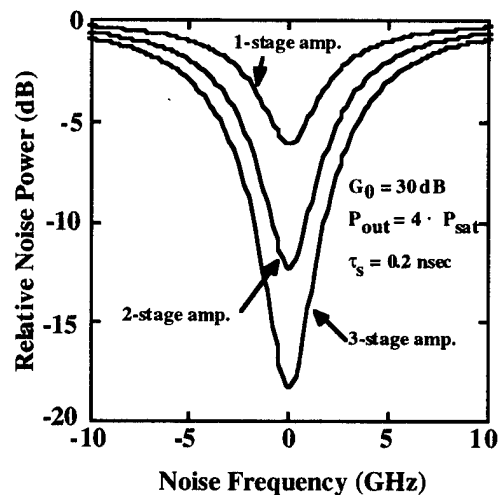


Fig. 8 Suppressed noise spectrum of sliced light by using cascaded SOAs.

# Application of synthetic aperture techniques to arrayed-waveguide grating passband control

M.C. Parker\*, F. Farjady\* and S.D. Walker<sup>+</sup>

\* Fujitsu Telecommunications Europe Ltd. Research,  
Northgate House, St Peter's St, Colchester, Essex, CO1 1HH, UK.  
*Tel:* +44 1206 363000, *Fax:* +44 1206 363009  
*Email:* M.Parker@ftel.co.uk, F.Farjady@ftel.co.uk

<sup>+</sup> University of Essex, Department of Electronic Systems Engineering,  
Wivenhoe Park, Colchester, Essex, CO4 3SQ, UK.  
*Tel:* +44 1206 872413, *Fax:* +44 1206 872900  
*Email:* stuwal@essex.ac.uk

## Summary:

Future WDM networks may require devices with dynamically controllable characteristics to provide extra functionality and reconfigurability [1]. The arrayed-waveguide grating (AWG) [2] has emerged as an important passive WDM component. Previous approaches to arrayed-waveguide grating passband modification have considered fixed device parameters [3] [4] and use of a trapezoidal-shaped active region [5] for device tuning. In this paper we show how dynamic passband control, in addition to tuning and free-spectral-range (FSR) adjustment, can be achieved using multiple, low-order polynomial-profiled electrodes.

Figure 1 shows a schematic of the two contact device used for simulations. The parabolic shaped electrode (B) causes increasing phase differences between adjacent guides resulting in passband widening due to superposition of the detuned spectra. In effect, this electrode introduces a synthetic aperture function. A side-effect of the synthetic aperture superposition is an

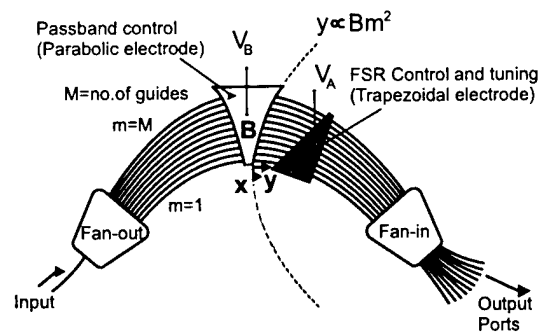


Figure 1: Schematic of AWG with parabolic and trapezoidal active regions

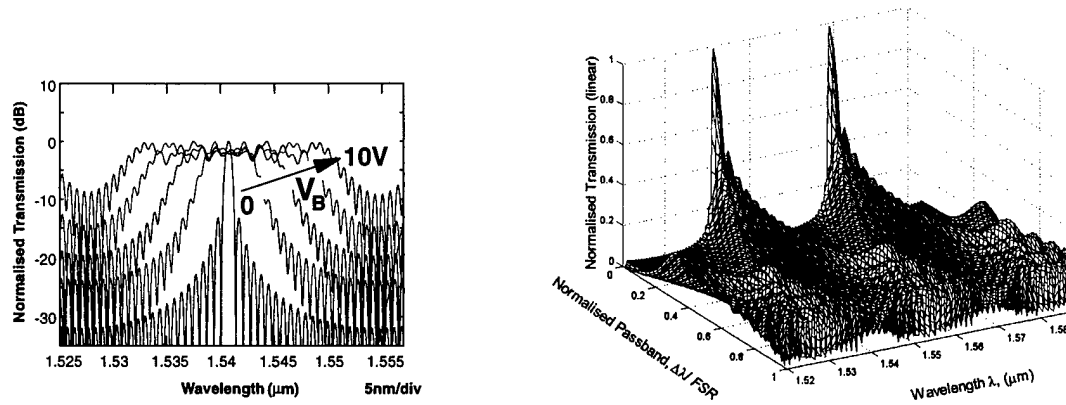


Figure 2: 2D and 3D plots of passband broadening as  $V_B$  is increased

associated centre-wavelength shift. This is removed by a compensating trapezoidal electrode (A) as shown, which provides the additional benefit of two-way wavelength tuning and FSR control. The basic equation describing the output amplitude spectrum  $t(\lambda)$  for an active AWG with multiple polynomial-profiled electrodes from one output port is:

$$t(\lambda) = \sum_{m=1}^M f_m^2 e^{j \frac{2\pi n_c \Delta l}{\lambda}} (m + Am + Bm^2 + Cm^3 + \text{higher orders of } m) \quad (1)$$

where  $\lambda$  is the wavelength,  $f_m$  the coupling coefficient for the  $m^{\text{th}}$  waveguide,  $n_c$  the refractive index,  $\Delta l$  the incremental path length difference between the waveguides, and  $M$  the total number of waveguides. The coefficients  $A, B, C, \dots$  etc. are proportional to the voltages  $V_A, V_B, V_C, \dots$  etc. applied to the trapezoidal, parabolic and higher-order polynomial-shaped electrodes respectively. In the present case, only orders up to  $m^2$  are considered, such that the coefficients  $C, D, \dots = 0$ . To achieve a broadened spectrum of 3dB-width  $\Delta\lambda$ , centred on a wavelength  $\lambda_1$ , the required values for  $A$  and  $B$  can be approximated to:

$$B \approx \frac{2(\Delta\lambda - \Delta\lambda_0)}{\pi\lambda_0(M-1)} \quad A \approx -(M-1)B + \frac{\lambda_0 - \lambda_1}{\lambda_0} \quad (2)$$

where  $\lambda_0$  and  $\Delta\lambda_0 = \frac{\lambda_0^2}{Mn_c\Delta l}$  are respectively the centre wavelength of the passband and the passband 3dB-width, when the applied voltages are zero, *i.e.* for the unbroadened spectrum. Simulations have been performed, assuming  $\text{LiNbO}_3$  as the device active material, with the strong electro-optic coefficient  $r_{33} = 30.8 \times 10^{-12} \text{mV}^{-1}$ . Additional device parameters have been modelled as  $M = 40$ ,  $\Delta l = 40 \mu\text{m}$ ,  $n_c = 2.2$ ,  $\Delta\lambda_0 = 0.7 \text{nm}$  and  $\text{FSR} = 27.7 \text{nm}$ . Both the applied voltages  $V_A$  and  $V_B$  are not expected to exceed 10V. Figure 2a shows the passband broadening functionality of the device, as  $V_B$  increases from 0 to 10V. As the passband width is increased, the passband remains substantially flat, demonstrating the utility of the synthetic aperture approach. Figure 2b shows a 3D plot of the active device's relative transmission across

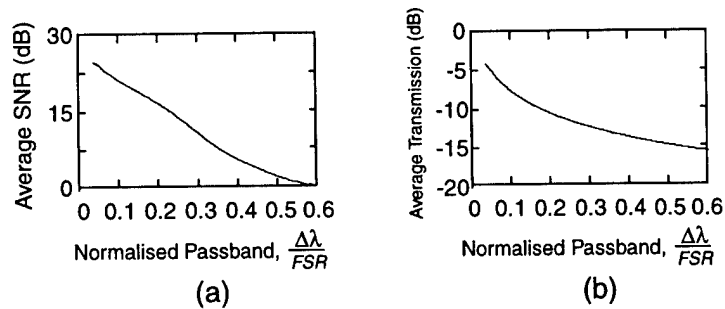


Figure 3: Filter characteristics as passband  $\Delta\lambda$  is broadened

two FSRs, as the voltage  $V_B$  is applied to its maximum, when  $\Delta\lambda = FSR$ . It demonstrates, as shown in figure 3a, that the maximum practical passband broadening occurs for  $\Delta\lambda = 0.56FSR = 15.5\text{nm}$ , when the out-of-band noise suppression (*i.e.* signal-to-noise ratio, SNR) of the device is reduced to 0dB. The concomittant reduction in transmission of the device passband is 16dB, as shown in figure 3b.

In conclusion, we have described a novel technique for dynamic passband control of an AWG using polynomial-profiled electrodes. Passband broadening from 0.7nm to 15.5nm is possible by applying voltages of up to 10V to two electrodes on LiNbO<sub>3</sub>. In principle, further higher-order polynomial-profiled electrodes could be added to achieve a range of tailored spectral filtering characteristics, with lower passband ripple and improved SNR. Using this device, the techniques of synthetic aperture theory may also be readily applied to issues such as dynamic spectral equalisation and segmented passbands.

## References

- [1] C.A. Brackett, A.S. Acampora, J. Sweitzer, G. Tangonan, M.T. Smith, W. Lennon K.-C. Wang, and R.H. Hobbs. A scalable multiwavelength multihop optical network: A proposal for research on all-optical networks. *IEEE Journal of Lightwave Technology*, 11(5/6):736–753, 1993.
- [2] C. Dragone, C.A. Edwards, and R.C. Kistler. Integrated optics  $N \times N$  multiplexer on silicon. *IEEE Photonics Technology Letters*, 3(10):896–899, 1991.
- [3] Y.P. Ho, H. Li, and Y.J. Chen. Flat channel-passband-wavelength multiplexing and demultiplexing devices by multiple-Rowland-circle design. *IEEE Photonics Technology Letters*, 9:342–344, 1997.
- [4] A. Rigny, A. Bruno, and H. Sik. Double-phased array for a flattened spectral response. *ECOC'97*, 3:79–82, 1997.
- [5] J. Stone. Tunable silicon based optical router. *US Patent*, #5515460.

---

**Integrated Photonics Research**

# **Photonic Nanostructures I**

**Tuesday, March 31, 1998**

**B. E. Little, Massachusetts Institute of Technology**

**R. W. Ziolkowski, University of Arizona**

Presiders

**ITuA**

**8:30am–10:00am**

Salon B

## **Advances in Photonic Crystals and Devices**

J. D. Joannopoulos  
Massachusetts Institute of Technology  
Department of Physics  
Cambridge, MA 02139  
joannop@MIT.EDU

During the last few years a new class of materials has emerged, called photonic crystals, which provide capabilities along new dimensions for the control and manipulation of light. A photonic crystal affects the properties of light in much the same way that a semiconductor affects the properties of electrons. Consequently, photons in photonic crystals can have band-gaps, localized defect-states, surface-states, etc. This new ability to mold and guide light leads naturally to many novel applications of these materials as microphotonic devices and device components. An introductory survey including recent exciting developments in the field of photonic crystals is presented.

## FDTD modeling of photonic nanometer-sized power splitters and switches

*Richard W. Ziolkowski*

Department of Electrical and Computer Engineering

The University of Arizona, Tucson, AZ 85721

Tel: (520) 621-6173, Fax: (520) 621-8076

E-mail: ziolkowski@ece.arizona.edu

Nanometer and micron sized optical devices are currently being explored for their applications in variety systems associated with communications, data storage, optical computing, etc. However, as the size of optical devices is pushed to the size of an optical wavelength and less, the need for more exact materials and response models is tantamount to the successful design and fabrication of those devices. Moreover, the time scales for many of these devices is rapidly approaching the femtosecond regime. For this reason the finite-difference time-domain (FDTD) method is receiving intensive study (see, for example, [1-3]). To understand the physics underlying the associated small-distance scale and short-time scale interactions, particularly in the resonance regime of the materials and the associated device structures, a first-principles, rather than a phenomenological, approach was considered to be the most desirable. As discussed in [4], this leads to a semiclassical Maxwell-Bloch model, i.e., a careful marriage between microscopic (quantum mechanical) material models of the resonant material systems and the macroscopic Maxwell's equations solver.

It has been further demonstrated that photonic bandgap (PBG) structures can be used to form nanometer sized waveguiding structures [5]. The ability of the FDTD approach to model finite-sized PBG structures with defects and to recover known behaviors has been demonstrated [6]. The Maxwell-Bloch FDTD simulator has been applied to modeling several VCSELs based upon PBG structures [7]. This paper illustrates preliminary efforts to model nanometer sized waveguiding structures that have resonant nonlinear materials built into them. Results for the basic sub-wavelength waveguiding structures including right-angle corners have been reproduced and extended to power splitters and defect-based switches. These structures are shown in Figures 1-3. The generalization of these results to the more general resonant material cases is currently under investigation.

To model the interaction of electromagnetic fields with multi-level atoms, a multi-dimensional FDTD Maxwell-Bloch simulator has been developed [7, 8]. The FDTD approach can handle ultra-fast single-cycle pulse cases as readily as multiple-cycle cases having an intrinsic carrier wave. It can incorporate complicated scatterers and materials with great flexibility. It can be run with or without the Bloch portion being turned-on. In this manner the basic electromagnetic properties of the structures can be determined without the more complex nonlinear material behaviors being present. Then the response of the same structures loaded with resonant materials can be evaluated. A Berenger PML [3] absorbing boundary condition is used to truncate the FDTD mesh.

The electric field in the simulator taken to be tangent to the dielectric interfaces associated with each region in the PBG structures shown in Figs. 1-3. An electromagnetic field is injected as a focused gaussian beam into the waveguide from a total field/scattered field boundary near the entrance to the waveguides. The coupling of the gaussian beam to the waveguide has not yet been optimized. It is felt that a better design of the input face of the waveguide would lead to a more complete coupling of the incident field to the waveguiding structure. Once all of the reflections

take place that are necessary to make the finite periodic structures on either side of the defect act as mirrors, the waveguides propagate all of the energy injected into them with only minor losses.

A square lattice with a row of one post defects was used for the waveguiding structures. The posts are assumed to be GaAs with  $\epsilon_r = 11.4$  surrounded by air. The radius of the rods is  $r = 0.18a$  where  $a = 0.4\lambda$  is the distance between the centers of the rods. With  $\lambda = 1.5 \mu\text{m}$ , one has  $a = 0.6 \mu\text{m}$  and  $r = 0.1 \mu\text{m}$ . This gives a guide width of  $500 \text{ nm}$ . The FDTD simulator has shown that the defect structure shown in Fig. 1 does act as a waveguide and that the Y-power splitter shown in Fig. 2 does split the power equally between the two branches. It has been found that the defect waveguiding structures, as long as they are not too near to each other, are decoupled. A 1 to  $1/N$  micron-sized power splitter could be constructed in principle with this approach.

The simulator has also been used to determine how much time it takes for the PBG structure to acquire its steady state behavior. Because of the time scales to reach steady-state, these PBG waveguiding structures are found to be useful primarily for continuous rather than pulsed wave applications.

The use of another single defect to control the power through each arm of the Y-power splitter was examined. It was found that more than a 3 : 1 switching of the power between the arms could be achieved with a single additional defect. More complex defect structures are also currently being investigated to determine how much isolation between the arms can be achieved.

This work was supported in part by the Office of Naval Research under grant number N0014-95-1-0636 and by the Air Force Office of Scientific Research, Air Force Materiel Command, USAF, under grant number F49620-96-1-0039.

1. R. W. Ziolkowski and J. B. Judkins, "NL-FDTD Modeling of Linear and Nonlinear Corrugated Waveguides," *J. Opt. Soc. Am. B*, vol. 11(9), 1565-1575, 1994.
2. J. B. Judkins and R. W. Ziolkowski, "Finite-difference time-domain modeling of nonperfectly conducting metallic thin-film gratings," *J. Opt. Soc. Am. A*, vol. 12(9), pp. 1974-1983, 1995.
3. A. Taflov, *Computational Electrodynamics*, Artech House, Norwood, MA, 1995.
4. Richard W. Ziolkowski, John M. Arnold, and Daniel M. Gogny, "Ultrafast pulse interactions with two-level atoms", *Phys. Rev. A*, vol. 52, no. 4, pp. 3082-3094, October 1995.
5. J. D. Joannopoulos, R. D. Meade, and J. N. Winn, *Photonic Crystals: Molding the Flow of Light*, Princeton University Press, Princeton, NJ, 1995.
6. R. W. Ziolkowski and S. J. Franson, "Finite-difference time-domain (FDTD) modeling of photonic band gap structures constructed from electric and magnetic materials," 1996 OSA Annual Meeting, Rochester, NY, October 1996.
7. R. W. Ziolkowski and S. J. Franson, "Finite-difference time-domain (FDTD) modeling of photonic band gap waveguide structures," 1997 OSA Annual Meeting, Long Beach, CA, October 1997.
8. Richard W. Ziolkowski, "Realization of an all-optical triode and diode with a two-level atom loaded diffraction grating," to appear in *Appl. Opt.*, November 1997.

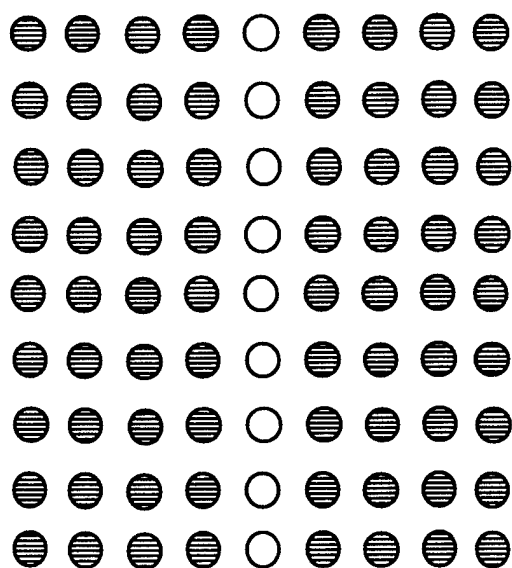


**Figure 1. Basic nanometer PBG waveguide structure.**

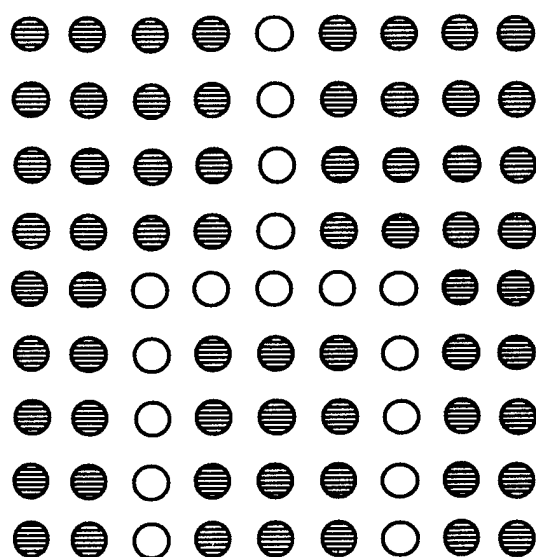


**Figure 2. Basic nanometer PBG power splitter.**

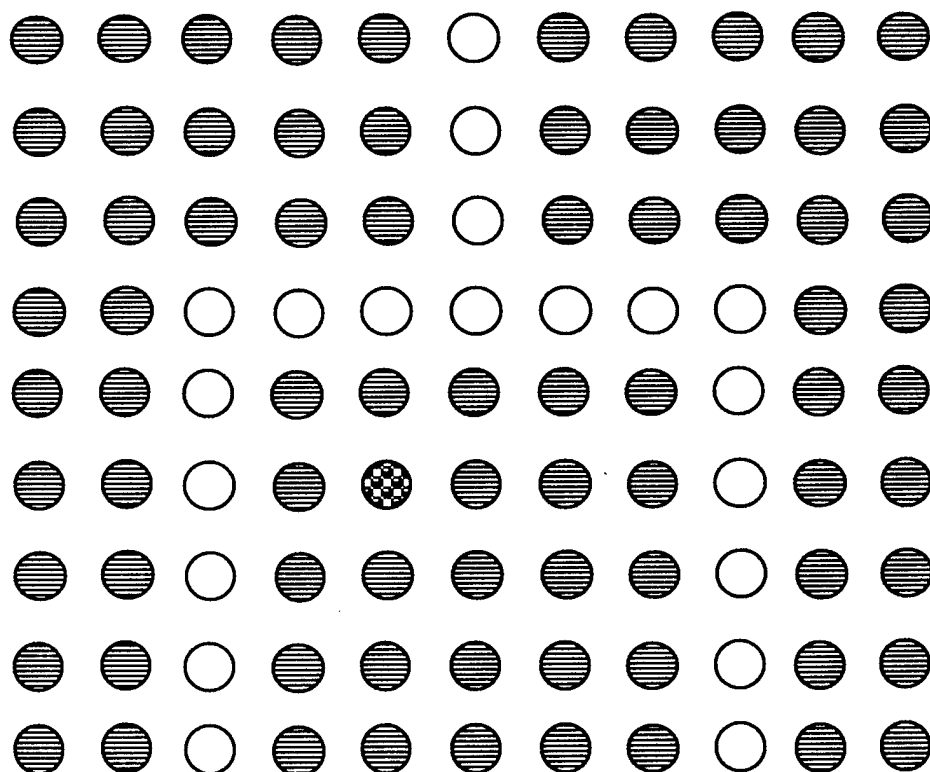


**Figure 3. Basic nanometer PBG defect switch.**

# Fabrication Processes for 3D Periodic Nanostructures and Photonic Crystals

Shojiro KAWAKAMI

Research Institute of Electrical Communication, Tohoku University

2-1-1 Katahira, Sendai, 980-77 Japan

Phone: +81-22-217-5522 FAX: +81-22-217-5523

e-mail: shojiro@kawakami.riec.tohoku.ac.jp

## Abstract

We review process technologies for 3D periodic nanostructures and photonic crystals. We then propose layer-by-layer deposition by bias sputtering, and demonstrate its usefulness. The mechanism of stationary pattern formation is elucidated.

## Introduction

Photonic bandgap structures[1,2], or photonic crystals, have many fascinating properties such as spontaneous-emission free lasers or radiation-free waveguide discontinuities, and attracted many theoreticians. By definition, photonic crystals require fabrication of 3D periodic nanostructures composed of high refractive index and low index materials with a large dielectric contrast. The spacial period is about half a wavelength in the medium. This requirement is quite severe. This paper discusses various techniques reported thus far, and then we propose a novel way of manufacturing (use of bias sputtering) and present experimental results indicating formation of stationary patterns. We finally discuss the role of several elementary processes of bias sputtering in the evolution of the surface shape during layer-by-layer deposition.

## Various Process Techniques

Before we review various techniques by different authors, we summarize important aspects comparison.

### ☆ To manufacture purely periodic structures:

- Flexibility on the choice of materials
- Flexibility on the type of symmetry and dimensions
- Capability to tailor geometry within the unit cell
- High degree of periodicity
- Sufficient number of periods (for example,  $> 10$ )

### ☆ To manufacture functional devices/waveguides:

- Flexibility to locally perturb periodicity
- Flexibility to accommodate/embed functional materials/devices within the periodic structure

Many different approaches have been tried to enable fabrication of photonic crystals. Some of them are summarized in Table 1. It will be understood that none of them sufficiently satisfies the above requirements.

### **A Novel Process for 3D Periodic Nanostructure Fabrication**

Replication of the surface bumps/pits in bias sputtering has been recognized by several authors[3]. We took advantage of this strange phenomenon to manufacture 3D periodic nanostructures in the following way.

We prepare a substrate, fused silica or single crystal silicon, having a hexagonal array of tiny holes. We deposit alternating a-Si and SiO<sub>2</sub> thin films. Bias sputtering is used when we make SiO<sub>2</sub> films. In the beginning, the top surface of each layer evolves, and after some transition layers, almost stationary pit patterns are established as shown in Fig. 1(10/20 periods)[4]. We also show the schematic configuration in (c). In other words, a 3D periodic nanostructure is successfully manufactured.

A point defect in a photonic crystal behaves like a resonant cavity, and a line of defects play the role of a waveguide. With this in mind, we then tried to form a family of line defects on a substrate. The AFM picture of Fig. 2 shows the top surface of one of samples after deposition of 10 periods. Bright/dark patterns are observed when it is illuminated by an incoherent source of 1.2 $\mu$ m wavelength(photographs not shown).

### **3D Pattern Physics: Evolution and “Convergence” to Stationary Patterns**

Evolution of the shape of the top surface of each layer is the key issue of the process explained in the previous section. The modelling of the process of surface evolution in the bias sputtering process has been investigated in [5].

We tried to identify the role of each microscopic process in bias sputtering. The elementary processes relevant to our experiments are:

1. Adsorption of neutral particles caused by their diffuse incidence.
2. Sputter-etching by incidence of charged gas ions, normal to the substrate plane.
3. Re-adsorption of target material during etching or deposition.

Simulation studies explained later support a very simple picture like this:

- Sputter etching forms the “shoulder part” which has a nearly constant slope.
- Diffuse incidence of neutral particles explains the formation of a well defined kink at the bottom.
- Redeposition fills the bottom part, and “self-adjusts” the depth of each hole or valley.

These simple arguments are supported by simulations given in Figs. 3 and 4. The experimental results are well fitted by simulations(shown in Fig. 5).

### **Conclusion**

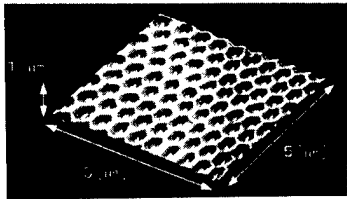
We reviewed a novel process to fabricate 3D periodic nanostructures with emphasis on photonic crystals. The process is flexible, reliable and versatile, and is expected to open a door to many novel devices and technologies.

### **References**

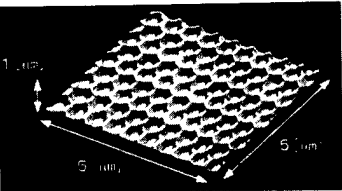
- [1] E. Yablonovitch, *Phys. Rev. Lett.*, **58**(20), pp. 2059–2062, 1987.
- [2] J. D. Joannopoulos et al., *Photonic Crystals* (Princeton Press, Princeton) 1995.
- [3] K. H. Guenther, *Appl. Opt.*, **20**(6), pp.1034–1038, 1981.
- [4] S. Kawakami, *Electron. Lett.*, **33**(14), pp.1260–1261, 1997.
- [5] S. Tazawa et al., *IEEE Trans. Semiconduct. Manufact.*, 5(1), pp. 27–33, 1992.

Table 1. Fabrication Techniques for Photonic Crystals

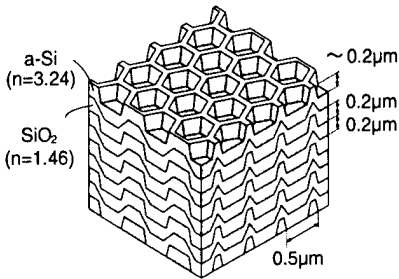
	material	method	sizes	periods	References
Cheng et al. (CALTECH,UCLA)	GaAs	RIE	0.35~0.46μm	4	J. Vac. Sci. Technol. B 13(6), 2696 (1995)
Noda et al. (Kyoto U.)	GaAs	wafer-bonding	4μm	1	Jpn. J. Appl. Phys. 35(7B), L909 (1996)
Feiertag et al. (Microtech. Mainz)	Resist (SiCN as replica material)	x-ray lithography (by SOR)	85μm	5	Appl. Phys. Lett. 71(11), 1441 (1997)
McIntosh et al. (MIT)	Al/polymer	additive lithography	2.83μm	3	Appl. Phys. Lett. 70(22), 2937 (1997)
Miguez et al. (CSIC)	SiO <sub>2</sub> sphere	self ordering	0.22μm	~∞	Appl. Phys. Lett. 71(9), 1148 (1997)
<b>Present Method (Tohoku U.)</b>	<b>SiO<sub>2</sub> /Si</b>	<b>Bias Sputtering</b>	<b>0.4~0.5μm</b>	<b>≥ 20</b>	Trans. IEICE J80-C-I(6), 296 (1997)



(a)



(b)



(c)

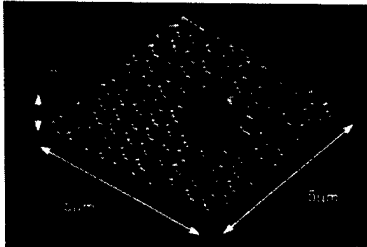


Fig. 2. AFM image of the surface of the multilayer with a line defect.

Fig. 1. Fabricated 3D periodic structures. AFM image of (a) 10 periods, (b) 20 periods. (c) Schematic configuration.

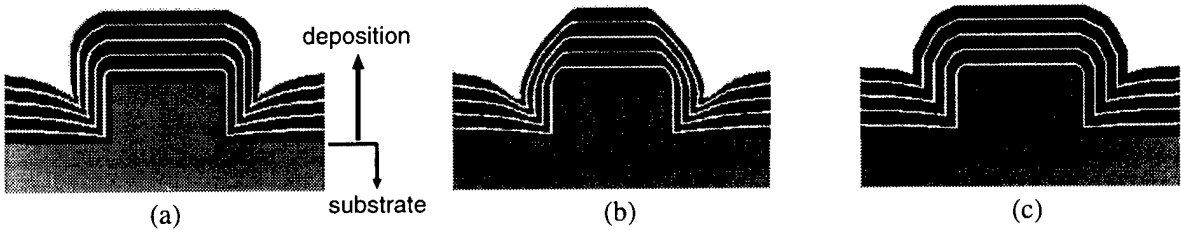


Fig.3. 2D simulation of evolution of the surface shape. (a) Diffuse incidence of neutral particle, (b) Angle-selective etching superposed on (a), and (c) Redeposition superposed on (a).

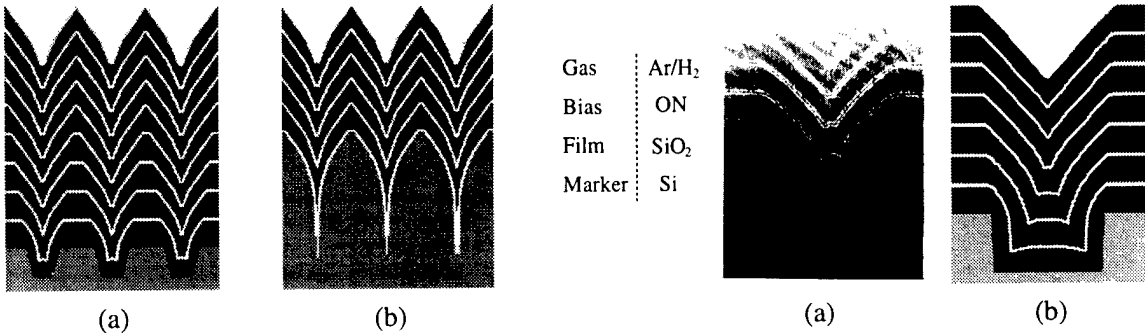


Fig. 4. Simulation of self-shaping processes. Starting from (a) shallow grooves, (b) deep grooves.

Fig. 5. Comparison of (a) experimental result and (b) simulation.

## Membrane Microresonator Lasers with 2-D Photonic Bandgap Crystal Mirrors for Compact In-plane Optics

*B. D'Urso, O. Painter, A. Yariv and A. Scherer*  
Electrical Engineering, Caltech, Pasadena, CA 91125

### Introduction

Fabrication of two dimensional photonic bangap crystals makes it possible to control the propagation of light within a plane. Confinement of light in the vertical direction can be attained by the use of a thin suspended membrane of high refractive index material. This waveguiding slab, which contains the 2-D photonic crystals can also be used to connect adjacent optical devices [1]. Microcavities based on photonic crystals can therefore be used to define either small laser sources or optically pumped switches. Emitted light from one or more microcavities can be used to pump others, forming a compact optical switching network. Here we design and fabricate such in-plane membrane microresonators with the purpose of connecting them in compact optical networks. Within the plane of light propagation, microcavities can be designed to interact through optical paths defined in the photonic bandgap crystals. Photonic crystals can thus provide the desired freedom in the geometrical design of the cavities as well as the coupling channels. We consider the use of a triangular array of air holes in a slab of material with a high dielectric constant [1-3], which has been shown to exhibit a bandgap for both TE and TM polarizations. The InGaAs/InGaAsP material system was chosen since it does not suffer from large surface recombination losses and is relatively easy to microfabricate structures into. It has previously [4] been used to demonstrate optically and electrically pumped whispering gallery mode microdisk lasers with radii down to 1  $\mu\text{m}$  and cavity thicknesses comparable to our designs.

### Procedure

A structure with six 12nm thick InGaAs quantum wells separated by five 12nm thick InGaAsP barriers and InGaAsP layers on the top and bottom of the quantum wells was grown by organometallic vapor phase epitaxy (OMVPE) on an InP substrate. A surface mask composed of 60 nm of  $\text{SiO}_2$ , followed by 5 nm Cr, 50 nm Au, and 70 nm of polymethylmethacrylate (PMMA) was deposited on top of this sample. The PMMA resist was then exposed with a Hitachi S-4500 field-emission electron microscope to define the 2-D photonic crystals and optical cavities. After developing in cellusolve/methanol, the patterns in the PMMA layer were transferred through the Cr and Au layers with an  $\text{Ar}^+$  ion beam. This metal mask was used to transfer the lithographic patterns into the  $\text{SiO}_2$  mask by using a  $\text{C}_2\text{F}_6$  reactive ion etching (RIE) process [5]. Finally, the lateral resonator structures were etched through the InGaAs/InGaAsP multiple quantum well layer by using chemically assisted ion beam etching (CAIBE) with an argon ion beam assisted by chlorine reactive gas. After the holes were etched through the InGaAs and InGaAsP layers, the InP substrate was removed by isotropic chemical etching with HCl through the microfabricated holes. This procedure left a suspended membrane of perforated InGaAs/InGaAsP material to create membrane microresonators.

Triangular and hexagonal cavities were designed using the effective index of refraction of the waveguide, determined from the propagation constant of the TE mode. Next, the band structure of a 2-D photonic crystal made by etching holes into a slab of material with this index of refraction was calculated using a plane wave expansion. The band structure of a triangular array of holes was then used to design the mirrors for the triangular and hexagonal cavities such that the emission wavelength of the InGaAs was within the bandgap of the lattice. We have developed and used a finite-difference time-domain (FDTD) [6-9] method to investigate the behavior of light in membrane microresonator cavities. The steady state modes were extracted using a numerical Fourier filter.

### Cavity Design and Fabrication

When taking into account the thickness of the waveguide, we determine an effective index of refraction of the waveguide layer of 2.6491. This value can be used to calculate the band structure of a triangular array of holes etched into the material. The band structure reveals the existence of a bandgap for TM (magnetic field parallel to axis of holes), but no bandgap for TE (electric field parallel to axis of holes). Thus, the array acts as a mirror for TM polarized light but not for TE polarization. The triangular cavity is designed with normalized frequency  $\omega a/2\pi c = 0.31$ . For the light emission peak of InGaAs at  $1.55\mu\text{m}$ , this requires a hole spacing  $a = 500\text{nm}$  and radius  $r = 150\text{nm}$ , which is well within the resolution range of electron beam lithography.

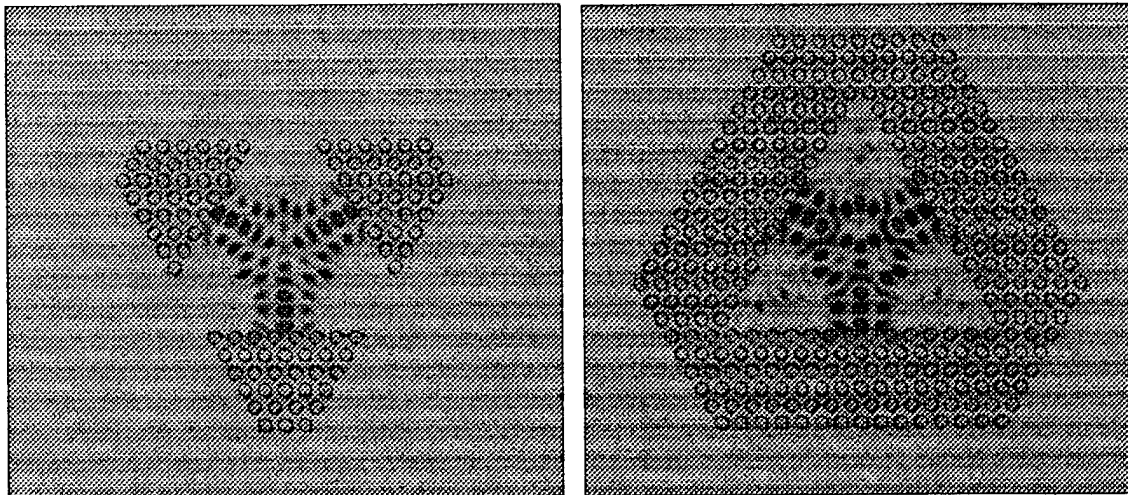
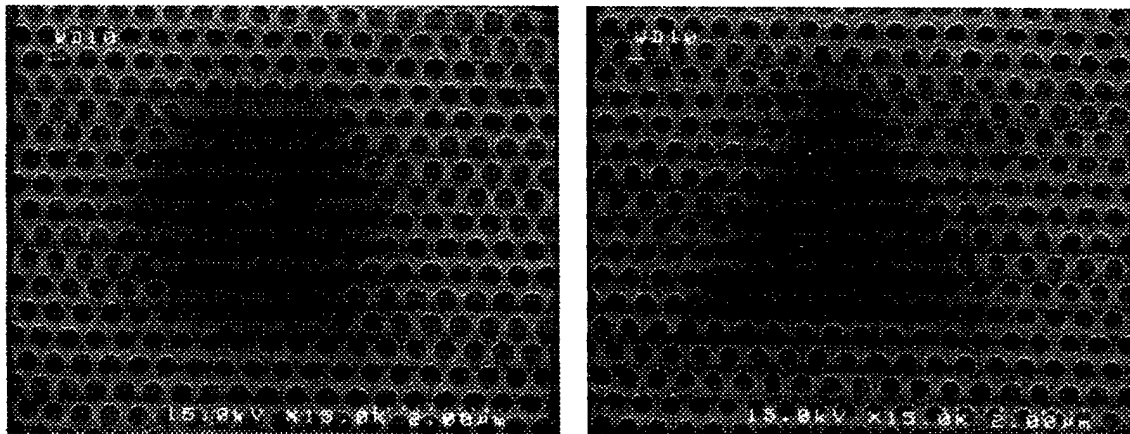


Figure 1. Calculated modes supported within thin triangular membrane cavities. Here the color indicates intensity (magnitude squared) of the magnetic field.

A triangular cavity of length  $7\mu\text{m}$  per side with the mirrors described above can be modeled with the FDTD method. In order to find a mode of the full cavity which reflects primarily off of the middle of the sides and not out of the corners, we begin by finding a mode of the cavity without mirrors on the corners figure 1a. The solution for this cavity is then used as the initial field for filtering in the complete cavity figure 1b. Notice that the mode interacts strongly with the center of each side and only weakly with the corners, as desired

The quality (Q) of these modes is also calculated with a two-dimensional FDTD method. The full triangular cavity without any output channels has a Q of 4300. The cavity Q for this mode is substantially reduced to a value of 900 when a coupling waveguide is included through the side of the triangular cavity which reflects a high field intensity. Examples of microfabricated hexagonal and triangular cavities are shown in Figure 2, where a scanning electron micrograph shows the geometry of these membrane microresonators. The distances between holes in the 2D photonic bandgap mirrors correspond to the optimized dimensions calculated earlier.

*Figure 2. SEM micrographs showing examples of microfabricated hexagonal and triangular optical cavities with  $\sim 5\mu\text{m}$  lateral dimensions.*



We have shown that photonic crystals can be used to localize light into a triangular cavity. In particular, we have designed a mirror and cavity for use with the InGaAs/InGaAsP system. We have also demonstrated the initial stages in the fabrication of the triangular cavity designed. Optical pumping of these structures will be attempted in the near future.

## References

1. J.D. Joannopoulos, R.D. Meade, J.N. Winn, *Photonic Crystals*, (Princeton University Press, 41 William Street, Princeton, NJ 08540, 1995)
2. S. Fan, P.R. Villeneuve, J.D. Joannopoulos, E.F. Schubert, Proc. Photonics West '97
3. T.F. Krauss, R.M. De La Rue, Appl. Phys. Lett., **68**, 1613, (1996).
4. A. Levy, R. Slusher, Appl. Phys. Lett., (1992)
5. J. O'Brien, O. Painter, C.C. Cheng, R. Lee, A. Yariv, A. Scherer, Electronics Lett., **32**, 2243, (1996)
6. M. Kanskar, P. Paddon, V. Pacradoui, R. Morin, A. Bush, J.F. Young, S.R. Johnson, J. Mackenzie, T. Tiedje, Appl. Phys. Lett., **70**, 1438, (1997)
7. M. Bartsch et al., Computer Physics Communications, **72**, 22 (1992)
8. D.H. Choi, W.J.R. Hoefer, IEEE Transactions on Microwave Theory and Techniques, **34**, 1464, (1986)
9. Z. Bi, Y. Shen, K. Wu, J. Litva, IEEE Transactions on Microwave Theory and Techniques, **40**, 1611 (1992)



**Integrated Photonics Research**

# **Lasers I**

**Tuesday, March 31, 1998**

**Jean Francois Vinchant, Alcatel Optronics, France**  
Presider

**ITuB**  
**8:30am-10:00am**  
Salon C

# Single Transverse Mode Active MMI InGaAsP/InP Laser Diode

Kiichi Hamamoto<sup>(\*)</sup>, Emilio Gini, Christoph Holtmann and Hans Melchior  
 Swiss Federal Institute of Technology  
 CH-8093 Zurich, Switzerland

Phone: +41-1-633-3773 Fax: +41-1-633-1109 E-mail: hamamoto@iqe.phys.ethz.ch

\* On leave from Optoelectronics and High Frequency Device Research Laboratories, NEC Corporation, Japan

**Abstract** A novel laser diode structure incorporating active multi-mode interferometers (MMI) realized in InGaAsP/InP achieves up to 90% higher single lobe and fiber coupled outputs at 1.3 $\mu$ m.

**1. Introduction** High output power single transverse mode laser diodes (LD) are attractive for several applications, for instance, long distance transmission and local area access. One way to obtain high output power from LD's is to utilize a multi mode waveguide<sup>(1)-(3)</sup> because it has a wide pumping area, which improves power saturation level, compared to regular single lobe LD. Among them, active multi-mode interferometer (MMI) LD's<sup>(3)</sup> are attractive since they offer the possibility for high power single transverse mode operation with a relatively simple structure. We have already confirmed<sup>(3)</sup> that active MMI waveguides work as LD's.

In this paper, we report the first significant output power increases by utilizing this active MMI-LD concept. Active MMI-LD's were implemented, together with regular LD's, in InGaAsP/InP buried hetero structures (BH) for 1.3 $\mu$ m. Increases in output power and slope efficiency of 90% and 20%, respectively, were achieved, while remaining single lobe far fields and good coupling to standard single-mode fibers (SMFs).

**2. Concept of the active MMI-LD** A schematic view of the active MMI-LD is shown in Fig. 1 (a). It consists of conventional single mode waveguides that are connected to 1x1-MMI couplers<sup>(4)</sup>. The MMI exhibits a larger width than the single mode waveguides. By proper design of the length and width of the MMI section, single mode optical field at the input is identically imaged at the MMI output (see Fig. 2). The resulting structure behaves as single transverse mode waveguide although the main part is designed as multi-mode waveguide with wider pumping area, compared to conventional single mode waveguides. The active MMI structures are designed such that index guiding is not disturbed by current injection induced refractive index changes.

**3. Design** The active MMI-LD concept has been realized, together with regular LD's, in InGaAsP/InP BH-LD structure for operation at  $\lambda=1.3\mu$ m. Figure 1 shows the schematics of the fabricated LD's. The widths of the waveguides in the MMI regions of the active MMI-LD are 6.5 $\mu$ m, their lengths 135 $\mu$ m. The widths of the single mode waveguides integrated at the input port, intermediate section, and output port as shown in Fig. 1 (a) are 2 $\mu$ m. Two MMI regions are integrated to result in a device length of 600 $\mu$ m and a total area of 2.4x10<sup>-5</sup>cm<sup>2</sup>. Regular single lobe LD's, for comparison, with 2 $\mu$ m width waveguides and the same device length of 600 $\mu$ m, covers the area of 1.2x10<sup>-5</sup>cm<sup>2</sup> (shown in Fig. 1. (b)). The active areas of the MMI-LD's are, thus, twice the active areas of the regular LD's.

The hetero epitaxial layer structure is the same for both the MMI-LD's and the regular LD's (shown in Fig. 1. (c)). The active layer is bulk 1.3 $\mu$ m-InGaAsP of 0.15 $\mu$ m thickness. p-InP and n-InP current blocking layers are inserted beside it. On them, p-InP cladding layer and p<sup>+</sup>-InGaAs contact layer are stacked. The double channel structure was used for current blocking<sup>(5)</sup>.

**4. Results and discussion** For the fabrication, metal organic vapor phase epitaxy (MOVPE) and  $\text{CH}_4/\text{H}_2$  reactive ion etching (RIE) were used. Both facets of the active MMI-LD's and the LD's were as-cleaved. Characteristics were evaluated in CW and in pulsed operation (pulse width: 10 $\mu\text{s}$ , duty cycle: 1%) at 20°C. Single facet emission and power coupled into standard single-mode fibers (SMF) was investigated.

Figure 3 shows the far field pattern of the fabricated active MMI-LD. The full width at half maximum angle ( $\theta_{//}=24^\circ$ ,  $\theta_{\perp}=29^\circ$ ) is similar to the angle of previously reported BH-LD<sup>(5)</sup>. The output power characteristics of the active MMI LD's and of the regular LD's are shown in Fig. 4 (a) and (b), both for emission from one facet and for coupling to a SMF. Typical active MMI-LD and regular LD characteristics are compared in table 1. The maximum output power of the active MMI-LD's in CW operation (27mW/facet) increases by 90%, compared to single mode LD's (14mW/facet). It is thought that the larger active area, namely larger pumping area, improves the saturation of the output power caused by thermal heating from current injection. The maximum output power of the active MMI-LD's under pulsed operation (82mW/facet) also increases by 40%, compared to single mode LD's (58mW/facet). This increase is mainly due to the difference in turn-on of the bypass current blocking layers<sup>(6)</sup>. The larger active area in active MMI-LD results in lower series resistance.

The slope efficiency of the active MMI-LD's (0.12W/A) also increases by 20%, compared to single mode LD (0.10W/A). This is because the MMI waveguide has a larger overlap between the optical field and the electric one, compared to single mode waveguides. It is thought that this larger overlap also contributes to the lower threshold current densities of the active MMI-LD's (3.8kA/cm<sup>2</sup>) as mentioned in tab. 1.

From the results of the power coupled into a SMF, shown in fig. 4 (a) and (b), it appears that the active MMI-LD's keep single transverse mode output up to higher powers than single mode LD's for both CW and pulsed operations.

**5. Summary** A novel large active area laser diode (active MMI-LD) was demonstrated in InGaAsP/InP BH-LD. The fabricated active MMI-LD's showed significant maximum output power and slope efficiency increases, compared to the conventional single mode LD. As the power coupled into SMF is also higher for active MMI-LD's than by single mode LD's, it seems that active MMI-LD's are suitable for the application of high power single lobe LD's.

**Acknowledgment** The authors would like to thank Juerg Eckner, Werner Hunziker and Marcus Duellk for technical support and useful discussions.

#### References

- (1) P. Vankwikelberge, et. al., J. Quantum Electron., 1987, **QW-23**, (6), pp. 730-737
- (2) A. Al-Muhanna, et. al., Appl. Phys. Lett., 1997, **71**, (9), pp.1142-1144
- (3) K. Hamamoto, et. al., 8th ECIO (Stockholm, Sweden), 1997, pp. PD5-1-PD5-4
- (4) L. B. Soldano et. al., J. Lightwave Technol., 1995, **13**, (4), pp. 615-627
- (5) I. Mito, et. al., Electron. Lett., 1982, **18**, (22), pp. 953-955
- (6) N. K. Dutta, et. al., J. Lightwave Technol., 1984, **LT-2**, (3), pp. 201-208

Tab. 1. Typical LD characteristics of the fabricated active MMI-LD and regular LD

	CW operation			Pulsed operation		
	Maximum Power	Slope Efficiency	Threshold	Maximum Power	Slope Efficiency	Threshold
Active MMI-LD	27 mW/facet	0.12W/A	92mA (3.8kA/cm <sup>2</sup> )	82 mW/facet	0.12W/A	74mA (3.1kA/cm <sup>2</sup> )
Regular LD	14 mW/facet	0.10W/A	65mA (5.4kA/cm <sup>2</sup> )	58 mW/facet	0.10W/A	58mA (4.8kA/cm <sup>2</sup> )

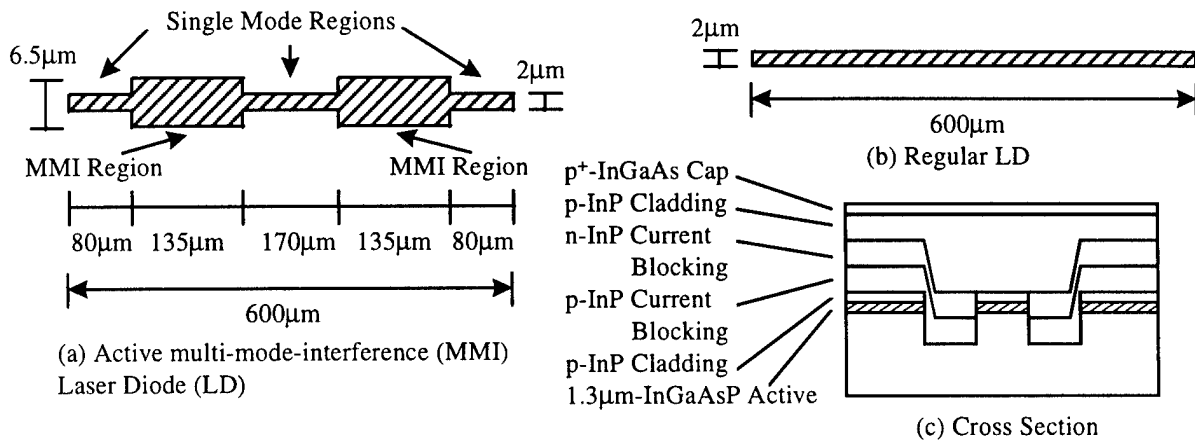


**Fig. 1. Multi-mode interferometers (MMI) and regular laser diodes (LD's)**

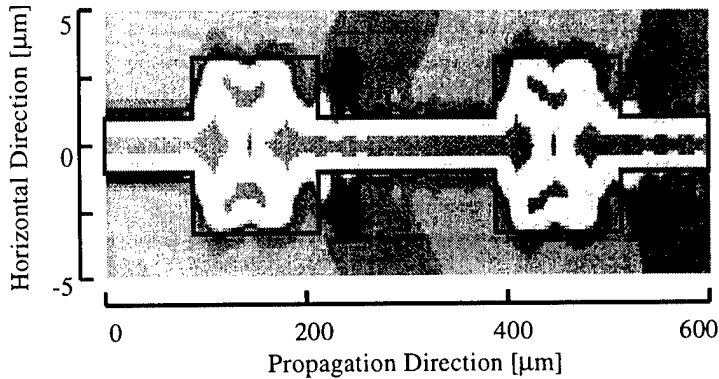


**Fig. 2. Simulated mode propagation through active MMI-LD** (gain=100cm<sup>-1</sup>, by 2-dimensional beam propagation method)

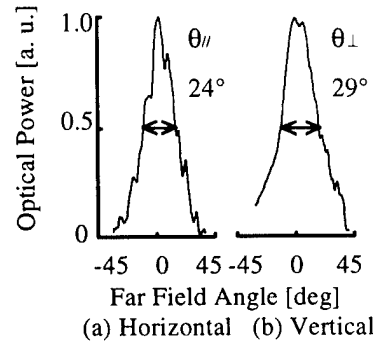
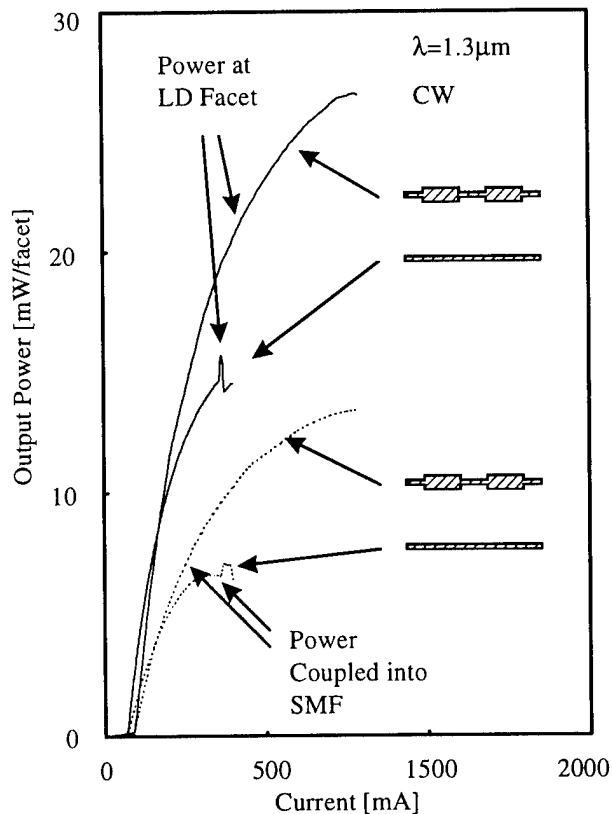
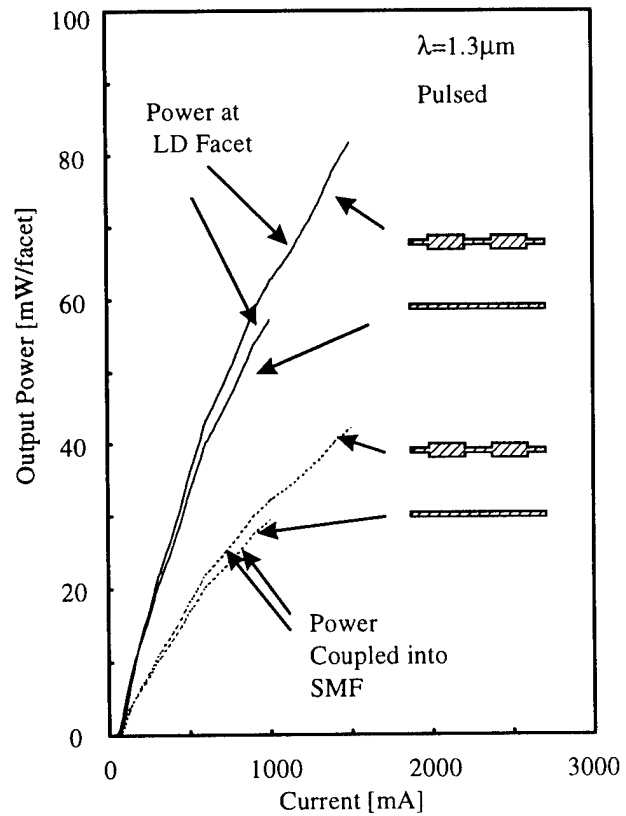


**Fig. 3. Far field pattern of active MMI-LD**



(a) CW Operation



(b) Pulsed Operation

**Fig. 4. Output power characteristics at active MMI-LD and LD in CW and pulsed operation** ( — : Power at LD Facet, ..... : Power coupled into single mode fiber (SMF))

## Integrated amplifier/multi-mode interference coupler laser for high optical power in a single-mode waveguide

F. Camacho, C.J. Hamilton, A.C. Bryce and J.H. Marsh

*Department of Electronics and Electrical Engineering,*

*University of Glasgow, Glasgow G12 8QQ, UK,*

Tel: + 44 141 3306008, Fax: + 44 141 3304709, E-mail: F.Camacho@elec.gla.ac.uk

High-power semiconductor lasers with a fundamental transverse mode are desirable for applications such as optical disk memories, free-space communications, second-harmonic elements, etc. For the generation of high optical power with a fundamental transverse mode, narrow stripe lasers are used. However, a major reliability concern for this type of semiconductor laser, because of the large optical power density at the mirrors, is facet degradation due to catastrophic optical damage (COD). This COD at the laser facet is due to absorption of the intense optical flux, which generates carriers, and the subsequent non-radiative recombination of these carriers leads to localised heating and oxidation of the laser facet. Two different techniques are usually employed to avoid COD: the first one is facet treatment [1,2], where the laser facet is chemically treated or coated to make it more difficult for the facet to oxidise, and the second technique makes use of non-absorbing mirrors (NAMs) [3,4].

In this paper, we present a new configuration for high optical power generation. Using quantum-well intermixing (QWI), we have monolithically integrated four amplifiers/lasers with a passive multi-mode interference (MMI) coupler and a passive output waveguide, as shown in Figure 1. For the light generated by the four amplifiers to recombine constructively at the single output waveguide, two conditions must be fulfilled: the light emission from the amplifiers must be locked in phase and a phase shift between the two inner and the outer arms is required. We believe the laser self-adjusts the phase length of the four amplifiers by adjusting the gain, and thus the wavelength and longitudinal mode that has the lowest threshold condition for the high power laser supermode overall is selected.

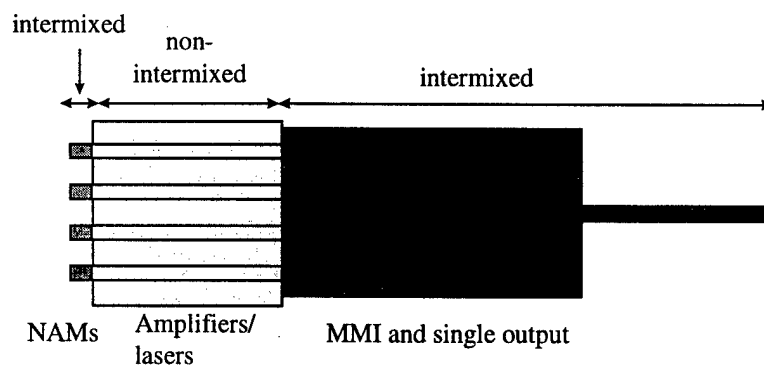


**Figure 1:** Schematic diagram of the integrated amplifiers/MMI semiconductor laser.

The device, fabricated with double quantum-well GaAs/AlGaAs material, comprises: a) four amplifiers (1 mm long and 4  $\mu\text{m}$  wide) with 30  $\mu\text{m}$  long NAMs at the facet side, and with a separation between waveguides of 2.5  $\mu\text{m}$ , b) a 4-to-1 MMI coupler (675  $\mu\text{m}$  long and 26  $\mu\text{m}$

wide) and c) a output waveguide (325  $\mu\text{m}$  long and 4  $\mu\text{m}$  wide). The total length of the device was 2 mm. The NAMs, MMI and output waveguide were fabricated using an initial QWI step to widen selectively the bandgap of these regions [5], giving a low-loss passive waveguide section. This integration technique is much easier, cheaper and has a higher yield than those involving material regrowth [3,4]. Furthermore, the use of QWI ensures perfect alignment between the active and passive sections of the device and results in a negligibly small reflection at the interface.

Figure 2 shows the light-current curve of our device. The threshold current was 120 mA, and the slope efficiency around 10% per facet. Even though the laser threshold current was quite low, equivalent to an injected current of 30 mA per single amplifier, the efficiency of our device was unexpectedly low. One reason for this low efficiency might be a high propagation loss in the passive areas of the device, but this should not be a problem because using QWI, the loss coefficient in the passive regions can be reduced to values as low as  $2\text{ cm}^{-1}$  [6]. However, it is also possible that the poor efficiency is related to the way we fabricated this device. In this first version of our device, the amplifiers, the MMI coupler and the output waveguide were shallow etched, to a depth around 200 nm above the active region. This is not the best configuration for the MMI, as its wall reflectivity would not be very high and the MMI could be very lossy. Devices with deep etched MMI and output waveguide (etched across the active region) are now being fabricated, and we believe these lasers will have a much higher efficiency.

Notwithstanding the above comments, an output power of over 180 mW per facet was obtained without any noticeable damage at any of the laser's facets, and at the passive side of the device the 180 mW was in a single ridge waveguide.

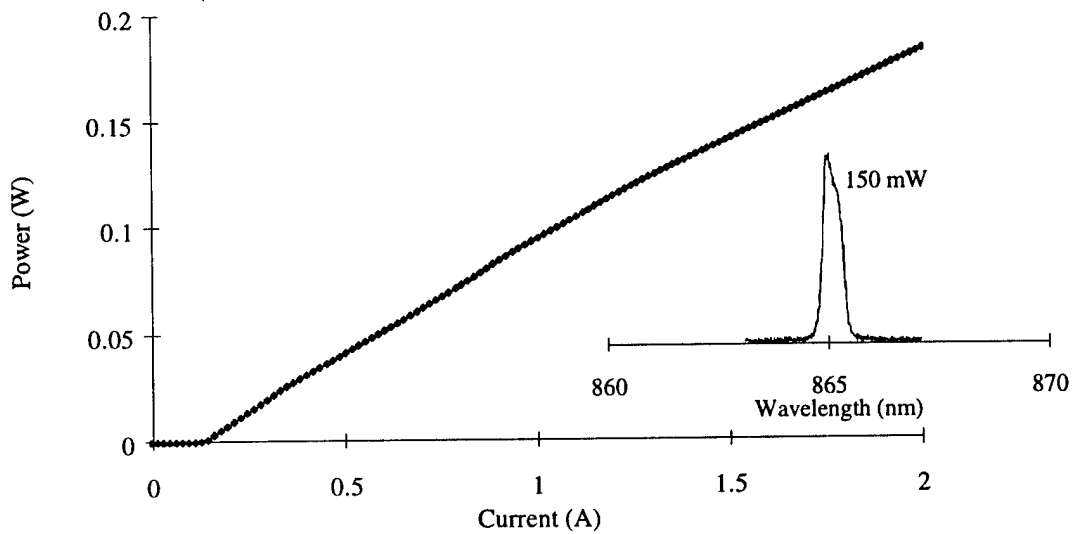


**Figure 2:** Light-current characteristic and optical spectrum of the device.

Figure 2 also shows the optical spectrum of the laser at an injected current of 1.5 A. The laser emission was centred at around 860 nm and the spectral width was 0.2 nm.

Figure 3 shows the near field images obtained from the front (single output waveguide) and back (four amplifiers) of our high power device. It can be seen that the output waveguide was single transverse moded, but there is some light at the right of the main peak due to leakage through the shallow etched slab. Because of the non-uniformity in the light generated at the four amplifiers, as can be seen in Figure 3, the MMI coupler does not have the imaging point at exactly the middle point of its output, but it is shifted from the centre. We believe this is the reason why the leakage light can be seen at the right of the output waveguide.

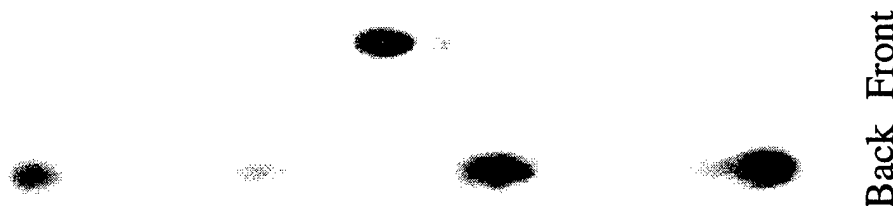


**Figure 3:** Near-field images from the front and back of the device.

Far field measurements on the amplifier side of the device showed that the light generated by the amplifiers was locked in phase, giving a stable far field pattern as the injected current was increased.

**In conclusion** we have shown a new configuration for high power semiconductor lasers. The device generated over 180 mW per facet, with single transverse mode operation out of the passive output waveguide. The device threshold was 120 mA and the efficiency around 10%.

### References

- <sup>1</sup> S. Kamiyama, Y. Mori, Y. Takahashi and K. Ohnaka, "Improvement of catastrophic optical damage level of AlGaInP visible laser diodes by sulfur treatment," *Appl. Phys. Lett.*, 1991, **58**, 23, pp. 2595-2597.
- <sup>2</sup> N.K. Dutta, W.S. Hobson, G.J. Zyzdik, J.F. de Jong, P. Parayanthal, M. Passlack and U.K. Chakrabarti, "Mirror passivation of InGaAs lasers," *Electron. Lett.*, 1997, **33**, 4, pp. 213-214.
- <sup>3</sup> H. Naito, M. Kume, K. Hamada, H. Shimizu and G. Kano, "Highly-reliable CW operation of 100 mW GaAlAs buried twin ridge substrate lasers with non-absorbing mirrors," *IEEE J. Quantum Electron.*, 1989, **25**, 6, pp. 1495-1499.
- <sup>4</sup> M. Matsumoto, K. Sasaki, M. Kondo, T. Ishizumi, T. Takeoka, H. Nakatsu, M. Watanabe, O. Yamamoto and S. Yamamoto, "High-power 780 nm AlGaAs narrow-stripe window structure lasers with window grown on facets," *Jpn. J. Appl. Phys.*, 1993, **32**, 5, pp. 665-667.
- <sup>5</sup> S.D. McDougall, O.P. Kowalski, J.H. Marsh, and C.N. Ironside, "Extended cavity ridge waveguide lasers operating at 1.5 $\mu$ m using a simple damage induced quantum well intermixing process," *Electron. Lett.*, 1997, **33**, pp. 1957-1958.
- <sup>6</sup> A.C. Bryce, F. Camacho, P. Cusumano and J.H. Marsh, "CW and mode-locked integrated extended cavity lasers fabricated using impurity free vacancy disordering," *IEEE J Selected Topics Quantum Electron.*, 1997, **3**, pp. 885-892.

# Efficient InP-based Integrable Spot-Size Converter

J. Stulemeijer<sup>1</sup>, A.F. Bakker<sup>2</sup>, I. Moerman<sup>3</sup>, F.H. Groen<sup>4</sup>, M.K. Smit<sup>1</sup>

<sup>1</sup>Delft University of Technology, Faculty of Information Technology and Systems,  
TTT Laboratory, P.O. Box 5031, 2600 GA Delft, The Netherlands,  
Tel. +31-15-2786106, Fax +31-15-2784046, Email J.Stulemeijer@et.tudelft.nl

<sup>2</sup>BBV Software BV, Enschede, The Netherlands

<sup>3</sup>University of Gent-IMEC, Department of Information Technology, Belgium

<sup>4</sup>Delft University of Technology, Faculty Applied Sciences, Delft, The Netherlands

## Abstract

An InP-based spot-size converter has been realized in a relatively simple technology, showing less than 3 dB coupling loss to a cleaved fiber for TE polarized light.

## Introduction

Most spot-size converters have a weakly guiding large waveguide at the fiber side and a small waveguide which has a much higher contrast at the rest of the chip. The spot-size conversion is achieved by deforming the mode of the high-contrast waveguide to the mode of the weakly guiding waveguide. The two waveguides can be in-line [1,2] or the waveguide with the higher contrast can be tapered to cutoff with the lower contrast waveguide located underneath. This can be done both in the lateral [3] and the transverse direction [4], see figure 1. A disadvantage of the lateral tapering is that the waveguide dimensions have to be controlled accurately into the sub-micron range; cutoff usually occurs at waveguide widths far below 1  $\mu\text{m}$ . Transverse tapering has the disadvantage of requiring a non-planar technology for a gradual reduction of the waveguide width. In this paper we present first results on a transverse tapering method based on a diffusion-limited etch which is compatible with the technology for realizing an integrated optical crossconnect [5].

## Taper design

We have chosen for a transverse tapering using a diffusion limited etch [6]. In this approach the etch rate is controlled by controlling the width of the slit in the etching mask, the wider the slit the lower the local etch rate at the center of the slit because of depletion of the etchant. For the weakly guiding

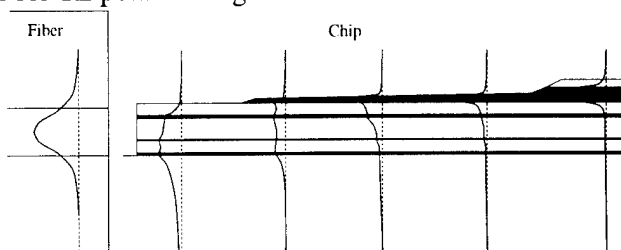


Figure 1 Schematic light distribution in SSC.

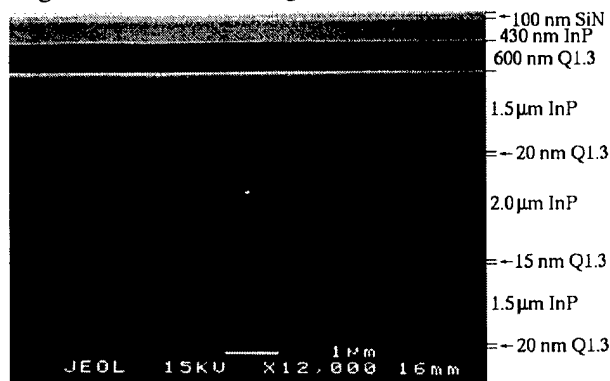


Figure 2 The layerstack.

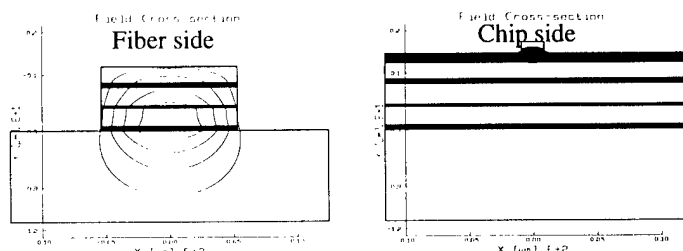


Figure 3 Spot at input and output of SSC.

waveguide we have chosen for a diluted InGaAsP/InP layer structure consisting of three thin quaternary layers embedded in InP.

Our strategy was to optimize the coupling efficiency to a fiber with a minimal thickness of the diluted waveguide structure by properly choosing the widths and distances for the quaternary layers. We arrived, using a 2D mode solver from BBV software, at a minimal transverse mode mismatch loss of 0.3 dB for a diluted waveguide width of only 5  $\mu\text{m}$  thickness with the following structure : 1500/20/2000/15/1500/20 nm InP/Q1.3/InP/Q1.3/InP/Q1.3, see figure 2.

It was chosen to make a large lateral taper in the upper high contrast waveguide. The field distribution, computed with a 2D mode solver, at the input and at the output of the SSC are shown in figure 3.

Care must be taken when the film is tapered down in height, because at the point where the mode couples from the upper film to the lower waveguide the height variation must be slow. This implies that a non-linear height profile is needed, otherwise the length of the SSC would become impractical. Furthermore it must be taken into account that the TE and TM mode have different heights at which they couple to the substrate. The non-linear profile was optimized using a 2D BPM in the transverse direction.

Finally the mode conversion loss of the entire SSC, as shown in figure 4, was computed using a 3D BPM, this gave a loss of 1.2 dB for the TE polarization.

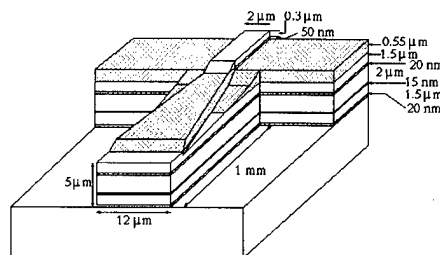


Figure 4 Schematic view of SSC.

## Fabrication

The fabrication of the SSCs was done in three lithographic steps. The wafer, with a layerstack as shown in figure 2, is grown with MOVPE. The first step in the process is the vertical tapering of the film layer using a diffusion limited etch, see ref. [6]. A layer of 100 nm SiN is deposited using a PECVD to serve as diffusion limiting etch mask. Next a pattern is defined in the SiN using contact lithography. The chip is etched in Br:CH<sub>3</sub>OH 1:2000 at 25°C for about one and a half minutes. This etch is isotropic and has the same etch rate for InP and InGaAsP. It was found that stirring was needed during the etch to guarantee a sufficiently uniform etch depth. The etch was interrupted three times to measure the etch depth such that the precise etch depth could be reached within 6% variation over the chip. The diffusion limited etch reached an etch rate of three times the etch rate in an open plane when 10% of the surface was left open by the diffusion limiter.

The next step is the etching of the ridge waveguides. This is done in a RIE with CH<sub>4</sub>/H<sub>2</sub> as etch gas and SiN as mask. The diffusion limited etch had left 70 nm of the initial 430 nm of the InP in the open planes, so an etch depth of 150 nm was necessary to etch 50 nm into the film.

Finally deep trenches are etched besides the SSC. The etch needs to go through 5  $\mu\text{m}$  of both InP and InGaAsP layers. H<sub>3</sub>PO<sub>4</sub>:HCl 4:1 and H<sub>2</sub>O:H<sub>2</sub>SO<sub>4</sub>:H<sub>2</sub>O<sub>2</sub> 10:1:1 are used as selective etches for InP and InGaAsP respectively. These etches are alternated until the etch depth of 5  $\mu\text{m}$  is reached. The SSC was put parallel to the [0 -1 -1]-direction in order to obtain perpendicular side walls in the InP etch. The final result is shown in figure 5.

The final result is shown in figure 5.

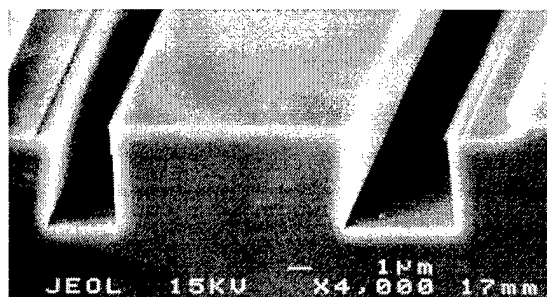


Figure 5 SEM picture of end of SSC.

## Results

Waveguides with small spots have been integrated with waveguides with spot size converters of various lengths on either side. For the waveguides with a normal small spot a propagation loss of  $0.7 \pm 0.2$  dB/cm was measured. The coupling loss from the end of the SSC to a SMF due to mode mismatch is below 1.2 dB (simulation: 0.3 dB). The total loss for coupling light from the fiber to the

chip through the SSC is shown in figure 6 as a function of taper length, for TE polarization. The losses for TM are worse by more than 3 dB per SSC. The alignment tolerances of the fiber for 1 dB extra coupling loss are  $\pm 2.6 \mu\text{m}$  and  $\pm 2.2 \mu\text{m}$  in the horizontal and vertical direction, respectively. The measured conversion loss is  $1.6 \pm 0.2 \text{ dB}$ .

## Discussion

The difference between measurement and simulation of mode overlap between fiber and SSC can be explained by the fact that the deep wet chemical etch did not go straight into the substrate, instead the side-walls incline slightly inwards making the waveguide about  $2 \mu\text{m}$  smaller.

The difference in performance of the SSC for TE and TM polarized can be explained as follows. As was mentioned above the TE and TM mode couple to the substrate at different heights of the film layer. From simulations it follows that the TM mode couples to the lower waveguide at a different position as the TE mode. At the position where TM couples to the low contrast waveguide, in the current design, the width of the waveguide is smaller than at the position where TE couples to the low contrast waveguide. This implies that the lateral mode-overlap between the upper waveguide and the lower waveguide is worse for TM than for TE. This translates directly into a higher conversion loss for TM polarization. In following design a taper in the upper waveguide can be inserted before the height of the film is tapered down.

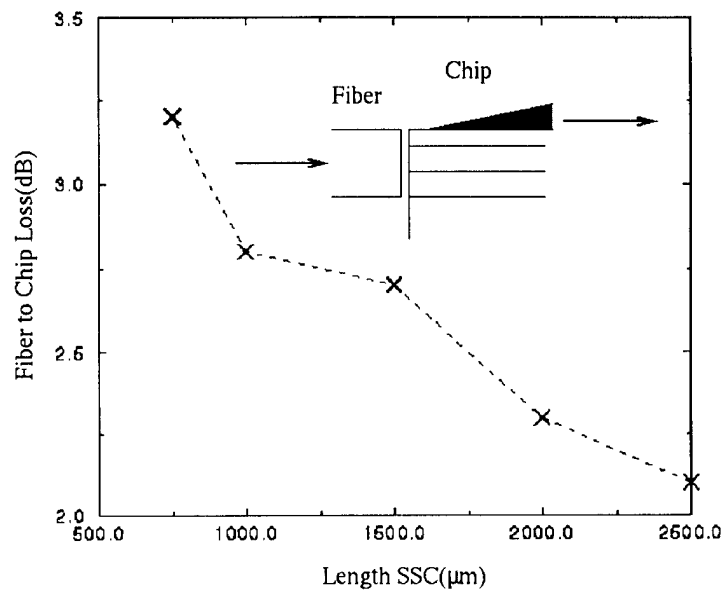


**Figure 6** Fiber-chip coupling losses as a function of SSC length.

## Conclusion

We have demonstrated an configuration for a SSC, which does not depend on regrowth. The fiber-chip coupling losses for both TE and TM agree well with simulations. Unfortunately the losses for TM are higher for the current design. The loss form a SMF to a waveguide with a spot of  $3 \times 2 \mu\text{m}$  is  $2.8 \pm 0.4 \text{ dB}$  for a SSC of 1 mm, for TE polarized light.

## References

- [1] T. Brenner, M. Bachman, H. Melchior, "Vertically tapered InGaAsP/InP waveguides for highly efficient coupling to flat-end single-mode fibers", *Appl. Phys. Lett.* **65**(7), 1994
- [2] I. Moerman, M. D'Hondt, W. van der Bauwhede, J. Haes, L. van Wassenhove, P. de Dobbelaere, R. Beats, P. van Daele, P. Demeester, W. Hunziker, C. Holtmann, "Vertically Tapered InGaAsP/InP Waveguides And Lasers Resulting in Low-Loss Fibre-Chip Coupling", *20<sup>th</sup> European Conference on Optical Communication*, 1994
- [3] G.A. Vawter, R.E. Smith, H. Hou, J.R. Wendt, "Semiconductor Laser with Tapered-Rib Adiabatic-Following Fiber coupler for Expanded Output-mode Diameter", *IEEE Photonics Technology Letters*, Vol. **9**(4), 1997
- [4] P. Albrecht, H. Heidrich, R. Löffler, L. Mörl, F. Reier, C.M. Weinert, "Polarization independent integrated mode transformer for uncladded InGaAsP/InP rib waveguides without epitaxial regrowth", *22<sup>nd</sup> European Conference on Optical Communication*, 1996
- [5] C.G.P. Herben, C.G.M. Vreeburg, D.H.P. Maat, K.J.M. Leijtens, M.K. Smit, F.H. Groen, J.J.G.M. van der Tol, P. Demeester, "A Compact Integrated InP-based Single- PHASAR Optical Crossconnect", submitted to *IEEE Photon. Technol. Lett.*
- [6] T. Brenner, M. Melchior, "Local Etch-Rate Control of Masked InP/InGaAsP by Diffusion-limited Etching", *J. Electrochem. Soc.*, Vol. **141**(7), 1994

## High power InGaAsP laser diodes with circular beam profile

Heonsu Jeon, Atul Mathur, and Mehrdad Ziari

SDL, Inc.  
80 Rose Orchard Way  
San Jose, CA 95134

Phone: 408-943-4322  
Fax: 408-943-1070  
Email: heonsuj@sdli.com

Asymmetric beam profile from a conventional laser diode is a major obstacle in achieving high coupling efficiency into a single mode fiber. Various techniques have been proposed and developed to solve this problem. Two major approaches are diluted waveguide design [1] and taper integration technology [2], and both schemes have been very successful in obtaining low divergence circular laser beam profile. Narrow beam divergence and circular mode profile can be, however, attainable at the expense of some penalty in laser performance due to lower optical overlap in the diluted waveguide case or due to losses from the taper. We report on a new taper fabrication process for a very low loss mode transformer, and the resultant experimental data on high power circular beam lasers.

The central waveguide structure of base wafer, grown using MOCVD epitaxy technique, consisted of two InGaAsP waveguide layers: a thick waveguide layer containing multiple quantum wells and a thin waveguide layer underneath. A smooth vertical taper was formed using a combination of non-selective and selective wet chemical etching techniques. Fig.1 schematically illustrates the fully processed device structure with the definitions of active, tapered, and passive sections. A strongly confined optical mode in the active section is gradually expanded along the taper in an adiabatic fashion. The expanded mode is then finally stabilized in the passive section

where only the underlying passive waveguide layer is left. Optical mode profile at the output facet and therefore beam divergence angle is solely determined by the thickness of the passive guiding layer. After a regrowth process for cap and contact layers, wafer was processed into ridge

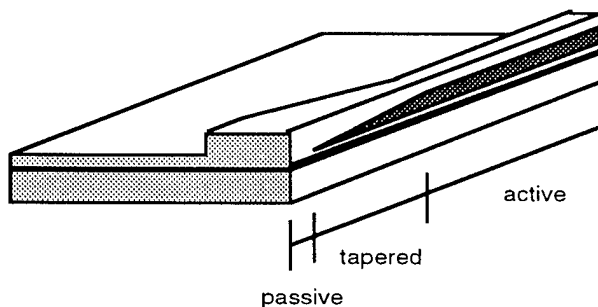


Fig.1 Schematic of the ridge waveguide laser device integrated with a vertically tapered mode transformer.

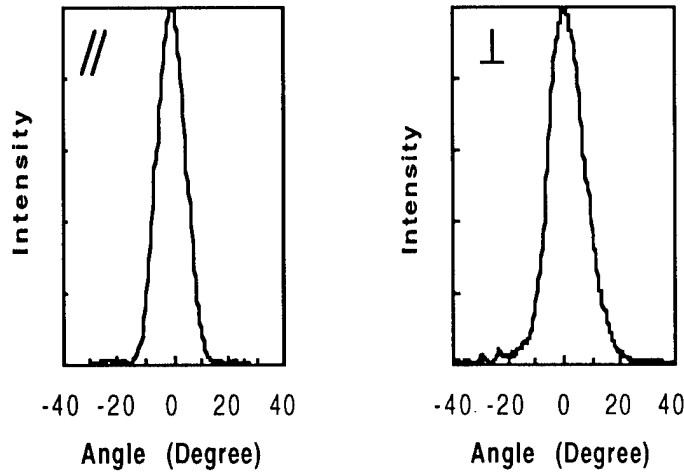


Fig.2 Far-field patterns from a typical tapered laser.

14° in the vertical directions, demonstrating a high quality symmetric circular laser beam profile. Especially, the 14° vertical divergence angle is a large improvement over ~40° for the non-tapered backside. Fig.3 displays the light output versus current characteristics, directly from a chip and after coupled into both a lensed and a cleaved single mode fibers. The demonstrated chip output

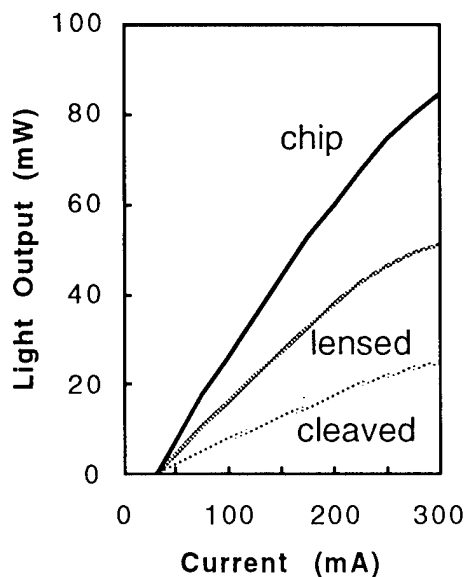


Fig.3 L-I characteristics of a tapered Fabry-Perot laser: from chip and after coupled into a lensed and a cleaved fiber.

waveguide lasers. Also shown in Fig.1 is the laterally tapered ridge structure toward the output facet to accommodate the expanded beam better. Cleaved laser devices were LR and HR coated on the front and rear facets, respectively, and bonded for cw testing.

Typical far-field patterns, as seen in Fig.2, showed smooth Gaussian-like profiles with the measured FWHM divergence angles of 12° in the lateral and

was well over 80mW while significant improvement in fiber coupling efficiency was readily obtained, upto 63% into a lensed fiber and 31% into a cleaved fiber. As a comparison, the corresponding coupling efficiencies of a non-tapered reference laser were 40% and 17%. Owing to the larger mode size, fiber misalignment tolerance has also been improved. The vertical tolerance measured in the butt-coupling scheme into a cleaved fiber was 3.7μm for the tapered laser diode and 2.8μm for a reference laser at -1dB extra loss from the maximum coupling. Our preliminary investigation also revealed that the taper loss is mainly governed by the background free-carrier

absorption loss (not by the radiation or scattering loss), indicating the high quality of our processed vertical taper.

The taper process technology has also been successfully applied to DFB laser fabrications for single longitudinal mode laser operation, yet with a circular beam profile. As demonstrated in

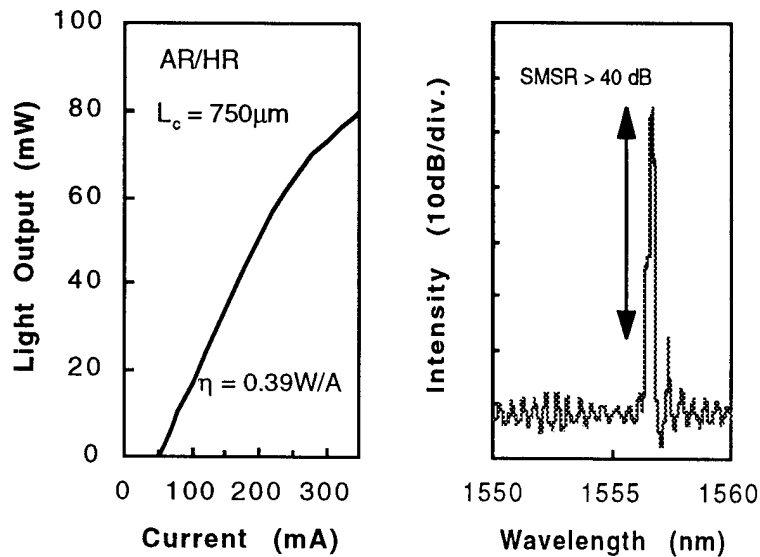


Fig.4 L-I and spectrum of a tapered DFB laser diode.

Fig.4, single DFB mode laser operation was achieved upto the output power level of greater than 80mW with the side mode suppression ratio of over 40dB. The FWHM divergence angles of the corresponding devices were  $12^\circ \times 14^\circ$  in the lateral and vertical directions. Some devices emitted laser output greater than 130mW even though they did not preserve single DFB mode operation at high current.

## References

1. For example, J.-M. Verdiell, M. Ziari, and D. F. Welch, "Low-Loss coupling of 980nm GaAs laser to cleaved singlemode fibre," *Electron. Lett.*, vol. 32, pp. 1817-1818, 1996.
2. For example, R. Ben-Michael, U. Koren, B. I. Miller, M. Young, M. Chien, and G. Raybon, "InP-based multiple quantum well lasers with an integrated tapered beam expander waveguides," *IEEE Photon. Technol. Lett.*, vol. 6, pp. 1412-1414, 1994; H. Kobayashi, M. Ekawa, N. Okazaki, O. Aoki, S. Ogita, and H. Soda, "Tapered thickness MQW waveguide BH MQW lasers", *IEEE Photon. Technol. Lett.*, vol.6, pp.1080-1081, 1994.

## Overview of integrated semiconductor multiwavelength lasers

C. R. Doerr

Bell Laboratories, Lucent Technologies  
791 Holmdel-Keyport Road, Holmdel, NJ 07733 USA  
(732) 888-7067, FAX: (732) 888-7007  
e-mail: crdoerr@lucent.com

### 1. Introduction

There are two main designs for creating multiple lasers at different wavelengths on a single chip with only one output. The first is to give each laser its own independent cavity and intracavity filter and then combine the lasers extra cavity, usually with a power combiner as in Fig. 1. Examples are the integration of distributed feedback (DFB) lasers[1] or distributed Bragg reflector lasers[2] and a power combiner in the same chip. The second is to have all of the lasers share a common intracavity filtering element which automatically has a single output, shown in Fig. 2. Examples are the MAGIC laser[3] and the waveguide grating router multifrequency laser[4]. Both types are useful as wavelength selectable and simultaneous multiple wavelength transmitters with external modulators and directly modulated simultaneous multiple wavelength transmitters.

### 2. Modal characteristics

Extremely important for long-haul and rather important for short-haul transmission is that the lasers oscillate in only one mode. For extra-cavity-combined lasers, single-mode operation is usually accomplished by making the lasers be quarter-wave shifted distributed feedback lasers. For intra-cavity-combined lasers, single-mode operation is accomplished by the semiconductor gain nonlinearities and minimizing the cavity lengths and filter bandwidths.[5] The gain nonlinearities insure that the lasing will occur in only one cavity mode at a time and prevents mode hopping. However, exactly in which cavity mode lasing will occur is uncontrolled. Because of their long cavities, intra-cavity-combined lasers tend to have a significantly narrower linewidth ( $\sim 1$  MHz) than extra-cavity-combined lasers ( $\sim 50$  MHz).

### 3. Channel spacing

The differences between lasing wavelengths in extra-cavity-combined lasers, each of which has its own independent filter, is not as well controlled as in intra-cavity-combined lasers. Precisely because intra-cavity combined lasers share the same intracavity filtering element the channel spacing is tightly controlled in intra-cavity-combined lasers, and the standard deviation of the channel spacing is essentially given by the cavity mode spacing (typically 3 GHz). Because of the less well controlled channel spacings of extra-cavity combined lasers, they are often limited to operation of only a single channel at a time, while intra-cavity combined lasers have been demonstrated in systems experiments with fast switching between channels[6],

simultaneous direct modulation of many channels[7], and simultaneous external modulation of many channels[8].

#### **4. Long-term wavelength stability**

The short cavities of extra-cavity-combined lasers implies that their oscillation wavelengths are more sensitive to index changes in the gain. DFBs are well known to shift by tens of GHz as the drive current is changed. On the other hand, the long cavities of intra-cavity-combined lasers shift only a few GHz with drive current. Also, the intra-cavity filter in these lasers is in passive material and so does not shift at all. Thus if the transmitters are expected to maintain a frequency stability of a few GHz over 25 years, extra-cavity-combined lasers will require external wavelength stabilization while intra-cavity-combined lasers may be able to do without it.

#### **5. Unwanted reflections**

Perhaps the most significant issue in integrated lasers is unwanted on-chip reflections. It can be shown that when the net reflectivity back into the laser exceeds approximately  $1/\alpha^2$ , where  $\alpha$  is the linewidth enhancement parameter, multimode lasing will result, depending on the relative phase of the reflected light. For extra-cavity-combined lasers, the most devastating unwanted reflection is the output facet. Very high quality anti-reflection coatings are usually applied to the output facet, and often a window is employed as well. Other reflections occur at the transition between the gain regions and the passive waveguide regions. For intra-cavity-combined lasers, there are fortunately no unwanted facet reflections. However, there are still active-passive transition reflections, which can encourage multimoding.

#### **6. Nonlinearities**

When there is an amplifier integrated in the output waveguide, there will be strong wave mixing between channels when more than one laser is operated simultaneously and cross-gain-modulation induced crosstalk when the channels are directly modulated. Thus for multiple simultaneous channel operation, neither design generally has a shared amplifier. However, even without a shared amplifier, intra-cavity-combined lasers can encounter instabilities due to wave mixing in the passive shared waveguide when three or more channels are operated simultaneously[9]. The instabilities arise when the mixing products overlap with other channels' cavity modes. Extra-cavity-combined lasers, although they will exhibit passive wave mixing, are not affected by it.

#### **7. Direct modulation speed and chirp**

The short cavities of extra-cavity-combined lasers permit much higher direct modulation speeds than that of intra-cavity-combined lasers, although with significantly more static and dynamic chirp. Intra-cavity-combined lasers can typically be modulated with good extinction ratios typically only up to speeds of 1.2 Gb/s[10] because of their long cavities. Intra-cavity-combined lasers exhibit much less static chirp[10,11], the total chirp essentially given by the linewidth enhancement parameter of the amplifiers.

#### **Acknowledgments**

C. H. Joyner, L. W. Stulz, R. Monnard, M. Zirngibl, R. C. Alferness, C. Dragone, J. M. Fernandes, and H. M. Presby.

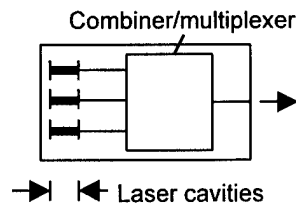


Fig. 1. Extra-cavity-combined lasers

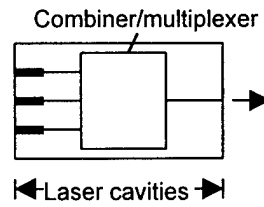


Fig. 2. Intra-cavity-combined lasers

## References

- [1] C. E. Zah, et. al., "Monolithic integration of multiwavelength compressive-strained multiquantum-well distributed-feedback laser array with star coupler and optical amplifiers," *Electron. Lett.*, vol. 28, pp. 2361-2362, 1992.
- [2] M. G. Young et. al., "A 16 x 1 wavelength division multiplexer with integrated distributed Bragg reflector lasers and electroabsorption modulators," *IEEE Photon. Technol. Lett.*, vol. 5, pp. 908-910, 1993.
- [3] J. B. D. Soole, et. al., "Multiple-stripe array grating in a cavity (MAGIC) laser: A new semiconductor laser for WDM applications," *Electron. Lett.*, vol. 28, pp. 1805-1807, 1992.
- [4] M. Zirngibl, C. H. Joyner, L. W. Stulz, U. Koren, M.-D. Chien, M. G. Young, and B. I. Miller, "Digitally tunable laser based on the integration of waveguide grating multiplexer and an optical amplifier," *IEEE Photon. Technol. Lett.*, vol. 6, pp. 516-518, 1994.
- [5] C. R. Doerr, "Theoretical stability analysis of single-mode operation in uncontrolled mode-selection lasers," *IEEE Photon. Technol. Lett.*, vol. 9, pp. 1457-1459, 1997.
- [6] R. Monnard, M. Zirngibl, C. R. Doerr, C. H. Joyner, and L. W. Stulz, "Demonstration of a 8-wavelength fast packet switching transmitter of 2.5 Gb/s bit stream," submitted to *IEEE Photon. Technol. Lett.*
- [7] R. Monnard, C. R. Doerr, C. H. Joyner, M. Zirngibl, and L. W. Stulz, "Direct modulation of a multifrequency laser up to 16 x 622 Mb/s," *IEEE Photon. Technol. Lett.*, vol. 9, pp. 815-817, 1997.
- [8] R. Monnard, et. al., "16 x 2.5 Gb/s long-haul transmitter with 50-GHz channel spacing using 2 multifrequency lasers," *LEOS*, PD2.1, 1997.
- [9] C. R. Doerr, R. Monnard, C. H. Joyner, and L. W. Stulz, "Simultaneous cw operation of shared angular dispersive element WDM lasers," to appear in *IEEE Photon. Technol. Lett.*
- [10] C. R. Doerr, "Direct modulation of long-cavity semiconductor lasers," *J. Lightwave Technol.*, vol. 14, pp. 2052-2061, 1996.
- [11] K. Liu and W. K. Wang, "Misalignment distortion penalty in moderate-speed directly modulated WDM systems and its reduction using fiber Bragg gratings," *IEEE Photon. Technol. Lett.*, vol. 9, pp. 1649-1651, 1997.

# Monolithic integration of a quantum well laser and an optical amplifier using an asymmetric twin-waveguide structure

P. V. Studenkov, M. R. Gokhale, J. C. Dries and S. R. Forrest

*Center for Photonics and Optoelectronic Materials (POEM),  
Department of Electrical Engineering, Princeton University, Princeton, NJ 08540  
Phone (609)258-4532, Fax (609)258-1954, E-mail forrest@ee.princeton.edu*

**Abstract:** We use a novel, asymmetric vertical twin-waveguide structure to demonstrate the monolithic integration of a 1.55 $\mu\text{m}$  wavelength InGaAsP/InP multiple quantum well (MQW) laser and a semiconductor optical amplifier. The laser and amplifier share the same strained InGaAsP MQW active layer, grown by gas-source molecular beam epitaxy. The asymmetric twin-waveguide structure uses the difference in modal gains to discriminate between the even and odd modes. An on/off ratio of 18dB at the SOA output is observed, with the amplifier current switched between zero and 3 kA/cm<sup>2</sup>.

Integrated optical amplifiers are important for photonic integrated circuits, to compensate for losses in fibers, splitters, waveguides and other devices. Monolithic integration of optical amplifiers with waveguides and lasers has been previously demonstrated using MOCVD regrowth [1], selective growth with a dielectric mask [2], bandgap alteration by quantum well intermixing [3], and integrated twin-waveguide (TG) scheme. The TG structure combines active and passive waveguides in a vertical directional coupler geometry [4]. It offers design flexibility, relatively simple fabrication and low cost due to the need for only a single epitaxial growth for the entire structure. The TG structure, however, suffers from a strong dependence of the waveguide coupling on device length due to the interaction between the two waveguide modes [5]. To address this problem, it is necessary to discriminate between the even and odd modes. In the TG laser [6] the discrimination was achieved by introducing additional loss to the even mode, thereby attenuating its interaction with the odd mode. Another approach, suitable for a traveling-wave semiconductor optical amplifier (SOA), is to make the modal gain

different for the even and odd modes. Fig. 1 shows the refractive index profile and calculated eigenmodes in an asymmetric twin-waveguide (ATG) structure.

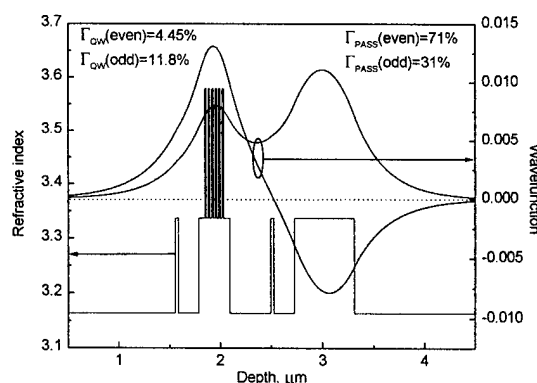


Figure 1. Refractive index profile and the two eigenmodes of the asymmetric twin-guide structure.

In this structure, the even and odd modes are split unequally between the guides, with the odd mode primarily confined to the active guide, and the even mode more strongly confined to the passive guide. The figure shows the confinement factors calculated for modes in both the quantum wells ( $\Gamma^{QW}$ ) and in the passive waveguide ( $\Gamma^{PASS}$ ). This structure can be used for integrating a traveling-wave SOA, with passive waveguide serving as an optical

interconnect layer. Light entering the twin-guide section of the SOA splits between the even (*e*) and odd (*o*) modes, with the coupling coefficients  $C_e$  and  $C_o$  given by the corresponding overlap integrals. The same coupling coefficients apply at the end of the TG section, where both modes are partially coupled into the output guide. For the structure in Fig. 1,  $C_o < C_e$ , hence the odd mode has a coupling disadvantage. On the other hand, the modal gain is higher for the odd mode which has a larger confinement factor in the quantum wells. Ignoring gain saturation effects, the total input-to-output transmission factor for the electric field is

$$E_{out}/E_{in} = C_e^2 e^{\Gamma_e^{QW} gL/2} + C_o^2 e^{\Gamma_o^{QW} gL/2 + i\Delta k \cdot L},$$

where  $\Gamma_o^{QW}$  and  $\Gamma_e^{QW}$  are the quantum well confinement factors,  $g$  is the gain of the quantum well stack,  $L$  is the length of the TG section, and  $\Delta k \cdot L$  is the phase difference between the even and odd modes at the output due to their slightly different propagation constants. If  $gL$  is sufficiently large, the odd mode is amplified much more than the even, and dominates the SOA output regardless of the phase. In this regime the even mode can be ignored, and the input-to-output power gain is  $P_{out}/P_{in} = C_o^4 e^{\Gamma_o^{QW} gL}$ . Hence, the asymmetric twin-guide structure uses gain, rather than a loss layer, to discriminate between the modes.

The ATG structure was grown by gas-source molecular beam epitaxy on a S-doped (100)  $n^+$  InP substrate. The structure is similar to the one described in Ref. [7], with the following differences: the active region contains six quantum wells for high gain, the InGaAs loss layer is omitted, and the thickness of the passive waveguide is adjusted to achieve the quantum well confinement factors of approximately 12% for the odd and 4% for the even mode. Fig. 2

shows the device geometry. Reactive ion etching was used to remove the active waveguide in the passive regions and form vertical facets for the laser and SOA.

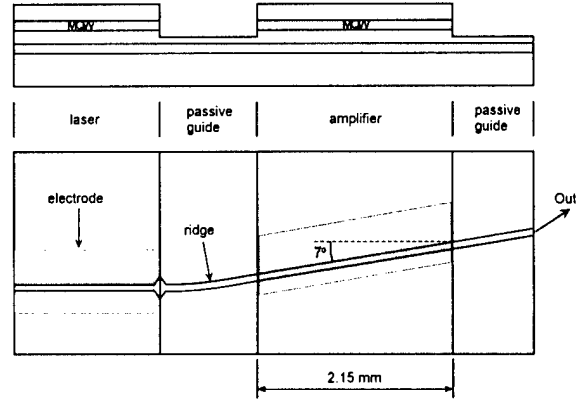


Figure 2. Schematic cross-section and top view of the integrated device.

The wet-etched ridge waveguide is  $3.8 \mu\text{m}$  wide; it runs perpendicular to the etched facet in the laser section, and is tilted at a  $7^\circ$  angle from the normal at both SOA facets to prevent optical feedback into the amplifier. The rear laser facet and the SOA output waveguide are cleaved.

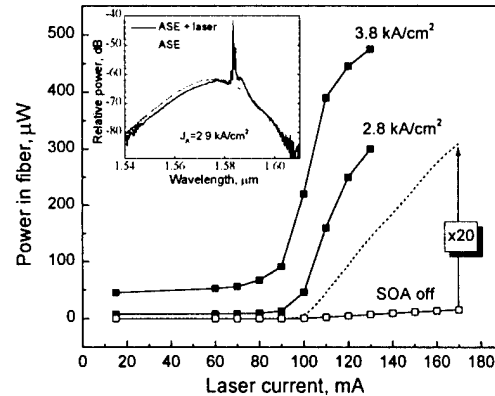


Figure 3. Light-current characteristics of the laser measured at the SOA output. Inset: typical spectra of ASE and amplified signal from the on-chip laser.

Amplified spontaneous emission spectra of integrated SOAs with 2.15 mm-long TG active regions are featureless, with a full width at half maximum of 30 nm (inset in Fig. 3). Gain

ripple in the integrated device is less than 1 dB at a current density of  $J_A = 4 \text{ kA/cm}^2$ , which is approximately four times the transparency current density for the active region. Fig. 3 shows light-current characteristics of the laser at the SOA output with no amplifier current, and with the amplifier biased at  $J_A = 2.8$  and  $3.8 \text{ kA/cm}^2$ . There is a 65 times increase in the slope of the L-I curve for  $J_A = 3.8 \text{ kA/cm}^2$ . At the same time there is no change in the spectrum or power emitted from the rear facet of the laser.

Fig. 4 shows the measured on/off ratio (R) at the output as a function of SOA current density for two different laser currents. The power in the "on" state includes amplified spontaneous emission. For a weak input signal, the largest on/off ratio observed was 18dB at  $J_A = 3.8 \text{ kA/cm}^2$ . The oscillations around  $J_A = 2 \text{ kA/cm}^2$  are believed to come from beating between the even and odd modes, whose relative phase at the SOA output is a function of current. As the gain increases further with  $J_A$ , the oscillations diminish since the odd mode starts to dominate due to its gain advantage. However, with larger input power, amplifier gain starts to saturate and the mode intensities no longer grow exponentially with distance. This reduces the gain advantage of the odd mode, and the output

power oscillations continue into higher current densities. Further optimization of the structure is needed to improve mode selection in the amplifier, thereby increasing its dynamic range.

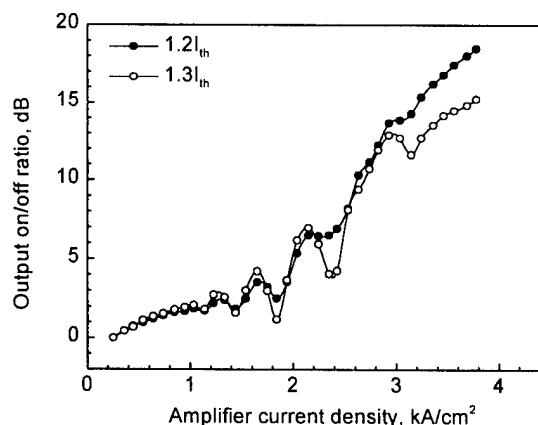


Figure 4. On/off ratio at the output versus amplifier bias, with laser power held constant at two different values.

In conclusion, we have demonstrated a monolithically integrated InGaAsP/InP MQW laser and optical amplifier using a novel, asymmetric twin-waveguide structure which uses gain to select between the two propagating modes. Traveling-wave amplifier performance with high internal gain and low gain ripple was obtained. Using the integrated amplifier as a laser output modulator, an on/off ratio of 18dB was observed. This shows the potential of the ATG design for low-cost photonic integration.

The authors gratefully acknowledge support from DARPA.

## References

1. K. R. Oh, J.-H. Ahn, J. S. Kim, S. W. Lee, H. M. Kim, K. E. Pyun and H. M. Park, *Electron. Lett.*, vol. 32(1), pp. 39-40, 1996
2. Hamamoto and K. Homatsu, *Electron. Lett.*, vol. 31(20), pp. 1779-81, 1995
3. J.-J. He, E. S. Koteles, P. J. Poole, Y. Feng, M. Davis, S. Charbonneau, R. D. Goldberg and I. V. Mitchell, "Integrated optoelectronics" Proc. of SPIE, vol. 2891, p. 2-9, 1996
4. Y. Suematsu, M. Yamada and K. Hayashi, *IEEE J. Quantum Electron.*, vol. QE-11(7), pp. 457-460, 1973
5. K. Utaka, Y. Suematsu, K. Kishino and H. Kawanishi, *Trans. IECE Japan*, vol. E-62, p. 319-23, 1979
6. L. Xu, M. R. Gokhale, P. Studenkov, J. C. Dries, C.-P. Chao, D. Garbuzov and S.R. Forrest, *IEEE Photon. Technol. Lett.*, vol 9, pp. 569-71, 1997



**Integrated Photonics Research**

# **Photonic Packaging I**

**Tuesday, March 31, 1998**

**Nan Marie Jokerst, Georgia Institute of Technology**  
Presider

**ITuC**

**8:30am–10:00am**

Saanich Room

## **Manufacturing Technology of VCSEL module**

J.Y. Kim

Samsung Electro Mechanics Co., South Korea

VCSEL based hologram module for optical disc is considered. The requirements are much different from optical communication products. Especially, a single transverse mode should be maintained to get a diffraction limited spot on the disc. The far field pattern of VCSEL is another important factor determining the characteristics of the hologram module.

The manufacturing processes including fabrication and assembly processes are also described. Since the window of VCSEL is small to get a single mode operation, it should be carefully protected during the fabrication process. In the assembly process, the relative position between VCSEL and photo detector is very important, and so a precise die bonding process is required.

The adjustment of holographic optical element(HOE) is critical to get the good performances in optical disc readout. The adjustment process and the effects of misalignment on the module performances are discussed.

Finally, some reliability issues as well as the yield problems are considered.

# Overview of MEMS Technology for Packaging Optoelectronic Components

Ming C. Wu

University of California, Los Angeles, Electrical Engineering Department

66-147D Engineering IV, Los Angeles, CA 90095-1594

Tel: 310-825-6859, Fax: 310-825-6954, Email: [wu@ee.ucla.edu](mailto:wu@ee.ucla.edu)

Recent advances of the Micro-Electro-Mechanical System (MEMS) technology has opened up many new opportunities for packaging of optoelectronic components. Silicon V-grooves are now widely used in fiber and optoelectronic packages. New dry etching and electroplating technique allows the fabrication of high-aspect-ratio structures. Furthermore, MEMS actuators and micropositioners enables new packaging schemes. Micro-XYZ stages with sub-micrometer accuracy permit on-chip optical alignment for advanced optoelectronic packages. In this paper, we will review the current state-of-the-art of the MEMS technologies, and discuss examples of MEMS-enabled optoelectronic packaging schemes.

## I. High-Aspect-Ratio Structures by Deep Etching or Electroplating

Precise V-grooves, pyramidal pits, and atomically smooth vertical sidewalls can be created by anisotropic etching of (100) and (110) silicon wafers. However, such structures are restricted by their crystal-orientation dependence. On the other hand, deep reactive ion etching (DRIE) allows etching of highly anisotropic, randomly shaped and located features into a single crystal silicon wafer. Marxer et al [1] has used DRIE to create vertical trenches with spring leaves to package single mode fibers for the MEMS optical switches fabricated by the same etching process. High-aspect-ratio structures can also be created by LIGA (German acronym for Lithography, Electroplating, and Molding) process. In contrast to the DRIE process, *metallic* microstructures can be produced by the LIGA process. Thus in addition to optical alignment [2], the LIGA structures can also be used for electrical interconnect as well as heat sinking. Fan *et al* has used the LIGA-deposited Ni to package an 8x1 vertical cavity surface-emitting laser (VCSEL) array to an 8x1 multimode fiber ribbon with passive alignment [3], as shown in Fig. 1. The VCSEL array is temporally clamped by a spring structure while the front contacts are soldered to the Ni blocks. Coupling efficiency of 60% has been obtained.

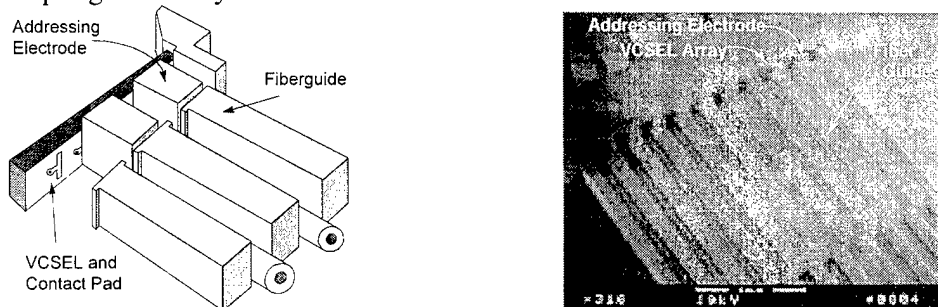


Fig. 1. Packaging of VCSEL array with ribbon fiber by LIGA microstructures.

## II. Microactuated Beam Steering Devices

Optical MEMS devices with integrated microactuators enable active optical alignment after the optoelectronic elements are fixed to the packages. The optoelectronic/fiber components can be

actively aligned after they are fixed by solders. Therefore, this scheme can correct the misalignment due to solder creeping or aging. Daneman et al. has proposed to use a surface-micromachined sliding/tilting mirror for laser-to-fiber coupling [4]. A coupling efficiency of 40% has been demonstrated.

Figure 2 shows another type of beam-steering device. By stacking two  $45^\circ$  mirrors in orthogonal directions, the optical beam can be shifted both horizontally and vertically using only in-plane microactuators [5]. By moving the lower  $45^\circ$  mirror, the optical beam is shifted in the horizontal direction. If the upper  $45^\circ$  mirror is moved, the optical beam is shifted in the vertical directions. This configuration is particularly suitable for surface-micromachined devices since only in-plane actuators are needed. The out-of-plane optical beam translation is achieved without using out-of-plane actuators. Three-axis optical alignment can be achieved by mounting the optical elements on a third translation stage that moves along the direction of optical axis. Two-dimensional beam steering and focusing/defocusing have been experimentally demonstrated [5].

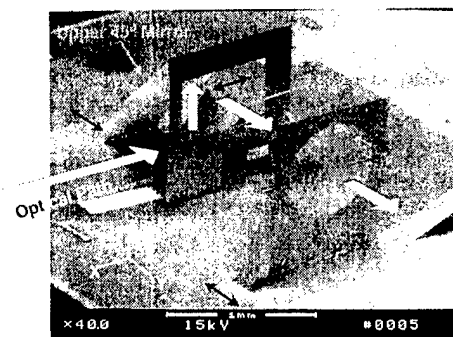


Fig. 2. Three-dimensional beam-steering device

### III. Micro-XYZ Stages

In contrast to the beam steering device, the XYZ micropositioning stages can physically move the optical elements in three directions. They are widely used in free-space optical systems. However, implementation of such XYZ stages with large travel distance and submicron accuracy is very challenging using the surface-micromachining technology. The Cornell University has demonstrated a nano-XYZ stage for scanning atomic force microscope using two sets of orthogonal comb drive actuators for XY stages and an out-of-plane torsion Z-stage [6], however, the travel distance is limited to below a few micrometers.

Vertical displacement is difficult to achieve for surface-micromachined structures. Recently, at UCLA, we have demonstrated a novel self-assembled vertical stage that can achieve large displacement with fine resolution [7]. It consists of five surface-micromachined polysilicon plates. The center plate is connected to four side support plates through polarity microhinges. Each support plate is in turn connected to a microactuator array. Here, the scratch drive actuator (SDA) is chosen for this application because it can produce large displacement with fine step resolution [8]. To raise the center platform, the SDA's on the opposite sides of the platform move in at the same speed. If the SDA's move in the same direction, lateral translation of the stage is achieved. Figure 3 shows the scanning electron micrograph (SEM) of the micro-XYZ stage holding a micro ball lens with  $300\text{-}\mu\text{m}$  diameter. Large displacements in all three axes ( $> 120\text{ }\mu\text{m}$ ) and fine step resolution ( $27\text{ nm}$ ) have been experimentally demonstrated. Another unique feature of such XYZ stage is that it is completely self-assembled by applying electrical

bias only. No manual assembly is required, which can greatly reduce the system cost. This will be discussed further in a later section.

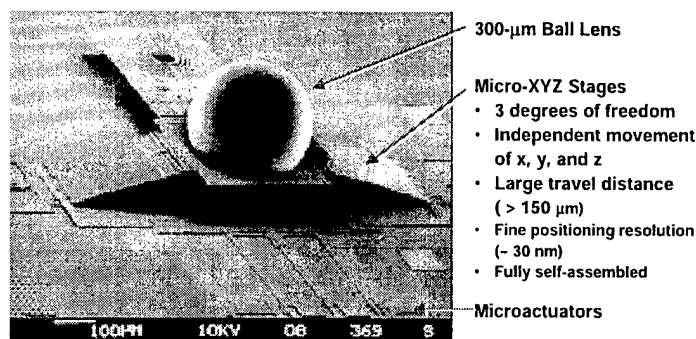


Fig. 3. Micro-XYZ stage with 3 degrees of freedom.

In summary, the micromachining technology has opened up many new possibilities for packaging optoelectronic components. Precise optomechanical structures can be produced by anisotropic etching, deep reactive ion etching, or by electro-plating. Furthermore, movable micromechanical structures to be integrated with the optoelectronic device or on the sub-mount. On-chip optical alignment with high optical coupling efficiency can be achieved. The work at UCLA is supported by DARPA.

#### REFERENCES

- 1 C. Marxer, M.-A. Gretillat, N.F. de Rooij, R. Battig, O. Anthamatten, B. Valk, and P. Vogel, "Vertical Mirrors Fabricated by Reactive Ion Etching for Fiber Optical Switching Applications," in Proc. 10th Workshop on Micro Electro Mechanical Systems (MEMS), pp. 49-54, 1997.
- 2 A. Muller, I. Ggtert, J. Mohr, and A. Rogner, "Fabrication of stepped microoptical benches for fiber and free space applications," *Microsystem Technologies*, vol.2, pp.40-45, 1996.
- 3 L. Fan, C. R. King, and M. C. Wu, "Self-Aligned VCSEL Array-to-Optical Fiber Ribbon Coupler Fabricated with the LIGA process," 1997 *Conference of Lasers and Electro-Optics (CLEO)*, Paper CME5, Baltimore, Maryland, May 18 - 23, 1997.
- 4 M.J. Daneman, O. Solgaard, N.C. Tien, N.C.; K.Y. Lau, and R.S. Muller, "Laser-to-fiber coupling module using a micromachined alignment mirror," *IEEE Photonics Technology Letters*, vol. 8, p.396-8, 1996.
- 5 L. Y. Lin, J. L. Shen, S. S. Lee, and M. C. Wu, "Surface-Micromachined Micro-XYZ Stages for Free-Space Micro-Optical Bench," *IEEE Photonics Technology Letter*, Vol. 9, No. 3, March, 1997.
- 6 Xu, Y.; MacDonald, N.C.; Miller, S.A. "Integrated micro-scanning tunneling microscope," *Applied Physics Letters*, vol.67, pp.2305-7, 1995.
- 7 T. Akiyama, D. Collard, and H. Fujita, "Scratch drive actuator with mechanical links for self-assembly of three-dimensional MEMS," *Journal of Microelectromechanical Systems*, vol.6, p.10-17, 1997.
- 8 L. Fan, M. C. Wu, K. Choquette, and M.H. Crawford, "Self-Assembled Microactuated XYZ Stages for Optical Scanning and Alignment," Proc. 1997 International Conferences on Solid-State Sensors and Actuators (Transducers 97), Paper 2A2.01, 1997.
- 9 L. Fan and M. C. Wu, "Self-Assembled Micro-XYZ Stages for Moving Micro-Ball Lenses," *International Conference on Optical MEMS and Their Applications (MOEMS 97)*, Nara, Japan, November 18 - 21, 1997.

# Hybrid 4×4 optical matrix switch module on silica based Planar Lightwave Circuit by self-align multiple chip bonding technique

J. Sasaki, H. Hatakeyama, T. Tamanuki, M. Yamaguchi,  
N. Kitamura, T. Shimoda, M. Kitamura, T. Kato and M. Itoh

Opto-Electronics and High Frequency Device Research Laboratories

S. Kitamura

Compound Semiconductor Device Division

NEC Corporation

4-1-1 Miyazaki, Miyamae-ku, Kawasaki, Kanagawa 216, Japan  
1753 Shimonumabe, Nakahara-ku, Kawasaki, Kanagawa 211, Japan  
Telephone: +81 - 44 - 856 - 2073, Facsimile: +81- 44 - 856 - 2224  
*E-mail: sasaki@oel.cl.nec.co.jp*

## 1. Introduction

Large capacity switching systems based on photonic technologies are attractive toward achieving high throughput telecommunication network against a large traffic increase [1]~[3]. Such systems require a number of multi-channel photonic functional devices, such as photonic matrix switches. Among a variety of photonic matrix switch structures, the gate type optical switch using semiconductor optical amplifier (SOA) gates is necessary, because of its high extinction ratio (low crosstalk), optical gain, and nanosecond switching time with a simple switching control scheme [4][5]. Hybrid integration of arrayed SOA gates onto a silicon (Si) platform with silica based planar lightwave circuit (PLC) seems to be a suitable way to achieve a practical gate type matrix switch module [6][7]. In order to realize such a hybrid integrated module, high precision multiple-chip assembly techniques for optical/electrical devices and optical fibers, with self-align manner [8]~[10], are necessary.

This paper describes the newly developed optical hybrid integration technology to assemble all of SOA gate arrays, electrical wiring chips and optical fiber arrays on a silicon platform with silica based PLC in a self-aligned manner. A 4×4 SOA gate matrix switch modules has been successfully realized by using the developed technology and spot-size converter integrated (SSC) SOA gate arrays.

## 2. Module structure

**Figure 1** shows a schematic diagram of the developed 4×4 optical matrix module. Four sets of silica optical waveguide 1:4 splitter and 4:1 combiner are formed on a Si platform. Four 4-channel SOA gate array chips are mounted on the platform. Two sets of single mode optical fiber (SMF) arrays are assembled in V-grooves fabricated at both ends of the platform. The following optical hybrid integration technologies have been developed for achieving this structure.

### (1) Si Platform with Silica-Based Optical Waveguides, metal electrodes and Fiber Guides:

In order to improve the layout flexibility, a multi-layer structure including metal wiring layers as well as silica waveguide layers is necessary. The conventional SiO<sub>2</sub> deposition processes degrade metal materials due to high temperature treatment exceeding 1000°C. Atmospheric pressure chemical vapor deposition (AP-CVD) using tetraethoxysilane (TEOS) as precursor has the promising feature of deposition temperature as low as 450°C [11]. By employing TEOS AP-CVD method, WSi is applicable as a conductor material. Moreover, WSi can also be utilized as etching mask in fabricating V-grooves on Si for optical fiber integration [11]. In the Si platform for the 4×4 switch, core dimension is 6μm and refractive index difference Δn is 0.8%. Minimum angle of the waveguide intersection is 37° so as to suppress inter-port crosstalk.

### (2) Simultaneous self-align assembly of multiple optical/electrical devices:

The self-align assembling technique using solder bumps is the most suitable candidate for assembling multiple chips simultaneously. We have developed solder bump technology using Au-80 wt% / Sn-20 wt% eutectic alloy solder to achieve high reliability. The SOA gates are first put on solder bumps formed on the platform. As the solder bump re-flowed, they are simultaneously self-aligned to their correct position by restoring force as a result of surface tension of the molten solder. The solder bumps are formed by mechanical punching method [10] to obtain high uniformity and cost reduction. The Au/Sn solder pieces are formed by punching an Au/Sn ribbon sheet using a micro punch and a die, then directly pressed against the solder-wettable pads. To achieve high precision vertically, stripe-type solder bumps, instead of spherical bumps usually employed in flip-chip bonding, has been developed [12]. The stripe-type bumps could reduce

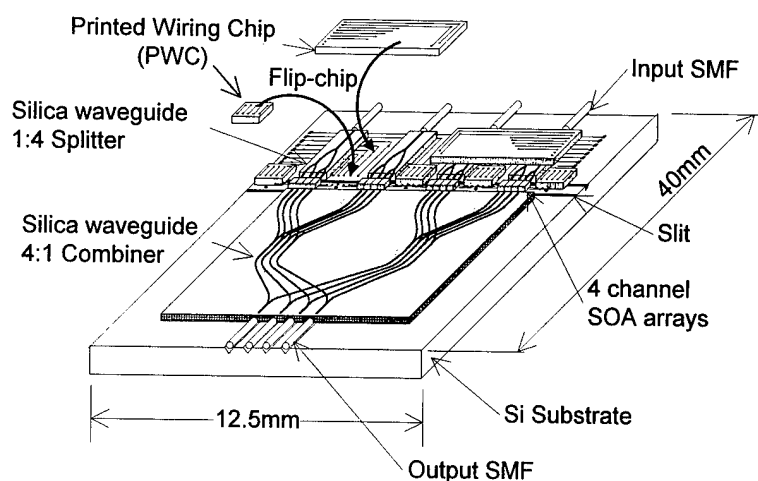


Figure 1 Schematic diagram of 4x4 optical gate matrix switch.

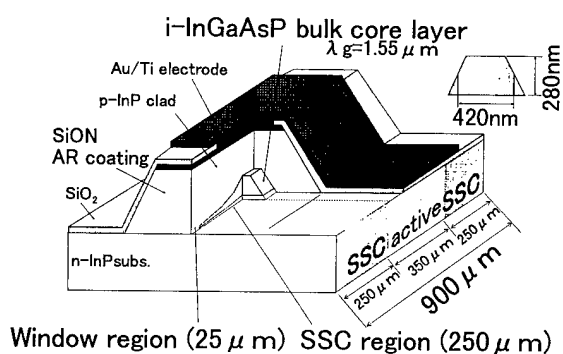


Fig. 2 Schematic diagram of SSC integrated SOA gate structure

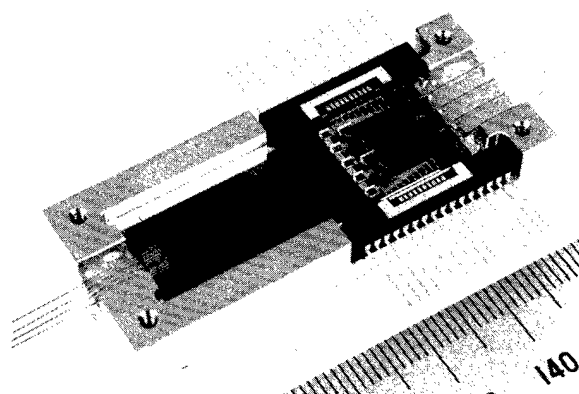


Fig. 3 Hybrid-integrated 4x4 optical gate matrix switch module

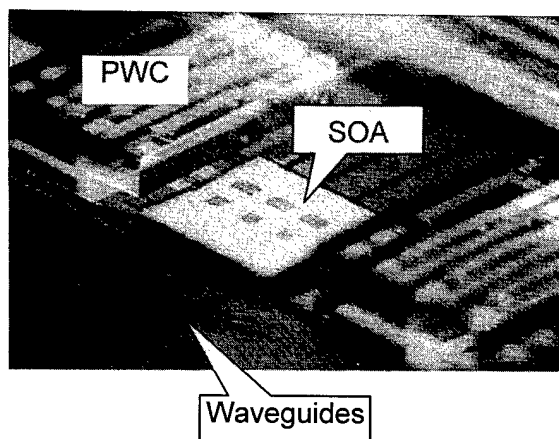


Fig. 4 SOA gates and printed wiring chips mounted on the PLC platform

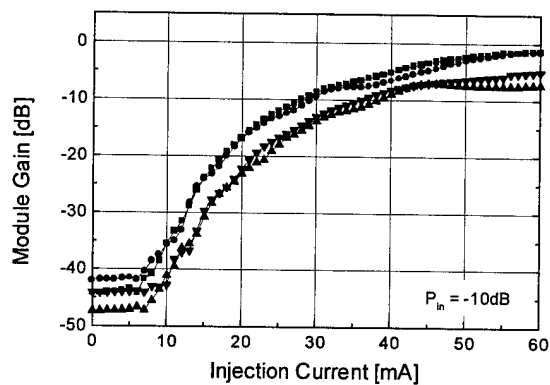


Fig. 5 Fiber-to-fiber gain as a function of injection current

height deviation due to solder volume deviation, as the case with conventional spherical bumps, by bump stretching. The positioning accuracy of less than  $\pm 1 \mu\text{m}$  is possible both in lateral and vertical directions.

### (3) Spot Size Conversion between Different Waveguides:

In hybrid optical module, coupling loss between optical devices and waveguides is usually inevitable due to mode field difference. To reduce such loss, spot-size converter was integrated on the SOA gate arrays. **Figure 2** schematically shows the structure of the polarization insensitive 4-channel SSC-SOA gate array [13][14]. The gate consists of a bulk InGaAsP active stripe ( $\lambda=1550\text{nm}$ ) and thickness-tapered SSC regions for both facet sides, which are grown by selective MOVPE simultaneously and buried in InP layers. Window regions of  $25\mu\text{m}$  long were formed at each of the facets to suppress residual facet reflectivity. Radiation divergence is  $13\sim 14^\circ$  (FWHM) in both azimuth and elevation plane, while they are approximately  $40^\circ$  in non-SSC devices. Typical on/off ratio is more than 40dB.

### (4) 3-Dimensional Electrical Signal Wiring:

In our module design, the silica waveguide facets facing SOAs are to be constructed by using mechanical sawing technique due to its easiness and low cost capability. However, this process also cut the electrical wiring patterns connecting to SOAs. To overcome this problem, we have employed printed wiring chips (PWCs) to achieve electrical connection over the slits formed by sawing process, as shown in Fig.1. The PWCs and SOAs are simultaneously mounted by the solder bump re-flow. Using this PWC technology, some electronic circuits such as driver IC chips may also be assembled.

## 3. Module Performances

**Figure 3** shows the photograph of the fabricated  $4\times 4$  optical switch module. The module is 54mm long, 22mm wide. The SSC-SOA gates and the printed wiring chips mounted on the PLC platform are shown in **Fig. 4**. The operation of all 16 SOAs has been confirmed after optical hybridization. Typical fiber-to-fiber gain as a function of injection current is depicted in **Fig. 5**. The insertion losses at injection current of 50mA were  $7 \pm 4 \text{ dB}$ . The coupling losses between SOAs and silica waveguides were estimated to be about 4 dB. The average coupling loss between the SMFs and silica waveguides was 1.8 dB, and average 1:4 splitting losses was 7.4dB per a side. Intersection losses in the combiner region were less than 0.1 dB. By switching the injection current between 0 and 50 mA, average extinction ratio as high as 40 dB has been obtained. This value is large enough for optical gates used to compose a cross-talk free matrix switch [1].

## 4. Summary

We developed hybrid integrated  $4\times 4$  matrix optical switch module. The developed  $4\times 4$  gate matrix switch consists of spot-size converter integrated semiconductor optical amplifier gate arrays and optical fibers on a Si platform with silica waveguides. Newly developed self-align multiple chip assembly technique using Au/Sn solder bumps and AP-CVD based Si platform technologies have enabled this integration.

## References

- [1] S. Takahashi, et al., *Technical Digest of Photonics in Switching '96*, vol. 2, Post deadline Paper, PThC1, pp.12~15, 1996.
- [2] H. Takeshita, et al., *Proceedings of ECOC/IOOC '97*, WE4C-2, 1997.
- [3] K. Sasayama, et al., *Proceedings of ECOC '94*, vol.2, pp.533~536, 1994.
- [4] D. Chiaroni, et al., *Proceedings of ECOC '95*, vol. 1, Mo.L.3.5, pp.115~119, 1995.
- [5] T. Kato, et al., *Technical Digest of IEICE '96 Spring Conference*, B-1106, 1996.
- [6] Y. Yamada, et al., *IEEE Journal of Lightwave Technol.*, vol. 10, No. 3, pp. 383~390, 1992.
- [7] I. Ogawa, et al., *Proceedings of CLEO/Pacific-Rim '97*, PD 2.3, 1997.
- [8] M. J. Wale, et al., *IEEE Trans. on CHMT*, vol. 13, No.4, 1990.
- [9] K. Katsura, et al., *Proceedings of IMC '90*, 105, 1990.
- [10] M. Itoh, et al., *Proceedings of ECTC '96*, pp. 1~7, 1996.
- [11] N. Kitamura, et al., *Technical Digest of Integrated Photonics Research '96*, IThB2-1, 1996.
- [12] J. Sasaki, et al., *Proceedings of LEOS '95*, OPMR 2.3, 1995.
- [13] S. Kitamura, et al., *IEEE Photonics Technol. Lett.*, 7, pp. 147~148, 1995.
- [14] H. Hatakeyama, et al., *Technical Digest of OECC '97*, 9C3-2, 1997.

## New promising technological approach for optoelectronic hybridization

P. Mottier, Cl. Massit, G. Parat and G. Grand  
CEA-LETI / Département de Microtechnologies  
17, avenue des Martyrs - 38054 Grenoble Cedex 09 - France  
Tel : 33 476889816 - Fax : 33 476889456 - e-mail : mottier@cea.fr

### Abstract

*A cost-effective technique for achievement of hybrid optoelectronics units is proposed. Compared to the previous ones, it offers relaxed alignment tolerances and high versatility. It has been demonstrated on a simple, but very demanding, unit consisting of a laser diode hybridized in front of an optical circuit integrated on Silicon.*

### Introduction

Large scale optical communication network deployment needs more and more complex optoelectronic units able to achieve the various required functions. However, it is clear that ideal material enabling all kinds of functions to be achieved does not exist. For example, glass or silicon based integrated optics are very well suited for passive function integration but not for optical source realization ! Therefore, a flexible monolithic optoelectronics technology still seems far away.

A way to overcome these difficulties is hybridization which many authors recommended a long time ago [1,2] and since that time numerous realizations have been carried out [3,4]. However these technologies have trouble leaving the labs for industry because of poor manufacturing yields inducing foreseeable high production costs. The main reasons are that the proposed solutions are firstly very demanding from the technological process accuracy point of view, secondly very specific to only one type of optoelectronic unit which prevents the development from being easily paid off on several products.

In this work, we propose a new technical approach which, in our opinion, provides many advantages, including versatility and low cost potentialities.

### Description of the proposed technical approach

It consists of a silicon « micro-bench » on top of which each of the required functions are flip-chip hybridized [figure 1]. All the optical chips are picked and placed on the substrate presenting previously achieved solder microbumps. Then all the devices are simultaneously self-aligned in the 3 directions by means of surface tension forces during the solder bumps reflow.

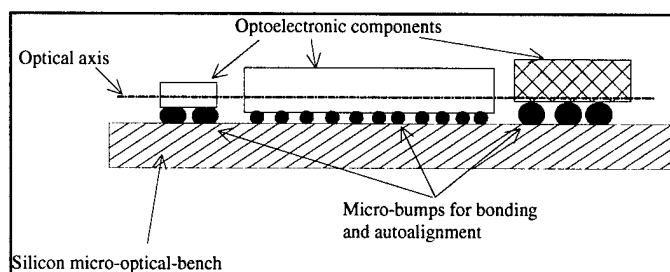


Figure 1 : Schematic view of the microbench concept

One key point is that the optical axis height of the different components is adjusted by simply controlling the solder cylinder radius before solder reflow. Supposing a very simple model where the solder volume is conserved during reflow, we get the following relation between the final height  $h$  of the bump versus the diameter  $d$  of the cylinder and the thickness  $t$  of the solder layer before reflow :

$$\frac{\pi}{6} h^3 = \frac{\pi}{4} d^2 t \quad \{1\}$$

Let us assume that we want to hybridize 2 devices with  $\Delta h$  difference between the optical axis depths. In order to compensate this difference, we have to vary the solder pad diameter  $d$  such that :

$$\left(1 + \frac{\Delta h}{h}\right)^3 = \left(1 + \frac{\Delta d}{d}\right)^2 \quad \{2\}$$

In previous works, the optical axis of the component to be hybridized had to be carefully positioned on the optical axis of the holding device [see for example reference 5 or 6]. So, « absolute » positioning is required

which implies accurate micro machining, therefore poor yield or/and high cost in an industrial environment. Here we propose a « relative positioning » which relaxes tolerances on device alignments. From the relations above, we plotted in figure 2 the variations on  $\Delta h$  (vertical misalignment) induced by a quite large variation on  $t$  ( $1\mu\text{m}$ ) versus the aimed solder thickness  $t$  and for different solder pad diameters  $d$ . The difference between optical axis height is assumed to be  $10\mu\text{m}$ . It can be seen that the induced vertical misalignment could be as low as  $0.2\mu\text{m}$  if we use sufficiently low diameter pads and high solder thickness. Of course, these results coming from a very simple model must be adjusted according to actual technological results, but they show all the interest of this approach.

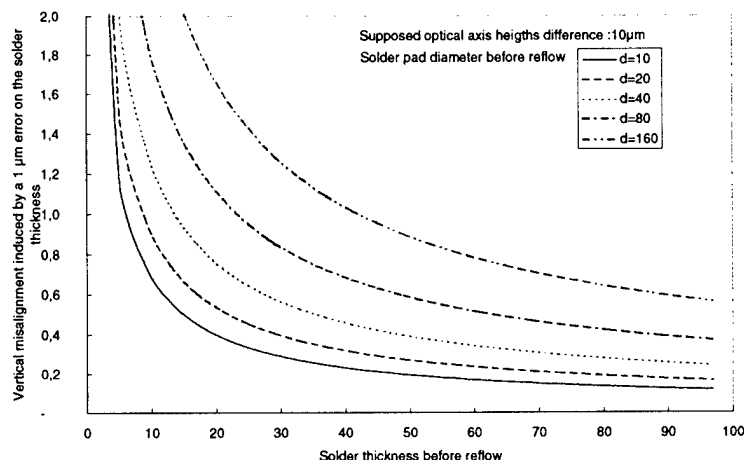


Figure 2 : Sensitivity of vertical misalignment to solder thickness control

Lastly, this technique is very versatile. Indeed, to hybridize a new type of component, instead of modifying its manufacturing process in order to add for example mechanical stops, we have only to deposit and pattern a metal layer on the wafer before dicing it. So only two conditions have to be verified, the first one is the technical compatibility, for example care must be taken concerning metal diffusion into the surface layers, particularly in the case of active devices such as lasers. But this problem can be easily overcome by a metal diffusion barrier. The second condition is the ability to pattern the metal layer adequately positioning the metal pads with respect to the optical axis. This last point only requires the presence of alignment marks.

The silicon microbench plays many roles. First, it is the 0 level reference in the z-direction. Second, it holds the required electrical lines for power distribution or signal outputs and the solder pads. Finally it allows efficient thermal dissipation. We do not deposit solder pads on the optical chips but on the microbench for two main reasons : first it minimizes the modifications of existing device manufacturing processes ; secondly we do not have to take into account the thickness dispersion which would occur if solder had been deposited separately on different wafers. In order to keep the process as low cost as possible, we used electroplating deposition. To validate this technical approach, we decided to test it on hybridization of a laser in front of  $\text{SiO}_2$  on Si optical waveguides.

### Experimental procedure

The defined optoelectronic units consist of a standard  $1.3\mu\text{m}$  Perot-Fabry laser diode aligned with a 1 to 2 beam splitter. We bought a full InP laser wafer [7]. Its manufacturing process flow was kept strictly standard. Only before the dicing step, we asked for an extra metal deposition and patterning. To carefully align the metal pads in relation to the laser optical axis, alignment marks were added on the mask limiting the emission channel. After the metal layer patterning, lasers are diced as usual. As metal is left only on very localized sites, it does not increase the difficulty of the operation. Some laser samples were fully characterized individually in order to have a laser behavior reference to be compared to the hybridized one.

The silica on silicon optical passive device was achieved in our laboratories. Its main interest lies in its sensitivity to the laser lateral misalignment. Here also, after standard wafer processing, metal deposition and patterning were carried out in the same manner as for the laser. Some samples were characterized in order to control their homogeneity and to measure the maximum coupling efficiency between the laser and the device output which will be the reference of the maximum available output.

Lastly, the microbench wafer was processed following standard microelectronics processes. 4 levels are required : Al,  $\text{SiO}_2$  passivation, TiNiAu and SnPb60/40 electroplating deposition. Afterwards a reflow leads to a pattern of solder microbumps.

After module hybridization [Figure 3], the alignment accuracy was carefully characterized first by a  $1.55\mu\text{m}$

interferometer able to measure distances through the Si substrate or with S.E.M. observations, then measuring the output optical power and comparing to the maximum that could be expected.

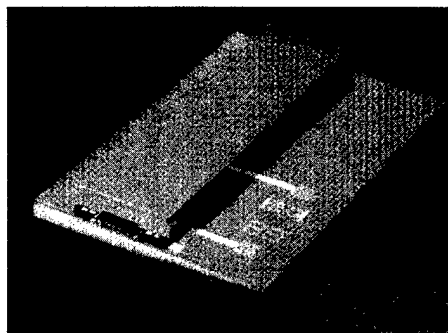


*Figure 3 : Hybrid optical unit*

### Results

After first runs aiming to adjust technological parameters, we obtained promising results. However, we noticed a  $-2\mu\text{m}$  systematic error in the z-direction due to the metal pattern design which was adjusted in the following runs. The last measurements showed a vertical alignment better than  $1\mu\text{m}$  with  $0.2\mu\text{m}$  for the best value.

Lateral misalignment was shown below  $0.50\mu\text{m}$  maximum value with a mean value around  $0.30\mu\text{m}$ . The longitudinal mean value between device endfaces is  $10.5\mu\text{m}$  with a quite large dispersion existing (from  $4$  to  $14.5\mu\text{m}$ ) due to the dicing uncertainty. However, in this direction, optical constraints are not too severe. Indeed, numerical simulation shows that insertion losses increase by only  $1\text{dB}$  for an air gap between devices varying between  $0$  to  $20\mu\text{m}$ .

From the optical point of view, no laser degradation was detected, not only the behavior versus applied voltage was the same, but also the lifetime does not seem to decrease. The power penalty due to misalignment was estimated to be within a few tenths of a dB. Finally, the ratio on the two output signals was better than  $0.9$  in agreement with the good lateral alignment mentioned above.

### Conclusion

Even though some improvements are still required, we demonstrated an original approach for complex hybrid optoelectronic unit manufacturing suitable for low cost mass production. Its main features are versatility, self-alignment, easy Z adjustment, and decrease in required processing accuracy. It needs only metal deposition and patterning on the surface of the chips to be able to hybridize them. We think this approach could be used for any kind of optical hybrid unit with no extra difficulty.

### References

- [1] S. Valette, J.P. Jadot, P. Gidon and A. Kevorkian, « Integrated optics and microelectronics : toward an integration on a single silicon chip », Proc. SPIE, Vol 864 Advanced Optoelectronic Technology, Cannes (F), November 18-20, 1987, pp. 125-133.
- [2] C.H. Henry, G.E. Blonder and R.F. Kazarinov, « Glass Waveguides on Silicon for Hybrid Optical Packaging », Journal of Lighthwave Technology, Vol. 7, No. 10, October 1989, pp1530-1539.
- [3] Y.C. Lee and N.R. Basavanhlly, « Overview : Solder Engineering for Optoelectronic Packaging », JOM, June 1994, pp. 46-50.
- [4] Q. Tan and Y.C. Lee, « Soldering Technology for Optoelectronic Packaging », Proceedings of 44<sup>th</sup> Electronic Components and Technology Conference, Orlando (USA), 28-30 May 1996, pp 26-35.
- [5] F. Mallecot, Cl. Artigue, F. Pommereau, F. Poingt, A. Bodere, D. Carpentier, T. Fillon, J.L. Gentner, F. Gerard, M. Goix, E. Grard, J.L. Lafraguette, L. Le Gouezigou, R. Ngo, A. Pinquier, G. Vendrome, G. Grand, P. Mottier, P. Gidon, A. Fournier, Wasler, G. Laude, « Hybrid silica multiwavelength optical source realized by passive alignment technique », Proceedings of Optical Fiber Communication Conference, OFC'95, San Diego (CA), February 26-March 3, 1995.
- [6] M.J. Wale, C.Edge, F.A. Randle and D.J. Pedder, « A new self-aligned technique for the assembly of integrated optical devices with optical fibre and electrical interfaces », Proceedings of European Conference on Optical Communication, ECOC'89, pp 368-371.
- [7] Lasers supplier : Thomson-CSF - Domaine de Corbeville - 91404 Orsay - France



---

**Integrated Photonics Research**

# **Photonic Nanostructures II**

**Tuesday, March 31, 1998**

**B. E. Little, Massachusetts Institute of Technology**

**R. W. Ziolkowski, University of Arizona**

Presiders

**ITuD**

**10:30am–12:00m**

Salon B

## Meso-optoelectronic devices and applications

A. F. J. Levi  
 Department of Electrical Engineering  
 University of Southern California  
 University Park, DRB118  
 Los Angeles, California 90089-1111

### Abstract

This talk presents a case for developing meso-optic technology based on its potential to enhance the capabilities of otherwise all-electronic systems.

### Introduction

Interconnect is an important factor which limits electronic system design. The interconnect distance, the number of signal lines per unit length (or form-factor) and the maximum signaling rate adversely constrain large electronic system designs to greater volumes, increased power consumption, and less than optimal bisection bandwidth [1]. In recent years there has been a concerted effort to develop optoelectronic technology to replace copper-based approaches for interconnect lengths greater than 1 m. Arrays of efficient, low-threshold current laser diodes and arrays of pin detectors have been used to provide an effective very high-performance replacement of copper-based interconnects. However, within the constraints of laser diodes and pin detectors there is a limit to which such components can effectively compete with electrical solutions. To insert optics deeper into the core of systems with interconnect lengths less than 1 m it is necessary to develop new devices and concepts which enhance functionality well beyond that of a laser diode or a pin detector and simultaneously ensure scalability to larger numbers of devices. This is both the challenge and application envisioned for meso-optics.

The development of the Vertical Cavity Surface Emitting Laser (VCSEL) has enabled the reduction in physical size (scaling) of laser diodes [2-4]. Active region volumes can approach  $10^{-14}$  cm<sup>3</sup> and optical resonator volumes can approach  $10^{-12}$  cm<sup>3</sup>. Significantly, scaling has also reduced threshold current to the  $\mu$ A range [4] and increased efficiency of VCSELs. On the other hand, scaling of VCSELs has not resulted in any increase in functionality. The device remains merely a diode. From an overall system perspective, without demonstrable additional functionality, diodes are of limited use. They may be used to establish dense arrays of point-to-point interconnects but, for example, they cannot be used to route or process optical signals. The limited functionality of VCSEL and pin-based components requires electronic circuits to perform routing and signal processing functions. A central challenge for researchers in the optoelectronic community is to develop new technologies for future, highly functional, integrated optical circuits that will be capable of replacing significant portions of otherwise all-electronic systems. The purpose of this talk is to show that such enhanced functionality may indeed be achievable.

### Coupled photon cavity experiments

The ability to digitally switch lasing wavelength is key to developing optoelectronic components with the needed functionality since it is anticipated that future logic or switching devices will use wavelength coding. To achieve this functionality requires investigation of active coupled-cavity devices. Recently this has been explored using hybrid active and passive components and sequential wavelength switching controlled by intracavity loss has been reported [5]. Applying knowledge gained from these experiments it has been possible to demonstrate the equivalent of an electronic SR flip-flop [6]. The hybrid wavelength-selective electro-optic flip-flop is able to toggle between two Bragg grating (BG) defined lasing wavelengths by application of electrical set and

reset signals. Because this is an early example of an essential functional building block for electro-optic components, it merits further discussion.

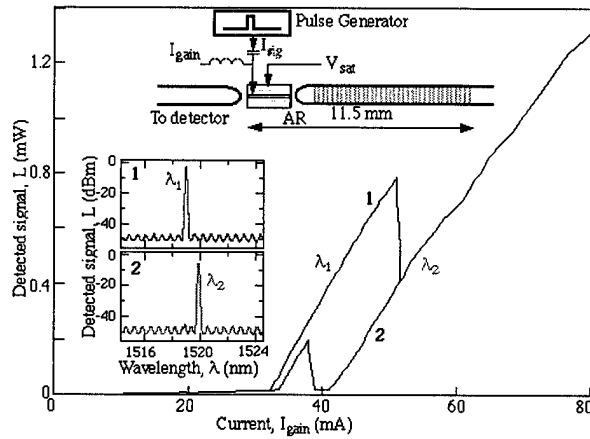


**Figure 1** - Measured light intensity versus gain-section current ( $L$ - $I_{\text{gain}}$ ) characteristic of a laser in an external cavity for saturable absorber voltage,  $V_{\text{sat}} = 0.9$  V. The inset is a schematic diagram of the experimental arrangement. The laser diode is a 500  $\mu\text{m}$  long InGaAs/InP buried heterostructure four quantum well device with an integrated saturable absorber. Optical feedback is provided by coupling emission from the AR coated facet into a single-mode fiber in which is embedded a dual reflection peaked BG. The measured optical spectrum of the light output at points 1 and 2 along the  $L$ - $I_{\text{gain}}$  curve are also seen as an inset.

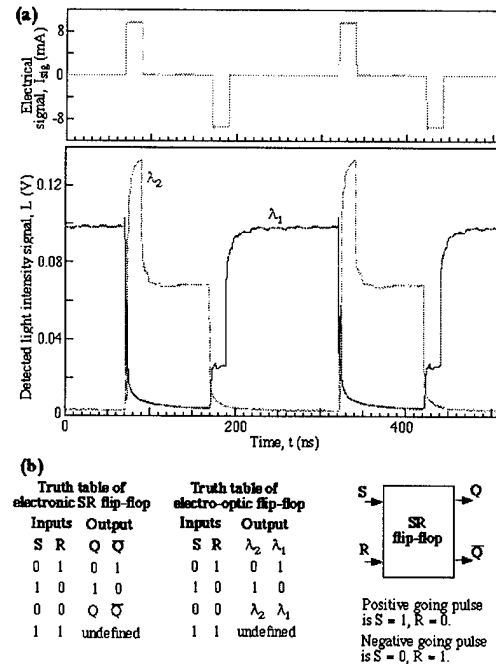


**Figure 2** - (a) Measured temporal response of the device acting as an electro-optical SR flip-flop. The laser is biased at  $I_{\text{gain}} = 50$  mA with the absorber bias  $V_{\text{sat}} = 0.9$  V. A 9 mA positive going electrical pulse applied to the device sets the lasing wavelength to  $\lambda_2$ . The device stays in that state until a -9 mA electrical pulse resets the device to lase at  $\lambda_1$ . (b) Truth table of a conventional electrical SR flip-flop and the electro-optical SR flip-flop. The positive (negative) going pulse mimics  $S = 1, R = 0$ , input ( $S = 0, R = 1$ ). The  $S = 0, R = 0$  input is equivalent to having no electrical pulse input to the electro-optical SR flip-flop.

Figure 1 shows a schematic diagram of the experimental arrangement. The laser diode used for these hybrid experiments is a 500  $\mu\text{m}$  long InGaAs / InP buried heterostructure four quantum well device with an integrated saturable absorber [7]. Optical feedback is provided by coupling emission from the anti-reflection (AR) coated facet into a single-mode fiber in which is embedded a dual reflection peaked BG. The 10.5 mm long BG has peaks in reflectivity of greater than 90% centered at wavelengths  $\lambda_1 = 1519.03$  nm and  $\lambda_2 = 1519.91$  nm with a -3 dB full-width optical bandwidth of 0.13 nm (16.9 GHz) and 0.12 nm (15.6 GHz) respectively. The measured photon-cavity resonance frequency is 14.7 GHz corresponding to a photon cavity round-trip time of 71 ps. Because the center wavelengths of the BGs are  $\Delta\lambda_{\text{BG}} = 0.89$  nm apart and since cavity modes of the imperfectly AR coated semiconductor laser are spaced  $\Delta\lambda_{\text{cav}} = 0.59$  nm apart,  $\Delta\lambda_{\text{BG}} = 1.5 \Delta\lambda_{\text{cav}}$ . Hence, coupled cavity effects select only one of the BG defined wavelengths as the lasing wavelength [5]. Hysteresis in the  $L$ - $I_{\text{gain}}$  characteristic due to coupled cavity effects may be exploited to build an electro-optic SR flip-flop.

The optical output of the laser is stable at both operating points 1 and 2 on the  $L$ - $I_{\text{gain}}$  shown in Fig. 1. Fig. 2 shows the device operating as a wavelength-selective electro-optic SR flip-flop. When

the laser is operating at point 1 and lasing at wavelength  $\lambda_1$ , a 9 mA 'set' electrical pulse applied to the laser for 20 ns switches the laser operating point to 2 and lasing occurs at wavelength  $\lambda_2$ . The laser continues to operate at point 2 with lasing at  $\lambda_2$  until a 20 ns -9 mA 'reset' electrical pulse switches the operating point to 1 with lasing at  $\lambda_1$ . Measurements indicate that the temporal response to set and reset signals can be as short as 2 ns. Optical emission at wavelength  $\lambda_2$  serves as Q output of the flip-flop while emission at wavelength  $\lambda_1$  serves as the Q-bar output. Significantly, the measured optical mode suppression ratio between the two lasing states is greater than -35 dB.

The speed of operation of the electro-optic SR flip-flop is limited to the 100 MHz range due to the turn-on delay as well as switching timing jitter. Improvements in speed may be obtained by using optical injection. Preliminary experiments indicate that the turn-on delay as well as timing jitter switching to wavelength  $\lambda_1$  ( $\lambda_2$ ) can be reduced by either continuously injecting photons into the laser at the wavelength  $\lambda_1$  ( $\lambda_2$ ) or by switching between the states using an optical pulse at  $\lambda_1$  ( $\lambda_2$ ).

Following this proof of concept, it is appropriate to consider scaling such devices to the meso-optic domain. This may require research into coupling between microdisk lasers or other novel devices [8-9].

The above illustration did not dwell on the sometimes subtle physics determining device behavior. The focus is the fact that functional opto-electronic devices can be made. Although not discussed in detail, it is worth mentioning that all-optical photonic logic devices are also possible to create. Meso-optic research is needed to scale such devices so that they may be integrated to provide the needed level of complex functionality in future photonic enhancements of otherwise all-electronic digital systems.

### Acknowledgment:

This work is supported in part by the Joint Services Electronics Program under contract #F49620-94-0022, the DARPA Ultra-II program, and the Air Force Office of Scientific Research under contract #F49620-97-1-0438.

### References

- [1] R. A. Nordin, A. F. J. Levi, R. N. Nottenburg, J. O'Gorman, T. Tanbun-Ek, and R. A. Logan, *J. Lightwave Technol.* **10**, 811 (1992).
- R. A. Nordin and A. F. J. Levi, *AT&T Technical Journal* **72**, (number 5) 37 (1993).
- [2] D. L. Huffaker, D. G. Deppe, K. Kumar, and T. J. Rogers, *Appl. Phys. Lett.* **65**, 97 (1994).
- [3] M. H. MacDougall, P. D. Dapkus, V. Pudikov, H. Zhao and G. M. Yang, *IEEE Photon. Technol. Lett.* **7**, 229 (1995).
- [4] G. M. Yang, M. H. MacDougall and P. D. Dapkus, *Electron. Lett.* **31**, 886 (1995).
- [5] A. P. Kanjamala and A. F. J. Levi, *Appl. Phys. Lett.* **71**, 300 (1997).
- [6] A. P. Kanjamala and A. F. J. Levi, unpublished.
- [7] K. Berthold, A. F. Levi, T. Tanbun-Ek, and R. A. Logan, *Appl. Phys. Lett.* **56**, 122 (1990).
- [8] A. F. J. Levi, *Solid State Electronics* **37**, 1297 (1994).
- [9] A. F. J. Levi, *Physics World* **9**, (number 11) 20 (1996).

# Photonic bandgap membrane microresonator

O. Painter, R. Lee, A. Yariv, and A. Scherer

Electrical Engineering/Applied Physics

California Institute of Technology, MS 200-36, Pasadena, Ca., 91125

(626)-395-4691, opainter@cco.caltech.edu

J. O'Brien

Department of Electrical Engineering

University of Southern California, 604 PHE MC 0271, Los Angeles, Ca., 90089

(213)-740-8682, jdobrien@usc.edu

## Abstract

We have designed and fabricated an optical microcavity formed from a defect in a two-dimensionally patterned, half wavelength thick, InGaAs/InGaAsP multi-quantum well membrane.

Optical microcavities hold the promise of improving the performance of light sources, such as lasers and light-emitting diodes. It has been evident for some time that the intriguing interplay between an atomic system and the electromagnetic field may be modified, and even performance tailored, by modifying the environment in which the the atomic system is placed.<sup>1</sup> High Q optical cavities, on the order of  $(\frac{\lambda}{2n})^3$  in volume, have been proposed for high efficiency, low power, and high speed modulation light sources.<sup>2</sup> Adequate fabrication techniques and optical design tools have only recently become available for the definition of such optical microcavities. For example, microlasers with sizes as small as 400nm have been fabricated by highly anisotropic etching a one dimensional epitaxial grown Fabry-Perot structure, and remarkably low threshold powers (of 2pJ) were measured in these devices.<sup>3</sup> More recently, whispering gallery mode lasers have been demonstrated, which rely on total internal reflection from the edge of a thin "microdisk", and have been demonstrated, both by electrical and optical pumping, to work well in the InGaAs/InGaAsP material system.<sup>4</sup> Although microdisks with diameters as small as  $1.5\mu\text{m}$  have been demonstrated, the overall mode volume is still rather large.

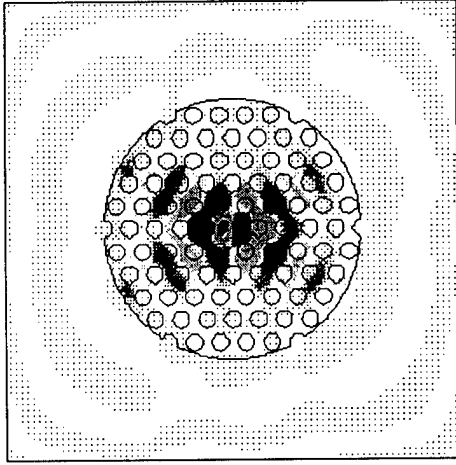


Figure 1: Two dimensional plot of the intensity of the magnetic field of the defect mode pattern (2D calculation only).

electric slab suspended in air to provide vertical confinement of the defect mode. The dielectric membrane is patterned with a hexagonal 2D array of air holes, with one hole missing to localize a defect mode. Using a finite-difference time-domain calculation<sup>9</sup> we first modeled the structure in two dimensions. To account for waveguide dispersion due to the strong vertical confinement, an effective index was calculated and substituted for the dielectric constant of the membrane in the 2D calculations. A plot of the magnetic field showing the defect mode is given in figure 1. With the aid of the 2D calculations we then proceeded to design and model a full 3D defect mode in the suspended membrane. The calculated Q of the defect mode in the thin membrane structure is approximately 380, and is limited by radiation in the vertical direction (not by the 5 or 6 layers of air holes surrounding the defect).

As mentioned earlier the defect mode was designed for the InGaAs/InGaAsP material system. A 6-layer InGaAs/InGaAsP multiple quantum well structure was grown by organometallic vapor phase epitaxy (OMVPE) onto a InP substrate. The total thickness of the grown quaternary material was 150nm, or approximately  $\lambda/2$ . This epitaxially grown layer was then coated with a  $\text{SiO}_2$  ion etch mask layer, which was in turn covered by a 50nm gold layer and a spun 80nm layer of polymethylmethacrylate (PMMA) electron beam resist. A Hitachi S-4500 field-emission electron microscope was used to define hexagonal arrays of circles. In the center of each pattern, a hole was left out, thereby creating a defect in the 2D photonic crystal. The pattern was then transferred into the Au and  $\text{SiO}_2$  surface mask using an argon ion mill followed by a reactive ion etch with  $\text{C}_2\text{F}_6$  as the reactive gas. The 2D pattern was etched through the multiple quantum well epitaxy and into the InP substrate by using a chemically assisted ion beam etch with a chlorine flux directed towards

In the work presented here, we have designed and fabricated a connected structure which utilizes the thin membrane of the microdisk, and incorporates a two dimensional (2D) photonic crystal with a defect to localize an optical mode in-plane. The membrane microresonator is based upon the successful work in microdisk lasers and the evolution of the processing of 2D photonic crystal mirrors.<sup>5-8</sup> Similar to the microdisks, the defect microcavity was designed around the InGaAs/InGaAsP material system due to its low surface recombination velocity and its relative maturity in laser sources. This also allowed us to design the photonic crystal for a relatively long wavelength of  $1.5\mu\text{m}$ , which eased the fabrication of the structure. The optical cavity design consisted of a  $\lambda/2$  thick di-

the sample surface. To complete the fabrication procedure for the membrane microresonator, the quantum well structure was undercut by immersing the sample into a hydrochloric acid InP selective etch, followed by a rinse in isopropyl alcohol. In figure 2 we show a series of SEM micrographs at different magnifications of the undercut membrane structure.

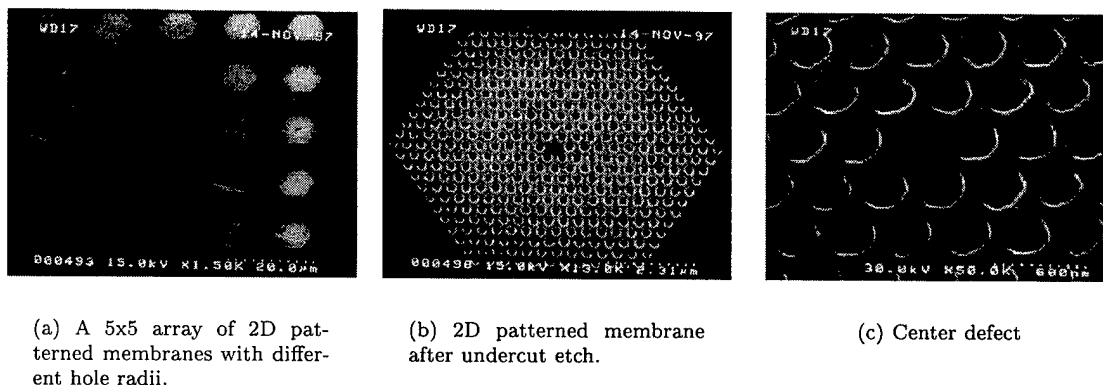


Figure 2: Various magnifications of the fabricated 2D patterned multi-quantum well membrane with a center defect.

Currently we are making passive and active (optically pumped) measurements of the membrane microresonators. We are also optimizing our current design to increase the cavity Q, as well as to implement a structure which is more solidly heat sunk and lends itself to electrical pumping as opposed to the optically pumped structure presented here.

## References

- [1] E. M. Purcell, *Physical Review* **69**, 681 (1946).
- [2] Eli Yablonovitch, *Physical Review Letters* **58**, 2059 (1987).
- [3] J. L. Jewell, J. P. Harbison, A. Scherer, Y. H. Lee, and L. T. Florez, *IEEE Journal of Quantum Electronics* **27**, 1332 (1991).
- [4] A. F. J. Levi, S. L. McCall, S. J. Pearton, and R. A. Logan, *Electronic Letters* **29**, 1666 (1993).
- [5] J. O'Brien, O. Painter, C.C. Cheng, R. Lee, A. Scherer, and A. Yariv, *Electronic Letters* **32**, 2243 (1996).
- [6] Thomas F. Krauss, Richard M. De La Rue, and Stuart Brand, *Nature* **383**, 699 (1996).
- [7] M. Kanskar, P. Paddon, V. Pacradoui, R. Morin, A. Busch, Jeff F. Young, S. R. Johnson, Jim Mackenzie, and T. Tiedje, *Applied Physics Letters* **70**, 1438 (1997).
- [8] T. Baba and T. Matsuzaki, *Japanese Journal of Applied Physics* **1** **35**, 1348 (1996).
- [9] B. D'Urso, O. Painter, J. O'Brien, T. Tombrello, A. Yariv, and A. Scherer, submitted to *JOSA: B* (unpublished).

## Dynamic analysis of lasing microcavities

Ira B. Schwartz and Ioana Triandaf  
*Special Project in Nonlinear Science*  
*U.S. Naval Research Laboratory*  
*Code 6700.3*  
*Plasma Physics Division*  
*Washington, D.C. 20375-5000 U.S.A.*  
*Phone: 202 404 8359*  
*FAX: 202 404 8357*  
*EMAIL: schwartz@nrls4.nrl.navy.mil*

Dynamics and active control of light dumping of lasing micorcavities are analyzed theoretically. Mean escape times for light dumping are controlled via cavity boundary perturbations.

### I. PHYSICS OF LASING MICROCAVITIES

The highest Q optical resonators are dielectric microspheres in which the high-Q modes are created by total internal reflection of light circulating just inside the surface of the sphere. These high-Q modes are referred to as "whispering gallery" modes or "morphology-dependent resonances". These resonances arise from angular momentum conservation. Deviations of the dielectric from spherical symmetry lead to spoiling of the high-Q modes. Small geometric deformations mix nearby modes and do not give a large degradation of their Q since rays impinge upon the boundary with a conserved angle of incidence and are trapped by internal reflection. At larger deformations many hundreds of modes are mixed and qualitative understanding of the Q-spoiling behavior is little understood ([1]). For small deformations the resonator is modeled by the wave equation ([2]), whereas for high deformations ray-optics models have been proposed ([3],[4]). Q degradation at large deformations is explained by rays which can escape refractively after multiple reflections. The ray dynamics is just the Hamiltonian dynamics of a point mass moving freely within a three-dimensional "billiard" (see [5]) and specularly reflecting from the surface, with the condition that if the angle of incidence with respect to the normal surface,  $\alpha$  falls below a critical angle,  $\sin(\alpha_c) = \frac{1}{n}$  then the ray escapes the dielectric according to Snell's law. The Q factor is proportional to the mean escape time spent by the rays inside the cavity ([1],[3]). The onset of escape corresponds to the appearance of chaos in the ray dynamics as a result of a KAM (Kolmogorov-Arnold-Moser) transition to chaos.

### II. THE MODEL

We simplify the model to that of a cavity of a microdisk laser which is described by a conformal transformation of the unit disk ([3]):

$$w(z) = \frac{z + bz^2 + cz^3}{(1 + 2b^2 + 3c^2)^{\frac{1}{2}}},$$

where b and c are real parameters. The boundary of the cavity is given by letting  $z = e^{i\phi}$ ,  $0 \leq \phi \leq 2\pi$ . To represent the dynamics one takes the Poincare surface of section which defines the angle of incidence as a function of the arc length ( a two-dimensional cut through a four-dimensional phase space). One studies the dynamics as the deformation parameter b is varied. For  $b = 0$  the trajectories are periodic quasi-periodic. As b increases, say to  $b = 0.11$ , a KAM transition to chaos is noticed: stable islands form around periodic orbits and a chaotic layer forms between islands ([3],[5],[6]), unbroken KAM tori persist for some finite range of the parameter. Further deformation leads to the brake up of such tori, as shown in Fig.1 and the trajectories can escape towards the chaotic region in the upper part of Fig.1, after which they exit the cavity tangentially, yielding Q spoiling. In Fig.2 a single escaping chaotic trajectory is shown.

### III. DYNAMICS AND Q-FACTOR CONTROL

Our purpose was to control the Q-factor by controlling the mean escape time of a group of trajectories started within a narrow angle of incidence. It is stated in ([3]) that it is desirable to be able to dump out light at will and have a type of control that would act as a Q switch. We calculated the mean escape time when the amplitude and frequency of a deformation pulse (of the  $b$  parameter) were varied. The mean escape time increases with increased frequency as expected. When the amplitude is increased we find that, in general, the larger the amplitude the shorter the mean escape time thus reducing the Q-factor.

This type of open loop control could not be used to prolong the mean escape time. For this purpose we use targeting along unstable manifolds of conveniently located unstable states as done for a  $CO_2$  laser [7]. The algorithm uses the natural dynamics of the system, namely unstable directions in the dynamics, to re-inject the iterates inside the cavity along these directions before they reach the critical escape angle. To find suitable unstable states we start from the undeformed state ( $b = 0$ ) and track orbits as  $b$  is increased, using continuation algorithms [8] and revealing bifurcation phenomena. Although the KAM transition to chaos has been well studied ([6]) an accurate bifurcation study with respect to parameters has not been done.

Using active control methods, one may manipulate the dynamics near a periodic unstable state lying near the escape regions. Then one can design open loop amplitude-frequency responses to sustain chaos while retaining internal reflection, thereby increasing the Q-factor. One potential candidate for control is the dynamics near a period-4 unstable state which can be identified in Fig. 2 by the density of rays around it.

Following [9] we showed that the type of dynamics followed by the trapped scattered light can be identified by looking at the maximum Lyapunov exponent as a function of the iterate. There are three types of trajectories: KAM tori, islands chains and chaos. We have found that for chaotic behavior the Lyapunov exponent are positive and decrease sharply with the number of iterations settling to a value one order of magnitude higher than the exponents for quasiperiodic behavior which are almost invariant as the number of iterations is increased and are very close to zero.

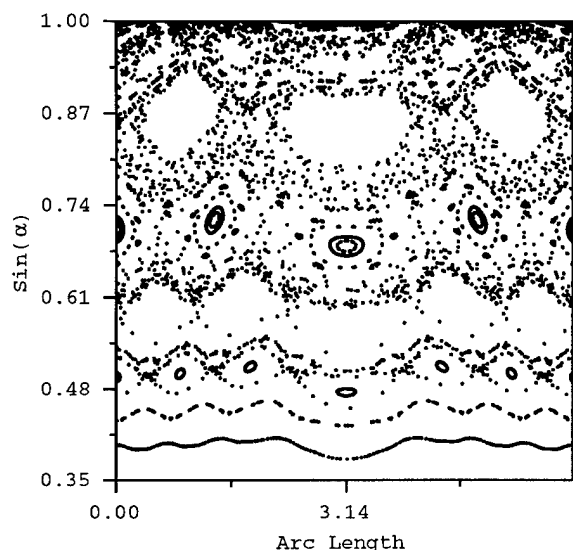


FIG. 1. Poincaré map of the angle of incidence versus arc length, showing KAM tori, islands chains and chaotic dynamics at  $b = 0.15$ .

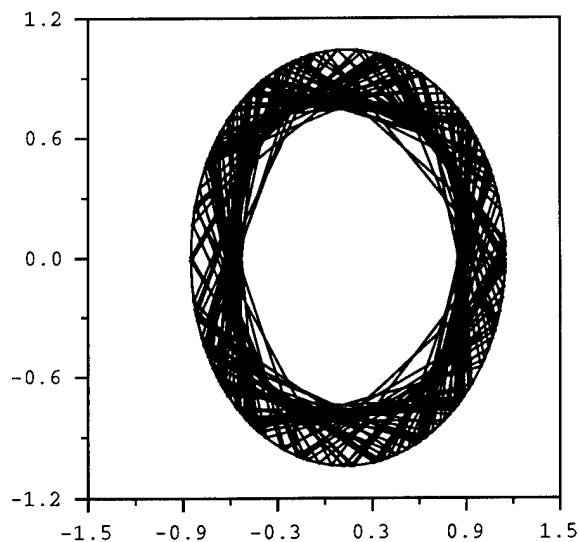


FIG. 2. The real-space trajectory at  $b = 0.15$  started with  $\sin\alpha = 0.77$ .

#### IV. REFERENCES

- [1] A. Mekis, J.U. Nockel, G.Chen, A.D. Stone and R.K.Chang, Phys. Rev. Lett., vol. 75, No. 14, 2682 (1995).
- [2] Jens U. Nockel and A. Douglas Stone, Nature, vol. 385, January 1997.
- [3] J.U.Nockel,A.D.Stone and R.K.Chang, Opt.Lett. 19,1693 (1994).
- [4] Jens U. Nockel, A. Douglas Stone, Gang Chen, Helene L. Grossman and Richard K. Chang, Optics Letters, vol. 21, No. 19, 1609 (1996).
- [5] M.V. Berry, Eur. J. Phys. 2, 91-102, (1981).
- [6] Edward Ott, 'Chaos in Dynamical Systems', Cambridge University Press, 1993.
- [7] Ira B. Schwartz and Ioana Triandaf, PRL, vol. 77, No. 23, 4740 (1996).
- [8] Ira B. Schwartz and Ioana Triandaf, Phys. Rev. A, Vol. 46, No. 12, 7439 (1992).
- [9] Lyman Hurd, Celso Grebogi, and Edward C. Ott, Hamiltonian Mechanics, Plenum Press 123-129 (1994).

## FDTD analysis and comparison of circular and elongated ring designs for waveguide-coupled microcavity ring resonators

S. C. Hagness, D. Rafizadeh<sup>(1)</sup>, S. T. Ho, and A. Taflove

Department of Electrical and Computer Engineering

Northwestern University, Evanston, IL 60208

phone: 847-491-8887, fax: 847-491-4455, email: s-hagness@nwu.edu

<sup>(1)</sup>current address: The Aerospace Corporation,

P. O. Box 92957 M2-246, Los Angeles, CA, 90009-2957

Waveguide-coupled microcavity ring resonators are composed of waveguides with large refractive index contrasts in the lateral direction. Since the lateral confinement of the mode is so strong, the diameter of the ring waveguide can be as small as a few micrometers with negligible bending losses. The key advantages of these compact resonators are the wide free spectral range and the potential for high-density integration. These devices may serve as micron-size narrowband tunable filters, frequency-domain switches, or intensity/phase modulators in high-density photonic integrated circuits.

The coupling of light between the adjacent waveguides and the ring is controlled by the width of the air gap and the coupling interaction length. The strong confinement of the waveguides requires very close proximity of the waveguide to the ring, resulting in the challenging fabrication of very narrow air gaps. Using electron beam lithography and nanofabrication techniques, we recently demonstrated high- $Q$  semiconductor microcavity ring and disk resonators with evanescent wave coupling to sub-micron-width waveguides across  $0.1\text{-}\mu\text{m}$ -wide air gaps with aspect ratios of more than 20:1 [1, 2]. Other lithography techniques have resulted in adjacent waveguides being fused to the ring, in which case the amount of coupling is much larger than desired [3]. An important step towards practical fabrication and commercialization of these devices is the exploration of designs that might alleviate the need for such narrow air gaps. In particular, a wider air gap may allow reliable and repeatable fabrication of these resonators with reduced sensitivity to fabrication variations.

In order to achieve the desired level of coupling (0.5-3%, depending on the scattering losses) with a wider air gap, the interaction length over which the coupling takes place must be increased. We previously investigated the possibility of curving the adjacent waveguide along the ring for this purpose [4]. Using finite-difference time-domain (FDTD) models to compute the coupling efficiency, we found that the coupling actually drops when the input waveguide curves along the ring for more than just a small fraction of the circumference of the ring. For example, when the adjacent waveguide curves along a  $5.0\text{-}\mu\text{m}$ -diameter ring for 1/8th of its circumference, the path length difference due to the differing bend radii of the ring and adjacent waveguides leads to significant phase mismatch between the signals in each waveguide.

Here, we investigate changing the shape of the ring instead of the adjacent waveguide in order to manipulate the coupling behavior. For example, the coupling interaction length can be increased by elongating the ring to form a racetrack configuration, as proposed recently [5]. In Figure 1, the FDTD-computed coupling efficiency, defined as the percentage of power that couples into the ring from the input waveguide, is graphed as a function of the width

of the air gap for two different microcavity ring resonators. The width of the ring and adjacent waveguides in all simulations is  $0.3\ \mu\text{m}$ . The refractive index of the waveguide core is 3.2 (semiconductor); the cladding index is 1.0 (air). The dotted-line curves represent the coupling efficiencies at  $\lambda=1.5$ ,  $1.55$ , and  $1.6\ \mu\text{m}$  for a  $5.0\text{-}\mu\text{m}$ -diameter circular ring resonator. The solid-line curves represent the coupling efficiencies for a racetrack ring resonator with  $5.0\text{-}\mu\text{m}$ -diameter circular sections and  $1.5\text{-}\mu\text{m}$ -long straight sections. These results illustrate the potential advantage of the racetrack resonator for allowing slightly wider air gaps while still achieving desired coupling levels.

Consider a  $5.0\text{-}\mu\text{m}$ -diameter circular ring resonator with a gap size of  $0.2\ \mu\text{m}$  between the ring and adjacent waveguides; the coupling efficiency of this design is approximately 2% at  $\lambda=1.5\ \mu\text{m}$ . The same coupling level can be achieved with a racetrack resonator using a gap size of  $0.3\ \mu\text{m}$  and straight-section lengths of  $2.1\ \mu\text{m}$ . We have computed the transmittance for circular and racetrack ring resonators. In order to make a direct comparison of the resonance characteristics, the cavities in both designs have identical perimeter lengths. To match the perimeter of the  $5.0\text{-}\mu\text{m}$ -diameter circular ring resonator and its coupling behavior in the  $1.55\text{-}\mu\text{m}$ -wavelength range, a racetrack ring resonator with  $3.66\text{-}\mu\text{m}$ -diameter curved sections and  $2.1\text{-}\mu\text{m}$ -long straight sections was modeled. The FDTD-computed transmittance data reveal that the Q for each resonator is about 3000 and the free spectral range is approximately 50 nm. Figure 2 shows visualizations of the steady-state electric field patterns in the circular and racetrack ring resonators for on-resonance single-frequency excitation at  $\lambda=1.56\ \mu\text{m}$ .

In summary, we have demonstrated that the resonance characteristics of the microcavity racetrack ring resonator are similar to those of the circular ring resonator. An elongated design such as the racetrack ring resonator allows the air gap to be slightly wider while maintaining the desired coupling levels. Such designs lessen the strict tolerances required in fabricating nanometer-scale features that are highly sensitive to fabrication variations.

## References

- [1] D. Rafizadeh, J. P. Zhang, S. C. Hagness, A. Taflove, R. C. Tiberio, K. A. Stair, and S. T. Ho, "Nanofabricated waveguide-coupled  $1.5\text{-}\mu\text{m}$  microcavity ring and disk resonators with high Q and 21.6-nm free spectral range," *Conference on Lasers and Electro-Optics*, Baltimore, MD, May 1997, postdeadline paper CPD23.
- [2] D. Rafizadeh, J. P. Zhang, S. C. Hagness, A. Taflove, K. A. Stair, R. Tiberio, and S. T. Ho, "Waveguide-coupled AlGaAs/GaAs microcavity ring and disk resonators with high finesse and 21.6-nm free spectral range," *Opt. Lett.*, vol. 22, pp. 1244–1246, Aug. 15, 1997.
- [3] J. S. Foresi, B. Little, G. Steinmeyer, E. Thoen, S. Chu, H. Haus, E. Ippen, L. Kimerling, and W. Greene, "Si/SiO<sub>2</sub> micro-ring resonator optical add/drop filters," *Conference on Lasers and Electro-Optics*, Baltimore, MD, May 1997, postdeadline paper CPD22.
- [4] S. C. Hagness, D. Rafizadeh, S. T. Ho, and A. Taflove, "FDTD microcavity simulations: Design and experimental realization of waveguide-coupled single-mode ring and whispering-gallery-mode disk resonators," *J. Lightwave Technol.*, vol. 15, pp. 2154–2165, Nov. 1997.
- [5] G. Griffel and S. Arnold, "Synthesis of variable optical filters using meso-optical ring arrays," *IEEE LEOS Annual Meeting*, San Francisco, CA, Nov. 1997.

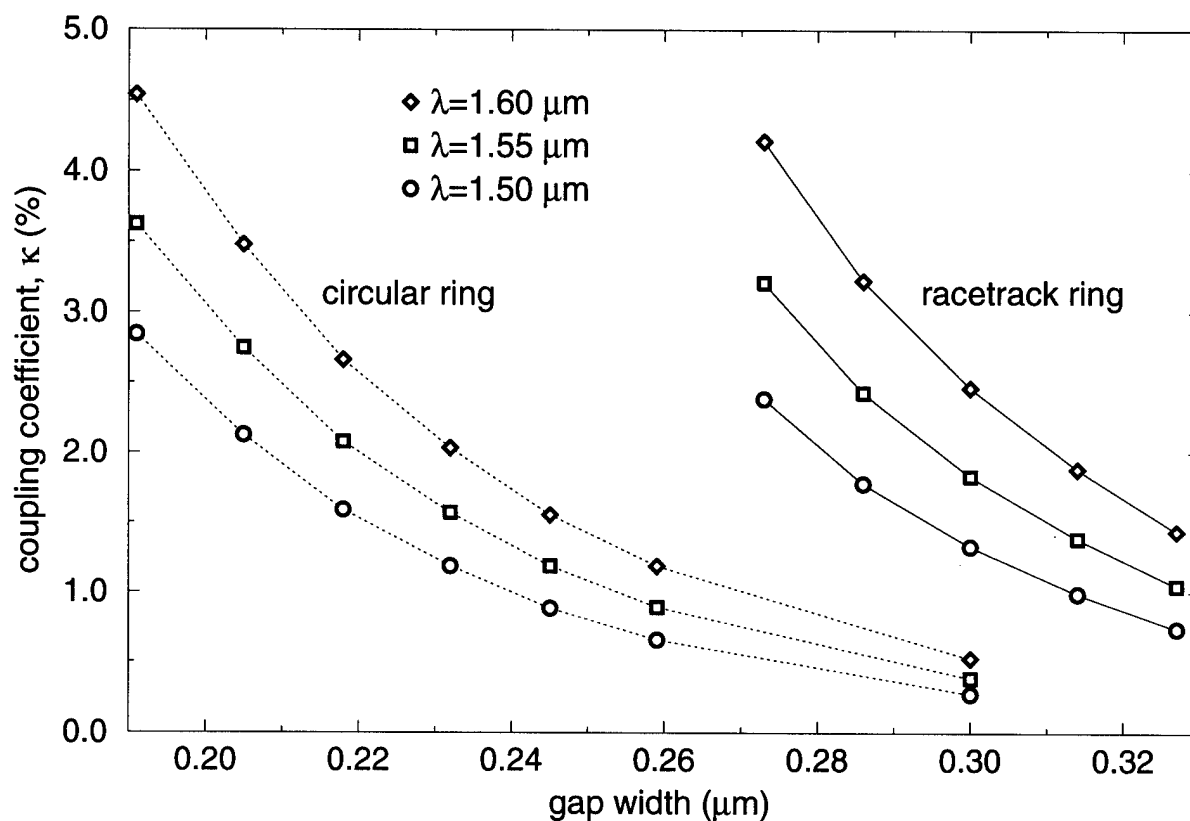


Figure 1. FDTD-computed coupling coefficients as a function of wavelength and gap size for a 5.0- $\mu\text{m}$ -diameter circular ring resonator (dotted lines) and a racetrack ring resonator with 5.0- $\mu\text{m}$ -diameter curved sections and 1.5- $\mu\text{m}$ -long straight sections (solid lines).

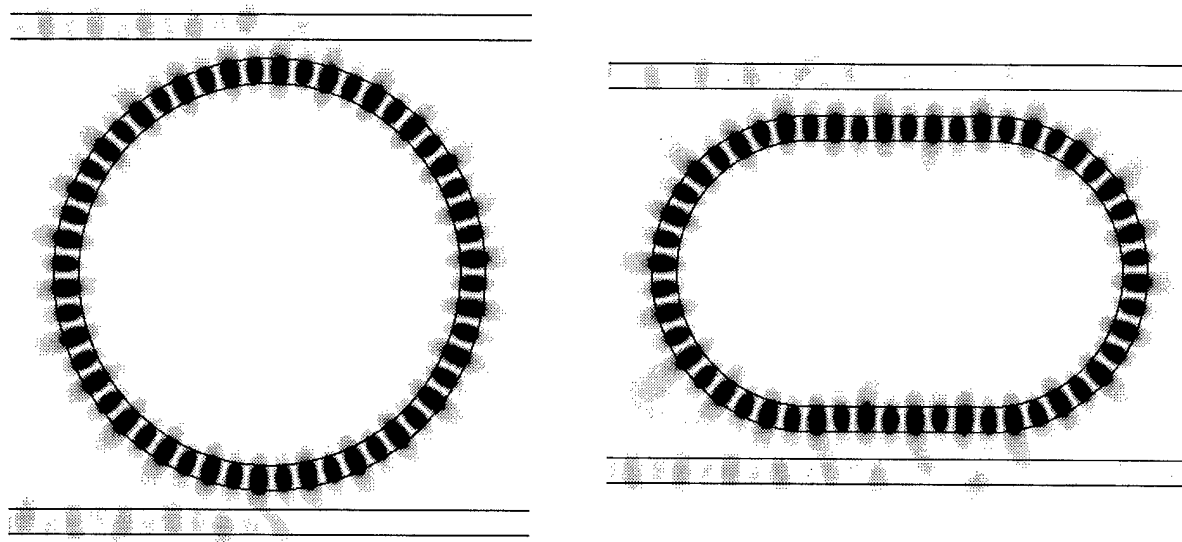


Figure 2. FDTD-computed steady-state electric field patterns in microcavity circular (left) and racetrack (right) ring resonators at an on-resonance excitation wavelength ( $\lambda = 1.56 \mu\text{m}$ ).

# Noise characteristics of two-polarization microcavity semiconductor lasers

**G. P. Bava (1) P. Debernardi (2)**

(1) Dip. di Elettronica, (2) Cespa-CNR, Politecnico di Torino,

Corso Duca degli Abruzzi, 24 10129, TORINO, ITALY

Tel. 011/5644165, Fax 011/5644089, E-mail: Pierluigi@polito.it

## Summary

Microcavity semiconductor lasers have been shown to be promising devices owing to their characteristics such as very low threshold current, large modulation bandwidth, etc.; in particular noise properties have been widely studied in recent years [1, 2], showing peculiar characteristics, but only with reference to single mode operation. However common microcavity structures present geometrical symmetries such that two modes, corresponding to orthogonal polarizations, can simultaneously lase [3, 4, 5, 6, 7]. The noise behavior of multimode semiconductor lasers has also been deeply investigated by several authors [8, 9]. However in these treatments different modes are coupled only through spontaneous emission. Instead in the microcavity structures supporting two orthogonal polarizations, ideally perfectly degenerate, the two modes are tightly coupled by different mechanisms which remove the degeneracy. They can be related for instance to slight geometrical asymmetries, material anisotropies etc., both inside the cavity and in the mirrors [7].

In the present work the two polarization behaviour of a microcavity semiconductor laser is analyzed as regards noise performances. The theory is developed by using Langevin noise sources in the quantum mechanical equation of motion for the field and electron operators. The two modes are assumed to be nearly degenerate: that is they present very similar resonant frequencies (with a spacing on the order of a few gigahertz according to experimental measurements) and decay constants. The coupling between the two polarizations includes also the effect of different electron spin populations, following the

model of Ref. [3]; however, on the basis of Ref. [9], in the present model only the difference in conduction band spin populations is included, since the valence band spin relaxation is much faster. To simplify the analytical treatment and the numerical computation only operating conditions where the two modes are locked at a common frequency is considered; this is the most important situation in practical applications (single frequency operation).

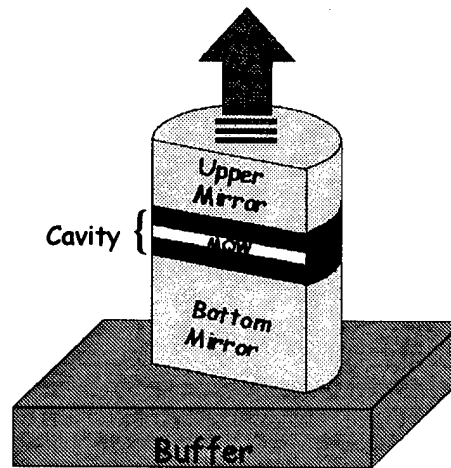


Figure 1: Schematic representation of the semiconductor post microcavity laser

For numerical evaluations we consider an air post structure with a multiple quantum well active region, whose schematic representation is depicted in the figure. The optical gain, the spontaneous emission (both global and in the lasing modes) and the electromagnetic model of the cavity and Bragg mirrors are computed self consistently; for such a device a complete model is presented in Ref. [10]. Instead for the effects of small geometrical asymmetries and anisotropies, phenomenological parameters are introduced.

The main purpose of the work is concerned with the evaluation of output amplitude and photon number fluctuation spectra. Two cases will be considered: the fluctuations of the total field (including the two polarizations) or the fluctuations of the dominant polarization.

Work carried out in the framework of ESPRIT-LTR Project ACQUIRE and with the financial support of Progetto Finalizzato MADESS II by Italian CNR.

## References

- [1] Y. Yamamoto, S. Machida and O. Nilsson, Phys. Rev. A, "Amplitude squeezing in a pump-noise suppressed laser oscillator", 34, 1986, p. 4025-4042.
- [2] Y. Yamamoto, S. Machida, G. Björk: "Microcavity semiconductor laser with enhanced spontaneous emission"; Phys. Rev. A, 44, 1991, p. 657-668.
- [3] M. San Miguel, Q. Feng and J. V. Maloney: "Light-polarization dynamics in surface-emitting semiconductor lasers", Phys. Rev. A, 52, 1995, p. 1728-1739.
- [4] M. Travagnin, M. P. van Exter, A.K. Jansen van Doorn and P. Woerdman: "Role of optical anisotropies in the polarization properties of surface-emitting semiconductor lasers", Phys. Rev. A, 54, 1996, p. 1647-1660.
- [5] J. Martin-Regalado, F. Prati, M. San Miguel, and N.B. Abraham: "Polarization Properties of Vertical-Cavity Surface-Emitting Lasers"; IEEE J. Quant. Electron., 33, 1997, p. 765-783.
- [6] M. Travagnin: "Linear anisotropies and polarization properties of Vertical Cavity Surface Emitting semiconductor Lasers ", Phys. Rev. A, 56, 1997, p. 4094-5005.
- [7] J.P. Woerdman, A.K. Jansen van Doorn and M. P. van Exter: "Simmetry breaking in vertical-cavity semiconductor lasers"; 1997 Spring Topical Meetings, Quantum Optoelectronics, paper QFB6, Incline Village, 19-21 March 1997, p. 129-131.
- [8] D. Marcuse: "Computer simulation of laser photon fluctuations: theory of single cavity laser": IEEE J. Quant. Electron., 20, 1984, p. 1139-1148.
- [9] Minoru Yamada: "Variation of intensity Noise and Frequency Noise with Spontaneous Emission Factor in semiconductor lasers"; IEEE J. Quant. Electron., 30, 1994, p. 1511-1519.
- [10] T.C.Damen, L.Vina, J.E.Cunningham, J.Shah and L.J.Sham: " Subpicosecond Spin Relaxation Dynamics of Excitons and Free Carrier in GaAs Quantum Wells", Phys.Rev.Lett. 67, 1991, p. 3432-3435.
- [11] G. P. Bava, P. Debernardi: "Spontaneous emission in semiconductor microcavity post lasers," to appear on IEE Proc. Optoelectronics.

---

**Integrated Photonics Research**

# **Modulators/Switches**

**Tuesday, March 31, 1998**

**S. Chandrasekhar, Lucent Technologies**  
Presider

**ITuE**  
**10:30am-12:00m**  
Salon C

## OPTICAL PROCESSING WITH ELECTROABSORPTION MODULATORS

**F. Devaux**

Alcatel Alsthom Recherche, Route de Nozay,  
91460 Marcoussis, France  
Ph : 33 1 69 63 11 78 Fax : 33 1 69 63 18 13

**A. Carencio**

France Telecom, CNET/DTD, 92220 Bagneux  
Cedex, France  
fabrice.devaux@aar.alcatel-alsthom.fr

Electroabsorption (EA) modulators were primarily intended for high-speed coding as an alternative to  $\text{LiNbO}_3$  Mach-Zehnder modulators. Beyond this application, EA modulators have been increasingly used for various optical processing functions thanks to specific properties (Table 1). For instance, the transfer function is highly non-linear and can be used for optical pulse generation. Another key feature of EA modulators is polarisation independent operation allowing optical processing in line or in the receiver part. We will focus in this talk on the use of multiple EA modulators, either in series or in parallel, for optical processing.

	$\text{LiNbO}_3$ Modulator	EA modulator
Frequency response *at 3dB	Linear decrease ( $\sim 0.1 \text{ dB/GHz}$ ) Very high bandwidth (40GHz*)	RC-like decrease (6 dB/octave) Very high bandwidth (50 GHz*)
Drive voltage	Moderate (3-6V)	Low (1.5-3V)
Insertion loss	Low [-4,-6 dB]	High [-8,-12 dB]
Chirp	Tunable or fixed [-5,5]	Fixed with limited range [-.5,5]
Transfer function	Sinusoidal, periodic	Highly non-linear vs V Linear vs current
Polarisation dependence	Yes	No
InP compatible	No	Yes

Table 1 : Comparison of  $\text{LiNbO}_3$  and electroabsorption (EA) modulators.

### EA MODULATORS IN SERIES

The series configuration is shown in figure 1a. Practically it is either two modulator modules [1] or a two-section modulator [2]. In the latter case, a simple electrical insulation defines the two sections. Depending on the application, a passive waveguide or an amplifier can be inserted between the two modulators to reduce the electrical cross-talk, if necessary, or provide optical gain [3].

In this configuration, each EA modulator can basically be operated in four ways : switching (i.e. NRZ coding), pulse shaping, linear modulation (small modulation depth) or photodetection. A practical example is to use the first modulator as a pulse shaping element and the second one to code the corresponding pulse stream. Such a coded pulse source was demonstrated at 20 Gb/s; it is made of two EA modulators, a separating amplifier and a DFB laser, all integrated on InP [3]. Another example is demultiplexing + detection. The first modulator is operated as a gate by applying a sinusoidal voltage, while the second one is biased to a high absorption part of the transfercurve to act as a photodetector of the demultiplexed pulses. Using the EA

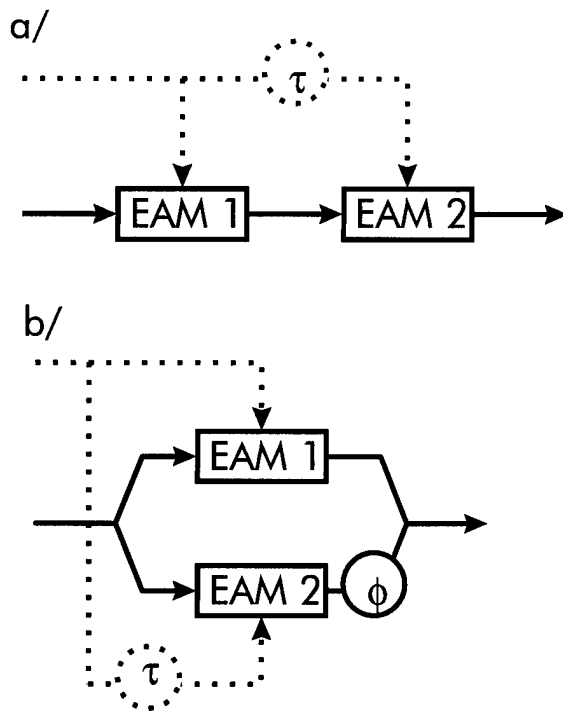


Figure 1 : EA modulators in series (a) or in parallel (b)

modulator as a photodiode affects slightly the design of the device because transit time has to be taken into account. In this case, also, the electrical crosstalk is an important parameter.

In a different way, EA modulators can be used in series to overcome the discrete device limitations. For instance, EA modulators as pulse shaping elements are limited to about 10% duty cycle and 15-30 dB extinction ratios (depending on active layer and waveguide technology), which prevents their use in optical time division multiplexing (OTDM). Two modulators in series, operated with the same electrical signal, should double the extinction ratio. On one hand more RF power is needed to compensate for the RF splitting losses. On the other hand, lower drive voltage is needed on each modulator. Since the transfer function is non-linear, the excess RF power may be positive or (more rarely)

negative, depending on the specifications. The duty cycle can then be reduced to about 5 %, or even more if the delay between the two RF signals is properly adjusted. A tandem of EA modulators was fabricated with on/off ratios as low as -55 dB and 4x20 Gb/s was demonstrated with low interference coherence noise [2]. Hybrid double modulation also allowed 8x10 Gb/s OTDM [1].

The performances can still be increased by adding other modulators. The number of modulator in series is mainly limited by residual absorption loss, unless the total device length is kept constant. In the last case, the modulator section lengths are reduced and ultra-high frequency operation is made possible, to the expense of drive voltage. The limit of this scheme is a travelling-wave EA modulator to go beyond 100 GHz bandwidth.

#### EA MODULATORS IN PARALLEL

EA modulators may be inserted in an interferometer as shown in Figure 1b. One of the arm is optically phase-shifted (typically 0,  $\pi/2$  or  $\pi$ ), and the two applied electrical signals are delayed by  $\tau$ . The output lightwave electric field is

$$E_{all} = (E(t) + E(t-\tau)e^{j\phi}) / 2 ,$$

where  $E$  is the field one would obtained with a single modulator. After Fourier transform, we obtain

$$E_{all}(f) = E(f)(1 + e^{j(\phi + 2\pi f\tau)}) / 2 .$$

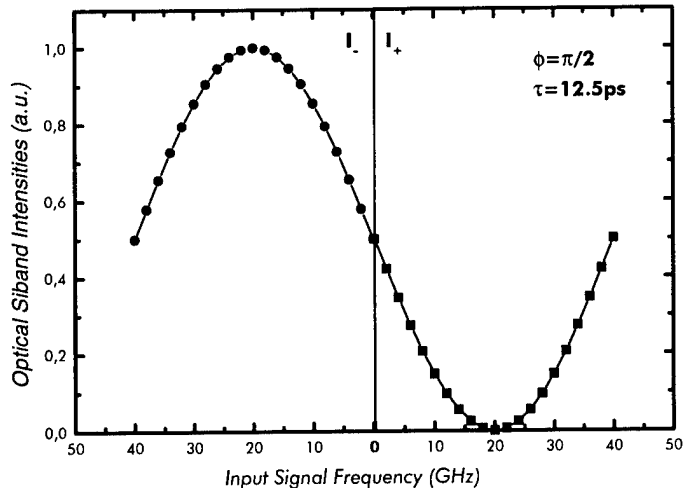


Figure 2 : First Side band amplitude of optical spectrum versus frequency of applied signal for device of figure 1/h

conversion can be obtained by changing the parameter of the interferometer (here  $\phi = \pi$ ). The configuration can be extended to  $N$  arms with  $N$  optical amplitudes and phases and  $N$  electrical phases. In such a way, arbitrary filter transfer function may be obtained: broadband SSB modulation may be approximated with a four-arm interferometer, arbitrary Partial Frequency Response coding such as modified duobinary, multilevel coding, etc.

The device acts as an electrical-to-optical filter, relating the optical to the electrical modulation spectra. In figure 2, for instance, the delay is  $1/4f_0$  and the optical phase shift  $\pi/2$ . The device acts as a Single-Side-Band (SSB) electrical-to-optical converter at modulation frequencies around  $f_0$ . Such a SSB source was demonstrated up to 40 GHz with DFB laser, interferometer and modulators integrated on InP [4]. It is shown in figure 3. In the same manner, electrical-to-optical duobinary

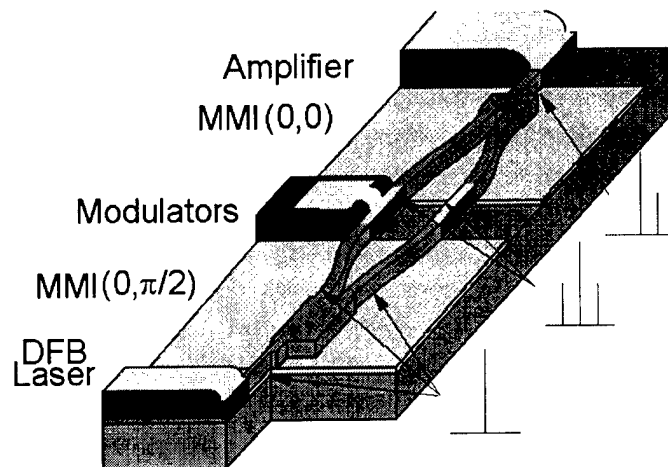


Figure 3 : Two EA modulators integrated with a DFB laser and an amplifier form a Single-Side-Band source

#### Reference :

- [1] Marcenac et al, « 80 Gb/s OTDM using electroabsorption modulators », ECOC'97, vol. 3, p. 23
- [2] Devaux et al, « Tandem of modulators for high on/off pulse generation (-55dB) », Electron. Lett. , vol. 33 (17), p.1491, 1997
- [3] Souli et al, « Tandem of EA modulators integrated with DFB laser and optical amplifier for 20 Gb/s pulse generation and coding at  $1.55\mu\text{m}$  », OFC'97, p. 141
- [4] Vergnol et al, « Fully integrated millimetric single-side-band lightwave source up to 40 GHz », ECOC'97, vol. 6, p. 45

# Low-Loss and Efficient InAsP/GaInP MQW Electroabsorption Waveguide Modulators for Analog Fiber-Optic Links

K. K. Loi, X. B. Mei, J. H. Hodiak, C. W. Tu, and W. S. C. Chang

Department of Electrical and Computer Engineering

University of California, San Diego

La Jolla, CA 92093-0407, USA

Phone: +1-619-534-3627, Fax: +1-619-534-2486, E-mail: kloi@sdcc3.ucsd.edu

## I. INTRODUCTION

A lithium niobate ( $\text{LiNbO}_3$ ) Mach-Zehnder interferometric modulator is a key optoelectronic component for an externally modulated microwave fiber-optic link. A high-speed electroabsorption (EA) modulator is an attractive alternative because it requires very low microwave drive voltage, and could potentially be integrated with laser and electronic driver circuitry. Recently, a high linearity analog link with a 116dBHz<sup>4/5</sup> spurious-free dynamic range has been demonstrated using an InGaAs multiple-quantum-well (MQW) EA modulator monolithically integrated with a laser [1]. However, the optical insertion loss of EA modulator is about 10dB [2]-[5], which is significantly higher than that of  $\text{LiNbO}_3$  modulator (3 to 5dB). We have designed and fabricated a low-loss EA waveguide modulator using strain-compensated InAsP/GaInP MQW's. We describe in this paper the high-frequency performance of the EA modulator for microwave subcarrier modulation in an 1.3 $\mu\text{m}$  analog fiber-optic link.

## II. DEVICE STRUCTURE AND FABRICATION

The  $p$ - $i$ (MQW)- $n$  waveguide modulator structure is grown on an  $n^+$  InP substrate using a gas-source MBE. The unintentionally doped region consists of six periods of 9.4nm thick compressively strained InAsP quantum wells and 10.6nm thick tensile strained GaInP barriers. The exciton absorption peak wavelength at zero external bias is located at 1.288 $\mu\text{m}$ . The active MQW region is embedded between 0.9 $\mu\text{m}$  thick lightly  $p$ -doped and  $n$ -doped InGaAsP layers. The two high-index quaternary passive waveguide layers enlarge the core of the waveguide mode, without producing any significant RF voltage drop. Ridge waveguides were fabricated using  $\text{CCl}_2\text{F}_2$  reactive ion beam etching. The ridge height is 1.9 $\mu\text{m}$  and the waveguide width ranges from 3 $\mu\text{m}$  to 6 $\mu\text{m}$ . The wafer was cleaved into bars with waveguide lengths between 65 $\mu\text{m}$  and 400 $\mu\text{m}$ . Quarter-wave  $\text{Al}_2\text{O}_3$  antireflection layers are deposited on the waveguide end facets at TRW. The residual reflectivity is less than 1% measured using an optical circulator.

## III. MODULATOR PERFORMANCE

Micromachined tapered single-mode fibers were used to couple TE polarized light into and out of the EA modulator. Table I summarizes the fiber-to-fiber optical insertion loss of a typical 4 $\mu\text{m}$  wide 215 $\mu\text{m}$  long device at various operating wavelength. The insertion loss is less than 5dB at a detuning energy ( $\Delta\text{det}$ ) larger than 24meV. Our results compare favorably with the lowest insertion loss reported ( $\leq 5\text{dB}$  at  $\Delta\text{det} \geq 32\text{meV}$ ) for a 1.55 $\mu\text{m}$  InGaAs/InAlAs MQW EA modulator which requires the regrowth of a semi-insulating InP burying layer [6].

The low-frequency (1kHz) electrical-to-optical transfer characteristic of the 4 $\mu\text{m}$  wide 215 $\mu\text{m}$  long device is illustrated in Fig. 1. The best electrooptic slope efficiency  $\eta$  was determined from the first derivative of its empirical optical transfer curve. The  $\eta$ 's obtained at various wavelength are also summarized in Table I. The slope efficiency is of prime importance for analog applications because it directly determines the transmitted microwave signal level and

RF link gain. The  $1.0\text{V}^{-1}$   $\eta$  achieved by the EA modulator is equivalent to a  $\text{LiNbO}_3$  Mach-Zehnder modulator with a half-wave voltage  $V_\pi$  of 1.6V. In comparison, a commercially available  $\text{LiNbO}_3$  modulator has a DC  $V_\pi$  of 12V with 18GHz bandwidth.

The *p-i-n* EA modulator structure can be utilized simultaneously as a compact optoelectronic transmitter-modulator and receiver-photodetector by adjusting the applied reverse bias [7]-[8]. At  $-5\text{V}$  external bias, the MQW EA modulator operates as an efficient waveguide photodetector with a measured DC responsivity better than  $0.62\text{A/W}$  (see Table I), which is 30% higher than the  $0.45\text{A/W}$  obtained using an InGaAsP Franz-Keldysh EA modulator [8].

The input reflection coefficient  $S_{11}$  and the small-signal frequency response of the MQW EA modulator were characterized from 45MHz to 40GHz. The measured  $S_{11}$  substantiates that the modulator input impedance can be represented by an equivalent lumped RC circuit. A  $3\mu\text{m}$  wide  $90\mu\text{m}$  long EA modulator terminated with a  $50\Omega$  load in parallel exhibits a 3dB electrical bandwidth of 23GHz. The measured modulation response correlates very well with the theoretical prediction based on the RC circuit model extracted from the  $S_{11}$  data. The RC time constant dictates the low-pass electrical bandwidth.

Fig. 2 displays the measured RF link gain as a function of frequency with input optical carrier power as the parameter. The link gain is the RF-to-RF efficiency between the output of the photodetector and the input to the EA modulator. A  $-26\text{dB}$  RF link gain has been recorded at  $16\text{mW}$  input optical carrier power and  $1.27\text{mA}$  received photodetector current. A higher RF link gain can be achieved using (1) photodetector with higher responsivity, (2) higher input optical power, (3) optical/electrical amplification. Data on the nonlinearity of the EA modulator is being collected and the performance of two-tone intermodulation distortion will be presented.

#### IV. CONCLUSION

We have demonstrated a very-low-loss, highly efficient, and high-speed EA waveguide modulator for microwave subcarrier transmission on optical fibers. A fiber-to-fiber optical insertion loss as low as 5dB and an equivalent half-wave voltage of 1.6V have been obtained.

#### V. REFERENCES

- [1] R. Helkey *et al.*, in *IPR '96 digest*, IMH-18, 217 (1996).
- [2] K. Wakita *et al.*, *IEEE Photon. Technol. Lett.*, vol. 3, 138 (1991).
- [3] Y. Chen *et al.*, *Appl. Phys. Lett.*, vol. 61, 10 (1992).
- [4] F. Devaux *et al.*, *IEEE Photon. Technol. Lett.*, vol. 5, 1288 (1993).
- [5] T. Ido *et al.*, *IEEE Photon. Technol. Lett.*, vol. 6, 1207 (1994).
- [6] K. Wakita *et al.*, in *OFC '97 digest*, WG-3, 137 (1997).
- [7] L. Westbrook *et al.*, *Electron. Lett.*, vol. 32, 1806 (1996).
- [8] R. Welstand *et al.*, *IEEE Photon. Technol. Lett.*, vol. 8, 1540 (1996).

**Table I** Performance of a  $4\mu\text{m}$  wide  $215\mu\text{m}$  long EA modulator at various operating wavelength

Wavelength ( $\mu\text{m}$ )	Detuning (meV)	Optical insertion loss (dB)	Slope efficiency ( $\text{V}^{-1}$ )	Responsivity@ $-5\text{V}$ (A/W)
1.30	8.9	8.5	2.07	0.658
1.31	16.2	5.5	1.27	0.663
1.32	23.3	5.0	1.03	0.649
1.33	30.4	4.9	1.01	0.640
1.34	37.4	4.7	0.99	0.620

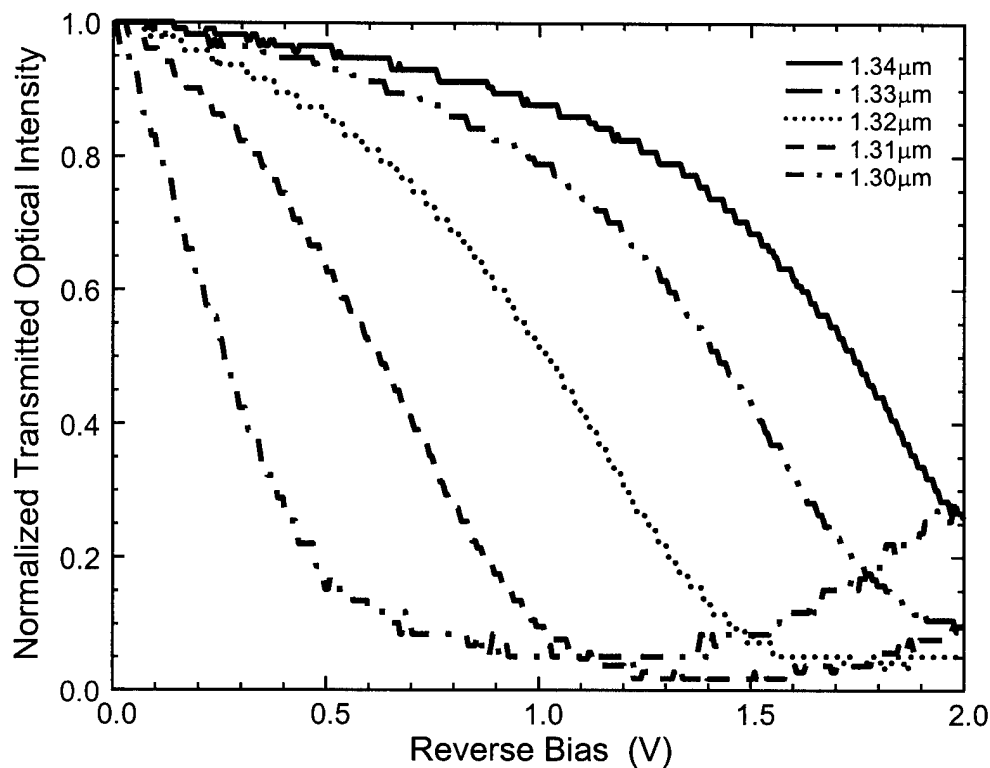


**Figure 1** Optical transfer curves (normalized to the zero-bias transmitted light intensity) at various wavelength

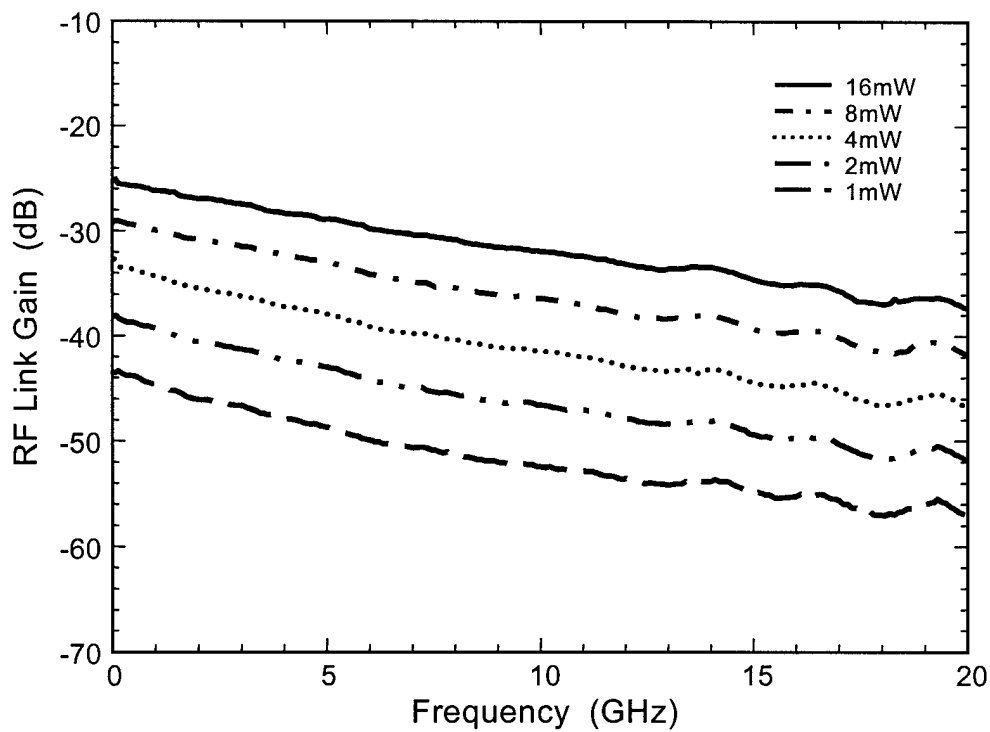


**Figure 2** RF link gain as a function of frequency at various input optical carrier power

# A COMPACT INTEGRATED PHASAR-BASED OPTICAL CROSSCONNECT ON InP

C.G.P. Herben, C.G.M. Vreeburg, D.H.P. Maat<sup>1</sup>, X.J.M. Leijtens, Y.S. Oei,  
F.H. Groen<sup>1</sup>, J.J.G.M. van der Tol<sup>2</sup>, P. Demeester<sup>3</sup>, and M.K. Smit

Faculty of Information Technology and Systems, Delft University of Technology, P.O. Box 5031,  
NL-2600 GA, Delft, The Netherlands, email: herben@et.tudelft.nl

<sup>1</sup>Research Group for Optics, Delft University of Technology, The Netherlands

<sup>2</sup>KPN-Research, Royal PTT Netherlands N.V., Leidschendam, The Netherlands

<sup>3</sup>University of Gent-IMEC, Department of Information Technology, Belgium

## I. Abstract

**We report the first InP-based integrated optical crossconnect. The device can crossconnect signals at four wavelengths independently from two input fibers to two output fibers. Total on-chip loss is less than 16 dB. Device size is 7x9 mm<sup>2</sup>.**

## II. Introduction

Wavelength selective switches such as optical crossconnects (OXC's) and add-drop multiplexers (ADM's) play a key role in advanced WDM-networks [1],[2]. Devices presently used in network experiments are assembled from a large number of discrete components, which makes them costly and voluminous. Integration will be necessary to reduce both cost and volume. First integrated wavelength selective switches reported were based on silica technology [3]. We have reported the first reconfigurable InP-based ADM [4]. This device showed good loss and crosstalk properties, but it was not polarization independent. To obtain a polarization independent wavelength selective switch both the PHASAR and the switches have to be insensitive to the polarization.

In this paper we report the first integrated InP-based polarization-independent crossconnect. The device, which can crossconnect signals at four wavelengths independently from two input fibers to two output fibers, has been realized by integrating a polarization dispersion compensated 16x16 PHASAR as reported by Vreeburg [5] with four polarization independent Mach-Zehnder Interferometer switches. Experimental results are found to be in good agreement with simulation results obtained with an advanced photonic circuit simulator [9].

## III. Design

The OXC consists of a single 16-channel polarization dispersion compensated PHASAR [5] and four Mach-Zehnder Interferometer space switches [10] connected in a fold-back configuration. The 2x2 electro-optical Mach-Zehnder Interferometer switches have phase sections orientated 28° from the [0 $\bar{1}$ 1]-direction (perpendicular to the small flat of the wafer) towards the [011]-direction to obtain polarization independent operation. In Fig. 1 the layout of the device is depicted. The channel spacing is 400 GHz (3.2 nm) and the device size is 8.5x6.4 mm<sup>2</sup>.

The fold-back configuration using a single PHASAR has been chosen to avoid additional losses caused by misalignment of the wavelength responses which will occur, due to nonuniformities of the wafer, if

the demultiplexer and the multiplexer are separate devices. Small thickness and composition non-uniformities will change the central wavelength of the PHASAR, a 2% variation in the layer-thicknesses results in a shift of the central wavelength of a few tenths of a nanometer, yielding a loss penalty of about 1 dB [8].

#### IV. Fabrication

The OXC was fabricated in a MOVPE grown layer stack as shown in Fig. 1. A 100 nm thick PECVD-SiN layer served as an etching mask for the waveguides. The pattern was defined using contact illumination with positive photo-resist and transferred in the SiN-layer by  $\text{CHF}_3$  reactive ion etching. The waveguides were etched employing an optimized  $\text{CH}_4/\text{H}_2$  etching and  $\text{O}_2$ -descumming process [7]. After removal of the SiN-layer, metallisation windows in photo-sensitive polyimide were made on the phase shifting sections of the switches. TiAu contacts on top of the phase shifting sections are fabricated by vacuum evaporation and lift off with image reversal photo-resist. The PHASAR has been made polarization independent by removing part of the top-layer of the waveguides in the triangular birefringence compensation section (see Fig. 1) down to a Q(1.3) etch stop layer using a selective etch ( $\text{HCl}:\text{H}_3\text{PO}_4=1:4$ )[5]. After removal of photo-resist the wafer processing is finished.

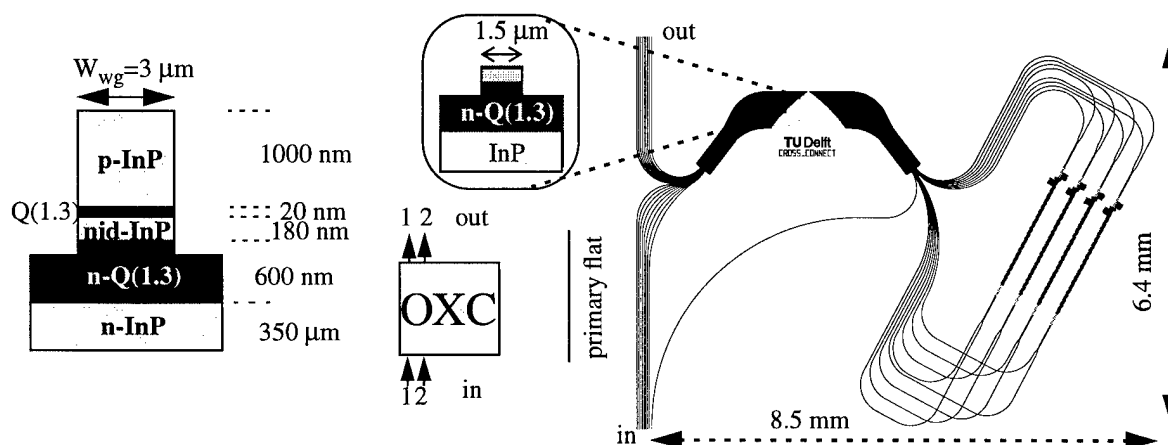


Fig. 1. Layout of the OXC and dimensions of the waveguide structures used.

#### V. Experiments and Simulations

The OXC was measured using the spontaneous emission spectrum of an EDFA as a broadband light source and a polarizer to select the polarization. Light was coupled in the chip by using microscope objectives, coupled out of the waveguides by a single mode tapered fiber and analyzed using an optical spectrum analyzer. Straight reference waveguides with a width of 3  $\mu\text{m}$  showed a propagation loss of 1.5 dB/cm for TE polarization (TM 1.7 dB/cm).

In Figure 2 the measured response is shown for both polarization states. The total on-chip loss is only 13 dB for TE and 16 dB for TM-polarization. It is composed as follows: PHASAR (which is passed twice) 2 times 2-3 dB (2 times 2.5-3.5 dB), MZI-switch 1.5 dB (2.5 dB), crossings 6 times 0.2 dB, 3 cm waveguide 3 times 1.5 dB/cm (3 times 1.7 dB). (Values between brackets are for TM-polarisation). The interband crosstalk level is low: <-40 dB indicating good performance of the PHASAR.

The main problem in the performance is the high intra-band crosstalk level of -13 dB. We analyzed the background of this crosstalk using the recently developed 16x16 PHASAR simulation module of our photonic circuit simulator [9]. Analysis of the results reveals that the crosstalk consists of three main contributions; one from the switch, one from the multiplexer (pass 1) and one from the demultiplexer

(pass 2). Because all signals are routed through the same PHASAR they will interfere with each other, which is visible in the oscillating character of the response. Using a value of -20 dB for the switch crosstalk, which is typical for our single-stage devices, it is seen from the simulations that the coherent interference results in a crosstalk penalty of about 5 dB.

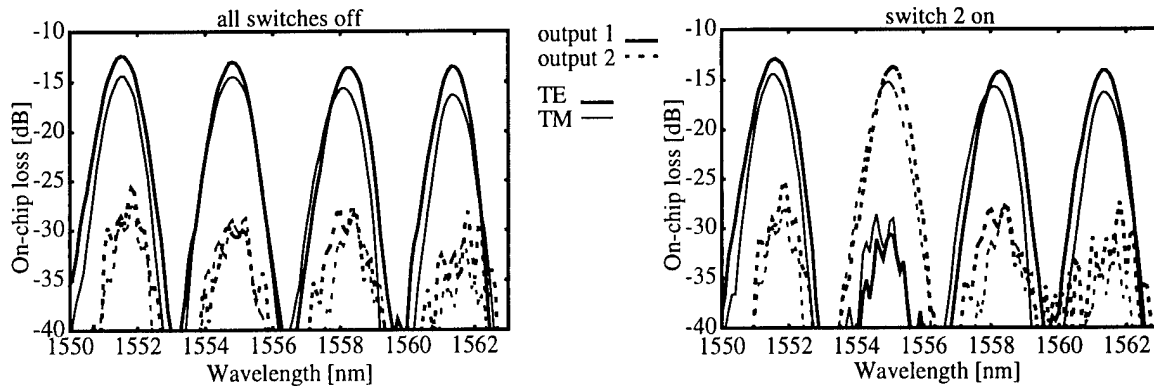


Fig. 2. Measured polarization independent response with all switches off (left) and with switch 2 on (right)

## VI. Discussion and Conclusions

A polarization independent integrated four-channel 2x2 crossconnect on InP is reported. This integrated OXC is realized using a single low-loss polarization dispersion compensated PHASAR [5] and Mach-Zehnder Interferometer electro-optical switches with specially oriented phase shifting sections [10] to cancel the polarization dependence of earlier designs [6]. The use of a single PHASAR both as demultiplexer and multiplexer was chosen to avoid loss penalties originating from misaligned wavelength responses of separate (de)multiplexers. Simulations show however, that this configuration results in a crosstalk penalty in the order of 5 dB.

## VII. References

1. C. Brackett et al., "A scalable multiwavelength multihop optical network: a proposal for research on all-optical networks," *IEEE J. of Lightwave Technol.*, vol. 11, no. 5/6, pp. 736-753, 1993
2. M.K. Smit et al., "PHASAR-based WDM-devices: principles, design and applications," *IEEE J. Sel. Topics Quant. Electron.*, vol. 2, no. 2, pp. 236-250, June 1996.
3. K. Okamoto et al., "16-channel optical add/drop multiplexer consisting of arrayed-waveguide gratings and double-gate switches," *Electron. Lett.*, vol. 32, no. 16, pp. 1471-1472, 1996
4. C.G.M. Vreeburg et al., "First InP-based reconfigurable integrated add-drop multiplexer," *IEEE Photon. Technol. Lett.*, vol. 9, no. 2, pp. 191-193, 1997
5. C.G.M. Vreeburg et al., "An improved technology for eliminating polarization dispersion in integrated PHASAR demultiplexers," *Proc 23rd Eur. Conf. on Opt. Comm. (ECOC '97)*, Edinburgh, UK, pp. 3.83-3.85, 1997
6. T. Uitterdijk et al., "Dilated, polarisation insensitive InP-based space switch," *Proc. 8th Eur. Conf. on Int. Opt. (ECIO'97)*, Stockholm, Sweden, 1997
7. Y. Oei et al., "Novel RIE-process for high quality InP-based waveguide structures," *Proc. 7th Eur. Conf. on Int. Opt. (ECIO'95)*, Delft, The Netherlands, pp. 205-208, 1995
8. N.N. Khrais et al., "Effect of cascaded misaligned optical (de)multiplexers on multiwavelength optical network performance," *OFC/IOOC '96 Technical Digest*, pp. 220-221, San Jose USA, 1996.
9. X.J.M. Leijtens et al., "S-matrix oriented CAD-tool for simulating complex integrated optical circuits," *IEEE J. Sel. Topics Quant. Electron.*, vol. 2, no. 2, pp. 257-262, 1996
10. R. Krahenbuhl et al., "Low-loss polarization insensitive InP/InGaAsP optical space switches for fiber optical communication," *IEEE Photon. Technol. Lett.*, vol. 8, no. 5, pp. 632-634, 1996

# InGaAsP/InP scaleable, photonic crossconnects using optically amplified suppressed modal interference switch arrays

Gregory A. Fish, Larry A. Coldren, Steven P. DenBaars

*Electrical & Computer Engineering, University of California, Santa Barbara, 93106*

6500fish@ucsbuxa.ucsb.edu,

Phone: (805) 893-8465

Fax: (805) 893-4500

## Introduction

Photonic space switches will be very attractive elements for future communication networks. While simulations and theory have predicted limitations on the size of an  $N \times N$  semiconductor switch to be near 50-100 channels[1], practical concerns, such as, optical loss and physical size have limited monolithic InP crossconnects to arrays no larger than  $4 \times 4$ . To address these issues, we report a novel, compact optical switch that combines zero insertion loss and low crosstalk with a scaleable, compact architecture to act as a building block for large  $N \times N$  photonic crossconnects.

The combination of optical switches with traveling wave amplifiers has been shown to be a very effective way to create a scaleable photonic crossconnect[2]. The traveling wave amplifiers can provide very high on/off ratios ( $> 40$  dB) while the optical switches eliminate splitting loss incurred at each junction in a crossconnect, making the design more scaleable. A schematic showing our implementation of this idea is shown in Fig. 1 a). Orthogonal input and output waveguides are connected through two suppressed modal interference (SMI) optical switches[3] and a small radius ( $250 \mu\text{m}$ ) curved amplifier to form a complete  $1 \times 2$  optically amplified suppressed modal interference (OASIS) switch element[4]. Sixteen OASIS elements can be combined to form a compact  $4 \times 4$  photonic crossconnect that occupies only a few square millimeters, as shown in Fig. 1 b).

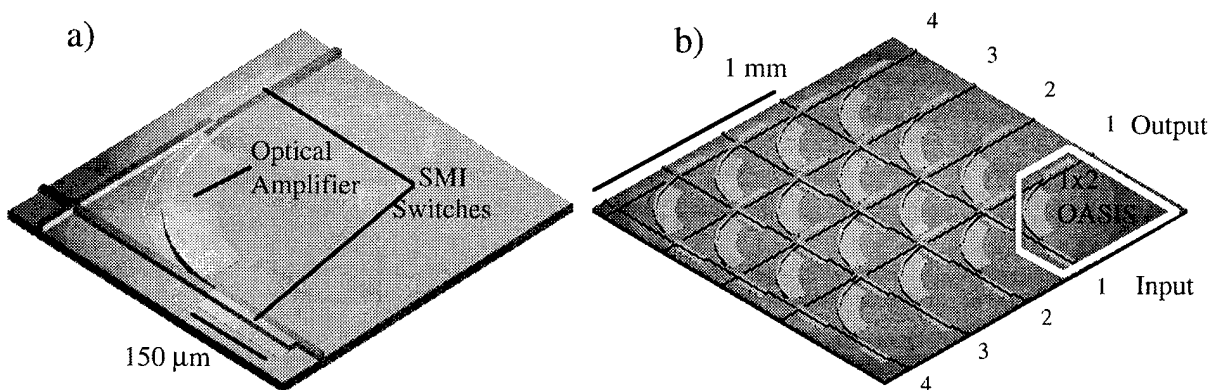


Fig. 1 a) Schematic drawing of an  $1 \times 2$  OASIS depicting orthogonal inputs and outputs connected by two SMI switches with a  $250 \mu\text{m}$  radius curved amplifier. b) Schematic drawing of a  $4 \times 4$  crossconnect consisting of 16 OASIS elements.

## Suppressed Modal Interference Switches

To gain an improvement over an amplifier gate array which simply uses splitters, the switches used in the OASIS have very little excess loss in the bar state, yet switch enough power into the amplified path that the cross state loss can be zero. To accomplish this, the SMI switches

have an input waveguide which is coupled off-center to a modal interference section exactly one beat length long. In the bar state, the modal interference causes the input mode appearing on the right half to be imaged on the left half at the output of the modal interference section, naturally bypassing the curved amplifier. In the cross state, current is injected into half of the modal interference waveguide eliminating its higher order modes, suppressing the modal interference, and guiding the light straight into the curved amplifier. Two dimensional beam propagation method (BPM) was used extensively in the design of the SMI switch and simulations illustrating the bar and cross state operation of the SMI switch are depicted in Fig 2 a) and b), respectively. Fig. 2 c) shows near field images taken from the end of a SMI switch (at  $L_\pi$  in Fig 2 a) portraying the evolution of switching as current is applied.

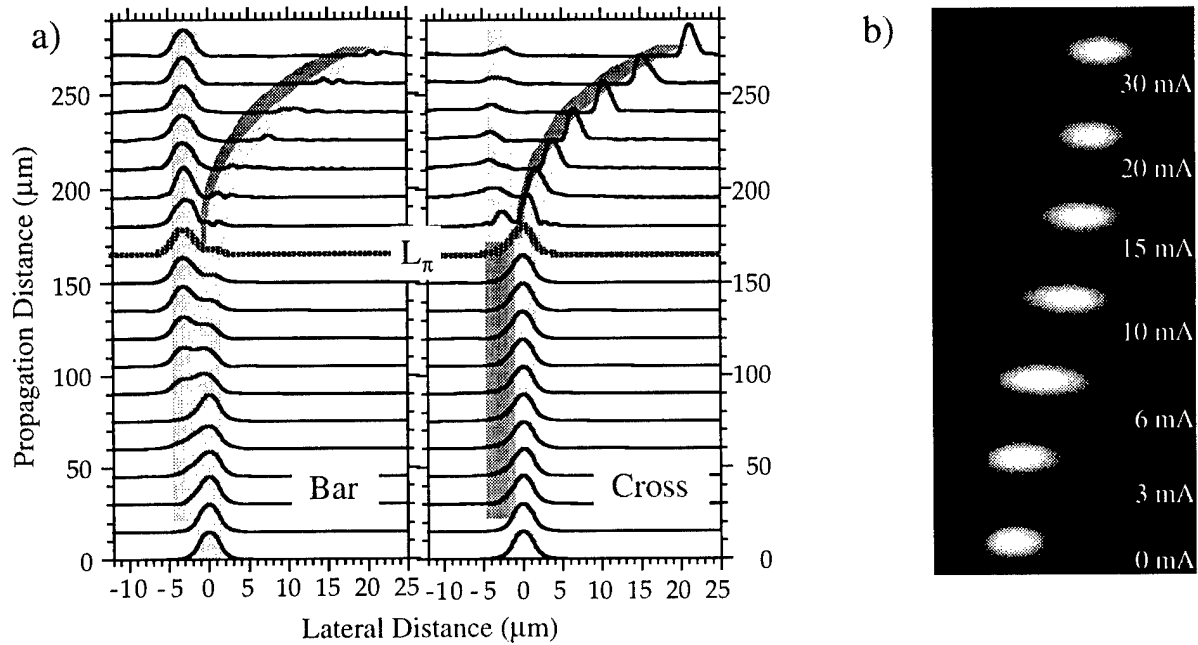


Fig. 2 a) BPM simulations illustrating the operation of the SMI switching element in the bar and cross state. b) Near field images taken at the end of an SMI switch (at  $L_\pi$ ) showing the evolution of the switching as current is applied.

### Combining SMI switches with amplifiers

Combining the SMI switches with a small radius amplifier is complicated by the different lateral index contrast required by the two elements. Switches must have small index contrasts to be effective while small radius bends require large index contrasts to reduce bending loss. To solve this problem, we etched additional cladding material from the outside of the curve, as shown in Fig. 1 a).

Fabrication of the OASIS involves only two MOCVD growth steps in which a base structure where a MQW active region is grown on top of a 0.35 μm thick InGaAsP ( $\lambda_g = 1.35\mu\text{m}$ ) waveguide layer. The active region is removed in the passive sections of the device and the p-cladding and contact layers are regrown including a stop etch layer to define the lateral index contrast of the switch waveguide. Ridge waveguides are dry etched using  $\text{CH}_4/\text{H}_2/\text{Ar}$  followed by a wet  $\text{H}_3\text{PO}_4/\text{HCl}$  clean up etch to the stop etch layer, this gives a well controlled uniform lateral waveguide contrast required for these type of devices. Further etching on the outside of the curve section follows using  $\text{CH}_4/\text{H}_2/\text{Ar}$  dry etching. Finally, the devices are covered with  $\text{SiN}_x$ , metallized and proton implanted to isolate the various sections and define the unbiased half of the SMI switches.

## Photonic Crossconnect Characterization

Prior to testing, a quarter wavelength thick  $\text{SiO}_2$  antireflection coating was applied to the input and output facets of a 4x4 OASIS crossconnect. The device is similar to the schematic shown in Fig 1 b), however, a 500  $\mu\text{m}$  long optical amplifier is added to both the output and input waveguides of the device to help overcome fiber coupling losses. To initially test the on-chip performance of the device, the input optical amplifier is pumped as a LED and its emission is collected (using a lensed optical fiber, radius 9  $\mu\text{m}$ ) from the orthogonal output facet after traversing the OASIS. Fig. 3 a) Shows the measured on/off ratio of input channel 1 to output channel 2 as the current to the two switches is increased at each curved amplifier bias. Unfortunately, the processing of this device caused the second switching element not to function properly resulting in an estimated 10 dB of loss. Fiber to fiber measurements were conducted on the same input and output channel of the 4x4 array using an external cavity tunable laser emitting at 1550 nm at an optical power of -20 dBm as the source. As illustrated in Fig 3 b), despite the one nonoperational SMI switch, an on/off ratio of 40 dB is achieved with an insertion loss of -3 dB if both input and output amplifiers are biased at 60 mA.

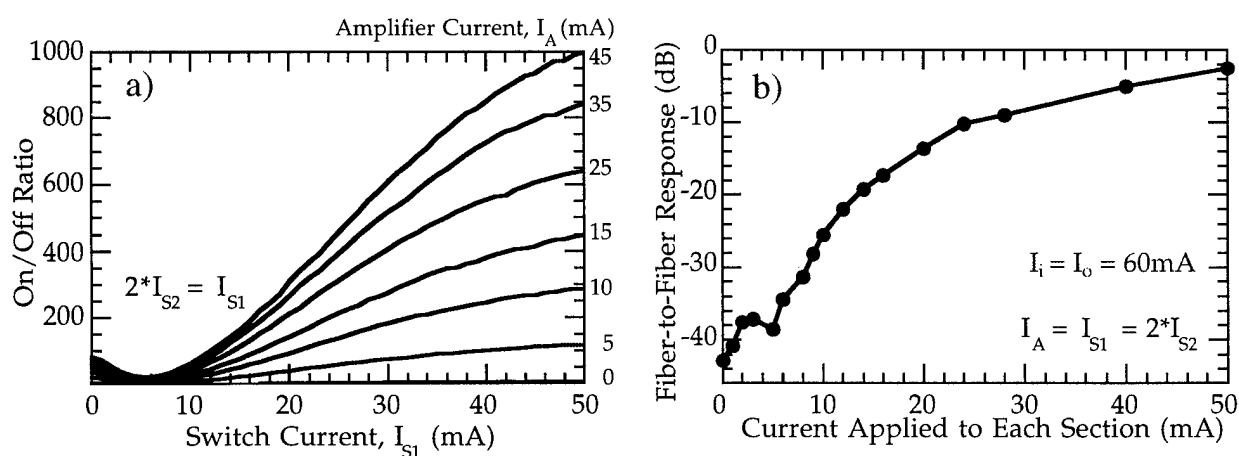


Fig. 3 a) On chip measured on/off ratios for input 1 to output 2 of a 4x4 OASIS crossconnect. b) Fiber-to-fiber response of the same channel with additional amplification from an input and output stage amplifier, showing 40 dB on/off ratios with -3 dB insertion loss.

## References

- [1] S. Yang and J. G. Yao, "Impact of crosstalk induced beat noise on the size of semiconductor laser amplifier based optical space switch structures," *IEEE Photonics Technology Letters*, vol. 8, pp. 894-6, 1996.
- [2] T. Kirihaara, M. Ogawa, H. Inoue, H. Kodaera, and K. Ishida, "Lossless and low-crosstalk characteristics in an InP-based 4\*4 optical switch with integrated single-stage optical amplifiers," *IEEE Photonics Technology Letters*, vol. 6, pp. 218-21, 1994.
- [3] G. A. Fish, L. A. Coldren, and S. P. DenBaars, "Compact InGaAsP/InP 1\*2 optical switch based on carrier induced suppression of modal interference," *Electronics Letters*, vol. 33, pp. 1898-900, 1997.
- [4] G. A. Fish, L. A. Coldren, and S. P. DenBaars, "Suppressed modal interference switches with integrated curved amplifiers for scaleable photonic crossconnects," *IEEE Photonics Technology Letters*, vol. 10, 1997.

# Polarization independent InP-based switch with relaxed fabrication tolerances

D.H.P. Maat<sup>1</sup>, C.G.P. Herben<sup>2</sup>, M.K. Smit<sup>2</sup>, F.H. Groen<sup>1</sup>, H. van Brug<sup>1</sup>, H.J. Frankena<sup>1</sup>, I. Moerman<sup>3</sup>

<sup>1</sup>Research Group for Optics, Department of Applied Physics, Delft University of Technology  
P.O. Box 5046, NL-2600 GA Delft, The Netherlands, email: maat@optica.tn.tudelft.nl

<sup>2</sup>Faculty of Electrical Engineering, Delft University of Technology, Delft, The Netherlands.

<sup>3</sup>Department of Information Technology, University of Gent-IMEC, Gent, Belgium.

## I. ABSTRACT

**A polarization independent MZI-switch is presented, of which the fabrication tolerances are relaxed by using double, orthogonal phase shifting sections.**

## II. INTRODUCTION

Optical space switches play a key role in advanced optical networks, both for WDM and single wavelength applications. One of the most important requirements for these switches is polarization independent operation since the fiber network does not maintain the state of polarization.

Making electro-optical Mach-Zehnder interferometer (MZI) switches polarization independent is usually performed by adjusting the angle of the phase shifting sections of these switches with respect to the wafer's crystal axes [1,2]. The angle for polarization independent operation turns out to be rather sensitive to variations in layer thickness and doping profile. In this paper experimental results are given of a switch in which two orthogonal phase shifting sections are applied to obtain polarization independence by applying proper voltages to the two electrodes. In this way variations in layer thickness and doping profile can be compensated by adjusting the switching voltages.

## III. PRINCIPLE OF OPERATION

The linear Pockels effect, one of the electro-optical effects that provide the refractive index change needed for switching, shows a dependence on the direction of the phase shifting sections with respect to the crystal axes. In phase shifting sections in the  $[1\bar{1}0]$  direction the Pockels effect increases the refractive index change whereas in phase shifting sections in the  $[110]$  direction it lowers the refractive index change. Due to this angular dependence and the fact that the Pockels effect only affects the TE polarization, the phase shift efficiency for TE is higher than that for TM in phase shifting sections in the  $[1\bar{1}0]$  direction, whereas in the  $[110]$  direction it is the other way around. Using this phenomenon, polarization independent switches have been fabricated by placing the phase shifting sections under an angle with respect to the wafer's crystal axes. The required angle is very sensitive for variations in the layer stack and in the doping profile. This sensitivity can be solved by splitting each phase shifting section into two orthogonal parts as shown in Fig. 1. The directions for the phase shifting sections are the  $[1\bar{1}0]$  and  $[110]$  directions. Using the  $[1\bar{1}0]$ -phase shifting section for switching, the TM switching voltage is higher than the TE switching voltage. Since the phase shifting efficiency in the  $[110]$  direction is higher for TM than for TE, both switching voltages can be made equal by applying a proper voltage on a  $[110]$ -phase shifting section. Doing this, it is possible to achieve polarization independent operation, which is not affected by deviations in the layerstack and in the doping profile.

## IV. FABRICATION

In our (MZI) switch MMI-couplers are used as 3 dB splitting and combining elements. In between are the two sets of phase shifting sections with a length of 1 mm. The width of the in- and output waveguides is 3  $\mu\text{m}$  to provide low loss. To enable the alignment of the 2  $\mu\text{m}$  wide contacts on top of the waveguides of the phase shifting sections, the latter have a width of 4.5  $\mu\text{m}$ . All bends in the switch have a radius of 500  $\mu\text{m}$ . For the transition from the 3  $\mu\text{m}$  to 4.5  $\mu\text{m}$  waveguides, and vice versa, 100  $\mu\text{m}$  long tapers have been used.

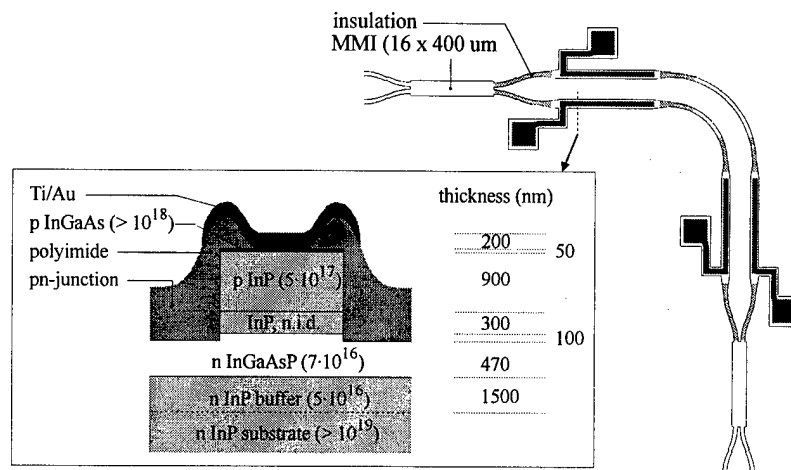


Fig. 1 Layout of the switch and cross section of the switch at the phase shifting sections (doping levels in  $\text{cm}^{-3}$ ).

The InGaAsP/InP/InGaAs layer stack was grown on a (001) oriented  $n^+$  substrate. The thicknesses and doping levels of the various layers are shown in Fig. 1. To provide sufficient distance between the optical field and the metal contacts (for low loss) the thickness of the p-InP is chosen to be 900 nm. The InGaAsP guiding layer is n-doped such that the switch is already close to polarization independence and at the same time has low loss [3]. The top InGaAs layer provides an ohmic contact to the Ti/Au metallization. The layer stack has been configured to enable switches to be integrated with a wavelength (de)multiplexer.

The production of the switch starts with removing the  $p^+$  InGaAs from the wafer, by using wet chemical etch, except in those regions where the metal contacts will be placed in a later stage of the production process. Then the waveguides are realised with a  $\text{CH}_4\text{-H}_2/\text{O}_2$  RIE/descum process, using (PECVD) silicon-nitride masking. In order to have electrical insulation between the four phase shifting sections of the switch, a section of the waveguides is etched down to the pn-junction at either side of each contact. Due to the dry etching of the waveguides in an  $\text{H}_2$  atmosphere the acceptors are passivated, which gives rise to high leakage currents. The acceptors have been reactivated using an RTP anneal step. Next, the pn-junction is passivated with cured polyimide. The switch is finished by depositing Ti/Au contacts on the phase shifting sections using a lift-off technique[4,5].

## V. MEASUREMENT RESULTS AND DISCUSSION

The switches have been measured at 1.5  $\mu\text{m}$  wavelength using microscope objectives for coupling light into and out of the waveguides of the switch. In Fig. 2 the output power of the cross output port as a function of the reverse bias on the  $[1\bar{1}0]$ -electrode is given for two bias values of the  $[110]$ -contact. This figure shows the possibility of tuning the switch into a polarization independent state. The right side of Fig. 2 shows almost polarization independent operation. The switching voltages are 4V and 12V for the bar state and 12 V and 12V for the cross state, applied on resp.  $[1\bar{1}0]$ -contact and the  $[110]$ -contact.

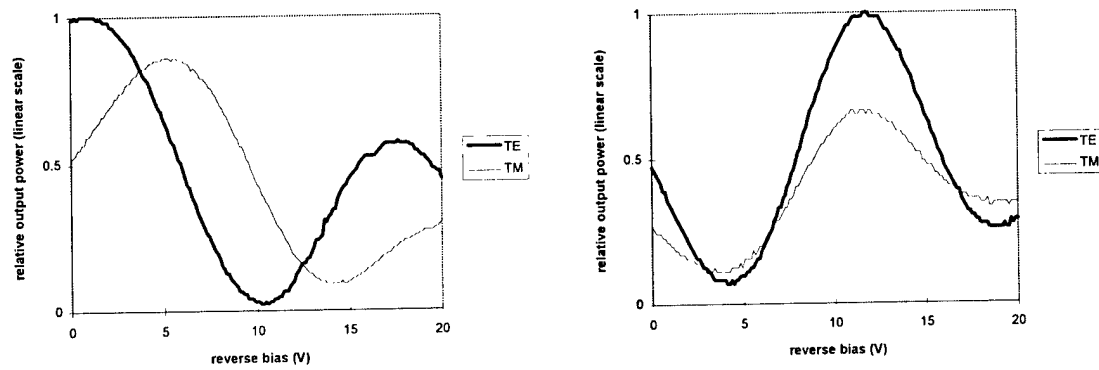


Fig. 2 Relative output power at the cross port as function of reverse bias on the  $[1\bar{1}0]$ -electrode for 0V (left) and 12V (right) reverse bias applied to the  $[110]$ -electrode.

In the bar state a small polarization dependence remains. This can be removed by lowering the voltage on the  $[110]$ -contact to 11V.

Due to a large offset between the TE and TM switching curves, shown in left side of Fig. 2, large adjustments are necessary to obtain polarization independent operation, resulting in large switching voltages. This can be solved by making the optical paths of both arms between the MMI's identical for both TE and TM when no bias is applied.

## VI. CONCLUSIONS

A polarization independent Mach-Zehnder switch is presented having double, orthogonal phase shifting sections in the  $[1\bar{1}0]$  and the  $[110]$  directions. It is shown that for this type of switch polarisation independent operation is achieved in a wide tolerance window for variations in layer thickness and doping profile.

## VII. REFERENCES

- [1] R. Krähenbühl et al., 'Low-Loss Polarisation-Insensitive InP-InGaAsP Optical Space Switches for Fiber Optical Communication', *IEEE Phot. Techn. Lett.*, vol. 8(5), pp 632-34, 1996.
- [2] D.H.P. Maat et al., 'An improved polarisation independent switch', *Proceedings of 1997 IEEE/LEOS Symposium - Benelux Chapter*, pp 193-196, 1997.
- [3] J.F. Vinchant et al., 'InP/InGaAsP guided-wave phase modulators based on carrier-induced effects: theory and experiment', *Journ. Lightw. Techn.*, vol. 10, no. 1, pp 63-69, January 1992.
- [4] T. Uitterdijk et al., 'Integrable Polarisation Insensitive InGaAsP Mach-Zehnder Switch', *Integrated Photonic Research*, vol. 6, 1996 OSA Technical Digest series, pp 486-489.
- [5] T. Uitterdijk, *Integrated Electro-Optical Switches on InP*, PhD Thesis, Delft University of Technology, 1997, ISBN 90-9010549-2.

**Integrated Photonics Research**

# **Photonic Packaging II**

**Tuesday, March 31, 1998**

**Robert J. Deri, Lawrence Livermore National Laboratory**  
President

**ITuF**

**10:30am-12:00m**

**Saanich Room**

## Molded Plastic Optics in Fiber Optic Transceivers

Ching-Long (John) Jiang

AMP Incorporated

61 Chubb Way, Somerville, NJ 08876

TEL: (908) 704-6581 FAX: (908) 575-9869

Conventional fiber optic transceivers use a transistor outline (TO) style ball lens as the light coupling element in the optical sub-assembly (OSA). This is shown in Figure 1. Molded plastic optics have been widely used in many applications. Naturally, for light coupling, most people would like to replace the TO-style OSAs with the molded plastic optics due to its lower cost. Furthermore, we provided additional functions in the molded plastic optics. These additional functions (fiber-receiving and light-bending) have been incorporated into one opto-mechanical device called a lens/receptacle. The new fiber optic transceiver using this multifunction lens/receptacle is shown in Figure 2.

Application of the lens/receptacle is best illustrated by comparing an SC-simplex datalink using the older generation TO header based package with the lens/receptacle package. An exploded view of the original 16-pin SC-simplex datalink is shown in Figure 1. Aside from the optoelectronic device and SC shroud, ten parts are required, including a plastic "ear" and stainless steel precision-bore active device mount (ADM). Note that the TO header is burned-in before aligning into the ADM, and is then soldered onto a ceramic board. The leads of the header are a source of unwanted parasitic capacitance and inductance; they are also effective antennas for transmission or reception of EMI. The reduced part count of the lens/receptacle package is shown in Figure 2. Note that the SC connector ears are integrated into the molded case, and that the molded lens/receptacle has a fiber stop inserted into the bore. Including the fiber stop, this assembly requires only four parts. The 45° prism in the lens/receptacle contains a total internally reflecting surface that conducts the non-collimated light stream between the integrally molded aspheric surfaces.

Performance improvements are achieved as well, as illustrated by a comparison of an older generation 22 pin package with a 13 pin package incorporating the molded lens/receptacle. Histograms of production data are presented for optical rise and fall time, LED coupled power at room

temperature and receiver sensitivity for both designs (see Figures 3-6). Higher edge speeds were expected and subtle power and sensitivity improvements were also observed. Within the comparisons for each metric, the total number of 13- and 22-pin parts is the same. The data were samples from a 100% final test database collected over a one month period. All the data are based on performance with 62.5  $\mu\text{m}$  core multimode fiber.

Rise time is a measure of the time it takes for fiber coupled power to rise from 10% to 90% of the peak state using a 125 Mbit/sec test pattern, and vice-versa for fall time. The drive circuits for the LED in the 13-pin and 22-pin packages are similar and incorporate a speed-up network that was re-tuned for the 13-pin package. LED type is the same for both designs. The rise time histograms in Figure 3 show a peak of 1.2 ns for the 13-pin, versus 1.8-1.9 ns for the 22-pin. Distribution of speed is also narrower for the 13-pin. The fall time histograms, Figure 4, again show a substantial advantage for the 13-pin package with a peak at 1.5 ns versus a 22-pin peak at 2.1 ns.

LED coupled power for the 13-pin datalink has a histogram peak at -16.0 dBm as shown in Figure 5; the 22-pin peak is at -16.2 dBm. While there appears to be more high power 22-pin parts and more low power 13-pin parts, 68% of the 13-pin parts are  $>-16.6$  dBm versus only 64% of the 22-pin parts. This suggests a tighter distribution and a general bias to higher power for the 13-pin parts, with a slight low power tail.

The receiver sensitivity comparison, Figure 6, is for a  $2^{15}-1$  pseudo-random bitstream. Here again there seem to be more high sensitivity 22-pin parts, but there are also more low sensitivity parts. Overall, the 13-pin data are more tightly distributed. Integration of the more desirable  $<-35.6$  dBm average-input-power sensitivity parts yields 70% of the 13-pin total and 67% of the 22-pin total. This performance has been achieved without anti-reflection coatings on the lens/receptacle, which is required in the sapphire lensed 22-pin package.

A molded plastic lens/receptacle has been developed for data link applications which reduces parts count, assembly steps and cost while improving performance. Products based on the lens/receptacle, including the new 13-pin and the 9 & 16-pin packages, are replacing TO header style packages.

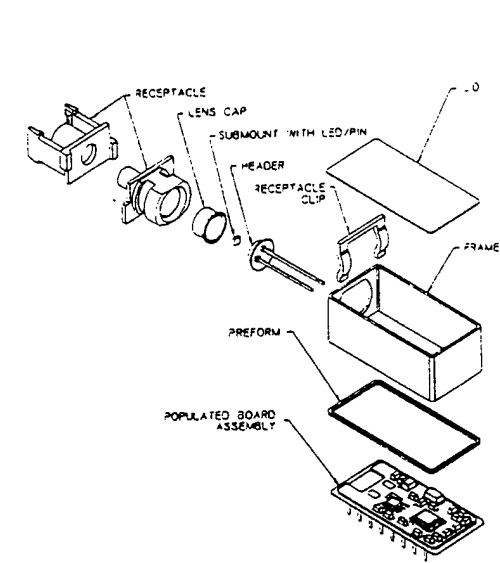


Figure 1. Exploded view of the old generation 16-pin SC-simplex datalink

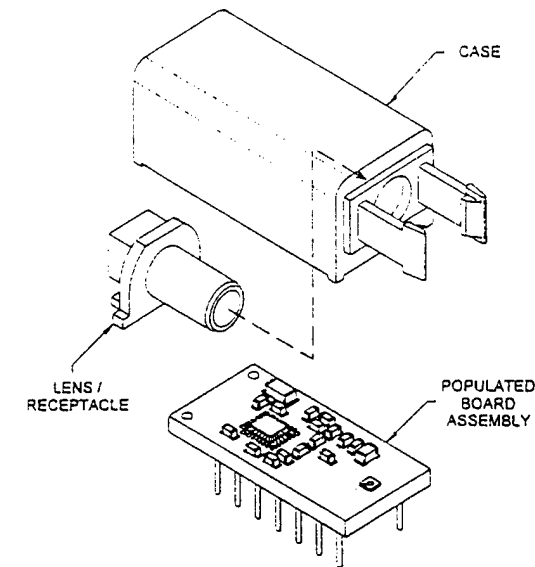


Figure 2. Parts comprising the lens/receptacle based 16-pin SC-simplex datalink

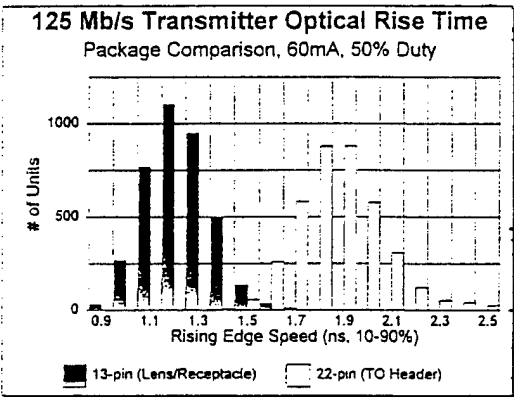


Figure 3. Rise time of production FDDI transceiver

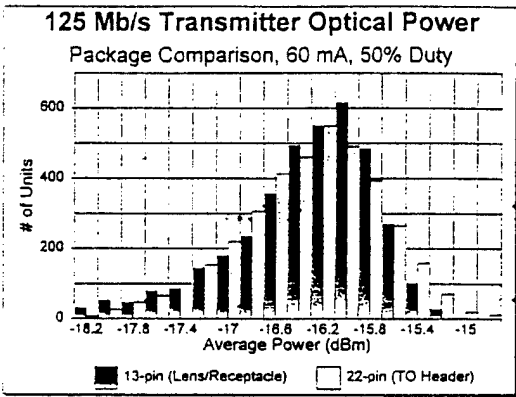


Figure 5. Coupled power of production FDDI transceiver

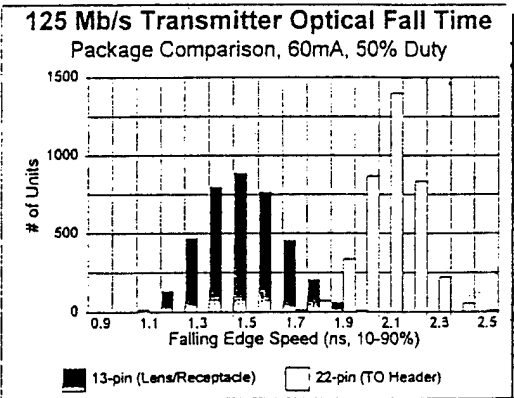


Figure 4. Fall time of production FDDI transceiver

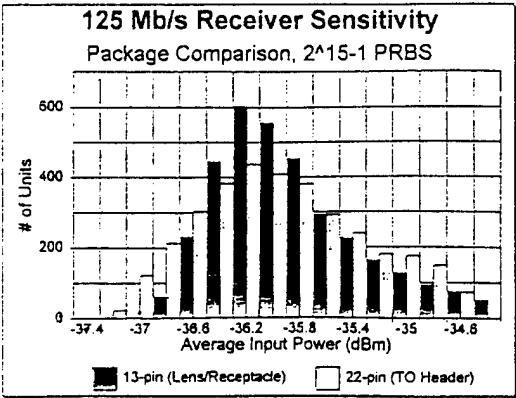


Figure 6. Sensitivity of production FDDI transceiver

## Flip-chip GaN LED with Highly Reflective Ag P-contact

You Kondoh\*, Satoshi Watanabe, Yawara Kaneko, Shigeru Nakagawa, and Norihide Yamada  
Hewlett-Packard Laboratories, 3-2-2, Sakado, Takatsu-Ku, Kawasaki-shi, Kanagawa 213, Japan  
Phone: +81-44-812-9757, Fax: +81-44-812-5247, E-mail\*: kondoh@jp.hpl.hp.com

### Introduction

GaN blue LEDs using a sapphire substrate were first introduced in 1981[1]. One of the differences between GaN LEDs and previous LEDs is that the p-contact and n-contact are located on the same surface of the LED chip. Currently, transparent electrodes are employed in GaN LED products for the p-contact to prevent the electrode itself from blocking off the light emission. However, it is difficult to achieve the electrode transparency higher than 60%. It is said that flip-chip(FC) assembly has some advantages to solve this problem, but no papers have yet been published which quantitatively evaluate the improvement in light output.

### Basic scheme

Fig.1 shows a schematic cross-sectional view of our FC-LED. A GaN LED chip is connected to the wiring circuit on a plastic substrate directly using Au ball bumps and In bumps. The LED chip has a highly reflective p-contact, which consists of three layers, Ag, Ni, and Au. It functions both as a low-resistive p-contact and high-reflective back-side mirror. The advantage of the FC-LED is greatly influenced by this back-side reflector. According to a rough calculation, the brightness of the FC-LED with 70-80% reflectance on the back-side p-contact, which is the same as conventional metal package, is expected to be 130-140% of a conventional GaN LED. If higher than 90% reflectance can be achieved on the p-contact of the FC-LED, it is expected to be twice as bright as a conventional GaN LED.

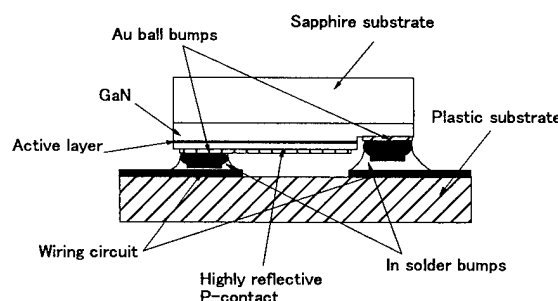


Fig.1 Schematic cross-sectional view of FC-LED

### Highly reflective p-contact

A three layer metal structure consisting of Ag, Ni, and Au was developed to achieve a highly reflective p-contact for our FC-LED. The Ag film is deposited first and acts as a highly reflective p-contact layer. The second layer, Ni acts as diffusion barrier, and the Au acts as bonding layer. Table 1 shows the measured reflectance for light at around 470nm of the 100nm-metal films deposited by EB evaporation. In general, Pd, Pt, and Ni are well-known as p-contact materials[2],[3],[4], but the reflectance of films of these metals is lower than 65%. A Ag film was used in our FC-LED because only Ag has the potential to be used as both a low-resistance p-contact layer and a high-reflectivity back-side mirror layer.

Table1 Reflectance of deposited metal film

Pd	Pt	Ni	Ag
63%	57%	52%	96%

It was also found that 50nm of Ag deposited by EB-evaporation is enough to obtain reflectance higher than 95%. Fig.2 indicates the effect of the Ni diffusion barrier layer. The combination of 100nm-Ag, 300nm-Ni, and 50nm-Au was the best selection as highly reflective p-contact system for our FC-LED. GaN chips were annealed at 450°C for 30min to reduce the resistance of p-contacts. A color change of the surface of Ag p-contact could be observed using an optical microscope after annealing and the measured reflectance reduction was larger than 40%, when a very thin or no Ni diffusion barrier layer was employed between the Ag layer and the Au layer. It is thought that Au from the Au bonding layer diffused into the Ag p-contact layer and caused the observed color change. A total reflectance of the back-side p-contact higher than 90% was achieved using this newly developed three layer metal system.

**FC fabrication**

Fig.3 shows a fabrication process of our FC-LED. Before the LED wafer was lapped, polished, and scribed, Au ball bumps were formed on p and n-contacts of every GaN chip using the ball bonding method. In contrast, In solder bumps were formed on a copper foil wiring circuit of the plastic substrate. The LED chip with Au ball bumps was heated up to 180°C, and aligned and pressed on the plastic substrate using die bonding method. Fig.4 (a), and (b) show SEM photographs of Au ball bump

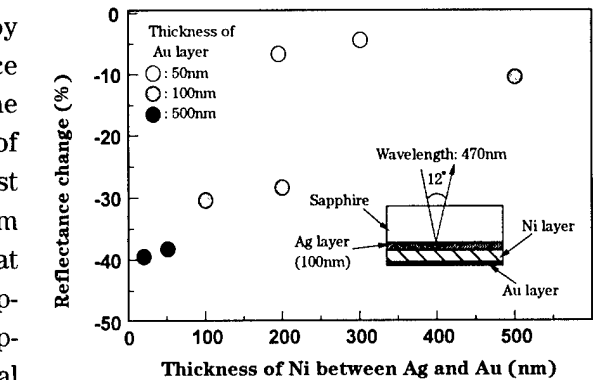


Fig.2 Reflectance change of Ag P-contact after annealing for several kinds of layer systems

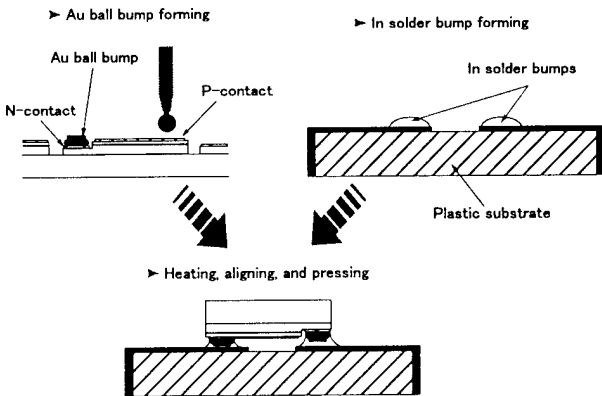
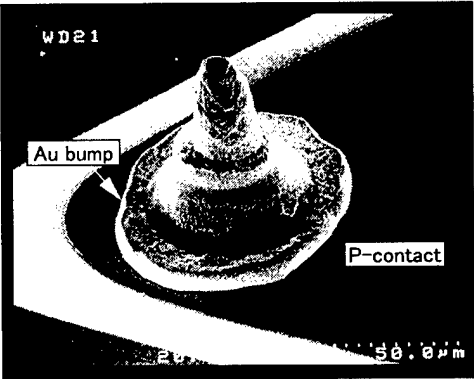
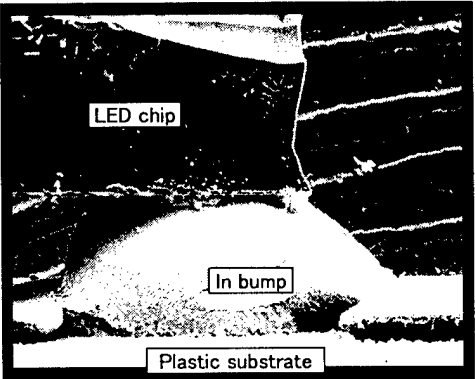


Fig. 3 Fabrication process of FC-LED



(a)



(b)

Fig.4 SEM photographs of Au ball bump (a) and bump inter-connection after bonding (b)

and bump inter-connection after FC bonding, respectively. Every Au ball bump has a small pin, which seems to stick into an In solder bump during FC bonding. The diameter of the pedestal of Au ball bump was about 100 $\mu$ m, and the maximum height including a pin was about 70 $\mu$ m. After the FC bonding, they were encapsulated with epoxy resin into a metal lead package to be estimated under the same condition as the conventional top-emitting LED.

### LED characteristics

Fig.5 shows the relative light output and operating voltage against the injected current of the FC-LED and the conventional top-emitting LED. Although these two kinds of LEDs were made from same GaN LED wafer, the measured light output of the FC-LED was about 210% of that of the conventional top-emitting LED at 20mA-injected current. The brightness is 7.01 m/W and the external quantum efficiency is about 12%. The light output saturated around 80mA in the case of the FC-LED. It is thought that this is due to the poor thermal conductivity of the plastic substrate used for mounting the FC-LED and that it can be improved by changing from a plastic substrate to one with a higher thermal conductivity. The operating voltage of the FC-LED was lower than the top-emitting LED for all values of injected current.

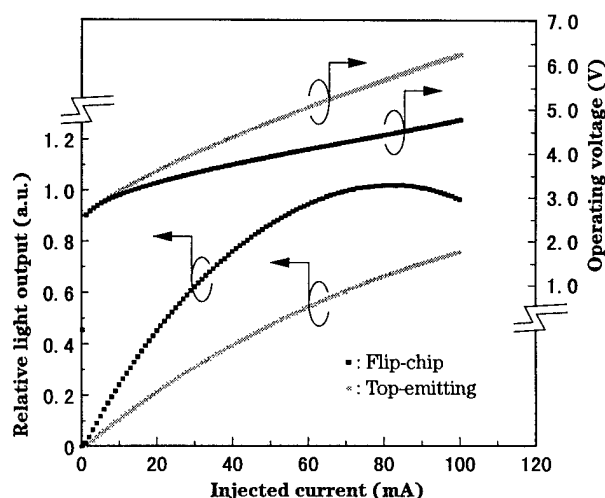


Fig.5 Relative light output and operating voltage against injected current of FC-LED and top-emitting LED

### Conclusion

The advantage of using the flip-chip technique for GaN blue LEDs was evaluated quantitatively. The FC-LED demonstrated in this paper is twice as bright as the conventional top-emitting LED, and could be operated at lower voltage. A highly reflective back-side p-contact structure consisting of Ag, Ni, and Au, which achieved higher than 90% reflectance, and an inter-connection technique using Au ball bumps and In solder bumps were developed for the new FC-LED.

### References

- [1] Y.Ohki, et al., Inst. Phys. Conf. Ser. No.63, 479 (1981)
- [2] Y.Yamaoka, et al., ICNS'97, 70 (1997)
- [3] T.I.Kim, et al., SPIE vol.3001, 88 (1997)
- [4] H.H.Berger, et al., Solid State Electron.15, 145 (1972)

## Non-peripheral epilayer cleaving of GaAs for hybrid device applications

*J. Fujita, M. Levy, and R. M. Osgood, Jr.*

*Microelectronics Sciences Laboratories, Columbia University, New York, NY 10027*

*Tel, (212) 854-8042 Fax (212) 860-6182 Email: juni@cumsl.ctr.columbia.edu*

### INTRODUCTION

Hybrid integration of bulk or waveguide devices of different material systems permits increased optical integration and enhanced complexity of device functionality on a single chip. For example, integration of thin bulk polarizers, reciprocal rotators, and a waveguide Faraday Rotator on silica has been used to demonstrate hybrid isolation performance.<sup>1</sup> Incorporation of these elements often requires the presence of high quality optical facets in combination with a deep groove or slot in a non-peripheral chip location. In the silica case, the polarizing element was inserted within the waveguide circuit by using a thin dicing saw to form a deep groove on a silica platform. Subsequently smooth facets were obtained by annealing the diced samples.

However, to date, techniques for achieving this same capability for compound semiconductor have not been reported. Facet fabrication in semiconductor materials makes use of one of several well-known etching techniques such as dry etching, wet etching, and photoelectrochemical etching. However, these techniques cannot be relied upon to produce the required high-quality deep etching, and vertical, smooth sidewalls needed for hybrid integration. In addition, many times the implementation of these techniques requires a long sequence of complex and/or costly processes.

In this paper, we describe and demonstrate a technique for fabrication of cleaved sidewalls at "mid-chip" on a GaAs slab waveguide, at the edges of  $\sim 100\mu\text{m}$  deep groove. Fabrication is accomplished via a deep undercut in the slab waveguide so as to allow easy cleavage of the overhang, resulting in a low-loss, free-space gap, with near-ideal minimal-loss characteristics. This technique takes advantage of the fact of the well known tendency of some compound materials, such as GaAs, to form easy cleavage planes that produce smoother sidewalls than are obtain with etching. This method also allows a flexibility in the choice of groove dimensions and produces cleaved surfaces with low coupling loss. In our experiment, we measure excess losses of less than 1dB in perfect (loss-less) cleaved sidewalls. The feasibility of integrating a bulk device is also studied by inserting a thin film polarizer and measuring the resulting optical performance.

### PROCEDURE

In order to produce grooves with cleaved sidewalls on GaAs waveguides, the etching process must form an undercut of the epilayer underlying the slab waveguide to be cleaved. In our experiment, photoelectrochemical etching is used to form both this over-hang and a high-aspect-ratio deep groove.<sup>2</sup> Since, the geometry of the etched features are dependent on the degree of hole confinement within each layer,<sup>3</sup> proper etching requires a considered choice of carrier concentrations in the waveguide and substrate layers.

The samples used here consists of  $n^+$  GaAs substrate containing a  $6\mu\text{m}$ -thick GaAs top layer, and a  $4\mu\text{m}$ -thick  $\text{Al}_{0.05}\text{Ga}_{0.95}\text{As}$  under layer. These rather thick epilayer layers are chosen so as to reduce diffraction of light exiting the waveguide into the free-space region. The top two layers are undoped with a carrier concentration of  $\sim 5 \times 10^{14} \text{cm}^{-3}$ . The samples are mounted in a quartz boat with a diluted acid  $\text{HCl}:\text{HNO}_3:\text{H}_2\text{O}=4:1:50$  and are covered with a quartz plate. A bias voltage of a few volts between substrate and top surface is applied between the top surface and the bottom substrate. Etching is accomplished by scanning a focused Ar-laser beam ( $\lambda=350\text{nm}$ ,  $2\omega \sim 2.8\mu\text{m}$ ) directly on the sample. The laser power and scan speed are chosen at

500 $\mu$ W and 1 $\mu$ m/sec, respectively. When illuminated in solution, the band offset between substrate and waveguide creates a carrier concentration difference in the GaAs/AlGaAs layers leading to a deep undercut. A plot of the undercut distance versus bias voltage is shown in Fig. 1. The plot shows that there is a threshold to establish undercut and deep etching. The inset of Fig. 2 shows a typical undercut formed by this technique. Note that the top two layers are not affected by the undercut.

The cleaved sidewall fabrication technique proceeds as follows: First, a relatively deep groove is made to form the undercut regions. The bias voltage for this groove is chosen so that the lateral undercut distance matches  $\sim 1/2$  of the desired cleave separation. Next, two grooves, which act as scribe marks, are made perpendicular to and at the end of the first deep groove. The location of the cleavage plane is determined by the length of these two laser-defined scribe marks. After the groove fabrication, the etched region forms an "H" shape with the inner region of the grooves being completely undercut. Finally, the cleaving is obtained by ultrasonic agitation.

## RESULTS

After fabrication, the quality of the facets is measured by coupling 1.55 $\mu$ m wavelength light across the groove. The total insertion loss through the fabricated groove is measured and compared with the case of a grooveless slab waveguide. An excess loss of 0.4dB is obtained over the theoretically computed diffraction and Fresnel losses. This result confirms that sidewall imperfections are minimal. ( $\leq 0.4$ dB) Figure 2 shows a cleaved facet obtained by the technique. To compare this result with other possible etching technique, similar grooves are fabricated with chemically assisted ion beam etching (CAIBE). The optical transmission measurement shows that there is a  $\sim 2$ dB excess loss due to facet imperfections for the CAIBE process in comparison to the cleaved facets.

To demonstrate the feasibility of integration, a 30 $\mu$ m-thick bulk polarizer, called lamipol,<sup>5</sup> is inserted on the groove. This lamipol has a high extinction ratio (up to 60dB) with a low insertion loss ( $\sim 0.4$ dB). The overall performance of the integrated waveguide polarizer is an extinction ratio of at least 20dB with an excess loss of 1dB. The lower measured value of the extinction ratio is limited by the dynamic range of our testing setup.

## CONCLUSION

We present a novel way to fabricate high quality non-peripheral epilayer cleaved facets in conjunction with a deep groove. As described above, this method yields cleaved sidewalls and feature size flexibility via a relatively short and simple process. The technique minimizes the coupling loss between a compound semiconductor waveguide when used to couple in mid-chip to any of several possible inserted free space devices; in this paper a lamipol polarizer was used to demonstrate the technique.

## REFERENCES

1. N. Sugimoto, H. Terui, A. Tate, Y. Katoh, Y. Yamada, A. Sugita, A. Shibukawa, and Y. Inoue, *IEEE J. Lightwave Tech.*, **14**, 2537 (1996).
2. D. V. Podlesnik, H. H. Gilgen, A. E. Willner, and R. M. Osgood, Jr., *J. Opt. Soc. Am. B*, **3**, 775 (1986).
3. M. N. Ruberto, A. E. Willner, D. V. Podlesnik, and R. M. Osgood, Jr., *Appl. Phys. Lett.*, **55**, 10 (1989).
4. R. Khare, E. L. Hu, D. Reynolds, and S. J. Allen, *Appl. Phys. Lett.*, **61**, 2890 (1992).
5. T. Sato, K. Baba, T. Hirozawa, K. Shiraishi, and S. Kawakami, *IEEE J. Quantum Electron.*, **29**, 175 (1993).

Fig. 1

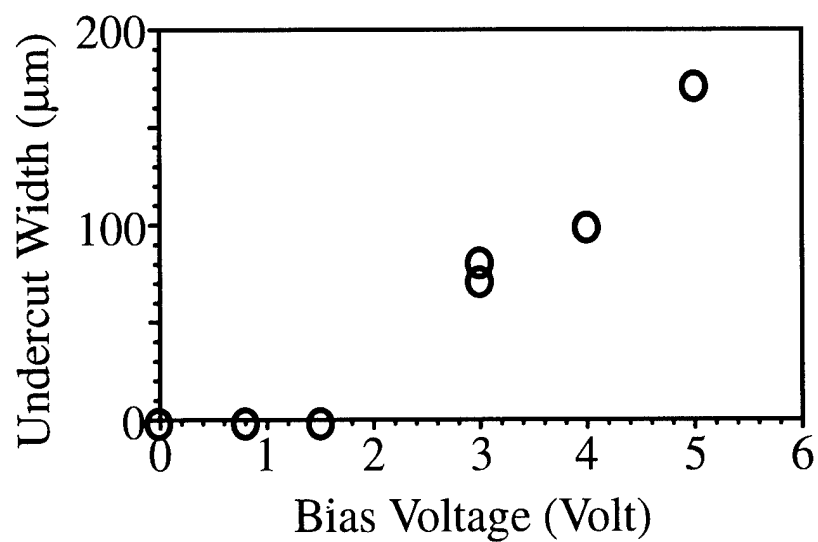
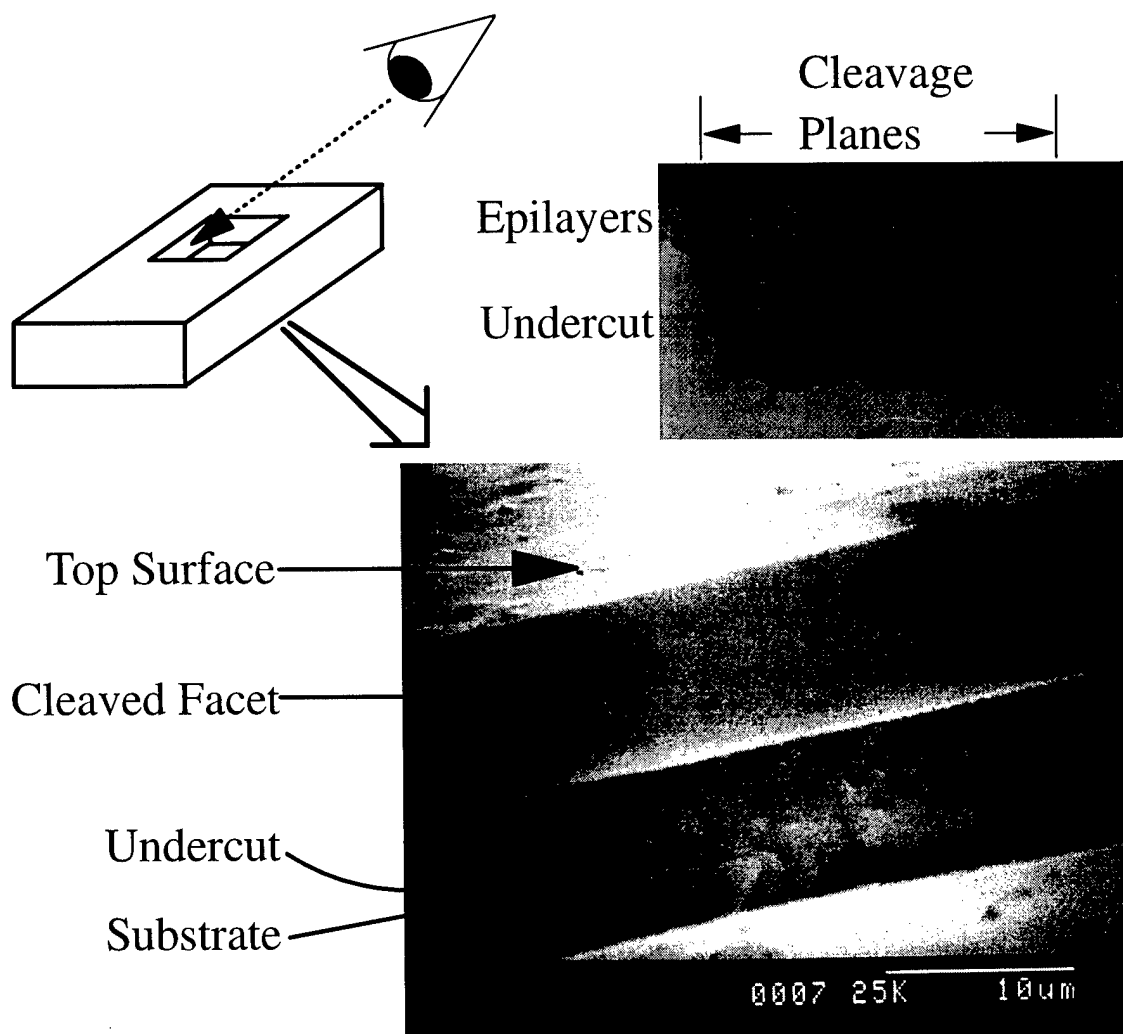
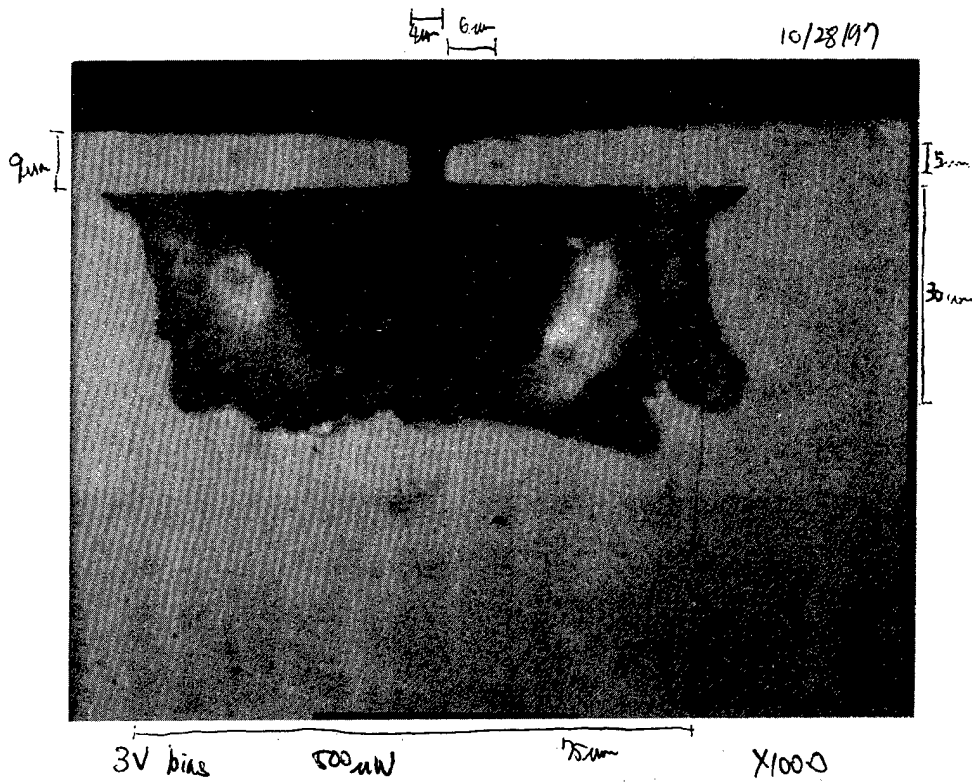
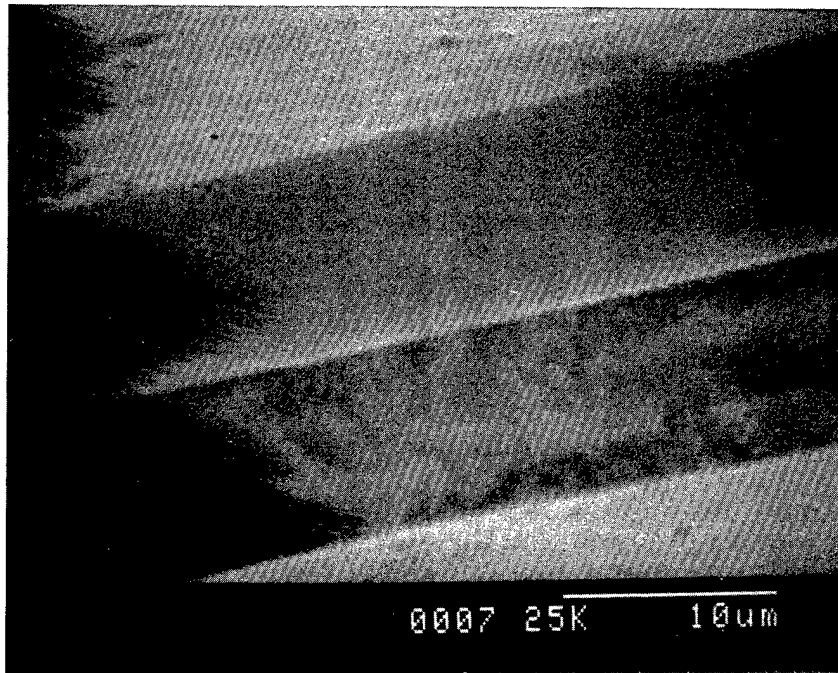


Fig. 2





## Alignment Tolerant Smart Pixel Bi-Directional Optoelectronic Links Using Co-Located Emitters and Detectors

Jeffrey Cross, Mikkel A. Thomas, and Nan Marie Jokerst

Smart pixel optoelectronic systems combine the use of highly complex digital and analog Si electronics coupled with optoelectronic devices, and offer numerous advanced optical interconnection schemes for system implementation. To realize cost effective smart pixel interconnect systems, alignment tolerant packaging is critical to the system design and implementation. We have demonstrated a highly alignment tolerant, single channel bi-directional link using co-located emitters and detectors [1]. For low-cost packaging, this single channel, bi-directional scheme is attractive since it reduces the packaging per link from two channels to one. This link was demonstrated at a relatively low speed for automotive and avionic signal distribution applications that require low sensitivity to electromagnetic interference but do not require high speeds. Herein we report upon the alignment tolerant system design, compare theory to experimental results for the demonstrated link, and expand the theory to predict the alignment tolerance for higher operating frequencies and for different emitter and detector options. Critical factors that influence the alignment tolerance of these links are the choice of emitter and detector. Options for optical emitters include vertical cavity surface emitting lasers (VCSELs), resonant cavity enhanced (RCE) light emitting diodes (LEDs) and LEDs, which differ primarily in their efficiency and divergence angle for this point to point interconnection. For detectors, the tradeoffs between P-i-N and metal-semiconductor-metal (MSM) detectors are absorbing area, responsivity, and noise. In this paper, we explore the system optimization of packaging alignment tolerance for low-cost free space optical links that utilize co-located emitters and detectors.

We have demonstrated a low cost, bi-directional fiber optic interconnect using a co-located emitter and detector [1], as shown in Figure 1(a). Using a large core plastic optical fiber, -3dB alignment tolerances were demonstrated for longitudinal separations over 1mm and lateral separation over 0.5mm. This system was designed for an operating frequency of 10kHz. The system shown in Figure 1 utilizes GaAs-based thin film emitters integrated onto silicon CMOS circuitry. The Si circuitry includes a Si detector, analog interface circuits, and digital signal processing circuitry. The system analysis uses radiometric propagation for LEDs to calculate the longitudinal and lateral alignment tolerance. The longitudinal alignment tolerance (i.e., optical coupling as a function of longitudinal separation) for the link shown in Figure 1(a) is shown in Figure 1(b), and shows excellent agreement between the model and experimental data. For large core fiber optic interconnects, the system analysis is similar to a previous result [3] assuming negligible modal dispersion within the fiber.

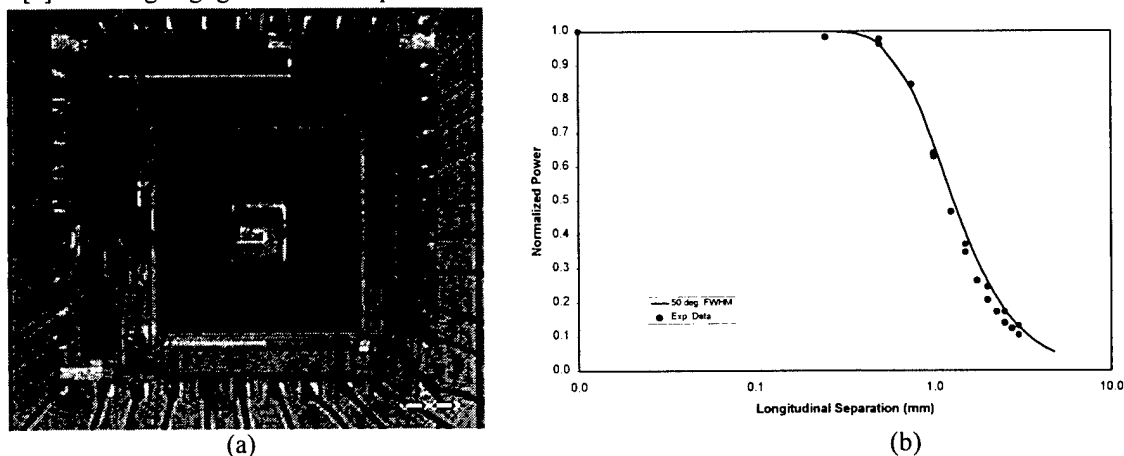


Figure 1 – (a) Photomicrograph of integrated CMOS circuit and (b) comparison between theoretical and experimental longitudinal alignment tolerance.

For the demonstrated link, the speed and responsivity of the system are limited by the Si CMOS detector. Small CMOS junction depths coupled with low Si absorption coefficients cause low responsivity, but phototransistor gain was used to improve the responsivity, which can result in slower speeds. Thus, to extend the model to higher frequencies, we use a co-located thin film integrated detector and emitter. This type of stacked thin film system has been previously demonstrated [2], in which the thin film devices are integrated on top of one another.

To extend the alignment tolerant link to higher speeds, a detector and emitter must be selected. The first design choice is between P-i-N detectors and MSM detectors. Although P-i-N detectors generally have larger responsivity than MSM detectors, inverted MSM (I-MSM) detectors [4] can be used that have a responsivity which is slightly less than that of P-i-N detectors, but which have significantly larger absorbing areas than P-i-N detectors. Assuming the MSM detector has a transit time of 5ps and a responsivity of  $0.7\text{A/W}$ , the system bandwidth will limit the absorbing area of the detector. Larger absorbing areas are desired because they provide the greatest degree of alignment tolerance. An MSM detector will have capacitance per unit area of  $3.1 \times 10^{-17}\text{F}/\mu\text{m}^2$  with finger width and finger spacing of  $1\mu\text{m}$  [5]. Typical input characteristics for interface receiver circuitry includes an input resistance of  $100\Omega$  and minimum input signal current of  $1\mu\text{A}$  [6].

The second design option that dictates coupling and alignment tolerance is the choice of emitter. Vertical cavity surface emitting lasers (VCSELs) have higher external quantum efficiency, and thus produce more optical power per unit drive current than with light emitting diodes (LEDs). However, LEDs have higher reliability and longer lifetime than lasers, and can be implemented into low-cost system designs because LEDs can satisfy the output power and bandwidth constraints while not incurring the increased cost associated with device fabrication and the complexity of the control circuitry. Typical VCSELs have an output power of  $27\text{mW}$  with an operating current of  $50\text{mA}$ , and can be directly modulated at frequencies of  $1\text{GHz}$  [7,8]. Gaussian beam propagation is used to calculate the longitudinal and lateral alignment tolerance for VCSELs. In addition, both LEDs and RCE LEDs have been modeled. LEDs and RCE LEDs have  $90^\circ$  and  $25^\circ$  divergence half angles, respectively, and are both bandwidth limited by carrier recombination; as the performance of the LED shifts to obtain higher speeds, the output power decreases. For LEDs operating below  $155\text{MHz}$ , the typical output power is  $1\text{mW}$  with  $50\text{mA}$  operating current. For the same drive current, for a  $-3\text{dB}$  bandwidth of  $790\text{MHz}$ , the output power drops to  $100\mu\text{W}$ , and, for a  $-3\text{dB}$  bandwidth of  $2.75\text{GHz}$ , the output power drops to  $2\mu\text{W}$  [9,10]. These system parameters for detectors and emitters have been used to determine the feasibility of implementing low cost, alignment tolerant packaged smart pixel optoelectronic system designs.

For the higher speed link model, an inverted square MSM with an edge length of  $200\mu\text{m}$  was used for operation up to  $1\text{GHz}$ ; the emitter was either a VCSEL with a diameter of  $40\mu\text{m}$  or a square LED with an edge length of  $50\mu\text{m}$ . The emitter drive currents used are the same to maintain constant power dissipation in the system. Using these system parameters, Figure 2 shows that these LED-based systems are functional over a large range of longitudinal separations up to  $750\text{MHz}$ , but fail at  $800\text{MHz}$  to  $1\text{GHz}$  for all values of longitudinal.

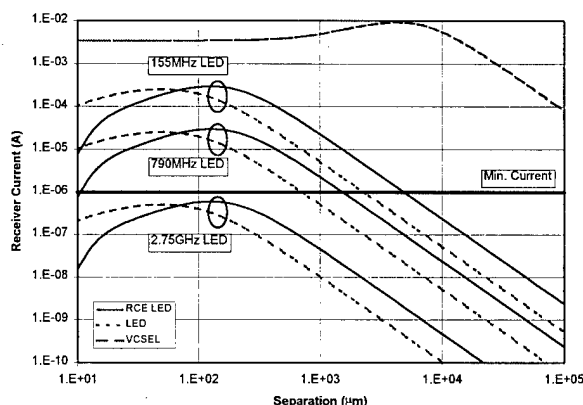


**Figure 2 – Input receiver current dependence on emitter-detector longitudinal separation for three different system bandwidths.**

The initial peaking in the input receiver current is due to the co-location of the emitter and detector; the emitter shadows the detector at close distances, but as the separation increases, the source divergence illuminates more of the detector area. In all cases, the VCSEL results in a higher degree of coupling for all longitudinal separations due to the smaller divergence angle and higher efficiency.

Figure 2 represents systems that have no lateral misalignment, but for low-cost applications, the system must be insensitive to variations in lateral position, as well. Figure 3 shows the lateral alignment tolerance (coupling) for various values of longitudinal separation. The lateral separations examined herein are for chip to chip free space interconnects, or for large core optical fibers, which can also be represented by this model. Again,

these curves show that the LEDs fail to produce sufficient coupling at speeds from 800MHz to 1GHz. However, the LEDs are more alignment tolerant than VCSELs for large transverse separations due to the larger divergence angle of the LEDs.

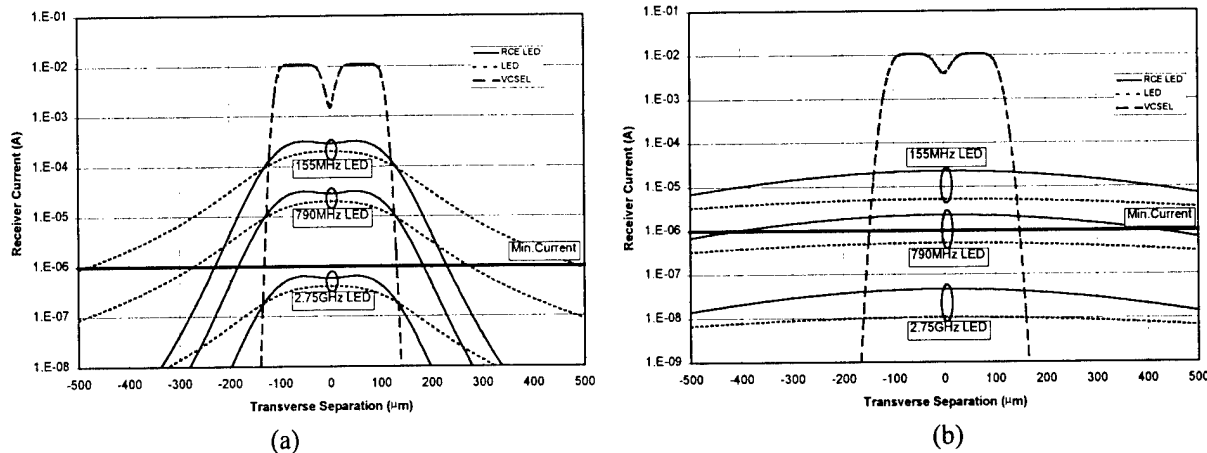


**Figure 3 – Input receiver current dependence on transverse separation for longitudinal separations of (a) 100μm and (b) 1000μm for three different system bandwidths.**

In conclusion, this paper reports the alignment tolerant packaging analysis for bi-directional co-located emitters and detectors for free space optoelectronic interconnects. For systems operating at frequencies <790MHz, low-cost applications can be successfully implemented using LEDs, with fairly large longitudinal and lateral displacements. For systems operating at frequencies >790MHz, the low efficiency and large divergence angle of LEDs prohibit these devices from typical system implementations. VCSELs are well suited for these higher speed applications, however, they have limited lateral alignment tolerance.

#### References:

- [1] J. Cross, A. Lopez-Lagunas, B. Buchanan, L. Carastro, S.-C. Wang, N. Jokerst, S. Wills, M. Brooke, and M. A. Ingram, "A single-fiber bi-directional optical link using co-located emitters and detectors", *IEEE Photon. Tech. Lett.*, vol. 8, pp. 1385-7, Oct. 1996.
- [2] S. Fike, Army Missile Command Final Report, 1997.
- [3] S.-C. Wang and M. A. Ingram, "A novel Fourier technique for calculating fiber-to-LED coupling efficiency with lateral and longitudinal misalignments," *J. Lightwave Tech.*, vol. 14, pp. 2407-13, Oct. 1996.
- [4] O. Vendier, N. Jokerst, R. Leavitt, "Thin-film inverted MSM photodetectors," *IEEE Photon. Tech. Lett.*, vol. 8, pp. 266-8, Feb. 1996.
- [5] J. Burm, K. I. Litvin, W. J. Schaff, and L. F. Eastman, "Optimization of high-speed metal-semiconductor-metal photodetectors," *IEEE Photon. Tech. Lett.*, vol. 6, pp. 722-4, June 1994.
- [6] M. Lee, O. Vendier, M. Brooke, and N. Jokerst, "Scaleable CMOS current-mode preamplifier design for an optical receiver," *Analog Int. Circ. Sig. Proc.*, vol. 12, pp. 133-44, Feb. 1997.
- [7] R. A. Morgan, J. A. Lehman, and M. K. Hibbs-Brenner, "Vertical-cavity surface-emitting lasers come of age," *Proc. SPIE*, vol. 2683, pp. 18-29, 1996.
- [8] C. A. Gaw, W. Jiang, M. Leiby, P. A. Kiely, and P. R. Claisse, "Characteristics of VCSELs and VCSEL arrays for optical data links," *Proc. SPIE*, vol. 3004, pp. 122-133, 1997.
- [9] T. J. de Lyon, J. M. Woodall, D. T. McInturff, R. J. S. Bates, J. A. Kash, P. D. Kirchner, and F. Cardone, "Doping concentration dependence of radiance and optical modulation bandwidth in carbon-doped Ga<sub>0.51</sub>In<sub>0.49</sub>P/GaAs light-emitting diodes grown by gas source molecular beam epitaxy," *J. Appl. Phys. Lett.*, vol. 60, pp. 353-5, Jan. 1992.
- [10] C. Van Hoof, H. De Neve, R. Mertens, I. Romandic, E. Goovaerts, and G. Borghs, "Gigahertz modulation of tunneling-based GaAs light emitters," *IEEE Photon. Tech. Lett.*, vol. 9, pp. 1463-5, Nov. 1997.

# Single-mode stability of Fabry-Pérot taper-lasers with external fibre Bragg gratings

E. Rönneberg, G. Vollrath, B. Hübner, Ch. Gréus, and H. Burkhard

Deutsche Telekom AG, Technologiezentrum, Am Kavalleriesand 3, D-64295 Darmstadt,  
Tel. +49-6151-832589, Fax +49-6151-834049, E-mail: roenneberg@10.dmst02.telekom400.dbp.de

## Abstract

We have theoretically and experimentally investigated the effect of variation of the resonator phase on the single-mode stability of Fabry-Pérot taper-lasers with external fibre Bragg gratings.

## Introduction

Low cost, frequency-stable lasers are a key component in DWDM (dense wavelength-division multiplexing) optical networks. One promising solution are Fabry-Pérot lasers with external fibre Bragg gratings (fibre grating laser, FGL). The emission wavelength of these devices is mainly defined by the Bragg wavelength of the fibre Bragg grating (FBG). FBGs are already available in mass production with high wavelength precision. The same type of lasers can be used for different wavelengths simply by using different FBGs. No further wavelength control is necessary, which makes those devices ideal for DWDM laser arrays.

In addition, lasers with monolithically integrated spot size converters (SSC, or taper) [1] provide higher alignment tolerances and shorter cavity lengths. This is because the grating can be written close to the cleaved fibre end which is placed directly in front of the laser. Short cavities lead to a higher modulation speed. We already achieved error free operation at 2.5 Gbit/s (back-to-back) even without an optical isolator (input return loss of the optical receiver >25 dB).

However, FGLs suffer from mode jumps caused by a shift of the resonator phase relative to the reflection band of the FBG. This can be caused either by variation of cavity length (i.e. distance between fibre and laser) or chip temperature. We have investigated these properties in theory and experiment on our SSC-FGLs.

## Device structure

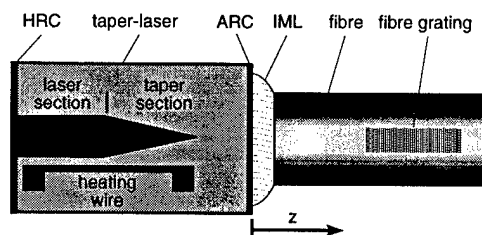


Figure 1: SSC-laser with external FBG.

The gain element consists of a 200  $\mu\text{m}$  long mushroom-type MQW Fabry-Pérot laser section and a monolithically integrated taper section of 300  $\mu\text{m}$  length [1]. The taper section also contains active material and can be pumped separately. Additionally, these devices feature integrated resistive heaters consisting of a thin Ti/Pt wire in the vicinity of the active zone.

The laser facet is high-reflection coated (HRC). The taper facet anti-reflection coating (ARC) is matched to the refractive index of the fibre which is butt-coupled to the taper facet. The ARC consists of a low cost single layer coating leading to a reflectivity of  $\approx 0.2\%$ . An index matching liquid (IML) is used to minimize reflections between semiconductor chip and fibre. The FBG used has a peak reflectivity of 0.4 at 1540 nm, a bandwidth (FWHM) of 0.4 nm, a length of  $\approx 2$  mm and is placed less than 1 mm away from the cleaved fibre end. Fig. 1 shows a schematic drawing of the device. For our experiments, the fibre is mounted on a piezo-driven nano-positioning stage in order to exactly align the fibre to the laser and to vary the distance in the z-direction between fibre (i.e. grating) and laser with high precision.

### Influence of the distance between laser and FBG

A laser mode must fulfill the roundtrip phase condition. By slightly changing the resonator phase (i.e. optical resonator length) the phase condition matches at a different wavelength within the reflection band. Larger variation of the phase shift moves the lasing mode towards the edge of the reflection band while the next mode on the other edge moves further inside it until this mode becomes dominant and a modejump occurs.

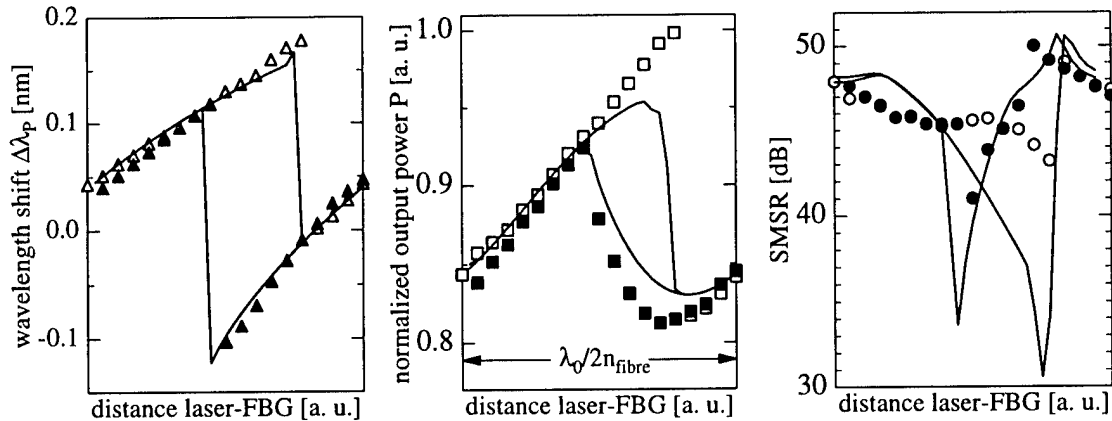


Figure 2: Measured wavelength shift  $\Delta\lambda_p$ , normalized optical power  $P$  and SMSR when moving the fibre away from (open symbols) and towards (solid symbols) the laser compared to simulations (lines).

The dependence of the optical properties of the FGL on the relative resonator phase was simulated with a transmission-line-model of a taper-laser [2]. A phase-shifting element has been inserted in order to vary the resonator phase. Fig. 2 shows simulations for a laser with a perfect ARC (solid lines) as well as the measured data of the shift of the emission wavelength from the Bragg wavelength ( $\Delta\lambda_p$ , left), the optical output power ( $P$ , middle) and the side-mode suppression ratio (SMSR, right) over the distance between laser and FBG. The data were recorded while moving the fibre from and back towards the laser. The range of the z-axis corresponds to a  $2\pi$ -phase shift, which is one half of the wavelength in the fibre, i.e. 514 nm.

The modejumps occur at different wavelengths and different z-axis positions depending on the direction of the variation of the phase shift (hysteresis) [3].

As expected, the plot of  $\Delta\lambda_p$  has a "saw-tooth" like shape. Both,  $\Delta\lambda_p$  and  $P$  are in very good agreement with the simulations. Instead of the SMSR, the relative stability of the lasing mode was derived in the simulations [4]. These two quantities can only be compared qualitatively. However, the general features are in agreement with the measured data. The SMSR ranges between 45 and 50 dB, being lower than 40 dB only in the vicinity of modejumps.

Since the power  $P$  is easy to monitor in laser modules, it would be an ideal control criterion of the laser parameters for stable laser operation. Therefore the shape of the  $P$ -graph is of special interest.

If the taper facet has a residual reflectivity like in a real device, one has to deal with two coupled resonators. We therefore inserted a second phase-shifting element in the simulations. An assumed reflectivity of the taper facet of 0.2 % leads to similar shapes of  $\Delta\lambda_p$  and SMSR. The amplitude of the jump of the optical power increases by a factor of nearly two, but maintains its general shape. For a reflectivity of 5 % additional modejumps occur. Thus, an ARC is necessary, but a low cost single layer coating like ours is sufficient. It therefore is possible to adjust the resonator phase using the power  $P$  to monitor the phase.

### Influence of the chip temperature

There are three factors affecting the chip temperature: The driving currents through the laser and taper sections ( $I_L$  and  $I_T$ , resp.) and the current  $I_H$  through the heating wire. Fig. 3 shows the plot of  $\Delta\lambda_p$  over  $I_H$ . As can be seen, the resonator phase can be varied by more than  $2\pi$ . This means, that the phase can always be adjusted to an optimum at any given z-axis position. Hence, a z-axis alignment while packaging is not necessary.

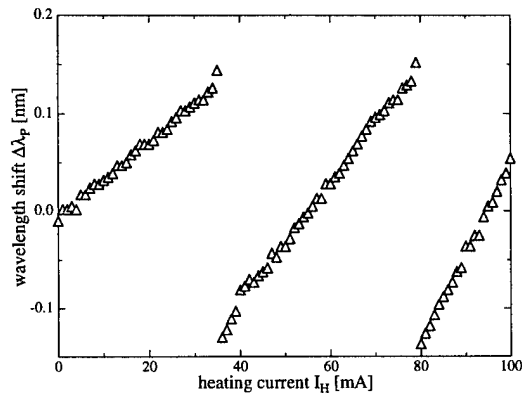


Figure 3: Wavelength shift  $\Delta\lambda_p$  vs. heating current  $I_H$ .

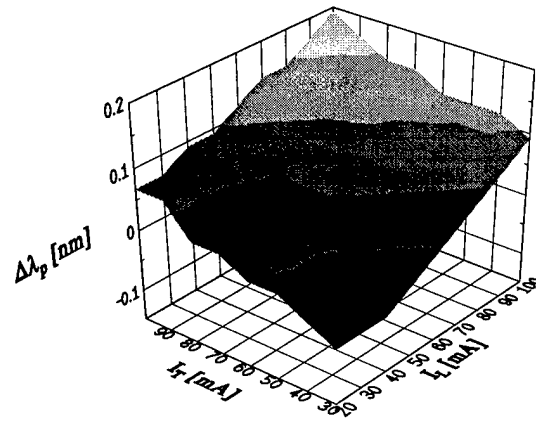


Figure 4: Wavelength shift  $\Delta\lambda_p$  vs.  $I_L$  and  $I_T$  for optimized z-axis position.

In Fig. 4 the dependence of  $\Delta\lambda_p$  on  $I_L$  and  $I_T$  for an optimized z-axis position is plotted. It can be seen that for currents  $I_L$  and  $I_T$  up to 100 mA the phase shifts by less than  $2\pi$ ; thus mode jump free operation can be achieved if the resonator phase is optimized. Since these measurements were carried out in CW operation, the phase shift will be smaller under direct modulation because temperature effects are smaller. Therefore the optimization of the resonator phase is less critical than in CW operation. The maximum overall wavelength shift of our SSC-FGL of 0.3 nm is very small compared to DFB-lasers, very low linewidth and chirp are also expected [5, 6]. This makes these devices suitable for DWDM applications with a channel spacing of 100 GHz or even less.

### Conclusion

We have simulated and measured the dependence of the single mode stability of SSC-FGLs on the resonator phase. We showed that mode-jump free operation is possible if the resonator phase is optimized. This optimization can be achieved by adjusting the chip temperature using the optical output power to monitor the phase. Therefore laser arrays for DWDM applications consisting of Fabry-Pérot taper-lasers and ribbons of FBGs are possible to create.

### References

- [1] R. Zengerle et al., *Electron. Lett.*, Vol. 31 (14), p. 1442, 1995
- [2] B. Hübner et al., *Proceedings ECIO*, ECIO 97, p. 200, 1997
- [3] P.A. Morton et al., *Appl. Phys. Lett.*, Vol. 64 (20), p. 2634, 1994
- [4] B. Hübner, PhD thesis, University of Würzburg, 1998
- [5] J-M. Verdiell et al., *SPIE*, Vol. 3038, p. 67, 1997
- [6] F.N. Timofeev et al., *Proceedings ECOC*, ECOC 97, tu1a, 1997



---

**Integrated Photonics Research**

# **Quantum Wells I: Carrier Transport in Quantum Well Devices**

**Tuesday, March 31, 1998**

**S. L. Chuang, University of Illinois, Urbana-Champaign**  
Presider

**ITuG**  
**1:30pm–3:00pm**  
Salon B

# Simulation of Nonlinear Gain and the Modulation of Quantum Well Laser Diodes

Karl Hess and Matt Grupen

University of Illinois

Beckman Institute

405 N. Mathews Ave.

Urbana, IL 61820

(217) 333-9734

k-hess@uiuc.edu

Direct small signal amplitude modulation of quantum well (QW) laser diodes is largely a problem of carrier transport. Important transport mechanisms include classical transport in the bulk regions of the laser [1] and the capture of bulk carriers into the quantum active region [2, 3, 4]. Within the quantum well, free carrier thermalization (spectral hole burning) [5, 6], nonequilibrium phonon distributions [7, 8], and hot carrier effects [7] also influence the differential gain and the modulation response.

The Minilase-II laser simulator treats these transport processes in a coupled, self-consistent manner. In this talk, the models used in the simulator will be briefly described. Simulated modulation responses will also be presented and compared directly to experimental measurements. The comparison will show how hot quantum carrier effects contribute to nonlinear gain.

Carrier transport, as modeled in Minilase-II, is represented by Figure 1, which shows a schematic diagram of the quantum well and the surrounding bulk regions. A two-dimensional cross section of the laser is discretized in real space, and certain one-dimensional cross sections of the QW are discretized in energy space. Transport in the bulk regions is treated with drift-diffusion theory [9]. At the interface with the QW, bulk carriers are injected ballistically by thermionic emission [9, 10] into states above the QW. These states are approximated by a three-dimensional parabolic continuum. Continuum carriers can ballistically transfer back into the bulk or scatter into states within the QW. Within the well, carriers are distributed spatially according to their wavefunctions, obtained by solving Schrödinger's equations in the effective mass approximation for a finite square well [11].

Quantum carriers are distributed in energy space by balancing their capture from the continuum with their recombination and scattering between energy points. The net transfer of electrons between two energy points  $i$  and  $j$  due to LO scattering is given by

$$S_{i \rightarrow j}^{\text{el-ph}} = s_{ij}^{\text{el-ph}} \delta(E_i - E_j - \hbar\omega_{\text{LO}}) g_i g_j f_i (1 - f_j) (n_q + 1) \Delta E_i \Delta E_j + s_{ij}^{\text{el-ph}} \delta(E_i - E_j + \hbar\omega_{\text{LO}}) g_i g_j f_i (1 - f_j) n_q \Delta E_i \Delta E_j \quad (1)$$

where  $s_{ij}^{\text{el-ph}} \delta(E_i - E_j \pm \hbar\omega_{\text{LO}})$  is the electron-phonon scattering probability,  $g_i$  is the density of states at energy point  $i$ ,  $f_i$  is the corresponding occupation probability, and  $\Delta E_i$  is the energy range associated with point  $i$ . To determine  $s_{ij}^{\text{el-ph}}$ , an electron-phonon total scattering rate of  $10^{13} \text{ s}^{-1}$  was assumed for equilibrium conditions at room temperature. A similar expression is used for holes. The resulting LO phonon emission rates are also used in a phonon rate equation to calculate the nonequilibrium LO phonon temperature. Acoustic phonons are assumed to be in thermal equilibrium everywhere in the laser. Electron-electron scattering between the two energy points is simulated by

$$S_{i \rightarrow j}^{\text{el-el}} = \begin{cases} s_{ij}^{\text{el-el}} g_i g_j f_i (1 - f_j) \Delta E_i \Delta E_j & \text{for } E_i > E_j \\ s_{ij}^{\text{el-el}} g_i g_j f_i (1 - f_j) \exp\left(\frac{E_i - E_j}{kT_{\text{el}}}\right) \Delta E_i \Delta E_j & \text{for } E_i < E_j \end{cases} \quad (2)$$

where the electron-electron scattering probability  $s_{ij}^{\text{el-el}}$  corresponds to a scattering rate of  $10^{14} \text{ s}^{-1}$  [12, 13]. Again, a similar expression is used for holes. The electron temperature  $T_{\text{el}}$  in (2) is determined by an energy balance which assumes that electrons and holes have equal temperatures and which ensures that carrier-carrier scattering conserves total carrier energy [14].

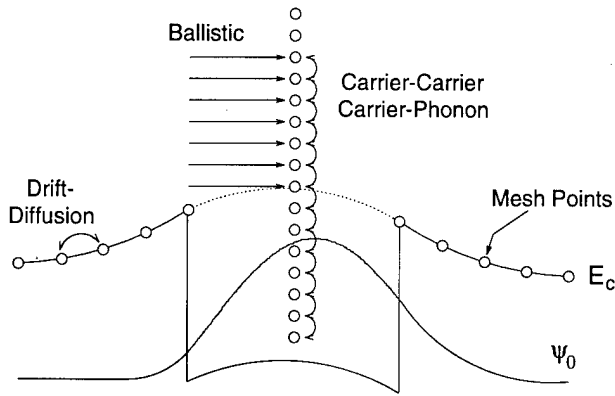


Figure 1: A schematic diagram of the QW and surrounding areas as discretized in Minilase-II.

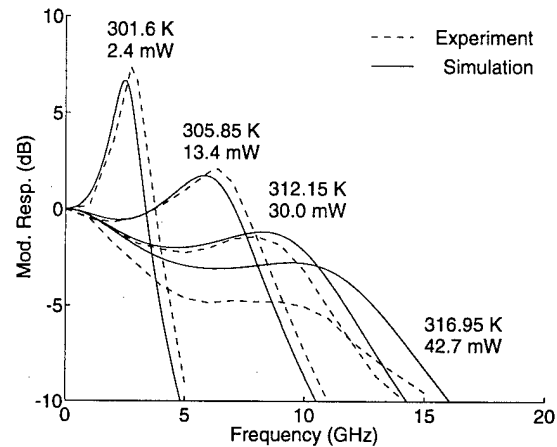


Figure 2: Measured [16] and simulated (including hot quantum carrier effects) modulation responses.

To simulate laser modulation, the photon dynamics must be calculated along with the carrier dynamics. Minilase-II determines the photon dynamics using photon rate equations that balance the emission of photons due to spontaneous and stimulated recombination with the internal and mirror losses for each relevant cavity mode. The mode gain and spontaneous emission rate in the active region are obtained from the band structure in the QW, calculated using an eight band  $\mathbf{k} \cdot \mathbf{p}$  method [15], Fermi's Golden Rule, and the density of cavity photon states. The cavity modes are determined by solving Maxwell's equations, approximated by the scalar Helmholtz equation [11].

To test the models used in Minilase-II, simulated small signal amplitude modulation responses are compared to experimental measurements. The experimental data comes from a paper published by R. Nagarajan *et al* [16]. The device considered contains a single intrinsic 80 Å compressively strained  $\text{In}_{0.2}\text{Ga}_{0.8}\text{As}$  QW surrounded by an intrinsic  $\text{Al}_{0.1}\text{Ga}_{0.9}\text{As}$  SCH that measures 3000 Å on each side of the well. It is an edge-emitting laser with a cavity length of 300 μm. Some of the measured responses from [16] are shown in Figure 2 along with simulated responses calculated for the same single facet output powers.

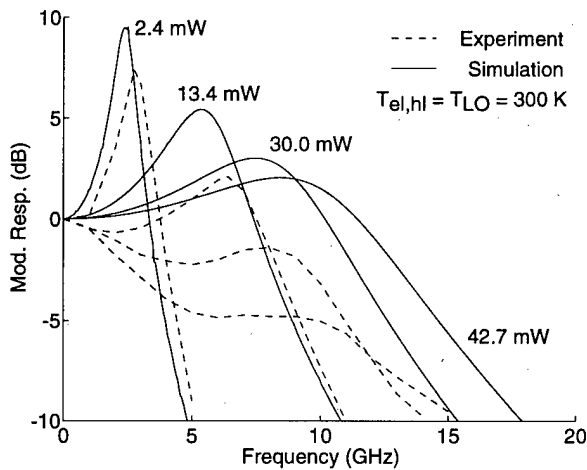


Figure 3: Measured [16] and simulated (no hot quantum carrier effects) modulation responses.

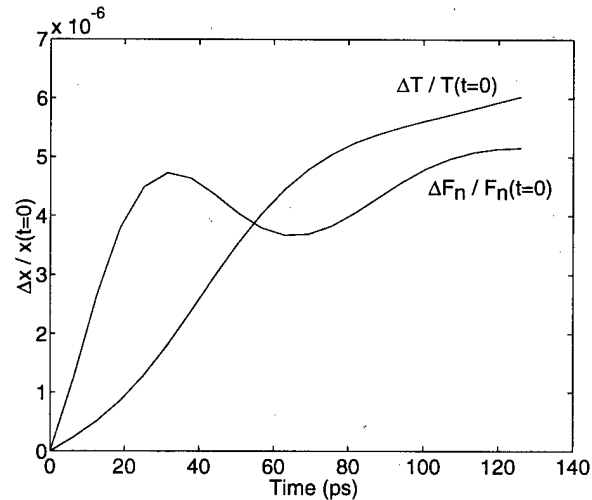


Figure 4: Small signal time evolution of quantum electron quasi-Fermi level (determined by the electron density) and quantum carrier temperature.

Figure 2 shows good agreement between simulation and experiment. The most significant disparity occurs at the highest power, which shows the experiment to roll off more than the simulation. This may be due to the assumption of equilibrium acoustic phonons. Although the carrier heating appears to be moderate,

Figure 3 shows that its effects are very significant. The simulations that neglect heating effects show much less roll off and gain saturation. Such a strong temperature dependence can be understood with the help of Figure 4. This figure shows the relative changes in the quasi-Fermi level for quantum electrons and the quantum carrier temperature as a function of time after a small increase in bias is applied to the 42.7 mW case of Figure 2. It shows that the relative increase in carrier temperature is comparable to the increase in quasi-Fermi level, i.e. while the injection of carriers is working to fill the lasing states, the increase in temperature works to empty these states.

The small signal amplitude modulation of a quantum well laser involves many different interacting carrier transport processes. The laser simulator Minilase-II contains models that are designed to treat these processes effectively. The models included in Minilase-II include classical bulk transport, the capture of bulk carriers into the quantum well, spectral hole burning, nonequilibrium LO phonons, and quantum carrier heating.

Modulation responses simulated by Minilase-II compare favorably with experimental measurements. The comparisons reveal that hot phonons and hot carriers are a significant part of QW laser dynamics. The modal gain is modulated by both injected carriers and carrier temperature. In other words, when pumping the lasing states, the rate that energy is removed from the QW is as much of a concern as the rate that carriers are injected into the QW.

## References

- [1] Nagarajan R, Mirin R P, Reynolds T E and Bowers J E 1993 *Electron. Lett.* **29** 1688–1689
- [2] Brum J A and Bastard G 1986 *Phys. Rev. B* **33** 1420–1423
- [3] Rideout W, Sharfin W F, Koteles E S, Vassell M O and Elman B 1991 *IEEE Phot. Tech. Lett.* **3** 784–786
- [4] Grupen M, Kosinovsky G and Hess K 1993 *International Electron Device Meeting Technical Digest* (Piscataway, New Jersey: IEEE) 23.6.1–23.6.4
- [5] Agrawal G P 1987 *IEEE J. Quantum Electron.* **QE-23** 860–868
- [6] Grupen M, Hess K and Rota L 1995 *Physics and Simulation of Optoelectronic Devices III, San Jose* vol 2399 ed M Osiński and W W Chow (Bellingham, Washington: SPIE) 468–479
- [7] Tsai C-Y, Tsai C-Y, Lo Y-H and Spencer R M 1995 *Appl. Phys. Lett.* **67** 3084–3086
- [8] Grupen M and Hess K 1995 to be published in *Proc. of the Fourth Internat. Workshop on Comp. Electron.*
- [9] Hess K 1988 *Advanced Theory of Semiconductor Devices* (Englewood Cliffs, New Jersey: Prentice Hall)
- [10] Grupen M, Hess K and Song G H 1991 *Proc. 4th International Conf. Simul. Semicon. Dev. Process., Zurich* vol 4 (Konstanz: Hartung-Gorre Verlag) 303–311.
- [11] Grupen M, Ravaioli U, Galick A, Hess K and Kerkhoven T 1994 *Physics and Simulation of Optoelectronic Devices II* vol 2146 ed W W Chow and M Osiński (Bellingham, Washington: SPIE) 52–67
- [12] Ridley B K 1988 *Quantum Processes in Semiconductors* (Oxford: Clarendon Press) 175
- [13] Kash J A and Tsang J C 1988 *Solid-State Electron.* **31** 419–424
- [14] Grupen M 1996 *Physics and Simulation of Optoelectronic Devices IV* vol 2693 ed W W Chow and M Osiński (Bellingham, Washington: SPIE) 374–385
- [15] Oyafuso F, von Allmen P, Grupen M and Hess K 1995 to be published in *Proc. of the Fourth Internat. Workshop on Computational Electronics*
- [16] Nagarajan R, Fukushima T, Ishikawa M, Bowers J E, Geels R S and Coldren L A 1992 *IEEE Phot. Tech. Lett.* **4** 121–123

# CARRIER TRANSPORT EFFECTS IN THE FREQUENCY MODULATION RESPONSE OF QUANTUM WELL LASERS

N. Mustafa<sup>1,2</sup>, L. Pesquera<sup>1</sup>, and I. Esquivias<sup>3</sup>

<sup>1</sup> Instituto de Física de Cantabria (CSIC-UC), E-39005 Santander, Spain.

<sup>2</sup> Departamento de Física Moderna, Univ. de Cantabria, E-39005 Santander, Spain.

<sup>3</sup> Departamento de Tecnología Fotónica, Univ. Politécnica de Madrid, Spain.

Return Address: L. Pesquera, Instituto de Física de Cantabria (CSIC-UC),

Facultad de Ciencias, Avda. de los Castros s/n, E-39005 Santander, Spain.

Phone: 34-42-201453 Fax: 34-42-201459 E-mail: pesquerl@ifca.unican.es

Carrier transport effects are very important when considering the dynamic response of Quantum Well (QW) lasers. Theoretical and experimental studies of the amplitude modulation characteristics have shown that the modulation bandwidth can be limited by carrier transport. However, there has been a few studies of the contribution of the carriers  $N_c$  in the core (barriers and separate confinement heterostructure) to the frequency modulation (FM) response of QW lasers. This contribution, that corresponds to the carrier-induced refractive index change, is enhanced by the larger optical confinement factor of the unconfined carriers. It has been shown that carrier transport from the core into the well layers can increase the FM efficiency [1], and have an important impact on the shape of the FM response [2] of InGaAs/InGaAsP QW lasers operating at 1.5  $\mu\text{m}$ . The contribution of barrier-state carriers to the linewidth enhancement factor [3] and to the laser dynamics under large signal modulation [4] can be also very important at large values of  $N_c$ , as it has been found for InGaAs/GaAs QW lasers operating around 1  $\mu\text{m}$ .

In this work we perform a theoretical study of carrier transport effects in the FM response of QW lasers. These effects include carrier diffusion across the separate confinement heterostructure and in the barriers, carrier capture into the QW (both processes characterized by a single effective capture time  $\tau_{cap}$ ), and carrier escape out of the QW (with effective escape time  $\tau_{esc}$ ). A rate-equation model for the carriers in the active layers  $N_w$ , the carriers in the core  $N_c$ , and for the optical field is used. We also consider the change in the laser frequency due to the refractive index changes in both the wells and the core. The laser parameters considered correspond [5] to ultra-high speed InGaAs/GaAs MQW lasers with intrinsic modulation bandwidth of 40 GHz. Transport effects are not important for the structures studied in Ref. [5] ( $\tau_{cap} = 5$  ps and  $\tau_{esc} = 500$  ps for a 48 nm GaAs upper core region at room temperature). Here we study the small signal FM response by assuming different values of  $\tau_{cap}$  and  $\tau_{esc}$  in order to analyze carrier transport effects.

Three terms contribute to the FM response [2]. The first one corresponds to the direct contribution of the active region, and represents the whole FM response for bulk lasers. This term comes from the increase of the refractive index in the QW  $n_w$  when  $N_w$  decreases, and it is proportional to the linewidth enhancement factor,  $\alpha = 1.5$ . The second term is due to the change of  $N_c$  induced by the change of  $N_w$  and it is proportional to the ratio  $\tau_{cap}/\tau_{esc}$ . Then it is not negligible only when both time constants are of the same order. The third term is due to the dependence of  $N_c$  on the injection current and it is proportional to the capture time. These two terms correspond to the change of the refractive index in the core  $n_c$  with the carrier density,  $dn_c/dN_c$ . Since the laser frequency is below the bandgap in the core,  $n_c$  can increase or decrease with the carrier density  $N_c$ . For undoped devices when  $N_c$  is smaller than about  $10^{18} \text{ cm}^{-3}$ ,  $dn_c/dN_c$  is positive at  $1 \text{ } \mu\text{m}$ , due to the bandgap shrinkage effect [6,7]. However, for higher carrier concentrations in the core bandfilling and plasma effects dominate yielding a negative differential refractive index. We have considered both negative and positive  $dn_c/dN_c$ , in order to analyze carrier transport effects for different possible devices. We show in Fig. 1 the modulus of the three contributions to the FM response in two different situations, not negligible capture time and small escape time. For  $\tau_{cap} = 30 \text{ ps}$  and large escape times the contribution of the carriers in the core is important at frequencies smaller than the cut-off frequency  $(2\pi\tau_{cap})^{-1}$ . For small escape and capture times the shape of the FM response can change due to the term proportional to  $\tau_{cap}/\tau_{esc}$ . This term has the same shape than the one due to  $N_w$ . Then, for positive values of  $dn_c/dN_c$  the FM response can become more flat due to the compensation of these two contributions, although the FM efficiency will decrease.

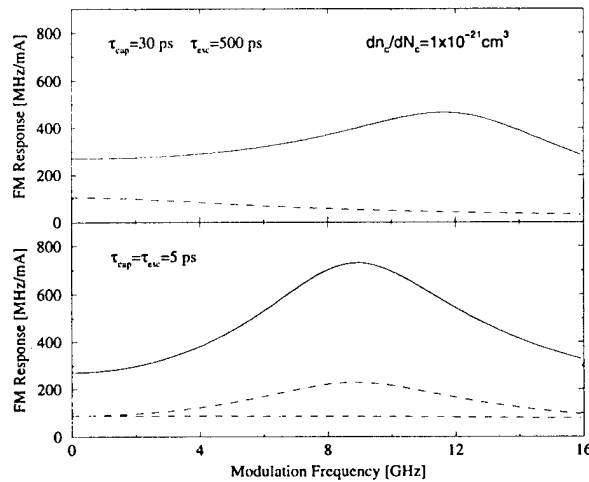


**Figure 1.** Magnitude of the different contributions to the FM response for a bias current of 80% above threshold: term proportional to the linewidth enhancement factor (solid line), capture time (dashed line) and to the ratio of capture and escape times (dotted line). In the upper figure the last contribution is negligible. In the lower figure the contributions due to  $N_c$  are magnified by a factor of 5.

The total FM response is shown in Fig. 2 for different values of the capture and escape times. Both positive and negative values of  $dn_c/dN_c$  are considered. When  $\tau_{cap}$  increases the FM efficiency increases (decreases) for negative (positive) differential refractive index. Also a more flat FM response is obtained in particular when  $dn_c/dN_c$  is positive, due to the different shapes of the contributions due to  $N_w$  and  $N_c$  (see Fig. 1). Also a decrease of the FM efficiency in this case can result in small chirping when increasing the capture time, and a zero static chirping can be obtained for a certain value of  $\tau_{cap}$ . Concerning the effect of the escape time, it is observed that the FM response is slightly more flat for positive differential refractive index, as discussed previously.

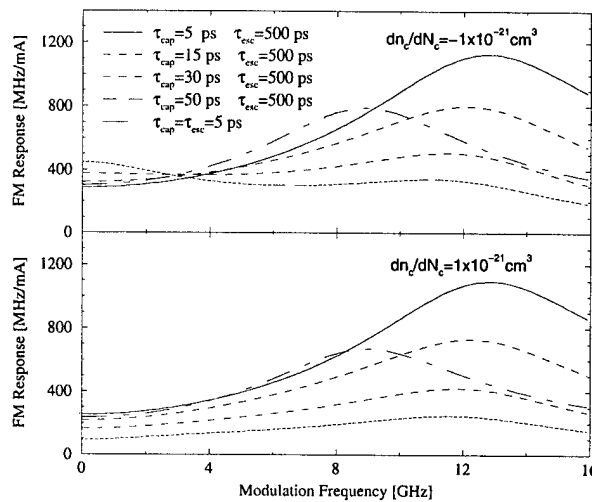


**Figure 2.** Magnitude of the total FM response for a bias current of 80% above threshold for different values of the capture times and two values, large and small, of the escape time.

## References

- [1] H. Yamazaki et al., IEEE Phot. Technol. Lett., **4**, 396 (1993).
- [2] R. F. S. Ribeiro et al., IEEE Phot. Technol. Lett., **7**, 857 (1995).
- [3] C. Z. Ning et al., IEEE J. of Select. Top. in Quantum Electron., **3**, 129 (1997).
- [4] D. Finzi et al., IEEE J. of Select. Top. in Quantum Electron., **3**, 142 (1997).
- [5] J. D. Ralston et al., IEEE J. of Quantum Electron., **29**, 1648 (1993).
- [6] H. C. Huang and S. Yee, J. Appl. Phys. **70**, 925 (1991).
- [7] B. R. Bennett et al., IEEE J. of Quantum Electron., **26**, 113 (1990).

## Optical gain enhancement in InP-based quantum-well lasers with $n$ -doped separate confinement heterostructure layers

Shunji Seki and Kiyoyuki Yokoyama

*NTT Opto-electronics Laboratories*

*3-1 Morinosato Wakamiya, Atsugi, Kanagawa, 243-01 Japan*

(Tel: 81-462-40-3279, Fax: 81-462-40-2859, Email: seki@aecl.ntt.co.jp)

Highly efficient 1.3- $\mu\text{m}$  strained-layer (SL) multiple-quantum-well (MQW) lasers operating over a wide temperature range have attracted much attention due to their applications to fiber-in-the-loop (FITL) and fiber-to-the-home (FTTH) systems [1]. For these applications, much effort has been focused on improving the device performance of long-wavelength lasers at elevated temperatures [2]-[5]. In this paper, we demonstrate that  $n$ -type doping in separate confinement heterostructure (SCH) layers exerts a great impact on optical gain over a wide range of temperature, and that this novel approach can lead to a significant improvement in the high-temperature performance of InP-based MQW lasers.

In InP-based SL-MQW structures, the spill-over of excess holes due to electrostatic deformation in band profiles plays a significant role in determining the device characteristics at elevated temperatures [4]. To accurately take this effect into account, the numerical approach involves solving the Poisson equation, the scalar effective-mass equation for the conduction band, and the multiband effective-mass equation for the valence band in a self-consistent manner [6].

We analyzed an SL-MQW structure sandwiched by an InGaAsP ( $\lambda_g=1.05\ \mu\text{m}$ , referred to as Q1.05 hereafter) SCH layer on an InP substrate. The SL-MQW stack consists of three 6-nm, 1.5%-compressively-strained InGaAsP quantum wells with 10-nm InGaAsP (Q1.05) barriers. The total thickness of the SCH layer was 50 nm. We studied three different types of doping profile: (a) an undoped SL-MQW with undoped SCH layers, (b) an undoped SL-MQW with  $n$ -doped SCH layers, and (c) an  $n$ -type modulation-doped (MD) SL-MQW with  $n$ -doped SCH layers. The donor concentration ( $N_d$ ) in the SCH layers was  $1.5 \times 10^{18}\ \text{cm}^{-3}$  and that in the barrier layers was  $1.0 \times 10^{18}\ \text{cm}^{-3}$ . In the type-(b) and (c) structures, the doping condition in the 10-nm InGaAsP SCH layer adjacent to the MQW stack was the same as that in the barrier layers. The peak-gain wavelength for the TE mode was 1.3  $\mu\text{m}$  at room temperature.

Figures 1(a), (b) and (c) show the valence-band profiles for 3-well SL-MQW structures with the three different doping profiles described above. The temperature is 373 K and the total sheet carrier density, which is the carrier density of the whole MQW structure including the QWs and the adjacent SCH regions, is  $9.6 \times 10^{12}\ \text{cm}^{-2}$ . The solid lines are the results obtained by a self-consistent numerical method and the dashed lines are the original band profiles. Due to the downward bending of the band profiles in the MQW region, the effective barrier height for the valence band ( $E_{VB}^{eff}$ ) becomes much smaller than the original value in the conventional SL-MQWs with the undoped SCH, as shown in Fig. 1(a). Owing to this reduction in  $E_{VB}^{eff}$ , the pile-up of holes in the SCH region can easily occur at elevated temperatures, leading to a significant deterioration in the high-temperature performance of

SL-MQW lasers [4].

On the other hand, in the SL-MQW structures with the  $n$ -doped SCH, the  $n$ -type doping causes a downward bending of the band profiles in the SCH region, as shown in Figs. 1(b) and (c). This downward bending in the SCH region cancels out that in the MQW region, and as a result, the overall band profiles resemble the original band profile. Hence,  $E_{\text{VB}}^{\text{eff}}$  becomes larger in these structures compared with the conventional SL-MQW structure. Since the  $n$ -type doping in the barrier region compensates the strong deformation in band profiles in this region,  $E_{\text{VB}}^{\text{eff}}$  becomes the largest in the type-(c) structure, as shown in Fig. 1(c). In this structure,  $E_{\text{VB}}^{\text{eff}}$  exceeds 175 meV, which is almost 50 meV larger than that in the conventional SL-MQW structure. It is, hence, expected that  $n$ -type doping in the barrier/SCH layers can profoundly suppress the pile-up of holes in those regions under high-temperature, high-injection conditions, which can bring about a marked improvement in the device performance of InP-based SL-MQW lasers at elevated temperatures.

Figure 2 shows the variations of the peak of optical gain with injected total sheet carrier density. The results calculated for the three different types of doping profile at two different temperatures are compared in this figure. The dotted, dashed and solid lines show the results for the type-(a), (b), and (c) structures, respectively. In the case of the undoped SL-MQW with the  $n$ -doped SCH, the optical gain at 373 K can be increased by about 60% at the injected carrier density of  $8 \times 10^{12} \text{ cm}^{-2}$ . When the  $n$ -type doping in the SCH is combined with the  $n$ -type modulation doping in the MQW, the optical gain is further increased and it becomes twice as large as that of the conventional structure. These results clearly indicate that the  $n$ -type doping in the SCH region exerts a significant impact on optical gain of InP-based SL-MQW structures over a wide range of temperature.

Another striking feature of these SL-MQW structures with  $n$ -doped SCH is their potential for reducing the power penalty ( $\Delta P_{\text{out}}$ ), which is the change in the light output power at a fixed drive current with increasing temperature. In Fig. 3,  $\Delta P_{\text{out}}$  with increasing temperature from 298 to 358 K is plotted as a function of drive current for the 3-well  $n$ -type MD-SL-MQW with the  $n$ -doped SCH (type-(c) structure). The experimental and calculated results for a conventional 6-well SL-MQW with an undoped SCH [7] are also shown for comparison. Here, the power penalty was calculated using the formula derived in [7]. In the  $n$ -type MD-SL-MQW with  $n$ -doped SCH,  $\Delta P_{\text{out}}$  can be reduced to less than one half of that in the conventional SL-MQW with the undoped SCH regardless of the amount of drive current. This marked reduction in  $\Delta P_{\text{out}}$  mainly arises from the fact that the  $n$ -type doping in the SCH region makes it possible to achieve larger optical gain at elevated temperatures as shown in Fig. 2.

In summary, we have proposed a novel SL-MQW structure that incorporates  $n$ -doped SCH layers with  $n$ -doped barrier layers. It has been demonstrated that the  $n$ -type doping increases the barrier height in the valence band effectively, thereby significantly enhancing the optical gain at elevated temperatures. Another significant feature of this approach is that the power penalty can be reduced to one half of that in conventional SL-MQW structures with an undoped SCH. On the basis of the results obtained in this study, we can conclude that SL-MQW structures with  $n$ -doped SCH layers have a great potential for realizing high-performance long-wavelength lasers operating over a wide range of temperature.

## References

- [1] J. Yoshida, *Tech. Dig. OFC'97*, Dallas, 275 (1997).
- [2] P. J. A. Thijs et al., *IEEE J. Lightwave Technol.* **12**, 28 (1994).
- [3] H. Oohashi et al., *Electron. Lett.* **31**, 556 (1995).
- [4] S. Seki et al., *IEEE J. Quantum Electron.* **32**, 1478 (1996).
- [5] Y. Sakata et al., *Tech. Dig. ECOC'97*, Edinburgh, 99 (1997).
- [6] S. Seki et al., *IEEE J. Select. Topics Quantum Electron.* **1**, 264 (1995).
- [7] S. Seki et al., *IEEE Photon. Technol. Lett.* **9**, 1205 (1997).

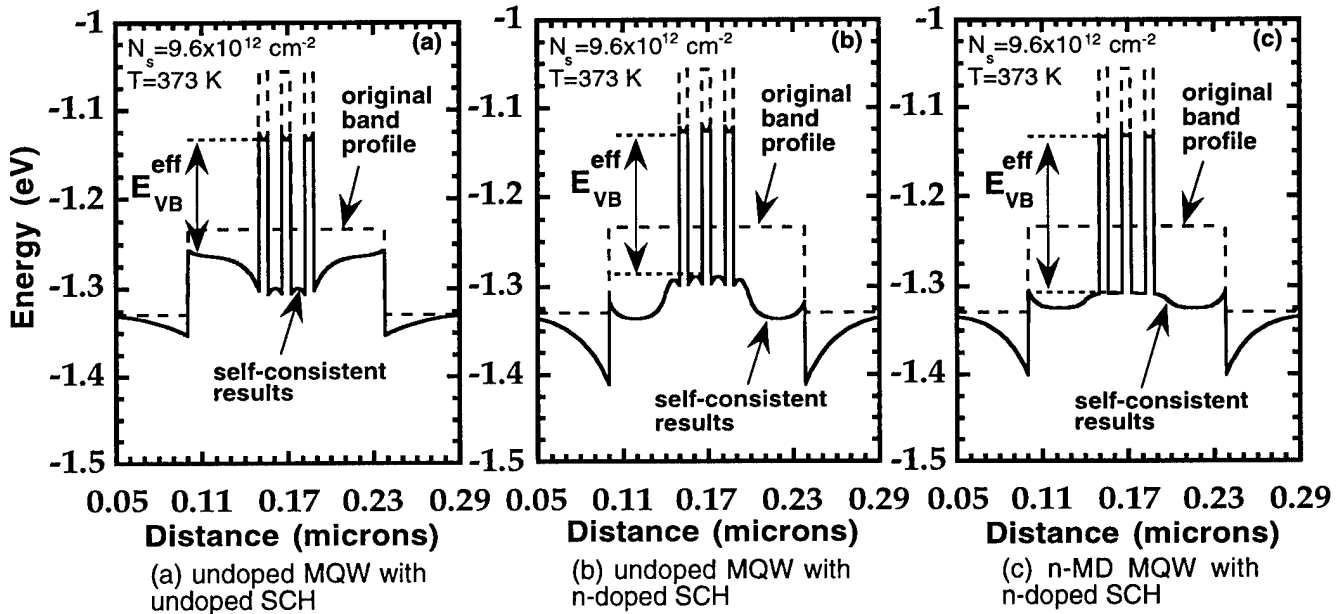


Fig. 1 Valence band profiles for 3-well SL-MQW structures with three different types of doping profile. The MQW stack consists of three 1.5%-compressively-strained QWs.

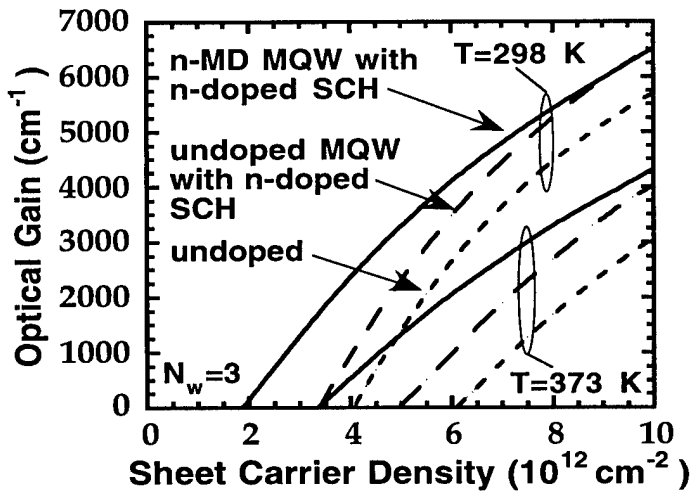


Fig. 2 Variations of the peak of optical gain with injected total carrier density.

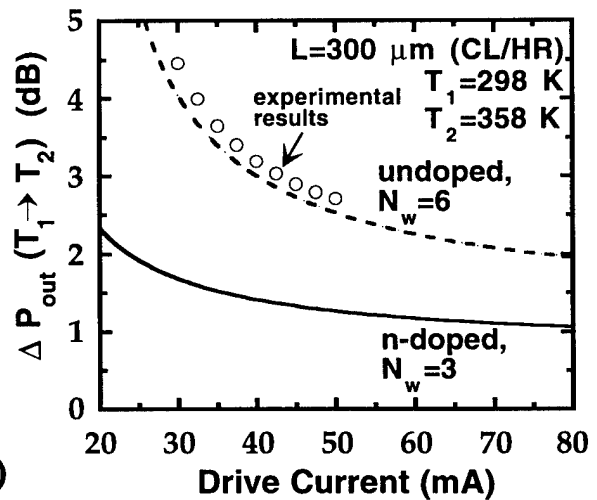


Fig. 3 Power penalty with increasing temperature from 298 to 358 K plotted as a function of drive current.

## Direct Measurement of Capture and Escape Rates in Quantum Well Active Layers

Kerry Vahala, Roberto Paiella, Guido Hunziker  
California Institute of Technology

Uzi Koren  
Lucent Technologies

In quantum well lasers and amplifiers, the transport of electrons and holes into and out of the quantum wells has been recognized as an important limiting factor in their dynamic response [1,2]. For example, each electron or hole involved in the emission of light in a quantum well laser is first transported to the lasing energy level by diffusion/drift to the active region and subsequently captured into the well. Quantum capture and escape phenomena in these structures are complicated processes that have been studied by various methods [3,4]. Recently, we introduced two distinct measurement techniques for the characterization of capture and escape processes in quantum well active layers. The results give a direct frequency-domain response function associated with the desired capture or escape process over a wide range of frequencies.

The first technique, polarization resolved four-wave mixing (FWM), provides frequency domain data on the carrier dynamics associated with inter-well transport [5]. This measurement is most sensitive to the escape rate from the quantum wells. The second, wavelength resolved four-wave mixing, provides the frequency response associated with the capture process [6]. Both techniques can measure their respective frequency response functions from low frequencies of a few GHz to high frequencies in excess of several 100 GHz. The two measurements can be made on a single device to map out both the capture and escape processes separately.

Four-wave mixing in semiconductor optical amplifiers involves input of two pump waves to the amplifier. These waves write dynamic gratings in the carrier density and temperature (the dominant mechanisms for pump detuning frequencies less than 200 GHz). This leads to modulation of the gain and refractive index and scatters energy from the original input waves into the FWM side

bands. The strength of these side bands as a function of detuning frequency reflects the underlying carrier dynamics of the quantum well system. An important feature of these FWM processes is that the formation of the dynamic gratings and the scattering are two entirely distinct processes. As such, they do not need to take place in the same spatial region of the semiconductor or involve the same energy levels. Specifically, by choosing the wavelength and polarization of the input waves appropriately, it is possible to selectively modulate carriers in certain regions of the semiconductor (or in certain energy states), and probe the optical response elsewhere.

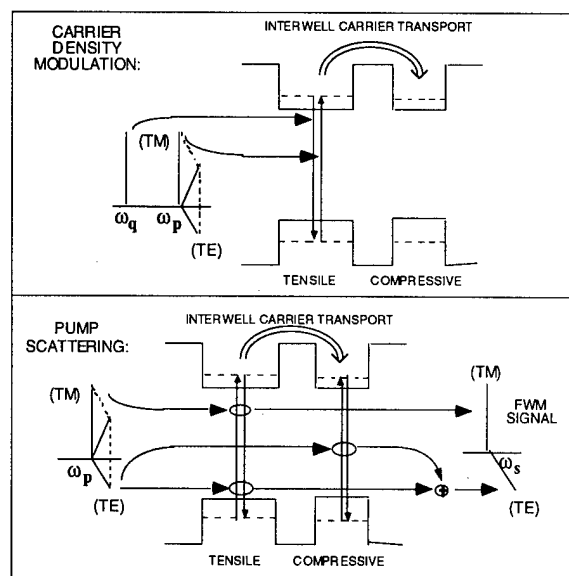


Figure 1: Selective excitation of tensile quantum wells and measurement of interwell transport by polarization resolved FWM.

**Interwell Transport:** This experiment uses a quantum well amplifier containing equal numbers of alternating tensile and compressive strained quantum wells. The

input waves were polarized as shown in figure 1 with TM polarized pumps. Since optical transitions are forbidden for the TM polarization in

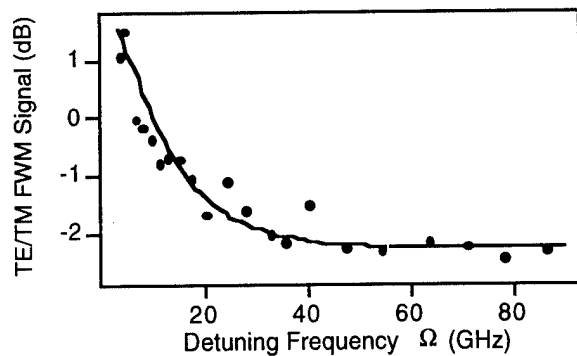


Figure 2: TE/TM FWM power versus detuning frequency showing enhancement below 40 GHz due to interwell transport.

compressive strained quantum wells, the induced modulation occurs only in the tensile wells. From there, the modulation can be transported to the compressive wells as indicated. Pump wave scattering occurs in two ways as shown in the figure. A conventional FWM TM component is generated by scattering of a TM pump component in the tensile wells. In addition, scattering of a TE wave (provided with one of the pump waves) will occur from modulation in the tensile well as well as from modulation transported to the compressive wells. By measuring the ratio of TE/TM FWM power versus frequency, we thus measure the effectiveness of the transport process. The measured ratio is plotted in

figure 2. At low detuning frequencies an enhancement due to the interwell transport of carrier modulation is apparent in the data. In addition a cut-off clearly appears for frequencies above 40 GHz indicating that the transport is inefficient for frequencies beyond this value.

**Capture Response** In a second measurement we have applied wavelength-selective four-wave mixing to induce carrier modulation in the barrier layers of the quantum well. This can be accomplished as shown in figure 3 using two single frequency lasers in the 1.3 micron band. The barrier modulation created by their photo-mixing will be captured into the quantum wells where the modulation can be probed using a 1.5 micron laser source that will be sensitive to the associated gain and refractive index variations.

By tuning the wavelength of one of the 1.3 micron lasers, it is possible to change the modulation frequency of the carrier density. The effectiveness of this modulation to scatter energy from the 1.5 micron laser beam and into the FWM signal will give direct information on the relaxation processes. We combine the 1.5 micron output with an optical local oscillator, and detect the beat frequency between the optical local oscillator and the FWM signal at a constant IF in the RF frequency band. In this way, the signal can be measured for mixing frequencies as low as a few GHz to as high as several 100 GHz.

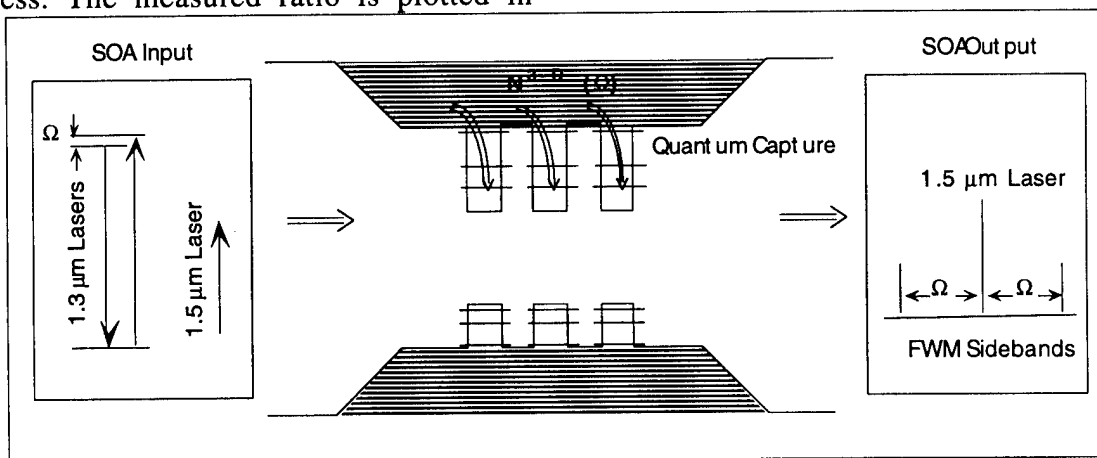


Figure 3: Schematic showing pump laser excitation of barrier states and probing of capture process. FWM sidebands are detected with an optical heterodyne receiver (not shown).

The raw response curve is shown in figure 4 and shows both a 20 dB/dec roll-off as well as a 40 dB/dec roll-off beyond a detuning frequency of 80 GHz. The 20 dB/dec roll-off is attributed to the stimulated interband lifetime of the carriers in the quantum well. By normalizing-out this constant roll-off, we arrive at the data presented in the inset to figure 4 showing more clearly the second pole at 80 GHz. This corner frequency should correspond to the capture rate for carriers

generated at the energy determined by the DFB laser wavelength. The magnitude of the capture rate in this particular measurement could be influenced by several factors. For example, the excitation energy used here places the carriers at the barriers edge and could enhance the capture process beyond, for example, what is more typical for carriers at higher energies. Other factors affecting this result will also be discussed.

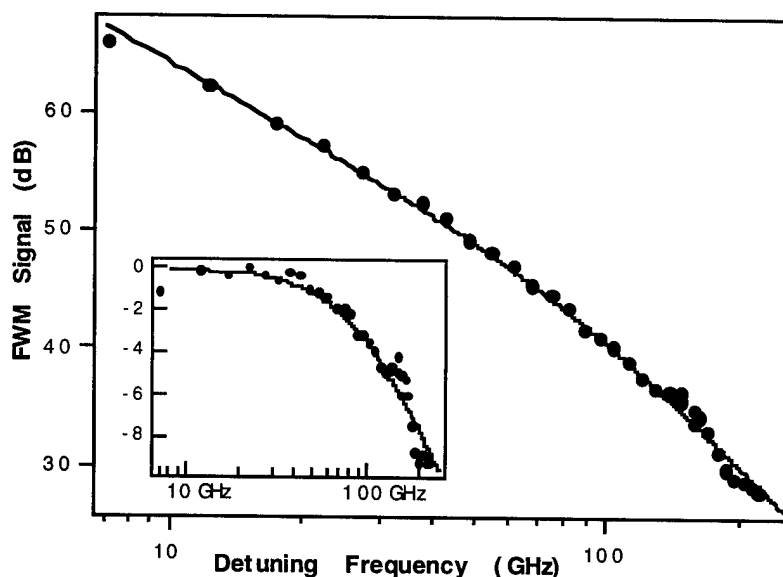


Figure 4: FWM signal versus the detuning frequency of the 1.3 micron pump lasers. Inset shows the same data with a 20 dB/dec roll-off factored out - leaving a response function including a possible capture pole at approximately 80 GHz.

## References

- [1] W. Rideout, W. F. Sharfin, E. S. Koteles, M. O. Vassell, and B. Elman, *IEEE Photon. Tech. Lett.*, Vol. 3, pp. 784 (1991)
- [2] S. C. Kan, D. Vassilovski, T. C. Wu, and K. Y. Lau, *Appl. Phys. Lett.*, Vol. 61, pp. 752 (1992)
- [3] S. Weiss, J. M. Wiesenfeld, D. S. Chemla, G. Raybon, G. Sucha, M. Wegener, G. Eisenstein, C. A. Burrus, A. G. Dentai, U. Koren, B. I. Miller, H. Temkin, R. A. Logan, and T. Tanbun-Ek, *Appl. Phys. Lett.*, Vol. 60, pp. 9 (1992)
- [4] S. Vassilovski, Ta-Chung Wu, Sidney Kan, K. Lau, C. Zah, *IEEE Photon. Tech. Lett.*, Vol. 7, pp. 706 (1995)
- [5] R. Paiella, G. Hunziker, K. J. Vahala and U. Koren, *Appl. Phys. Lett.*, Vol. 69, pp. 4142 (1996)
- [6] R. Paiella, G. Hunziker, K. J. Vahala and U. Koren, *Appl. Phys. Lett.*, Vol. 71, (25) (1997)



**Integrated Photonics Research**

# **Silicon Based Optoelectronic Technology**

**Tuesday, March 31, 1998**

**Richard A. Soref, Rome Laboratory, AFRL/SNHC**  
Presider

**ITuH**  
**1:30pm-3:00pm**  
Salon C

## Fabrication and characterization of a 1-to-48 fanout H-tree structure for clock signal distribution system

Linghui Wu, Bipin Bihari, Jianhua Gan, and Ray T. Chen  
Microelectronics Research Center, Department of Electrical and Computer Engineering  
The University of Texas at Austin, Austin, TX 78758  
Phone: (512) 471-7035      FAX: (512) 471-8575

Suning Tang  
Radiant Research, Inc., 9450 Research Blvd., Suite IV305, Austin, TX 78759  
Phone: (512) 338-4670      FAX: (512) 338-4645

Randy Wickman  
Cray Research, Inc., 655 Lone Oak Dr., Eagan, MN 55121

### Summary

The clock rate is one of the important parameters determining system performance in the high-speed computing environments. The state-of-the-art VLSI circuits are capable of operating and generating ultra-high clock rates ( $> 1$  GHz). However, clock signal distribution systems based on electrical interconnect technologies fail to keep up with the cycle times and pulse widths needed to synchronize the operation of logic devices over long distances. This timing bottleneck is a consequence of the variations in the transmission line propagation losses and dispersion, different packaging environments, and impedance discontinuities at the interfaces of the chips and boards. Further, capacitive loading, switching noise and signal cross-talk alter the clock signal waveform and become critical at high clock rates and large system lengths. These bottlenecks manifest themselves as clock skew and timing jitter in synchronous clock signal distribution systems. An array of novel optical interconnect architecture has been proposed to circumvent these bottlenecks [1-3]. For example, the latest T-90 microprocessor machines from Cray Research incorporate up to 36 processor-boards with a system clock speed of 500 MHz. All the boards in this system are synchronized to a central clock using an optical clock signal distribution system utilizing a high power semiconductor laser operating in conjunction with single-mode optical fiber array at  $1.3\ \mu\text{m}$ . Within the each board the clock signal distribution is still all electrical which puts a limitation on the further improvements in the overall system speed. The guided wave optical clock distribution system can effectively resolve this bottleneck at board-level applications.

A novel board-level optical clock signal distribution system based on polymeric channel waveguides in conjunction with waveguide output couplers and fast photodetectors will be discussed in this presentation. The guided wave optoelectronic interconnect network under development will be inserted into the Cray supercomputer boards to become an additional interconnection layer along with the electrical interconnection layers. The Cray T-90 supercomputer board consists of 52 vertical electrical interconnection layers with the board size of  $14.48 \times 26.67\ \text{cm}^2$  [4], and in order to implement an additional optoelectronic interconnection layer (OIL) for high-speed clock signal distribution, the Si-CMOS process compatibility and planarization of the OIL are the two major concerns required to be addressed. These two issues could be effectively handled by application of polyimide based waveguide structures. Our approach utilizes low-loss polyimides for optical channel waveguides which are Si-CMOS process compatible and all associated components including waveguides, waveguide grating couplers and waveguide splitters can be easily planarized.

In the OIL all the optical paths have to be of equal lengths to minimize the clock skew problems. A waveguide H-tree structure can provide the equal path lengths for 1-to-many fanouts. The optical components required for constructing such a H-tree system include low loss polymer-based channel waveguides, waveguide output coupler, and 3 dB 1-to-2 waveguide splitters. We

have constructed a 1-to-48 fanout H-tree waveguide structure using polyimide planarization and photolithographic technique. Fig. 1 shows a photograph of the waveguide H-tree system constructed using Ultradel 9120 polyimide. The optical clock signal delivered by an optic fiber will be coupled into the input end of the OIL. At the output end the optical signal will be coupled-out by surface-normal grating coupler and will be converted into the electrical signal by a fast-photo detector.

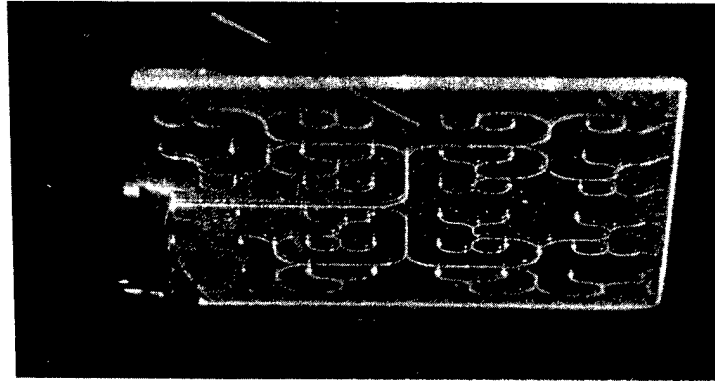


Fig.1 Photograph of the 1-to-48 fanout H-tree on quartz substrate using Ultradel 9120 polyimide. He-Ne laser beam at  $\lambda=633$  nm was coupled into the input end using a prism coupler.

High-speed operation and massive fanout requirements impose stringent conditions on the material selection, minimization of waveguide propagation loss, and optimization of output coupling efficiencies. Ensuring enough optical power at the end of photodetectors for high-speed operation is essential. For example, the total optical splitting power budget is 18 dB (3x6) in an optical H-tree system (capable of providing 64 fanouts), which consists of six stages of 1-to-2 (3 dB) optical fanout. If the optical power at the input end is 10 dBm, and a 1.3 GHz optical receiver (having a sensitivity of -18 dBm at 1 GHz), [5] is used at output end for signal detection, the total insertion loss (output coupling loss plus waveguide propagation loss) should be less than 10 dB. Experimentally estimated loss at each fanout of the H-tree structure shown in Fig. 1 is 38.04 and 34.44 dB at operating wavelengths of 633 and 830 nm, respectively. These loss figures can be further improved by optimizing the feature size at the 1-to-2 waveguide splitters and purifying the polyimide.

To ensure the desired electrical and mechanical properties imposed by the Cray supercomputer board, and to meet the required optical properties for the low-loss waveguide formation, Ultra-9000 series photosensitive polyimides (Amoco Chemicals) [6] are used for the waveguide fabrication. Fully cross-linked polyimides have an excellent thermal stability ( $T_g = 400^\circ\text{C}$ ) and optical transparency. The high  $T_g$  is critical for it to survive wire-bonding and metal deposition process, which makes it compatible with silicon CMOS processing. To fabricate the channel waveguides, the photosensitive polyimide was first spin-coated on the substrate, followed by a soft-curing process to remove the solvent. After the UV exposure, a post-exposure bake at  $175^\circ\text{C}$  was made following a process to form the H-tree waveguides. Finally, the fabricated H-tree was post-baked at  $260^\circ\text{C}$  to remove residual solvent and to improve its solvent resistance.

Efficient output coupling is another important factor to be addressed for reasonable performance from the OIL. We are investigating polymer-based tilted waveguide gratings as potential approach. Note that a  $45^\circ$  waveguide end mirror is not suitable in this case because of the requirement of planarization imposed by the vertical integration of the other electrical interconnection layers. The tilted grating waveguide couplers can surface-normally couple the optical signal into and out of a channel waveguide. The surface-normal feature of fanout beams and the planar compact device structure convert the most difficult three spatial and three angular multiple alignment problem into a single step 2-D planar one. Fig. 2 shows a photograph of such

an input-grating coupler on glass substrate. Because of the reciprocity of the tilted grating coupler same structure can be used for output coupling as well. We have experimentally estimated an output efficiency of  $\sim 35\%$ , which has potential for further improvements. Our theoretical prediction indicate that an efficiency as high as 70% is achievable by using high index polyimides and fine tuning the grating parameters such as grating period, depth, and tilt angles [7].

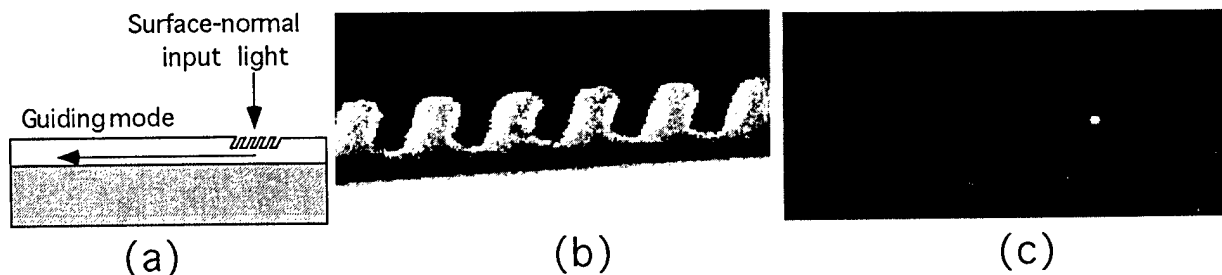


Fig. 2. (a) The schematic of a surface-normal input coupling using tilted grating. (b) SEM micrograph of polyimide tilted-grating with tilt angle of  $\sim 32^\circ$ . (c) The photograph of coupling a surface-normal input laser into the 9120D polyimide waveguide.

Experiments are underway to verify the bandwidth of H-tree structure in conjunction with waveguide grating coupler, and results will be discussed in detail in the presentation. Preliminary measurements were performed on a straight channel waveguide launching an 1-GHz optical signal generated by a laser diode at  $1.3 \mu\text{m}$  and a high-speed transmitter (2556T, Force Inc.), and detecting by a high-speed receiver (2556R, Force Inc.) and a Tektronics 11403 Digitizing Oscilloscope. The sinusoidal 1-GHz modulation applied on the transmitter was provided by a HP 8656B signal generator. Initial observations indicate that the speed of the optical signal was limited by the transmitter bandwidth (1.3-GHz) and the speed of the (HP 8656B) signal generator (1-GHz), rather than the channel waveguide length.

In conclusion, we present results and progress towards our effort to construct an optoelectronic interconnection layer for the high-speed massive clock signal distribution for the Cray T-90 supercomputer board. The optical interconnection layer under development employs optical multimode channel waveguides in conjunction with surface-normal waveguide grating couplers. Equalized optical paths are realized using an optical H-tree structure having 48 optical fanouts which could be increased to 64 without any additional complication introduced.

## 5. References

1. Ray. T. Chen, H. Lu, D. Robinson, Michael Wang, Gajendra Savant, and Tomasz Jansson, "Guided-wave planar optical interconnects using highly multiplexed polymer waveguide holograms," *IEEE J. Light. Technol.*, vol. 10, pp. 888-897, 1992.
2. Bradley D. Clymer and Joseph W. Goodman, "Optical clock distribution to silicon chips," *Opt. Eng.*, vol. 25, pp. 1103-1108, 1986.
3. R. W. Wickman, "Implementation of optical interconnects in GibaRing supercomputer channel", *Proc. SPIE*, vol. CR62, pp. 343-356, 1996.
4. Suning Tang and Ray T. Chen, "1-to-42 optoelectronic interconnection for intra-multichip-module clock signal distribution," *Appl. Phys. Lett.*, vol. 64, pp. 2931-2933, 1994.
5. Data Sheet of VSC7810, Vitesse Semiconductor Corporation.
6. T. C. Kowalczyk, T. Kosc, and K. D. Singer, P.A. Chhill, C. H. Seager, and M. B. Meinhardt, A. J. Beuhler and D. A. Wargowski, "Loss mechanism in polyimide waveguides," *J. of Appl. Phys.*, vol. 76, no. 4, pp. 2505-2508, 1994.
7. Feiming Li, Linghui Wu, Bipin Bihari, Suning Tang and Ray T. Chen, "Unidirectional surface-normal wave-guide grating couplers for wafer-scale MCM interconnect," to be submitted to *IEEE Photonics Tech. Lett.*

# Waveguide-Fed SiGe Avalanche pin Photodetector Grown on SOI Substrate with 0.2A/W External Responsivity at 1.3 $\mu$ m

T. Yoshimoto\*, S. Thomas, K.L.Wang and B.Jalali

Electrical Engineering Department,  
University of California Los Angeles,  
CA 90095-1594, USA

## Abstract

We demonstrate a SiGe avalanche photodetector grown on a silicon-on-insulator(SOI) passive waveguide. The thick SOI waveguide couples the light from an optical fiber into the SiGe detector with strain-limited thin absorption region. The detector exhibits low dark current, sharp breakdown and an external responsivity of 0.2A/W at 1.3 $\mu$ m.

\* On leave from Department of Electronic and Information Engineering,  
Hokkaido Tokai University, Sapporo, 005 Japan

SiGe photodetector operating at  $1.3\mu\text{m}$  and  $1.55\mu\text{m}$  constitute an attractive alternative to III-V based device. The ability to integrate SiGe detectors with conventional silicon integrated circuits can result in a low cost silicon based OEIC technology [1-4]. Since the strain limits the maximum thickness of SiGe layers, waveguide detectors are preferred over normal incident structure. While the internal efficiency is increased in waveguide photodetector structure, the overall performance is severely limited by the poor coupling efficiency from fiber into the thin SiGe waveguide core. One attractive solution is to integrate the detector with an SOI waveguide that has a large core and high numerical aperture. Using etch and regrowth, an integrated device based on a pin junction photodetector butt coupled to a passive SOI waveguide has been demonstrated[2]. Here we demonstrate an avalanche photodetector (APD) based on evanescent coupling between a passive SOI waveguide and a SiGe waveguide over layer. The device is simple to fabricate and shows excellent electrical characteristics with  $0.2\text{A/W}$  external responsivity before AR coating.

$n^+\text{Si}$	500Å
$n^+\text{Si}$	1500Å
$i\text{Si}_{0.56}\text{Ge}_{0.44}$	66Å
$i\text{Si}$	480Å
$\times 12$	
$p^+\text{Si}$ buffer	8000Å
$p^-\text{Si}$	$2\mu\text{m}$
$\text{SiO}_2$	$1\mu\text{m}$
Si Substrate	

Fig.1 Layer structure for the detector.

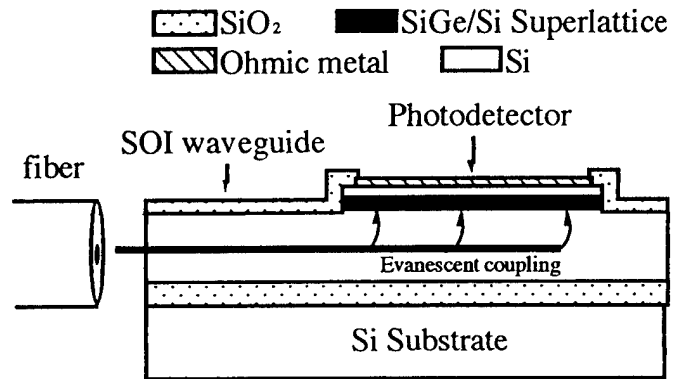
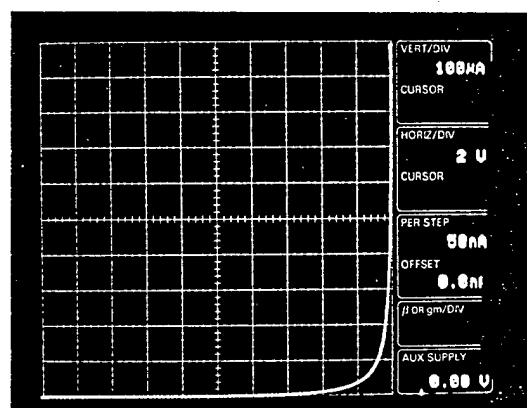


Fig.2 Schematic structure of waveguide coupled photodetector.

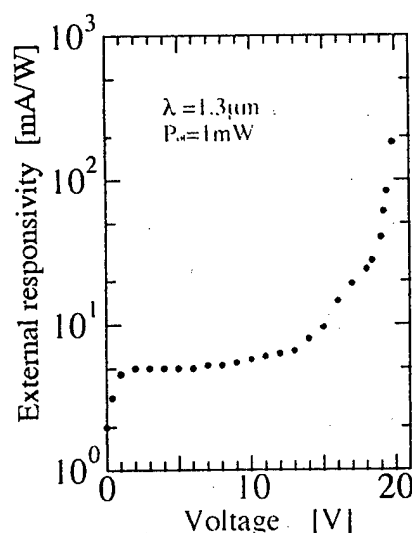
Figure 1 shows the layer structure for the detector. The substrate is (100) oriented SOI wafer( $\text{SiO}_2$   $1\mu\text{m}$ ,  $p\text{-Si}$   $2\mu\text{m}$ ). The  $8000\text{Å}$   $p^+$  layer( $p=8\times 10^{18}\text{cm}^{-3}$ ) serves as the buffer and contact. A 12 period undoped  $66\text{Å}$   $\text{Si}_{0.56}\text{Ge}_{0.44}$  /  $480\text{Å}$   $\text{Si}$  is used as the absorption region. The top contact is formed by a  $1500\text{Å}$   $n=5\times 10^{18}\text{cm}^{-3}$  and a  $500$

$\text{\AA}$   $n=1 \times 10^{19} \text{cm}^{-3}$  layers. The layers were grown by solid source molecular beam epitaxy (MBE). The growth temperature was  $500^\circ\text{C}$  for the the buffer layer and superlattice layer and from  $400^\circ\text{C}$  to  $600^\circ\text{C}$  for the top layer.

The device was fabricated using standard processing technology. An Al top contact was evaporated and patterned with wet chemical etching. The waveguide was defined using reactive ion etching (RIE) of Si and SiGe layers. The detector area is  $30 \times 500 \mu\text{m}$ . After the RIE step, a  $5000 \text{\AA}$   $\text{SiO}_2$  passivation layer was deposited by plasma enhanced CVD (PECVD) at  $300^\circ\text{C}$ . Figure 2 shows the waveguide coupled photodetector structure. Light is coupled from a single mode fiber into the cleaved facet of the SOI waveguide. In the photodetector region, the light transfers into the higher refractive index SiGe absorption layer via evanescent coupling.



(a)



(b)

Fig.3 (a) Measured reverse bias characteristics, (b) Measured external responsivity at  $1.3 \mu\text{m}$  wavelength as a function of applied bias.

The device shows excellent current-voltage characteristics indicating the high quality of epitaxial layers. Figure 3(a) shows the measured reverse bias characteristics. The reverse leakage current is  $70 \text{pA}/\mu\text{m}^2$  at  $10 \text{V}$  with a sharp breakdown at the

reverse bias of 20V. Figure 3(b) shows the measured external responsivity of the device for  $1.3\mu\text{m}$  incident light. As the applied bias is increased beyond 15V, the external responsivity increases rapidly by the avalanche multiplication process. The external responsivity at 20V reaches 0.2A/W corresponding to the avalanche multiplication factor of  $M=34$ .

**Acknowledgements** The authors would like to acknowledge Dr. F. Coppinger and Dr. F. Huang for useful discussion. Help from Mr. A. Kane and Mr. S.Yegnanarayanan for device fabrication process is also acknowledge. This work was supported by DARPA.

## References

- (1) S.Luryi, T.P.Pearsall, H.Temkin, and J.C.Beam, "Waveguide infrared photodetector on a silicon chip," *IEEE Electron Device Lett.*, vol.7, pp.104-107, 1986.
- (2) A.V.P.Kesan, P.G.May, E. Bassous, and S.S.Iyer, "Integrated waveguide-photodetector using Si/SiGe multiple quantum wells for long wavelength applications," in *Proc. IEDM*, San Francisco, CA, 1990, pp.26.7.1-4.
- (3) B.Jalali, L.Naval, and A.F.Levi, *J.Lightwave Technol.*, "Silicon-based receivers for optical data links," vol.12, pp.930-935, June 1994.
- (4) A.Splett and K.Petermann, "Ultimate performance of SiGe/Si multiquantum well waveguide-photodetector combinations," in *ECOC'94. 20th European Conf. Optic. Commun.*, Firenze, Italy, Sept. 25-29, 1994, vol.2., pp.861-4.

## Gbit/s Integrated Si/InGaAs Telecommunication Photodetectors

B. F. LEVINE

Bell Laboratories, Lucent Technologies,  
600 Mountain Ave, Murray Hill, NJ 07974

The advantages of directly bonding Si and III-V wafers to fabricate novel integrated devices which maximize the advantages of each material are well known<sup>1,2</sup>. We will discuss planar high performance  $\lambda=1.55\mu\text{m}$  telecommunication photodetectors on a Si substrate. The fused Si/InGaAs interface is in the center of the active device region, and therefore, these detectors can be used to study, in detail, the interface characteristics which are important for both PINs and avalanche photodiodes (APDs). Our detectors show high internal quantum efficiency ( $\eta \approx 100\%$ ), high speed (RC limited frequency response of 21 GHz), record low dark current ( $I_d < 100$  pA at a bias of 4 V), a long generation recombination lifetime of 400 ns, and a forward bias ideality factor of  $n=1.1-1.2$ . In addition, capacitance-voltage measurements and absolute photocurrent noise measurements show no evidence of charge trapping, recombination centers or a conduction bandgap discontinuity at the heterointerface. Thus, the Si/InGaAs interface is nearly ideal for high performance PINs and APDs.

1. A. R. Hawkins, T. E. Reynolds, D. R. England, D. I. Babic, M. J. Mondry, K. Streubel, and J. E. Bowers, Appl. Phys. Lett. **68**, 3692, (1996).
2. B.F. Levine, A.R. Hawkins, S. Hiu, B.J. Tseng, C.A. King, L.A. Gruezeke, R.W. Johnson, D.R. Zolnowski, and J.E. Bowers, Appl. Phys. Lett. **70**, 2449, (1997).

## Silicon-on-Insulator Waveguide Bragg Gratings

Jolyon Tidmarsh and John Drake

Bookham Technology Ltd., 90 Milton Park, Abingdon, Oxfordshire, OX14 4RY, U.K.

### Introduction

Grating based devices are attractive in dense wavelength division multiplexing systems, (DWDM). An alternative approach to fiber gratings can be based on silicon waveguides which can be fabricated successfully using SOI rib waveguides. Bookham's proprietary ASOC™ technology<sup>1,2</sup> is based on the formation of single mode rib waveguides<sup>3</sup> offering excellent properties in the 1.3 and 1.55 micron telecommunications bands. A cross section of an ASOC™ waveguide is shown in figure 1. The advantages offered by ASOC™ include low loss, low birefringence waveguides, mass production capability utilizing established Si technology, and hybrid/monolithic integration of active components. DWDM devices based on SOI waveguides could therefore offer significant advantages over competing technologies such as fibre and silica by enabling lower cost, increased functionality and potential for subsystem integration.

This paper describes the design, fabrication and performance results of such waveguide grating structures and their potential applications in DWDM.

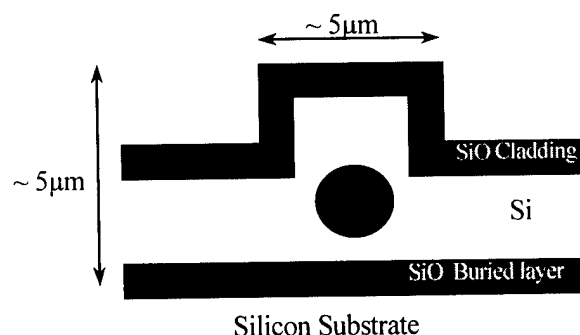


Figure 1. Cross section of the ASOC™ waveguide

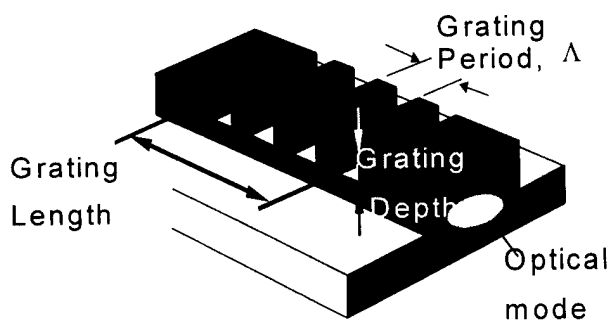


Figure 2. Schematic of ASOC™ waveguide grating

### Grating design

Bragg waveguide gratings are formed by modulating the propagation constant of the optical mode. On SOI waveguides, this is achieved by etching slots across the waveguide to modulate the effective refractive index ( $n_{\text{eff}}$ ) of the waveguide as shown in figure 2.

At each  $n_{\text{eff}}$  step a fraction of the optical power is reflected back down the waveguide. A reflected beam will only result at wavelengths where the phase difference between each of the reflections is an integer number of wavelengths. This gives the Bragg condition,

$$\lambda_{\text{Bragg}} = 2n\Lambda N$$

This relates the wavelength at which the reflectance is greatest,  $\lambda_{\text{Bragg}}$  the Bragg wavelength, to the period of the grating,  $\Lambda$ , and the average effective index of the waveguide in the grating region,  $n$ .  $N$  is an integer representing the grating order. As  $N$  increases the grating period increases making the required lithography easier, however the reflector becomes much less efficient. Hence for operation in the 1550nm telecommunications window the grating period needs to be approximately 220nm for a first order grating.

The optical properties of the Bragg grating are determined by the grating period, mark:space ratio, grating length and etch depth.

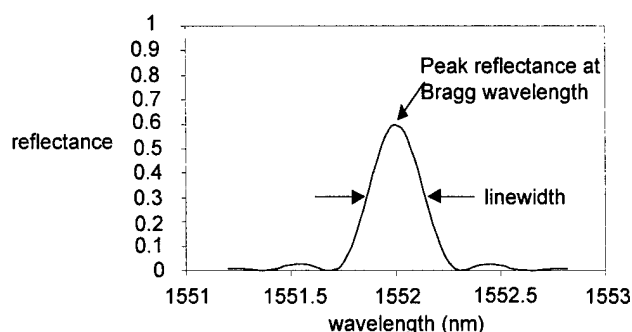


Figure 3. Schematic of reflection spectrum

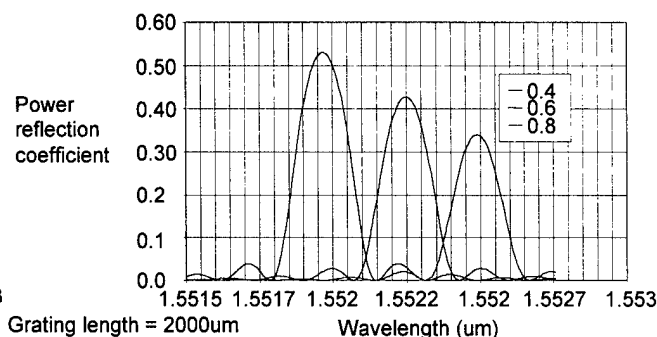


Figure 4 – simulated reflection spectra

The design of the gratings was determined from the required spectral linewidth and peak reflectance and these are both related to the grating length and the coupling coefficient,  $K$ .  $K$  is a function of the etch depth and the mark:space ratio. Using a computer programme spectral plots were attained for various grating lengths and etch depths. The graph below shows reflectance spectra for three etch depths of 0.4, 0.6 and 0.8  $\mu\text{m}$  for a 2mm long grating.

### Fabrication

The 220nm period gratings were patterned using direct write electron beam lithography to produce the 110nm lines and spaces. The pattern was transferred into the waveguide using dry etching. A range of different etch depths and lengths were produced. A typical ASOC<sup>TM</sup> waveguide grating is shown in figure 5 opposite.

### Results

The grating spectra were measured using a tunable laser, wavemeter and personal computer to collect the data. The input light was set to be plane polarised and the ASOC<sup>TM</sup> chips were mounted on a temperature stabilised mount.

Figure 6 shows the reflection spectrum from a 2mm long 0.8  $\mu\text{m}$  deep grating.

As can be seen there are slight sidemodes and the peak is very clean. The spectrum is very close to that simulated in figure 4. We have measured gratings with linewidths from 70 to 300pm.

For application in DWDM devices the ability to produce gratings with a variety of Bragg wavelengths is very important. The chart below shows reflection spectra from gratings produced on the same wafer, all taken at the same temperature.

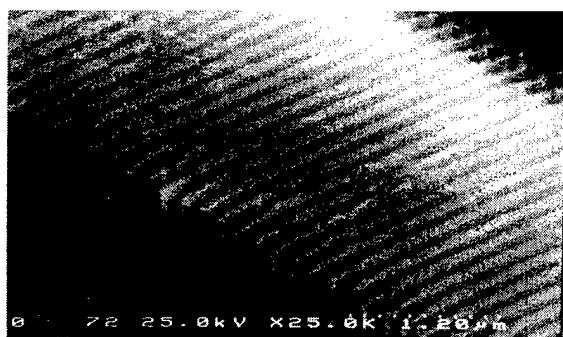
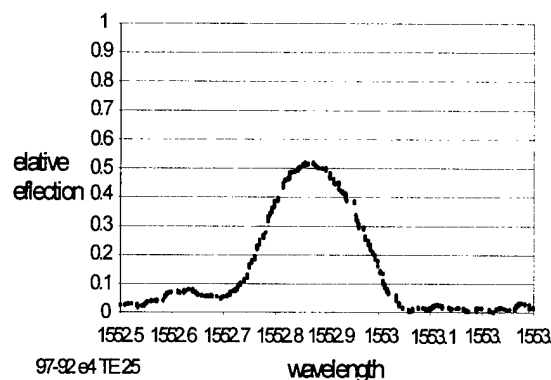
Figure 5 – ASOC<sup>TM</sup> waveguide grating

Figure 6 – Measured Reflection spectrum

In order to enhance the channel registration accuracy in such systems it may be useful to tune the Bragg wavelength and this can be done by changing the temperature of the ASOC<sup>TM</sup> chip. This causes a change in the bulk refractive index of silicon and for the grating to expand mechanically. In this way

the thermal coefficient of the Bragg wavelength has been measured to be  $86\text{pmK}^{-1}$ . The major contribution to this is the thermal change in the refractive index of Si.

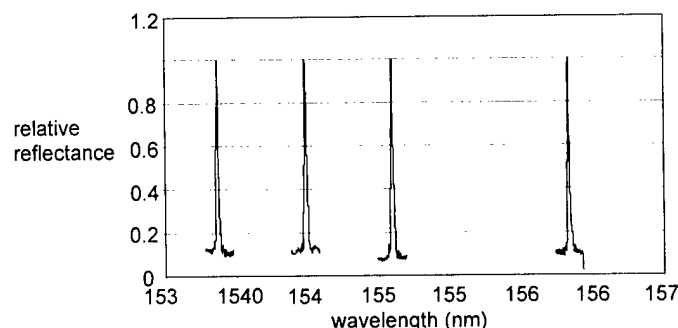


Figure 7. Reflection spectra from four waveguide gratings

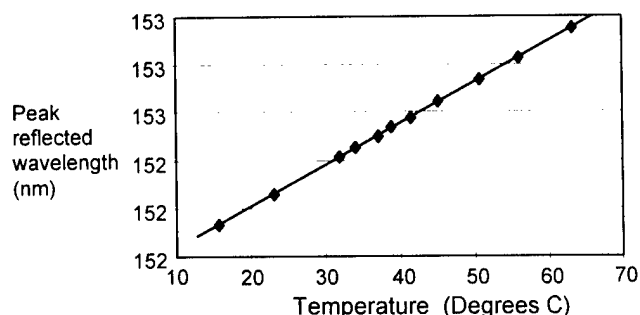


Figure 8 Variation of Bragg wavelength with temperature

### Possible Applications

One possible application of these gratings is to produce an 'add-drop multiplexer'. Two identical waveguide gratings arranged between two 50-50 couplers in a Mach-Zender configuration can achieve this function<sup>4</sup>. In the figure below, a stream of eight wavelengths enters at port A and is split equally into the grating regions of the two arms. Light in the specified wavelength range is reflected back and exits the device at port B. The remaining light propagates through the device and exits at port D. In this case the design wavelength is dropped from the incoming signal. This configuration can also be used to simultaneously add light at this wavelength.

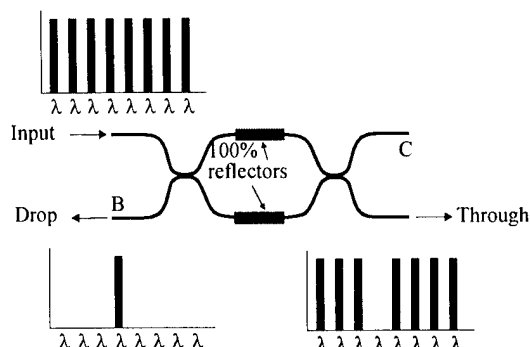


Figure 9 Add Drop Multiplexer

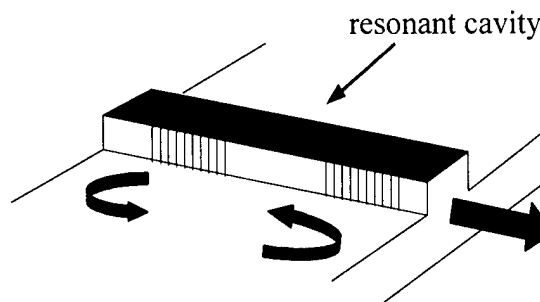


Figure 10 Silicon Resonator

A second application is the production of optical resonators – formed by placing a section of unperturbed waveguide between two gratings. Such a structure may be useful in an all silicon light emitting device<sup>5</sup>.

### References

- 1 A.Harpin, SPIE 3007, p.128(1997)
- 2 T.Bestwick, "Integrated Optics: Moulding Photonic Components into Solutions", Photonics Spectra p132 February 1997
- 3 R A Soref, J Schmidtchen and K Petermann, IEEE J.Quantum Electronics. 27 p1971 (1991)
- 4 C M Radgale, T J Reid et al, Electronics Letters, 28 no 8, p712. (1992)
- 5 J Foresi, L Giovane et al, Proc. MRS Fall Meeting 1997 (to be published)

## AMORPHOUS SILICON LIGHT MODULATORS FOR I.R. FIBER OPTIC DIGITAL COMMUNICATIONS

G. Cocorullo<sup>1,3</sup>, F. G. Della Corte<sup>1</sup>, R. De Rosa<sup>2</sup>, I. Rendina<sup>1</sup>, A. Rubino<sup>2</sup> and E. Terzini<sup>2</sup>

<sup>1</sup>Consiglio Nazionale delle Ricerche - Istituto di Ricerca per l'Elettromagnetismo e i Componenti Elettronici (IRECE-CNR), Via Diocleziano 328, I-80124 Napoli - Italy  
tel. + 39.81.5707999 - fax + 39.81.5705734

<sup>2</sup>Ente per le Nuove Tecnologie, l'Energia e l'Ambiente - Centro Ricerche Portici (ENEA-CR Portici), Via del Vecchio Macello, I-80055 Portici (Napoli) Italy  
tel. + 39.81.7723111 - fax + 39.81.7723344

<sup>3</sup>Università della Calabria - Dipartimento di Ingegneria Elettronica,  
I-87036 Rende (Cosenza) Italy

A growing and renewed interest is addressed to silicon for the possibility it gives of integrating VLSI electronic circuits with photonic devices onto the same chip [1]. The new thin film silicon technology, in particular, seems to be a good candidate for this purpose. Besides the classical Chemical Vapor Deposition (CVD) technique, requiring substrate temperatures usually in excess of 550 °C, the Plasma Enhanced CVD (PECVD) at lower temperature (200 ÷ 300 °C) is finding interesting applications in the fabrication of amorphous silicon-based optoelectronic devices, which are compatible with the standard microelectronic technology. The biggest advantage offered by this technique is the possibility of tuning the band-gap by varying the gas phase composition in the plasma. Thanks to this peculiarity several amorphous silicon-based optoelectronic devices have been fabricated, like light emitting diodes [2], photodetectors [3,4], optocouplers [5] and low-loss optical waveguides [6].

In this paper a new amorphous silicon based light modulator, integrated in a low loss rib-like waveguide, is reported. The device consists of a Fabry-Perot interferometric cavity which modulates light by exploiting the strong Thermo-Optic Effect (TOE) present in a-Si [7].

The modulator fabrication steps are as follows. The starting material is a 500-μm-thick, Sb highly doped, <100> oriented, crystalline silicon wafer. A planar waveguiding structure, consisting of a 0.4-μm-thick a-SiC undercladding layer and a 3-μm-thick a-Si core layer, is deposited on it by low temperature PECVD. Details on deposition conditions can be found in [6]. The strong radiation confinement, obtained thanks to the refractive index step profile ( $n \approx 3.4$  and  $2.9$  for a-Si and a-SiC respectively), and the very low absorption coefficient ( $\alpha < 0.1 \text{ cm}^{-1}$ ) of the a-Si layer in the  $1.3 \div 1.5 \text{ μm}$  wavelength range, give rise to a guiding structure characterized by propagation losses as low as  $0.7 \text{ dB/cm}$  [6]. A  $0.1\text{-μm}$ -thick tungsten layer is then deposited by e-beam evaporation. This film is then patterned by photolithography to define, at the same time, the resistive film and the ribs. In particular, a selective etch based on a  $\text{KH}_2\text{PO}_4/\text{KOH}/\text{K}_3\text{Fe}(\text{CN})_6$  solution is used for tungsten. Subsequently, using tungsten as the mask, the rib is created by reactive ion etching in a standard  $8\% \text{ O}_2/\text{CF}_4$  mix at room

temperature. The etching depth is 1.2  $\mu\text{m}$ . The last step was the evaporation and definition of 1- $\mu\text{m}$ -thick Al bond pads. When crossed by a current pulse, the tungsten layer acts as a resistive heater activating the thermo-optic modulation.

Waveguides with widths of 20, 30, 40, and 50  $\mu\text{m}$  have been realized, and then Fabry-Perot modulators with various lengths obtained by substrate cleaving. A schematic of the devices, with the relative thickness of the films, is reported in fig. 1.

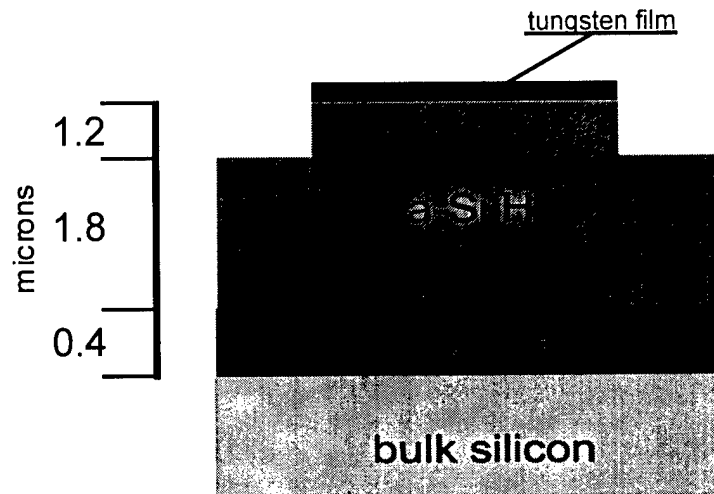


Fig. 1 Cross section of the rib waveguide Fabry-Perot modulators. The ribs are 20-, 30-, 40-, and 50- $\mu\text{m}$ -wide.

A preliminary device characterization has been performed by measuring the modulated reflected light intensity. To this aim the cleaved modulators have been bonded on TO39 metal cases. A 1.3- $\mu\text{m}$ -DFB fiber pigtailed laser diode has been coupled to the first input arm of a 3-dB Y-branched single mode fiber coupler. The single output fiber of the coupler goes to the modulator while the second input arm is coupled to an InGaAs photodetector. Typically, 30 dB overall insertion losses between source and detector were measured. These very high loss values are mainly due to the poor fiber-to-fiber alignment setup and to the dimensional mismatch between the 5- $\mu\text{m}$ -core monomode fiber and the modulator input face, which greatly limit the collection efficiency of the reflected beam. For this reason, the signal detection necessitates of a high transimpedance, limited bandwidth current amplifier.

The modulation pattern at the repetition frequency of  $\sim 600$  kHz measured in a 1-mm-long, 30- $\mu\text{m}$ -wide cavity is reported in fig. 2 (upper trace). The driving voltage pulses (lower trace) have an amplitude of 18 V and a duty cycle of 0.2. In this case the tungsten film has a resistance of 600  $\Omega$ . Maximum repetition frequencies of about 700 kHz were measured in the same device. This limit was mainly due to the low bandwidth of the detection apparatus, and we think it does not represent the actual speed limit of the device under test.

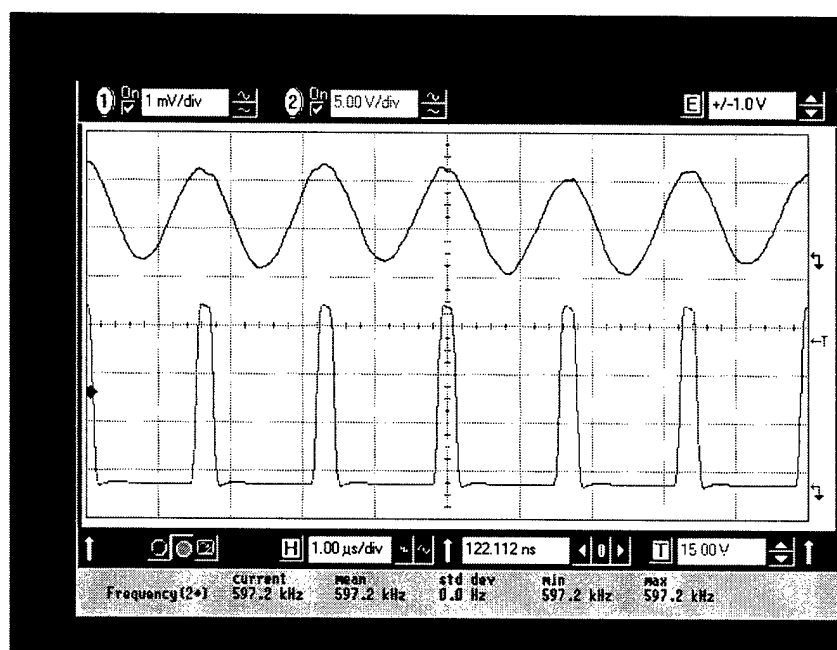


Fig. 2 Experimental plots of the driving voltage pulses (lower trace) and the corresponding light intensity modulation pattern (upper trace).

The preliminary results carried out indicate that modulation frequencies beyond 1 MHz could be reached in similar devices, but with a smaller waveguide cross-section, therefore characterized by a lower thermal capacitance. Furthermore, the evaluation of different undercladding materials is under way with the aim of exploiting a more thermally conductive layer between the a-Si waveguide core and the heat-sinking substrate, as for instance ZnO or other conductive oxides. Moreover, these materials show lower refractive indexes compared to that of a-SiC, which should allow an improvement of the guiding characteristic even with thinner undercladding layers.

## REFERENCES

- [1] R. A. Soref, Proc. IEEE, **81** (20), 1687 (1993)
- [2] O. B. Gusev, A.N. Kuznetsov, E. I. Turekov, M. S. Bresler, V. K. Kudoyarova, I. N.Yassievich, B. P. Zakharchenya, W. Fuhs, Appl. Phys. Lett., **70**, 240 (1997)
- [3] P. P. Deimel, B. B. Heimhofer, G. Krötz, H. J. Lilienhof, J. Wind, G. Muller, E. Voges, IEEE - Photon. Tech. Lett., **7**, 499 (1990)
- [4] M. Okamura, S. Suzuki, IEEE - Photon. Tech. Lett., **6**, 412 (1994)
- [5] D. Kruangam, T. Sujaridchai, K. Chirakawikul, B. Ratwises, S. Panyakeow, 17<sup>th</sup> Int. Conf. on Amorphous and Microcrystalline Semicond., Budapest, HU, 1997
- [6] G. Cocorullo, F. G. Della Corte, R. De Rosa, I. Rendina, A. Rubino, E. Terzini, 17<sup>th</sup> Int. Conf. on Amorphous and Microcrystalline Semicond., Budapest, HU, 1997
- [7] G. Cocorullo, F. G. Della Corte, I. Rendina, C. Minarini, A. Rubino, E. Terzini, Opt. Lett., **21**, 2002 (1996)



**Integrated Photonics Research**

# Electrooptic Materials and Devices

**Tuesday, March 31, 1998**

**William Minford, Lucent Technologies/Bell Laboratories**  
President

**ITul**  
**1:30pm–3:00pm**  
Saanich Room

# INFLUENCE OF PHASE STATE OF $\text{Li}_{1-x}\text{H}_x\text{NbO}_3$ WAVEGUIDING LAYER ON RATE OF COPPER EXCHANGE AND PHOTOREFRACTIVITY

S.M. Kostritskii

Physics Dept., Kemerovo State University, 650043 Kemerovo;

Fax: (3842) 525383; E-mail: root@chsb.kemgu.kemerovo.su

Yu.N. Korkishko, V.A. Fedorov

Chemistry Dept., Moscow Institute of Electronics Technology,

103498 Moscow, Zelenograd, Russia;

Fax: (095) 5302233; E-mail: korkishk@chem.miet.zgrad.ru

The copper exchange of waveguides, containing the different  $\text{Li}_{1-x}\text{H}_x\text{NbO}_3$  phases, is investigated. The significant increase of holographic sensitivity, depending on phase state, is observed because of the copper exchange.

The previous studies of the proton-exchanged  $\text{LiNbO}_3$  waveguides [1,2] allowed to identify the different crystallographic phases  $\text{Li}_{1-x}\text{H}_x\text{NbO}_3$ , considering that there the phase transitions occur when the proton concentration  $x$  in the exchanged-layer is gradually varied, which cause a sudden variation of the cell parameters. Most interesting for waveguide fabrication is the fact that most of these discontinuities and phase transitions can already be seen on a rather simple diagram, which was called in Ref.[2] as "the structural phase diagram". Thus, the seven different crystallographic  $\text{Li}_{1-x}\text{H}_x\text{NbO}_3$  phases (the  $\alpha$ ,  $K_1$ ,  $K_2$ ,  $\beta_1$ ,  $\beta_2$ ,  $\beta_3$ ,  $\beta_4$  phases) were identified [2,3]. The results obtained previously demonstrate the substantial difference in the chemical bonding [3] and the some properties [3,4] of the different phases. Evidently, the difference of other fundamental properties of the  $\text{Li}_{1-x}\text{H}_x\text{NbO}_3$  phases should be expected. Our interest is focused on the phase dependence of an additional copper exchange, as the promising prospects of the combined proton and copper exchange for fabrication of photorefractive  $\text{LiNbO}_3$  waveguides were discovered [5,6]: The additional copper exchange of the proton-exchanged  $\text{LiNbO}_3$  waveguides allows to increase its photorefractive sensitivity (PRS) up to one thousand times. Also, it was reported [5,7], that the PRS depends on a proton concentration  $x$  by the very complex manner. However, this dependence was not investigated in detail, as the structural phase diagram for  $\text{Li}_{1-x}\text{H}_x\text{NbO}_3$  system is not taken into account yet. Therefore, the main aim of our work consists of study both the copper exchange and the photorefractive properties of the different  $\text{Li}_{1-x}\text{H}_x\text{NbO}_3$  phases.

To realize the proton-exchanged  $\text{LiNbO}_3$  waveguides containing the different phases we have used either a simple proton exchange, varying the temperature and the acidity of the melt and the duration of the exchange to modify the parameters of the waveguide, or a two step process, where the exchange is followed by annealing whose duration and temperature further modify the waveguide parameters. PE waveguides were fabricated in optical grade Z-cut  $\text{LiNbO}_3$  substrates. Here it are described results obtained on samples, which were fabricated in our previous work [2-3]. The phase state of the  $\text{Li}_{1-x}\text{H}_x\text{NbO}_3$  layers have been determined by using X-ray diffraction, IR-reflection, attenuated total reflection and m-line spectroscopy methods, Table 1.

The successive copper exchange have been carried out in a melt of the benzoic acid mixed with 1 mol.%  $\text{Cu}_2\text{O}$  and 1.2 mol.% lithium benzoate (LB) at 230°C during 10 min. The LB is added in mixture for suppression of the marked extra proton exchange, which is possible to change a phase state and a refractive index profile.

The copper content in the waveguides is determined by measuring optical absorption of the samples in the UV and the visible region with the help of a Cary 17D spectrometer. We have found that the copper exchange induces of a new composite band in an absorption spectrum between 340 and ~600 nm, Fig.1. The intensity and shape of this band are very different in the waveguides, which had contained the different  $\text{Li}_{1-x}\text{H}_x\text{NbO}_3$  phases before the copper exchange. As, the most intensive copper-induced absorption is observed in the Z1 sample, Fig.1a. The computer fitting of difference spectrum (optical density  $D$  as versus photon energy) between the Z1 sample and the standart undoped  $\text{LiNbO}_3$  plate demonstrates the two pronounced bands at 2.6 and 3.3 eV. In accordance with well known data (see citations in Refs.[5,6]) the band at 3.3 eV corresponds to absorption on the  $\text{Cu}^+$  ions. The nature of second band is not known yet and it will be subjected to our further study. Note, that main difference between the studied samples, concerning to the shape of the copper-induced composite band, consists of a ratio between intensities of the bands at 2.6 and 3.3 eV: As, in the copper-doped Z12 sample's spectrum the band at 2.6 eV is not observed, but in the other samples this band is observed. This band has a maximum contribution in shape of the composite band in case of the Z1 sample, Fig.1. These data allow to assume, that a valence state of Cu defects, appearing in proton-exchanged  $\text{LiNbO}_3$  waveguides because of the additional copper exchange, depends on the phase state of a  $\text{Li}_{1-x}\text{H}_x\text{NbO}_3$  layer. Moreover, a value of the integral intensity of the copper-induced absorption has

the specific values for samples, containing the different phases before the copper exchange. This fact indicates, that the rate of the copper exchange depends clearly on the phase state of a  $\text{Li}_{1-x}\text{H}_x\text{NbO}_3$  waveguiding layer and, what is why, this rate is proportional to  $x$  only in limits of a given phase. We have found, that the rates of the copper exchange for different phases differ by up to 20 times.

Table 1. Samples notation, and phase state of waveguiding layers on the different samples.

sample notation	phases before copper exchange	phases after copper exchange
Z1	$\beta_4, \beta_3, \beta_1$	$\beta_1$
Z3	$\beta_1$	$\beta_1$
Z5	$\beta_2, \beta_1$	$\beta_1$
Z6	$\beta_1$	$\beta_1$
Z7	$\beta_3, \beta_1$	$\beta_3, \beta_1$
Z8	$K_1 (\text{HT}), \alpha$	$\alpha$
Z9	$K_2 (\text{LT}), K_1 (\text{LT}), \alpha$	$K_2 (\text{LT}), K_1 (\text{LT}), \alpha$
Z10	$K_1 (\text{LT}), \alpha$	$K_1 (\text{LT}), \alpha$
Z11	$K_2 (\text{HT}), K_1 (\text{HT}), \alpha$	$K_1 (\text{HT}), \alpha$
Z12	$\alpha$	$\alpha$

Here the phases are indicated in order their sequence from the surface inside a waveguide.

It is important to note, that in many cases the change of the phase state of waveguiding layer is induced by the copper exchange, table 1. This conclusion is clear consequence of the characteristic changes of the relationship between a crystal deformation  $\varepsilon_{33}$  and a refractive index increment  $\delta n_e$ .

To investigate light induced refractive index changes  $\Delta n$ , the holographic gratings are written in planar  $\text{LiNbO}_3$  waveguides utilizing an argon-ion laser (wavelengths of 457.9 and 488 nm). For this purpose two slightly focused beams are coupled into and out waveguide using two rutile prisms. During the build-up of the refractive index grating, the diffraction efficiency  $\eta$  is measured as a function of time by blocking one of the beams for a short time (50 ms) and measuring the ratio of diffracted and total light intensity of the outcoupled beams. In steady state the saturation value of diffraction efficiency  $\eta^s$  is reached, Fig.2. We have observed, that the effective holographic recording in any sample becomes possible only after the additional copper doping. An increase of  $\eta^s$  with increasing an input light power  $P_{\text{in}}$  occurs in all copper-exchanged waveguides, and the maximum value  $\eta^s (\text{max})$  has the very different values in the different waveguides. The highest values of  $\eta^s (\text{max})$  are obtained in the copper-exchanged Z8, Z11 and Z12 samples.

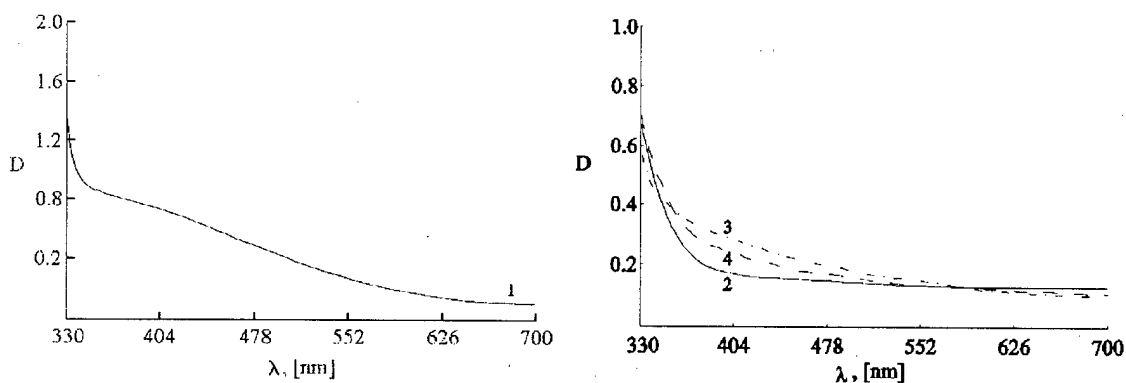


Fig. 1. Optical absorption spectra of different samples: shown is the optical density  $D$  versus light wavelength  $\lambda$  (in [nm]): Curve 1 - Z1 sample after copper exchange (CE); curve 2 - sample Z11 before CE, but the same spectra are observed for any undoped sample (Table 1); curve 3 - Z11 sample after CE; curve 4 - Z12 sample after CE.

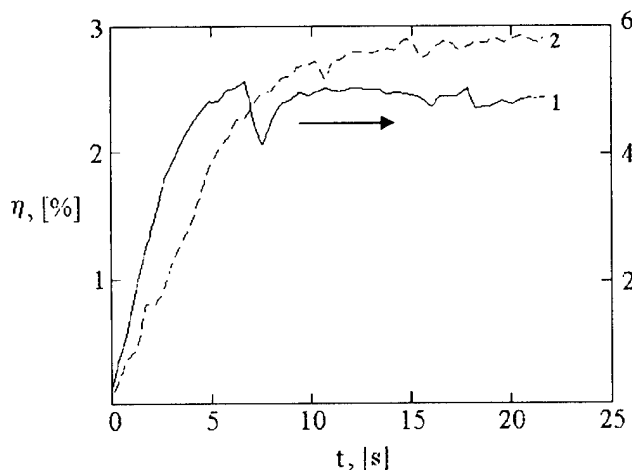


Fig.2. Time evolution of writing of a holographic grating at  $\lambda = 488$  nm and  $P_{in} = 700$  mW in the copper exchanged waveguides fabricated in the Z11 sample (curve 1, the result obtained with two  $TM_3$  modes) and Z12 sample (curve 2 obtained with two  $TM_2$  modes). Here it are shown the  $TM_i$  modes, which allow to reach the highest value of  $\eta^s$  (max) in a given waveguide.

The comparison with undoped samples shows that copper presence increases the efficiency of holographic recording  $\eta^s$  (max) more than in fifty times and decreases essentially a characteristic time of the photorefractive response in all waveguides, e.g., the effective holographic recording becomes possible for 2 - 5 seconds in the Z11 and Z12 samples after the copper exchange, Fig.2. At the same time, there is a strong difference between different  $TM_i$  modes, and the change of the  $\eta^s$  (max) at the variation of mode order  $i$  is very different in the waveguides, containing the different  $Li_{1-x}H_xNbO_3$  phases. To compare  $TM_i$  modes of different waveguides, we determine the values of the holographic sensitivity  $R$  from the rate of hologram build-up in the initial stage:

$$R = d\{(\eta)^{1/2}\}/d(P_{in} t) \big|_{t \rightarrow 0} \quad (1)$$

The measurements point out that  $R$  depends clearly on input power  $P_{in}$ , so that we can write:

$$R = R_l + R_q P_{in} \quad (2)$$

We have found, that there is crucial influence of the phase of the waveguiding layer on the values of  $R_l$ ,  $R_q$  and ratio  $R_q/R_l$ . The maximum values of  $R_l$  and  $R_q$  are reached in Z12 and Z11 samples, respectively: As, at  $\lambda = 488$  nm we have observed:  $R_l = 13.2 \cdot 10^{-3} (W s)^{-1}$  and  $R_q = 1.72 \cdot 10^{-2} (W^2 s)^{-1}$  in the copper-doped Z12 sample, and  $R_l = 0.49 \cdot 10^{-3} (W s)^{-1}$  and  $R_q = 6.8 \cdot 10^{-2} (W^2 s)^{-1}$  in the copper-doped Z11 sample, but in these samples undoped by Cu the values of  $R$  don't exceed the  $10^{-5} (W s)^{-1}$  at the same experimental conditions. Moreover, from the comparison of the different modes in a given waveguide we can conclude that the  $R_q$  is almost proportional to the copper-induced absorption, i.e. is proportional to copper concentration on the propagation depth of a mode. According to [6,7], we may expect that the photorefractive properties of the Z1 - Z10 samples should be considerably improved by additional treatment in the  $LiNO_3$  melt, when the changes of hydrogen concentration and copper valence state occur simultaneously. Therefore, the all copper-exchanged  $Li_{1-x}H_xNbO_3$  waveguides with any phase state may have, in principle, a some interest for fabrication of the photorefractive integrated-optical devices for a given application.

## REFERENCES

1. Yu.N. Korkishko and V.A. Fedorov, J.Appl.Phys., v.83, pp.1010- 1017, 1997.
2. Yu. N. Korkishko and V.A. Fedorov, J.Selected Topics of Quantum Electronics, v.2, pp.187-196.
3. Yu. N. Korkishko, V.A. Fedorov and M.P. De Micheli, Proc. ECIO-8, pp.56-59, Royal Institute of Technology, Stockholm, 1997.
4. K. El Hadi, P. Baldi, M.P. De Micheli, D.B. Ostrowsky, F. Laurell, Proc.ECIO-8, pp.358-361, Royal Institute of Technology, Stockholm, 1997.
5. S.M. Kostritskii and O.M. Kolesnikov, J.Opt.Soc.Am. B, v.11, pp. 1674-1682, 1994.
6. F. Rickermann, D. Kip, B. Gather and E. Kratzig, phys.stat.sol. (a), 150, pp.763-772, 1995.
7. S.M. Kostritskii, J.Nonl.Opt.Phys.&Mater., v.6, No3, 1997.

## Evolution of Crystal Phases and Refractive Index Profiles in X-cut Annealed Proton-Exchanged LiTaO<sub>3</sub>

David B. Maring, Yuri N. Korkishko<sup>†</sup>, Robert F. Tavlykaev, Ramu V. Ramaswamy, and John M. Zavada<sup>††</sup>

Photonics Research Lab, 339 Larsen Hall, University of Florida, Gainesville, FL 32611  
Tel: (352) 392-9265, Fax: (352) 392-4963, tavl@eel.ufl.edu

<sup>†</sup>Moscow Institute of Electronic Technology, Moscow 103498, Zelenograd, Russia

<sup>††</sup>U.S. Army Research Office, Research Triangle Park, North Carolina 27709

### Introduction

Lithium Tantalate (LiTaO<sub>3</sub>) attracts considerable interest as a material for integrated optics due to its large electro-optic and nonlinear coefficients, similar to those of Lithium Niobate (LiNbO<sub>3</sub>), but most importantly, due to its much higher threshold for optical damage than LiNbO<sub>3</sub>. Guided-wave devices implemented in this material will exhibit a much higher power handling capability than LiNbO<sub>3</sub>, making them ideal for a variety of high-throughput applications. Currently, the Annealed Proton Exchange (APE) technique is used almost exclusively for the fabrication of waveguides in LiTaO<sub>3</sub>, owing to its simplicity and the fact that it can be performed at temperatures below the Curie point. Low-loss waveguides with high index increments can be achieved with this process. However, the APE process in LiTaO<sub>3</sub> is known to exhibit a number of anomalies which to date, are not fully understood. In particular, APE waveguides in LiTaO<sub>3</sub> have been found to exhibit significant short-term and long-term instabilities of the refractive index increment [1]. It has been shown that the total hydrogen content, and refractive index, increase upon annealing and that the index decreases when proton concentration exceeds a certain level [2]. These peculiar behaviors have suggested a nonlinear dependence of proton concentration on refractive index which may result in buried index profiles for certain fabrication conditions, as we have recently confirmed by direct observation [3]. To explain the observed abnormal behavior, it is therefore important to understand the relationship between proton concentration and index increment, i.e. the phase diagram, in APE waveguides in LiTaO<sub>3</sub>. Moreover, knowledge of the phase diagram is indispensable in developing advanced high-throughput electro-optic and nonlinear guided-wave devices with low-loss and temporally stable performance.

It should be noted that the aforementioned specifics of the APE process in LiTaO<sub>3</sub> have complicated a complete and accurate reconstruction of the phase diagram for this material, while that for LiNbO<sub>3</sub> is fairly well known [4,6]. In this paper, we present for the first time a complete phase diagram for APE X-cut LiTaO<sub>3</sub>, relating the proton-induced lattice deformation ( $\epsilon''_{33}$ ), calculated through Rocking Curve measurements, to extraordinary refractive index increment ( $\Delta n_e$ ), obtained by index profiling. We analyze the evolution of the refractive index profile through the stages of post-exchange annealing. Modifications of the index profile from step-like, to buried, and eventually Gaussian profiles are clearly demonstrated, explaining the previously observed anomalies. Additionally, regions of the phase diagram that are likely to correspond to highly unstable, as well as stable, waveguides are identified.

### Fabrication and Measurement Techniques

Planar waveguides were fabricated in X-cut LiTaO<sub>3</sub> by proton exchange using a variety of sources: pyrophosphoric acid, benzoic acid, ammonium dihydrophosphate, stearic acid and palmetic acid. Exchange and anneal times and temperatures were varied as deemed necessary to produce a sufficient number of data points across the phase diagram. It was found that pyrophosphoric acid and ammonium

dihydrophosphate provided the highest proton concentrations possible without causing surface cracks on the sample. This limit of proton concentration is reached after exchanging in pyrophosphoric acid at 260°C for 20 minutes. Because further exchanges lead to surface cracking, it is this concentration induced lattice deformation which determines the upper limit of our phase diagram.

Waveguide index profiles for the extraordinary index were obtained for all samples fabricated by using a reflectivity technique [5]. It is quintessential to use direct profiling of waveguides, since indirect techniques (IWKB and the like) produce errors when applied to non-monotonic (buried) profiles, as is the case with LiTaO<sub>3</sub> under certain fabrication conditions. Furthermore, at high concentrations, waveguides can support few to no modes and IWKB cannot be used at all. For direct profiling, the focused beam of a laser ( $\lambda=632.8\text{nm}$ ) scanned the waveguide cross-section and the variation  $\Delta I$  in intensity  $I$  of light due to the presence of the refractive index profile was measured. The index profile was then determined from the measured  $\Delta I$  using the known relationship [5]:

$$\frac{\Delta n}{n_b} = \frac{1}{4} \left( n_b - \frac{1}{n_b} \right) \frac{\Delta I}{I}$$

where  $\Delta n$  and  $n_b$  are the local increment and bulk index (ordinary or extraordinary), respectively. Approximately half of the substrate surface was bevelled at an angle  $\alpha$  of 2° to magnify the depth profiles by  $1/\sin\alpha$  times.

Lattice deformations  $\epsilon''_{33}$  in the exchanged region of each sample were determined by measuring rocking curves with a double-crystal x-ray diffractometer [6]. According to x-ray diffraction theory, the maximum angular shift on the rocking curve due to the presence of protons corresponds to the surface value of strain.

### Results and Discussion

Fig. 1 shows the complete phase diagram for APE, X-cut, planar waveguides in LiTaO<sub>3</sub>. Surface values of extraordinary index increment  $\Delta n_e$  were plotted versus surface values of lattice strain  $\epsilon''_{33}$ . This figure illustrates that the index increment has an approximately linear dependence on lattice deformation, and therefore on proton concentration, within each phase. However, the slope of this dependence is different for each phase and the transitions between phases are marked by sharp discontinuities. Note that the slope difference between the  $\beta_1$  and  $\beta_2$  phases is small, making them difficult to distinguish. As a result, a single linear fit was used through both of them.

Analysis of this phase diagram leads to an explanation of the aforementioned phenomena of reduced index increment with increasing proton concentration. As proton concentration is increased via proton exchange, stress and index increase through the first four phases. However, once the concentration is high enough to produce a deformation value of about  $\epsilon''_{33} = 4$ , further increase of protons and stress leads to a decrease in index. The anomaly of increased index increment upon short annealing can also be explained. If a single-step proton exchange process is sufficient enough to supply the required proton concentration, and induced stress, to form waveguides largely within the  $\beta_3$  or  $\beta_4$  phase, then subsequent annealing will cause a reduction of stress, and hence an increase in index.

A unique perspective of how the concentration induced stress impacts the waveguide index profile can be obtained by tracking the evolution of the index profile and corresponding rocking curves as we move through the phases from higher to lower values of lattice deformation  $\epsilon''_{33}$ . Typical examples of index profiles are illustrated by insets in Fig.1. Inset 1 shows the index profile for an as-exchanged waveguide with an  $\epsilon''_{33}$  value of 11.4. There is no surface index increment, however, there are large variations in index change below the surface. Rocking curves for this sample also clearly indicate the presence of at least two phases within the APE layer,  $\beta_4$  and  $\beta_3$ , with the  $\beta_4$  phase being the uppermost, or surface layer. Lower-stress phases are also present but there is not a sharp enough strain discontinuity between them to be discerned on the rocking curves. It is likely that the presence of multiple phases and resulting non-uniform stresses is what leads to the index variations observed. Inset 2 depicts a waveguide with a step-like index

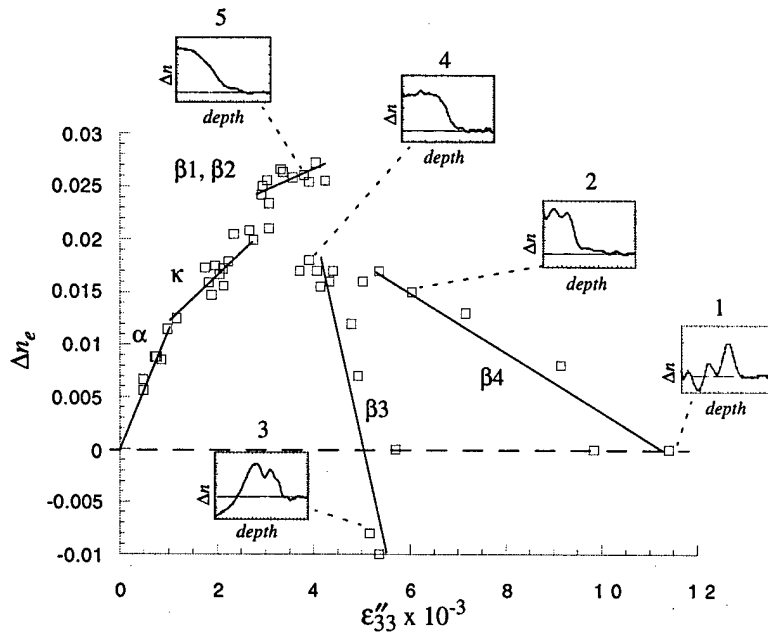


Fig. 1. Phase diagram for X-cut LiTaO<sub>3</sub>. Typical waveguide index profiles for various regions are shown as insets.

and index variations below the surface are less noticeable. Likewise, the surface value of index rises until the profile is no longer buried. Inset 4 shows such a waveguide with an  $\epsilon''_{33}$  value of 4.06, at the low-stress end of the  $\beta_3$  phase. Waveguides in this region have a characteristically Fermi-like index distribution with a peak value for  $\Delta n_e$  below the surface of about 0.016, nearly the same value as that of the low-stress end of the  $\beta_4$  phase. Lastly, inset 5 depicts a waveguide profile with a surface  $\epsilon''_{33}$  value of 3.84. This Gaussian-like index distribution is characteristic of the  $\beta_1$ - $\beta_2$  phases, as well as the  $\kappa$  and  $\alpha$  phases.

The long-term stability of waveguides existing within the different phases of our diagram has also been investigated. The results will be presented at the conference.

### Conclusion

We have presented, for the first time, a complete phase diagram for APE X-cut LiTaO<sub>3</sub>. Completion of this diagram has provided explanations for several of the previously reported anomalies associated with the APE process in LiTaO<sub>3</sub>, most notably the decrease in index with increasing proton concentration and the increase in surface index upon short annealing durations. We have identified at least two high-stress phases which are highly unstable with time. Experiments are currently underway to characterize the long-term stability of the remaining lower-stress phases.

### References

1. P. Matthews and A. Mickelson, *J. Appl. Phys.*, vol. 71, no. 11, p. 5310, June 1992.
2. H. Åhlfeldt, J. Webjörn, F. Laurell, and G. Arvidsson, *J. Appl. Phys.*, vol. 75, no. 2, p. 717, Jan. 1995.
3. D. B. Maring, R. F. Tavlykaev, and R. V. Ramaswamy, *Integrated Photonic Research*, vol. 6, 1996 OSA Technical Digest Series, IWB3-1, p. 435.
4. J. M. Zavada, H. C. Casey, Chang-Ho Chen, and A. Loni, *Appl. Phys. Lett.*, vol. 62, no. 22, p. 2769, May 1993.
5. D. B. Maring, R. F. Tavlykaev, and R. V. Ramaswamy, *Elec. Lett.*, vol. 32, no. 16, p. 1473, Aug. 1996.
6. V. A. Fedorov and Y. N. Korkishko, *Ferroelectrics*, v. 160, p. 185-208, 1994.

profile and a smaller  $\epsilon''_{33}$  value of 6.03, as may be obtained through annealing. Rocking curves for this region show an increasing content of the additional  $\beta_3$  phase. Inset 3 shows a profile for a waveguide with an  $\epsilon''_{33}$  value of 5.16, essentially in the  $\beta_3$  phase. Waveguides in this region are characterized by buried index profiles. Rocking curves also reveal the distinct presence of a  $\beta_2$  phase layer, beneath the  $\beta_3$  layer. Note again that the index variations, and perhaps the fact that it is buried, are likely due to the presence of multiple phases with well-defined stress transitions between them. As further annealing is performed and stresses are reduced, the presence of the  $\beta_2$  phase becomes more pronounced on rocking curves

## Integrated Optical Ti:Er:LiNbO<sub>3</sub> DBR-Laser with Fixed Photorefractive Grating

CH. BECKER, A. GREINER, TH. OESSELKE, A. PAPE, W. SOHLER, H. SUCHE

Universität-GH Paderborn, Angewandte Physik  
Warburger Straße 100, D-33098 Paderborn, Germany  
Fax: +49-5251-603422; e-mail: suche@physik.uni-paderborn.de

**Introduction:** Recently, integrated optical Ti:Er:LiNbO<sub>3</sub> DBR-(Distributed Bragg Reflector-) lasers have been developed with holographically defined ion beam etched surface grating for narrowband optical feedback [1]. However, DBR-lasers with etched surface gratings suffer from several drawbacks: The fabrication technology is complicated [2]. Grating inhomogeneities induce extra losses of the lasing mode. The overlap of the grating and the lasing mode is very small requiring a long interaction length. The pump mode is partially coupled to substrate modes resulting in high extra losses; therefore, pumping through the Bragg-grating is not possible.

Photorefractive gratings, as successfully used in fiberoptic DBR- and DFB-lasers [3], are a very promising alternative, avoiding all the drawbacks mentioned above. We report in this contribution the first DBR-waveguide laser ( $\lambda = 1531\text{nm}$  (and  $\lambda = 1546\text{nm}$ )) in Er-diffusion-doped LiNbO<sub>3</sub> with a fixed photorefractive grating in an Fe-doped Ti-diffused strip waveguide; the device is pumped by a laser diode ( $\lambda \approx 1480\text{nm}$ ).

**Laser Fabrication:** A schematical diagram of the laser is presented in Fig. 1. It is fabricated in a 70mm long X-cut LiNbO<sub>3</sub> substrate, which has been Er-doped over 43mm by an indiffusion of a 15nm thick, vacuum-deposited Er-layer at 1120°C during 120h. Subsequently, the remaining surface has been iron-diffusion doped (33nm, 1060°C, 72h) to increase the photorefractive sensitivity for grating fabrication. Finally, a 8 $\mu\text{m}$  wide, 97nm thick, photolithographically defined Ti-stripe parallel to the c-axis has been indiffused forming the optical channel guide. The sample has been annealed at 500°C for 3h in flowing Ar (0.5l/min) to enhance the Fe<sup>2+</sup>/Fe<sup>3+</sup>-ratio, which determines the photorefractive susceptibility.

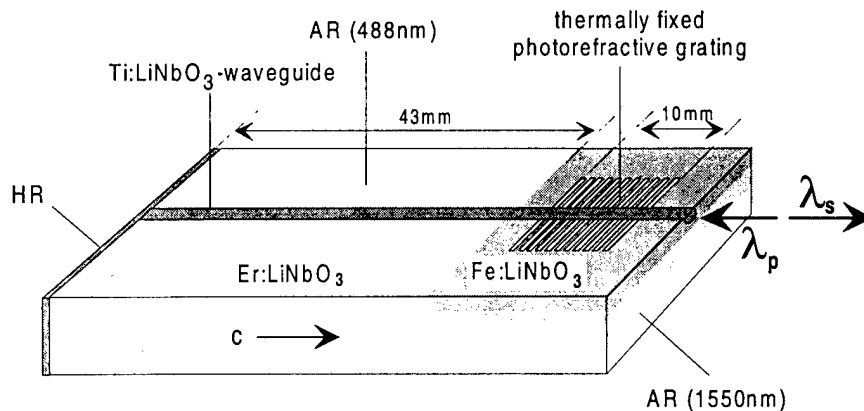


**Fig. 1:** Schematical structure of the Ti:Er:LiNbO<sub>3</sub> DBR waveguide laser with photorefractive grating in the Fe-doped section. HR: Highly reflecting dielectric mirror; AR: anti-reflection coating.

The laser resonator consists of a broadband dielectric high reflector on the polished waveguide end face of the Er-doped section. The end face of the Fe-doped section has been antireflection coated for fibre butt coupling. Finally, the upper and lower sample surfaces have been AR-coated to avoid interference effects during the grating writing.

The grating has been written using a holographic setup with the 488nm line of an Ar-laser. The periodic illumination leads to a corresponding excitation of electrons from  $\text{Fe}^{2+}$ -states; they are redistributed by drift, diffusion and the photovoltaic effect in  $\text{LiNbO}_3$ . The latter is the dominant transport mechanism along the optical c-axis. Finally, the electrons are trapped by acceptor states ( $\text{Fe}^{3+}$ -ions) in areas of low optical intensity. This redistribution generates a periodic space charge field which modulates the refractive index via the electrooptic effect and generates in this way a narrowband Bragg-reflector grating.

A grating fabricated at room temperature is not stable. Therefore, it has been written by a 2-hours exposure at  $170^\circ\text{C}$ . At this temperature protons in the crystal become mobile and compensate the periodic electronic space charge [4, 5]. After cooling to room temperature, these ions are frozen at their high temperature positions. Homogeneous illumination with the collimated beam of a 100 W halide lamp then leads to a nearly homogeneous redistribution of the electronic charge, developing in this way a stable ionic grating as a replica of inverse polarity of the initial electronic space charge distribution.

**Laser Properties:** The laser has been first characterized as passive device. The erbium and the iron concentration profiles are Gaussian-like with surface concentrations of  $1.15 \cdot 10^{20}$  ( $3.3 \cdot 10^{19}$ )  $\text{cm}^{-3}$  and 1/e-penetration depths of  $4.7(63)\mu\text{m}$  for  $\text{Er}(\text{Fe})$ , respectively.

The Ti-diffused optical waveguide is single mode for wavelengths around 1550nm, with the fundamental TM-mode slightly larger than the TE-mode ( $8.5\mu\text{m}(\text{width}) \times 4.8\mu\text{m}(\text{depth})$  and  $8.4\mu\text{m} \times 4.5\mu\text{m}$ , respectively). The scattering losses are as low as 0.02dB/cm in a reference channel without Er-doping. For the Er-doped waveguide scattering losses of about 0.2dB/cm are estimated by the comparison of modelled and measured laser results. Absorption coefficients for the Er-doped section have not been measured, but can be estimated to be about 1.4(8.5)dB/cm at 1480(1531)nm wavelength for TE-polarised light. These values can be inferred from mode-size and absorption cross section measurements for  $\alpha$ -polarised light.

The high reflector has reflectivities of about 80% for both, signal- and pump wavelengths. In this way double pass pumping of improved absorption efficiency is achieved. The spectral characteristics of the holographically written grating has been determined by slightly pumping the device and measuring the backscattered amplified spontaneous emission from the Er-doped section transmitted through the grating. This yielded a minimum transmission of about 40%, corresponding to a reflectivity of about 60%. Due to an electronic compensation of the ionic grating the reflectivity drops slowly as function of time. However, this compensation can be easily reversed by homogeneous illumination. Fig. 2 shows the specific result measured for the optimum output coupling of the DBR-laser. The halfwidth of the grating is about 0.11nm.

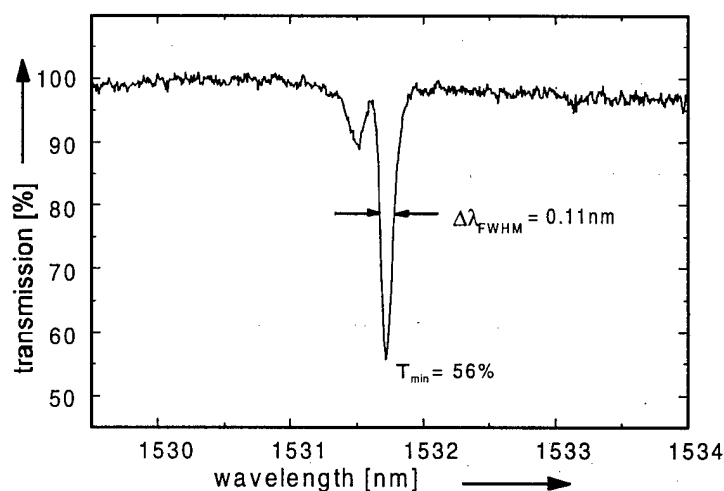


**Fig. 2:** Transmission of a fixed grating after homogeneous illumination versus wavelength.

To operate the DBR-laser, a pigtailed diode laser ( $\lambda_p \approx 1480\text{nm}$ ) has been used for pumping. A fiberoptic wavelength division multiplexer (WDM) launched up to 110mW of pump power into the DBR-laser and simultaneously extracted the laser emission in backward direction.

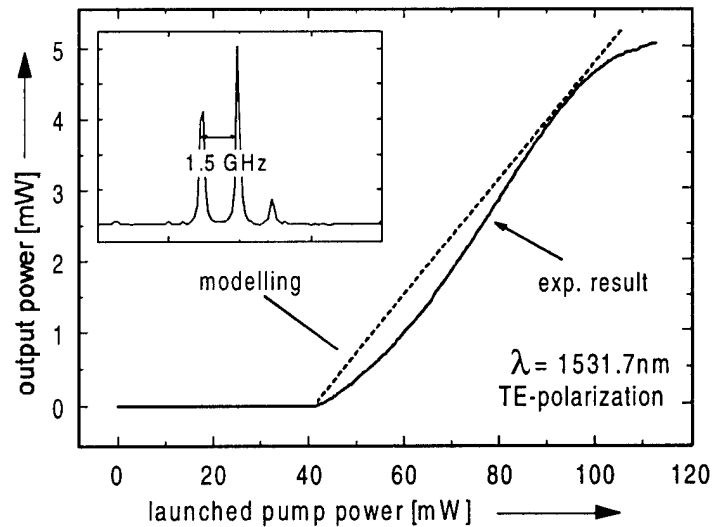


**Fig. 3:** Power characteristics of the DBR-laser. Inset: axial mode spectrum (TE-polarised).

Laser emission could be achieved in both, TE- and TM-polarisation. The actual polarization was determined by the location of the axial eigenmodes with respect to the peak reflectivity of the Bragg reflector. By thermal drift alternating TE- and TM-emission could be observed, respectively. TE-polarization for both, pump and emission, has yielded the maximum output power (see Fig. 3), as the smaller TE-modes result in a better overlap with the erbium concentration profile. To suppress TM-emission, a stripe of silver paste operating as a TE-pass polarizer has been deposited across the waveguide close to the high reflector. The bandwidth of the grating of  $\approx 0.11\text{nm}$  has led to the simultaneous emission of three longitudinal modes (see inset of Fig. 3) with a central wavelength of 1531.7nm. The output power of the DBR-laser has been monitored as function of the reflectivity of the Bragg grating, starting with a reflectivity of about 60%. The maximum TE-polarized output power of 5.1mW has been measured for a grating reflectivity of about 45%.

Modelling results predict a significant potential for improvements. Assuming 0.1dB/cm waveguide scattering losses, an optimized Er-diffusion and output coupling through the grating, up to 32% slope efficiency and 15mW output power at 80mW of launched pump power seem to be feasible at the same emission wavelength.

**Acknowledgement:** We thank Prof. Krätzig and Dr. Kip of the University of Osnabrück, Germany, for helpful discussions about the photorefractive effect and for vacuum depositing the Fe-layers needed for diffusion doping.

#### References:

- [1] J. Söchtig, R. Groß, I. Baumann, W. Sohler, and H. Schütz, R. Widmer, *Electron. Lett.*, **31**, pp. 551-552 (1995)
- [2] J. Söchtig, H. Schütz, R. Widmer, H.W. Lehmann, R. Groß: *Proc. SPIE Conf. on Nanofabrication and Device Integration*, **2213**, pp. 97-98 (1994)
- [3] J. Hübner, P. Varming, and M. Kristensen, *Electron. Lett.* **33** (2), pp. 139-140 (1997)
- [4] J.J. Amodei, D.L. Staebler, *Appl. Phys. Lett.*, **18**, pp. 540-542 (1971)
- [5] Buse, K., Breer, S., Peithmann, K., Kapphan, S., Gao, M., Krätzig, E.: *Phys. Rev. (B)*, **56** (3), pp. 1225-1235 (1997)

# Drive Voltage Reduction in Mach-Zehnder Electrooptic Modulators Using Systems Approach

Nadir Dagli

Department of Electrical and Computer Engineering

University of California  
Santa Barbara, CA 93106

Phone: (805) 893 - 4847

Fax: (805) 893 - 3262

e-mail: dagli@ece.ucsb.edu

## Introduction

A crucial component for high speed digital and analog fiber optic links is the optical modulator. Most commonly used high speed modulators are electroabsorption and Mach Zehnder types. Electroabsorption modulators are small lumped components that offer bandwidth extending up to 40 GHz with drive voltages around three volts [1]. Although it is possible to reduce the drive voltage further, this comes at the expense of reduced electrical bandwidth due to increased device capacitance. On the other hand Mach-Zehnder electrooptic modulators can be realized in traveling wave configuration, hence very wide bandwidths can be realized [2]. Traveling wave configuration also helps to reduce the drive voltage. Therefore, Mach-Zehnder electrooptic modulator is the only candidate for operation beyond 40 GHz. However, the drive voltage for very wide bandwidth devices is around five volts. Although drive voltages of about three volts seem to be realizable at 30 GHz, drive voltages around five volts are very difficult to realize at frequencies in excess of 30 GHz. Therefore reducing the drive voltage of Mach-Zehnder electrooptic modulators without degrading frequency response is a very important and challenging task. In this paper a systems approach is presented to realize a system having the characteristics of a Mach-Zehnder electrooptic modulator. System uses two high speed Mach-Zehnder electrooptic modulators together with other fiber components. The composite system behaves just like a Mach-Zehnder electrooptic modulator with a significantly reduced drive voltage. Furthermore, it has exactly the same electrical frequency response of the modulators it contains.

## Basic idea

The main electric field component at the output of a push pull driven Mach-Zehnder electrooptic modulator can be expressed as

$$a_{out} = B \left[ \cos\left(\frac{\pi}{2} \frac{v(t)}{V_\pi}\right) \right] \cos(\omega_0 t - \beta L)$$

$V_\pi$  is the drive voltage required to turn the modulator completely off,  $\omega_0$  is the optical angular frequency,  $\beta$  is the unperturbed phase constant in the modulator and  $L$  is the length of the modulator. We can manipulate this equation into the following form assuming a sinusoidal drive voltage

$$a_{out} = B [\cos(m \cos(\omega_m t))] \cos(\omega_0 t - \beta L)$$

where  $m = (\pi/2)(V_{max}/V_\pi)$  is a dimensionless number.  $V_{max}$  is the peak of the available drive voltage and  $\omega_m$  is the angular electrical frequency. In practice  $m$  could be very small since  $V_{max}$  is limited at high frequencies. For example for a modulator that operates at 100 GHz  $V_{max} < 0.1$  V, whereas  $V_\pi > 5$  V. Therefore  $m < 0.03$ . We can expand the modulating part of the optical waveform using well known expansions in terms of Bessel functions and obtain

$$a_{out} = B [J_0(m) - 2 \sum_{n=1}^{\infty} J_{2n}(m) \cos(2n\omega_m t)] \cos(\omega_0 t - \beta L)$$

For  $0 < m < \pi/2$  it is an excellent approximation to keep only  $J_0(m)$  and  $J_2(m)$  terms in the previous expansion since  $J_4(m)/J_2(m) < 5 \times 10^{-2}$  in this range. Then the output spectrum of the modulated optical wave will look like as shown in Fig. 1. In other words it is an AM modulated waveform of modulation index  $J_2(m)/J_0(m)$ . When the modulating voltage is large enough to turn the modulator fully on and off, i.e., when  $m = \pi/2$   $J_2(m)/J_0(\pi/2) = 0.529$ . As  $m$  gets smaller, as it happens under realistic drive conditions, modulation index drops sharply to zero. In reality since  $m$  is low modulation index is always low.

The basic idea in this work is to engineer the output spectra of a modulator for any  $m$  such that the output spectra is converted to that of  $m = \pi/2$ . This way an electrical signal not strong enough to turn the modulator fully off can do so. The output spectra manipulation can be done as shown in Fig.

1. The idea is to generate two output spectra in which the carrier terms are out of phase and sidebands are in phase. Then adding these two spectra one can extract the side bands. Finally adding a carrier term of appropriate amplitude to the remaining side band spectra one can generate the spectra of a fully modulated optical waveform. Obviously this approach requires two output spectra hence two modulators along with other fiber components. There are various ways to achieve this spectra engineering and one particularly useful implementation is shown in Fig. 2.

### Analysis of the composite modulator

In this system the wave labeled  $a_1$  is split into two waves of equal amplitude and a  $90^\circ$  phase shift between them. These waves are the inputs to the two Mach Zehnder modulators. The spectra of the optical wave at different points are shown in Fig. 2. The modulators are driven by the same voltage form except that the drive signals to the two modulators are phase shifted  $90^\circ$  with respect to each other. Then partially modulated waveforms  $a_3$  and  $a_4$  with spectra shown in Fig. 2 are generated. Running these waveforms through a 3 dB coupler one obtains only the carrier in one of the outputs ( $a_7$ ) and the sideband spectra in the other ( $a_8$ ). After  $90^\circ$  phase shifting the carrier one can split it into two parts in a 3 dB splitter. One part is fed back after an amplification to the input for carrier recycling. The other part is added to the sideband spectra after appropriate attenuation  $\alpha$ . The optical output of the composite system can be expressed as

$$a_{out} = B \frac{J_2(m)}{J_2(\frac{\pi}{2})} \frac{\sqrt{2}}{2 - J_0(m)} \left[ \frac{\alpha}{\sqrt{2}} \frac{J_2(\frac{\pi}{2})}{J_2(m)} \frac{J_0(m)}{J_0(\frac{\pi}{2})} J_0(\frac{\pi}{2}) + 2J_2(\frac{\pi}{2}) \cos(2\omega_m t) \right] \cos(\omega_0 t - \beta L)$$

where  $A$  is the amplification in the feedback path and  $\alpha$  is the attenuation. If  $\alpha$  is chosen such that

$$\alpha = \sqrt{2} \frac{J_2(m)}{J_2(\frac{\pi}{2})} \frac{J_0(\frac{\pi}{2})}{J_0(m)} J_0(\frac{\pi}{2})$$

and the approximate expansion introduced in earlier is used then the transfer function becomes

$$a_{out} = B \frac{J_2(m)}{J_2(\frac{\pi}{2})} \frac{\sqrt{2}}{2 - J_0(m)} \left[ \cos(\frac{\pi}{2} \omega_m t) \right] \cos(\omega_0 t - \beta L)$$

Obviously this is the output of a fully modulated modulator even though the available modulating voltage amplitude is much smaller than the  $V_\pi$  of a single modulator. One can make the amplitude of the output waveform unity by choosing the feedback amplification as

$$A = \frac{1}{J_0(m)} \left[ 2 - \sqrt{2} \frac{J_2(m)}{J_2(\frac{\pi}{2})} \right]$$

Fig. 3 shows the required attenuation and amplification needed for full on/off modulation as a function of drive voltage reduction defined as  $V_\pi/V_{max}$ . For small  $m$ ,  $J_0(m) \approx 1$  and  $J_2(m) \approx 0$  hence the required amplification is around 2. In other words a modest amplification of 6 dB in the feedback path should be sufficient. In a practical system the actual amplification should be higher to compensate for the insertion loss of the modulators and the propagation loss of the other fiber components. But the additional gain for proper operation is less than 6 dB which is very modest. Attenuation values are high but easy to realize using a fiber attenuator.<sup>14,15</sup> From this figure it is obvious that at least a five fold improvement is possible. Larger improvements can be possible if more accurate amplification and attenuation control is performed. This can be done using a small part of the output and feeding this into a feedback controller to control the required amplification and attenuation.

### Conclusions

In this paper a system using two high speed Mach-Zehnder electrooptic together with other fiber components is proposed. The composite system behaves just like a Mach-Zehnder electrooptic modulator with a significantly reduced drive voltage. Furthermore, it has exactly the same electrical

frequency response of the modulators it contains. It is shown that drive voltage reduction at the order of 5 is easily achievable. Higher reductions could be possible if more accurate feedback techniques are used to precisely control the required amplification and attenuation.

#### References

- [1]. T. Ido, S. Tanaka, M. Suzuki, M. Koizumi, H. Sano and H. Inoue, "Ultra High Speed Multiple Quantum Well Electroabsorption Modulators with Integrated Waveguides," *J. Lightwave Technol.*, vol. 14, pp. 2026-2034, 1995.
- [2]. R. Spickermann, S. R. Sakamoto, M. G. Peters and N. Dagli, "GaAs/AlGaAs Traveling Wave Electrooptic Modulator with Electrical Bandwidth Greater Than 40 GHz," *Electronics Letters*, vol. 32, pp. 1095-1096, 1996.

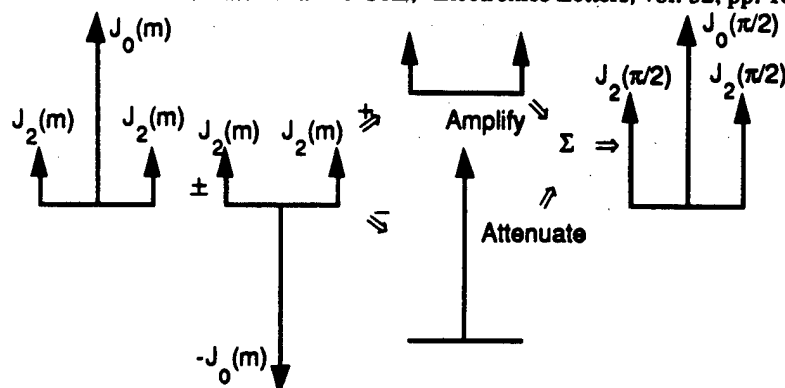


Figure 1. Diagram demonstrating the spectra manipulation utilized to convert a partially modulated optical output of a Mach-Zehnder to a fully modulated output waveform.

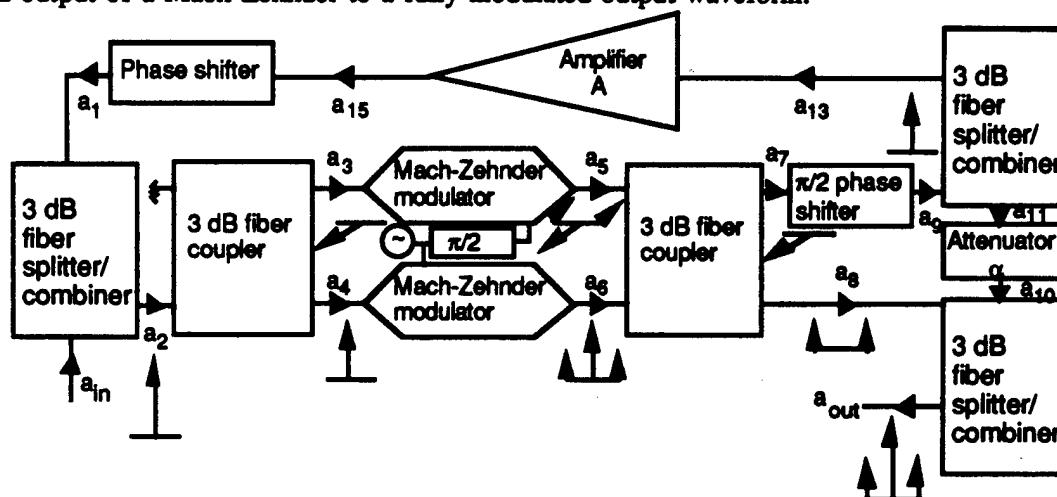


Figure 2. Block diagram of the composite modulator.

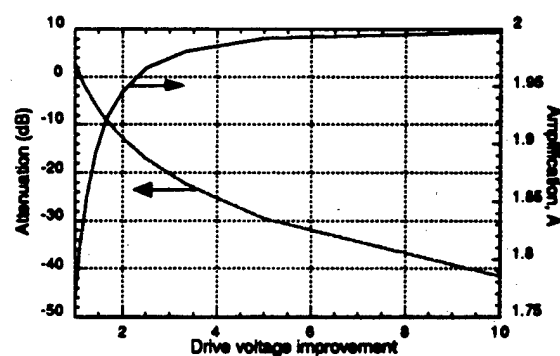


Figure 3. Required amplification  $A$  and attenuation  $\alpha$  as a function of drive voltage reduction.

# 10-GHz Mode-Locked Ti:Er:LiNbO<sub>3</sub> Waveguide Laser

R. WESSEL, A. GREINER, W. QIU, H. SUCHE, AND W. SOHLER

Universität-GH Paderborn, Angewandte Physik  
Warburgerstraße 100, D-33098 Paderborn, Germany

Fax-No.: ++49-5251-603422; e-mail: r.wessel@physik.uni-paderborn.de

**Abstract:** Mode-locked laser operation with a stabilized, packaged and diode-pumped Ti:Er:LiNbO<sub>3</sub> waveguide laser has been demonstrated at 1561-nm (TE) and 1575-nm (TM) wavelength with 14% slope efficiency. Pulse widths of < 10 ps at 10-GHz pulse repetition rate have been measured.

**Introduction:** Mode-locked lasers emitting in the third telecommunication window are promising sources for (soliton) transmission systems. Of particular interest are (harmonically) active mode-locked lasers due to their possibility to synchronize the pulse repetition rate to the high frequency system clock.

Lithium niobate is an attractive material to develop integrated solid state lasers. It has excellent electrooptic properties, allows the incorporation of Er up to the solid solubility limit without fluorescence quenching and the fabrication of high quality Er-doped waveguides. Using a monolithically integrated intracavity phase modulator as mode locker (FM-type mode locking) and a broadband Fabry Perot waveguide cavity fundamental and harmonic mode locking have already been demonstrated [1],[2]. However, the output power of these lasers was low and the emission wavelength (1531nm, 1602nm) was not matched to the third telecommunication window.

In this paper we report a diode-pumped, pigtailed and packaged harmonically mode-locked laser with a pulse repetition frequency up to 10 GHz. The laser emits 10-ps-long pulses of more than 100-mW peak power at 1562-nm and 1575-nm wavelength, respectively, depending on the polarization of the pump.

**Device fabrication:** Half (with respect to the X-direction) of the Z-cut (Y-propagation) LiNbO<sub>3</sub> substrate has been doped near the surface by indiffusion of 28 nm of vacuum-deposited Er at 1130°C during 125 h. Subsequently, photolithographically delineated 7- $\mu$ m-wide and 98-nm-thick Ti-stripes have been indiffused at 1060°C during 8h to form the 66.5mm long waveguide channels (see Fig. 1).

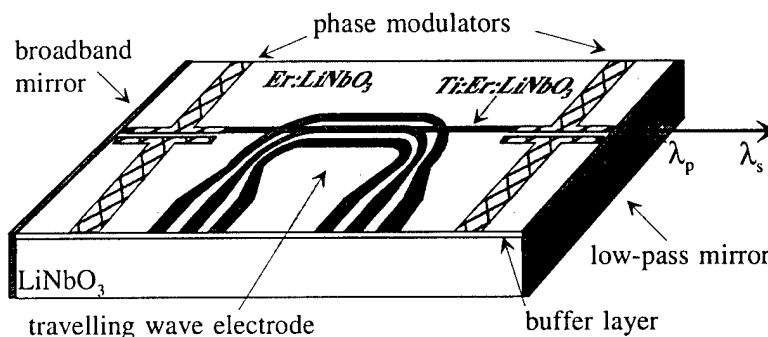


**Fig. 1:** Mode-locked Ti:Er:LiNbO<sub>3</sub> waveguide laser. (New laser design with two phase modulators)

To avoid excess losses of the TM-mode an 0.6- $\mu$ m-thick insulating SiO<sub>2</sub> buffer layer has been vacuum deposited onto the substrate surface prior to the electrode fabrication. The electrode structure of the intracavity travelling wave phase modulator (mode locker) is a symmetrical coplanar microstrip line with a gap to hotline width ratio of 0.75. It has been fabricated by photolithographic lift-off of a sandwich of 30-nm sputtered Ti and 120-nm sputtered Au as a first step. Subsequently, the Au-structure was electroplated up to a thickness of 6  $\mu$ m using a cyanidic Au-electrolyte.

The laser cavity is comprised of a broadband high reflector on the rear side to achieve double-pass pumping and of a pump input coupler of optimized output coupling for the signal on the front face (see e.g. [3]). Both mirrors consist of a stack of 13 and 14  $\text{SiO}_2/\text{TiO}_2$ -layers, respectively, directly deposited onto the polished waveguide endfaces using  $\text{O}_2^+$ -ion assisted reactive evaporation.

The pump input side of the cavity was pigtailed with the common branch of a fiberoptic wavelength division demultiplexer (WDM) to allow coupling of a pigtailed pump laser diode and extraction of the laser output in backward direction. The WDM has standard (9/125 $\mu\text{m}$ ) fiber pigtails. Finally, the pigtailed laser has been packaged including isolation, thermo-electric temperature control ( $< \pm 0.01\text{K}$ ) and two cascaded 10/90% power splitters. FC/PC connection is provided for the pump input, for the laser output (90%), for monitoring of mode-locking stability (1%) and to derive a control signal for the pump feedback stabilization (9%).

**Experimental results:** The mode-locked Er-doped laser has been investigated in terms of power characteristics, pulse width, spectrum and time-bandwidth product for mode locking at different harmonics (2nd, 5th and 10th) of the axial mode frequency spacing. To drive the mode locker the rf-signal from a highly stable generator was boosted using a narrow-band low-noise amplifier and then fed via a bias tee to the travelling wave electrodes of the intracavity phase modulator. The electrodes are terminated AC-coupled by a 50- $\Omega$  load.

To pump the  $\text{Ti:Er:LiNbO}_3$ -waveguide laser a high-power (up to 150 mW from the laser pigtail) laser diode of about 1480-nm center-wavelength and 12-nm spectral width has been used. The pump power was launched through the WDM into the mode-locked laser. Up to 140 mW of incident pump power were available at the common branch of the WDM. The polarization and wavelength of the emission can be adjusted by the pump polarization. With  $\pi(\sigma)$ -polarized pumping the Er-laser emits at 1575 (1562) nm  $\pi(\sigma)$ -polarized. Threshold pump power and slope efficiencies are 56 mW (65 mW) and 14.4%(13.2%) for  $\pi(\sigma)$ -polarized emission, respectively. Both, slope efficiency and output power are more than an order of magnitude better than previously reported results [1],[2].

To suppress relaxation spiking of the laser during mode locking 9% of the laser output were detected and the detector signal fed to a specially designed control circuit. This circuit generates and superimposes a correction component to the injection current of the pump laser diode to suppress relaxation oscillations by controlled pumping. Up to -42 dB reduction of the spectral power density at the dominant peak of the noise spectrum around 450 kHz has been achieved leading to a relative intensity noise (RIN) of the laser of -82.3 dB/Hz for 3.5 dBm of DC-electrical power (detector signal into 50  $\Omega$ ). At frequencies above 100 MHz the laser output is almost shot noise limited.

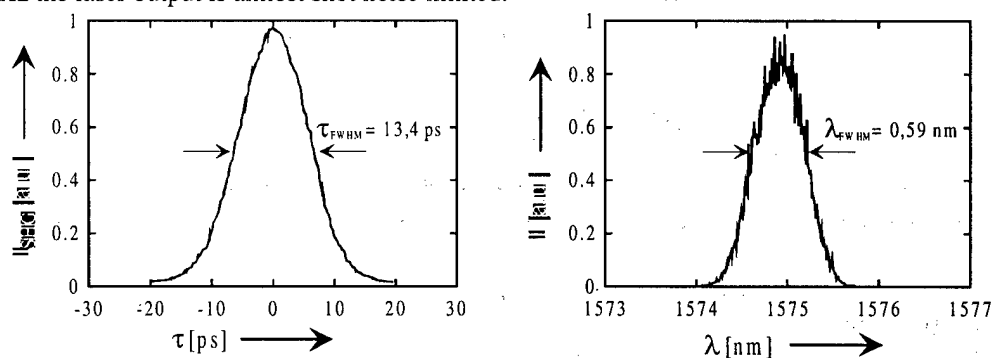


**Fig. 2:** Autocorrelation trace as function of the relative pulse delay (left) and spectral power density versus wavelength (right) for mode locking at the 10th harmonic (10.295 GHz) in  $\pi$ -polarized emission with 33.2-dBm rf-power.

Results obtained with mode-locked operation are shown in Fig. 2 for the 10th harmonic and  $\pi$ -polarized emission. With 33.2 dBm of rf-power a pulse width of 9.5 ps (FWHM) has been determined by deconvolution of the autocorrelation trace assuming a Gaussian pulse shape. Together with the spectral width of 0.59 nm a time bandwidth product of 0.68 results.

First Bit Error Rates (BER) have been measured with a pulse repetition rate of 2 GHz. The driving frequency was limited by the bit error measurement set up. A LiNbO<sub>3</sub> intensity modulator with an extinction ratio of 23 dB was used for the digital encoding. With a pseudo random bit pattern of  $2^7-1$  length a BER of  $1.9 \cdot 10^{-9}$  was detected during half an hour. To achieve this result, the RF-drive frequency had to be detuned about 500 kHz from the frequency of minimum time-bandwidth product.

This detuning was necessary to reduce high-frequency noise detected at the optimum locking frequency. This noise is well known for harmonical mode locking as beat noise of supermodes [4]. Therefore, we developed an improved laser design with two additional phase modulators, indicated in Fig. 1. By active spatial averaging of the standing wave intensity pattern of the supermodes the beat noise is reduced. With this laser design we measured the spectral power density at the lowest beat noise component. In Fig. 3 the results are shown for 5th harmonic mode locking at optimum locking frequency (time-bandwidth product = 0.49). With 2 MHz push-pull phase modulation the noise maximum is reduced by -24 dB.

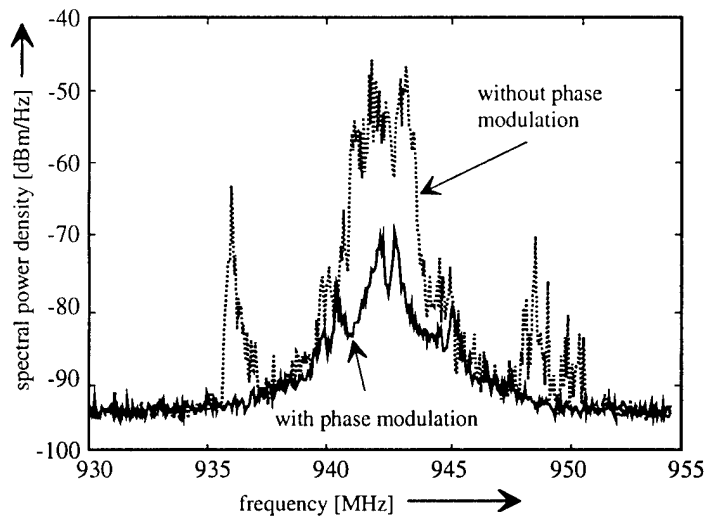


**Fig. 3:** Electrical spectral power density at the lowest beat noise component at 5th harmonic mode locking and  $\sigma$ -polarized emission with (solid line) and without (dashed line) phase modulation

**Conclusions:** We have demonstrated a harmonically mode-locked Ti:Er:LiNbO<sub>3</sub> waveguide laser of drastically improved performance compared to former results. Output power and slope efficiency have been improved by more than an order of magnitude. By feedback controlled pumping the RIN of the laser could be reduced by -42dB. A Bit Error Rate of  $10^{-9}$  at 2nd harmonic mode locking during half an hour has been achieved. With an improved laser design it was possible to reduce the high-frequency beat noise by -24 dB.

#### References:

- [1] H. Suche, R. Wessel, S. Westenhöfer, W. Sohler, S. Bosso, C. Carmannini, and R. Corsini, *Opt. Lett.*, **20**, No. 6, pp. 596-8 (1995)
- [2] H. Suche, I. Baumann, D. Hiller, and W. Sohler, *Electr. Lett.*, **29**, pp. 1111-2, (1993)
- [3] I. Baumann, R. Brinkmann, M. Dinand, W. Sohler, and S. Westenhöfer, *IEEE J. Quantum Electron.*, **32**, No. 9, pp. 1695-1706 (1996)
- [4] A. E. Siegman, "Lasers", (University Science Books, Mill Valley, California, 1986), pp. 1073-4

# Fabrication of New Abrupt Waveguide Bends in Lithium Niobate

Tzyy-Jiann Wang, Pei-Kuen Wei, and Way-Seen Wang.

Institute of Electrical Engineering

National Taiwan University

Taipei 10617, Taiwan, ROC

Tel: +886-2-363-5251, FAX: +886-2-362-1950

E-Mail: wswang@cc.ee.ntu.edu.tw

## I. Introduction

In optical integrated circuit, waveguide bends are used to change the optical wave propagation direction. They are important structures in many devices, such as couplers and modulators, to prevent the unwanted crosstalk between neighbor waveguides and make the device design become flexible. However, the bend loss is serious for bend angle larger than  $2^\circ$ . This restricts its application on devices with bend angle  $< 1^\circ$  and makes the device very long.

In integrated optics, lithium niobate ( $\text{LiNbO}_3$ ) is one of the most promising materials because of its high optical quality, excellent electro-optical property, and mature waveguide fabrication technology. In this work, we present a new abrupt waveguide bend structure in  $\text{LiNbO}_3$ . This bend utilizes a microprism fabricated by proton exchange to compensate the phase difference between the inner and outer sides of the wavefront, which is required to make the wavefront properly tilt to enter into the bent waveguide. The microprism is designed by a modified phase compensation rule in the viewpoint of phase match. From experiment, it is found that a great improvement of bend loss is achieved.

## II. Design

The new abrupt waveguide bend consists of a nickel-indiffused (NI) waveguide bend and a microprism, as shown in Fig.1. A microprism fabricated by proton exchange is placed on the bend corner. As the optical field propagates through the microprism, the inner side of its wavefront goes through a longer distance in the microprism than the outer one. Since the refractive index of the microprism is higher than that of the substrate, the phase of the inner side is delayed more than that of the outer one. This results in the tilt of the wavefront. By an appropriate design of the microprism such that the tilt angle of wavefront is equal to the bend angle of waveguide, most of the optical field can enter into the waveguide after the bend and only little optical power is lost.

From [1], the microprism half-length  $L$  can be designed by

$$(n_p - n_f) \cdot L = n_{eff} \cdot \tan(\theta/2) \cdot \left[ W_{eff} + \left( \frac{L}{\sin(\theta/2)} + W_{eff} \right) \cdot \left( \frac{1}{\cos(\theta/2)} - 1 \right) \right] \cdot \sqrt{\frac{n_f}{n_p}} \quad (1)$$

where  $n_p$  and  $n_f$  are the refractive indexes of the microprism and the waveguide,  $n_{eff}$  is the effective index of the guided mode,  $W_{eff}$  is the effective width of the waveguide,  $\theta$  is the bend angle. From several works, it is found that the extraordinary refractive index change caused by proton exchange in benzoic acid is  $\Delta n_e = 0.12$  [2]. In this design,  $n_p = 2.2028 + 0.12$  is chosen. For a diffusion-type waveguide,  $n_f$  is not a constant, but varies along the lateral and the depth directions. The determination of  $n_{eff}$  requires additional measurement and make microprism design process difficult. Because the difference between  $n_f$  and  $n_{eff}$  is small, for convenience, they are approximated as the substrate index  $n_s$  in this design. Simulation results by the semivectorial finite difference beam propagation method [3] show that the determination of  $L$  by this approximation is effective in the microprism design and the calculated  $L$  is close to the optimal one. As to  $W_{eff}$ , its value is set as three times of the waveguide width  $W$  in order to include most of the optical power.

### III. Fabrication and results

The abrupt waveguide bends are fabricated on a z-cut, y-propagating LiNbO<sub>3</sub> substrate. In the experiment, the NI waveguide is chosen, because it can be fabricated at lower diffusion temperature [4], no additional LiO<sub>2</sub> outdiffusion suppression is required during the diffusion process. In addition, it has the low-loss characteristic. From previous work [5], it is found that the proton change rate is reduced as Ni ions pre-exist in LiNbO<sub>3</sub>. As the range of the microprism and the waveguide are overlapped, this effect will give rise to an inhomogeneous microprism. However, when the pattern of waveguide and microprism are in different masks, any mask misalignment will cause a gap between the microprism and the waveguide, and result in the increase of bend loss. To overcome the above problem, a novel self-alignment method is used.

Fig. 2 displays the fabrication process of the waveguide bend. First, a Si film is sputtered on LiNbO<sub>3</sub> substrate and patterned as the microprism shape by photolithography. This structure is shown in Fig. 2(a). In order to form the NI waveguide, a Ni stripe with width  $W=4\mu\text{m}$  is deposited by the e-beam evaporation to a thickness of 400Å. As shown in Fig. 2(b), in the region of microprism, the Ni stripe is placed on the Si film of the microprism pattern. Thus, during the diffusion process at temperature  $T=900^\circ\text{C}$  for 30 min, no Ni ions will enter into the microprism part of substrate. Additional experiments show that little Si ions are diffused into the substrate during the diffusion process and only negligible reduction of the proton exchange rate is observed. Then a Cr film is deposited on the substrate as the proton exchange mask. When the substrate is put in the diluted hydrofluoric acid, the Si film of the microprism shape is etched and the Cr film on the top of it is removed just like the common lift-off process. Fig. 2(c) shows the structure at this step. To form the proton-exchanged microprism, the substrate is immersed in the benzoic acid at  $240^\circ\text{C}$  for 4 hr. After proton exchange, the Cr film is removed. Finally, the waveguide end face is polished for laser light coupling. Fig. 2(d) shows the overall structure of the new abrupt waveguide bend.

Abrupt waveguide bends of  $\theta=4^\circ$ ,  $6^\circ$ ,  $8^\circ$ , and  $10^\circ$  with and without the microprism are fabricated. The bend loss measurement is made at the wavelength  $0.6328\mu\text{m}$  using a chopped beam and a lock-in detection. The normalized transmitted power is calculated by referring to the transmitted power of a straight waveguide. The experimental results show that the normalized transmitted power of the abrupt waveguide bend without microprism for  $\theta=4^\circ\sim 10^\circ$  is below 1%. As to the new structure, the waveguide bend with microprism of different half-length  $L$  for the same bend angle are fabricated and measured in order to obtain the better performance of device. The difference from the  $L$  calculated by (1),  $\pm 1\mu\text{m}$ , is considered. The normalized transmitted power for microprism with various values of  $L$  and  $\theta$  is listed in Table I. The normalized transmitted power can be as high as 46%, 39%, 36%, and 42% for  $\theta=4^\circ$ ,  $6^\circ$ ,  $8^\circ$ , and  $10^\circ$ , respectively.

### IV. Conclusion

A new abrupt waveguide bend in LiNbO<sub>3</sub> with proton-exchanged microprism is fabricated. The microprism designed by the phase compensation rule with approximation is proved to be effective in reducing the bend loss. To our knowledge, the improvement of bend loss is the greatest for the diffusion-type abrupt waveguide bend with  $\theta=4^\circ$ ,  $6^\circ$ ,  $8^\circ$  and  $10^\circ$  in LiNbO<sub>3</sub>. The microprism fabrication parameters have not been optimized yet. In the future, we will continue to improve the fabrication process and optimize the related fabrication parameters.

### V. References

- [1] H.-B. Lin, J.-Y. Su, P.-K. Wei, and W.-S. Wang, "Design and application of very low-loss abrupt bends in optical waveguides," *IEEE J. Quantum Electron.*, vol. QE-30, pp. 2827-2835, Dec. 1994.
- [2] J. L. Jackel, C. E. Rice, and J. J. Veselka, "Proton exchange for high-index waveguides in LiNbO<sub>3</sub>," *Appl. Phys. Lett.* Vol. 41, no. 7, pp.607-608, Oct. 1982.

- [3] P. L. Liu and B. J. Li, "Study of form birefringence in waveguide devices using the semivectorial beam propagation method," *IEEE Photon. Technol. Lett.*, vol. 3, no. 10, pp. 913-915, 1991.
- [4] Y.-P. Liao, D.-J. Chen, R.-C. Lu, and W.-S. Wang, "Nickel-diffused lithium niobate optical waveguide with process-dependent polarization," *IEEE Photon. Technol. Lett.*, vol. 8, no. 4, pp. 548-550, Apr. 1996.
- [5] R.-S. Chen, T.-J. Wang, and W.-S. Wang, "Wet-etched ridge waveguides in Y-cut lithium niobate", *J. Lightwave Technol.*, vol.15, no.10, pp. 1880-1887, Oct. 1997.

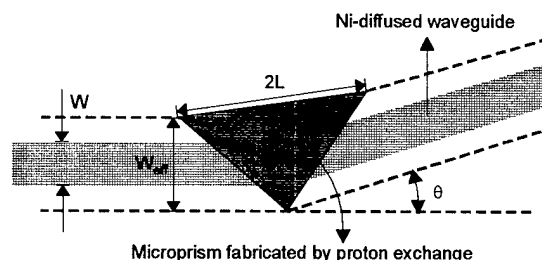


Fig. 1 The new structure of abrupt waveguide bend with microprism in  $\text{LiNbO}_3$ .

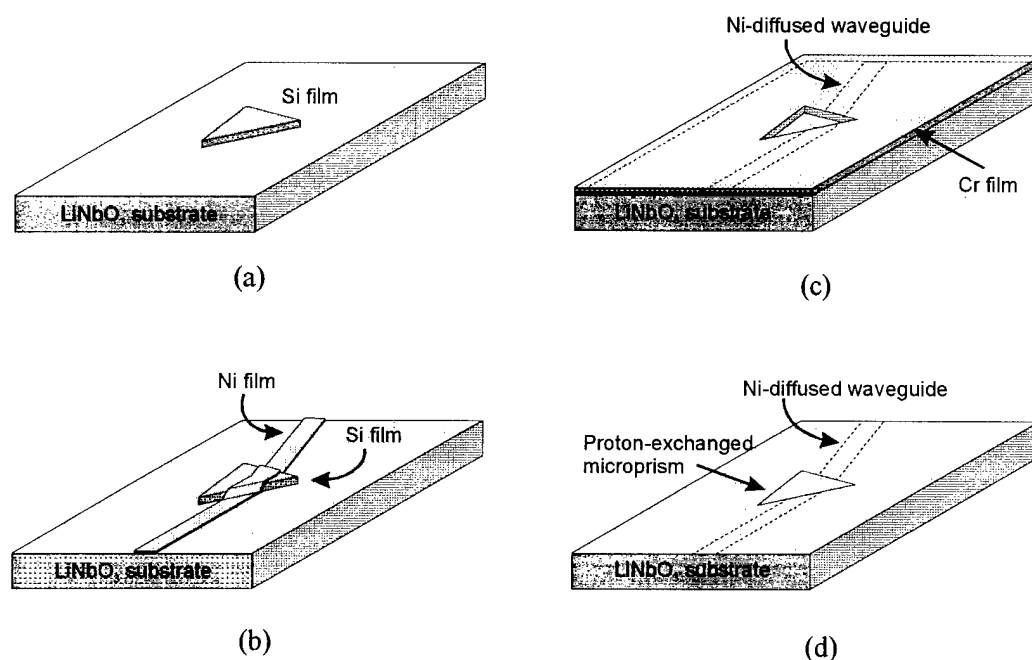


Fig. 2 Fabrication process of the improved waveguide bend with proton-exchanged microprism in  $\text{LiNbO}_3$ .

half-length ( $\mu\text{m}$ )	bend angle			
	4°	6°	8°	10°
L-1	31.62%	27.39%	<b>36.06%</b>	<b>41.83%</b>
L	<b>45.83%</b>	<b>38.73%</b>	35.36%	34.64%
L+1	21.21%	25.50%	23.45%	20.0%

Table I. The normalized transmitted power of the new structure with microprism.



**Integrated Photonics Research**

# **Quantum Wells II: Heterojunction Engineering, Optical Gain and Electro- Absorption**

**Tuesday, March 31, 1998**

**Joseph P. Donnelly, MIT Lincoln Laboratory**  
Presider

**ITuJ**  
**3:30pm–5:00pm**  
Salon B

# InGaAs/InAlAs Asymmetric Triple Coupled Quantum Well for Blue-Chirp Electroabsorption Optical Modulators

*Masaki Kato, Kunio Tada and Yoshiaki Nakano*

Department of Electronic Engineering, University of Tokyo  
7-3-1 Hongo, Bunkyo-ku, Tokyo 113-8656, Japan  
Phone: +81-3-3812-2111(ext. 6777), Facsimile: +81-3-5802-3313  
E-mail: mkato@jungfrau.t.u-tokyo.ac.jp

## Introduction

EDFA has made the external modulator a key device for long-haul, high-speed optical transmission systems. In such systems the product of the square of bit rate and the transmission length is limited by the modulator's chirp parameter and the fiber dispersion, where transmission distance can be extended through negative-chirp or blue-chirp operation. However, most electroabsorption (EA) modulators have positive chirp parameter, and blue-chirp operations are only achievable at the sacrifice of insertion loss and extinction ratio [1-4].

In this paper, we propose a novel potential-tailored quantum well structure composed of two ternary materials lattice-matched to InP,  $\text{In}_{0.53}\text{Ga}_{0.47}\text{As}$  wells and  $\text{In}_{0.52}\text{Al}_{0.48}\text{As}$  barriers, which is able to bring about blue-chirp operation in EA modulators without the trade-off mentioned above.

## Calculation

As illustrated in Fig. 1(a), the quantum well proposed here contains three wells separated by two thin barriers. The widths of side wells are optimized so as to promote the penetration of electron and heavy hole wavefunctions into the side wells under small electric field, and so as to maintain exciton oscillator strength required for modulation. Shown in Fig. 2(a) and (b) are absorption coefficient spectra of this asymmetric triple coupled quantum well (ATCQW) and a conventional rectangular quantum well (RQW) as a reference, respectively. In the calculation of absorption coefficients, we took into account the effect of valence band mixing on the basis of  $\mathbf{k} \cdot \mathbf{p}$  perturbation theory [5] with 4×4 Luttinger-Kohn Hamiltonian and the effect of excitons using the non-variational approach [6]. The change in the refractive index was calculated from the change in the absorption coefficient using the Kramers-Kronig relation and, finally, the chirp parameter  $\beta_c$  was calculated using the following equation,

$$\beta_c = \frac{4\pi}{\lambda} \frac{\Delta n}{\Delta \alpha},$$

where  $\lambda$ ,  $\Delta n$  and  $\Delta\alpha$  are the operation wavelength, the refractive index and absorption coefficient changes, respectively. Figure 3 shows the relationship between the refractive index change and the absorption of the modulator, where the differential slope of the curves corresponds to the chirp parameter of small signal modulation. As can be seen, the RQW's chirp parameter is always positive, whereas the ATCQW gives rise to negative chirp parameter over a wide range of applied electric field. Therefore, blue-chirp operation is obtainable without introducing excess insertion loss.

## Discussion

In order to achieve both blue-chirp operation and low insertion loss, a large Stark shift of exciton absorption peak and abrupt reduction of exciton oscillator strength are required [7]. In the ATCQW, as illustrated in Fig. 1(b), electron and heavy hole quickly separate under electric field by tunneling into the wells on opposite sides. This is equivalent to applying a large field to the well, thus producing the large Stark shift shown in Fig. 2(a). At the same time, exciton oscillator strength decreases abruptly because overlap between electron and heavy hole wavefunctions becomes very small. In the RQW, on the other hand, since the Stark shift is much smaller and strong exciton absorption is maintained even at high electric field (Fig. 2(b)), negative chirp parameter is not achievable.

## Conclusion

We have proposed a lattice-matched ternary InGaAs/InAlAs asymmetric triple coupled quantum well and numerically simulated its electroabsorption characteristics. It has been found that, in EA modulators incorporating this ATCQW, negative chirp parameter is possible over a wide range of operation condition without increasing insertion loss. This work was supported by the Mombusho Grant-in-Aid #09450029 and JSPS-RFTF program #97P00103.

## References

- [1] J. F. Fells, M. A. Gibbon, I. H. White, G. H. B. Thompson, R. V. Peny, C. J. Armistead, E. M. Kimber, D. J. Moule and E. J. Thrush, *Electron. Lett.*, **30**, pp. 1168-1169, 1994.
- [2] F. Dorgeuille and F. Devaux, *IEEE J. Quantum Electron.*, **30**, pp. 2565-2572, 1994.
- [3] K. Morito, R. Sahara, K. Sato, Y. Kotaki and H. Soda, *Electron. Lett.*, **31**, pp. 975-976, 1995.
- [4] K. Yamada, K. Nakamura, Y. Matsui, T. Kunii and Y. Ogawa, *IEEE Photon. Technol. Lett.*, **7**, pp. 1157-1158, 1995.
- [5] J. M. Luttinger and W. Kohn, *Phys. Rev.*, **97**, pp. 869-883, 1955.
- [6] J. P. Loehr and J. Singh, *Phys. Rev. B*, **42**, pp. 7154-7162, 1990.
- [7] K. Wakita, K. Yoshino, I. Kotaka, S. Kondo and Y. Noguchi, *IEEE Photon. Technol. Lett.*, **8**, pp. 1169-1171, 1996.

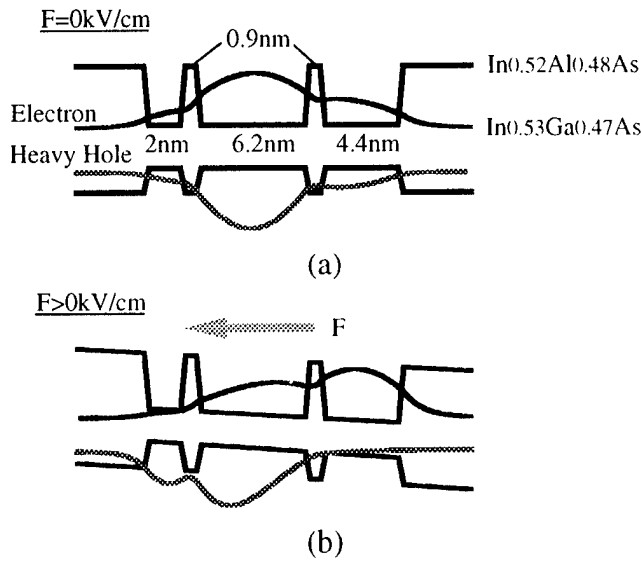


**Fig. 1** Asymmetric triple coupled quantum well and wavefunctions for electron and heavy hole at zero electric field (a) and under electric field (b).

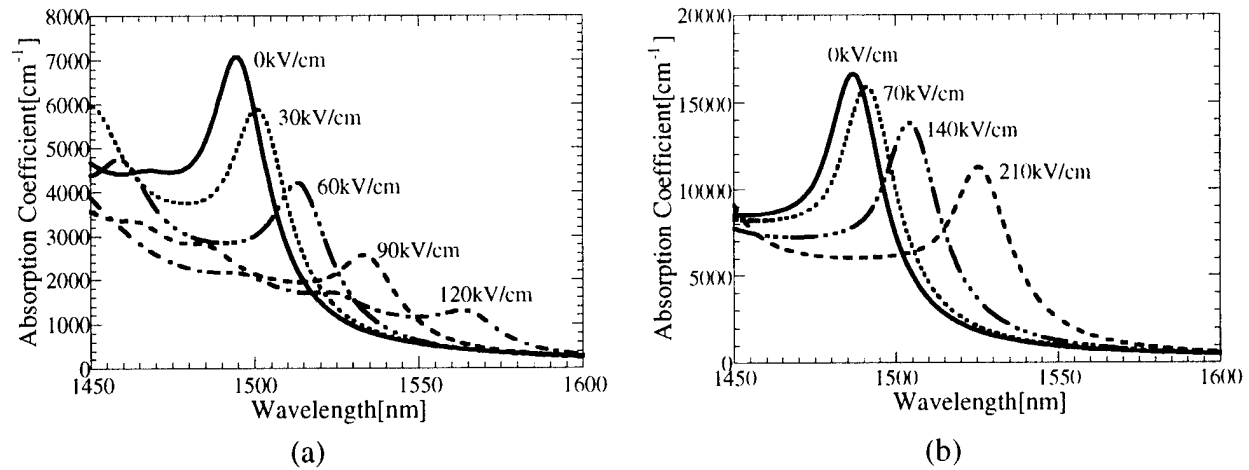


**Fig. 2** Absorption coefficient spectra of the asymmetric triple coupled quantum well (a) and 7 nm thick In<sub>0.53</sub>Ga<sub>0.47</sub>As / In<sub>0.52</sub>Al<sub>0.48</sub>As rectangular quantum well (b).

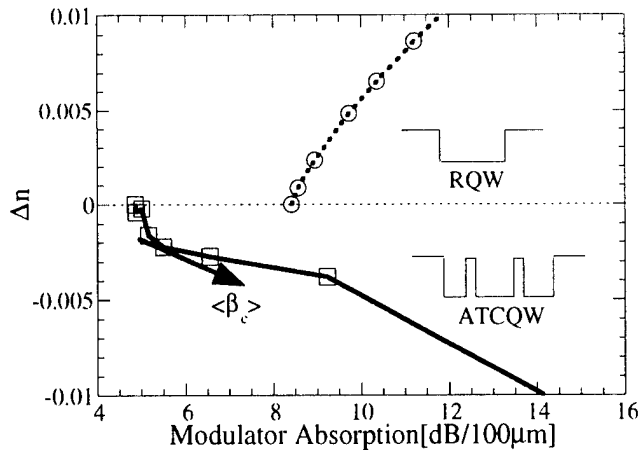


**Fig. 3** The relation between refractive index change and absorption in the modulator. The solid line with squares is for ATCQW and the dotted line with circles for RQW. The square markers for ATCQW are plotted every 15 kV/cm step of electric field whereas the circle markers for RQW every 35 kV/cm step. The differential slope of the curves  $\langle \beta_c \rangle$  corresponds to chirp parameter.

# MQW waveguide electroabsorption modulators on InGaAsP with absorption edge merging

A. Ahland, D. Schulz, E. Voges

University of Dortmund, Lehrstuhl Hochfrequenztechnik

D-44221 Dortmund, Germany

Phone: +49-231/755-5567 Fax: +49-231/755-4631

e-mail: ahland@hft.e-technik.uni-dortmund.de

**Abstract:** An optimized InGaAsP based MQW modulator with low chirp is proposed. The TE-absorption is enhanced by field induced heavy and light hole absorption merging.

**Introduction:** There is an increasing interest in external modulators in order to exploit the vast bandwidth of optical fibre communication networks operating at  $\lambda = 1.55\mu\text{m}$  wavelength. Particularly for high bit-rate, long haul optical fibre transmission systems the performance restrictions of directly modulated lasers have lead to an intensive study of external modulators. A monolithic identical layer integration of laser and modulator [1] combines a simple processing with good modulation behavior. In this context the chirp parameter is one of the utmost performance parameters, because it results in a frequency broadening of the signal and restricts long-haul transmission. Especially MQW electroabsorption modulators are very attractive, as they provide a large absorption change under a relative low applied voltage due to the effect of the excitonic absorption. The modulation behavior is greatly enhanced by a field induced merging of heavy hole (hh) and light hole (lh) transitions. Up to now a similar effect is only known from GaAsP/AlGaAs QWs [2] and from GaInAs/AlInAs QWs [3]. On the other hand GaInAsP is much easier to process because Al easily oxidizes. Unfortunately GaInAsP based QWs have got an electron dominated Stark effect, due to their large valence band discontinuity. We present an optimized three layer quantum well composed of tensile and compressive strained GaInAsP, in which the different behavior of heavy and light holes results in an enhanced field dependence. As compressive strained layers show a lower valence band discontinuity the saturation behavior is improved. Additionally, this structure offers the possibility of an identical layer integration with a laser when a second laser quantum well structure is added allowing laser operation at  $\lambda = 1.55\mu\text{m}$ .

**Modeling:** The dielectric function  $\epsilon(\omega)$  is calculated with a bilocal density matrix formalism [4, 5] valid for excitonic transitions as well as for the interband absorption including band mixing. The formalism includes the creation of electron-hole pairs. The dielectric response is related to the real part of the bilocal electron-hole amplitude. No Kramers-Kronig relation has to be evaluated with this approach, the refractive index and the chirp factor are calculated directly from the dielectric function. This avoids tedious integral evaluations as well as the influence of the integration limits on the results. The electron-hole amplitude is expanded in  $k$ -space into the exciton eigenfunctions. The subbands which build a basis for the exciton eigenfunctions are obtained by solving the

stationary Schroedinger equation with k-p operators of orders up to 8x8.

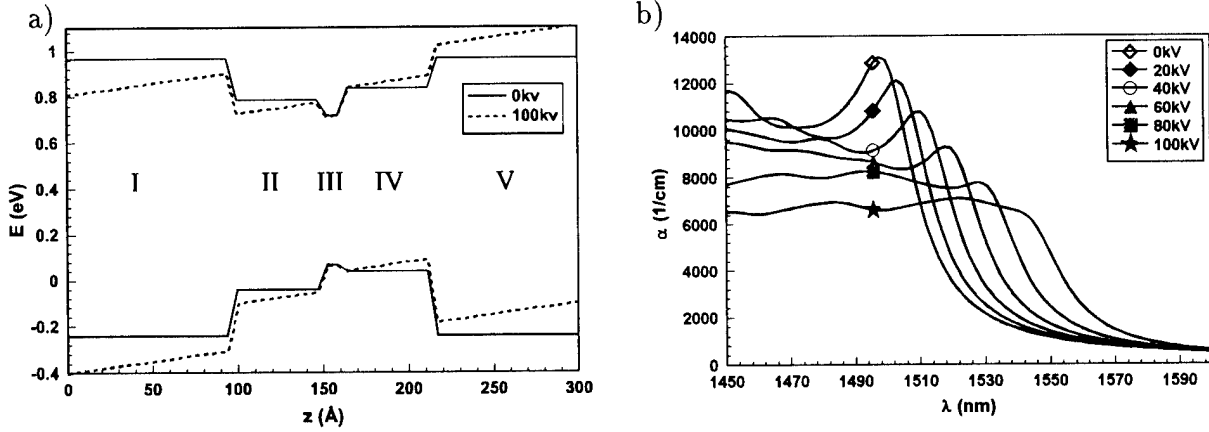


Figure 1: a) Confinement potential of the structure based on  $\text{Ga}_{0.1}\text{In}_{0.9}\text{As}_{0.2}\text{P}_{0.8}$  (I+V),  $\text{InAs}_{0.5}\text{P}_{0.5}$  (II) with 52Å width,  $\text{InAs}_{0.7}\text{P}_{0.3}$  (III) with 12Å width,  $\text{Ga}_{0.6}\text{In}_{0.4}\text{As}$  (IV) with 52Å width, b) absorption

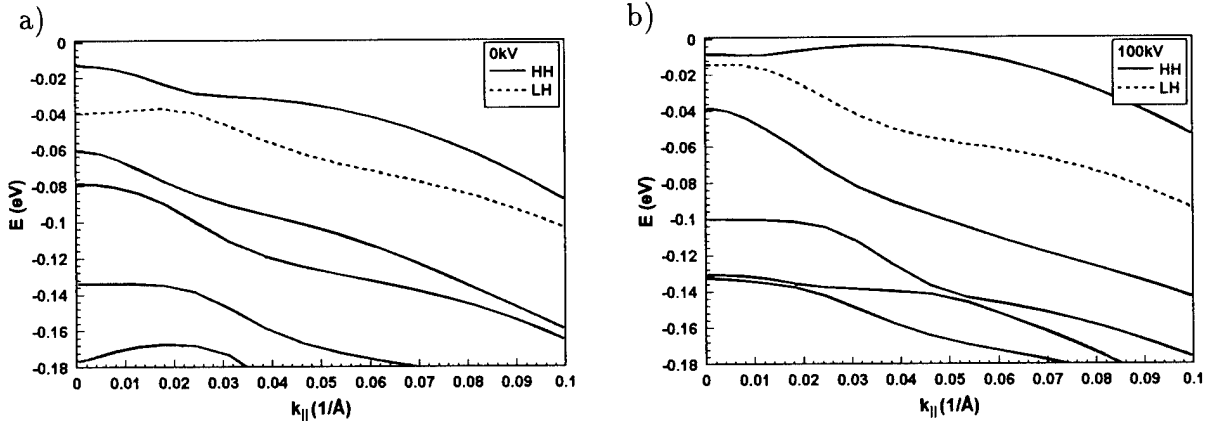


Figure 2: Bandstructure at 0kV/cm (a) and 100kV/cm (b)

**Results:** The device structure proposed is shown in fig. 1a. The layers II and III are compressive strained, layer IV is tensile strained. Because of the very small width of four monolayers ( $\approx 12\text{\AA}$ ) there is no bound state in the layer III, but the overlap of the electron and hole wave function is increased, resulting in a much smaller reduction of the absorption with an applied voltage. The absorption  $\alpha$  is shown in fig 1b for different applied voltages. Depending on the direction of the applied voltage, the hole wave function is shifted into the tensile or compressive strained layer. At about 100kV/cm the absorption edges of light and heavy holes begin to merge which is shown in the subband structure in fig. 2 with an external field of 0kV/cm (a) and 100kV/cm (b) applied. The band mixing results in an upward bending of the heavy hole band, which gives an increased joint density of states. This compensates the decrease of the absorption due to the quantum confined Stark effect (QCSE). The Stark shift is 25meV for a field variation of 100kV/cm. The chirp factor is defined by

$$\alpha_H = \frac{4\pi}{\lambda} \frac{\Delta n'}{\Delta \alpha} \quad (1)$$

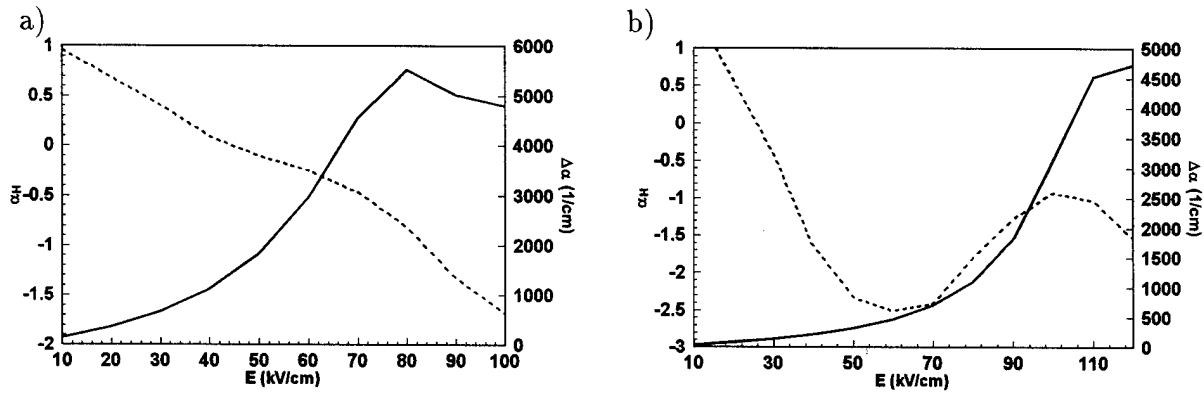


Figure 3: Differential absorption (straight) and  $\alpha_H$  (dashed) at  $\lambda = 1.53\mu\text{m}$  (a) and  $\lambda = 1.55\mu\text{m}$  (b)

with the refractive index change  $\Delta n'$ . The differential absorption  $\Delta\alpha$  and chirp factor  $\alpha_H$  for  $\lambda = 1.53\mu\text{m}$  and  $\lambda = 1.55\mu\text{m}$  is shown in fig. 3. For transmission with standard single mode fibers  $\alpha_H$  should be slightly negative. Most important are the parts related to the highest signal power. Thus for a system analysis it is recommended to average over the first 3dB of the signal [6]. The average chirp  $\alpha_{H3dB}$  varies between +0.35 and -1.1 for  $\lambda = 1.53\mu\text{m}$  and  $1.55\mu\text{m}$ , respectively. These values depend on the absolute contrast ratio ( $CR$ ), which is estimated by

$$CR = 10 \log(e^{\Delta\alpha\gamma L}) \approx 4.343 \Delta\alpha\gamma L. \quad (2)$$

A confinement factor  $\gamma$  of 0.2 and a modulator length  $L$  of  $50\mu\text{m}$  is assumed. Because of the high differential absorption  $\Delta\alpha$  a modulator length of  $50\mu\text{m}$  is sufficient for a  $CR$  of more than 20dB. By the small length the capacity is reduced which results in a greatly enhanced cutoff frequency. Because this QW remains transparent for positive bias, this structure can be used for an identical layer monolithic integration of a laser and modulator. An additional QW has to be included into the active layer to achieve gain.

## References

- [1] A. Ramdane, A. Ougazzaden, F. Deveau, F. Delorme, and M. Schneider, *Electron. Lett.*, vol. 30, pp. 1980–1981, 1994.
- [2] B.N. Gomati, N.G. Anderson, F. Agahi, C.F. Musante, and K.M. Lau, *Appl. Phys. Lett.*, vol. 62, no. 26, pp. 3473–3475, 1993.
- [3] T. Schwander et al, *Proc. of Integrated Photonics Research, Boston*, vol. 6, pp. 298, IPR'96.
- [4] H. Mikkelsen, *Optoelectronic modulators in bulk, multiple quantum well and superlattice*, Shaker, Aachen, 1994.
- [5] A. Stahl und I. Balslev, *Electrodynamics of the semiconductor band edge*, Springer, 1987.
- [6] F. Dorgeuille and F. Devaux, *IEEE J. Quantum Electron.*, vol. 30, no. 11, pp. 2565–2572, 1994.

# Design of polarization insensitive semiconductor optical amplifiers at 1300 nm

Sangin Kim\*, WoonJo Cho, Xiaobo Zhang, Mark Hopkinson, Anand Gopinath

University of Minnesota

Department of Electrical and Computer Engineering

200 Union Street S. E.

Minneapolis, MN 55455

Tel: 612-625-3054 Fax: 612-625-4583

email: gopinath@ece.umn.edu

\*Currently at: Korea Telecom

17 Woonyun-Dong, Suhcho-Ko

Seoul, Korea

email:sangin@strl.kotel.co.kr

## 1 Introduction

Semiconductor Optical Amplifiers find applications as switches and wavelength convertors. Linearization of the gain may lead to use as amplifiers, especially at 1300 nm, where the fiber amplifiers based on the fluoride fibers are not very efficient. We discuss the design of 1300 nm semiconductor optical amplifiers (SOAs) suitable for integration. These amplifiers have a small value of tensile strain in the wells to attempt to equalize the TE and TM mode gains. We have designed and built amplifiers with this design, and we present measured results. We believe this is the first report of these amplifiers using tensile strain in AlInGaAs material system.

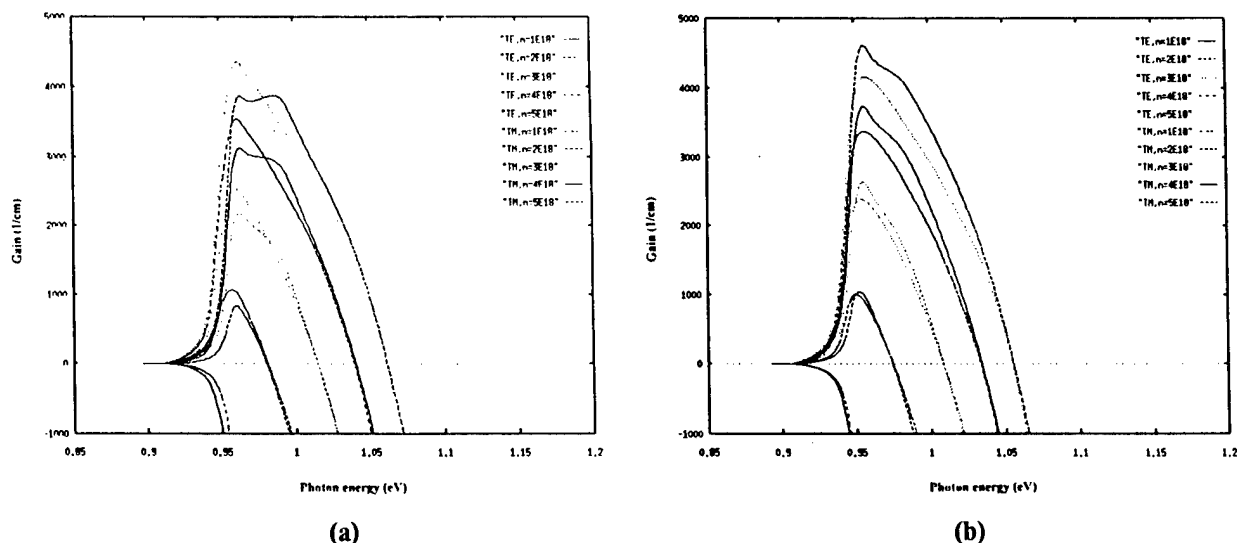


Figure 1: Calculated gain spectra in 10 nm quantum wells with (a) 0.25% tensile strain and (b) 0.35% tensile strain in AlInGaAs wells and 1.1  $\mu\text{m}$  AlInGaAs barriers.

## 2 Gain Calculations

$k \cdot p$  calculations were performed for both InGaAsP, and AlInGaAs to obtain their band structure, using the  $8 \times 8$  Hamiltonian using the envelope function approximation [1].

Subsequent calculations obtain the gain of the quantum wells with appropriate barriers. In Figure 1, we show the results of our gain calculations for the AlInGaAs quaternary with 0.25% strain, which indicates that the gain of the TE and TM modes are not quite equal. Similar calculations have also been performed for the AlInGaAs quaternary with 0.35% strain in the wells, which show much better gain equalization. We have also examined the alternatives: alternate compressive/tensile wells, strained-balanced compressive wells-tensile barriers and decided that the simplest structure for the crystal grower is the tensile strained wells.

## 3 Design of Ridge Waveguide Structure

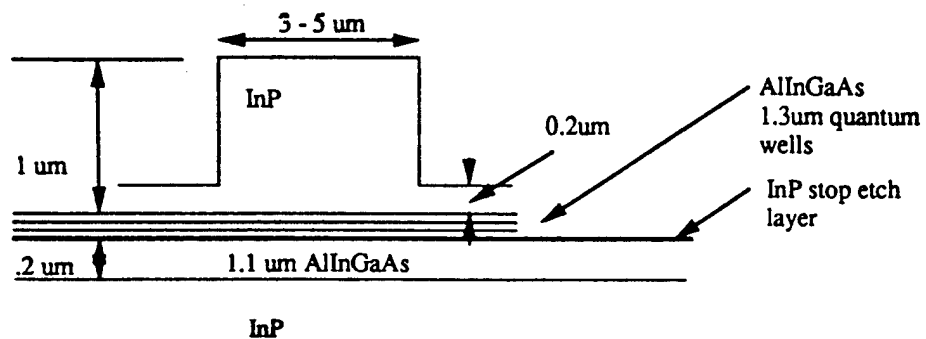


Figure 2: Ridge guide structure of the AlInGaAs amplifier

The amplifier structure was designed as a single mode ridge waveguide, and shown in Figure 2. The quantum wells were placed at the top of the separate confinement structure with an InP stop etch layer below the wells. Thus, for integration of this amplifier, the cladding layer, and the quantum wells may be etched off, and then the cladding layer is regrown on the InP stop etch layer. In the case of the AlInGaAs, the feasibility of regrowth remains because of this InP layer.

We chose the AlInGaAs/InP material system for the amplifier structure, since the wells in the conduction band are deeper [2]. The InP cladding layer was etched by reactive ion etching using  $\text{CH}_3/\text{H}_2$ , and the process was optimised to obtain nearly vertical side walls. The metalization was Ti-Pt-Au for the p-type contact, and Ni-Ge-Au for the n-type contact, however the former resulted in high contact resistance, and this will require to be optimized or changed. Both lasers and amplifiers were fabricated. Since our anti-reflection coating technology has not yet been developed, for the present the guides are at 7 degrees to the facet.

## 4 Results

Lasers in the AlInGaAs material with 0.25% strain in the wells, grown for this project showed a threshold current density of about  $5.56 \text{ KA/cm}^2$ , which is rather high. We are currently growing similar wafers with lower threshold current densities, and we will report on these at the meeting. Tests on lasers of different length gave a transparency current density of  $2.57 \text{ KA/cm}^2$ , with the high threshold material, and this is also high. The loss coefficient was estimated at  $623 \text{ cm}^{-1}$ , which is also very high.

The amplifiers were tested and Figure 3 shows the amplifier gain of a  $350 \mu\text{m}$  long structure, for both TE and TM polarizations, with TE gain being 7.9 dB, and with a 2.2 dB difference in gain for the TM polarization, indicating that a little more tensile strain, of the order of 0.35% is required to equalize the gain. We have also measured the gain spectra of the amplifier at different drive current. The spontaneous emission peaks around 1330 nm, with the difference in the TE and TM polarization being less than 5 nm.

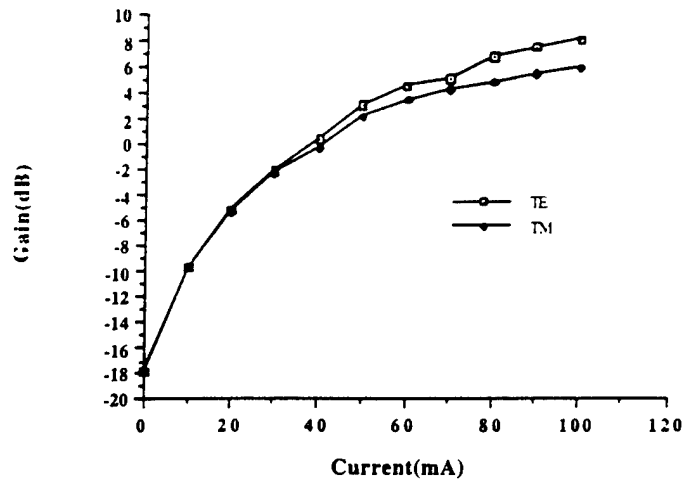


Figure 3: Gain plotted against drive current for  $350 \mu\text{m}$  long device with 0.25% tensile strain.

## 5 Summary

The design of polarization insensitive semiconductor optical amplifiers with quantum wells has been discussed. The amplifiers built have been tested and show polarization gains which are close to each other for the 0.25% tensile strain structures, and would be better for the 0.35% tensile strain structure.

## References

- [1] E. O. Kane, J. Phys. Chem. Solids, **1**, 82, 1956.
- [2] C.-E. Zah, R. Bhat, B. N. Pathak, F. Faivre, W. Lin, M. C. Wang, N. C. Andreakis, D. M. Hwang, M. A. Koza, T-P Lee, Z. Wang, D. Darby, D. Falnders, J. J. Hseih, J. Quantum Electron., **30**, 511, 1994.

# Many-body optical gain of wurtzite InGaN quantum-well lasers

Seoung-Hwan Park and Shun-Lien Chuang

Department of Electrical and Computer Engineering, University of Illinois at Urbana-Champaign,  
1406 West Green Street, Illinois 61801

Phone: (217) 333-3359

Fax: (217) 333-5701

E-mail: s-chuang@uiuc.edu

Wide band-gap semiconductors, including GaN, AlN, InN, and their ternary compounds, have drawn a lot of attention for their potential electronic and optoelectronic device applications. Room-temperature continuous-wave operation of strained InGaN multiquantum well (MQW) laser diodes with a lifetime of many thousand hours has been demonstrated recently [1,2]. With the progress in blue-green lasers, theoretical models for the electronic and optical properties of these wurtzite QW structures become very important. Recently, it has been pointed out [3-5] that many-body Coulomb effects are expected to be important in the wide band-gap semiconductors because of the large exciton binding energies in these systems. However, many fundamental properties of band structures and optical gain with many-body effects of the strained wurtzite GaN-based QW lasers, in particular, InGaN QW lasers are not well understood.

In this paper, we present theoretical results on the optical gain of wurtzite  $\text{In}_x\text{Ga}_{1-x}\text{N}/\text{In}_y\text{Ga}_{1-y}\text{N}$  QW lasers taking into account the many-body effects. Spectra broadening is calculated by taking into account the carrier-carrier (C-C) scattering. The optical spectra are obtained by using the spontaneous-emission transformation method [6-8]. The valence band structures and the band-gap renormalization are calculated as a function of strain or the well thickness. Also, these results are compared to those of GaN/ $\text{Al}_x\text{Ga}_{1-x}\text{N}$  QW

lasers. Our theoretical gain spectra of wurtzite InGaN QW lasers are also compared with experimental data obtained by Nakamura *et al.* [1].

Figure 1 shows the valence subband structures as a function of strain for 3.5 nm  $\text{In}_x\text{Ga}_{1-x}\text{N}/\text{In}_y\text{Ga}_{1-y}\text{N}$  and GaN/ $\text{Al}_{0.2}\text{Ga}_{0.8}\text{N}$  QW lasers. It is shown that subband energies of InGaN QW laser with small strain lie close to each other. However, it is expected that the increase of the compressive strain leads to improved laser characteristics, because the subband energy spacing is relatively large compared to that of QWs with smaller strain, as shown in Fig.1. Also, we know that subband energies of InGaN QW lasers lie closer to each other than those of GaN/ $\text{AlGaN}$

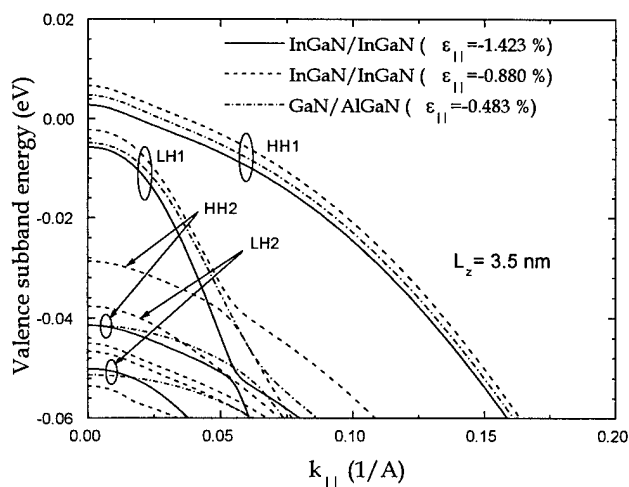


Fig.1 The valence subband structures as a function of strain for 3.5 nm  $\text{In}_x\text{Ga}_{1-x}\text{N}/\text{In}_y\text{Ga}_{1-y}\text{N}$  and GaN/ $\text{AlGaN}$  QW lasers.

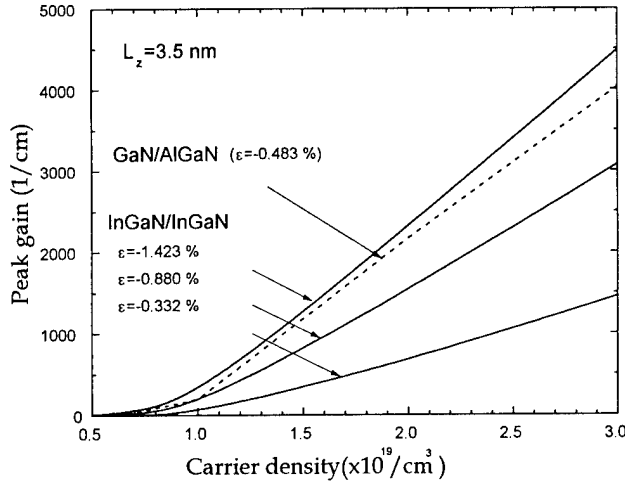


Fig.2 The peak gains in the TE polarization as a function of the injected carrier density for 3.5 nm  $\text{In}_x\text{Ga}_{1-x}\text{N}/\text{In}_y\text{Ga}_{1-y}\text{N}$  and  $\text{GaN}/\text{Al}_{0.2}\text{Ga}_{0.8}\text{N}$  QW lasers.

the InGaIn QW lasers at the same strain. That is, in a case of InGaIn QW lasers, larger strain is necessary to achieve lasing conditions similar to  $\text{GaN}/\text{Al}_{0.2}\text{Ga}_{0.8}\text{N}$  QW lasers.

Figure 3 shows the gain spectra of 3.5 nm  $\text{In}_{0.15}\text{Ga}_{0.85}\text{N}/\text{In}_{0.02}\text{Ga}_{0.98}\text{N}$  QW lasers. The solid and dashed lines are results calculated with many-body effects and the free-carrier theory, respectively. The gain spectra with many-body effects are compared with the only available experimental data so far for 3.5 nm

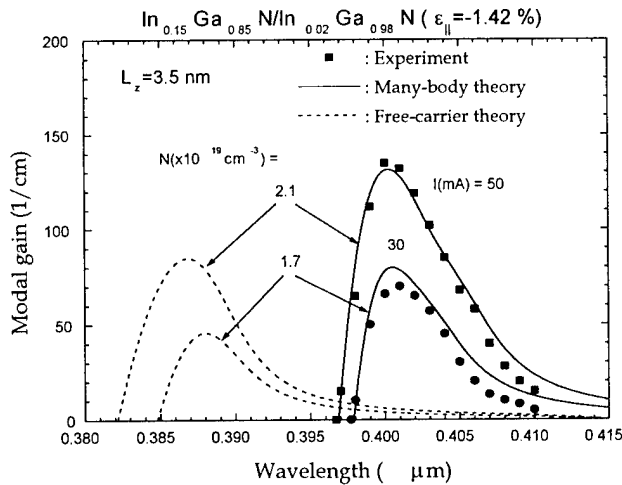


Fig.3 The gain spectra of 3.5 nm  $\text{In}_{0.15}\text{Ga}_{0.85}\text{N}/\text{In}_{0.02}\text{Ga}_{0.98}\text{N}$  QW lasers.

QW lasers for the same strain. This is attributed to the fact that InGaIn QW lasers have a smaller well depth than  $\text{GaN}/\text{AlGaIn}$  QW lasers for the same strain. Thus, it is expected that  $\text{GaN}/\text{AlGaIn}$  QW lasers show better laser characteristics than those of the InGaIn QW lasers with the same strain.

Figure 2 shows the peak gains in the TE polarization as a function of the injected carrier density for 3.5 nm  $\text{In}_x\text{Ga}_{1-x}\text{N}/\text{In}_y\text{Ga}_{1-y}\text{N}$  and  $\text{GaN}/\text{Al}_{0.2}\text{Ga}_{0.8}\text{N}$  QW lasers. It is shown that QW lasers with a larger strain shows improved laser gain compared to those with a smaller strain. As mentioned above, this is attributed to the fact that the subband energy spacing increases with compressive strain. Also, a  $\text{GaN}/\text{AlGaIn}$  QW laser shows a larger peak gain than those of

$\text{In}_{0.15}\text{Ga}_{0.85}\text{N}/\text{In}_{0.15}\text{Ga}_{0.85}\text{N}$  QW lasers. The symbols are experimental results from Ref.[1] at injection currents  $I=30$  and  $50$  mA, where the absorption line is assumed to be  $\sim 130 \text{ cm}^{-1}$ . Carrier densities are chosen to give the best fit to the experimental spectra. It is shown that the calculated gain spectra is in reasonably good agreement with the experiment. However, carrier densities are smaller than those estimated indirectly in Ref.[1]. We believe that our model provides a direct estimation of the carrier density. Further experimental and theoretical investigations are required to confirm the exact values of the carrier densities at a given current. Also, it is shown

that the gain peak with many-body effects is larger than of that of the free-carrier theory and shows a smaller blue-shift with increasing current.

Figure 4 shows the quasi-Fermi energy separation  $\Delta F$  and the band-gap renormalization (BGR) as a function of carrier density for a 3.5 nm  $\text{In}_{0.15}\text{Ga}_{0.85}\text{N}/\text{In}_{0.02}\text{Ga}_{0.98}\text{N}$  QW laser.

In the case of the free-carrier theory, the band filling effect is the main cause for the carrier density dependence of the peak gain energy. Thus, the peak gain energy obtained from the free-carrier theory is blueshifted with an increasing carrier density. On the other hand, the BGR decreases with increasing carrier density and contributes to the redshift of the gain peak. This results in the smaller blueshift for gain spectra with many-body effects compared to that of the free-carrier theory as shown in Fig.3.

In summary, theoretical results of the optical gain of wurtzite InGaN QW lasers taking into account the many-body effects are presented. The inclusion of compressive strain shows better lasing performance because of the increase of the subband energy separation in the valence band. The calculated gain spectra of  $\text{In}_{0.15}\text{Ga}_{0.85}\text{N}/\text{In}_{0.02}\text{Ga}_{0.98}\text{N}$  QW lasers are in reasonably good agreement with measured gain spectra. It is also shown that the gain peak shows a smaller blueshift than that of the free-carrier theory because of the large band-gap renormalization.

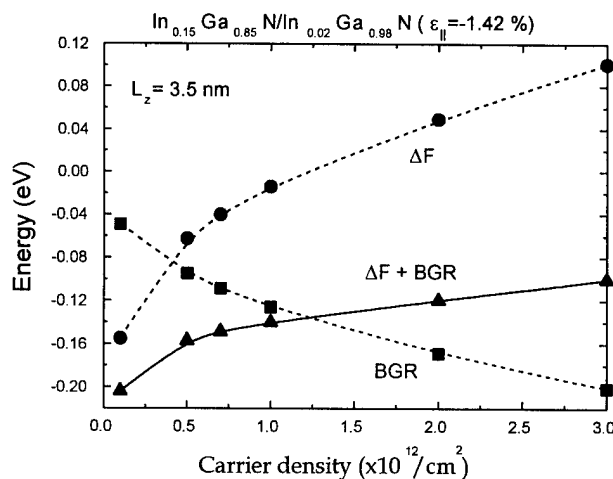


Fig.4 The quasi-Fermi energy separation  $\Delta F$  and the band-gap renormalization (BGR) as a function of carrier density for a 3.5 nm  $\text{In}_{0.15}\text{Ga}_{0.85}\text{N}/\text{In}_{0.02}\text{Ga}_{0.98}\text{N}$  QW laser.

## REFERENCES

- [1] S. Nakamura, IEEE J. Sel. Topics Quantum Electron. **3**, 712(1997).
- [2] S. Nakamura, LEOS'97, Postdeadline paper 1.1, November 1997.
- [3] H. Haug and S. W. Koch, *Quantum Theory of the Optical and Electronic Properties of Semiconductors*, (World Scientific, Singapore, 1993).
- [4] W. W. Chow, S. W. Koch, and M. Sargent III, *Semiconductor-Laser Physics*, (Springer, Berlin, 1994).
- [5] S. H. Park and D. Ahn, Appl. Phys. Lett. **71**, 398(1997).
- [6] S. L. Chuang, J. O'Gorman, and A. F. J. Levi, IEEE J. Quantum Electron., **29**, 1631 (1993).
- [7] C. S. Chang, S. L. Chuang, J. Minch, W. Fang, Y. K. Chen, and T. Tanbun-Ek, IEEE J. Sel. Topics Quantum Electron. **1**, 1100(1995).
- [8] S. H. Park and S. L. Chuang, Appl. Phys. Lett., accepted.

## Wavefunction Engineering: Optimizing Heterostructure Design

L. R. Ram-Mohan\* and J. R. Meyer†

\*Departments of Physics and ECE, WPI, Worcester, MA 01609

†Code 5613, Naval Research Laboratory, Washington, DC 20375

*Computational tools permit wavefunction engineering of optical properties of semiconductor heterostructures with complex geometries, e.g., the Interband Cascade Laser, and allow optimizing specific physical properties.*

The concept of bandgap engineering has been useful as a central theme over the past decade in the design of quantum semiconductor heterostructures for device applications. Recent advances in the techniques for the growth of increasingly complex structural configurations, with modulation of material parameters, have come hand in hand with improved computational tools. The interplay between modeling and MBE growth has a new focus today defined by the concept of “wavefunction engineering”.

Multi-band **k.P** modeling based on the finite element method (FEM) has the ability to include interface boundary conditions in a very natural manner, while accounting for the spatial variation of virtually every material parameter. The presence of external electric and magnetic fields can also be included in the calculations. With a few elements placed in different physical regions, energy eigenvalues and wavefunctions are obtained with very high accuracy. Furthermore, the visual representation of energy bands, wavefunctions, and variations of the matrix elements has provided an effective feed-back while designing the geometry of layers and their composition, and has led to a better appreciation of the physics.<sup>1</sup>

Recently, improved type-II InAs/GaInSb/InAs/AlSb quantum well “W” lasers have been designed,<sup>2</sup> keeping the paradigm of wavefunction engineering in focus. Samples grown to specifications suggested by simulations showed lasing with emission wavelengths between 3.2 $\mu$ m and 4.5 $\mu$ m.<sup>3</sup> The flexibility to design 4-constituent layers with thickness and composition variation that suppress Auger losses and enforce a 2D density of states provides a superb example of wavefunction engineering.

Inspired by the inter-subband quantum cascade laser, the mid-IR interband cascade laser has been explored, optimized, and modeled by detailed simulations.<sup>4</sup> Type-II antimonide interband cascade laser samples grown by MBE to these designs at the University of Houston have lased at 3 $\mu$ m up to 225 K, and with collected output powers of up to 430 mW/facet at 100 K (with 1.3 photons emitted for every injected electron).<sup>5</sup>

We also review other applications of the FEM simulations: FEM calculations have been used to analyse photoluminescence data on quantum wells under super-high pressure upto 100 kbars.<sup>6</sup>

The energy levels of a compositionally asymmetric quantum well (ASQW) include states with resonant occupation in the well region. These participate strongly in the optical transitions and in  $\chi^{(2)}$ . Physically such structures need not have any bound states, and this was verified experimentally for structures designed using FEM calculations.<sup>7</sup> States localized in surface quantum wells and above single barriers show a rich spectrum which has been explored experimentally, and model calculations using FEM have been used to analyse the data. Such structures could have useful applications in the design of photodetectors.<sup>8</sup>

The discovery that carriers with energies above the barrier height in superlattices are very strongly localized in the barrier layers and have quantum-well-like spectra is leading to a new spectroscopy of above-barrier states. Their applications have yet to be explored.<sup>9</sup>

The finite element approach and wavefunction visualization permitted the analysis of level degeneracy of energy levels in quantum wires (QWW). It is remarkable that the finite barrier removes the accidental degeneracies of rectangular wires with commensurate sides. The theoretical exploration of the optical properties of stacked quantum wires, a structure called the checker-board superlattice (CBSL), was feasible using the FEM. In such laterally-confined systems, control over optical nonlinearities in the CBSLs of quantum wires, the energy band structure, as well as optical nonlinearities can be controlled by the choice of superlattice periodicity. An increase by 1-2 orders of magnitude, with control over the polarization dependence of  $\chi^{(3)}$  due to band nonparabolicity has been predicted.<sup>10</sup>

Recently, we have extended our FEM modeling to include quantum wires of arbitrary cross-section. We show that wavefunction localization and hence the optical properties can be controlled through heterostructure design, in a manner similar to our examples for layered structures.<sup>11</sup>

#### References:

1. L. R. Ram-Mohan and J. R. Meyer, *J. Nonlinear Opt. Phys. & Mat.* **4**, 191 (1995).
2. J. R. Meyer, C. A. Hoffman, F. J. Bartoli, and L. R. Ram-Mohan, *Appl. Phys. Lett.* **67**, 757 (1995).
3. J. I. Malin, C. L. Felix, J. R. Meyer, C. A. Hoffman, J. F. Pinto, C.-H. Lin, P. C. Chang, and S.-S. Pei, *Electron. Lett.* **32**, 1593 (1996); C. L. Felix, J. R. Meyer, I. Vurgaftman, C.-H. Lin, S. J. Murry, D. Zhang, S.-S. Pei, *IEEE Phot. Tech. Lett.* **9**, 734 (1997).
4. I. Vurgaftman, J. R. Meyer and L. R. Ram-Mohan, *IEEE Photonics Tech. Lett.* **9**, 170 (1997); I. Vurgaftman, J. R. Meyer and L. R. Ram-Mohan, *IEEE J. Quantum Electron.*, in press (1997).
5. C. L. Felix, W. W. Bewley, I. Vurgaftman, J. R. Meyer, D. Zhang, C.-H. Lin, R. Q. Yang, and S.-S. Pei, *IEEE Phot. Tech. Lett.* **9**, 1433 (1997).
6. E. M. Baugher, M. Chandrasekhar, and L. R. Ram-Mohan, *J. Phys. Chem. Solids* **56**, 323 (1995).
7. D. Dossa, et al, *Appl. Phys. Lett.* **59**, 2706 (1991); C. Parks, et al, *Phys. Rev. B* **45**, 14215 (1992).
8. C. Parks, et al, *Sol. St. Commun.* **92**, 563 (1994).
9. F. C. Zhang, et al, *Phys. Rev. Lett.* **68**, 3220 (1992); N. Dai, et al, *Phys. Rev. B* **50**, 18153 (1994).
10. J. Shertzer and L. R. Ram-Mohan, *Phys. Rev. B* **41**, 9994 (1990). L. R. Ram-Mohan and J. Shertzer, *Appl. Phys. Lett.* **57**, 282 (1990).
11. L. R. Ram-Mohan, B. Butler, J. Sullivan, J. Kramer and D. Dossa, to be submitted (1997).



**Integrated Photonics Research**

# **Novel Silicon Based Structures**

**Tuesday, March 31, 1998**

**Gregory A. Magel, Texas Instruments, Inc.**  
President

**ITuK**

**3:30pm-4:45pm**

**Salon C**

## Si-based Nanostructures for Optoelectronics

Kang L. Wang

Electrical Engineering Department, UCLA

Los Angeles, CA 90095-1594

Phone: 310-825-1609, Fax: 310-206-4685, email: wang@ee.ucla.edu

### Abstract

This talk will address the current status of Si-based optoelectronics and explore the opportunities for monolithic integration of optoelectronic integrated circuits (OEIC) based on the advantages of nanostructures. Device applications of Si-based quantum dots, with emphasis on light emission and detection, will be discussed. Other optoelectronic components will also be briefly reviewed. Si-based nanostructures can now be prepared by several methods for sizes down to as small as a few nanometers. We will review different growth modes as well as their control for improving the optical properties.

**Introduction:** Among the driving forces of Si-based optoelectronic technology is its potential as a strong contender for low cost high-speed high data rate local area networks (LANs), long distance fiber optic communications and on-chip interconnections. The potential of Si-based optoelectronics in this area has been reviewed by Soref.<sup>1</sup> Another driving force comes from the fact that as the feature size of electronic devices and integrated circuits is continuously scaled down to below 100 nm, on-chip global interconnection may become a bottleneck as reflected in the SIA NTRS.<sup>2</sup> One of the potential solutions is to use optoelectronic interconnects for long distance global interconnections. The basic elements of Si-based optoelectronic technologies include detectors, modulators, optical waveguides and, eventually, sources as well as their integration schemes with electronic drivers. A schematic of such a system is illustrated in Fig. 1. To date, OEIC devices and circuits have been based on GaAs and InP materials technologies. Wafer bonding techniques, used to achieve III-V OEICs on Si substrates, are complicated and expensive in the realization of OE and electronic chips in a hybrid technology. For OEICs, the major challenge is to have efficient Si-based light sources (lasers or light emitting diodes). For optical fiber communication with wavelengths in the range of 1.3  $\mu\text{m}$  to 1.55  $\mu\text{m}$ , achieving highly efficient and high-speed optical receivers may be another major challenge due to the small absorption coefficient of Si in this wavelength range.

This talk will first address two of the primary components to monolithic integration: Detectors and Light Emitters. These two areas are of concern as there are some fundamental issues to be resolved in Si-based light emitters, and detectors in the 1.3 - 1.5  $\mu\text{m}$  wavelength range. Towards this end, the subject of "nanostructures" may provide major advances in these areas. The latter portion of this presentation will briefly highlight pertinent issues of other components such as modulators and waveguides. (The integration with electronic IC's will not be discussed due to the limited scope of this paper.) The demand of low cost OEICs coupled with the efforts in nanostructure research, as a result of the continuing scaling effort in CMOS, provides the impetus for exploring the use of nanostructures to resolve some of hurdles for monolithic integration of OEICs. The latter will undoubtedly greatly benefit the progress of Si-based optoelectronic devices and circuits.

**Detectors:** First, in detectors, the control of the detection wavelength, particularly in the range from 1.3 to 1.5  $\mu\text{m}$ , demands the use of narrow bandgap materials such as SiGe beyond the usual low Ge contents. In order to obtain sufficient absorption at 1.3  $\mu\text{m}$ , a Ge content greater than 50 % is required. The problem with high Ge concentration films is that they are limited by the critical thickness due to the presence of strain. (For example, for 60% Ge, the critical thickness is less than 10 nm and consequently, the absorption in such a thin film will be extremely small). The key issue in the realization of high Ge content films will be the growth of these materials with minimal dislocation densities. SiGeC has also been proposed and demonstrated to reduce the strain in pin avalanche photodiode detectors with a Ge content of about 60%, yielding a detection wavelength extending beyond 1.3  $\mu\text{m}$ <sup>3</sup>. However, the detectivity remains low due to the thin SiGeC absorption region. More recently, we have demonstrated a SiGe avalanche photodetector in a waveguide structure grown on SOI in order to improve the detectivity. A thick SOI waveguide is used to couple the light from an optical fiber into a multi-period SiGe detector with a strain-limited thin absorption region. An external responsivity of 0.2A/W at 1.3  $\mu\text{m}$  has been achieved due to the use of the waveguide structure. New approaches to improve the material growth are needed and they may include the use of lateral over growth, compliant substrate and template (or patterned substrate) growth. The use of quantum dots in the interband transition may make the transition energy much higher than the interested 1.3-1.5  $\mu\text{m}$  range. On the other hand, intersubband detection of Si/SiGe quantum wells appears to work only for the infrared region ( $\lambda > 2 \mu\text{m}$ ), even with the transition from the spin orbital state to the heavy hole band, which has been previously shown to give a high transition energy. With additional quantum confinement through the use of structures such as quantum dots, transition wavelength of near 1-2  $\mu\text{m}$  seems to be possible, thereby making intersubband detectors viable.

**Light Emitters:** Light emitters have been fabricated based on many Si-based structures including those using rare Earth elements<sup>4</sup>, quantum confinement, strain, and other band engineering. The use of short period superlattices has been pursued for sometime based on the Brillouin zone-folding concept. However, the results have not been extremely fruitful due to the fact that the symmetry properties of the wavefunctions of the X valley in the conduction band and the  $\Gamma$  valence band do not yield high oscillator strength. Quantum dots have been reported to yield high optical efficiency due to quantum confinement. Among one of the first investigated is porous Si, which is difficult for LED fabrication due to the instability of the contact formation that is necessary for carrier injection. It is possible to fabricate small (<100nm in diameter) SiGe quantum dots-based using patterning and etching, and LEDs operating at room temperature have been demonstrated.<sup>5</sup> The quantum confinement however, does not change the symmetry properties of the wavefunctions involved in the transition even for sizes down to a few monolayers, unless the lattice is extensively distorted in some manner. The process of nanostructure formation gives rise to a large strain (or lattice distortion) which markedly increases the luminescence yield. The light emission mechanism for this kind of LEDs is strain and nanofabrication induced lattice distortion which could change the symmetry properties of the wavefunctions involved in the transition to effectively make the structure "pseudo-direct gap".<sup>5</sup> There are a number of projects being carried out by laboratories around the world<sup>6</sup> in the formation of Si and Ge based micro-crystallites buried in  $\text{SiO}_2$  media. These buried micro-crystallites are primarily formed through the use of ion implantation and post-implantation thermal annealing. Efficient light emissions in the visible range have been demonstrated by several groups, however, the light emission band seems to be too broad and the exact wavelength

of the emission is difficult to control. We have recently been experimenting on SiGe quantum dots using ordered mesoporous sol gel silica coated Si substrates with some promising results.<sup>7</sup> The idea here is to use the volume shrinkable sol gel silica as a template, and put semiconductor atoms into the mesoporous matrix to form lattice distorted and mechanically shrunk SiGe quantum dots. Since the pore size is controlled by the surfactant molecular size, dots can be formed in the silica matrix with highly controllable size and the size uniformity, which are crucial for strong and sharp light emission for emitter applications. Our preliminary data also showed that both dots on the top and inside the porous matrix surface of the silica film can be formed.<sup>9</sup>

Another approach is to use intersubband transition in order to avoid the problem of "indirectness" of the transitions from the valence to the conduction bands. As stated previously, the intersubband transition energy of quantum wells lies in long wavelength range ( $> 5 \mu\text{m}$ ). For light emitters based on intersubband transition, Si/SiGe heterojunction should work almost identically to that of direct gap III-V materials, since the transition occurs in the same band for intersubband transitions. Thus, quantum cascade lasers<sup>8</sup> should work in SiGe/Si quantum wells. With the use of quantum dots in lieu of quantum wells, the spectrum energy will be increased to close to that required for communication applications. Quantum dot cascade lasers may be fabricated on Si-based materials in a foreseeable future to work hand-in-hand with intersubband detectors and modulators.

In addition to using Si-light emitters and the obvious hybrid approach bonding III-V direct gap light emitter to the Si chip, the recent progress in new polymers may give effective light emission for monolithic integration of light sources with Si-based electronics (CMOS). Indeed, the recent progress in conjugated semiconductor polymers has led to the successful demonstration of efficient light emitting diodes with a relatively low operating voltage (3.1 - 3.5 V). Tuning of different optical spectra has also been achieved by changing the chemical structure of the polymer such as changing the side groups and the backbone structures.<sup>9</sup> These devices have now been shown to have a relatively good external quantum efficiency of about a few percents (and an internal quantum efficiency of about 10 percent). The advantage of the polymer LED is the low temperature process, which could be easily adopted into the backend of Si processes. Quantum confinement in these polymers may also lead to higher quantum efficiency.

**Preparation of nanostructures:** There are many methods, which can be used to fabricate Si-based nanostructures. These include self-assembled quantum dots prepared by MBE, CVD, and those by patterned growth. Ge dots on Si have been successfully prepared by MBE and CVD.<sup>10</sup> One of the challenges in self-assembly techniques is to establish the underlying principles of controlling the size and its distribution so as to tune the energy of optical transitions. Strain control has been established to be one of the mechanisms. However, a sharper distribution will be needed to warrant the requirement of size control. The technique described above using templates or patterned substrates offers yet another alternate method to improve the control. Many templates, which are based on the choice of the molecular size and structure, have a potential for giving excellent control. Further work needs to be performed in this area.

The placement of the quantum dots is another important challenge to the self-assembly methods. The registration of the patterned dots will be needed for subsequent processing and for integration with electronic circuits. Through the use of patterned substrate, the strain and geometry effects have been shown to yield relatively well-arranged patterns. Further work will provide new avenues and the understanding of self-registration in the fabrication of nanostructures using the self-assembly techniques.

**Other components:** Among modulators, waveguides and other components, waveguides will be briefly discussed next. The larger index of refraction of strained SiGe as compared to Si will give improved waveguiding. Likewise, the use of SOI will facilitate waveguiding. Low loss waveguides have been successfully fabricated and it appears that there are no fundamental issues involved for applications in local network, inter-chip and on chip interconnection applications. In modulators, Mach-Zehnder interferometers and other related devices have been fabricated. An excellent review can be found in ref. 1. Likewise, interband and intersubband modulators based on SiGe/Si quantum wells have been discussed previously. Particularly, the use of asymmetric quantum wells can increase the sensitivity of the Stark effect, making them more effective in the modulation efficiency and depth. Excellent reviews of this type of work are readily available<sup>11</sup>. In intersubband modulators, with the use of quantum dots, it may be possible to increase the transition energy as discussed above and thus to have the modulator working in the 1-2  $\mu\text{m}$ .

In summary, there is a strong need to develop Si-based optoelectronics, which can be integrated with CMOS and BiCMOS for low cost, high data rate applications. The directions of research will be to use nanostructures to further increase luminescence yield and to improve the tuning of the working wavelength and the efficiency both for detection and emission. In addition, it is critical to achieve the fundamental understanding of the mechanisms for improving the optical properties of these quantum confined structures. High-speed modulators will be of great interest in view of the fact that other sources may be used for the substitution of Si-based light emitter.

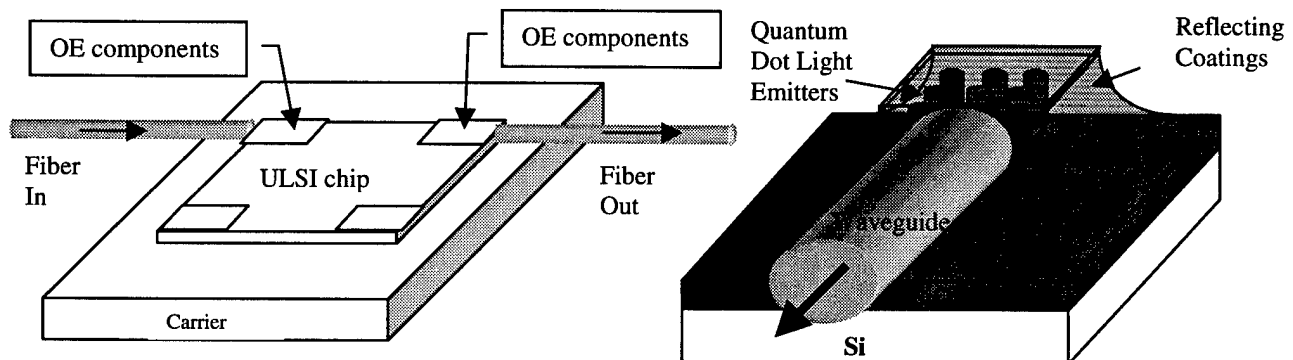


Fig. 1. OE components for inter-chip interconnection (left). Similar chips can also be used for intrachip global interconnects. Likewise, OEIC on Si can be used for local network applications. On the right, a quantum dot array is illustrated as a source. Similar structures can be implemented for detectors and modulators.

**Acknowledgments:** The author wishes to acknowledge the support of this work by SRC and DARPA.

- 
- <sup>1</sup> Richard A. Soref, "Silicon-based Optoelectronics", IEEE Proceedings, 81, 1687-1706 (1993)
- <sup>2</sup> SIA, The National Technology Roadmap for Semiconductors, Technology needs, 1997. S. Harrell, T. Seidel and B. Fay, "National Technology Roadmap for Semiconductors and SEMATECH Future Directions," Microelectronic Engineering, 30, 11 (1996).
- <sup>3</sup> F. Y. Huang and K. L. Wang, "Normal incidence epitaxial SiGeC photodetector near 1.3  $\mu\text{m}$  wavelength grown on Si substrate", Appl. Phys. Lett., 69, 2330-2332 (1996).
- <sup>4</sup> F. Y. Ren, J. Michel, Q. Sun-Paduan, B. Zheng, R. Kitagawa, D. C. Jacobson, J. M. Poate, and L. C. Kimerling, "IC compatible processing of Si:Er for optoelectronics", Materials research Society Symposium Proceedings, 298 (1993)
- <sup>5</sup> Y.S.Tang, S.Hicks, C.M.Sotomayor Torres, W.-X.Ni, C.D.W.Wilkinson & G.V.Hansson, "X-ray diffraction and room temperature light emission of Si-SiGe quantum dots" in Proc. SPIE Vol.3007, ed. by B. Jalali et al, p.p.170-177(1997)
- <sup>6</sup> For example, see reports from different groups around the world in the MRS Fall Meeting, Symposium C on "Materials and Devices for Silicon-Based Optoelectronics", Boston, , Dec. 1-5, 1997
- <sup>7</sup> Y.S.Tang, S.Cai, G.Jin, K.L.Wang, H.Soyez & B.Dunn, "SiGe quantum dots prepared on ordered mesoporous silica coated Si substrate" Appl. Phys. Lett. 71, 2448 (1997); and "Control of sizes and optical emission of SiGe quantum dots prepared on ordered mesoporous silica coated Si wafer" MRS Fall Meeting, Symposium C on "Materials and Devices for Silicon-Based Optoelectronics", Boston, , Dec. 1-5, 1997
- <sup>8</sup> G. Scamarcio, F. Capasso, J. Faist, C. Sirtori, D. L. Sivco, A. L. Hutchinson and A. Y. Cho, "Tunable Interminiband infrared emission in superlattice electron transport", Appl. Phys. Lett., 70, 1796-1798 (1997).
- <sup>9</sup> Y. Yang, "Polymer Electroluminescence Devices", MRS Bulletin, 22, 31-38 (1997).
- <sup>10</sup> T. I. Kamins, E.C. Carr, R. S. Williams, and S. J. Rosner, "Deposition of three-dimensional Ge islands on Si(001) by chemical vapor deposition at atmospheric and reduced pressures", J. Appl. Phys. 81, 211-219 (1997).
- <sup>11</sup> J. S. Park, R. P. G. Karunasiri, and K. L. Wang, "Observation of large Stark shift in  $\text{Ge}_x\text{Si}_{1-x}/\text{Si}$  multiple quantum wells", J. Vac. Sci. Technol. B8, 217-220, (1990); R. P. G. Karunasiri, Y. J. Mii and K. L. Wang, "Tunable infrared modulator and switch using Stark shift in step quantum wells", IEEE Electron Device Letters, 11, 227-229, (1990).

## ENHANCEMENT OF PROPAGATION CHARACTERISTICS IN ALL-SILICON WAVEGUIDE BY ION IMPLANTATION.

Giuseppe Cocorullo\*, Francesco G. Della Corte, Mario Iodice and Ivo Rendina,  
I.R.E.C.E. – National Research Council, Via Diocleziano 328, 80124 Napoli, Italy,  
Tel. +39 81 570 7999, Fax +39 81 570 5734, E-mail: iodice@irece1.irece.na.cnr.it

\* also with University of Calabria, DEIS, Rende (CS), Italy

Pasqualina M. Sarro,  
DIMES – TuDelft, Feldmanweg 17, 2628 CT, Delft, The Netherlands  
Tel. +31 15 278 7708, Fax +31 15 278 7319, E-mail: sarro@dimes.tudelft.nl

**Abstract** – A 7.0 dB/cm propagation loss improvement and higher confinement are achieved by ion-implantation in all-silicon waveguides matched to fiber size. Simulations for optimized structures predict 4.0 dB/cm attenuation.

**I. INTRODUCTION** – Silicon is the most important material for electronics, but it is also becoming more and more interesting for integrated optic applications. Because its optical absorption for wavelengths greater than  $1.2\ \mu\text{m}$  is very small ( $\alpha < 0.1\ \text{cm}^{-1}$ ), silicon meets the requirements for low loss optical waveguides. Important advantages of silicon for this kind of applications are its low cost and cheap manufacturing technology. In the last years low loss waveguides have been demonstrated in silicon on silicon (SOS) [1], silicon on insulator (SOI) [2] and silicon-germanium on silicon [3] materials. In order to keep the processing cost low the first typology is obviously attractive, because SOS waveguides can be fabricated by a single etching process in standard epitaxial silicon.

**II. BASIC PRINCIPLES** – In SOS structures the vertical confinement of the radiation is obtained through the plasma dispersion effect. A heavily doped silicon substrate, in fact, presents a slightly lower refractive index with respect to an intrinsic epitaxial layer grown on it. Therefore they can act respectively as the lower cladding and the guiding layer of a slab waveguide. As a drawback, high doping also causes an increase of the optical absorption, which, in turn, induces a degradation in the waveguide characteristics. This effect is particularly strong because of the deep penetration of the optical field in the lossy substrate due to the small refractive index variation between core and cladding. Single-mode rib SOS waveguides based on this effect with propagation losses between 15 and 20 dB/cm have been demonstrated [1]. Two ways to reduce the propagation losses are to use thicker epitaxial layer with low doping level or increase the substrate doping level [4]. While the first solution is self-explanatory, the latter needs some discussion. In fact, a higher substrate doping increases its optical absorption, but improves the radiation confinement in the loss-less epitaxial layer. The net result is a global improvement of the waveguide propagation losses. It should be noted, however, that substrates with higher doping are difficult to obtain and therefore a reduction of the propagation losses can be obtained only by recurring to thicker epitaxial layers ( $\geq 20\ \mu\text{m}$  [4]), at expenses of the ease and efficiency of coupling to standard single-mode optical fibers. Moreover, the realization of SOS waveguides in very thick epitaxial layer is very expensive and not fully compatible with standard microelectronic processes. Here we propose a technique to realize low-loss high-confinement SOS waveguides, starting from moderately or low doped substrate. Ion implantation is used to form a heavily doped lower cladding, between epilayer and substrate. Preliminary results on a  $6 \times 6\ \mu\text{m}^2$  cross section waveguide are reported, showing that propagation losses can be reduced to 4.0 dB/cm.

**III. WAVEGUIDE FABRICATION AND MEASUREMENTS** – The starting material was a  $0.02\ \Omega\cdot\text{cm}$   $n^+$  doped ( $\approx 1.5 \times 10^{18}\ \text{cm}^{-3}$  Sn) silicon (100) substrate. After a thermal oxidation of 45 minutes at  $1000\ ^\circ\text{C}$ , to form an ion channeling prevention oxide, the arsenic ion implantation was performed, with an energy of 150 keV and a dose of  $5.0 \times 10^{15}\ \text{cm}^{-2}$ . After the oxide stripping and the dopant drive-in and activation, an  $H = 6.0\ \mu\text{m}$  intrinsic ( $\leq 1.0 \times 10^{13}\ \text{cm}^{-3}$  As) silicon epitaxial layer was grown. Then a 500 nm thick  $\text{SiO}_2$  layer was sputtered and, using standard lithography and buffered HF etching, defined in stripes having widths in the range between 2 and  $24\ \mu\text{m}$ . In a  $\text{KOH:H}_2\text{O}$  solution ribs were etched  $1.5\ \mu\text{m}$  deep into the epitaxial layer. Due to the etchant anisotropy the average widths  $W$  of the waveguides exceeded the widths of the  $\text{SiO}_2$  stripes and ranged between 4 and  $26\ \mu\text{m}$ . According to [5], single mode behavior is assured for  $W \leq 8.0\ \mu\text{m}$ . At the same time, another  $\langle 100 \rangle$  silicon wafer, with a slightly higher

doping ( $2.0 \times 10^{18} \text{ cm}^{-3} \text{ Sn}$ ), was processed in the same way, except for the ion implantation step. The chosen substrate doping level is the minimum value that, for the given geometry, allows optical propagation into the channel. So, the resulting waveguides are geometrically identical to the implanted ones, except for the presence of the lower cladding, whose effect on the propagation characteristics have to be discussed. Waveguide propagation losses were therefore measured by means of the cut-back method. The radiation produced by a  $\lambda = 1.3 \mu\text{m}$  DFB laser diode, pigtailed to a single-mode  $5 \mu\text{m}$  core fiber, was then fired into the waveguide by butt-coupling, and the transmitted light monitored at the output with an InGaAs photodiode. The waveguide was then shortened twice at least by cleaving, and the transmitted light measured at each step. From the measured data, the net propagation losses in dB/cm were estimated

through the formula:  $\alpha = 10 \cdot \log_{10}(P_1/P_2)/(L_1 - L_2)$ , where  $P_1$  and  $P_2$  are the output powers measured at two different lengths  $L_1$  and  $L_2$ . Fig.1 reports the measured propagation losses in dB/cm versus the waveguide width  $W$  for both the implanted and the non-implanted structures. The implant in the substrate produces a useful effect for waveguides narrower than  $13 \mu\text{m}$ , with a maximum loss improvement of about 7 dB/cm for the  $4.0 \mu\text{m}$  wide device. As confirmed by numerical simulations, discussed in the following, for larger waveguides ( $W \geq 13 \mu\text{m}$ ) the ion implant in the substrate increases the global losses. The reason for this behavior lays in the fact that in large waveguides the optical radiation broadens laterally into the epilayer, while a smaller and smaller fraction will propagate through the lossy substrates. Therefore, for comparably field distributions in the substrate, the non-implanted structure will take advantage of the less absorbing cladding.

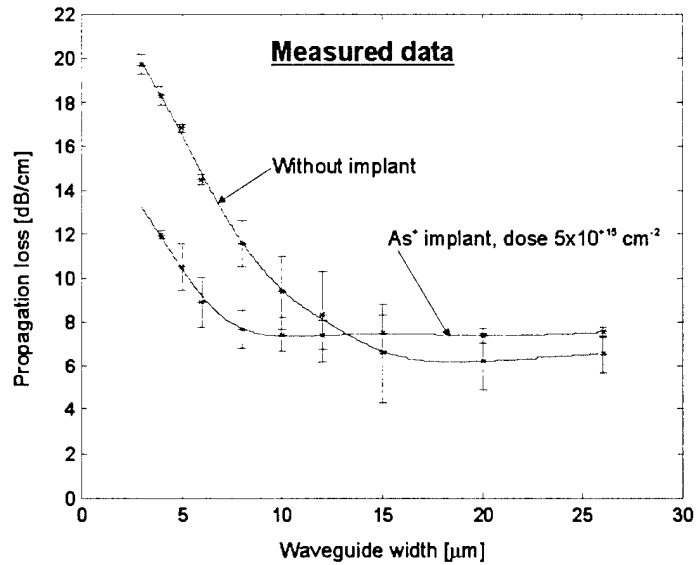


Fig.1 Measured propagation losses vs. waveguide width

IV. WAVEGUIDE ANALYSIS – The doping profile across the epitaxial layer and substrate as calculated by the ion implantation simulator available in the process simulator SUPREM-3 are reported in Fig.2. The resulting real refractive index ( $n$ ) profile is also shown. In order to perform optical simulations the real refractive index profile

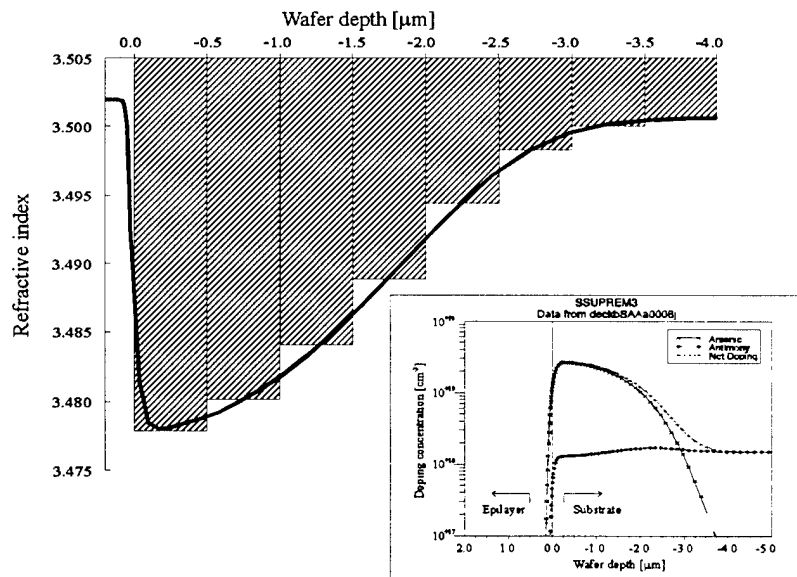
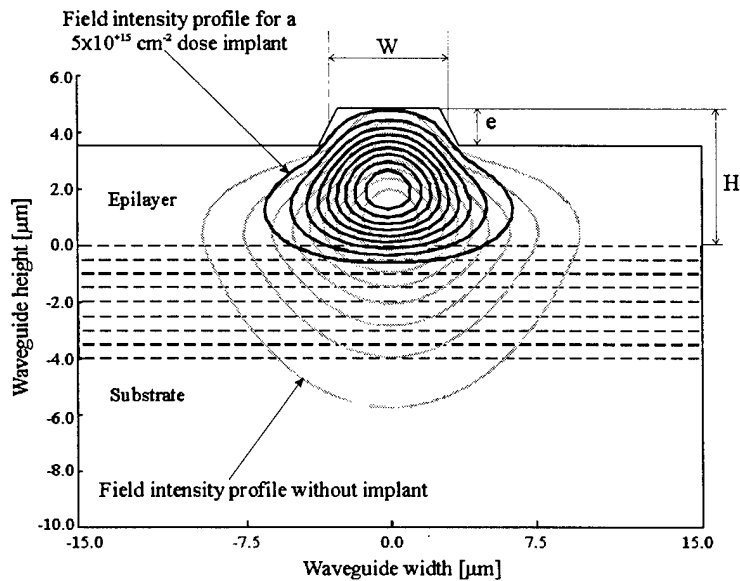


Fig.2 Refractive index and doping profile in the substrate

was discretized in eight regions,  $0.5 \mu\text{m}$  thick each. Using this discretization we calculated the global attenuation and the transverse field profile by means of a 2-D finite difference (FD) mode solver. Fig.3 shows the transverse cross section of the realized waveguide with  $W = 6.0 \mu\text{m}$ , together with the optical field intensity level curves for both implanted (black lines) and non-implanted waveguides (gray lines). The horizontal dashed lines mark the borders between the constant  $n$  regions introduced for the simulation. The effect of the  $n$  profile produced by ion implantation is clearly an enhancement of the vertical confinement. This fact, together with a propagation loss reduction, produces



fabrication process.

Fig.3 Waveguide cross section and field intensity profiles.

V. CONCLUSION – In this paper we experimentally demonstrated the possibility of realizing single-mode rib waveguides in a epitaxial silicon layer on lightly-doped silicon substrate, using ion implantation to form the lower cladding. The main advantages of the proposed technique are the independent choice for the substrate doping and the relatively small thickness for the epitaxial layer. These features allow a great flexibility in the design of optical circuits together with standard electronic devices, bringing new possibilities for the realization of optoelectronic integrated circuits (OEIC's).

#### REFERENCES.

- [1] R. A. Soref, J. P. Lorenzo, "All-silicon active and passive guided-wave components for  $\lambda=1.3$  and  $1.6 \mu\text{m}$ ", *IEEE J. Of Quantum Electron.*, vol. 22, no. 6, pp. 873-879, 1986.
- [2] A. Rickman et al., "Low-Loss Planar Optical Waveguides Fabricated in SIMOX Material", *IEEE Photon. Technol. Lett.*, vol. 4, no. 6, pp. 633-635, 1992.
- [3] A. Splett et al., "Low loss optical ridge waveguides in a strained SiGe epitaxial layer grown on silicon", *Electron. Lett.*, vol. 26, no. 14, pp. 1035-1037, 1990.
- [4] A. Splett and K. Petermann, "Low Loss Single-Mode Optical Waveguide with Large Cross-Section in Standard Epitaxial Silicon", *IEEE Photon. Technol. Lett.*, vol. 6, no. 3, pp. 425-427, 1994.
- [5] R. A. Soref, J. Schmidtchen and K. Petermann, "Large single-mode rib waveguides in GeSi-Si and Si-on-SiO<sub>2</sub>", *IEEE J. Of Quantum Electron.*, vol. 27 no. 8, pp. 1971-1974, 1991.

also a field profile better matched with the standard single-mode optical fiber. In Fig.4 the measured propagation losses are reported as a function of the waveguide width  $W$ , for a waveguide with a  $5 \times 10^{15} \text{ cm}^{-2}$  dose implant, compared with the simulated attenuation. In the same figure the simulated losses for a similar waveguide, with a  $10^{16} \text{ cm}^{-2}$  dose implant, are also shown. The difference between the measured and the simulated curve can be explained observing that the numerical simulation can not take into account the material defect losses, surface roughness losses and all the undesired scattering phenomena that occurs in real waveguides. We believe that a further reduction of the losses down to the estimated minimum values is possible by improving

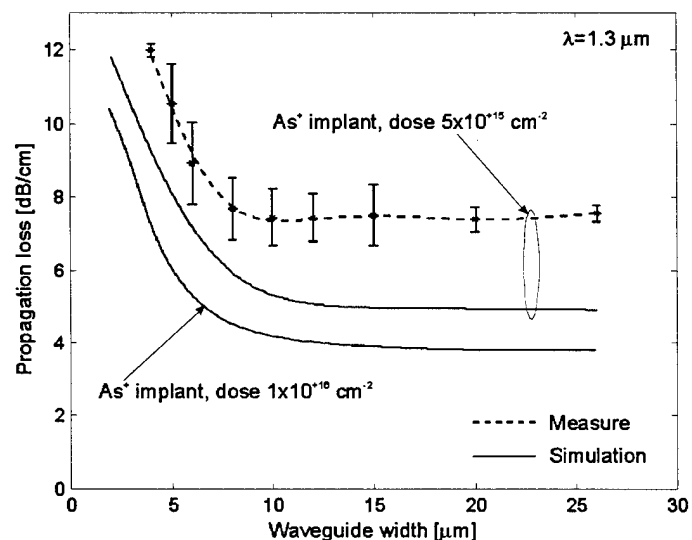


Fig.4 Measured and simulated attenuation vs. waveguide width.

## Bistable Si-Micromachined Fiber Switches

M. Hoffmann, P. Kopka, T. Groß, E. Voges  
 Universität Dortmund, Lehrstuhl für Hochfrequenztechnik  
 Otto-Hahn-Str. 6, D-44227 Dortmund, Germany  
 Tel. +49 - 231 - 755 - 4619 ; Fax: +49 - 231 - 755 - 4631  
 E-Mail: hoffmann@hft.e-technik.uni-dortmund.de; kopka@hft. ...

### Abstract

A bistable single-mode fiber optical 1x2 switch based on silicon-micromechanics has been fabricated. The input fiber is switched and fixed in a V-groove clamp using thermal actuators.

### Introduction

Optical switches and arrays of individual operating switches are important for optical communication networks, especially for optical backbone networks which are under development, e.g. in the ACTS-project COBNET (Corporate Optical Backbone Network) [1], for bypassing and network reconfiguration in the SDM-part. They have to be low cost devices with low insertion loss and cross talk and necessarily long term stability. Present micromechanical approaches have no bistable behavior and are complicated in fabrication [2, 3]. Here, we present a new design that allows the fabrication of bistable fiber switches on <100> silicon substrates employing standard technologies such as KOH-etching and thin film sputtering.

### Operation

The switch is based on thermally driven silicon actuators for fiber movement and fiber clamping. The principle of operation is shown in Fig. 1a,b The input fiber is fixed in the left position (state I). During the switching cycle the output cantilever is thermally bend down by the bimaterial effect, the input fiber relaxes in a middle position. The left arm of the U-shaped cantilever is heated and moves the input fiber to the right due to thermal expansion. Both actuators are switched off, the fiber is clamped in the right position (state II).

The fiber on the input cantilever as well as the two output fibers are positioned in V-grooves. The V-groove clamp for the output fibers is thermally actuated by the bimaterial effect. The chromium thin film heater on the lower part of the clamp has a higher heat expansion coefficient than the silicon causing a bending of the cantilever. The power for this bending is 1.3 W due to the small effect and the broad cantilever. For horizontal movement of the input fiber, the length variation due to thermal expansion is converted into an angular displacement. The heat is generated in chromium thin film heaters on top of the beams. It should be noted that this cantilever has a length of 20 mm, the thermal expansion is 5µm per 100K temperature increase resulting in an angle of 0.5° which is enough to move the fiber. The power required for this action is 200 mW. The total power of approx. 1.5 W is only needed for several 10 milliseconds due to the bistable operation.

### Optical design

Optical fiber switches promise low insertion loss (<1 dB) and very low cross talk (< -60 dB). While the cross talk is always achieved, the insertion loss is limited by the coupling efficiency between two fibers. For an insertion loss of less than 1 dB the radial misalignment between the two fibers has to be less than 1 µm, the angular displacement has to be ≤0.5°. The axial

displacement is less critical, it should be below 25  $\mu\text{m}$ . (Fabry-Perot resonances have to be suppressed by e. g. index fluides.)

Silicon V-grooves are well known devices for the precise fiber alignment to fulfill the radial offset condition. The condition for the angular displacement is satisfied by a proper design of the input cantilever length ( $\geq 20 \text{ mm}$ ) as shown before.

### **Fabrication**

These switches can easily be fabricated on standard  $\langle 100 \rangle$  silicon wafers using silicon nitride masked wet anisotropic etching in KOH. At first, a groove is etched from the back side of the wafer. Then the complete switch including the fiber V-grooves is structured on the top side. In a further step the thin film heaters are defined using a low-stress chromium lift-off process. The thin film heaters are isolated against silicon by silicon nitride. Chromium shows a very good adhesion to silicon nitride and it is neither etched nor detached during the KOH wet etching. The depth of the V-grooves is defined by the geometry of the mask due to the etch stop at  $\langle 111 \rangle$  planes. The etch-through of the wafer is achieved in a simple way: At first, all rectangular silicon areas which are exposed to KOH are etched like a V-groove. But if these V-grooves meet with the back side groove, fast etching  $\langle 110 \rangle$  planes are exposed and horizontal etching starts. This etching step is limited by  $\langle 111 \rangle$  planes resulting in V-grooves on the side walls. However, due to the allowable tolerances ( $\pm 10 \mu\text{m}$ ) compared to the etch rate (15  $\mu\text{m/h}$  for  $\langle 110 \rangle$  plains in 20% KOH at 45°C) a time controlled process with nearly vertical side walls is also possible. The resulting thickness of the cantilevers is about 100  $\mu\text{m}$ . The fibers are glued to the V-grooves using UV-curing resin. For a well defined vertical position of the fibers an additional upper V-groove clamp also fabricated by wet chemical etching is put up-side-down above the output cantilever. This upper clamp will be extended to a complete cover which seals the device.

### **Results**

First 1x2 bistable micromechanical fiber switches have been fabricated. They show an excellent operation of the actuators. The power required for the horizontal shift is below 200 mW. The fiber clamp was opened with 1.3 W. First optical measurement have also been performed. The low cross talk ( $< -60 \text{ dB}$ ) was confirmed. The insertion loss found at an early device was 4-5 dB. The main reason for the high insertion loss are tolerances within the fiber clamp. A new design was finished and will remove the deviations. Target specifications are insertion losses well below the insertion loss of typical integrated optical devices.

### **Conclusion**

These new bistable fiber switches offer a simple way for a mass production of low cost single mode and multimode switches with standard technologies. The main advantages against integrated optical solutions are low cross talk, two long term stable states without power consumption and potentially a verily low insertion loss.

Due to the small dimensions (3 mm width x 50 mm length) switch arrays can easily be fabricated. An array of 12 switches will have a width of 36 mm, only. Furthermore, the switch principle can be extended from 1x2 switches to e.g. 1x4 switches. A fabrication on  $\langle 110 \rangle$  silicon substrates is under development. Furthermore, the micromechanical switch can also be driven by piezoelectric actuators.

### Acknowledgment

This work is supported by the ECC within the ACTS project AC069 COBNET (Corporate Optical Backbone NETwork).

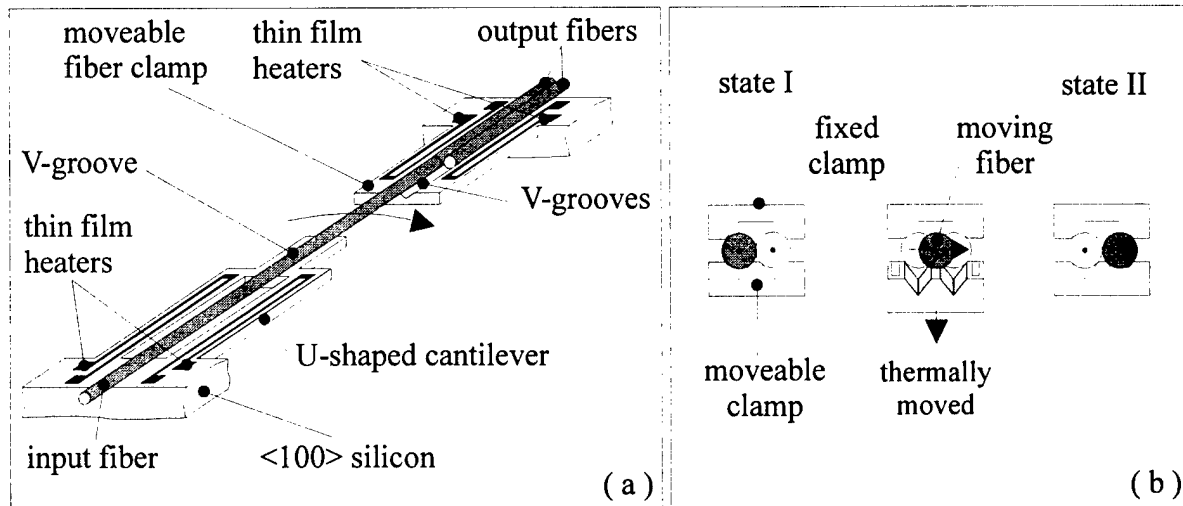


Fig. 1a: Scheme of the bistable fiber switch

Fig. 1b: Operation of the fiber clamps

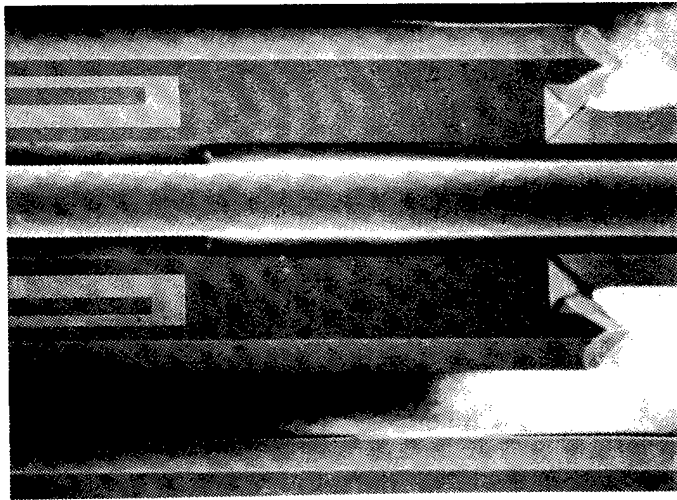


Fig 2: SEM-photo of the end section of the U-shaped cantilever showing the input fiber in a V-groove and the heating electrodes for angular displacement.

- 1 W. Denzel, B. Meekers: "Photonics in the Backbone of Corporate Networks - The ACTS COBNET Project", Proc. of NOC'97, Antwerp, Belgium, June 1997, Part 3, Edts. D.W. Faulkner and A.L. Harmer, IOS Press, Amsterdam, 1997, pp. 25-32.
- 2 E. Ollier, P. Labeye, F. Revol: "Micro-opto mechanical switch integrated on silicon", Electron. Lett., 31, No. 23 (1995), pp.2003-2005
- 3 L.A. Field, D.L. Burriesci, P.R. Robrish, R.C. Ruby: "Micromachined 1x2 optical fiber switch", Sensors and Actuators A 53 (1996), pp. 311-315

## Polarization-Insensitive Vycor-Based Optical Waveguide for Planar Lightwave Circuits on Silicon Substrate Fabricated by Aerosol Flame Deposition

Hyung Gon Jeong, Yong Tae Lee, Young Yun Chun, Jong Ha Moon\*, Hyung Jong Lee

Dept. of Physics, Chonnam National Univ., Yonobong-Dong 300, Kwangju 500-757, S. Korea

\*Dept. of Ceramic Eng., Chonnam National Univ., Yonobong-Dong 300, Kwangju 500-757, S. Korea

The glass film produced by FHD (Flame Hydrolysis Deposition)[1] or CVD (Chemical Vapor Deposition)[2] method has high-silica composition similar to that of an optical fiber and hence low propagation losses of planar optical waveguides may be achieved easily. However, the high-silica glass film has very lower thermal expansion than the Si wafer and hence the glass layers on top of the silicon substrate are under compressive stress, which warp the wafer resulting in the difficulty of photo-lithography of waveguide circuits and the polarization dependence of the devices due to stress-induced birefringence.

The multicomponent glasses containing some alkali oxides, such as Pyrex[3] or Vycor[4], have similar thermal expansion to that of Si wafer ( $3 \times 10^{-6}$ ), and the problems of the mismatch of thermal expansion between the high silica and the silicon substrate can be solved by using such glass system. However, such glass film is not available in the CVD technology. Furthermore, the FHD method needs precursors with high vapor pressure and such source containing sodium is not available. FHD also uses chlorine rich flame which is another difficulty in producing glasses containing alkali oxides.

In this study, the sodium borosilicate glass film for producing stress-free planar lightwave circuits is fabricated by AFD process[5]. The method of AFD is similar to that of FHD in the use of flame, but different in the transportation of the precursors. AFD process changes a liquid sol into aerosol using the ultrasonic generator of 1.5MHz, and make it oxidized in the flame of  $O_2$  and  $N_2$  and deposit it on the top of Si wafer. In AFD the liquid sol of macro-molecules composed of each constituents by atomic unit such as Si, B, Na, and Al is used as precursor, and carried into the flame in the form of aerosol by the carrier gas. Whereas each sources in FHD are evaporated separately and react in the flame with different reactivity. Therefore, the composition of the precursors is conserved in the glass film and the homogeneity of the glass film can be obtained more easily in AFD. The glass composition in this study is belong to the Vycor glass region, where the thermal expansion is expected to be low, but the crystallization due to phase separation may easily occur. Therefore, the effect of  $Al_2O_3$  on the phase separation and light-guiding properties of sodium borosilicate glass waveguide is investigated.

Phase separation of sodium containing glass may deteriorate the transmittance of light. Generally, clear glass may be produced in Vycor glass of  $66SiO_2-27B_2O_3-7Na_2O$ . However, this glass is easily crystallized due to phase separation by tempering or slow cooling after melting. The substitution of  $Si^{+4}$  by  $Al^{+3}$  provides an electrochemical potential for alkali ions ( $Na^+$ ) to segregate to  $Al^{+3}$  site to maintain electroneutrality and inhibits crystallization according to the

random network model of glass structure. Thus, we try to add  $\text{Al}_2\text{O}_3$  to the system to prevent glass film from crystallizing. Fig. 1 shows the surface morphology with addition of  $\text{Al}_2\text{O}_3$  of  $66\text{SiO}_2\text{-}27\text{B}_2\text{O}_3\text{-}7\text{Na}_2\text{O}$  glass consolidated at  $1200^\circ\text{C}$  for 1hr and quenched to room temperature in air. The thickness of glass films is  $14 \pm 1 \mu\text{m}$ . When  $\text{Al}_2\text{O}_3$  of 1.5wt% is added to the system, large crystallines like flower are grown. As the amount of  $\text{Al}_2\text{O}_3$  increases the size of the precipitated crystallines gradually decreases and such crystalline phase are not observed for the glass film with over 6wt%  $\text{Al}_2\text{O}_3$  at all. Therefore, in the case of the fabrication of glass film by AFD process the addition of 6wt%  $\text{Al}_2\text{O}_3$  to  $66\text{SiO}_2\text{-}27\text{B}_2\text{O}_3\text{-}7\text{Na}_2\text{O}$  glass inhibits completely crystalline from forming under the air-quenching condition after melting. On the other hand, the surfaces of (a) to (c) glass film containing some crystalline phase is more rough than the case of (d) without crystallization, which means that compositional inhomogeneity took place in glass film due to phase separation.

Fig. 2 shows the refractive index of  $66\text{SiO}_2\text{-}27\text{B}_2\text{O}_3\text{-}7\text{Na}_2\text{O}$  glass system. As the amount of  $\text{Al}_2\text{O}_3$  increases from 1.5 to 6wt% the refractive index increases linearly from 1.4610 to 1.4701. As mentioned in introduction, the difference of the thermal expansion coefficient between glass film and Si substrate induces compressive stress to glass layer. Fig. 3 shows the TE and TM mode index spectra of  $66\text{SiO}_2\text{-}27\text{B}_2\text{O}_3\text{-}7\text{Na}_2\text{O}$  glass film doped with 1.5 wt%  $\text{Al}_2\text{O}_3$ , measured with prism coupler. The mode index of TE is fairly in accordance with that of TM, which suggests that the birefringence of the glass film is very small. The birefringence increases linearly in proportional to the content of  $\text{Al}_2\text{O}_3$  as shown in Fig. 4. The mode index difference between TE and TM of 6wt%  $\text{Al}_2\text{O}_3$   $66\text{SiO}_2\text{-}27\text{B}_2\text{O}_3\text{-}7\text{Na}_2\text{O}$  glass film without any crystallization is  $8 \times 10^{-4}$ . This large value may be attributed to the condition of air quenching. When above specimen was annealed for 72 hrs at  $470^\circ\text{C}$ , which was just below the expected glass transition temperature, the value of TE-TM was minimized to less than  $2 \times 10^{-4}$  as shown in the Fig. 5. Therefore, it is possible to produce the glass film nearly free of stress and further reduction of birefringence seems to be possible.

The core slab of the waveguide was deposited on the base layer of above mentioned glass system. The composition of core slab was the same as the base layer except for the doping of Zr. The refractive index of the core was controlled by the content of Zr. Fig. 6 shows the near field of the guided mode. with waveguide core of 0.74%. Propagation loss of the slab guide with 6 wt%  $\text{Al}_2\text{O}_3$ , measured by prism coupler, is estimated to be less than 0.34 dB/cm at  $1.52 \mu\text{m}$ , which is comparable to 0.1 dB/cm, the typical loss of high-silica FHD materials. The loss measurement was carried out without any further effort to reduce the loss and expected to be reduced further by proper optimization.

## References

1. M. Kawachi, M. Yasu and T. Eda, *Electronics Lett.*, **19** (15), 583 (1983).
2. B. H. Verbeek, C. H. Henry, N. A. Olsson, K. J. Orlowsky, R. F. Kazarinov and B. H. Johnson, *J. of Lightwave Technol.* **6**, 1011 (1989).
3. J.-H. Jean, T.-H. Kuan and T. K. Gupta, "Crystallization inhibitors during sintering of Pyrex borosilicate glass," *J. Mat. Sci. Lett.* **14**, 1068 (1995).

4. Milos B. Volf, "Chemical Approach to Glass", Glass science and Technology 7, pp183-192.
5. T. F. Morse, A. Kilian and L. Reinhart, "Aerosol Techniques for glass Formation", J. of Non-Crystalline Solids **129**, 93 (1991).

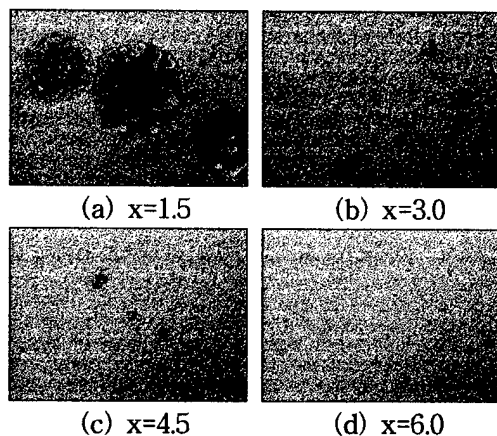


Fig.1 Surface of the Vycor films. 50 $\mu$ m; —  
(66SiO<sub>2</sub>-27B<sub>2</sub>O<sub>3</sub>-7Na<sub>2</sub>O + xAl<sub>2</sub>O<sub>3</sub> wt%)

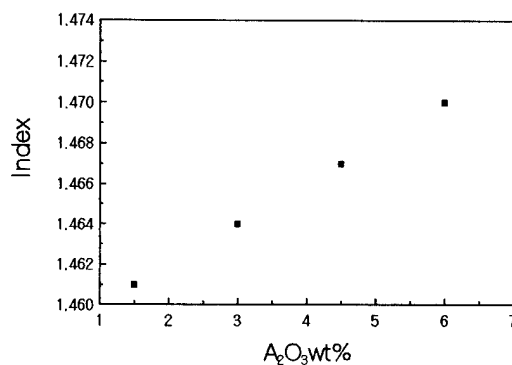


Fig.2 Refractive index of the Vycor glass film.  
(66SiO<sub>2</sub>-27B<sub>2</sub>O<sub>3</sub>-7Na<sub>2</sub>O + xAl<sub>2</sub>O<sub>3</sub> wt%)

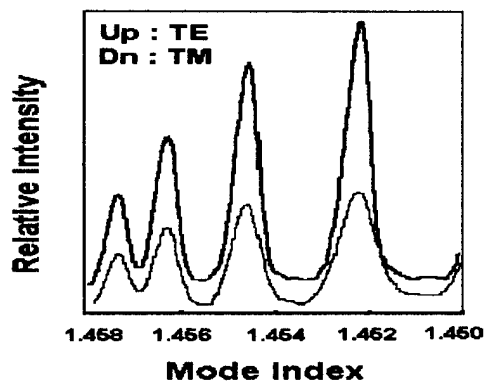


Fig.3 Mode index of the Vycor glass film.  
(66SiO<sub>2</sub>-27B<sub>2</sub>O<sub>3</sub>-7Na<sub>2</sub>O + 1.5Al<sub>2</sub>O<sub>3</sub> wt%)

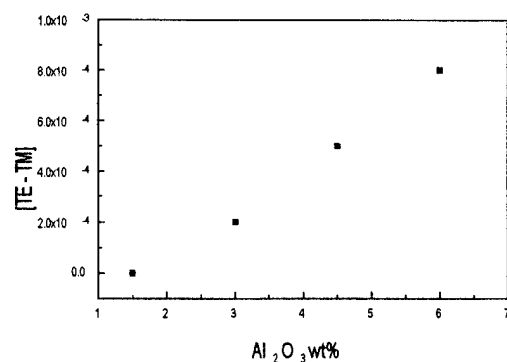


Fig.4 Birefringence of the Vycor glass films.  
(66SiO<sub>2</sub>-27B<sub>2</sub>O<sub>3</sub>-7Na<sub>2</sub>O + xAl<sub>2</sub>O<sub>3</sub> wt%)

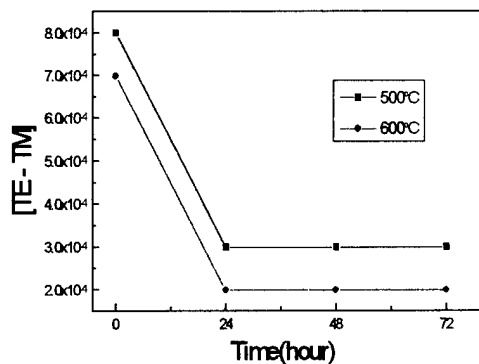


Fig.5 Birefringence reduction of the Vycor optical waveguide.



Fig.6 Near field of the Zr-doped Vycor optical waveguide.



**Integrated Photonics Research**

# Polymer Based Devices

**Tuesday, March 31, 1998**

**Lewis Aronson, Hewlett-Packard**  
Presider

**ITuL**  
**3:30pm–4:30pm**  
Saanich

# 3D directional coupler device with 9 channels in three layers

Th. Hennig, Ch. Wächter, W. Karthe, A. Bräuer

*Fraunhofer Institute for Applied Optics and Precision Engineering, D-07745 Jena, Schillerstraße 1*

e-mail: hennig@iof.fhg.de phone: +49|3641/807436 fax: +49|3641/807600

Ch. Véron

*Friedrich-Schiller University Jena, Institute for Solid State Theory and Theoretical Optics*

H. Wolter

*Fraunhofer Institute for Silicate Research Würzburg*

## ABSTRACT

Numerical and experimental results of investigating a compact monomode powersplitter with a three-dimensional layout are presented. It is shown that the chosen configuration is advantageous with respect to production tolerances.

## I. INTRODUCTION

The communication society of the next century requires increasing bandwidths for personal and business communication and entertainment.

In comparison to free space interconnects, Integrated Optics (IO) has a low channel density [1]. Reasons are the unfavourable aspect ratio, the restriction to mainly one waveguiding layer in one plane and the in/output spacing due to the geometry of the fibre ribbons or low crosstalk demands. To overcome this, some concepts for waveguide structures with several planes of waveguides were suggested, recently.

The use of three dimensions in IO offers some advantages e.g. the possibility of basically new device functions, the design of cross free layouts and the simultaneous horizontal as well as vertical coupling to reduce the device length.

Recently, three-dimensional directional coupler devices in two different polymers with horizontal and vertical coupling were reported [2]. Up to now, only a few more devices and concepts are known which use the third dimension [3] - [7].

In this paper we present a new multilevel powersplitter which is based on a consequent three-dimensional guiding scheme, i.e. the simultaneous coupling in both transverse directions. This device was first proposed in [2].

## II. DEVICE LAYOUT AND MODELLING

We investigate rectangular arrays of waveguides as one approach to higher splitting ratios and new devices schemes. Due to coupling and symmetry equidistributions or other relevant splitting ratios can be found.

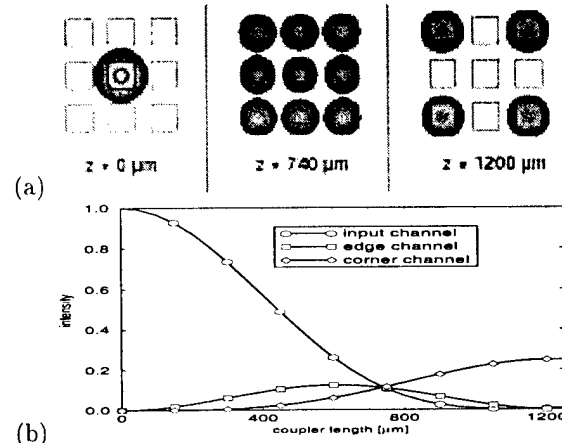


Fig. 1. Modebeating in a 3x3 matrix of waveguides:  
(a) isoline plot  
(b) intensities in the middle of the waveguides  
parameter set: waveguide crosssection  $4.8 \mu\text{m} \times 4.8 \mu\text{m}$   
vert. gap = horiz. gap =  $3 \mu\text{m}$   
 $\lambda = 1310 \text{ nm}$ ,  $\Delta n = 1 \times 10^{-2}$

The simulations are made by a modebeating algorithm, similar to that implemented in [8]. It allows the simulation of arbitrary couplers with z-invariant geometry. The Eigenvalue problem is solved by a vectorial two-dimensional finite element method (FEM). The excitation of the modes is calculated by their overlap-integrals with input fields.

In extension to a coupler with 4 coupling waveguides arranged [2] a configuration with 9 waveguides shows promising features.

The power oscillates between the input channel in the middle and the channel in the corners of the 3x3 waveguide array, see Fig. 1 for field evolution and parameters. At a length of  $740 \mu\text{m}$  the guided power is equally distributed among all nine channels. Further on, at a length of  $1200 \mu\text{m}$ , the intensity resides in the four corner guides.

In agreement with previous results [2] it does not seem to be realistic to find a layout which preserves the intensity relations in 9 guides when the individual channels are separated, e.g. by bends. That's why we concentrated on a layout where the 1x4 splitting

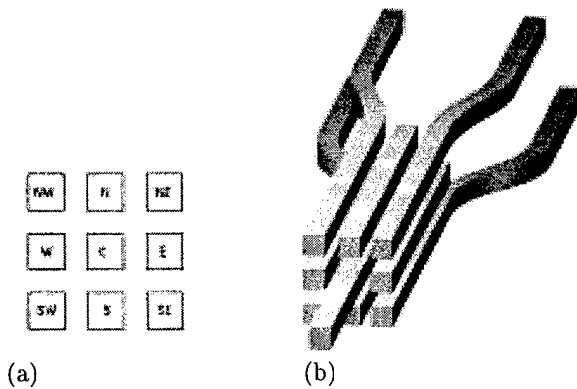


Fig. 2. Modebeating in a 3x3 matrix of waveguides:  
(a) cross section of the coupling region with labeling of the waveguides  
(b) three-dimensional device layout

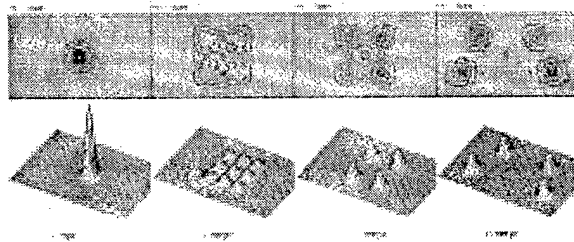


Fig. 3. 3D SE BPM Simulation of a 3 layer 1x4 powersplitter:  
upper row - isolineplots of the cross section  
lower row - 3D plots of the  $H_y$  component of the magnetic field  
please mention the different parameter set:  
waveguide cross section  $6\mu\text{m} \times 6\mu\text{m}$   
vert. gap = horiz. gap =  $3\mu\text{m}$   
 $\lambda = 1310\text{nm}$ ,  $\Delta n = 6 \times 10^{-3}$

is used. This 1x4 powersplitter has three waveguide layers, with nine individual channels in the coupling region (Fig. 2(a)), where one guide serves as input and four guides serve as output (Fig. 2(b)).

In contrast to the normal DC (1x2) and the  $2 \times 2_{geo}$ -coupler (1x4) [2] we point out that the intensity in all waveguides is at a fault tolerant minimum or maximum (see Fig. 1(b)). This is very advantageous with respect to production tolerances.

To determine whether or not this layout suffers from bend coupling we simulated the device by means of a full vectorial 3D series expansion beam propagation (3D SE BPM) [9]. Calculations confirmed that this three layer  $1 \times 4_{IN/OUT}$ -coupler is highly symmetric. No bend coupling in the output bend region occurs due to the greater distance of the output waveguides when the N-, E-, S- and W-waveguides (comp. Fig. 2(a)) on the edges of the 3x3 array are terminated.

BPM calculations showed furthermore that the split-

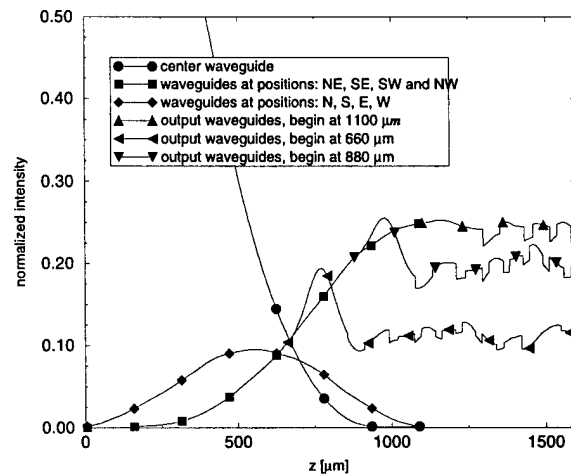


Fig. 4. BPM Simulation of a 1x4 powersplitter with mismatched coupling length. The end of the coupling region is varied (660, 880, 1100  $\mu\text{m}$ ). The 1100 micron coupling region matches best, but the splitting ratio is in every case perfect within numerical error limits.

ting ratio does not depend on refractive index drifts of the waveguide or the cladding material. Such drifts change the coupling length and a given device is "cut" at the wrong point. The loss of such a device will be higher, but the splitting ratio remains constant (Fig. 4). The same happens if the thicknesses of the buffer layers are mismatched similarly and, therefore, the vertical coupling is different from the horizontal.

### III. FABRICATION AND DEVICE CHARACTERIZATION

Polymers are the material of choice because of the flexibility of its properties and the variety of technologies. The material for three-dimensional IO has to fulfill some requirements. Essential is that layers (structured or not) should be stable against the following technology steps, therefore they should form three-dimensional networks to achieve chemical and thermal stability.

We concentrated on an ORMOCER [10] because ORMOCERs offer the opportunity of tailoring the material properties by modification of one of its components (organic, inorganic, metallic complex and functional groups) to the demands of IO and UV structuring. A three-dimensional inorganic network with organic acrylate crosslinks is the product of an UV initiated sol-gel reaction.

Up to now ORMOCERs, with its excellent thermal stability and acceptable losses in the communication wavelengths range were mostly used in IO for replication techniques [11]. Because oxygen inhibits the photoinitiation of acrylates, UV structuring of thin layers

turned out to be difficult. The oxygen inhibition prevents or slows down the hardening of those layers of the prepolymerized resin. To solve this problem we use an inert atmosphere during photostructuring.

Index tuning of the material was realized by blending the ORMOCER with an acrylate. We choose Dodecandiol-di-methacrylate (DDD) to decrease the buffer layer index. Adding an amount DDD of 35% of the mass of the resin to the ORMOCER, results in an refractive index decrease of  $\Delta n = 0.006$ .

Equipment for planar technologies like spin coating, hotplate and mask aligner is used to produce three-dimensional polymeric structures. The waveguides with rectangular cross section were produced by proximity exposure of a liquid layer of ORMOCER spun on an index matched buffer layer. The viscosity of the material is tuned by a common solvent. The unexposed material was washed out by Iso Butyl Methyl Ketone (MIBK) and the guides were dried to remove indiffused MIBK. The next buffer layer planarizes the rectangular waveguides very well. This is an important fact because other technologies - like chemical vapor deposition - does not. The next layers of waveguides were produced on top of the planarizing buffer layer. The mask is adjusted to the underlying structures through a system of special Moiré-alignment marks. By means of an alignment tool and a weak microscope we achieve alignment accuracy of approximately 1 micron.

A stack of 3 low index buffer layers and 3 high index structured waveguide layers was eventually covered with a fourth buffer layer.

We call this the 7-layer-3-mask technique. It indicates a M-layer-N-mask technique where M counts  $M=2N+1$ . The mask index N means that the N waveguide layers can be patterned independently with different structures according to the special layout of the device.

Fig. 5(a) shows the end face of a 3-layer 1x4 powersplitter with independently structured layers. The waveguide cross section is approximately quadratic. In Fig. 5(b) a nearfield pattern of such a coupler as 1x4 powersplitter is depicted at  $\lambda = 1550 \text{ nm}$ . It is to be seen that despite a small misalignment of the third guiding layer the splitting ratio is symmetric. Detailed measurements are presented at the conference.

#### IV. CONCLUSIONS

A three-dimensional symmetric 1x4 powersplitter is presented. Three waveguiding layers are applied including an area of a nine channel directional coupler. This new IO device has no direct two-dimensional analogies. Because of the special three-dimensional

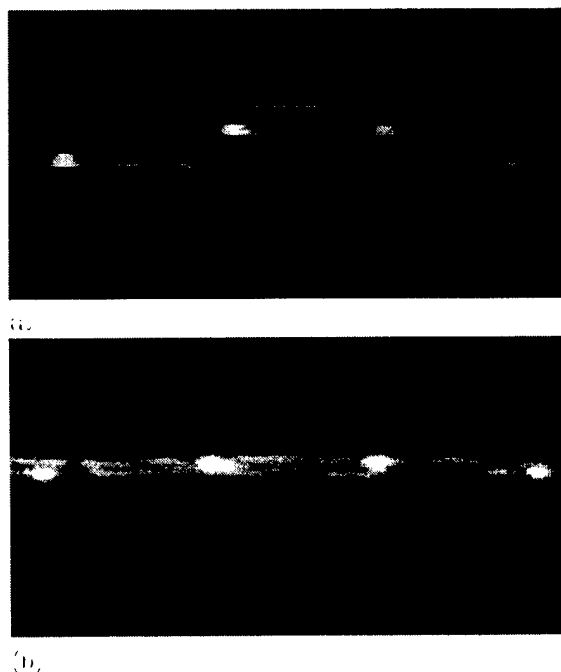


Fig. 5. First three-dimensional 3-layer 1x4 powersplitters: (a) microscope picture of the end face with the NE-, SE-, SW-, NW-waveguides (waveguide separation at this point: 50 and 150 microns in the upper and lower layer), (b) near field at  $\lambda = 1550 \text{ nm}$  (waveguide separation: 250 and 750 microns)

layout the device functionality is very tolerant against technology variations.

This device proves, that the stacking of more than two waveguide layers of structured ORMOCER is possible to produce complex three-dimensional integrated optical devices with a high overall number of layers involved.

#### REFERENCES

- [1] Linda Jean Camp, Rohini Sharma, and Michael R. Feldman, "Guided-wave and free-space optical interconnects for parallel-processing systems: a comparison", *App. Opt.*, vol. 33, no. 26, pp. 6168-6180, 1994.
- [2] Th. Hennig, Ch. Wächter, L. Friedrich, P. Dannberg, W. Karthe, A. Bräuer, and Ch. Véron, "New three-dimensional (1x4) directional coupler devices in polymers", in *Proc. ECIO'97*, 1997, p. PD2.
- [3] Thomas A. Tunnillio and Paul R. Ashley, "Demonstration of a polymeric registered multilevel mach-zehnder intensity modulator array", in *Integrated Photonics Research Techn. Digest*, IEEE, 1993, pp. 86-89.
- [4] P. C. Noutziou, G.L. Yip, and J. Albert, "A new directional coupler for optimum edge-coupling to an embedded photodetector", in *Proc. ECIO'93*, 1993, pp. 127-129.
- [5] Senichi Suzuki, Keizo Shuto, and Yoshinori Hibino, "Integrated-optic ring resonators with two stacked layers of silica waveguide on Si", *Phot. Techn. Lett.*, vol. 4, no. 11, pp. 1256-1258, 1992.
- [6] Makoto Hikita, Yoshito Shuto, Michiyuki Amano, Satoru Tomaru, and Haruki Kozawaguchi, "Optical intensity modulation in a vertically stacked coupler incorporating electro-optic polymer", *Appl. Phys. Lett.*, vol. 63, no. 9, pp. 1161-1163, 1993.
- [7] S. Asakawa, Y. Kokubun, T. Baba, and M. Ohyma, "Three-dimensional optical interconnects by stacked ARROW waveguides", *Int. Phot. Res.*, vol. 10, pp. 292-295, 1993.
- [8] C.M. Weinert and N. Agrawal, "Threedimensional simulation of multimode interference devices", *Int. Phot. Res.*, pp. 287-289, 1994.
- [9] M. Majd, A. Spielt, and K. Petermann, "A novel finite-difference beam-propagation method for large  $\Delta n$  and  $\Delta z$ ", *Int. Phot. Res.*, p. 90, 1991.
- [10] H. Wolter, W. Glaubitt, and K. Rose, "Multifunctional (meth)acrylate alkoxy-silanes: a new type of reactive compounds", *Mat. Res. Soc. Symp. Proc.*, vol. 271, pp. 719-724, 1992.
- [11] P. Dannberg, A. Bräuer, W. Karthe, and H. Wolter, "Ormocer-based monomode waveguide elements fabricated by replication technique", in *Techn. Digest Vol. 1, 10th IOOC*, 1995, p. 71.

## Polymeric Optical Space Switches

Norbert Keil, Huihai Yao, Crispin Zawadzki  
Heinrich-Hertz-Institut für Nachrichtentechnik Berlin GmbH  
Department Material Technology  
Einsteinufer 37, D-10587 Berlin, Germany  
Tel.: 00 49 30 31002 590; Fax: 00 49 30 31002 426; e-mail: keil@hhi.de

### Introduction

Data-intensive applications like desktop video-conferencing, video-on-demand and multimedia for business and education are creating an exponentially increasing demand for telecommunications bandwidth. A single-mode fiber's potential bandwidth is nearly 50 Tbps, which is nearly four orders of magnitude higher than electronic data rates of a few gigabits per second (Gbps), an essential solution to bandwidth problem is to use optical switching devices which provide network configuration at the optical level to form optical transparent networks. Besides that, optical switches are important for network protecting, routing in telecommunications, data communications, CATV, LAN, and in sensor and measurement techniques.

Polymers have a number of features that make them very attractive for high-performance integrated optical switches. They provide low optical loss and the combination of their large thermo-optic (TO) coefficient and low heat conductivity results in low electric switching power with ms-response time. This paper reviews the state of the art in polymeric optical space switches.

### Polymer waveguide technology

The prerequisite for any practical waveguide devices is the ability to form stable channel waveguides with low loss in the infrared region. Polymeric materials have the potential of very low material loss. Eldada *et al* reported losses below 0.01, 0.04 and 0.06 dB/cm at 840, 1300, and 1550 nm, respectively [1], for fluorinated acrylates. Compared with these data, the actual losses of polymeric channel waveguides are still rather high, especially at 1.55  $\mu\text{m}$ . Imamura *et al* realized channel waveguides with a loss of only 0.1 dB/cm at 1.31  $\mu\text{m}$  using deuterated and fluorinated PMMA providing highly controllable refractive indices [2]. At 1.55  $\mu\text{m}$ , the actual loss of polymer optical waveguides amounts to 0.4 dB/cm or more [3,4]. A key requirement for practical applications is the thermal stability of the optical material properties. The synthesis of low loss polymer waveguides with high thermal ( $T_g > 250^\circ\text{C}$ ) and high environmental stability attracts much attention at moment [3-5].

The basic structure of polymeric optical switches is a multilayer stack consisting of a Si-substrate acting as a heat sink, a buffer layer, a guiding layer, a top cladding and a metal heater. Polymeric films can be produced using spin-coating; the channel waveguides may be fabricated in different ways. The two major fabrication methods used for polymeric waveguide TO switches are reactive ion etching (RIE) [6,15,18-20], and UV-exposure of the polymers [7-12]. Thin metal layers may be produced by deposition or sputtering and structuring into micro heating elements using photolithography and chemical etching.

## Polymeric optical space switches

Two kinds of polymeric optical switches, i. e., the interferometric-type switch relying on modal interference and the digital optical switch (DOS) relying on adiabatic mode evolution, have been investigated. Polarization insensitive switching with low crosstalk at low power consumption has been obtained for both type of switches.

### Interferometric-type switches

Hida *et al* reported a Mach-Zehnder Interferometer (MZI) type 2x2 switch at  $1.3\ \mu\text{m}$  exhibiting low crosstalk ( $-40\ \text{dB}$ ) in conjunction with very low switching power ( $4.8\ \text{mW}$ ) [6]. However, in comparison with a directional-coupler (DC) switch, the total length of a MZI is about three times as large which renders this type of switch less suitable for the implementation of large switching matrices. The first polymer-based 2x2 DC switch exhibiting  $< -25\ \text{dB}$  crosstalk at  $1.55\ \mu\text{m}$  was realized at HHI in 1994 [7]. Based on that element, a 4x4 DC switch [8] and a 4x4 DC matrix [9] were reported for the first time by HHI in 1994 and 1995, respectively.

For improving the device performance in terms of crosstalk and fabrication tolerances, a 2x2 DC switch exhibiting  $< -40\ \text{dB}$  crosstalk was implemented first at HHI in 1996 [10]. This switch is operated as a symmetrical version coupler ( $\Delta\beta=0$ ) at low bias ( $3\ \text{mW}$ ) to turn the coupler into the *cross* state ( $-42\text{dB}$ ) and then as an asymmetrical version coupler ( $\Delta\beta\neq 0$ ) to reach the *bar* state ( $-45\ \text{dB}$ ) at a switching power of  $20\ \text{mW}$  (Fig. 1). Due to excellent device performance and high fabrication tolerances, this switch was used as a building block for constructing the first polymer-based 4x4 switching matrix [11], exhibiting crosstalk of  $< -30\ \text{dB}$  at either switching state.

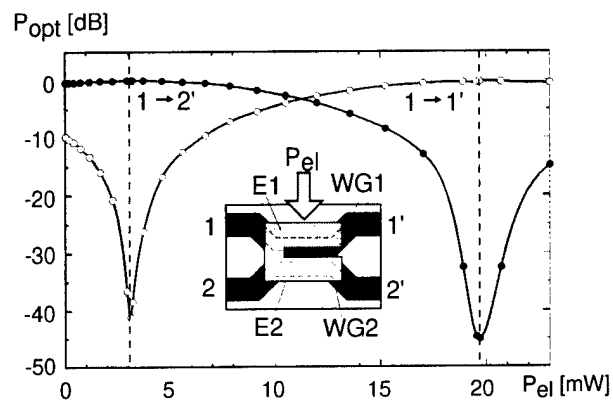


Fig. 1: 2x2 DC switch: transfer characteristics, ( $\lambda = 1.55\ \mu\text{m}$ ).

### Digital optical switches (DOS)

The digital optical switch (DOS) based on adiabatic modal evolution ideally exhibits a steplike response leading to a defined switching state as long as the applied switching power exceeds a given threshold value. This robust switching behaviour allows for relaxation of the technological tolerances and eliminates the need for a precise switching power control. Besides that, the DOS is polarization and wavelength insensitive, albeit at the expense of significantly higher switching power.

AKZO reported the first polymeric 1x2 DOS in 1991 [12], and TU Berlin [13], HHI [14], and NTT [15] followed in the years of 1995, 1996 and 1997, respectively. The polymer waveguide 1x2 DOS consists of a symmetrical Y-branch with a very small branching angle of typical  $0.1^\circ$  as shown schematically in the inset of Fig. 2. Two heating electrodes are placed on top of each branch. As an example, the measured optical transfer characteristics of a 1x2 DOS fabricated at HHI is shown in Fig. 2 [14]. The crosstalk remains below  $-20\ \text{dB}$  for a switching power of  $P_{el} \geq 60\text{mW}$  and below  $-30\ \text{dB}$  for  $P_{el} \geq 110\text{mW}$ .

The 1x2 DOS can be used as a building block for constructing 1xN and NxN switches and matrices. At HHI, a 1x4 and a 2x2 DOS consisting of three and four 1x2 DOS have been demonstrated [16] with average crosstalk of -27.5 and -37.5 dB, respectively. A 2x2 DOS based on a symmetric X-crossing consuming less electrical power was introduced by HHI in 1996 [17].

AKZO Nobel has fabricated the first 1x8 DOS in 1995 [18] and a 1x16 DOS is in the developmental stage at present. They reported also the first polymeric

8x8 digital switching matrix consisting of 112 single 1x2 DOS in 1996 [19]. At AKZO Nobel, volume production has started, and 1x2-, 1x4-, 1x8- and 2x2-DOS are commercial available now [20]. As an example, JDS FITELE uses 16 of the AKZO Nobel's BeamBox™ 1x8 DOS for constructing a 8x8 switching matrix [20].

## Conclusion

The growth of Internet and Intranet traffic has unleashed a demand that has led carriers to require more and more sophisticated photonic devices in hurry. This demand leads to an all-optical network with the optical switch representing one of the key devices. Different kinds of polymer-based switches have been investigated and fabricated. Some of them are already in volume production and commercial available. Low crosstalk in combination with low power consumption was obtained for both the interferometric-type and the digital optical switches. These polymeric switches are expected to find wide applications in telecommunications, CATV, LAN, and in sensor and measurement techniques.

## Reference

- [1] Eldada, *et al*: IEEE J. Lightwave Technol., **14**, 1704 - 1413, (1996).
- [2] Imamura, *et al*: Electron. Lett., **27**, 1342-1343, (1991).
- [3] Usui, *et al*, IEEE J. Lightwave Technol., **14**, 2338 - 2342, (1996).
- [4] Keil, *et al*: Micro Mat'97, Berlin, 1038, (1997).
- [5] Yardley, *et al*, POF'97, Kauai, Hawaii, 80 - 81, (1997).
- [6] Hida, *et al*: IEEE Photonic Technol. Lett., **5**, 782-784, (1993).
- [7] Keil, *et al*: Electron. Lett., **30**, 639 - 640, (1994).
- [8] Keil, *et al*: OFC'94, San José, Postdeadline Session, PD-14, (1994).
- [9] Keil, *et al*: OFC'95, San Diego, Postdeadline Session, PD-17, (1995).
- [10] Keil, *et al*: Electron. Lett., **32**, 655 - 657, (1996).
- [11] Keil, *et al*: Integrated Photonics Research'96, Boston, 633 - 636, (1996).
- [12] Möhlmann, *et al*: SPIE **1560**, 426 - 432, (1991).
- [13] Moosburger, *et al*: ECOC'95, Brussels, 1063 - 1066, (1995).
- [14] Keil, *et al*: NOC'96, Heidelberg, 196 - 203, (1997).
- [15] Watanabe, *et al*: ECIO'97, Stockholm, 474 - 477, (1997).
- [16] Keil, *et al*: POF'97, Kauai, Hawaii, 115 - 118, (1997).
- [17] Keil, *et al*: Electron. Lett., **32**, 1470 - 1471, (1996).
- [18] Horsthuis, *et al*: ECOC'95, Brussels, 1059 - 1062, (1995).
- [19] Borreman, *et al*: ECOC'96, Oslo, 5.59 - 5.62, (1996).
- [20] BeamBox™ NEWSLETTER, Akzo Nobel, Volume 2, June, (1997).

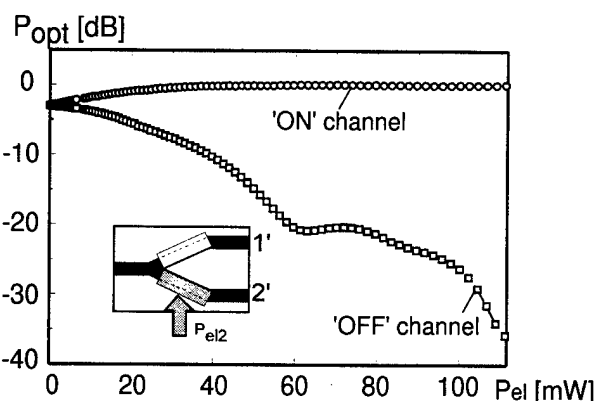


Fig. 2: 1x2 DOS: transfer characteristics, ( $\lambda = 1.55 \mu\text{m}$ ).

# Organic Light Emitting Diodes for Integrated Optics

Yutaka Ohmori and Katsumi Yoshino

Department of Electronics, Osaka University

Yamada-oka, Suita, Osaka 565 Japan

Tel: +81 6 879 7758, Fax: +81 6 879 7774, E-mail: ohmori@ele.eng.osaka-u.ac.jp

## Abstract

Organic light emitting diodes with plastic waveguides has been proposed for integrated optical circuits with plastic optical devices. Emission characteristics organic light emitting diodes have been discussed for integration with polymer waveguides and the plastic circuits.

## 1. Introduction

Recently, organic light emitting diodes (OLEDs) are developed rapidly to realize flat panel display devices. Many research workers [1-9] concentrated in OLEDs, because they have high brightness, low consumption of power, low driving voltage, and light weight, and can be made on flexible substrates, such as plastic substrates. Research works on OLEDs are for white light, multicolor emitting devices. Many organic materials for OLEDs have been developed, and the devices can be made by simple fabrication process, such as spin coating for polymer materials and organic vapor deposition technique for low molecular dye materials. In this paper, OLEDs with plastic waveguides has been proposed for integrated optical circuits, and emission characteristics of some types of OLEDs are discussed for integration of polymer waveguides or plastic optical circuits.

## 2. Device structure of integrated optical circuit

### 2.1 Device structure of proposed integration

Figure 1 shows a schematic description of OLED on a plastic substrate with optical circuits. There are two types of integration with optical circuits, since two types of light emission can be obtained from OLEDs, i.e., edge and surface emission types. In the case of edge emission type, which is shown in Fig. 1(a), light comes from the emissive layer along the substrate. On the other hand, as shown in Fig. 1(b), light comes through the substrate in the surface emission type. In the latter case, we can use transparent substrate and transparent electrode such as indium-tin-oxide (ITO) electrode. We can also use plastic transparent substrate for integrating OLEDs with plastic waveguide devices. Two kinds of organic materials (polymer [3-5] and low molecular dyes [1,2]) have been developed for light emitting sources in the OLEDs .

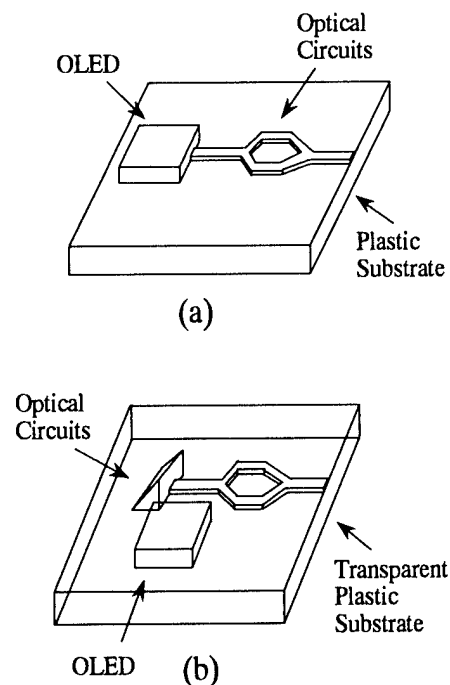


Fig. 1 Schematic description of proposed integration of OLED with polymer waveguide devices.

## 2.2 Device structure of organic light emitting diodes

Device structure of typical OLEDs are schematically shown in Figs. 2(a) and (b) for polymer and low molecular materials, respectively. In the case of polymer OLEDs, as shown in Fig. 2(a), the OLEDs are fabricated by spin coating method on a transparent substrate. As a transparent anode, we used ITO electrode.

On the other hand, OLEDs using low molecular dye materials are fabricated by organic molecular beam deposition (OMBE) technique on a transparent substrate. In this case, we can easily fabricate a layer structure with carrier transporting and emissive layers. We can also fabricate organic multiple quantum well (MQW) structure [7,8] using OMBE.

The emission wavelength can be selected by the emissive materials from ultraviolet to infrared, for example, utilizing polysilane or phthalocyanine, respectively.

## 3. Emission characteristics of organic light emitting diodes

Emission characteristics of the typical OLEDs fabricated by 8-hydroxyquinoline aluminum ( $\text{Alq}_3$ ) and N,N'-diphenyl-N,N'-(3-methyl phenyl)-1,1'-biphenyl-4,4'-diamine (TPD) are discussed comparing two kinds of device structure of heterostructure and MQW structure diodes. In Fig. 3, device structure and molecular structures used in this experiment are shown.  $\text{Alq}_3$  and TPD are used for emissive layer which emits green light at 520nm and carrier transporting layer, respectively. Heterostructure diode consists of 53.6-nm-thick  $\text{Alq}_3$  and 53.6-nm-thick TPD. MQW structure diode consists of 15 periods of 3.9-nm-thick  $\text{Alq}_3$  and 3.9-nm-thick TPD layers.

As shown in Fig. 4, the peak emission spectrum from the MQW structure shifts to the shorter wavelength and the full-width at half-maximum (FWHM) of the emission from the

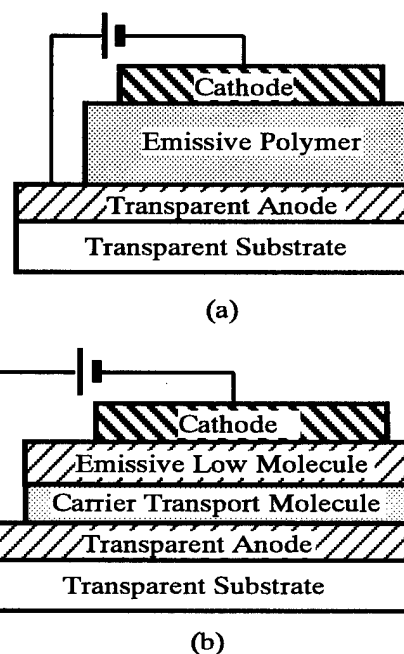


Fig. 2 Schematic description of typical OLEDs fabricated with polymer (a) or low molecular materials (b).

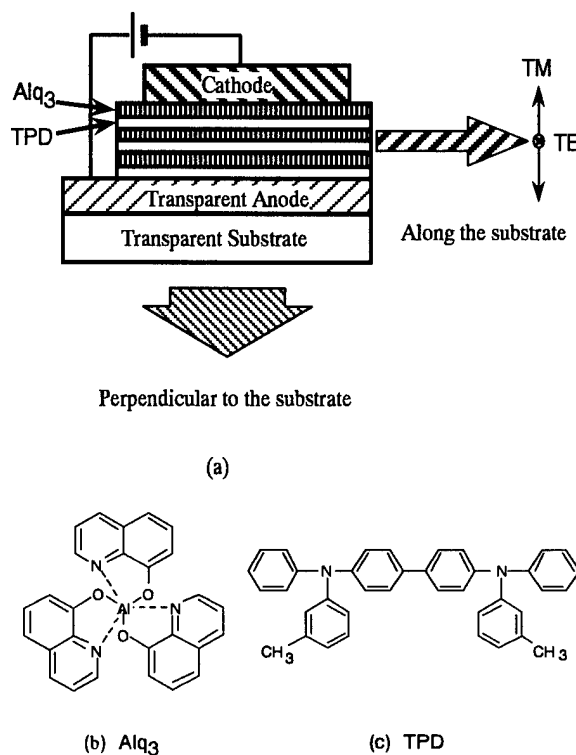


Fig. 3 Device structure of OLED (a) and molecular structure used for the device(b).

MQW structure decreases compared with the heterostructure and they both decrease as the layer thickness become thinner.

Polarization characteristics of the EL emission from the  $\text{Alq}_3/\text{TPD}$  MQW system ( $\text{Alq}_3/\text{TPD}$ ; 20nm/20nm, 5periods) are also shown in Fig. 4. The EL emission spectrum of TE and TM modes in the  $\text{Alq}_3/\text{TPD}$  MQW system is same even in the short-period system. The intensity in the TE mode is stronger than that in the TM mode, and the intensity ratio of TM and TE modes becomes unity in the short-period MQW system. The FWHM of the TE mode is smaller than that of the TM mode in the MQW system. This may be due to the energy distribution in the short-period MQW system or the difference in the reflection at the interface of the electrodes.

In Fig. 5, full-color emission spectra from the single OLED [9] are shown. The device consists of three different emissive layers and are driven independently.

#### 4. Summary

In summary, we demonstrated OLEDs fabricated on a transparent electrode and can emit various colors from a single device. The OLEDs are one of the promising devices which can be composed with integrating plastic optical circuits for optical integration.

#### References

- 1) C. W. Tang and S. A. VanSlyke: *Appl. Phys. Lett.* **51** (1987) 913 .
- 2) C. W. Tang, S. A. VanSlyke and C. H. Chen: *J. Appl. Phys.* **65** (1989) 3610 .
- 3) J. H. Burroughes, D. D. C. Bradley, A. R. Brown, R. N. Marks, K. Mackay, R. H. Friend, P. L. Burns and A. B. Holmes: *Nature* **347** (1990) 539.
- 4) Y. Ohmori, M. Uchida, K. Muro and K. Yoshino: *Jpn. J. Appl. Phys.* **30** (1991) L1938.
- 5) Y. Ohmori, M. Uchida, K. Muro and K. Yoshino: *Jpn. J. Appl. Phys.* **30** (1991) L1941.
- 6) F. F. So, S. R. Forrest, Y. Q. Shi and W. H. Steier: *Appl. Phys. Lett.* **56** (1990) 674.
- 7) Y. Ohmori, A. Fujii, M. Uchida, C. Morishima and K. Yoshino: *Appl. Phys. Lett.* **62**(1993)3250.
- 8) Y. Ohmori, A. Fujii, M. Uchida, C. Morishima and K. Yoshino: *Appl. Phys. Lett.* **63**(1993)1871.
- 9) N. Tada, A. Fujii, Y. Ohmori and K. Yoshino: *IEEE Trans. Ele. Device*, **44** (1997) 1234.

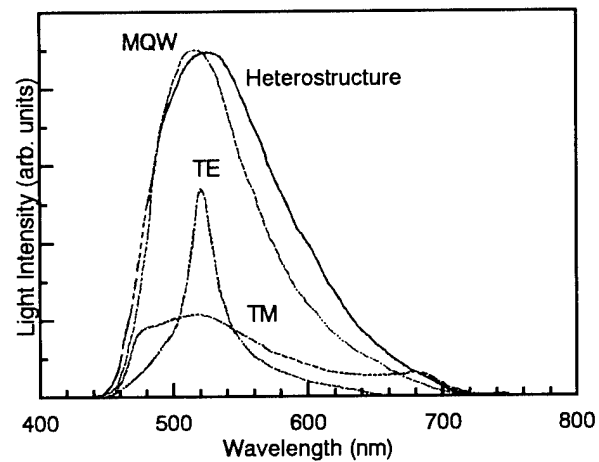


Fig. 4 Typical emission characteristics of the OLED through the substrate (MQW or Heterostructure) or along the substrate (TE or TM).

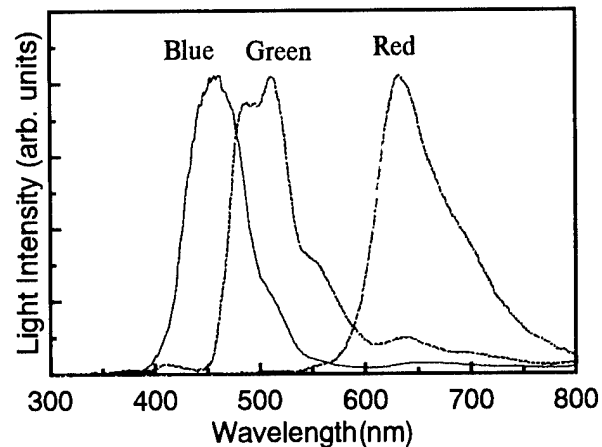


Fig. 5 Full color emission spectra from single OLED.

---

**Integrated Photonics Research**

# Device Simulations I

**Wednesday, April 1, 1998**

**K. A. Shore, University of Wales, Bangor, U. K.**  
Presider

**IWA**  
**8:30am–10:00am**  
Salon B

## Design and Simulation of Phased-array Wavelength Router with Flat Response using Fourier Optics Concept

Namhoon Kim and Youngchul Chung

Department of Electronic Communications Engineering, Kwangwoon University

447-1 Wolgye-Dong Nowon-ku, Seoul, Korea 139-701

TEL:+82-2-940-5138, FAX:+82-2-941-7855, e-mail:y chung@daisy.kwangwoon.ac.kr

### ABSTRACT

*A new design of passband-flattened phased-array wavelength router based on Fourier optics concept is presented. The simulation results show that the bandwidth is 0.8nm at -1dB, insertion loss about 6dB, and the crosstalk less than -23dB at all the channel wavelengths, which are 1.6nm(200 GHz) separated from adjacent channel around 1550nm wavelength range.*

One of the key components to accomplish the WDM all-optical network is phased-array wavelength router[1]. The spectral response of conventional phased-array wavelength router have parabolic shape, and the bandwidth is limited. The spectral response of optical filter should be as flat as possible for the reliable operation of the system, because in the actual system, the optical source's frequency could possibly be deviated[2][3][4][5]. In order to acquire the desired flat response, this letter presents the design of phased-array wavelength router with flat passband using Fourier optics concept.

The passband-flattened phased-array wavelength router consists of input waveguides, first slab waveguide and arrayed waveguides with the constant path-length difference which includes the removed waveguide region, second slab waveguide, and output waveguides.

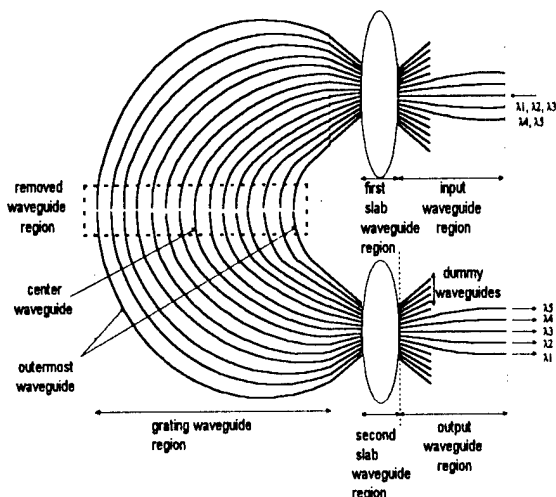


Fig. 1 The schematic layout of NxN phased-array wavelength router with flat response

The input beam radiates to the first slab waveguide and then excites the arrayed waveguides. After travelling through the arrayed waveguides, the light beam converges into the focal position in the second slab waveguide. Fig. 1 shows schematic layout of the NxN phased-array wavelength router with flat passband. To obtain a flat passband, it is necessary to produce the rectangular field distribution at the output plane of the second slab waveguide. As the field distribution in the output plane of the second slab waveguide is the Fourier transform of the field in the input plane of the second slab waveguide, such a rectangular field distribution could be realized when the field distribution at the input plane of the second slab waveguide obeys a sinc function

distribution[5]. In order to obtain sinc function distribution at the input plane of the second slab waveguide, the transmitted optical power is controlled by removing certain length of each waveguide in the array. Fig. 2 shows schematic diagram of power attenuation method in order to acquire the field distribution, which is similar to a sinc function in the input plane of the second slab waveguide. In Fig. 2, the region 2 is the phase reversal region in the sinc function distribution. We can reverse the phase in the region 2 using half wavelength waveguide insertion.

The first zero crossing point from the center waveguide in the array is given by

$$x_0 = \frac{\lambda_0 z}{W n_s} \quad (1)$$

where  $z$  is focal length of the second slab waveguide,  $n_s$  effective index of the second slab waveguide,  $W$  the width of rectangular function, and  $\lambda_0$  the center wavelength.

Therefore, through the proper design, the field distribution at the input plane of the second slab waveguide can be controlled to be a sinc function, resulting

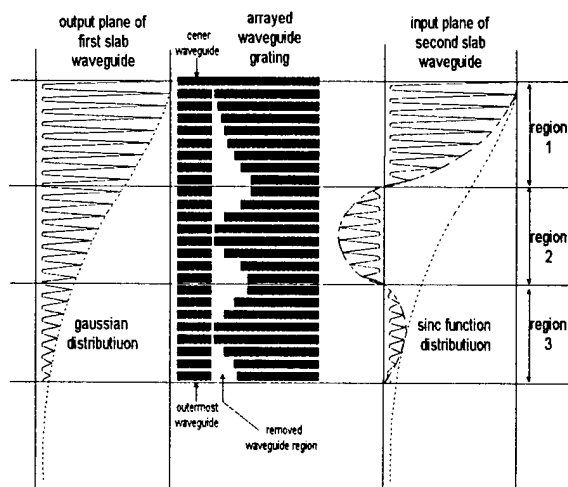


Fig. 2 Schematic diagram showing power attenuation method in order to acquire field distribution, which is similar to sinc function in the phased-array wavelength router with flat passband

in the rectangular field distribution at the output plane of the second slab waveguide.

Fig. 3 shows the field distribution at the array without and with removal of certain length of waveguides in the array.

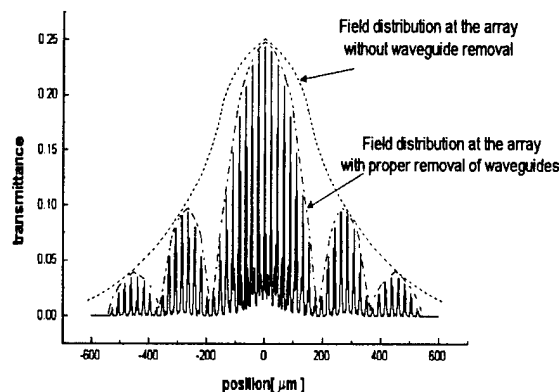


Fig. 3 Field distribution at the array without and with removal of certain length of waveguides in the array

To illustrate the design concept, we consider the waveguide structure as shown in Fig. 4.

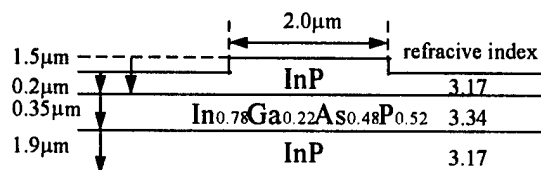


Fig. 4 Waveguide structure which simulated by beam propagation method

With this waveguide structure, the 7x7 phased-array wavelength router is designed. The channel spacing is 1.6nm and the diffraction order is 134. The phased-array waveguides are designed in such a way that 180° phase reversal occurs at every 82.5 μm (i.e 8 waveguides) from the center of the second slab waveguide input.

Fig. 5 shows relative phase difference and power attenuation as a function of the length of removed waveguide section. In Fig. 5 (a), the phase difference ( $\Delta\phi$ ) between phases with and without removal of waveguide is plotted as a function of

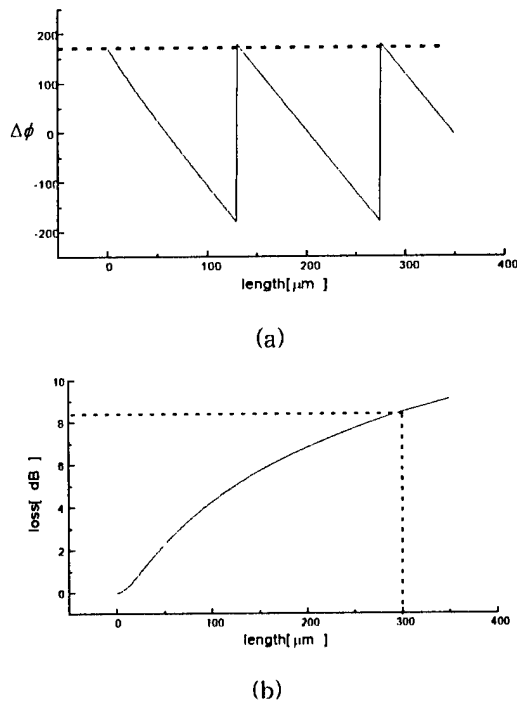


Fig. 5 (a)Relative phase difference (b)Power attenuation as a function of removed waveguide length.

removed waveguide length. This phase should be compensated by inserting the waveguide section, whose length is

$$\Delta L = \frac{\lambda_0}{2\pi n_c} \Delta\phi \quad (2)$$

The length of the removed section is tabulated in Table. 1.

Table. 1 Length of the removed section (Waveguide number "0" and "24" represent center and outermost waveguide in the array)

Waveguide number	0	1	2	3	4	5	6	7	8
Length of removed section [ $\mu\text{m}$ ]	0	6	14	23	32	44	200	317	690
Waveguide number	9	10	11	12	13	14	15	16	
Length of removed section [ $\mu\text{m}$ ]	780	255	75	18	14	6	50	780	
Waveguide number	17	18	19	20	21	22	23	24	
Length of removed section [ $\mu\text{m}$ ]	1140	255	75	23	0	0	50	270	

The BPM simulation is performed for the star coupler structure which includes the removed waveguide sections. The wave propagation through the array waveguides

is accommodated through the multiplication of phase factors.

The simulated spectral responses of 7x7 phased-array wavelength router are shown in Fig. 6. The BPM simulation shows that the bandwidth is 0.8nm at -1dB, insertion loss about 6dB, and the crosstalk less than -23dB, which are 1.6nm(200 GHz) separated from adjacent channel around 1550nm wavelength range[6].

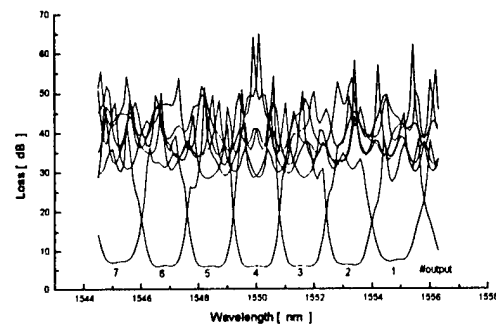


Fig. 6 Spectral response of 7x7 phased-array wavelength router when 4-th input port is excited

In summary, we designed the phased-array wavelength router with flat passband through the proper removal of waveguide sections and the resulting wave front shaping, the simulation results of which show the expected performance.

#### [REFERENCES]

- [1] C. Dragone et al, IEEE Photon. Technol. Lett. vol. 3, no. 10, 1991
- [2] K. Okamoto and A. Sugita, Electronics letters vol. 32, no.18, 1996
- [3] J.B.D.Sooile, M.R.Amersfoort, A.Rajhel, H.P.LeBlanc, et al. IEEE Photon. Technol. Lett., vol. 8, no. 10, pp. 1340-1342, 1996
- [4] Meint K. Smit, and Cor van Dam, IEEE J. Quantum Electron., vol. 2, no. 2, pp. 236-250, 1996
- [5] K. Okamoto and H. Yamada, Opt. Lett., vol. 20, no. 1, Jan 1995
- [6] Youngchul Chung and Nadir Dagli, IEEE J. Quantum. Electron., vol. 26, no. 8, pp. 1335-1339, 1990

## Improved Extinction Ratio in Ultra Short Directional Couplers Using Aymmetric Structures

Boo-Gyoun Kim\*, Ali Shakouri, Bin Liu, and John E. Bowers

Department of Electrical and Computer Engineering

University of California, Santa Barbara, CA 93106

Tel. (805) 893 8775, Fax (805) 893 7990

bgkim@opto.ucsb.edu

\* Permanent address: SoongSil University, Seoul 156-743, Korea

Directional couplers are critical components in photonic integrated circuits used in optical communication networks. The conventional directional couplers with laterally arranged waveguides can not achieve very short coupling lengths due to extreme sensitivity to fabrication variations and limitations to produce uniformly very narrow gap layers [1]. However, vertical directional couplers can obtain a short coupling length which is smaller than  $100\ \mu\text{m}$  [2]. The difficulty of separating the two vertical coupled waveguides into two distinct inputs and outputs limits the application of these couplers. Recently, a novel fused vertical coupler (FVC) with a very short coupling length of  $73\ \mu\text{m}$  was demonstrated, that can solve this problem [3]. To use the FVC in large switching fabrics, it should have the short coupling lengths and low crosstalk. In this paper, we analyze various means to improve the extinction ratio in FVCs using slight asymmetry in the structure.

The two-dimensional index profile of the FVC is reduced to one dimension using the effective index method. The structure is composed of two waveguides A and B with effective indices  $n_a$  and  $n_b$ , and thicknesses  $d_a$  and  $d_b$ . They are separated by an inner cladding region, index  $n_{ci}$  and thickness  $t$ . The outer cladding regions have indices  $n_{ca}$  and  $n_{cb}$ . The two waveguides in FVC are very close together ( $t = 0.2\text{--}1\ \mu\text{m}$  separation). To model accurately the crosstalk in this strongly coupled waveguide structure, an improved coupled mode theory (ICMT) is used, which takes into account the finite overlap integral between the modes of individual waveguides [4,5]. Assuming that the power is incident into the waveguide A without the loss of generality, the extinction ratio after a distance equal to the coupling length is defined as  $P_b/P_a$  where  $P_a$  and  $P_b$  are the guided mode powers in waveguides A and B respectively. The wavelength used in the calculation is  $1.55\ \mu\text{m}$ .

Fig. 1 and Fig. 2 show the extinction ratio and coupling length of TE and TM modes as a function of refractive index of waveguide A using ICMT and also 2D finite difference beam propagation method (BPM). The parameter values used in the calculation are  $n_b = 3.37$ ,  $n_{ca} = n_{cb} = n_{ci} = 3.17$ ,  $d_a = d_b = 0.5\ \mu\text{m}$ , and  $t = 0.6\ \mu\text{m}$ . We can see that the data calculated by ICMT agrees very well to that by BPM. The extinction ratio larger than 50 dB for TE (TM) mode occurs at  $n_a = 3.367$  ( $n_a = 3.366$ ) and the coupling length in this case is  $51\ \mu\text{m}$  ( $47\ \mu\text{m}$ ). The extinction ratio and the coupling length in the symmetric case for TE (TM) mode are 16.4 dB (15.7 dB) and  $52\ \mu\text{m}$  ( $48\ \mu\text{m}$ ). We can see that the extinction ratio is increased considerably at the expense of having less than 100 % power transfer to the waveguide B by slight detuning of the two waveguide eigenmodes as Chuang showed in [7]. The coupling length is not significantly affected by making the waveguides asymmetric.

When the waveguides are separated by  $0.6\ \mu\text{m}$ , the asymmetry defined by  $n_b - n_a$

required to achieve the highest extinction ratio for TE (TM) mode is 0.003 (0.004). Having index of waveguide A within  $\pm 0.019\%$  ( $\pm 0.021\%$ ) of the optimum value for TE (TM) mode, one can achieve the extinction ratio larger than 30 dB [Fig. 3]. As the separation between the two waveguides decreases, more asymmetry is needed but the tolerance to obtain an extinction ratio larger than 30 dB increases [Fig. 3]. This facilitates fabrication of passive asymmetric couplers or setting the voltage or current in active components. Fig. 4 shows the coupling length of the optimum asymmetric coupler for the different values of  $n_a$  corresponding to Fig. 3 and its percent difference with the symmetric case as a function of waveguide separation. The coupling length decreases and the percent difference increases as the separation decreases. By making the waveguides very close to each other ( $< 0.4\ \mu\text{m}$ ) one can achieve ultra short coupling lengths less than  $30\ \mu\text{m}$  and at the same time maintain the extinction ratio larger than 30 dB. One can see in Fig. 5 that, in the symmetric case, even though the coupling lengths are comparable to those of the asymmetric case, the extinction ratio severely deteriorates to less than 15 dB when the separation between the two waveguides is less than  $0.55\ \mu\text{m}$ .

To confirm that the effect of detuning of the two waveguide eigenmodes on the extinction ratio of the FVC comes from the slight difference in the shapes of the two waveguide eigenmodes, the extinction ratio and coupling length of TE and TM modes as a function of width of waveguide A rather than the refractive index are calculated with the parameter values for  $n_a = n_b = 3.37$ ,  $n_{ca} = n_{cb} = n_{ct} = 3.17$ ,  $d_b = 0.5\ \mu\text{m}$ , and  $t = 0.6\ \mu\text{m}$ . An extinction ratio larger than 42 dB for TE (TM) mode occurs at  $d_a = 0.486\ \mu\text{m}$  ( $0.484\ \mu\text{m}$ ) while the extinction ratio in the symmetric case was around 16 dB. Also, we calculated the extinction ratio and coupling length of TE and TM modes as a function of refractive index of the inner cladding layer. The extinction ratio changes considerably ( $> 15\text{dB}$ ) when the refractive index of the inner cladding layer changes in the asymmetric case, on the other hand, the extinction ratio does not change much as a function of the refractive index of the inner cladding layer in the symmetric case. A slight asymmetry can equalize the overlap integral of one of the waveguide modes with the symmetric and antisymmetric supermodes of the coupler and thus increase the extinction ratio.

In conclusion, we have shown that one can facilitate ultra short vertical directional couplers (coupling length 10–200  $\mu\text{m}$ ) while maintaining a high extinction ratio larger than 30 dB with slight asymmetry in the coupled waveguide structure. Shorter asymmetric couplers have an extinction ratio which is more fabrication tolerant.

This research was supported by the DARPA Center MOST.

#### References

1. J. E. Zucker, K. L. Jones, M. G. Young, B. I. Miller, and U. Koren, *Appl. Phys. Lett.* 55, 2282 (1989).
2. F. Dollinger, M. Borcke, G. Bohm, G. Trankle, and G. Weimann, *Electron. Lett.* 32, 1509 (1996).
3. B. Liu, A. Shakouri, P. Abraham, B.-G. Kim, and J. E. Bowers, to be presented in OFC'98.
4. A. Hardy and W. Streifer, *J. Lightwave Technol.* 3, 1135 (1985).
5. S.-L. Chuang, *J. Lightwave Technol.* 5, 5 (1987).
6. S.-L. Chuang, *IEEE J. Quantum Electron.* 23, 499 (1987).

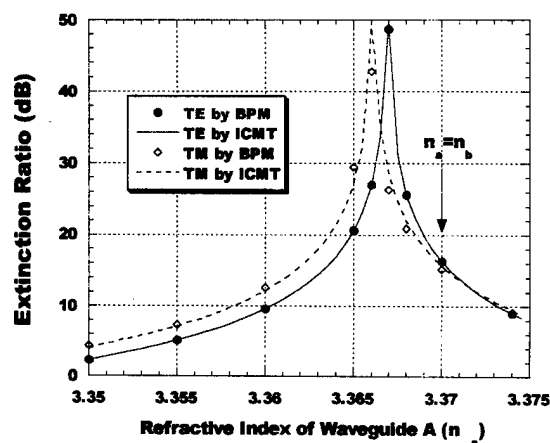


Figure 1: Extinction ratio for TE and TM modes as a function of the index of waveguide A calculated using ICMT and BPM.

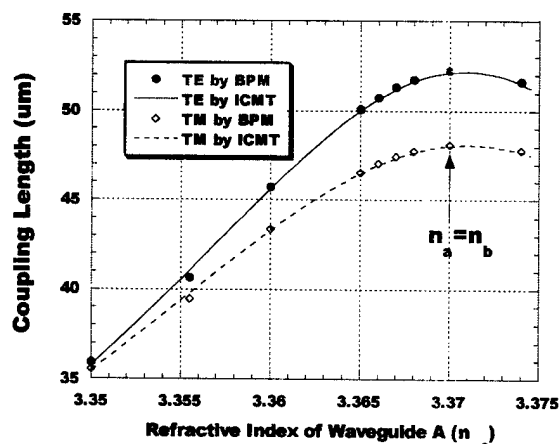


Figure 2: Coupling length for TE and TM modes as a function of the index of waveguide A calculated using ICMT and BPM.

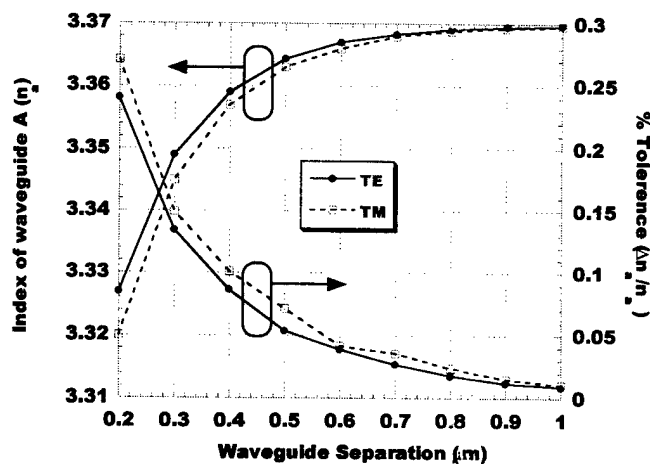


Figure 3: Index of waveguide A for maximum extinction ratio and tolerance on that to achieve > 30dB extinction ratio as a function of waveguide separation.

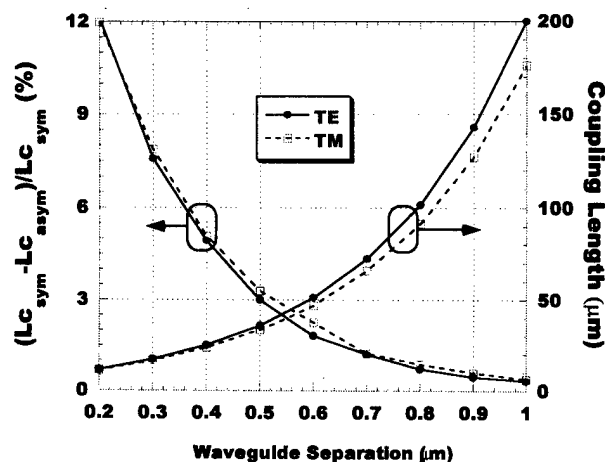


Figure 4: Coupling length of the asymmetric coupler for the different values of  $n_a$  corresponding to Fig. 3 and its difference with symmetric case as a function of waveguide separation.

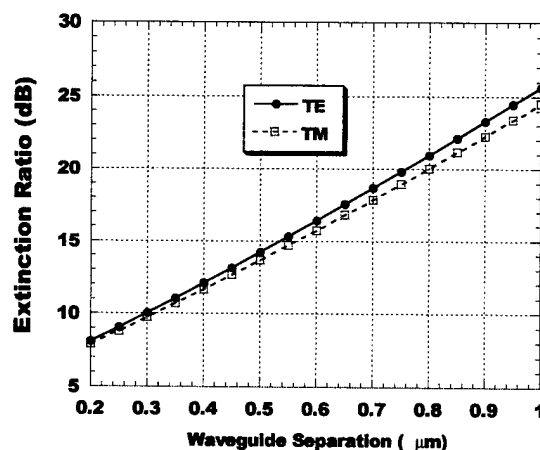


Figure 5: Extinction ratio for TE and TM modes for the symmetric coupler as a function of waveguide separation.

# AMPLIFICATION OF STRONG PICOSECOND OPTICAL PULSES IN SEMICONDUCTOR OPTICAL AMPLIFIERS

J.M.Tang and K.A.Shore

University of Wales, Bangor,  
School of Electronic Engineering and Computer Systems,  
BANGOR, LL57 1UT, UK

Tel: +44(1248)382618. Fax: +44(1248)361429.  
e-mail: alan@sees.bangor.ac.uk

**Introduction:** The amplification of ultrashort optical pulses in Semiconductor Optical Amplifiers (SOAs) has been the subject of considerable research interest, because the ultrafast carrier dynamics in SOAs is important for tailoring devices with applications in optical frequency conversion [1], high speed optical signal manipulation in optoelectronic integrated circuits and for understanding the high-speed modulation response of semiconductor lasers. With a view to such applications, numerical investigations have been undertaken of the picosecond pulse saturation behaviour of SOAs [2]. The effect of nonlinearity on the chirp characteristics of picosecond pulse amplification have also been reported [3].

**Analysis:** In this paper the amplification of strong picosecond optical pulse in SOAs is investigated taking into account nonlinear gain, two-photon absorption (TPA) and ultrafast nonlinear refraction (UNR). The model has in other work been shown to give very good agreement with published experimental results on the propagation of strong picosecond optical pulses in semiconductor optical amplifiers at the transparency point [4]. It was shown there that the effects of two-photon absorption and ultrafast nonlinear refraction are very important in determining the output pulse properties for pulse energy larger than 1pJ. The model used is the first which takes account of the above nonlinear mechanism whilst also retaining amplitude and phase (and hence spectral) information of the propagating pulse. Here the application of the model is extended with a view to investigating the temporal and spectral features of amplified short optical pulses.

**Results:** The parameters used in the calculations are representative for InGaAsP semiconductor materials for operating at a wavelength of  $1.5\mu\text{m}$ . Fig.1 shows the normalised output pulse shape for different small signal gain of the SOAs when the input pulse duration and energy are 1ps and 31pJ. For comparison the corresponding results without considering the TPA effect are also plotted in Fig.1. The salient features are that the amplified pulse width is broadened significantly (more than 1.8 times), and the broadened pulse width are enhanced greatly with increasing the

small signal gain of the SOAs. This is because above the injected transparency current, both nonlinear gain compression and the TPA take place, whilst nonlinear gain compression effect is damped at the transparency point. As can be seen in Fig.1, for increasing small signal gain there is a significant change in the symmetry of the pulses. The TPA effect decreases the gain experienced by the pulse by heating carriers in the active region, simultaneously the energy absorbed by TPA also results in increasing the inversed carrier density with recovery time much larger than the pulse width. Therefore the combination of the two processes leads to the output pulse shape varying with the small signal gain of the SOAs.

Under the same conditions as in Fig.1, the pulse spectra given in Fig.2, shows that the spectra vary from asymmetrical at the transparency current to symmetrical at relatively high injected current. Furthermore, the broadened spectra also shifts towards longer wavelength side for larger small signal gain. This results from the gain saturation and the UNR, which lead to negative chirp in the pulse leading edge. It should be also noted that for different small signal gain the spectral peak at short wavelength side changes very slowly in comparison with the longer wavelength side. This behaviour can be explained by considering Fig.1. We can see from Fig.1, that the pulse trailing edge does not change significantly with the small signal gain since the strong carrier depletion in the pulse leading edge causes very small gain experienced by the pulse trailing edge. The TPA is thus dominant in the pulse trailing edge. Therefore the small change in the pulse trailing edge is generated, causing nearly equally positive chirp occurring in the region for all the cases.

**Acknowledgements:** J.M.Tang is supported by the Wynn Humphrey Davies Studentship of the University of Wales, Bangor and by SEECs, University of Wales, Bangor. This work is also partly supported by the UK EPSRC under grant GR/L03262.

## References

- 1 A.D'Ottavi et al., IEEE J.Select Topics in Quantum Electron., Vol.3, pp.522-527, 1997.
- 2 A.Mecozzi and J.Mork, J.Opt.Soc.Am.B, Vol.14, pp.761-770,1997.
- 3 J.M.Tang, P.S.Spencer and K.A.Shore, Electron. Lett., Vol.32, pp.1293-1294, 1996.
- 4 J.M.Tang and K.A.Shore, "Effect of two-photon absorption nonlinearity on short pulse propagation in semiconductor optical amplifiers at transparency," Submitted.

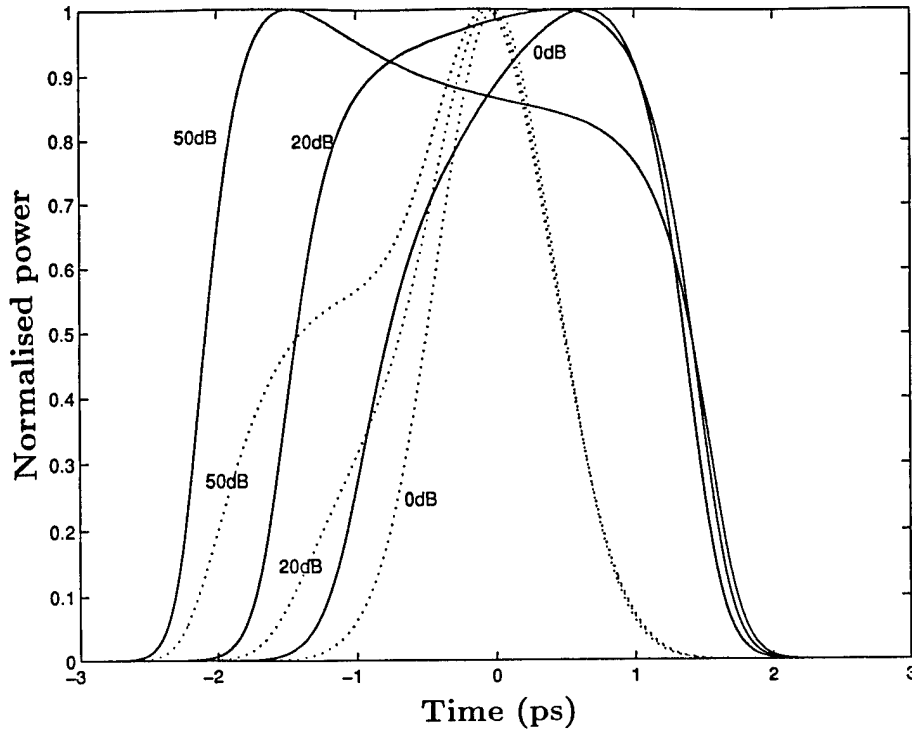


**Fig.1.** Normalised output pulse shape of input 1ps pulse with energy of 31pJ for different small signal gain of the SOAs. Solid (dotted) line includes (does not include) TPA effect.

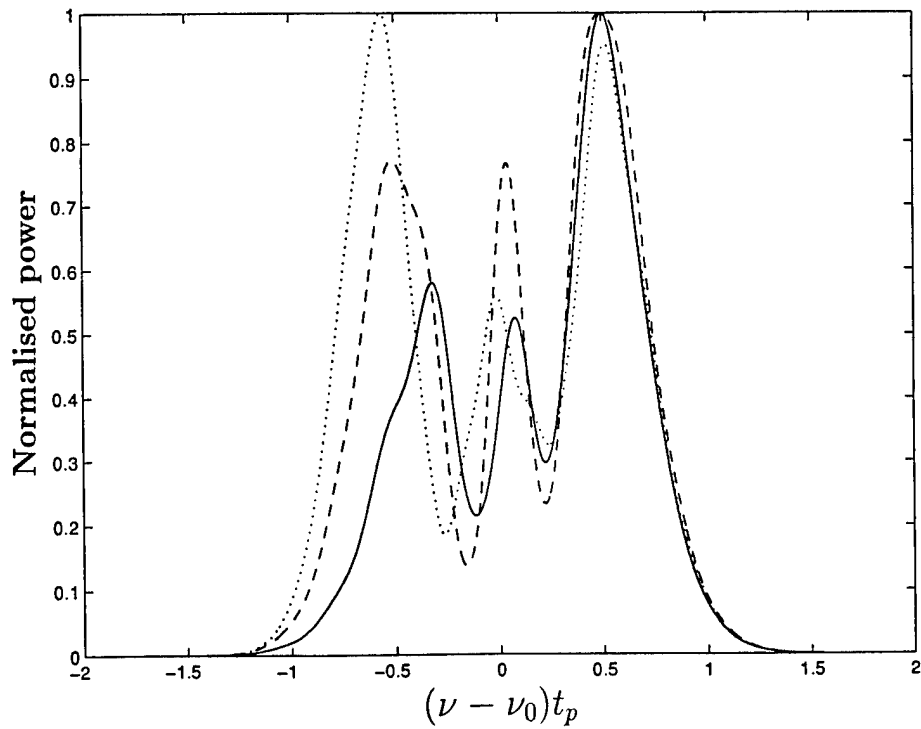


**Fig.2.** Spectra of 1ps, 31pJ input pulse for different small signal gain of the SOAs. Solid, dashed and dotted lines are with the small signal gain of 0dB, 10dB and 20dB respectively.  $\Delta\nu = \nu - \nu_0$  is the frequency difference,  $t_p$  and pulse width  $t_0$  have the relation of  $t_0 \approx 1.665t_p$  for Gaussian pulse.

# Application of a hybrid implicit-explicit FDTD scheme to nonlinear distributed Bragg resonators

Vien Van and Sujeet K. Chaudhuri

*Department of Electrical and Computer Engineering  
University of Waterloo, Waterloo, Ontario, Canada, N2L 3G1  
Tel. (519) 885-1211, Fax. (519) 746-3077  
Email: vvan@maxwell.uwaterloo.ca*

## 1. Introduction

With the increasing availability of computer resources, the Finite-Difference Time-Domain (FDTD) method by virtue of its versatility has become a powerful numerical tool for analyzing optical wave-guiding devices. Recently there has also been a growing interest in applying the method to nonlinear structures [1,2]. To date, however, only explicit time-stepping is employed in the discretization because the resulting propagator is extremely simple, but the scheme places a severe constraint on the time step and grid sizes in order to yield stable solutions in nonlinear media [2,3]. The stability condition can be relaxed by using an implicit discretization scheme but at the expense of extensive computational resources. By applying implicit discretization only to regions of nonlinear materials in the waveguide and employing the conventional explicit scheme in the linear material regions, we can combine the advantages of both schemes to give an efficient algorithm for handling waveguides of mixed linear and nonlinear materials.

## 2. Formulation of the hybrid FDTD scheme

In the proposed hybrid scheme, a partially-implicit discretization scheme is used to solve for the field in the regions of nonlinear materials, while the field in the linear medium regions is obtained using the explicit scheme. Fig. 1 shows a mesh superposed on a region of mixed linear and nonlinear media. A node is designated as being explicit if it falls in a linear region and implicit if it belongs to a nonlinear region. For an explicit node  $i$ , the conventional finite-difference equation for the 2D scalar wave equation for TE modes is

$$(\epsilon_r)_i \frac{E_i^{N+1} - 2E_i^N + E_i^{N-1}}{(c\Delta t)^2} = \frac{E_{i_L}^N - 2E_i^N + E_{i_R}^N}{(\Delta z)^2} + \frac{E_{i_A}^N - 2E_i^N + E_{i_B}^N}{(\Delta x)^2}, \quad (1)$$

where  $\epsilon_r$  is the relative permittivity. For the implicit regions, a weighted-average time-stepping scheme is used which is stable and does not introduce an amplitude attenuation factor. The discrete equation for an implicit node  $j$  with possibly explicit neighbours is

$$\begin{aligned}
\frac{(\epsilon_r E)_j^{N+1} - 2(\epsilon_r E)_j^N + (\epsilon_r E)_j^{N-1}}{(c\Delta t)^2} = & \frac{1}{4} \left[ \frac{E_{j_L}^L - 2E_j^{N+1} + E_{j_R}^L}{(\Delta z)^2} + \frac{E_{j_A}^L - 2E_j^{N+1} + E_{j_B}^L}{(\Delta x)^2} \right] + \\
& \frac{1}{2} \left[ \frac{E_{j_L}^N - 2E_j^N + E_{j_R}^N}{(\Delta z)^2} + \frac{E_{j_A}^N - 2E_j^N + E_{j_B}^N}{(\Delta x)^2} \right] + \\
& \frac{1}{4} \left[ \frac{E_{j_L}^M - 2E_j^{N-1} + E_{j_R}^M}{(\Delta z)^2} + \frac{E_{j_A}^M - 2E_j^{N-1} + E_{j_B}^M}{(\Delta x)^2} \right]
\end{aligned} \tag{2}$$

where in general, for a nonlinear medium,  $\epsilon_r$  is a function of the electric field  $E$ . The time indices  $L$  and  $M$  are assigned as follows: if a neighbour node  $j_\eta \in \{j_L, j_R, j_A, j_B\}$  is also an implicit node, then  $L(j_\eta) = N+1$  and  $M(j_\eta) = N-1$ ; otherwise  $L = N$  and  $M = N$ . This convention of assigning time indices to the neighbour nodes minimizes the numerical discontinuity, and hence reflection, at the interfaces between explicit and implicit regions.

The above hybrid scheme has been observed experimentally to be stable when the time step and grid sizes satisfy the CFL stability condition in the linear medium regions. Since the overall stability of the hybrid scheme is determined by the stability in the linear medium regions alone, nonlinearity in the structure does not affect the choice of the grid sizes or time step. This is in contrast with the purely explicit scheme where, in general, stronger nonlinearity requires the grid sizes and time step be further reduced below the CFL limit in order to ensure stability [3]. Simulations using the hybrid scheme have also demonstrated the self-phase modulation effect in nonlinear slab waveguides and power-dependent phase-matching condition in nonlinear distributed feedback structures [4].

### 3. Application to nonlinear DBR filters

We applied the hybrid FDTD scheme to the nonlinear distributed Bragg resonator (DBR) shown in Fig. 2. The structure consists of four grating regions alternating with three quarter-wave phase shift regions having Kerr-type nonlinearity. Each grating in turn is composed of alternating linear and Kerr-type nonlinear materials. The numbers of periods are  $N_1 = N_4 = 20$  and  $N_2 = N_3 = 40$ . Fig. 3 shows the incident pulse and the reflected signal, which consists of four consecutive pulses due to reflections from the four gratings. The reflection spectra normalized by the incident spectrum at two incident power densities, 1W/m and 3W/m, are shown in Fig. 4. The peak reflection coefficients are greater than unity because spectrum broadening associated with self-phase modulation causes the reflected spectrum at these wavelengths to gain in magnitude over the incident spectrum. Also due to Kerr nonlinearity, the grating steps in the permittivity appear higher at larger incident power, causing the reflection spectrum at 3W/m incident power to be shifted by nearly 5nm toward longer wavelengths compared to the spectrum at 1W/m incident power. Such a power-dependent filter response may be used to discriminate both wavelength and signal power in a multi-channel optical communication system.

#### 4. Conclusions

We presented a hybrid implicit-explicit FDTD scheme for simulating nonlinear optical wave-guiding devices and demonstrated its application to nonlinear DBR filters. The scheme is expected to provide improved stability over the purely explicit scheme in regions of nonlinear materials.

#### References

- [1] Jamid, H.A. and Al-Bader, S.J., "Finite-difference time-domain approach to nonlinear guided waves", *Electron. Lett.*, vol. 29, no. 1, pp. 83-84, 1993.
- [2] Ziolkowski, R.W. and Judkins, J.B., "Nonlinear finite-difference time-domain modeling of linear and nonlinear corrugated waveguides", *J. Opt. Soc. Am. B*, vol. 11, no. 9, pp. 1565-1575, Sep. 1994.
- [3] Kunz, K.S and Luebbers, R.J., *The Finite Difference Time Domain Method for Electromagnetics*. Boca Raton: CRC Press Inc., 1993.
- [4] Van, V., Chaudhuri, S.K. and Chu, S.T., "A hybrid implicit-explicit FDTD scheme for solving the scalar wave equation in non-linear optical waveguides", *Proc. AP-S*, vol. 1, July 1997.

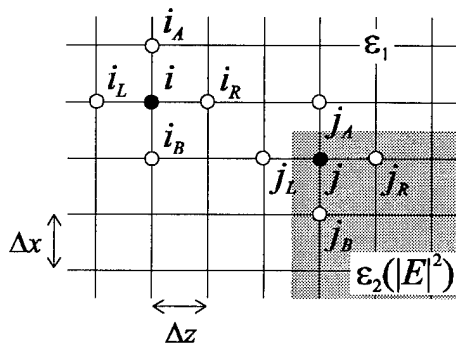


Fig. 1. Grid superposed on both linear and nonlinear medium regions.

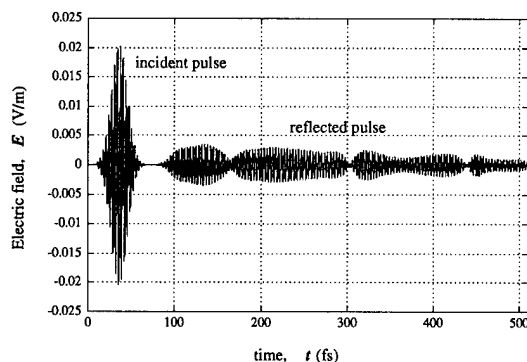


Fig. 3. Incident and reflected pulses in the nonlinear DBR filter ( $P_{inc} = 1 \text{ W/m}$ ).

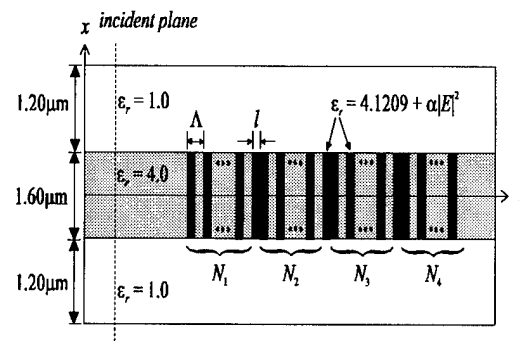


Fig. 2. Nonlinear DBR filter structure.

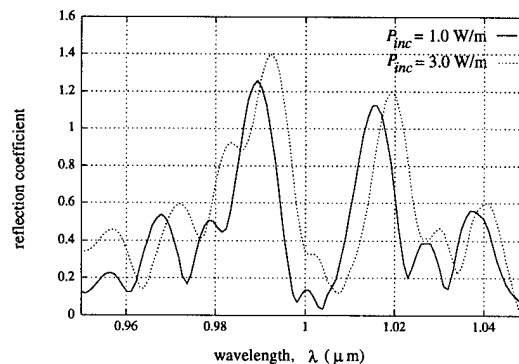


Fig. 4. Reflection spectra of the nonlinear DBR filter at  $P_{inc} = 1 \text{ W/m}$  and  $3 \text{ W/m}$ .

# Efficient analysis of non-symmetric periodic optical devices

Stefan F. Helfert

Allgemeine und Theoretische Elektrotechnik

FernUniversität, D-58084 Hagen

Phone: +49 2331 987 1144 Fax: +49 2331 987 353

e-mail: Stefan.Helfert@FernUni-Hagen.de

**Introduction:** Periodic structures (e. g. Bragg gratings) are important optical devices. The particular importance of fiber gratings was recognized by publishing a Special Issue of the Journal of Lightwave Technology featuring current research into these structures [1]. In case of a high number of periods, the numerical algorithms for analysis of such devices may have difficulties concerning the numerical stability, CPU-time and memory space. The most important problem (numerical stability) can be avoided by performing an impedance transfer as described in [2]. Recently, an algorithm was developed for analysis of symmetrical periodic devices with a moderate numerical effort [3],[4] which combines the numerical stable impedance transfer with Floquet's theorem [5]. The symmetry relates to the  $z$ -dependence of the period only, the cross section may be arbitrary, and the input and output side of the device may be different. Besides these symmetrical devices, the non-symmetrical structures also have a significant importance. Examples can be found in [6] and [7]. In the first paper is shown that the electric behavior of a VCSEL-structure can be improved by including a high doped region in the mirrors to reduce the voltage drop. The second one deals with a dielectric antenna with unequally spaced radial variations. In this paper we propose a new approach for analysis of asymmetric periodic structures combining the impedance transfer with Floquet's theorem. Its application for analysis of a grating with 1000 periods reduces the CPU time from 1 hour to 1.5 minutes.

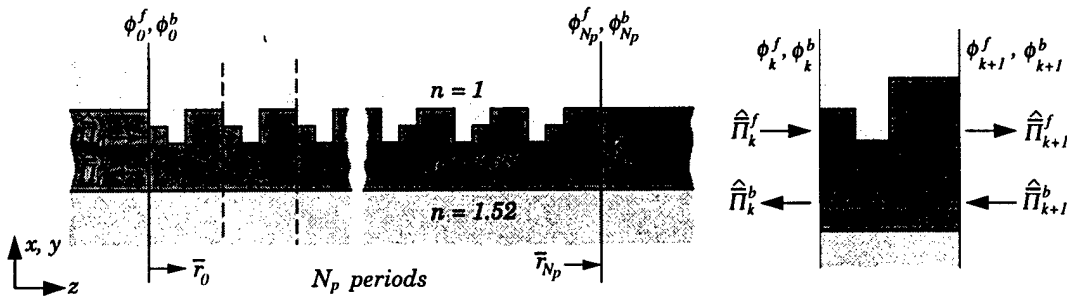


Fig. 1 a: Example of an asymmetric periodic structure, b: one period

**Theory:** The combination of Floquet's theorem and the impedance transfer was applied for the MoL-BPM, a beam propagation algorithm (BPM)[8] based on the method of lines (MoL)[9], which is described comprehensively in [10]. First, we divide the device into homogeneous sections in the direction of propagation (here  $z$ ). Then, after computing the magnetic field from a vector potential [5] we derive a wave equation for each homogeneous sector, which we discretize in transverse directions, resulting in a system of coupled differential equations. Transformation to principle axes results in a system of decoupled differential equations which can easily be solved (see [10]):

$$\frac{d^2}{dz^2} \hat{\Pi} - \hat{\Lambda}^2 \hat{\Pi} = 0 \implies \hat{\Pi}(z) = e^{-\hat{\Lambda}z} \hat{\Pi}^f(0) + e^{\hat{\Lambda}z} \hat{\Pi}^b(0) \quad (1)$$

It should be mentioned that a transformation to principle axes corresponds to an expansion of the field in eigenmodes. Thus, the potentials in transformed domain, represent the amplitudes of the eigenmodes of the homogeneous sections. Especially, for the analysis of 3D-devices we should use only a reduced set of these eigenmodes to keep the numerical effort moderate. At the interfaces between homogeneous sections the tangential field components have to be matched. Combining them into supervectors, we can write the following relation between the transformed potentials and the fields:

$$\begin{pmatrix} \mathbf{E} \\ \mathbf{H} \end{pmatrix} = \begin{bmatrix} \overline{\mathbf{M}}_E & \overline{\mathbf{M}}_E \\ \overline{\mathbf{M}}_H & -\overline{\mathbf{M}}_H \end{bmatrix} \begin{pmatrix} \hat{\Pi}^f \\ \hat{\Pi}^b \end{pmatrix} \quad (2)$$

$\overline{\mathbf{M}}_E$  and  $\overline{\mathbf{M}}_H$  are matrices, obtained by including  $\Pi$  into Maxwell's equations and then discretizing in the transverse directions (in analogy to the discretization of the wave equation). To apply Floquet's theorem

into the analysis, we divide the structure (Fig. 1a) into equal periods (Fig. 1b). Due to the analytic solution in  $z$ -direction we may easily determine the transfer matrix for the transformed potentials at the ports of one period (see Fig. 1b):

$$\left( (\hat{\Pi}_{k+1}^f)^t, (\hat{\Pi}_{k+1}^b)^t \right)^t = \mathbf{A}_P^t \left( (\hat{\Pi}_k^f)^t, (\hat{\Pi}_k^b)^t \right)^t \quad (3)$$

Next, we compute the eigenvalues and eigenvectors of  $\mathbf{A}_P^t$  and obtain:

$$\mathbf{A}_P^t = \begin{bmatrix} \mathbf{X}_{11} & \mathbf{X}_{12} \\ \mathbf{X}_{21} & \mathbf{X}_{22} \end{bmatrix} \begin{bmatrix} e^{-\Gamma_1} & \\ & e^{+\Gamma_2} \end{bmatrix} \begin{bmatrix} \mathbf{X}_{11} & \mathbf{X}_{12} \\ \mathbf{X}_{21} & \mathbf{X}_{22} \end{bmatrix}^{-1} \quad (4)$$

with  $\text{Re}\{\Gamma_{1,2}\} > 0$ . Unlike the symmetrical case, the submatrices of the eigenvectors are different in general. The eigenvalues are reciprocal (i. e.  $\Gamma_1 = \Gamma_2$ ), only when calculating with all modes. If the eigenmode system is reduced, this relation does not hold any longer. Nevertheless, we can introduce Floquet modes. They propagate in the following way:

$$\phi_{k+1}^f = e^{-\Gamma_1} \phi_k^f \quad \phi_{k+1}^b = e^{+\Gamma_2} \phi_k^b \quad (5)$$

In view of the analogy with homogeneous sections we use the superscripts  $f$  and  $b$  to indicate forward and backward propagation, though the terms exponentially increasing and decreasing modes appear more accurate. Concatenating  $N_p$  periods we must multiply  $N_p$ -times with the exponential factors, to obtain the relation between the Floquet modes at the input of the first and the output of the  $N_p$ th period. The relation between modes of the homogeneous sections and the Floquet modes are:

$$\hat{\Pi}^f = \mathbf{X}_{11}\phi^f + \mathbf{X}_{12}\phi^b \quad \hat{\Pi}^b = \mathbf{X}_{21}\phi^f + \mathbf{X}_{22}\phi^b \quad (6)$$

To obtain compact expressions we transform the fields according to:

$$\bar{\mathbf{E}} = (\bar{\mathbf{M}}_E)^{-1} \mathbf{E} \quad \bar{\mathbf{H}} = (\bar{\mathbf{M}}_H)^{-1} \mathbf{H} \quad (7)$$

resulting in:

$$\begin{pmatrix} \bar{\mathbf{E}} \\ \bar{\mathbf{H}} \end{pmatrix} = \begin{bmatrix} \bar{\mathbf{S}}_{11} & \bar{\mathbf{S}}_{12} \\ \bar{\mathbf{S}}_{21} & -\bar{\mathbf{S}}_{22} \end{bmatrix} \begin{pmatrix} \phi^f \\ \phi^b \end{pmatrix} \quad \text{with} \quad \begin{bmatrix} \bar{\mathbf{S}}_{11} & \bar{\mathbf{S}}_{12} \\ \bar{\mathbf{S}}_{21} & -\bar{\mathbf{S}}_{22} \end{bmatrix} = \begin{bmatrix} \mathbf{X}_{11} + \mathbf{X}_{21} & \mathbf{X}_{12} + \mathbf{X}_{22} \\ \mathbf{X}_{11} - \mathbf{X}_{21} & \mathbf{X}_{12} - \mathbf{X}_{22} \end{bmatrix} \quad (8)$$

Analyzing the structure shown in (Fig. 1a) we start with a load impedance  $\mathbf{Z}_E$  at the output of the grating. We obtain:

$$\bar{\mathbf{E}} = \bar{\mathbf{Z}}_E \bar{\mathbf{H}} \quad \text{with} \quad \bar{\mathbf{Z}}_E = \bar{\mathbf{M}}_E^{-1} \mathbf{Z}_E \bar{\mathbf{M}}_H \quad (9)$$

Introducing this expression into (8) yields the relation between the forward and backward propagating Floquet modes at the output port:

$$\phi^b = \bar{\mathbf{r}}_{N_p} \phi^f \quad \text{with} \quad \bar{\mathbf{r}}_{N_p} = (\bar{\mathbf{Z}}_E \bar{\mathbf{S}}_{22} + \bar{\mathbf{S}}_{12})^{-1} (\bar{\mathbf{Z}}_E \bar{\mathbf{S}}_{21} + \bar{\mathbf{S}}_{11}) \quad (10)$$

Due to the propagation of the Floquet modes (5) we can transfer the reflection coefficient to the input port and obtain in case of  $N_p$  periods:

$$\bar{\mathbf{r}}_0 = e^{-\Gamma_2 N_p} \bar{\mathbf{r}}_{N_p} e^{-\Gamma_1 N_p} \quad (11)$$

Introducing this input reflection coefficient ( $\bar{\mathbf{r}}_0$ ) into (6), we obtain a relation between the forward and backward propagating modes of the homogeneous sections and the forward propagating Floquet mode. Thus, giving e.g. an incident mode  $\hat{\Pi}^f$  we can determine the reflected part  $\hat{\Pi}^b$  and the Floquet modes at the input. To calculate the field inside the structure (5) is used only for propagation of  $\phi^f$ . Performing a transfer of the reflection coefficient analogous to (11), we can compute the backward propagating Floquet mode using an expression similar to (10). Knowing, the amplitudes of both Floquet modes we can calculate the related field components. Since for the transfer of the reflection coefficient as well as for the propagation of  $\phi^f$  only exponential decreasing terms are used, the numerical problems are eliminated.

**Numerical results:** To prove the validity of the algorithm proposed, the asymmetric periodic structure shown in Fig. 1 was examined. Since it consists of three homogeneous sections, the extension of the Floquet algorithm to non-symmetric devices was necessary. To check the numerical stability up to thousand periods were examined (Fig. 2), and the results were compared with those obtained by the well known admittance transfer approach (e.g. [2]). The numerical difference was less than  $10^{-10}$ , which shows the correct application of Floquet's theorem. To compute the reflectivity for 1000 periods only, the

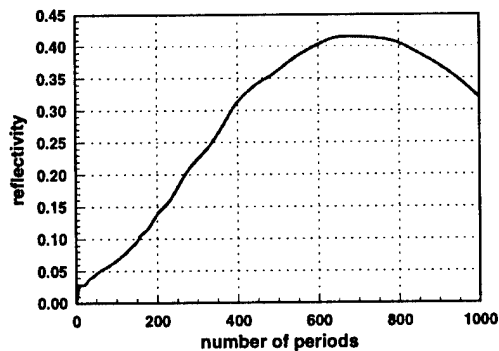


Fig. 2: Reflectivity of the fundamental mode as function of the number of periods

admittance transfer needed 1 hour, whereas the approach with Floquet's theorem could reduce this time to 1.5 minutes. Thus, an enormous reduction of the numerical effort is obtained for this case. As mentioned before, to analyze three dimensional devices with a moderate effort a reduction of the eigenmode system is required. Fig. 3 is a plot of the reflectivity for 1000 periods vs. the number of eigenmodes. It should be noted, that the reflectivity reaches a steady state using 45 eigenmodes. The total number of lines (=number of eigenmodes) was 138. Thus, for an exact computation only a third of all modes is really necessary. Fig. 4 shows the power flow inside the grating. As should be expected, the power is decreasing with the number of periods. The results obtained with all eigenmodes ( $n_r = 138$ ) and those obtained with a reduced set ( $n_r = 60$ ) agree very well, which proves again that a reduction of the number of eigenmodes is possible.

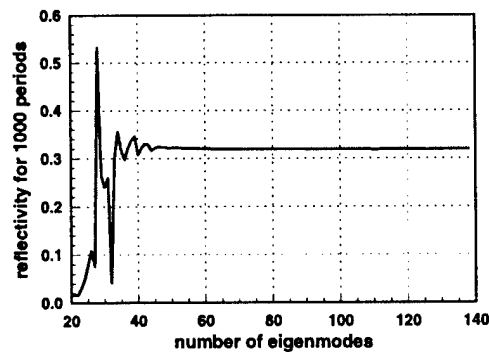


Fig. 3: Reflectivity of the fundamental mode as function of the number of eigenmodes

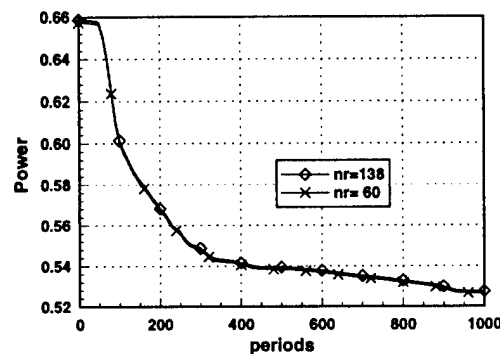


Fig. 4: Power flow

**Conclusion:** An efficient algorithm has been developed for the analysis of asymmetric periodic optical devices. It is numerical stable, even in case of a high number of periods, and the numerical effort remains moderate.

## References

- [1] *J. Lightwave Technol., Special Issue on Fiber Gratings, Photosensitivity, and Poling*, vol. 15, Aug. 1997.
- [2] R. Pregla, "The Method of Lines as Generalized Transmission Line Technique for the Analysis of Multilayered Structures", *AEÜ*, vol. 50, no. 5, pp. 293-300, Sep. 1996.
- [3] S. Helfert and R. Pregla, "A Very Stable and Accurate Algorithm for the Analysis of Periodic Structures with a Finite Number of Periods", *Proc. Prog. Electr. Res. Symp. (PIERS)*, Hong Kong, 1997, vol. 1, p. 105.
- [4] S. Helfert and R. Pregla, "Efficient analysis of periodic structures", submitted to *J. Lightwave Technol.*
- [5] R. E. Collin, *Field Theory of Guided Waves*, Series of Electromagnetic Waves. IEEE press, New York, 2 edition, 1991.
- [6] K. J. Ebeling, U. Fiedler, R. Michalzik, G. Reiner, and B. Weigl, "Efficient Vertical Cavity Surface Emitting Laser Diodes for High Bit Rate Optical Data Transmission", *AEÜ*, vol. 50, no. 5, pp. 316-326, 1996.
- [7] H. Kubo and Y. Mahara, "Dielectric Rod Waveguide with Unequally Spaced Radial Variations", in *1997 URSI North American Radio Science Meeting*, Montreal, Canada, July 1997, p. 117.
- [8] M. D. Feit and J. A. Fleck, "Light Propagation in Graded Index Optical Fibers", *Appl. Opt.*, vol. 17, pp. 3990-3998, 1978.
- [9] R. Pregla and W. Pascher, "The Method of Lines", in *Numerical Techniques for Microwave and Millimeter Wave Passive Structures*, T. Itoh, (Ed.), pp. 381-446. J. Wiley Publ., New York, USA, 1989.
- [10] R. Pregla, "MoL-BPM Method of Lines Based Beam Propagation Method", in *Methods for Modeling and Simulation of Guided-Wave Optoelectronic Devices*, W.P. Huang, (Ed.), number PIER 11 in Progress in Electromagnetic Research, pp. 51-102. EMW Publishing, Cambridge, Massachusetts, USA, 1995.

# Mode engineering in periodically segmented waveguides

D. Ortega, J M Aldariz and J. S. Aitchison,

Department of Electronics and Electrical Engineering,  
University of Glasgow, Glasgow. G12 8QQ  
e-mail: D.Ortega@elec.gla.ac.uk

## Abstract.

We report on the fabrication and testing of  $\text{Ti:LiNbO}_3$  periodically segmented waveguides (PSWs) and the use of a 3D finite difference beam propagation method (3D FD BPM) to simulate the evolution of the optical field.

## Summary.

$\text{LiNbO}_3$  is a well established material in the field of integrated optics, it possesses a unique combination of properties and characteristics, which allows a large number of active and passive integrated devices to be fabricated. Here we propose to use PSWs to increase the functionality of integrated components. The use of PSWs has been extended to many material systems, such as  $\text{LiNbO}_3$  [1],  $\text{KTP}$  [2],  $\text{InP}$  [3], and glass [4]. Initially PSWs were used to obtain quasi-phase matched (QPM) second harmonic generation (SHG) [5]. Recently PSWs have been employed in asymmetric Y-junction wavelength demultiplexers [6], asymmetric couples wavelength filters [4] and in tapers [3] [7].

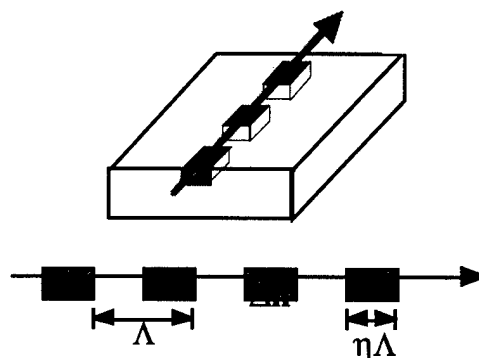


Fig 1. A Periodic segmented waveguide (PSW).  $\Lambda$  is the period and  $\eta$  the duty-cycle

In a PSW the increase in the refractive index ( $\Delta n$ ) is modulated periodically during fabrication, this is shown schematically in Fig 1. As a consequence of the segmentation, the losses in the guide are increased and the index difference is reduced when compared to a continuous waveguide. The application of PSWs in integrated optics rely on the possibility of controlling the effective index with duty cycle, and at the same time use its period for phase matching applications. This combination opens the gates to a range of novel devices. Here we will investigate the propagation of light in a PSW and consider the mode sustained by the waveguide and the segmentation losses. We

will show that a PSW can be represented by a equivalent continuous waveguide and that the duty-cycle controls the modal properties.

A PSW can be represented by an equivalent continuous waveguide with the same depth and width, in which the average index difference,  $\Delta n'$ , is taken to be the weighted average of the index along the direction of propagation. In the case of step index waveguides this is represented by Eq. 1 .

$$\Delta n' = \eta \Delta n \quad \text{Eq 1}$$

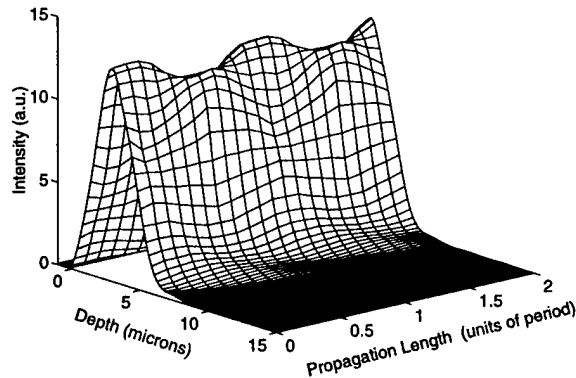


**Fig. 2.** Depth intensity profile along two periods of a step index channel PSW of period  $17.5 \mu\text{m}$ , duty cycle 0.5, width  $5 \mu\text{m}$ , depth  $5 \mu\text{m}$  and an increase in the refractive index of 0.0215. The operating wavelength is  $1.55 \mu\text{m}$ . The intensity profile was calculated by adding all the intensity points in the transversal direction for a given depth.

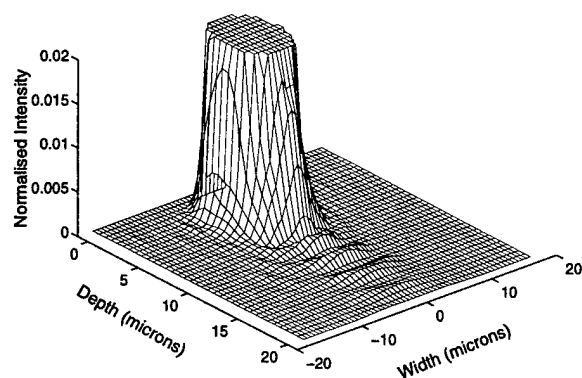
Using a 3D finite difference beam propagation method (3D FD BPM) we generated the optical field supported by a PSW, this can be seen in Fig 2. The optical field is repeated after each period, except for a reduction in the amplitude due to

segmentation losses (the losses associate with the modulation of the refractive index). For this reason we term the intensity distribution along a period the quasi-mode of a PSW.

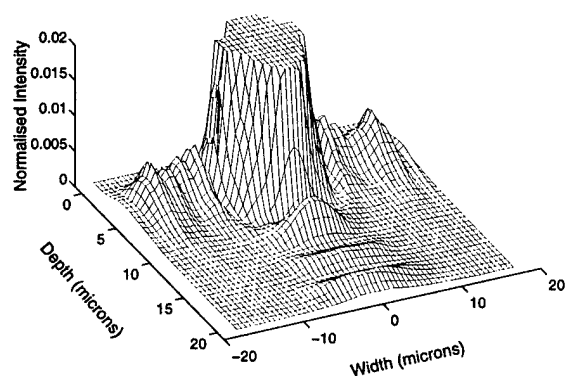
The radiation losses for PSW of period  $17.5$  and  $30 \mu\text{m}$  can be seen in Fig 3. Careful control of the optical field at the boundaries (to minimise noise) permitted us to quantify the radiation losses for different periods and duty-cycles. Until now the segmentation losses were only investigated for 2D structures, considering only the radiation toward the substrate. However as show in Fig 3, at larger periods, the dominant loss mechanism is in the horizontal direction.

The validity of Eq 1 has been demonstrated experimentally by investigating the cut-off wavelength of  $\text{Ti:LiNbO}_3$  PSWs. A series of waveguides were fabricated with different periods and duty-cycles. The cut-off wavelength of these PSWs were then compared with the expected results for the equivalent continuous waveguide [1]. Errors between predicted and measured values were 2%, and are attributed to fabrication uncertainties and measurement errors. Once the validity of Eq 1 has been demonstrated, the 3D BPM was used to compare the modes size of PSWs and the equivalent continuous waveguide described by Eq 1. The agreement between the two sets of results, directly confirm that Eq 1 can be used to

describe PSWs, and indicate that the 3D BPM accurately simulate PSWs.



(a)



(b)

**Fig 3.** A 3D detail of the intensity distribution in a PSW of period a)  $17.5 \mu\text{m}$  and b)  $30 \mu\text{m}$ . The duty-cycle, width, depth and increase in the refractive index are those of Fig 2. The intensity has been normalised to one.

We will show how this detailed knowledge of the behaviour of quasi-modes in a PSW can be used to describe grating assisted coupled mode interactions.

## Conclusions.

We have demonstrate that PSWs sustain quasi-modes, associate with these modes there are radiation losses which have been quantify using a 3D BPM. We have shown that the increase of the refractive index can be controlled with the duty-cycle. Since the phase matching wavelength is a function of the period, then we can precisely control the increase of the refractive index and the phase matching wavelength limited only by the photolithographic processing.

## References.

- [1] D. Ortega, R M De La Rue, and J S Aitchison, "Cut-off wavelength of periodically segmented waveguides in  $\text{Ti:LiNbO}_3$ ", *Journal of Lightwave technology*, Accepted for publication in the February 1998 issue.
- [2] J. D. Bierlein, D. B. Laubacher, and J. B. Brown, "Balanced phase matching in segmented  $\text{KTiOPO}_4$  waveguides", *Appl. Phys. Lett.* **56**, pp. 1725 - 1727, (1990).
- [3] F. Dorgeuille, B. Mersali, S. Francois, G. Herve-Gruyer, and M. Filoche, "Spot size transformer with periodically segmented waveguides based on  $\text{InP}$ ", *Optics Letters*, **20**, pp. 581 - 583, (1995).
- [4] Z. Weissman, F. Saint-Andre and A. Kevorkian, "Asymmetric directional couplers using buried ion-exchange, periodically segmented waveguides in glass.", *Proc. ECIO'97*, pp. 52 - 55, Stockholm April 1997.
- [5] Z Weissman, A Hardy, M Katz, M Oron, and D Eger, "Second harmonic generation in Bragg-resonant quasi-phase matched periodically segmented waveguides", *Optics Letters*, **20**, pp. 674-676, (1995).
- [6] Z. Weissman, D. Nir, S. Ruschin, and A. Hardy, "Asymmetric Y-junctions wavelength demultiplexers based on segmented waveguides", *Appl. Phys. Lett.*, **67**, pp. 302 - 304, (1995).
- [7] M. H. Chou, M. A. Arbone, and M. M. Fejer, "Adiabatically tapered periodic segmentation of channel waveguides for mode-size transformation and fundamental mode excitation", *Opt. Lett.* **21**, pp. 794 - 796 (1996).



**Integrated Photonics Research**

# **Lasers II: WDM/VCSELS**

**Wednesday, April 1, 1998**

**R. M. DeLaRue, University of Glasgow, U. K.**  
Presider

**IWB**  
**8:30am–10:00am**  
Salon C

# **Vertical cavity surface emitting lasers with spatially adjustable DBR reflectivity to enable free space photonic repeaters**

**Aaron E. Bond and P. Daniel Dapkus**

University of Southern California, University Park Campus, PHE504-MC0271

Los Angeles CA 90089-0271 (213) 740-4414 Voice, (213) 740-6022 Fax

bond@csl-sun.usc.edu, dapkus@mizar.usc.edu

Selective oxidation of AlAs [1] to form  $\text{AlO}_x$  within an epitaxial structure has been an enabling technology for high performance vertical cavity surface emitting lasers (VCSEL).  $\text{AlO}_x$  has been used to fabricate apertures to confine current flow and to provide lateral mode confinement[2]. In addition, the large index of refraction contrast between  $\text{AlO}_x$  and semiconductors has been used to fabricate high contrast distributed Bragg reflectors (DBRs) [3]. We have used these properties of the  $\text{AlO}_x$  to fabricate VCSELs with adjustable reflectors that allow the fabrication of both top and bottom emitting high performance VCSEL's side by side on the same wafer. This technology can be used for fabricating general purpose photonic repeaters and complex smart pixels in free space optical systems.

The DBRs in our VCSEL structure are designed so that the top and bottom mirror reflectivity can be altered in selective locations of the wafer to enhance either top or bottom emission while achieving devices with essentially the same performance. The top and bottom DBRs are hybrid structures containing conventional 87% AlGaAs / GaAs pairs for the part of the mirror structures near the active region and  $\text{AlO}_x$ /GaAs DBRs for part of the mirrors most remote from the active region. Thirteen pairs of 87% AlGaAs / GaAs are used in the bottom DBR, and ten are used in the top to compensate for the air/GaAs interface on the top. The  $\text{AlO}_x$  / GaAs portions of the DBR are selectively oxidized in different portions of the wafer to enhance either top or

bottom emission. Five pairs of AlAs/GaAs are grown at the top and bottom of the layer structure with the AlAs thickness chosen so that it will be one quarter wavelength after oxidation. To achieve bottom emission all of five of these pairs at the top are oxidized and only three on the bottom are oxidized. The remaining two pairs do not substantially affect the bottom reflectivity because they are phase mismatched when unoxidized. Top emission is achieved by selectively oxidizing all of the bottom AlAs/GaAs pairs and only three of the top pairs. The top two are removed. This approach yields calculated reflectivities that will result in the same threshold current and quantum efficiency for both types of device. The 87% AlGaAs/GaAs mirrors are left undoped to keep the optical losses to a minimum, and contact is made to the p and n GaAs layers with intracavity contacts [4].

Using this approach we have fabricated top and bottom emitting lasers from the same epitaxial wafer. To facilitate the fabrication and testing, the devices were fabricated in different parts of the wafer during subsequent processing runs. The performance of these devices serve as a feasibility test for monolithically integrated

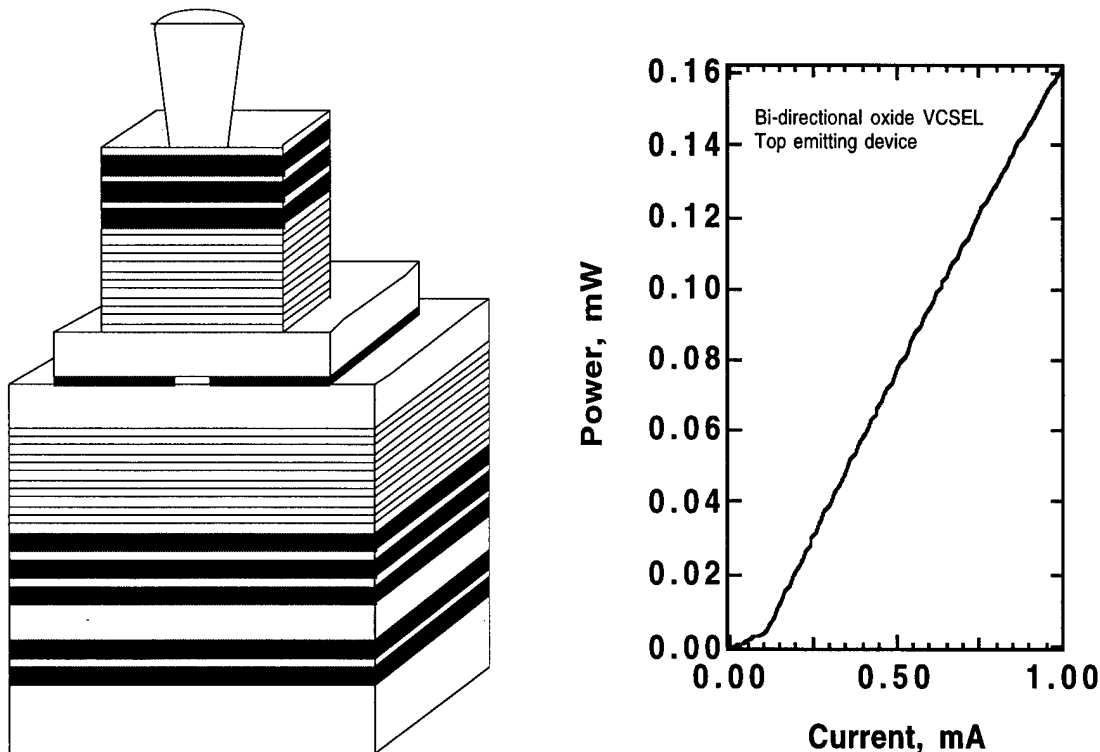


**Fig. 1** Epitaxial structure and performance characteristics of top emitting VCSEL's with adjustable mirror reflectivity

structures. We expect to demonstrate monolithic integration shortly. Our top emitting devices have a typical threshold of 100 -110  $\mu\text{A}$  with a differential efficiency of 18-20%.

Using the same epitaxial structure from the same wafer our bottom emitting devices achieved a performance similar to the top emitting structures. They have a threshold of 110 - 120  $\mu\text{A}$  with a differential slope efficiency of 17 -18%.

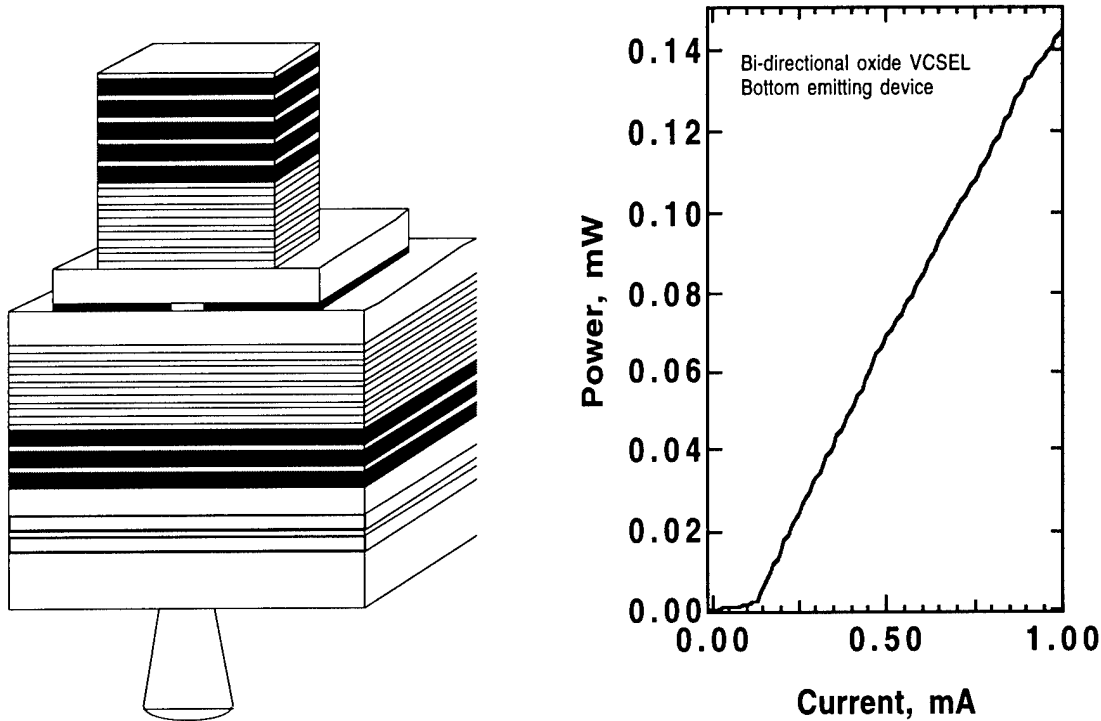


**Fig. 2** Bottom emitting device cross section, and performance results.

The similarity in performance between the top and bottom emitting structures validates the design concept and portends the monolithic integration of these devices with detectors and electronics into photonic repeater smart pixels.

1. Dallesasse, J. M., Holonyak, N. Jr., Sugg, A.R., Richard, T. A., and El-Zein, N.: "Hydrolyzation oxidation of  $\text{Al}_x\text{Ga}_{1-x}\text{As-AlAs-GaAs}$  quantum well heterostructures and superlattices", *Appl. Phys. Lett.*, 1990, **57**, (26), pp. 2844-2846
2. Huffaker, D.L., Deppe, D. G., and Kumar, K.: "Native-oxide defined ring contact for low threshold vertical-cavity lasers", *Appl. Phys. Lett.*, 1994, **65**, (1), pp. 97-99
3. MacDougall, M. H., Zhao, H., Dapkus, P. D., Ziari, M., and Steir, W. H.: "Wide-bandwidth distributed Bragg reflectors using oxide/GaAs multilayers," *Electron. Lett.*, 1994, **30**, pp.1147-1149
4. Yang, G. M., MacDougall, M. H., Dapkus, P. D.: "Ultralow threshold current vertical-cavity surface-emitting lasers obtained with selective oxidation," *Electron. Lett.*, 1995, **31**, pp. 886-888

# First demonstration of highly TM reflective and highly polarisation selective diffraction gratings (GIRO-gratings) for long wavelength VCSELs

S. Goeman, S. Boons, B. Dhoedt, K. Vandeputte, K. Caekebeke, R. Baets, P. Van Daele

## Abstract

We present experimental results on surface relief gratings in GaAs and InP with high reflectivity (>85%) and polarisation selectivity to normal incidence. The potential for polarisation stabilisation with a reduced mirror complexity for long wavelength VCSELs is discussed.

## 1. Introduction

Although short wavelength VCSELs (850 and 980 nm) are commercially available, these devices still show unstable output polarisation and transversal multimode behaviour. Several solutions have already been proposed to overcome these problems. Using AIAs oxidation in the top DBR mirror offers beside current confinement an improvement of transverse monomodal operation[1].

Concerning the polarisation problem, rectangular[2] or elliptical[3] etched post structures or growth on (311) substrates[4] have been proposed. This causes anisotropy of the gain, leading to pinning of the polarisation. Als surface relief gratings have been proposed to solve the polarisation stability problem[5][6]. In this paper we propose a structure not only showing polarisation selectivity but also a high reflectivity for TM polarisation. This property is of specific interest to long wavelength VCSELs in view of the low refractive index contrast in these devices leading to rather complex mirror structures (wafer fusion[7], metamorphic growth[8]) and associated electrical and thermal problems. Using the approach presented, it is possible to stabilise the polarisation and to decrease the number of DBR pairs of the top VCSEL mirror, possibly leading to a smaller electrical and thermal resistance. In section 2 we will shortly discuss the design and fabrication while section 3 shows experimental results of GaAs and InP based GIRO-gratings (GIant Reflectivity to 0 order). Section 4 presents calculations showing that the fabricated GIRO-gratings on top of a reduced DBR stack will lead to complete polarisation control and a reduced electrical and thermal resistance.

## 2. Design and fabrication

As shown in [9], semiconductor-air gratings can be designed to offer high polarisation selectivity and high TM reflectivity upon normal incidence from the semiconductor side. As proof of principle we have first fabricated these gratings for operation with a tuneable CO<sub>2</sub>-laser (9-11 $\mu$ m)[10]. In the present paper we will report on experimental results of GaAs and InP based GIRO-gratings for the wavelength region of 1.55  $\mu$ m. Fig.1-2 show theoretical results for the TM and TE reflectivity of a GaAs grating over a large period and depth range. These results show a large region of high TM reflectivity (>90%) while the TE reflectivity is low (<20%). In view of this large area it is feasible to fabricate highly TM reflective and highly polarisation selective gratings. GaAs and InP based GIRO-gratings have been fabricated based and the grating parameters are summarised in table 1.


Material	GaAs	InP
	$\Lambda = 900 \text{ nm}$	$\Lambda = 880 \text{ nm}$
	$d = 500 \text{ nm}$	$d = 525 \text{ nm}$
	$\eta = 50\%$	$\eta = 50\%$

Table 1: GIRO-grating parameters

These gratings were fabricated using holographic exposure and Ti evaporation, to produce the etch mask, and subsequent reactive ion etching. Since we have to measure the grating reflectivity from the substrate side, the samples were polished under a wedge angle (3 deg). This allows to measure the reflectivity of the polished interface and the grating interface, as seen from substrate side, separately. By comparing these two measurements it is possible to extract the reflectivity of the grating structure.

## 3. Experimental results

Fig. 3 shows a SEM picture of an InP GIRO-grating. We see a well defined grating with vertical walls and a filling factor close to 50%. Fig.4 shows the measurement results (error bar of +/- 5%) and a comparison with theoretically calculated values. The calculations agree well with the measurements (almost within the measurement error) and the grating parameters used in the calculations agree well with the SEM parameters

(table 2). This grating shows a maximum TM reflectivity of 85% for  $\lambda=1550$  nm and polarisation selectivity of more than 60% over the entire wavelength region. Fig.5 gives the measurement results and a comparison with theory for the GaAs GIRO grating. The polarisation selectivity of this grating is more than 50% over the whole wavelength region and the maximum TM reflectivity is 85% for  $\lambda=1490$  nm. As for the InP grating, the calculations agree well with the measurement (within the measurement error) and the grating parameters used in the calculations agree well with the SEM parameters (table.2).

	SEM parameters	fitted parameters
GaAs GIRO-grating	period = 900 nm depth = 450-480nm filling factor 40-45%	period= 900 nm depth = 465 nm filling factor 45%
InP GIRO-grating	period = 880 nm depth = 580-600 nm filling factor 50%	period = 880 nm depth= 580 nm filling factor 50%

Table 2: SEM parameters and fitted parameters for the GaAs and InP GIRO-grating

#### 4. GIRO-grating in combination with DBR stack

In this section we examine the performance of a GIRO grating on top of a DBR stack in comparison with a pure DBR mirror. Since the GIRO grating has an intrinsically high TM reflectivity, we can reduce the number of DBR pairs needed to obtain a highly reflective mirror. Since the underlying DBR stack will decrease the polarisation selectivity we want to find out what the remaining polarisation selectivity would be. For this purpose we use the fitted parameters of the InP grating of section 3. Fig.6 shows the comparison of a pure InGaAsP( $n=3.46$ )/InP( $n=3.17$ ) DBR of 34.5 periods and a combination of an InP GIRO-grating on top of a 20 period InGaAsP/InP DBR stack. As the calculations show, the maximum reflectivity of the pure DBR and the TM reflectivity of GIRO/DBR combination are comparable (i.e. 99.7%). The maximum TE reflectivity of the GIRO/DBR combination is only 96.2 %. The polarisation selectivity of the GIRO/DBR is still larger than 3% which should be more than enough to obtain complete polarisation control. In addition, the total mirror thickness is reduced roughly by 1/3. This will influence the electrical and thermal resistance of InP based VCSEL mirrors. Further calculations show that with more optimised gratings it should be possible to obtain a larger polarisation selectivity for the GIRO/DBR combination (i.e. in the order of 10%) while the number of DBR pairs could further be reduced to half the thickness of a pure DBR stack.

#### 5. Conclusion

In this paper we have described the design, fabrication and experimental results of highly polarisation selective and highly TM reflective gratings in GaAs and InP. Good agreement between experimental results and theory was found. Furthermore we have indicated the potential of these gratings for long wavelength VCSELs: in combination with a DBR stack, these gratings would lead to a reduced number of DBR pairs and a remaining polarisation selectivity of more than 3%.

#### Acknowledgement

This work is partly funded by the European ACTS024-VERTICAL project and the Belgian DWTC-project IUAP-13. S. Goeman and B. Dhoedt also acknowledge financial support of the Flemish IWT.

#### Reference

- [1] K.L. Lear et al, Electr. Lettr. Vol. 31 No. 3, p209, 1995
- [2] T. Yoshikawa et al, Appl. Phys. Lettr. 66(8), 20 Feb 1995
- [3] T. Mukaihara et al, Phot. Tech. Lettr. Vol.5 no.2, Febr 1993
- [4] M. Takahashi et al, J. of Selec. Topics in Quant. Electr. ,Vol. 3 No. 2 April 1997
- [5] T. Mukaihara et al, IEEE ISCL 94
- [6] J.H. Ser et al, Appl. Phys. Lettr. 66(21), May 1995
- [7] D.I. Babic et al, Quantum Electronics, Vol. 28, p 475, 1996
- [8] H. Gebretsadik et al, IEEE LEOS '97, San Francisco, paper TuU3
- [9] B. Dhoedt et al, Diffr Optics and Micro-Optics '96, post-deadline paper, J Tu B30
- [10] S. Goeman et al, IEEE LEOS '97, San Francisco, paper MA5



Fig.1 TM reflectivity GaAs GIRO grating, filling factor 50 %. Black region: TM reflectivity > 90%

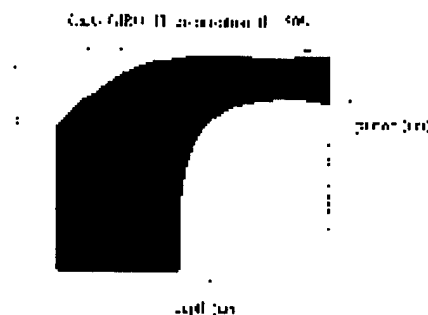


Fig.2: TE reflectivity GaAs GIRO grating, ff=50%. Black region: TE reflectivity < 20%

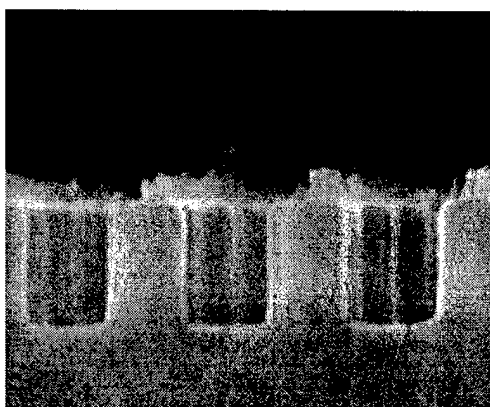


Fig.3: SEM picture of an InP GIRO grating

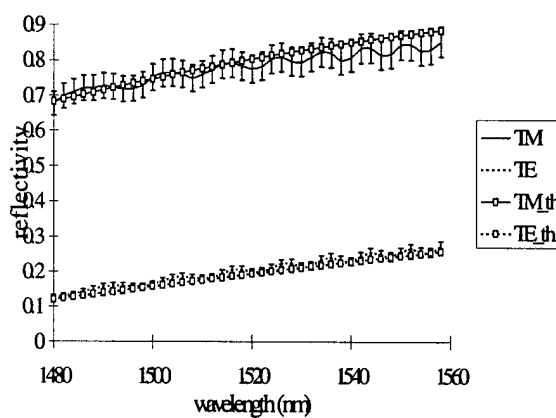


Fig.4: TM and TE reflectivity of InP GIRO grating and comparison with theory for the wavelengths of 1480 to 1560 nm

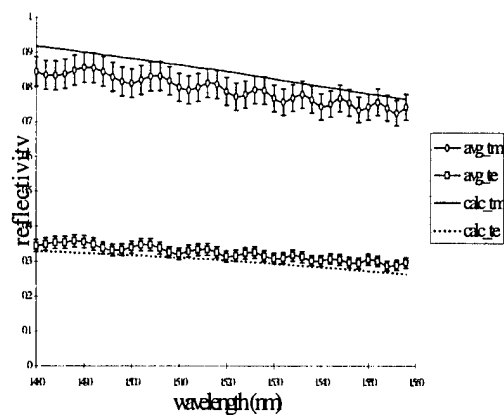


Fig.5: TM and TE reflectivity of GaAs GIRO grating and comparison with theory for the wavelengths of 1480 to 1560 nm

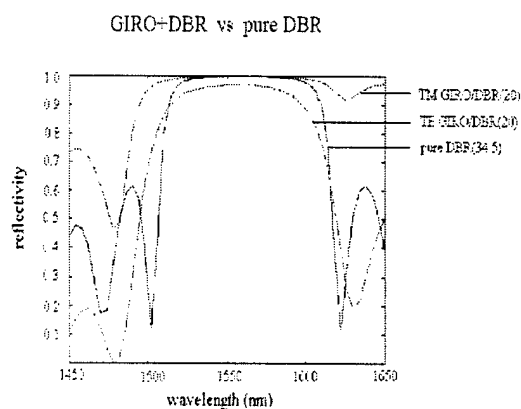


Fig.6: Comparison of the reflectivity of a pure DBR (34.5 periods) and the combination GIRO/DBR (20 periods). Theoretical calculations

# Compact semiconductor lasers with photonic microstructure mirrors and oxide apertures

Thomas F. Krauss<sup>a,b</sup>, Axel Scherer<sup>a</sup>, John S. Roberts<sup>c</sup> and Richard M. De La Rue<sup>b,d</sup>

<sup>a</sup> California Institute of Technology, MS 200-36, Pasadena, CA 91125, USA.

<sup>b</sup> Permanent address: Optoelectronics Research Group, Department of Electronics and Electrical Engineering, University of Glasgow, Glasgow G12 8QQ, Scotland, U.K.  
E-mail: t.krauss@elec.gla.ac.uk Tel.: +44 141 330 5220 Fax: +44 141 330 6002

<sup>c</sup> Department of Electronics and Electrical Engineering, Sheffield University, Sheffield S1 3JD, England, U.K.

<sup>d</sup> Communications Research Lab, Nukuikitamachi 4-2-1, Koganei, Tokyo 184, Japan

## 1. Introduction

Following the demonstration of DBR lasers with very high reflectivities from deeply etched, 1-D, third order Bragg reflector waveguide mirrors [1], we have achieved a further milestone towards the realisation of ultracompact, integrated, light emitting devices by also using selective oxidation in the GaAs/AlGaAs system. 90  $\mu\text{m}$  long AlGaAs/GaAs laser devices that use a cavity formed by one microstructured 6-period mirror and a single dry-etched output facet have been realised. The best threshold current we achieved was 13 mA, using a GaAs/InGaAs active layer with 3 quantum wells. We expect a substantial further improvement of this value by using shorter cavities, narrower oxide apertures and microstructured mirrors on both sides, following this demonstration of technological feasibility.

The combination of selective oxidation in the GaAs/AlGaAs system [2,3] and microstructuring of the semiconductor material [1,4-7] offers a wealth of opportunities to the design of novel light emitting devices; *microstructuring* the semiconductor host into a 'photonic lattice' or 'photonic crystal' allows the control of the light emission and propagation processes inside the material [4]; *selective oxidation* provides a means of restricting or channeling the flow of carriers and can be used to achieve further optical confinement. By carefully designing the epitaxial material and the processing sequence, a powerful combination of both concepts is achieved.

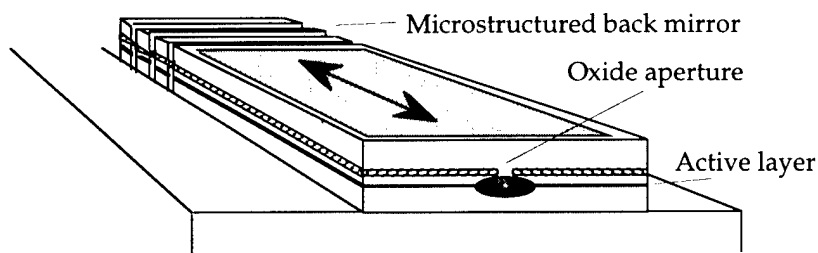


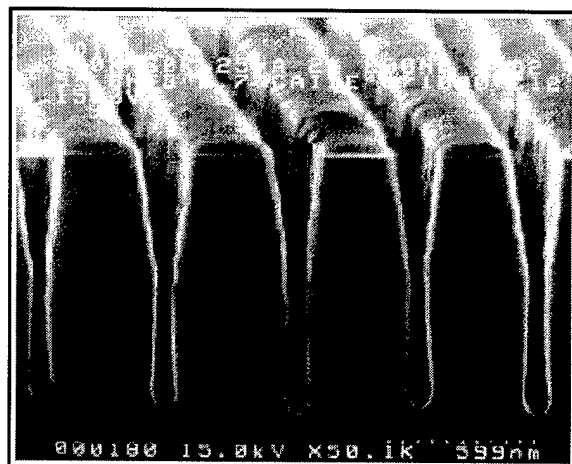
**Figure 1** Sketch of the laser cavity using a deeply etched microstructure to form the back mirror and a simple etched facet at the front. The oxide aperture is indicated at the front facet.

## 2. Design considerations

The epitaxial laser structure was grown by MOCVD and is very similar to the material used in previous experiments [1]. It contains 3 InGaAs quantum wells (18% In) placed 0.5  $\mu\text{m}$  below the top surface of the material. A 100 nm thick layer of 76% AlGaAs, is placed 120 nm above the quantum wells to form the oxide aperture. Despite this thin top cladding, we found a very low threshold current density of around 200 A/cm<sup>2</sup> for infinitely long broad area lasers. The main reasons for using a thin cladding are the fabrication limitations imposed by the microstructured mirrors; as discussed previously [6,7], we have demonstrated that the best design for a deeply-etched waveguide-based Bragg mirror consists of a lattice with a relatively large semiconductor/air ratio, ie. with a low air-filling factor. A broadband high reflectivity mirror can be achieved so long as the (third-order) periodicity corresponds closely enough to the target wavelength [6,7]. Making lattices with a low air fill-factor means etching very narrow features into the semiconductor. This is technologically difficult and limited, in practise, to an etch depth of about 1  $\mu\text{m}$ ,

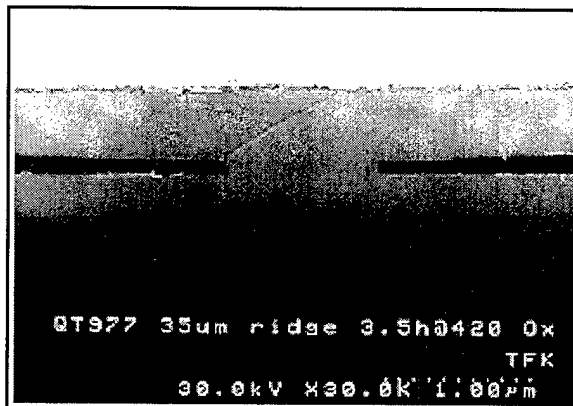
emphasizing the need for a thin top cladding layer. The cross-section of such a mirror is shown below. An additional advantage of the thin top cladding is that diffusion of the dopants is limited during epitaxial growth. Dopant diffusion has been shown [3] to cause current spreading underneath the oxide aperture, thereby extending the effective width of the laser filament.

**Figure 2** Cross-section of a microstructured Bragg mirror. The etch depth is  $1\ \mu\text{m}$ , the period is  $500\ \text{nm}$  and the etched slots are  $60\text{--}100\ \text{nm}$  wide. The active layer is placed  $0.5\ \mu\text{m}$  below the surface. The fabrication sequence for the mirror is as follows: First, narrow lines are written into electron-beam resist (PMMA, 950k molecular weight,  $120\ \text{nm}$  thick) using a converted ISI scanning electron microscope at  $30\ \text{kV}$ . The pattern is then transferred into a  $200\ \text{nm}$  thick  $\text{SiO}_2$  mask by Reactive Ion Etching (RIE) with  $\text{CHF}_3$ . Finally, the semiconductor is etched by Chemically Assisted Ion Beam Etching (CAIBE), using a beam of Ar-ions accelerated to  $1500\ \text{V}$  and chlorine as the chemically reactive gas. From a threshold and efficiency analysis, we determined a reflectivity as high as  $95\ \%$  for this type of waveguide mirror [1].



The Al-fraction of around  $80\%$  that we chose for the oxidation layer was motivated by the need to control the oxidation process; as is well known, the oxidation rate of  $\text{Al}_x\text{Ga}_{1-x}\text{As}$  increases exponentially with the aluminium fraction  $x$  [8], so a lower value for  $x$  results in a longer, more easily controlled oxidation time. Typically, we observed a rate of  $5\ \mu\text{m}/\text{h}$  at a temperature of  $420^\circ\text{C}$ . Figure 2 shows a very promising result achieved with a testpiece, where an aperture-width of  $1\ \mu\text{m}$  was obtained. Whether or not apertures of this size can be reproducibly made on a device level remains to be seen, although there are indications that good uniformity can be achieved indeed [2]. By using two high-reflectivity mirrors, for example, the device length can certainly be shrunk to well below  $50\ \mu\text{m}$ , reducing the length over which aperture uniformity is required.

**Figure 3** Oxide apertures of  $1\ \mu\text{m}$  width have been achieved with a testpiece of our laser material, which demonstrates the possibility of making very narrow laser stripes. The oxidation conditions were  $3.5\ \text{h}$  at  $420^\circ\text{C}$  with a flow of nitrogen bubbling through water heated to  $95^\circ\text{C}$ .



### 3. Fabrication and Results

The order of the processing sequence is critically important. We found, for example, that the device surface is very sensitive to damage before oxidation, i.e. even the GaAs top contact layer oxidised in the steam environment when it had been subjected to ion bombardment beforehand. Ion bombardment occurs during the fabrication of the microstructured mirrors (Fig. 2), so they had to be made last. We started the fabrication process by wet-etching ( $\text{H}_2\text{SO}_4:\text{H}_2\text{O}_2:\text{H}_2\text{O}$ ,  $4:1:50$ ,  $100\ \text{nm}/\text{min}$  at  $5^\circ\text{C}$ )  $0.7\ \mu\text{m}$  deep grooves to define the lateral extent of the cavity and to expose the high Al-content layer for the subsequent oxidation process. The devices were oxidised for  $1.5\ \text{h}$  at  $420^\circ\text{C}$ , which yielded  $8\ \mu\text{m}$  of native oxide on either side of an aperture width of  $11\ \mu\text{m}$ , with an initial mesa width of  $27\ \mu\text{m}$ . Next, the top contacts (Ni/Au,  $20\ \text{nm}/100\ \text{nm}$ ) were defined by lift-off, followed by the fabrication of the microstructured mirror (Fig. 2). Finally, a standard n-type contact (AuGe/Ni) was deposited on the back of the sample. Devices were tested cw on an HP 4145 parameter analyser using a silicon photodiode and the result for a  $92\ \mu\text{m}$  long device is shown in figure 4.

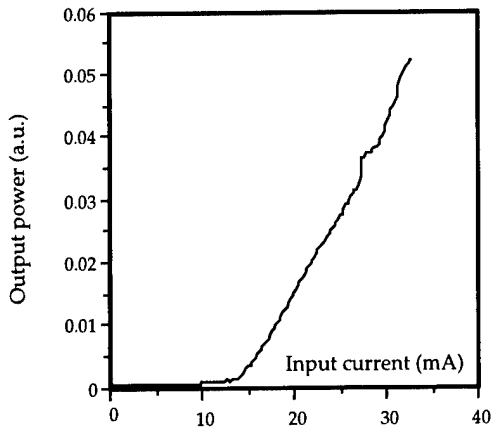


**Figure 4** Light-current (L-I) curve, measured cw, of an oxide-aperture laser with one microstructured and one simple etched facet. The device length is  $92\ \mu\text{m}$  and the width of the pumped aperture is  $11\ \mu\text{m}$ .

#### 4. Conclusion

The key result we derive from this work is that photonic microstructures can be used in conjunction with the selective "steam" oxidation of high Al-fraction AlGaAs, when process compatibility is properly taken into account. The successful operation of a semiconductor laser that uses both techniques opens the door to many other types of compact light sources and photonic crystal - based devices. For example, using high-selectivity mirrors on both facets and shrinking the device - size will allow edge-emitting lasers with an active area on the order of  $10\text{-}20\ \mu\text{m}^2$ , similar to the size of VCSEL's that have shown thresholds below  $100\ \mu\text{A}$  [3]. Such compact waveguide lasers will be essential in high packing density photonic microcircuits and may be combined with other functional devices via photonic crystal - based waveguides and bends [9]. Alternatively, by using clever design and graded layers of AlGaAs, the direction of the oxidation-front can be controlled, leading to the realisation of electrically pumped devices embedded into truly three-dimensional active semiconductor photonic crystals [10] that control most or all of the spontaneous emission generated inside [4].

This work was supported, in part, by the EPSRC of the UK under the microstructured photonic materials (MPM) programme, and by the Army Research Office of the U.S. through DARPA. TFK gratefully acknowledges support by the Royal Society of the UK. We also wish to thank Reginald Lee for invaluable help with the measurements.

#### 5. References

1. T.F. Krauss, O. Painter, A. Scherer, J.S. Roberts and R. M. De La Rue, "Photonic microstructures as laser mirrors", accepted for publication in *Optical Engineering*, April 1998.
2. Y. Cheng, P.D. Dapkus, M.H. MacDougall and G.M. Yang, "Lasing characteristics of high-performance narrow-stripe InGaAs-GaAs quantum-well lasers confined by AlAs native oxide", *IEEE Phot.Tech.Lett.* 8 (2), pp.176-178, 1996.
3. G.M. Yang, M.H. MacDougall and P.D. Dapkus, "Effects of current spreading under oxide current aperture in vertical-cavity surface-emitting lasers", *J.Appl.Phys.* 80 (9), pp.4837-4840, 1996.
4. E. Yablonovitch, "Inhibited spontaneous emission in solid state physics and electronics", *Phys. Rev. Lett.*, 58, pp. 2059-2063, 1987.
5. T. Baba, M. Hamasaki, N. Watanabe, P. Kaewplung, A. Matsutani, T. Mukaiharu, F. Koyama, and K. Iga, "A novel short-cavity laser with deep-grating distributed bragg reflectors", *Jap.J. of Appl. Phys. Pt. 1* 35 (2B), pp. 1390-1394, 1996.
6. T.F. Krauss and R.M. De La Rue, "Optical characterisation of waveguide based photonic microstructures", *Appl. Phys. Lett.* 68 (12), pp. 1613-1615, 1996.
7. T.F. Krauss, B.Voegele, C.R. Stanley, and R.M. De La Rue, "Waveguide microcavity based on photonic microstructures", *IEEE Phot.Tech.Lett.* 9 (2), pp. 176-178, 1997.
8. J.-H. Kim, D.H. Lim, K.S.Kim, G.M.Yang, K.Y.Lim and H.J.Lee, "Lateral wet oxidation of  $\text{Al}_x\text{Ga}_{1-x}\text{As}$ -GaAs depending on its structures", *Appl. Phys. Lett.*, 69 (22), pp.3357-3359, 1996.
9. A. Mekis, J.C. Chen, I. Kurland, S. Fan, P.R. Villeneuve and J.D. Joannopoulos, "High transmission through sharp bends in photonic crystal waveguides", *Phys. Rev. Lett.* 77 (18), pp.3787-3790, 1996.
10. R.M. De La Rue and T.F. Krauss, "Strategies for the fabrication of photonic microstructures in semiconductors", in 'Microcavities and Photonic Bandgaps: Physics and Applications' (J.G. Rarity and C. Weisbuch, eds.), pp.175-192, Kluwer, Dordrecht, 1996 (invited).

## **Simultaneous time-window gating and wavelength conversion using an injection locked Fabry-Perot laser diode**

L.Y.Chan, H. K. Tsang, S. P. Yam and C. Shu

Department of Electronic Engineering,  
The Chinese University of Hong Kong,  
Shatin, N.T.,  
Hong Kong.

Tel. No.: (852)2609-8252 , Fax. No.: (852)2603-5558, E-mail: lychan@ee.cuhk.edu.hk

Future optical broadband integrated service digital network (B-ISDN) and optical ATM networks require all-optical switching for demultiplexing high-speed time-division-multiplexed signals [1]. Recent works on all-optical demultiplexers employ nonlinear effects in either semiconductor optical amplifiers [2] or fiber loop mirrors [3], both of which require high optical power to achieve the desired nonlinear phase shift. In this paper, we use dual-wavelength injection-locking of a commercially available Fabry-Perot (FP) laser diode [4] to demultiplex a 1555.8nm signal in the time-domain and simultaneously perform wavelength conversion to 1562.4nm. This new scheme for time division demultiplexing has the advantage of operating with relatively low input optical powers.

The experimental set-up for the all-optical time-gating device is depicted in Fig.1. The FP laser diode, which acts as the demultiplexer, is a commercial one with a center wavelength of 1560nm. The cavity length is 1mm which gives a relatively small mode spacing ( $\sim 0.4$ nm), thus allowing easier longitudinal mode-matching with the input signals. The power from the cw operated FP laser was 1mW and the peak powers for the input 2GHz 1555.8nm pulse train and the 250MHz 1562.4nm gating signals were 2.1mW and 0.34mW respectively. It is necessary to adjust the polarization of the 1555.8nm signal to match the TE mode of the FP laser for efficient injection-locking. The 1555.8nm input and 1562.4nm gating signals were injection-locked to two longitudinal modes of the FP laser diode with side-mode suppression ratios (SMSR) of 30dB and 22dB respectively (as shown in Fig.2).

Fig.3 shows the temporal profiles of the input 2GHz signal (1555.8nm), and the input 250MHz gating signal (1562.4nm). The demultiplexed output was complemented and also underwent a wavelength translation to 1562.4nm.

In conclusion, a simple and low power all optical demultiplexer has been demonstrated using dual-wavelength injection locking of a FP laser diode. A wide-wavelength range of input signals can be demultiplexed by this method. Continuous tuning can be achieved for mode-matching of the injected signal by thermally control the FP laser diode. If wavelength translation or signal inversion is not desirable, the demultiplexer may be operated in cascade to re-invert the signal and shift the wavelength back to the original input wavelength.

### References

- [1] F. Masetti, J. M. Gabriagues, O. Guittard and J. B. Jacob, J. Lightwave Tech., **LT-13**, 2142 (1995).
- [2] R. Ludwig and G. Raybon, ECOC'93, Postdeadline paper ThP12.2 (1993).
- [3] T. Morioka, S. Kawanishi, K. Uchiyama, H. Takara and M. Saruwatari, Electron. Lett., **30**, 591(1994).
- [4] J. Horner and E. Patzak, IEEE J. Quantum. Electron., **QE-33**, 596(1997).

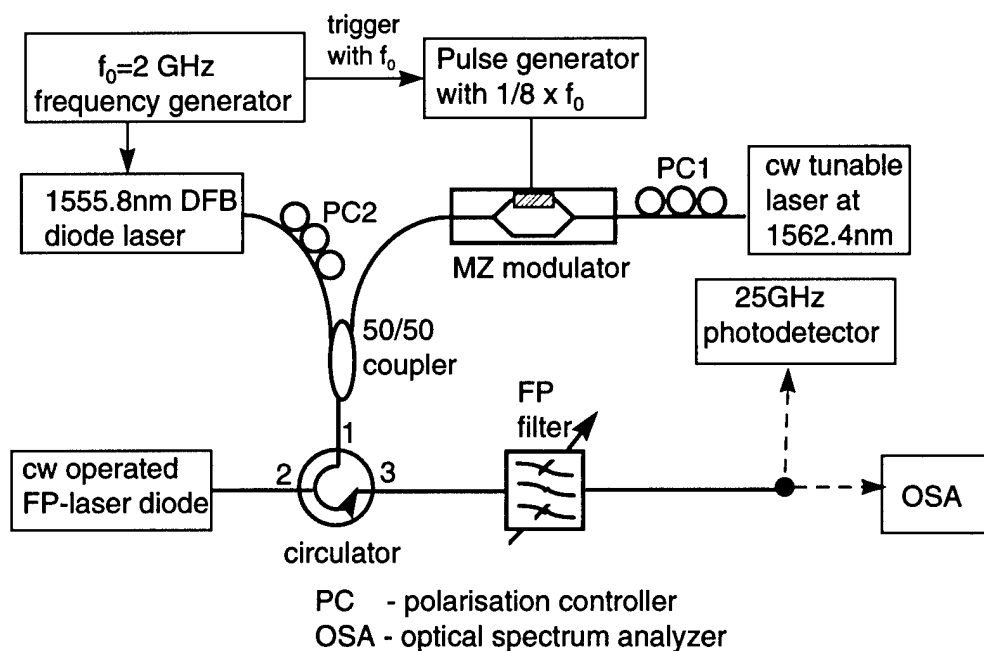


Fig.1 The experimental set up for the all-optical time-gating device by dual-wavelength injection locking of a FP laser diode.

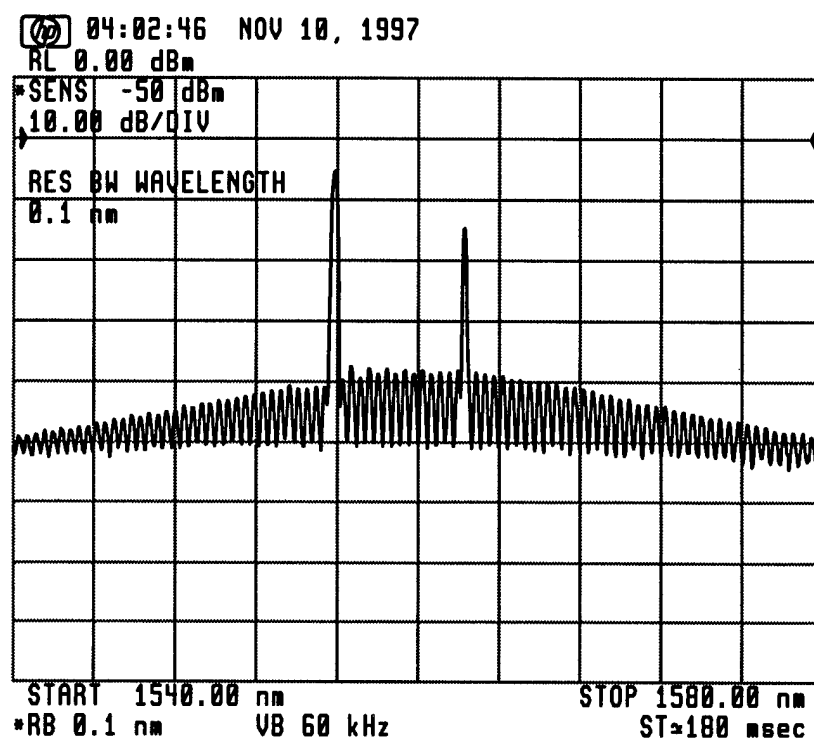


Fig.2 The spectrum of the dual-wavelength injection-locked FP laser diode, The 1555.8nm input pulse (left peak) and the demultiplexed 1562.4nm signal (right peak).

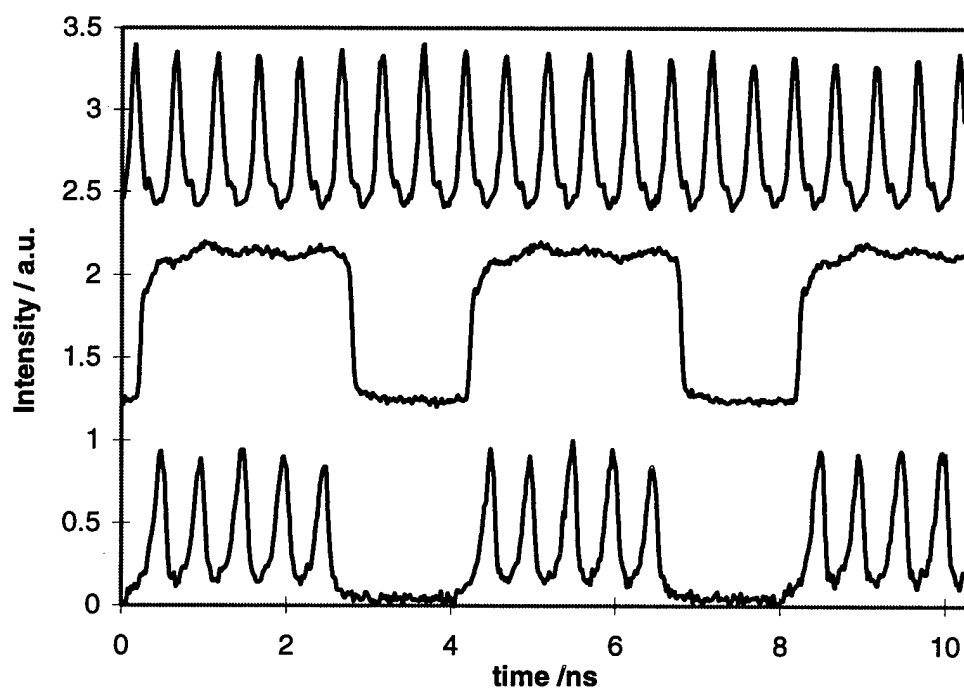


Fig.3 The temporal profiles for: (Top) The input 2GHz 1555.8nm injection- locked pulse train. (Middle) The input 250MHz time-gating signal in 1562.4nm. (Bottom) The output demultiplexed, inversely wavelength converted 1562.4nm signals after the FP filter.

## Semiconductor Integrated Devices for All-Optical Wavelength Conversion

S. J. B. Yoo

*Bellcore*

*331 Newman Springs Road, Red Bank, NJ 07701*

Wavelength conversion serves a number of important functions in Wavelength Division Multiplexing (WDM) networks including wavelength contention resolution and distribution of network control and management requirements. The role of wavelength conversion is expected to be more critical as the traffic load increases and as the traffic pattern becomes more dynamic. A large number of wavelength conversion mechanisms have been proposed and demonstrated to date [1]. Among these, semiconductor based wavelength converters exploit highly nonlinear optical responses and high degrees of integration capabilities to achieve excellent performances. This paper reviews and compares all-optical semiconductor integrated wavelength converters in light of WDM network applications.

There are countless issues to be considered in comparing wavelength conversion techniques. Table I lists some of the key comparison issues. These issues are grouped in three large categories: signal quality, configuration, and performance. *Signal quality* includes signal-to-noise ratio, chirp, amplitude distortion, and extinction ratio, and largely determines the bit-error-rate and the cascability of wavelength converters. *Configuration* is related to the actual implementation of the wavelength conversion in the wavelength-interchanging-cross-connect (WIXC) which is a network element that cross-connects nodes with wavelength conversion when needed. This configuration issue is closely linked to the mapping function of the wavelength converter and the resulting WIXC architecture. This category includes control requirements, dynamic ranges of input signals, polarization dependence, filtering requirements, and wall-plug power requirements. Lastly, the *performance* includes conversion efficiencies, conversion bandwidths, and bit-rate (or signal bandwidth) limits. In contrast to these comparison issues, all wavelength converters, regardless of what mechanism is used, must accurately register wavelengths.

Depending on the mapping functions and the form of control signals, wavelength converters can be classified into three categories: optoelectronic, optical gating, and wave-mixing wavelength converters. The optoelectronic wavelength converter executes a simple detection, amplification, and a re-transmission of the signal (O/E-E/O). The optical gating wavelength converter cross-modulates the probe wave according to the input signal wave, thereby transfers the information from input wavelength to the probe wavelength. According to the cross-modulation mechanism, this category is divided into two sub-categories: cross-amplitude modulation and cross-phase modulation. A large number of wavelength conversion mechanisms lie in this category. Cross-gain modulation in semiconductor amplifiers (SOA), saturable absorption in semiconductor waveguides, and cross-phase modulation in SOA, a *T*-gate lasers are a several examples of many optical gating wavelength converters. Lastly, wave-mixing wavelength converters achieve wavelength conversion via nonlinear optical mixing of a pump wave and a signal wave. The generated wave has an optical frequency that is a linear combination of the frequencies of the pump and the signal waves. This category includes four-wave-mixing (FWM) and difference-frequency-generation (DFG), and this is the only category of wavelength converters that offers strict transparency.

Following the categories described above, one can look into comparison issues that are common to each category. Optical gating and wave-mixing wavelength converters are considered

all-optical wavelength converters in that signal modulation information does not propagate in the form of an electrical signal anywhere in the wavelength converter. The wave-mixing wavelength conversion is the only category that offers strict-transparency. Optoelectronic and optical-gating wavelength converters offer limited-transparency, at best digital transparency up to a bit-rate determined by the speed of the electronics or the cross-modulation mechanism. The wave-mixing wavelength conversion is a variable-input-variable-output wavelength converter capable of simultaneously converting multiple channels[2]. Optoelectronic and optical-gating wavelength converters are variable-input-fixed-output wavelength converters without a multi-channel conversion capability.

TABLE I. Wavelength Converter Comparison Issues

	COMPARISON ISSUES	COMMON ISSUE
signal quality	s/n ratio chirp amplitude distortion extinction ratio	wavelength registration
configuration	WIXC architecture control and stability polarization dependence optical filtering dynamic range of input signal wall-plug power requirement	
performance	conversion efficiency conversion bandwidth bit-rate-limit and dependence transparency	

Semiconductor based all-optical gating wavelength conversion mechanisms include saturable absorption in diode lasers [3,4,5], cross-gain modulation in SOAs [6,7,8], cross-gain modulation in T-gate lasers [9], and cross-phase-modulation in SOAs utilized in Mach-Zehnder or Michelson interferometer configurations [10,11,12]. The bit-rates for these wavelength converters are typically limited to  $\sim 1$  Gb/s by the carrier life time [13], however, in case of SOAs and Lasers, bit-rates of  $\sim 10$  Gb/s and even 40 Gb/s have been demonstrated by exploiting the shortened carrier lifetime due to a stimulated emission processes [14,15,16]

Semiconductor based all-optical wave-mixing conversion mechanisms include FWM in SOAs [17,18], in diode lasers, and in passive waveguides [19], and DFG in quasi-phasematched semiconductor waveguides. The fundamental difference between FWM and DFG process lies in the fact that FWM is a higher order effect than DFG and thus it generates additional cross-mixing terms. FWM in SOAs also shows steep wavelength dependent conversion efficiency since the finite carrier lifetime affects the spectral characteristics. DFG in AlGaAs showed multi-channel conversion of 2-channels, 8-channels, and 17-channels with no significant cross-talk or cross-mixing terms [20,21].

With the exception of DFG in semiconductor waveguides, all semiconductor wavelength converters show finite polarization dependent conversion efficiency unless a careful design is employed. Recent reports on SOA based XGM, XPM, and even FWM wavelength converters indicate polarization dependence below 1 dB.

Table II summarizes the comparison of semiconductor integrated wavelength converters.

TABLE II. Comparison of Various Wavelength Conversion Techniques

	Optoelectronic Conversion	Cross-gain-modulation in semiconductor amplifiers	Cross-phase-modulation in semiconductor amplifiers	Four-wave-mixing in semiconductor amplifiers	Difference-frequency-generation in semiconductor waveguides
signaling category	variable-input-fixed-output	variable-input-fixed-output	variable-input-fixed-output	variable-input-variable-output	variable-input-variable-output
transparency	limited	limited	limited	strict	strict
chirp parameter	$= \alpha$ transmitter	$\alpha > 1$	$ \alpha  < 1$	chirp reversal	chirp reversal
polarization sensitivity	insensitive	sensitive unless special	sensitive unless special	sensitive unless special	insensitive,
optical filtering	not needed	must filter input signal	not needed if counter-pro.	must filter pump & non-conj.	must filter input signal
conversion efficiency	17 dB for 10 Gb/s	8 dB for 10 Gb/s	-2 dB for 10 Gb/s	-7 dB	-4 dB
conversion bandwidth	extremely broad	$\sim 6$ THz	$\sim 6$ THz	$\sim 1$ THz	$\sim 30$ THz
bit-rate-limit	$\sim 10$ Gb/s (depends on electronics)	$\sim 2.5$ Gb/s, 10-40 Gb/s for high power	$\sim 2.5$ Gb/s, 10-40 Gb/s for high power	$\sim 1$ Tb/s (depends on detuning)	$> 10$ Tb/s
advantages	<ul style="list-style-type: none"> <li>• ready for deployment.</li> <li>• improves signal to noise ratio</li> </ul>	<ul style="list-style-type: none"> <li>• simple configuration</li> <li>• gain in conv. eff.</li> </ul>	<ul style="list-style-type: none"> <li>• reduces chirp</li> <li>• reduces distortion</li> </ul>	<ul style="list-style-type: none"> <li>• chirp reversal</li> <li>• transparent</li> </ul>	<ul style="list-style-type: none"> <li>• chirp reversal</li> <li>• transparent</li> <li>• no excess noise</li> <li>• broad bandwidth</li> </ul>
disadvantages	<ul style="list-style-type: none"> <li>• cost increase with bit-rate and number of elements</li> <li>• limited transparency</li> </ul>	<ul style="list-style-type: none"> <li>• high noise figure, distortion, and chirp.</li> <li>• limited transparency</li> </ul>	<ul style="list-style-type: none"> <li>• narrow dynamic range of input power</li> <li>• limited transparency</li> </ul>	<ul style="list-style-type: none"> <li>• large ASE noise</li> <li>• narrow conversion bandwidth</li> </ul>	<ul style="list-style-type: none"> <li>• phasematching has to be achieved by careful fabrication.</li> </ul>

## REFERENCES

1. S. J. B. Yoo, *J. of Lightwave Tech.*, **14**, 955, (1996)
2. S. J. B. Yoo, *Bellcore Internal Memorandum* (1991), also in *U. S. Patent 5,434,700* (1993).
3. H. Kawaguchi, et al, *Electron. Lett.*, **23**, 1088 (1987). **24**,
4. Hitoshi Kawaguchi, et al, *IEEE J. Quant. Electron.* **24**, 2153 (1988).
5. H. Nobuhara, K. Kondo, S. Yamakoshi, and K. Wakao, *Electron Lett.*, **25**, 1485 (1989).
6. Serge Dubovitsky, et al, *IEEE Photon. Tech. Lett.* **6**, 804 (1994)
7. Jay M. Wiesenfeld, et al, *IEEE Photon. Tech. Lett.* **5**, 1300 (1993).
8. B. Mikkelsen et al, *ECOC '93*, Paper ThP 12.6
9. Chih-Cheng Lu, et al, *IEEE Photon. Tech. Lett.* **8**, 52 (1996).
10. T. Durhuus, et al, *IEEE Photon. Tech. Lett.* **6**, 53 (1994)
11. F. Ratovelomanana, et al, *IEEE Photon. Tech. Lett.* **7**, 992 (1995)
12. X. Pan, et al, *IEEE Photon. Tech. Lett.* **7**, 995 (1995)
13. B. Glance, et al, *Electron. Lett.*, **28**, 1715 (1992).
14. J. M. Wiesenfeld, et al, *Electron. Lett.*, **30**, 720 (1994).
15. B. Mikkelsen, et al, *ECOC '93*, postdeadline paper, Thp 12.6 (1993)
16. S. L. Danielsen, et al, *OFC'96*, paper PD-12.
17. G. P. Agrawal, et al, *J. Opt. Soc. Am. B*, **5**, 147 (1988)
18. Jianhui Zhou, et al, *IEEE Photon. Tech. Lett.*, **6**, 984 (1994).
19. H. Q. Le et al, *IEEE Photon. Tech. Lett.* **4**, 878 (1992)
20. S. J. B. Yoo, et al, paper *OFC '95* PD-13.
21. S. J. B. Yoo, et al, *Appl. Phys. Lett.*, **68**, p. 2609, (1996).

**Integrated Photonics Research**

# Device Simuations II

**Wednesday, April 1, 1998**

**Anand Gopinath, University of Minnesota**  
Presider

**IWC**  
**10:30am–11:45am**  
Salon B

# Modeling of Normal and Backward Integrated Electroabsorption Modulator and Laser

A. Hsu, W. Fang, and S. L. Chuang

Department of Electrical and Computer Engineering  
University of Illinois at Urbana-Champaign  
1406 West Green Street  
Urbana, Illinois 61801

Integrated optoelectronic devices are critical components in optical communications systems due to enhanced performance and cost-efficient production. For example, the integrated electroabsorption modulator - laser (EML) is used in optical communications systems. Wavelength division multiplexed systems offer increased system capacity, and ideas for integrated wavelength-tunable laser sources have been investigated. Tanbun-Ek et al.<sup>1</sup> have recently proposed an integrated wavelength-tunable device which consists of a distributed-feedback (DFB) laser and an integrated modulator which serves as the wavelength-tuning section using the electroabsorption effect.

In this paper, we theoretically investigate and compare the two integrated devices described above, namely (1) the normal EML and (2) the integrated wavelength-tunable laser or backward EML. Both modelled devices consist of a DFB laser section which is 360  $\mu\text{m}$  long and a 260  $\mu\text{m}$  modulator section separated by an 80  $\mu\text{m}$  isolation section. The difference between these devices is that for the normal EML, the DFB facet is high-reflection (HR) coated and the modulator facet is anti-reflection (AR) coated while for the backward EML, the DFB facet is AR coated and the modulator facet is HR coated. With reverse voltage bias, the modulator of the EML attenuates the light from the AR facet. For the modulator of the WTL, a particular voltage bias will affect the effective phase of the HR side and induce spatial hole burning which will cause the lasing mode to change. Hence, the modulator section selects the lasing mode of the backward EML with an applied voltage bias.

We model the longitudinal optical fields in the integrated devices using the transfer matrix and coupled-mode theory. A more detailed description of this model is given elsewhere.<sup>2</sup> We derive a transfer matrix for the forward and backward propagating electric fields for each section. The fields propagating through the entire device is found by multiplying the transfer matrices of each section together. The amplified spontaneous emission (ASE) spectrum is modeled by including an infinitely thin current sheet as an equivalent spontaneous emission source. The photon density profile is obtained from the forward and backward propagating electric field envelopes at each position along the cavity. Dispersion effects are also included in the model.

Longitudinal spatial hole burning is taken into account in the theoretical model using a far-above threshold approximation. First we solve for the photon density profile. Then, we calculate new gain and carrier density profiles which are approximately the inverse of the photon density profile. Then we again solve for the photon density profile and continue this iterative process until we obtain a self-consistent solution. A change in carrier density induces a change in refractive index through the linewidth enhancement factor and can have a significant effect on the threshold gain condition.

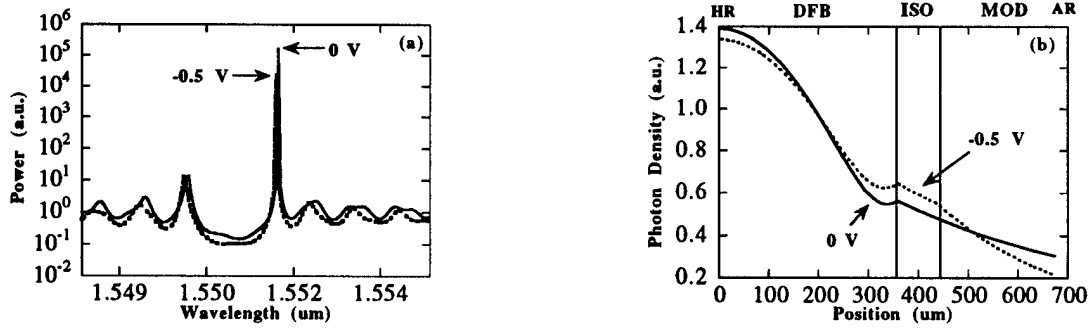


Figure 1: (a) Calculated spectrum of a normal EML at a modulator bias voltage of 0,-0.5 V. (b) Calculated photon density profile at a modulator bias voltage of 0,-0.5 V.

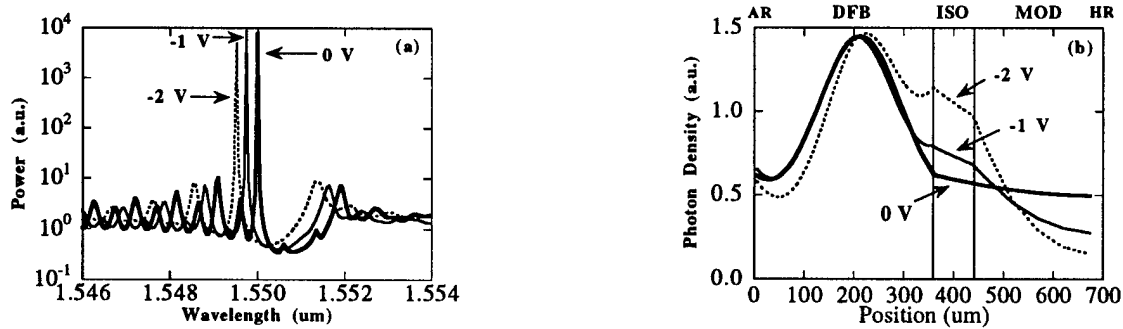


Figure 2: (a) Calculated spectrum of the backward EML at a modulator bias voltage of 0,-1,-2 V. (b) Calculated photon density profile at a modulator bias voltage of 0,-1,-2 V.

Using this model, we calculate the far-above threshold spectrum and longitudinal photon density profile for two integrated devices, the normal EML and the backward EML. For both devices, we used an HR reflectivity of 99%, an AR reflectivity of 1%, a grating pitch of 237.42 nm. Figure 1(a) shows the theoretical calculation for the spectrum far-above threshold as a function of modulator voltage bias in a normal EML. The voltage bias effect on the gain in the modulator is modelled by including an additive factor  $(dg/dV)V_{mod}$ , where  $dg/dV = 40 \text{ cm}^{-1}/\text{V}$  and is the increase in gain per unit voltage. A negative modulator voltage indicates absorption. As expected, a reverse bias voltage attenuates the modes of the spectrum. The photon density profile of the EML, shown in Fig. 1(b), illustrates the effect of the modulator voltage bias. Since the isolator and modulator sections are homogeneous, an analytic solution can be found for an effective reflection coefficient at the DFB-isolator interface. Physically, the reverse bias voltage increases the absorption in the modulator section which can be seen by the more rapidly decreasing photon density for the -0.5 V case. This increased absorption acts to increase the effective reflection coefficient at the DFB-isolator interface.

We then investigate the effects of a negative voltage bias applied at the modulator of a backward EML. For this case, the value of  $dg/dV$  used for the modulator is also  $40 \text{ cm}^{-1}/\text{V}$ . The calculated spectrum and photon density profile are shown in Fig. 2(a) and 2(b), respectively. The spectrum shows that the lasing mode changes with applied voltage. This is due to the modulator which changes the magnitude and phase of the effective reflection coefficient at the DFB-isolator interface. For the photon density profiles, the attenuation in the modulator and increased effective reflection coefficient are evident which is similar to the case for the normal EML. The difference between the two cases is that for the normal EML, the photon density is much greater at the DFB facet due to

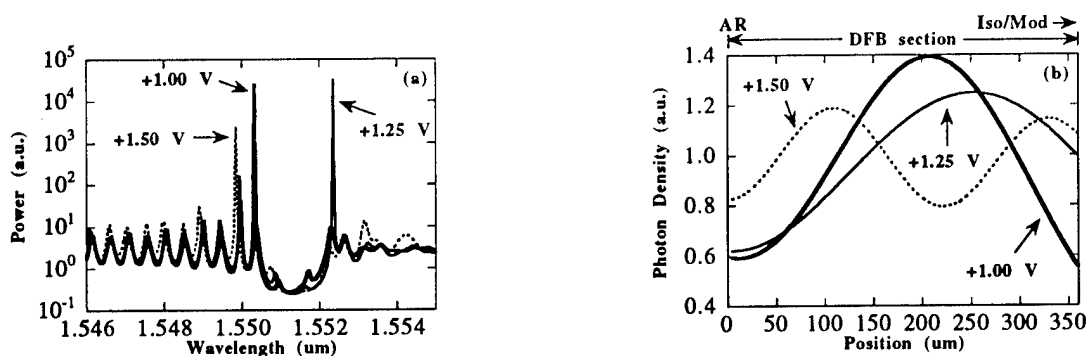


Figure 3: (a) Calculated spectrum of the backward EML at a modulator bias voltage of +1.00,+1.25,+1.50 V. (b) Calculated photon density profile at a modulator bias voltage of +1.00,+1.25,+1.50 V.

the enhanced optical feedback created by the HR coating and grating.

For positive bias voltages, the calculated spectrum and photon density profiles are shown in Fig. 3(a) and Fig. 3(b) respectively. The wavelength tuning here is markedly different from the previous negative bias voltage case. This produces spatial hole burning effects in the DFB laser cavity which perturbs the photon density profile from the  $V=+1.00\text{V}$  case to the  $V=+1.25\text{ V}$  case. This changes the threshold gain condition and a new lasing mode is selected. A further increase to  $V=+1.50\text{ V}$  forces the photon density profile into a new mode pattern which results in another shift in the wavelength of the lasing mode. This mode-selection behavior was observed in experimentally measured spectrum of an integrated wavelength-tunable laser.<sup>3</sup> In general, the wavelength tuning via spatial hole burning is a stronger mechanism than wavelength tuning via phase shifting.

In conclusion, the spectrum and photon density characteristics of an EML and an integrated wavelength-tunable laser have been investigated and compared. Accurate modeling of these effects in integrated devices can lead to a better understanding of physical mechanisms of these devices and provide optimization for future designs.

## REFERENCES

- [1] T. Tanbun-Ek, L. E. Adams, G. Nykolak, C. Bethea, R. People, A. M. Sergent, P. W. Wisk, P. F. Sciortino Jr., S. N. G. Chu, T. Fullowan, R. Pawelek, and W. T. Tsang, "Broadband Tunable Electroabsorption Modulated Laser for WDM Application," *IEEE J. Selected Topics Quantum Electron.*, Vol. 3, No. 3, pp. 960-967, 1997.
- [2] W. Fang, A. Hsu, S. L. Chuang, T. Tanbun-Ek, and A. M. Sergent, "Measurement and Modeling of Distributed-Feedback Lasers with Spatial Hole Burning," *IEEE J. Selected Topics Quantum Electron.*, Vol. 3, No. 2, pp. 547-554, 1997.
- [3] A. Hsu, W. Fang, and S. L. Chuang, "Integrated tunable laser with mode-selection modulator," *SPIE Photonics West 98*.

# Calculations of Highly Nondegenerate Four Wave Mixing Characteristics of $\lambda/4$ -Shifted DFB Lasers

Jacques W. D. CHI, K. Alan SHORE\* and Jean LE BIHAN

Ecole Nationale d'Ingénieurs de Brest, Laboratoire RESO  
Technopôle Brest-Iroise, C.P. 15, 29608 BREST Cedex, France

\* University of Wales, Bangor, School of Electronic Engineering and Computer Systems,  
Dean Street, Bangor, Gwynedd LL57 1UT, U.K.

Tel: +44 (0) 1248 382618 Fax: +44 (0) 1248 361429 e-mail: alan@sees.bangor.ac.uk

## 1. Introduction

It has been shown recently that highly nondegenerate four wave mixing (HNDFWM) can be used to achieve efficient THz-range frequency conversion in  $\lambda/4$ -shifted (QWS) distributed feedback lasers (DFB) [1], [2]. In comparison with the use of a travelling-wave optical amplifier (TWA) as the mixing medium [3], this approach has important advantages in terms of reductions of electrical current and amplified spontaneous emission (ASE) noise due to laser action, as well as system simplification arising from the self-generated, dynamical single mode (DSM) pump wave. All these attributes imply significant potential for the use of DFBs in system applications which exploit wavelength division multiplexing.

It is appreciated that DFB lasers behave approximately as a TWA for transmitted waves whose frequencies are located outside the DFB stopband, as is the case for HNDFWM with THz-range pump-probe detunings. Kuwatsuka et al. [2] have indeed used a TWA model to explain their experimental results. This theoretical approach is simple to use and gives analytical results in some cases [3] but fails to deal with waves whose frequencies are within or near the stopband, and, moreover, cannot study the DFB-reflected waves - which may have severe consequences on system performance. These problems can be resolved using a coupled-wave approach [1] which is used in this paper to study HNDFWM in medium-coupled ( $\kappa L \sim 1$ ) QWS-DFBs. Such lasers give a good compromise in terms of lasing threshold, gain level, and side-mode suppression ratio [4].

Calculations have been performed using device parameters typical of a DFB laser operating at a wavelength  $\lambda = 1.55 \mu\text{m}$ . It is noted that for small detunings ( $< 20 \text{GHz}$ ) injection locking and carrier depletion effects may become significant [5] but these are ignored in the present calculations and hence results at such small detunings are not considered here.

## 2. Results and discussion

The influence of pump power on HNDFWM efficiency for the case  $\kappa L = 1.1$  is shown in Fig. 1. Here it is assumed that the pump wavelength is at the gain peak thus giving rise to a symmetric response for positive and negative pump-probe detunings. In consequence only the results for positive detunings are illustrated. Experimentally observed asymmetry in HNDFWM efficiencies for positive and negative detuning are a consequence of the pump

wavelength being detuned from the gain peak [2]. As expected from the gain clamping effect, the probe transmission remains unchanged for different pump powers. Outside the DFB stopband the FWM-induced conjugate transmission increases  $\sim 6$  dB per pump power doubling. The dips appearing beyond 3.1 THz in these curves arise from the combined effects of the DFB gain and the FWM phase mismatch. These features cannot be explained by a simple TWA model. As can be seen in Fig. 1, the model shows excellent agreement with the experiment for detunings up to  $\sim 2$  THz. The divergence at higher detunings is a consequence of an assumed parabolic gain profile which leads to an under-estimate of the gain for longer wavelength [6].

Fig. 2 shows the influence of the coupling strength  $\kappa L$  on probe- and conjugate transmissions. As expected, smaller  $\kappa L$  value results in higher probe- and conjugate gains, since higher electrical excitation is then needed to sustain the same pump output. From Figs. 1 and 2, it is clear that there is a compromise between  $\kappa L$  value, pump power and conversion efficiency.

Investigations have also been undertaken of the DFB reflection effects for different pump powers and for different DFB coupling coefficients. It is found that higher gain or higher pump power results in a stronger conjugate reflection, while the reflected probe power is unchanged for different pump levels. These reflected powers are likely to be re-injected into transmission channels as deleterious noise. The consequences of such reflected signals must be carefully considered in practical applications.

### Acknowledgements

This study has been undertaken within the framework of the French-British Council ALLIANCE project, "Multi-contact Opto-electronic Tuning Structures (MOTS)". The work of KAS is also partially supported by the UK EPSRC under grant GR/L03262. The authors thank Dr H. Kuwatsuka of Fujitsu for supplying a copy of reference [2] prior to publication.

### References

- [1] J. Chi, K. A. Shore, and J. Le Bihan, "Highly non-degenerate four-wave mixing in uniform and  $\lambda/4$  shifted DFB lasers", IEEE J. Quantum Electron., **33**, November 1997
- [2] H. Kuwatsuka, H. Shoji, M. Matsuda, and H. Ishikawa, "Nondegenerate four-wave mixing in a long-cavity  $\lambda/4$ -shifted DFB laser using its lasing beam as pump beams", IEEE J. Quantum Electron., **33**, November 1997
- [3] A. Mecozzi, et al, "Four-wave mixing in traveling-wave semiconductor amplifiers", IEEE J. Quantum Electron., **31**, 689-699, 1995
- [4] H. Soda, et al, "Stability in single longitudinal mode operation in GaInAsP/InP phase-adjusted DFB Lasers", IEEE J. Quant. Electron., **23**, 804-814, 1987
- [5] W.M. Yee, and K.A. Shore, "Nearly degenerate fourwave mixing in laser diodes with non-uniform longitudinal gain distribution", J. Opt. Soc. America B, **11**, 1211-1218, 1994
- [6] J. Minch, et al, "Theory and experiment on the amplified spontaneous emission from distributed-feedback lasers", IEEE J. Quantum Electron., **33**, 815-823, 1997

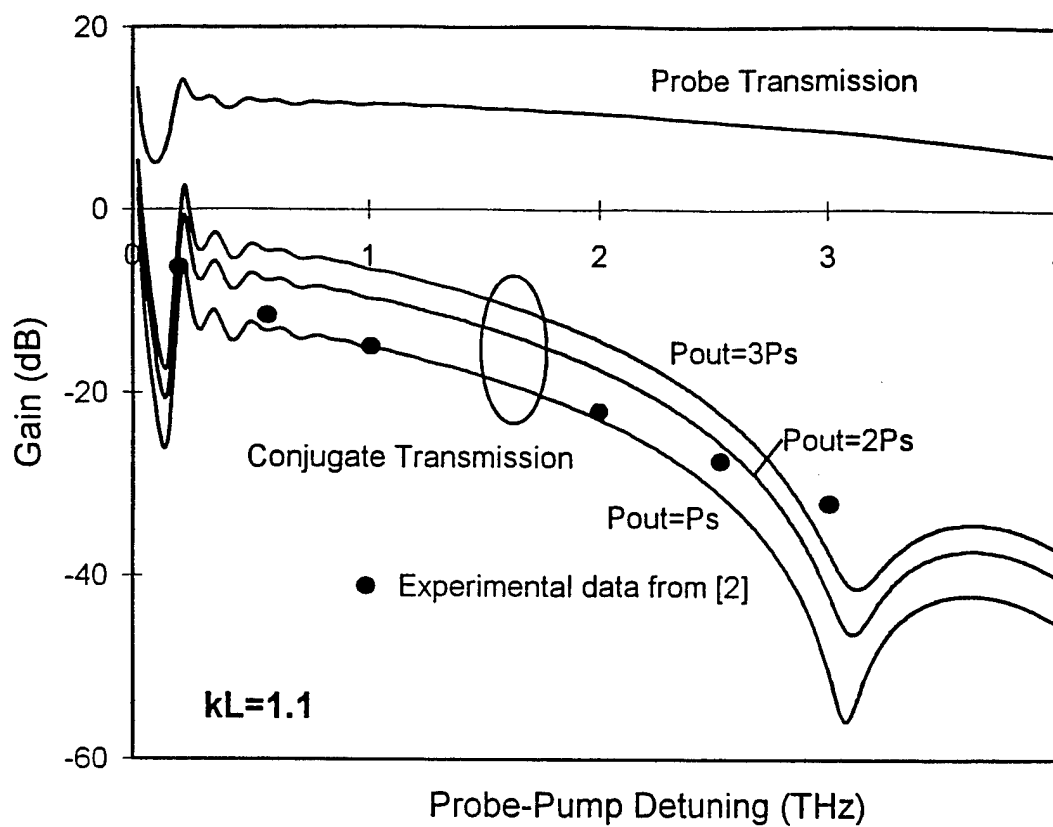
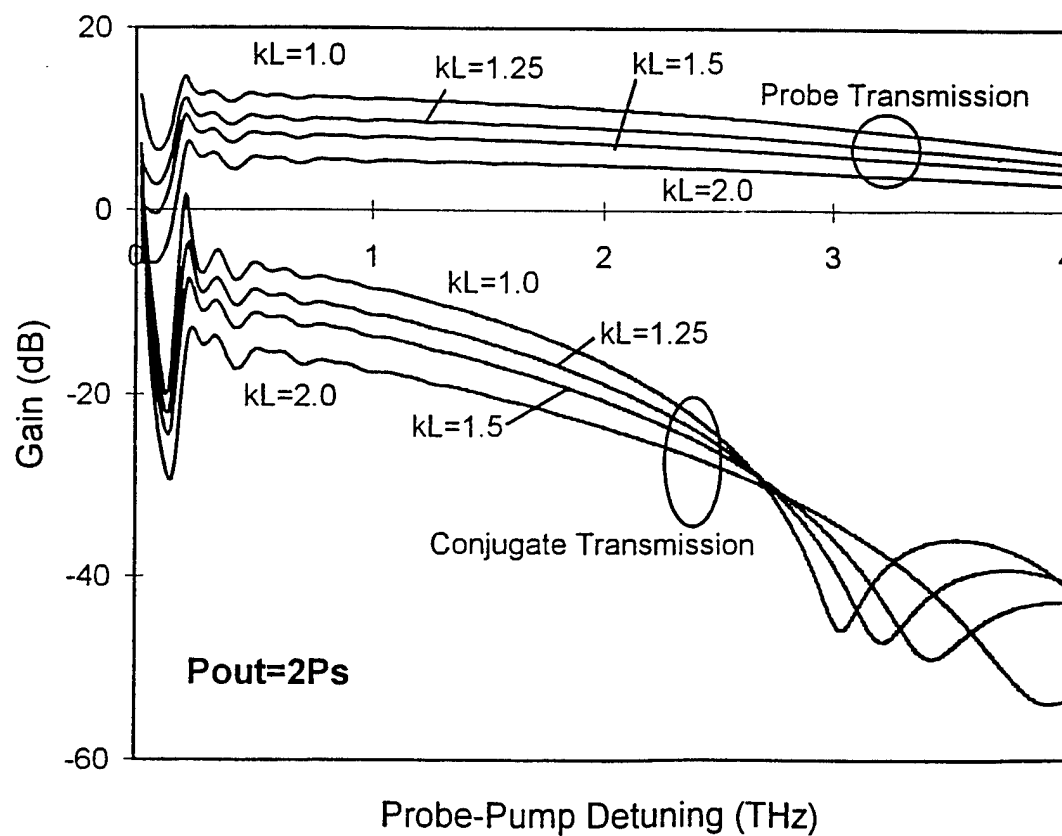


FIGURE 2



## Numerical Investigation of Leaky-Mode Coupling in VCSELs

G. Ronald Hadley  
 Sandia National Laboratories  
 Albuquerque, New Mexico 87185-5800  
 (505)844/4015  
 (505)844/8985 (FAX)  
 grhadle@sandia.gov

### SUMMARY

Recent advances in Vertical-Cavity Surface-Emitting Laser (VCSEL) technology that have led to higher efficiencies and lower thresholds have opened up a new realm of applications for these devices. In particular, phase-locked arrays of VCSELs<sup>1</sup>, previously thought to be impractical due to thermal considerations, now look extremely attractive as high-power and high-brightness sources. In addition, a new understanding of waveguiding in VCSELs<sup>2</sup> has led to practical methods for designing phase-locked arrays employing either evanescent or leaky-mode (antiguided) coupling. The latter type of coupling is particularly attractive in light of previous calculations<sup>1</sup> that predict especially strong mode discrimination against higher-order lateral modes. In this paper we report the first detailed simulation of leaky-mode coupling between two VCSEL pixels performed without the use of simplifying assumptions such as the effective index model. The results of this simulation are, however, found to be in good agreement with previously-developed simple theories<sup>3</sup> of leaky-mode coupling.

The structure chosen for examination consists of two 3- $\mu\text{m}$ -wide pixels in rectangular geometry (of infinite extent into the page) connected by a coupling region of varying width as shown in Fig. 1. The coupling region is assumed to be fabricated by etching prior to regrowing the upper mirror stack and may be of either higher or lower effective index than the pixel region (Fig. 1 shows a high-index, antiguided coupling region). Electrical and optical confinement at the outer edges is provided via a tapered oxide layer although this aspect of the device is inconsequential to the present study. The active region of the structure contains 5 quantum wells with spatial gain profiles that may be chosen arbitrarily. We calculate the in-phase and out-of-phase modes near threshold for this structure with the use of a fourth-order-accurate finite difference model<sup>4</sup> in an attempt to investigate the properties of both evanescent and leaky-mode coupling. The fundamental (in-phase) leaky mode for a coupling width of 0.75  $\mu\text{m}$  is shown in Fig. 2. This optimum width for in-phase operation was chosen using the effective index model and a simple formula developed previously to describe leaky-mode coupling in edge-emitting geometries<sup>3</sup>. The calculated mode discrimination against the out-of-phase mode was found to be

about 3 times the mirror loss. As the width was increased to  $1.1\text{ }\mu\text{m}$ , the threshold gain became equal for the two modes, again in agreement with simple theory<sup>3</sup>. *These calculations confirm the ability to engineer in-phase or out-of-phase operation for leaky-mode-coupled pixels by varying the coupling width and/or index step.*

Next, the strength of leaky-mode coupling in VCSELs was investigated by introducing a strong quantum well gain asymmetry between the two pixels and watching for changes in mode shape. Even for a gain imbalance of 100%, no discernable changes in mode shape were observed. This result implies that the coupling was sufficiently strong so that gain introduced into the right pixel was equally shared by the left pixel. This further implies that *leaky-mode-coupled arrays may be pumped peripherally without a significant degradation of the far-field pattern*. In contrast, a similar calculation was performed for two evanescently-coupled pixels with similar index step by merely reversing the direction of the etch shown in Fig. 1. The resulting in-phase amplitude profile is shown in Fig. 3 for the same case of 100% gain imbalance. As is seen, the un-pumped left pixel has diminished considerably in intensity because its mirror losses are not replenished efficiently by light coupled over from the right pixel.

In conclusion, these calculations confirm our previous understanding of leaky-mode coupling for the case of VCSELs fabricated using cavity length modulation to affect variations in effective index. The coupling strength has been shown to be high, and preference for the in-phase or out-of-phase mode may be engineered into the mask layout. As is the case for edge-emitters<sup>3</sup>, the resulting operation is expected to be insensitive to thermally-induced index changes because of the large magnitude of the index step. Numerous applications are envisioned for leaky-mode coupling in VCSELs, including optical logic gates and high-power high-brightness arrays.

1. G. Ronald Hadley, "Modes of a two-dimensional phase-locked array of vertical-cavity surface-emitting lasers, Opt. Lett. 15,1215(1990).
2. G. Ronald Hadley, "Effective index model for vertical-cavity surface-emitting lasers", Opt. Lett. 20,1483(1995).
3. G. Ronald Hadley, "Index-guided arrays with a large index step", Opt. Lett. 14,308(1989).
4. G. Ronald Hadley, "Low-truncation-error finite difference equations for photonics simulation II. Vertical-cavity surface-emitting lasers", to be published in the Journal of Lightwave Technology, January 1988.

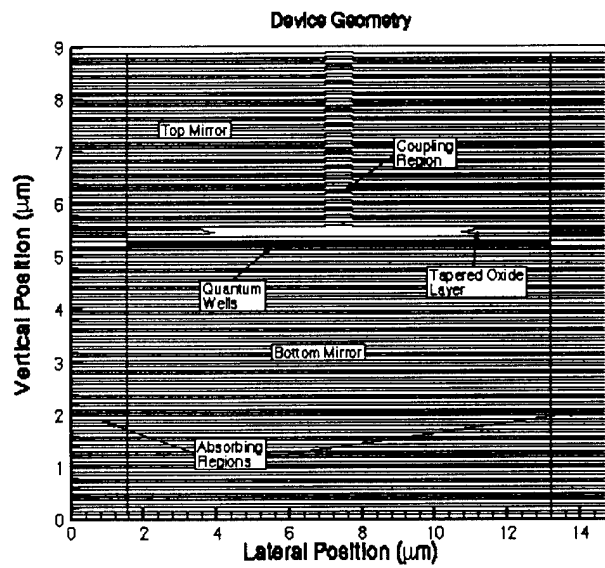


Figure 1. Device geometry for leaky-mode coupling

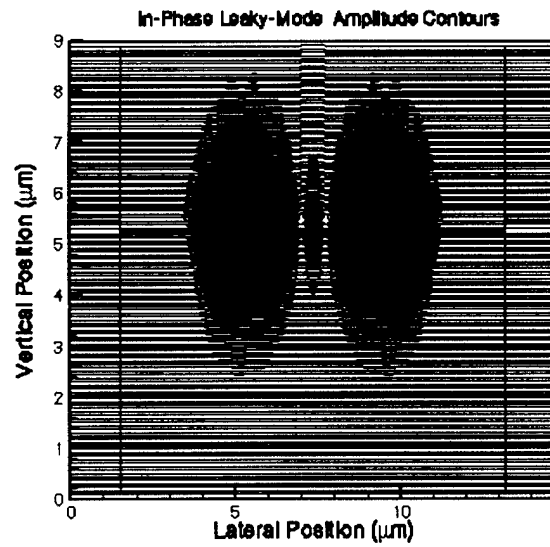


Figure 2. Amplitude contours for in-phase leaky mode at a coupling width of  $0.75 \mu\text{m}$

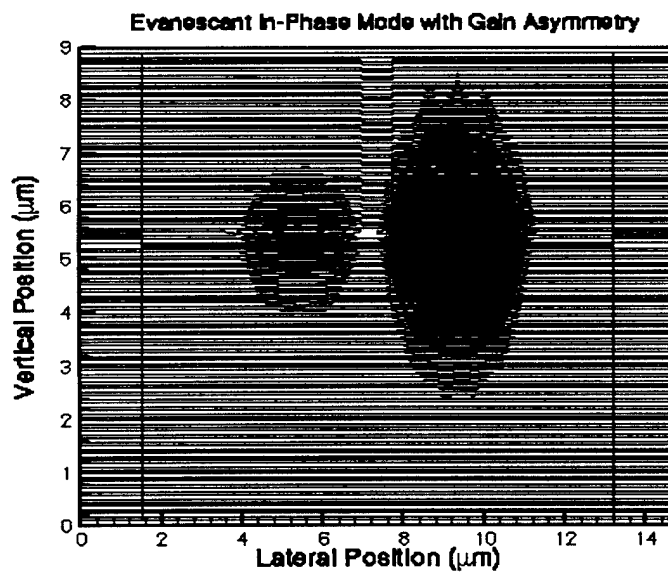


Figure 3. Amplitude contours for the in-phase evanescent mode with 100% gain imbalance; i.e. zero gain in the left pixel and twice the normal gain in the right pixel.

## Noise properties and selection of transverse modes in external cavity vertical cavity surface emitting lasers

J. Dellunde

Departament d'Estructura de la Materia, Facultat de Física, Universidad de Barcelona, Diagonal 647, E-08028, Barcelona, Spain.

A. Valle, L. Pesquera,

Instituto de Física de Cantabria (CSIC-UC), Facultad de Ciencias, E-39005 Santander, Spain.

K. A. Shore,

University of Wales, Bangor School of Electronic Engineering and Computer Systems, Bangor, LL 57 1 UT, Wales, UK.

Return Address: A. Valle, Instituto de Física de Cantabria (CSIC-UC), Facultad de Ciencias, Avda. de los Castros s/n, E-39005 Santander, Spain.  
Phone: 34-42-201465 Fax: 34-42-201459 E-mail: vallea@besaya.unican.es

The use of Vertical Cavity Surface-Emitting Lasers (VCSELs) in optical data links requires that consideration must be given to the device performance including the effects of optical feedback (OF). The modification of the transverse mode structure owing to OF has been studied in a VCSEL supporting the two lowest order modes ( $LP_{01}$  and  $LP_{11}$ ) [1,2]. Preferential excitation of either mode can be effected by appropriate choice of optical feedback delay,  $\tau$  [1,2]. On the other hand, solitary VCSEL supporting those modes has low mode partition noise (MPN) as is seen from its double peak RIN spectrum [3]. In this work we study the RIN spectrum of a multi-mode VCSEL subject to weak optical feedback. We show that the RIN double peak structure and low MPN are maintained in the presence of OF. Variations in the optical feedback delay are shown to alter the RIN spectrum from a twin peak to a single peak structure due to transverse mode selection. It is also shown that multiple reflections in the external cavity can affect the mode selection depending on the optical feedback delay.

In this work a cylindrical weakly-index guided VCSEL is considered. The model incorporates the spatial dependence of carrier and optical field profiles [1]. Attention is focused on the competition between  $LP_{01}$  and  $LP_{11}$  modes. Lang-Kobayashi rate equations for the complex mode amplitudes and a carrier continuity equation are solved numerically. Carrier evolution takes into account spatial hole burning (SHB) and diffusion effects. We always consider a stable cw situation since we assume from weak to moderate feedback and a very short external cavity. Low frequency enhancement of RIN, known as Mode Partition Noise (MPN), is observed in multimode laser diodes. It arises

when individual modes fluctuate in an anticorrelated way due to strong competition for the carriers. MPN is reduced when only  $LP_{01}$  and  $LP_{11}$  modes have appreciable power because of their small region of spatial overlap that leads to reduced carrier competition [3]. This is illustrated in Fig. 1 (a) where the RIN spectrum is shown for a solitary VCSEL when the power of  $LP_{01}$  is 0.1 times the power of  $LP_{11}$ . A double peak RIN spectrum is obtained for both modes. Peaks appear at frequencies corresponding to the relaxation oscillation frequencies of both transverse modes. The effect of OF is shown in Fig. 1 (b) where again a RIN double peak structure and low MPN are obtained.  $\tau$  has been chosen to make OF favours the mode with smaller power. Now the relation between both powers is inverted. Also the mode that has higher low frequency RIN is inverted. OF can also be chosen to completely suppress a particular transverse mode [1]. Then a change in RIN spectrum is obtained: from a twin peak to a single peak structure.

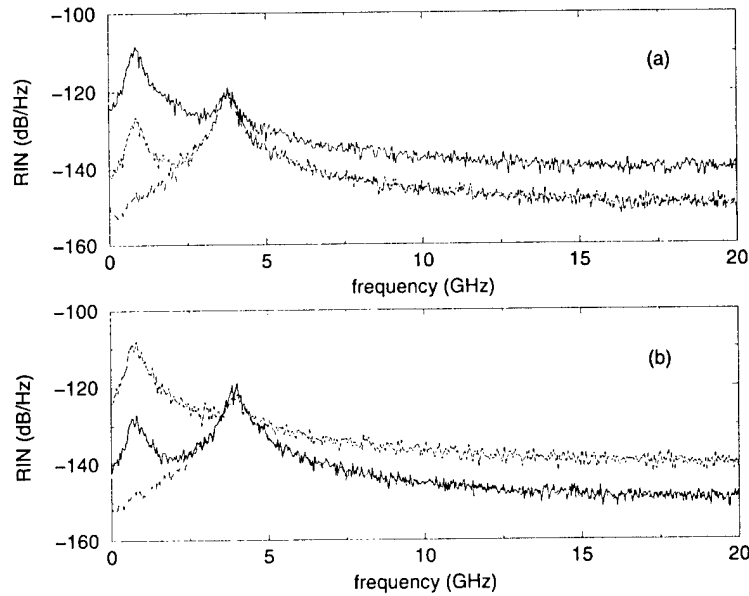


**Figure 1.** RIN spectrum for a solitary VCSEL (a) and for a VCSEL with optical feedback (b). The injected current is  $9\text{ kA/cm}^2$ , the external reflectivity is  $R_{ext} = 9.8\%$  and  $\tau = 2.0028$  ps.  $LP_{01}$ ,  $LP_{11}$ , and total power are plotted with solid, dashed and dotted lines respectively.

Optimum transverse mode selection can be achieved when  $(\omega_2 - \omega_1)\tau \approx (2n + 1)\pi$  where  $\omega_1$ ,  $\omega_2$  are the frequencies of  $LP_{01}$  and  $LP_{11}$ , respectively, and  $n$  is an integer [1]. In this case the maximum difference between threshold gains,  $g_{th,i}$ , of both modes due to OF is obtained. Multiple reflections affect only slightly mode selection since  $g_{th,2} - g_{th,1}$  does not depend on the second reflection. The effect of multiple reflections is important when  $(\omega_2 - \omega_1)\tau \approx (2n + 1/2)\pi$  as is seen from Fig. 2 where  $g_{th,i}$  and threshold currents,  $J_{th,i}$ , are plotted as a function of  $\tau$ . Now,  $g_{th,2} - g_{th,1}$  depends

on the second reflection leading the observed changes in Fig. 2. Multiple reflections favour the selection of  $LP_{01}$  at high current values. However, at low currents the range of  $\tau$  at which  $LP_{01}$  is selected decreases. The main effect of multiple reflections on  $LP_{11}$  mode selection is to shift the  $\tau$  range at which this mode is selected. Changes in threshold currents are related to the corresponding changes in threshold gains as is seen by comparing Figs. 2(a) and (b). We note that the achieved mode selection is only slightly worse than the one obtained when  $(\omega_2 - \omega_1)\tau \approx (2n + 1)\pi$  meaning in this way that any value of  $\tau$  such that  $(2n + 1/2)\pi < (\omega_2 - \omega_1)\tau < (2n + 1)\pi$  is appropriate to implement the feedback mode control mechanism.

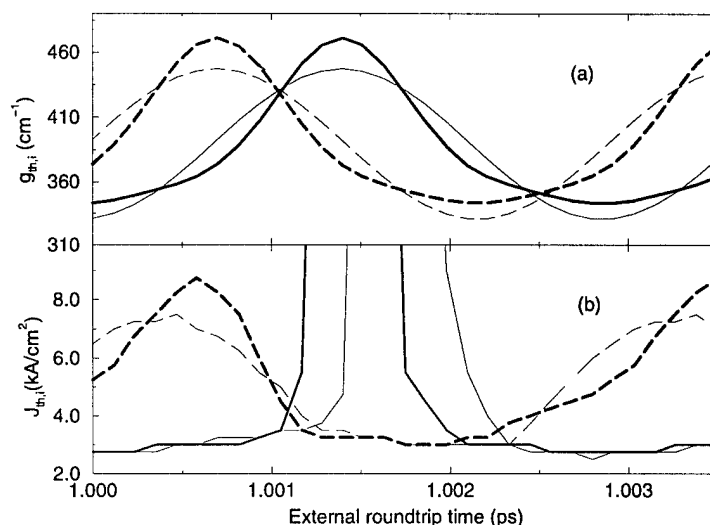


**Figure 2.** (a) Threshold gain and (b) Threshold current vs  $\tau$ . Solid and dashed lines correspond to  $LP_{01}$  and  $LP_{11}$ , respectively. Thin and thick lines correspond to one and multiple reflections, respectively. The external reflectivity is 9.8%.

In conclusion, we have shown that RIN spectrum double peak structure and low MPN are maintained in the presence of OF. We have also shown that multiple reflections in the external cavity can affect the mode selection depending on the optical feedback delay.

## References

- [1] J. Dellunde, A. Valle, and K. A. Shore, JOSA B, **13**, No. 11, 2477 (1996).
- [2] J. Y. Law, and G. P. Agrawal, IEEE J. of Selec. Topics in Quant. Electron. **3**, No. 2, 353 (1997).
- [3] J. Y. Law, and G. P. Agrawal, IEE Phot. Technol. Lett., **9**, No. 4, 437 (1997).

## Simulation of Scattering and Reflection Problems via Solution of the 2D Helmholtz Equation

Frank Schmidt, Konrad-Zuse-Zentrum, Takustr. 7, D-14195 Berlin-Dahlem, Germany  
Phone + 49 - 30-84185 - 174, Fax + 49 - 30-84185 - 107, e-mail: frank.schmidt@zib.de

The numerical simulation of wave propagation in integrated optics or fiber optics devices is one of the central tasks in the design of effective components. Fortunately, most of the practical structures can be modeled based on a uni- or bidirectional wave propagation. Simulation tasks of this kind can be solved by a number of different methods, most prominent here are the various types of Beam Propagation Methods (BPM). The central idea of BPM's, from its origin, has been to solve the scalar Helmholtz equation approximately by a reformulation of the boundary value problem to an initial value problem. This concept is very close to the working principle of a large number of optics components. Some structures, however, require simulation tools which are able to take into account arbitrary directions of reflections. For such type of problems it is natural, to go back to the scalar Helmholtz equation

$$\Delta u(x, y) + n^2(x, y)k_0^2 u(x, y) = 0, \quad u \in H^1(\Omega), \quad (1)$$

defined on some bounded domain  $\Omega$ , and to solve it as boundary value problem. That is, one prescribes the incident field along the whole boundary and obtains the interior solution  $u(x, y)$ . Exactly this idea has been proved to be of great practical relevance in simulation of grating structures [1]. The alternative choice is to solve the time-dependent wave equation by means of a finite-difference-time-domain (FDTD) method. This approach has been shown to be successful over a general class of structures [2]. It is advantageous, if the response with respect to an arbitrary time-dependent input is analyzed. In the problem class under consideration, however, where a time-harmonic incident wave is given, it is more efficient to solve the problem directly in its time-harmonic form. The central problem arising here is to construct transparent boundary conditions for general smooth boundaries and to find a suitable formulation of the interior problem, which allows for a direct implementation of these boundary conditions.

Our approach is based on a variational formulation of both the Helmholtz equation and the boundary operator. In standard fashion, we obtain the variational form of (1) by multiplication with a test function  $v \in H^1(\Omega)$  and integration by parts

$$-(\nabla v, \nabla u) + (v, n^2 k_0^2 u) = - \int_{\Gamma} \mathbf{n} v \nabla u \, ds \quad u, v \in H^1(\Omega), s \in \Gamma \quad .$$

Here  $\Gamma$  denotes the boundary and  $(v, u) = \int_{\Omega} v^* u \, dx dy$ . The function  $u(s), s \in \Gamma$ , may be considered as a superposition of incoming and outgoing waves,  $u(s) = u_{in}(s) + u_{out}(s)$ . Suppose a boundary operator  $\tilde{b}(s)$  is given, which relates the normal derivative to the boundary values as  $\mathbf{n}(s) \nabla u_{out} = \tilde{b}(s) u_{out}$  with  $\mathbf{n}(s)$  the outward normal vector. Then it follows  $\mathbf{n} \nabla (u_{in}(s) + u_{refl}(s)) = \mathbf{n} \nabla u_{in}(s) - \tilde{b} u_{in}(s) + \tilde{b} u(s)$ . With the reformulation of the boundary operator  $\tilde{b}(s)$  in its variational form,

$$b(v, u) = \int_{\Gamma} v^*(s) \tilde{b}(s) u(s) \, ds \quad ,$$

we have finally

$$\begin{aligned}
 a(v, u) + b(v, u) &= - \int_{\Gamma} v^* \mathbf{n} \nabla u_{\text{in}} ds + b(v, u_{\text{in}}) \\
 &\downarrow \\
 (\mathbf{A} + \mathbf{B})\mathbf{u} &= \mathbf{r}.
 \end{aligned}$$

Here the matrices  $\mathbf{A}$ ,  $\mathbf{B}$  and the vector  $\mathbf{r}$  are obtained using standard finite-element test functions  $v$ . The matrix  $\mathbf{A}$  is the conventional finite-element system matrix of the Helmholtz equation,  $\mathbf{B}$  is the discrete version of the boundary operator and realizes the transparency of the boundary. The right hand side vector  $\mathbf{r}$  contains the information about the incident wave. Many techniques to approximate the boundary operator  $\tilde{b}(s)$  for similar problems are known. There are the local operators based on operator factorizations [3] and [4], classical absorbing boundary conditions [1], the nonlocal approaches based on eigenfunctions expansions [5] and DtN-type operators [6], further the advanced absorbing boundary layers (including the PML-technique) analyzed in [7]. A new and exact technique based on algebraic considerations for Schrödinger-type equations has been published recently [8]. A generalization of this method to be applicable also to Helmholtz-type equations with arbitrary (smooth) boundaries will be presented in the paper.

Typical applications of the simulation method are given in Figs 1 and 2. Fig. 1 shows the reflection of the fundamental mode of a waveguide from a thin dielectric mirror. In this case, the exterior domain is not homogeneous, because it contains the waveguide. Note, that no artificial reflections from the boundary are observable. The second example concerns the reflection of a Gaussian beam from a metallic grating. It demonstrates that any detail of a reflecting structure can be modeled. Both examples are discretized such that the algebraic systems contain about 20,000 unknowns. The CPU-time to solve algebraic equations of this dimension with standard library routines is less than 1 minute on a SUN Ultra 1 work station.

## References

- [1] G. R. Hadley. Numerical simulation of reflecting structures via solution of the 2D Helmholtz equation. In *Integrated Photonics Research*, volume 3, pages ThD1-1, San Francisco, California, February 17-19 1994.
- [2] W. P. Huang, S. T. Chu, A. Goss, and S. K. Chaudhuri. *IEEE Phot. Tech. Lett.*, 3(6):524, 1991.
- [3] B. Engquist and A. Majda. Absorbing boundary conditions for the numerical simulation of waves. *Mathematics of Computation*, 31(139):629-651, July 1977.
- [4] A. Bayliss, M. Gunzburger, and E. Turkel. Boundary conditions for the numerical solution of elliptic equations in exterior domains. *SIAM J. Appl. Math.*, 42:430-451, 1982.
- [5] C. I. Goldstein. A finite-element method for solving Helmholtz type equations in waveguides and other unbounded domains. *Math. of Comput.*, 39, 1982.
- [6] D. Givoli. *Numerical methods for problems in infinite domains*, volume 33 of *Studies in Applied Mechanics*. Elsevier, 1992.
- [7] D. Yevick, J. Yu, and F. Schmidt. Analytic studies of absorbing and impedance-matched boundary layers. *IEEE Photonics Technology Letters*, 9:73-75, 1997.
- [8] F. Schmidt and D. Yevick. Discrete transparent boundary conditions for Schrödinger-type equations. *J. Comput. Phys.*, 134:96-107, 1997.

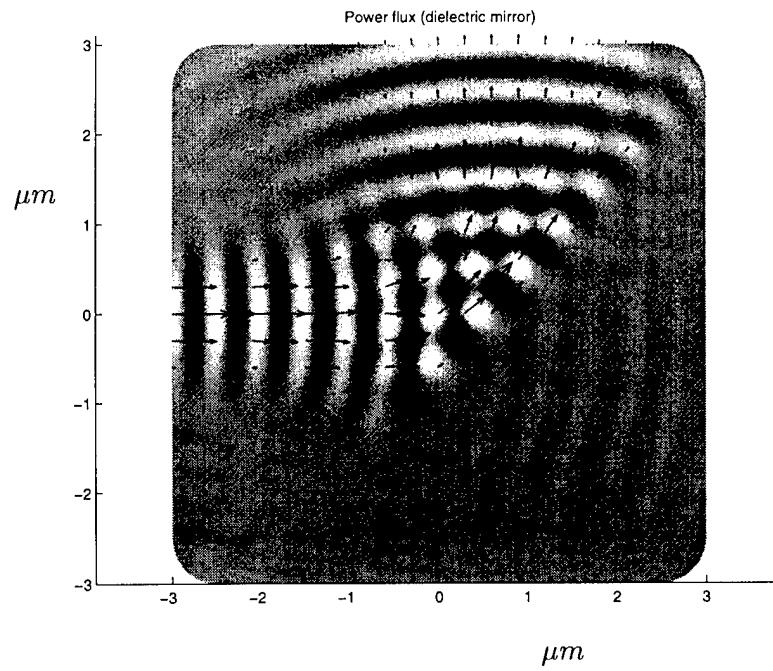


Figure 1: Reflection of the fundamental mode of a waveguide from a dielectric mirror – intensity distribution and power flux

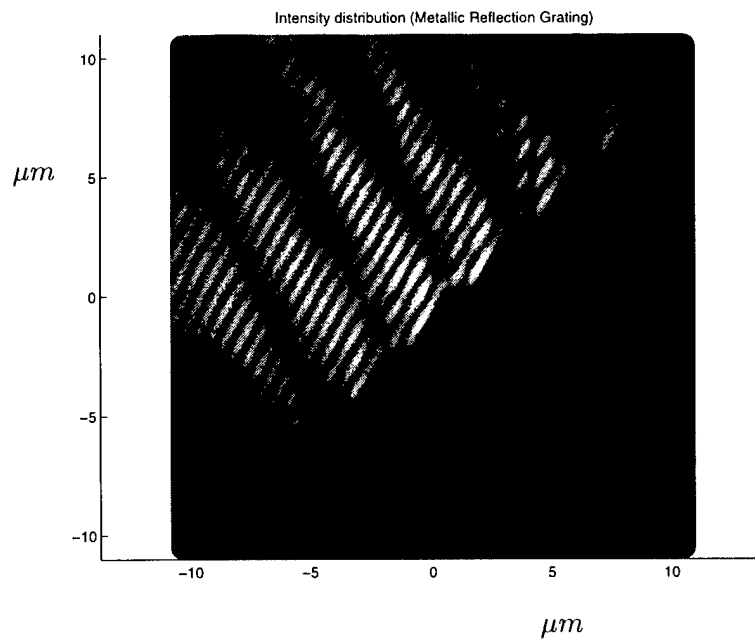


Figure 2: Reflection of a Gaussian beam from a metallic grating – intensity distribution

**Integrated Photonics Research**

# Multimode Optical Interconnects

**Wednesday, April 1, 1998**

**Lewis B. Aronson, Hewlett-Packard**  
President

**IWD**  
**10:30am-12:00m**  
Salon C

## **VCSEL Devices and Packaging for Fiber Optic Transceivers (Invited)**

**Michael S. Lebby**  
**Phoenix Applied Research Center**  
**Motorola**  
**2100 East Elliot Road,**  
**Tempe, Az 85284**  
**email: AYPH10@email.mot.com**

### **Keywords:**

**VCSELs, Array laser packaging, Autopower control, Packaging,  
 Optoelectronics, Discrete laser packaging, Semiconductor laser packaging**

### **Introduction**

Over the last few years, Motorola has been applying a different kind of semiconductor laser technology to a family of datalink and discrete products. The laser technology is commonly referred to as Vertical Cavity Surface Emitting Lasers (VCSELs). This technology is now emerging from advanced development and research laboratories into the market place, and there is a number of introductory texts, in addition to journal articles that describe the technology [1]. Motorola, has chosen the VCSEL technology to be the backbone of its optical program and has developed products such as the OPTOBUS™ datalink [1,2,3], which interconnects arrays of VCSELs inside a small, compact module via parallel fiber ribbon to receiver modules. As an extension to this technology, Motorola has designed new and novel ways to package the VCSELs. This paper will detail, in addition to the packaging used in OPTOBUS™, two approaches to discrete VCSEL packaging that are commercially competitive; the flip-chip and the angled angle TO-can. The essence of both these package designs is what is usually termed as 'auto-power control' (APC). This allows a feedback mechanism to feedback a signal to the laser, to control or change its output power level with respect to system conditions. Usually, this is accomplished by back facet monitor photodetectors in conventional edge emitting laser systems. As the VCSEL does not have facets, alternative solutions have to be developed; the flip-chip and angled TO-can are shown to be good candidates.

### **Concept of Auto-power control with VCSELs**

In commercial datalink systems, the semiconductor laser output power varies with temperature and degrades with duration of operation and lifetime. In many of today's applications such as CD-audio, CD-ROM, barcode scanners, high speed optical interconnect etc., require a semiconductor laser to maintain a constant output power across a temperature range within a specified system operation lifetime. Since the VCSELs counterpart, the edge emitting laser diode emits light from both facets, an autopower control or APC scheme can be implemented by monitoring the laser emission from the back facet of the laser. Even though the VCSEL output power is less sensitive to temperature, and VCSELs without APC have been used for some relatively low speed data communications though good system design such as OPTOBUS™ [1,2], further expanding the commercial VCSEL potential requires packaging a VCSEL with APC capability.

The VCSELs referred to in this paper are grown on GaAs substrates, and due to the absorptive nature of the material, any VCSELs with wavelengths shorter than 870nm will not emit backward through the substrate, unless the substrate is removed. Note: that the VCSELs used in OPTOBUS™ and other discrete products that include serial datalinks tend to be mostly 850nm. Therefore, the conventional APC approach for the edge emitting diode is not viable for this type of VCSEL. The edge emitter, with its back facet monitor detectors can easily achieve less than 10% stabilized output power over a wide temperature range and this has been implemented into CD types of applications where power stability is

important at the 1-2% range. In other applications such as serial datalinks, the requirement for stability is less (ranging between 5-10%), which means that if the VCSEL was to compete with the edge emitter for power stability, at least the above specifications need to be demonstrated.

#### Auto power control using the VCSEL flip-chip

APC using flip-chip has been accomplished by flip-chip mounting of a GaAs photodetector to a 1X2 VCSEL array. The detector and VCSEL array is then mounted to a standard TO-can using wirebonding. The type of TO-can is a TO-56 header with three electrodes. The primary VCSEL output power stabilization is achieved by monitoring the secondary VCSEL output power. A photodetector (PD) is flip-chip mounted onto one of the VCSELS to monitor its power variation.

The flip-chip concept assumes that these two VCSELS are identical in temperature performance and degradation behavior. The concept was developed from the reliability and failure analysis work on 850nm VCSEL arrays at Motorola for the OPTOBUS™ program [1,2]. The reliability results show that the degradation of one VCSEL next to another VCSEL was similar enough to allow an effective APC solution to be developed. Figure 1 shows how the concept is realized.

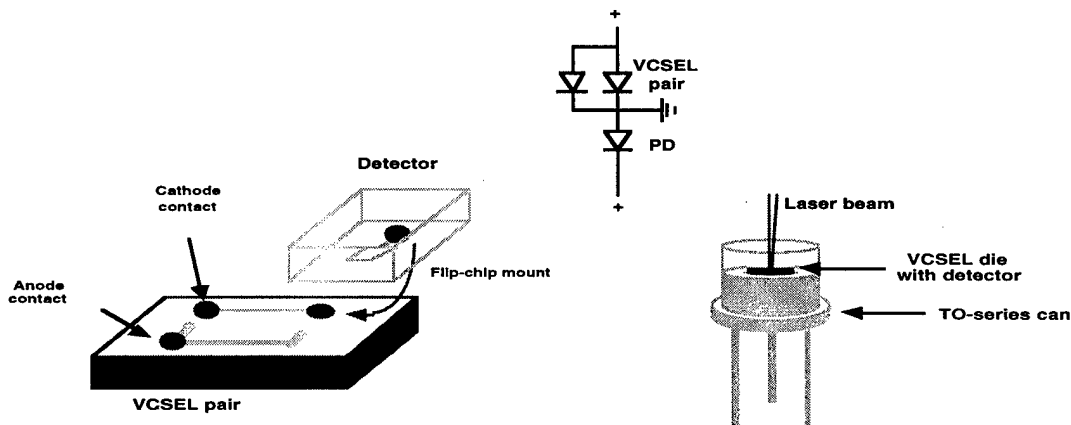


**Figure 1. Schematic of the a 1X2 VCSEL array with photodetector**

Although the reliability results show acceptable degradation rates, to further minimize the difference between these two VCSELS a small closely spaced array of 1X2 is utilized. The array implies that the same fab process and epitaxial growth run is used for both the VCSELS, thereby improving the probability that both VCSELS are similar in operation as well as lifetime. The two VCSELS are electrically connected in parallel, as shown in Figure 1. The laser driver will run both VCSELS simultaneously. The detector has an anode contact on the light receiving side and a cathode on the substrate side. It is flip-chip mounted onto the VCSEL array with its light aperture and its anode bonded onto the secondary VCSEL cathode. The VCSEL-PD chip set becomes a three terminal device (VCSEL-anode, VCSEL-cathode/PD-anode, and PD-cathode), and is mounted onto a TO-56 header.

The APC demonstration is shown in Figure 2, where the temperature is varied from 0 to 65°C, and the targeted VCSEL output power variation is only 0.8% from 1 mW at 0°C and 0.4% at 65°C, well within the required +/- 1% needed for the most stringent applications.

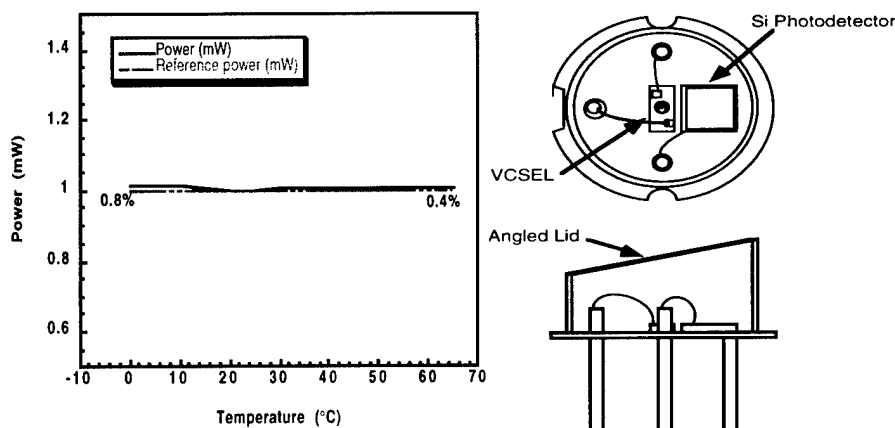


**Figure 2. The primary VCSEL output variation with temperature when APC is activated. Figure 3. Plan view and cross-section of the VCSEL APC solution using an angled lid**

#### Auto power control using the VCSEL with angled lid TO-56 package

Automatic power control of a laser is used to maintain a constant light output power from a laser that is subject to thermal and degradation effects. Typically a portion of the output light of the laser is used to generate a photocurrent that is used in a feedback loop that drives the laser. Results are presented for a VCSEL and photodetector mounted on a 4 lead TO56 header in which an angled lid is used to reflect a portion of the emitted laser beam onto the photodetector.

In the approach described here an angled, partially reflecting lid is used to reflect a portion of the emitted laser beam onto a photodetector that is mounted at the side of the VCSEL die. A cross sectional and plan view of the fabricated part is shown in Figure 3.

With the APC feedback loop enabled on the laser driver, power measurements were made over temperature at three different nominal output powers 0.3, 0.6, and 1mW. The results at 0.3mW are shown in Figure 4, illustrating both the actual power variation and the normalized power variation.

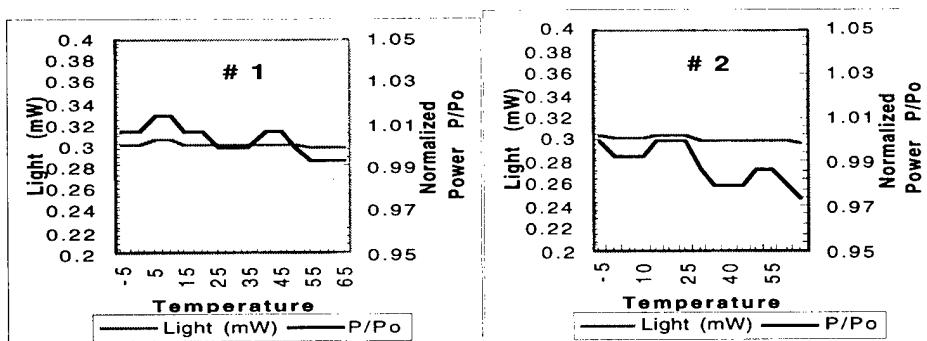


**Figure 4. Power Variation over -5 to 65°C for slanted lid packages with APC at a nominal 0.3mW output power**

For both packages the output power was capable of being maintained to within 4% of the nominal value. Therefore, APC using a slanted lid has been demonstrated, the performance shown with the two packages was reasonable considering the method of manufacture, and the feedback control that was used.

#### Array Packaging of VCSELs for OPTOBUS™

The success of the OPTOBUS™ parallel array interconnect is based on the use of AlGaAs Vertical Cavity Surface Emitting lasers at 850 nm in conjunction with some unique optoelectronic packaging concepts. These concepts will be discussed briefly with respect to the packaging of VCSEL arrays. The one notable difference between the above package concepts for VCSELs is that OPTOBUS™ is an optical interconnect system that has been designed to tolerate the VCSEL output power variances over life, and therefore does not need APC. This puts more stringency onto the VCSEL devices themselves through tighter output power specifications over temperature, but allows for more simpler system design. The packaging approach of the VCSEL and PIN arrays used in OPTOBUS™ use a multilayer Tape Automated Bonded (TAB) leadframe approach [2]. The leadframe contains separate signal and ground layers. The ground layer provides for a coaxial-like environment (low inductance and effective signal coupling to the ground plane).

### Conclusions

Two different types of VCSEL APC both achieving output power stability of 1% in the flip-chip experiment and better than 4% with an angled lid TO-package have been demonstrated. Clearly, these experiments show that better performance can be achieved through manufacturing, which makes the concepts very competitive for commercial application. An alternative VCSEL package concept has also been demonstrated using TAB technology that does not require photodetectors for APC. This package technology couples VCSEL arrays to waveguides to fiber ribbons. The resulting challenge is whether APC could be (or should be) incorporated into a package design for arrays. Clearly, if APC could be incorporated, then the VCSEL specifications might be allowed to relax.

### Acknowledgments

The VCSEL program spans multiple Motorola organizations and thus there are simply too many individuals to acknowledge personally. However, special thanks must be made to three groups: (1) The VCSEL/Detector production fab, (2) The discrete VCSEL manufacturing and (3) The OPTOBUS™ team.

### References

- [1] W. B. Jiang and M. S. Lebby, "Handbook of Fiber Optic Data Communication"; Chapters 2 and 15; Academic Press, 1997 ISBN#0-12-437162-0 (Excellent reference for an introduction to VCSEL technology)
- [2] M. Lebby, C. A. Gaw, W. B. Jiang, P. A. Kiely, C. L. Shieh, P. R. Claisse, J. Ramdani, D. H. Hartman, D. B. Schwartz, J. Grula, "Use of VCSEL arrays for parallel optical interconnects", Proc SPIE, 2683, 81 (1996)
- [3] C. L. Shieh, M. S. Lebby, and J. Lungo, "Method of making a VCSEL," US 5,468,656 (1995)
- [4] M. L. Lebby, C. A. Gaw, W. B. Jiang, P. A. Kiely, P. R. Claisse, and J. Grula, "Key challenges and results of VCSELs in data links," LEOS '96, WV2 (Boston, MA, Nov., 1996)
- [5] P. Claisse, W. Jiang, M. Lebby, B. Webb, P. Sanchez, L. Boughter, D. Cotney, P. Kiely, M. Roll, B. Lawrence, "Automatic Power Control of VCSELs using an angled lid TO-56 package", To be presented at ECTC in Seattle, May 1998

OPTOBUS™ and GUIDECAS™ are trademarks of Motorola

## **Optical interface issues in VCSEL-based multimode fiber-optic interconnects**

D. Haritos, K. Giboney, A. Yuen, P. Rosenberg, B. Lemoff, L. Aronson, L. Buckman,  
J. Straznicky, K. Wu, and D. Dolfi

Hewlett-Packard Laboratories, 3500 Deer Creek Road, Palo Alto, CA 94304

dean\_haritos@hpl.hp.com (650) 857-4256 (650) 813-3626 (fax)

Recent efforts in parallel fiberoptic data link research and development have concentrated on making the transition from demonstration platforms to production modules. This entails focusing on both volume manufacturability and cost, but without sacrificing performance advantages over conventional copper links. One critical component that must be optimized in these regards is the optical interface, which integrates the emitters, input and output fiber coupling, and the detectors. Key issues that must be addressed by the optical interface in order to satisfy performance concerns include coupling efficiency, modal noise, bandwidth-distance, and eye safety. The Parallel Optics for Network Interconnects (PONI) program, a DARPA-sponsored consortium led by Hewlett-Packard Labs<sup>1</sup>, is investigating these issues in order to create a second-generation fiberoptic data link with enhanced capabilities and performance (see figure 1). It will feature 12 channels at >1Gbit/s/ch over >100 meters.

Link performance is dependent in large part upon the optics. An obvious concern is coupling efficiency, which should be maximized to reduce the emitter drive current required. Since many parallel links for intermediate distances (hundreds of meters) rely on graded-index multimode fiber (GI MMF), this problem is not as trivial as simply matching the core size and numerical aperture (NA) with the input beam, as with step-index fibers. In GI MMF, the NA can be shown to be radially dependent such that the maximum NA is accepted by the fiber at the center of the core; the acceptance NA then decreases monotonically to zero at the edge of the core.

A second optics-related performance issue in MMF is modal noise. Modal noise arises when a signal exhibiting modal fluctuations is transmitted through a region with mode-selective loss (MSL). For example, if an emitter has an output beam exhibiting transverse mode hops (modal fluctuations), any resultant fluctuations in power coupled into the fiber due to MSL become modal noise. At the receiver end, if the output spot size is larger than the detector, the lost light can be mode-selective. In that case, any modal fluctuations in the fiber will translate to modal noise at the receiver. Hence it is seen that low modal noise relies on efficient coupling.

The bandwidth-distance product is fundamental to high-bitrate communications. Bandwidth-distance is limited in MMF by modal dispersion, which refers to the different propagation velocities of the various fiber modes. Since a number of fiber modes make up one bit, their different velocities result in a temporal spread of the pulse at the output of the fiber. While selective mode launches are under investigation for increasing bandwidth-distance, the PONI program is currently planning to approach an overfilled launch (OFL) condition by launching into as many fiber modes as possible. The OFL condition is satisfied by a lambertian

source such as a light-emitting diode, and is used by fiber companies to test the bandwidth-distance of their production fibers.

An important commercialization issue that PONI is addressing is eye safety. One method for ensuring eye safety is open fiber control (OFC), which functions to turn off the lasers should the link be broken. An algorithm is then required to restore power to the lasers when the link is reconnected. PONI is attempting to meet class I IEC and CDRH eye safety without OFC. To do so, it is imperative to design for a minimum-power output beam that is uniform over a broad NA.

The challenge in optical fiber links lies in solving all the above problems simultaneously. The challenge is augmented in PONI by our focus on low-cost manufacturability. It is therefore essential for an optical element coupling light to or from the fiber to have a minimal number of pieceparts, a simple assembly process with few steps, and a small number of precision features. There is also the issue of active vs. passive alignment. To move to passive alignment, tolerances must be maximized in the optics such that a misalignment of the interface does not degrade performance of the link.

One final concern is system architecture. Since most applications demand that the fiber ribbon be parallel to the substrate of the module, a 90° bend is required to interface the VCSELs (vertical cavity surface-emitting lasers) and photodetectors to the fibers. PONI is investigating both an optical and an electrical bend in an effort to find the lowest-cost high-performance solution. The optical bend is more difficult from an optics standpoint, but can reduce electrical parasitics since all optoelectronic components can reside on the same substrate as the ICs, hence shortening electrical paths. Since parasitics limit the maximum achievable data rate, the optical bend might be preferred.

One advance PONI has made toward simplifying the optical interface design involves the emitters used. PONI leverages experience with VCSEL arrays gained in the previous DARPA-sponsored HP-led program, the Parallel Optical Link Organization (POLO)<sup>2</sup>, and makes a further technological advance by transitioning from proton-implanted (PI) to oxide-confined (OC) VCSELs. While OC VCSELs have a number of advantages such as low threshold, their most important characteristic from the optics side is the relative stability and uniformity of their output pattern, owing to the strong index-guiding provided by the oxide layer. This is an advantage over the PI VCSELs used in POLO, which had unstable and less uniform outputs. The smaller modal fluctuations reduce the potential for modal noise. In addition, the stable uniform output pattern is advantageous in terms of eye safety, as peaks in nonuniform optical beams may not be eye safe.

Any optical interface must necessarily make tradeoffs between the various concerns described above. An interface providing 100% coupling efficiency but requiring tight alignment tolerance is not an appropriate solution because of the high manufacturing cost. Similarly, an eye-safe solution with high alignment tolerance but low coupling efficiency would have its own disadvantages such as high drive current and potential for modal noise. It is instructive to study some examples.

Motorola's OPTOBUS<sup>3</sup> and HP's POLO<sup>4</sup> both utilize tapered waveguides for their optical interface. Figure 2 shows a simulation<sup>5</sup> of a tapered cylindrical waveguide. One advantage of tapers is alignment tolerance of emitter to waveguide, as a wider end-face allows for large offsets. Another is that the tapering effects an NA broadening by a factor dependent upon the ratio of input to output diameter, which enhances eye safety. However, since the number of bounces rays make in the taper depends on their incident angles, a discretized "bullseye" pattern consisting of bright rings rather than a uniform power distribution is seen to form if the input is diverging. This may act to degrade eye safety. In addition, molding capabilities set a lower bound on the output diameter, which would ideally be smaller than the fiber core (50 or 62.5  $\mu\text{m}$  for GI MMF).

AMP has described an interface incorporating input and output lenses with a 45° mirror in between for accomplishing an optical bend.<sup>6</sup> A similar interface without the bend is modeled in figure 3. The first lens acts to collimate the light, while the second acts to focus it at the fiber face. This configuration, like the taper, can be used to engineer the output NA. The advantage is that the focusing allows the dimensions of the lenses to be unconstrained, whereas with the taper it is preferable to have the output diameter on the order of the fiber core diameter. The disadvantage of this interface, as with any lensed interface, is that any offset of the emitter from the optical axis results in both a translation and an angular shift in the output beam. These two effects are especially detrimental to GI MMF coupling due to its radially-dependent NA.

The path to a high-performance, low-cost manufacturable link involves playing all these tradeoffs against each other in the optical interface design. It is necessary to keep in mind that packaging concerns are as important as optical performance, since an interface with fantastic performance is completely worthless if it cannot be implemented cheaply and reproducibly.

<sup>1</sup> DARPA contract number MDA 972-97-3-0008 (under guidance of David Honey).

<sup>2</sup> DARPA contract number MDA 972-94-0038 (under guidance of Anis Husain).

<sup>3</sup> Schwartz, D., et al., "A Low-Cost High-Performance Optical Interconnect," *IEEE Transactions on Components, Packaging, and Manufacturing Technology – Part B* 19, 532-539 (1996).

<sup>4</sup> Giboney, K., "Parallel-Optical Interconnect Development at HP Laboratories," presented at *SPIE Optoelectronic Interconnects and Packaging IV* (1997).

<sup>5</sup> All simulations performed using Optical Research Associates' *LightTools* v. 2.0.0.

<sup>6</sup> Heiney, A., et al., "Polymer Molded Lenses for Optoelectronics," *45th Electronic Components and Technology Conference*, 170-176 (1995).

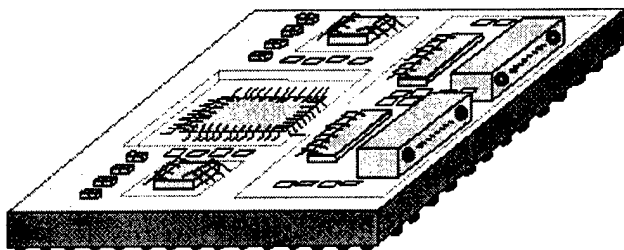


Figure 1: PONI module and its components.

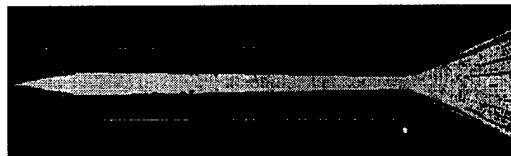


Figure 2: Cylindrical taper waveguide. Note the NA conversion.



Figure 3: Straight waveguide with input and output lenses.

## Simple fabrication of WDM filters for byte-wide, multimode cable interconnects

R.J. Deri, H.E. Garrett, S. Gemelos, R.E. Haigh, B.D. Henderer, J.D. Walker, and M.E. Lowry  
Lawrence Livermore National Laboratory, Livermore, CA 94550

Parallel optical interconnects over multimode fiber (MMF) ribbon cable are emerging as a robust, high-performance data link technology [1,2,3]. This technology has primarily been implemented as single wavelength, point-to-point links, and can be significantly enhanced by wavelength division multiplexing (WDM) to increase both point-to-point bandwidth as well as create more complex interconnect topologies and routing approaches. The combination of byte-wide transmission for high channel bandwidth with WDM for interconnect routing is particularly attractive for ultrascale computing platforms[4]. Research in this area suggests that WDM transceivers for point-to-point links can be realized.[5,6] Exploiting the potential richness of WDM networks, however, also requires a low-loss routing fabric which includes small footprint add/drop multiplexers. Low insertion loss is critical for this technology because the transceivers exhibit link power budgets well below that of telecom WDM systems and because the multimode fiber cabling precludes the use of optical amplifiers. While high-performance filters can be realized for single-fiber applications[7], achieving high-performance devices with ribbon cable is significantly more complicated. Complications arise from the MMF's high NA=0.275 and large core (62.5 $\mu$ m), which render array collimation difficult, and the difficulty of maintaining good filter performance at the high angles of incidence needed to minimize loss in a 3-port (2-output) device. Here we demonstrate a suitable approach to fabricating such filters, which is simple, involves primarily passive alignment, and provides high performance and connector alignment. We demonstrate a dual wavelength link through a cascade of eight WDM filters.

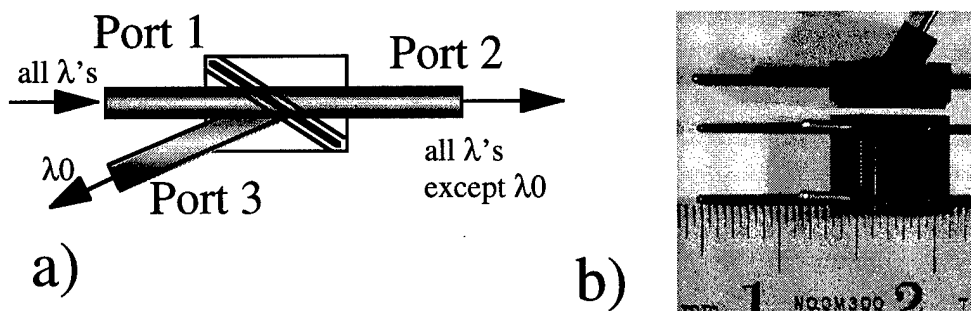


Fig. 1: Filter schematic (a) and photograph (b) showing top and side views with guide pins.

Our filters are 3-port devices suitable for add/drop multiplexing, which employ thin film interference filters sandwiched between MMF ferrules as shown in figure 1. In contrast to previous reports of related devices,[8] we employ high index materials for the filter coating to minimize bandpass spreading and polarization sensitivity while maintaining a substantial angle of incidence (30 degrees) to ease optomechanical packaging, and use commercially available "MT" connector ferrules to maintain fiber alignment. These ferrules use injection molded plastic to provide low cost, precision optical positioning of 12 parallel fibers via passive (guide-pin) alignment, [9] and are frequently used for transceiver and cable connectorization. Guide pin alignment enables 95% passive assembly of our filter, and can therefore provide low cost filters with available ferrule technology. Since the filter body is built from ferrules, the devices are already aligned for external connectors. This approach yields a small filter footprint (7.8x6.4x5.7 mm<sup>3</sup>) which is limited by ferrule size.

Filter assembly begins by populating three MT ferrules with 62.5 $\mu$ m GRIN core MMFs and preparing endfacets with a wafer saw. Facets are cut to 30° (ports 1, 2) or 60° (port 3) in the filter region and a thin film interference filter is then epoxied onto one 30° face. Port 1 and 2 ferrules are then epoxied together, using completely passive, guide pin alignment. Wafer sawing exposes the fiber-filter interface to enable access for port 3, and the port 3 ferrule is aligned with guide pins providing angular registration and position registration perpendicular to the three fiber plane (fig. 1a). In this procedure, care is required only in controlling the depth of the port 3 exposure saw cut and in longitudinal alignment of port 3 along the port 1-to- port 2 axis. Saw cut depth is controlled via microscope inspection during the cutting. We positioned port 3 longitudinally using active alignment-- which could be eliminated with a modified ferrule body design.

Device insertion loss depends strongly on diffractive loss during propagation outside the MMFs near the filter. Small gaps between all three ferrule faces are required to minimize loss; this is achievable for port 3 only for larger angles of incidence.[8] However, filter response is degraded at high incidence due to polarization dependence and angular dependence of the center wavelength, which is exacerbated by both large MMF NA and filter tilt. We overcome this problem with high-index filter material (AlGaAs) which is compatible with 30° tilt. For this first demonstration we used filter layers consisting of 31 quarter-wave AlGaAs layers sandwiched between TaO<sub>x</sub> single-layer AR coatings. The AlGaAs was grown by MBE on a GaAs substrate, which was removed by selective etching. Our filters were designed for a  $\approx$ 40 nm add/drop band about 840 nm (fig. 2), for compatibility with commercially available byte-wide transceivers with moderate wavelength tolerances.

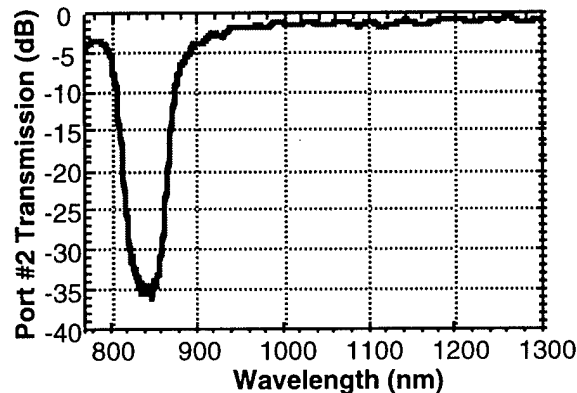


Fig. 2: Typical filter wavelength response for port 2 transmission.

Fabricated filters exhibit steep skirts, low insertion loss and good crosstalk isolation. The filters exhibit steep skirts (fig. 2) and a weak polarization dependence of the bandwidth ( $\approx$ 7 nm), which are not achievable with low index layers at 30° tilt. Insertion losses for our first two batches of filter modules are shown in Table I. The mean fiber-to-fiber insertion loss between ports 1 and 2 is 1.0 to 1.1 dB, with the best fibers exhibiting just under 0.7 dB loss. Filter loss uniformity is rather low, with standard deviations  $\leq$ 0.12 dB for batch #2. (The somewhat higher nonuniformity of batch #1 reflects an imperfect cleaning procedure which was improved for batch #2.) Uniformity on port 2 is very important because it impacts the maximum number of filters which can be serially cascaded in ring networks. The devices exhibit excellent wavelength crosstalk rejection in port 2, and acceptable rejection in port 3. The port 3 values, which we believe are limited by AR coating quality, can be improved by cascading an additional in-line (2-port) filter.

Potential diffractive loss in these filters raises concern about mode selective loss (MSL), which can introduce bit error rate floors in MMF systems. We measured the effective MSL in our

devices by comparing the fluctuation in monochromatic laser light transmission due to fiber agitation against that induced by known mode selective losses created by a variable, index-matched gap between two fiber endfacets. Because the filter MSL was quite low, it was determined by measuring the MSL of multi-filter cascades. This experiment detected MSL for port 1-to-port 2 transmission at 1310 nm, and MSL=  $0.34 \pm 0.1$  dB for port 1-to-port 3 transmission at 850 nm. This mode selective loss is quite low, and not expected to impact link performance.

**Table I: Measured filter performance at 850 and 1310 nm**

Batch	Module	loss 1-2 (dB) (mean $\pm$ sigma)	loss 1-3 (dB) (mean $\pm$ sigma)	Crosstalk 1-2 (dB, worst)	Crosstalk 1-3 (dB, mean)
#1	#1	1.08 $\pm$ 0.35	1.30 $\pm$ 0.28	-33.2	-12.2
#1	#2	0.99 $\pm$ 0.36	1.30 $\pm$ 0.40	-35.8	-11.2
#2	#3	0.99 $\pm$ 0.07	0.94 $\pm$ 0.12	-34.6	-15.2
#2	#4	1.12 $\pm$ 0.12	1.24 $\pm$ 0.09	-34.6	-15.0
#2	#5	1.18 $\pm$ 0.08	1.17 $\pm$ 0.08	-36.5	-14.9
#2	#6	1.03 $\pm$ 0.05	2.12 $\pm$ 0.12	-32.5	-14.6

We used these filters to demonstrate a dual wavelength link with commercially available, byte-wide transceivers at 850 and 1310 nm.  $2^{23}$ -1 PRBS signals at 500 and 1000 Mbit/s/fiber for the two wavelengths respectively, were routed through a serial cascade of up to eight filters and  $\approx 40$ m of 62.5 $\mu$ m core, GRIN fiber. This link exhibited 9dB insertion loss and yielded a bit error rate below  $1 \cdot 10^{-14}$ , including crosstalk effects between different wavelengths and different fibers in the ribbon cables. Shaking of the fiber to induce potential error rate floors from MSL had no effect, indicating that the filters introduce negligible mode selective loss.

In conclusion, we have demonstrated a simple fabrication approach for compact, high-performance WDM filters which are compatible with existing byte-wide transceivers. The filters are constructed from widely available ferrules to minimize alignment and connectorization costs, and exhibit low loss, sharp skirts, reasonable crosstalk suppression, and a negligible mode selective loss  $\leq 0.4$  dB. Here we demonstrated filter bandwidths of  $\approx 40$  nm; simulations show that our design is suitable for channel separations as small as 15-30 nm, and 5-10nm with some modification. This technology directly enables several interesting WDM interconnects, such as chordal rings. More significantly, its combination with recent advances in byte-wide WDM sources (eg: [6]) will enable byte-wide WDM fabrics with appreciable source routing capability and high channel bandwidth.

This work was performed under the auspices of the U.S. Department of Energy by Lawrence Livermore National Laboratory under contract No. W-7405-Eng-48, and was partially supported by ARDC funding.

## References

- [1] Y.-M. Wong et al., *J. Lightwave Technol.* LT-13, 995 (1995).
- [2] M. Lebbby et al., *Proc. 1996 Electron. Components & Technol. Conf.*, p. 279 (1996).
- [3] K. S. Giboney, *Proc. SPIE Optoelectron. and Packaging IV* (February 1997).
- [4] R.J. Deri et al., *Proc. 3d Massively Parallel Proc. using Opt. Interconn.*, p. 62 (1996).
- [5] S.Y. Hu et al., in *Proc. 1997 IEEE LEOS Annual Mtng.*, paper TuJ4 (1997).
- [6] C. Chang-Hasnain, in *Proc. 1997 IEEE LEOS Annual Mtng.*, paper WJ1 (1997).
- [7] L. Aronson et al., presented at *OFC '97* (postdeadline paper).
- [8] H. Yanagawa et al., *J. Lightwave Technol.* LT-7, p. 1646 (1989).
- [9] T. Satake et al., *Proc. 1994 Electron. Components & Technol. Conf.*, p. 994 (1994).

# Four Channel Multimode Wavelength Division Demultiplexer Based on Photopolymer Volume Holographic Gratings and Substrate-guided Waves

Charles C. Zhou, Sean Sutton and Ray T. Chen  
Microelectronics Research Center  
University of Texas at Austin  
Austin, TX 78712

Boyd V. Hunter, Paul Dempewolf  
LightPath Technologies Inc.  
6820 Academy Parkway E., NE  
Albuquerque, NM 87109

Wavelength division multiplexing (WDM) and demultiplexing (WDDM) techniques are the two key technologies for upgrading optical communication system bandwidth. The use of WDM technologies not only provides high speed optical communication links, but also provide advantages such as higher data rates, format transparency, and self-routing. Over the past twenty years, many kinds of WDDM device technologies have been developed and demonstrated [1-4]. WDDM devices using dispersive photopolymer or dichromated gelatin (DCG) volume holographic gratings have been recently reported [5-7]. In this paper, we report an integrated four-channel multimode fiber compatible WDDM system with four semiconductor lasers operating at 750, 780, 810 and 840 nm, respectively. The device is demonstrated using the combination of graded index (GRIN) lenses, photopolymer based holographic gratings and substrate-guided waves.

A four channel WDM/WDDM is designed for multimode fiber transmission systems. Multimode fibers are widely used in short haul optical communications. The schematic of a four channel wavelength division multiplexed and demultiplexed optical transmission system is shown in Fig. 1(a). The four discrete wavelengths are provided by semiconductor laser arrays. The four wavelengths are multiplexed into one 50  $\mu\text{m}$  multimode fiber for transmission. At the receiving end, a wavelength division demultiplexer is used to separate the discrete wavelengths for O/E conversion. The integrated four channel polymer holographic grating based WDDM structure is shown in Fig. 1(b). At the input end, the surface-normal incoming multiple wavelength light is collimated by a quarter pitch GRIN lens and diffracted by the volume holographic grating into substrate guided waves. The input holographic grating is designed using the phase-matching principle. The volume holographic grating has slanted fringes induced by the refractive index modulation inside the photopolymeric film. Since the input holographic grating is dispersive, the input multiple wavelengths are diffracted into different bouncing angles. The substrate-guided lights are separated spatially as they propagate along the waveguiding plate. The device length should be long enough so that the output spots will not overlap each other[8]. The collimated spot size is determined by the numerical aperture of the fiber and the GRIN lens. At the output end, they are coupled out surface-normally by a holographic grating. The light can be detected with a photodiode array. Since the substrate-guided waves maintain the mode symmetry along the optical path, the output light spots can be efficiently coupled into fibers using focusing GRIN lenses at the output end. Due to the beam reversal principle, the reverse use of the WDDM device automatically results in a WDM device. The advantage of this device structure is the adjustability of channel wavelength separation. For any desired wavelength separation, we simply change the device length or the input hologram diffraction angle to achieve low crosstalk output light spots without changing device structure. The use of GRIN lenses and surface-normal coupling avoid pigtailling from waveguide edges and free space packaging, thus result in more rugged and reliable devices.

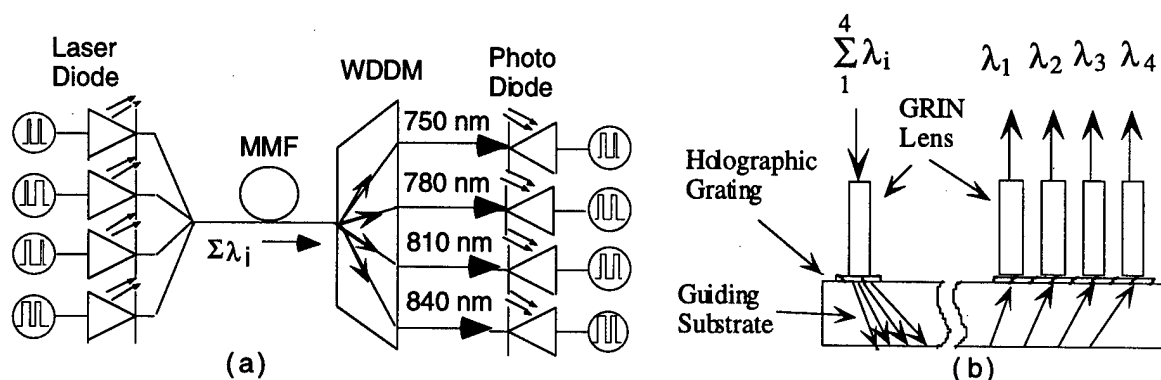


Fig.1 (a) The schematic of a four channel WDDM multimode optical transmission system, (b) The WDDM based on GRIN lenses, holographic gratings and substrate-guided waves.

The WD(D)M devices demonstrated previously are mostly using tunable laser sources. In our experiment, the four discrete near IR wavelengths of 750 nm, 780 nm, 810 nm and 840 nm are provided by four SHARP LT series edge-emitting semiconductor lasers packaged with ST receptacles. A 30 nm wavelength separation is used to avoid crosstalk caused by temperature-induced wavelength changes. Each laser diode has a 3 mw output power rating. The light from each edge-emitting laser is lens-coupled into a multimode fiber. Due to the mode mismatch between the edge-emitting laser diode and the multimode fiber, 0.5mw is normally coupled into the 50/125  $\mu\text{m}$  graded index multimode fiber from a laser. At the input end, four individual wavelengths are wavelength-division-multiplexed into a multimode fiber. A photo of the wavelength-division-multiplexing (WDM) module is shown in Fig. 2(a). The multiplexed light propagates through a spool of multimode fiber with 2km length. It is then connected to a fiber-pigtailed quarter pitch GRIN lens using an ST connector. The light is collimated by the quarter pitch GRIN lens with a diameter of 2 mm. The volume holographic grating is fabricated using 10  $\mu\text{m}$  thick DuPont photopolymer films with a maximum refractive index modulation of up to 0.02. A 514 nm Argon Ion laser is used to crosslink the photopolymer film and the center replay wavelength is selected to be 795 nm. An average diffraction efficiency of 23%, 38%, 37% and 24% is experimentally confirmed for randomly polarized light operating at 750, 780, 810 and 840 nm channels separately. The four channel WDDM is integrated on a BK7 glass substrate glass with a thickness of 7 mm. A CCD-based image system is used to measure the output light parameter. A picture of the light output spots at device output length of 200 mm is shown in Fig. 2(b). The measured crosstalk is less than -40 dB. The system insertion losses are -23dB, -21dB, -20dB, -22dB respectively for 750 nm, 780 nm, 810 nm and 840 nm. We can see that mode symmetry is maintained, which promises a high coupling efficiency to a fiber by using a focusing GRIN lens. The symmetrical mode dot focused on the planar GRIN lens surface facilitates fiber end-face coupling. The optical spectrum of the four channel WDDM device used is shown in Fig. 2(c). The results show that the four channel WDDM system can be easily extended to more channels.

In summary, we have demonstrated an integrated four channel wavelength division demultiplexer using holographic gratings and substrate-guided waves. The WDDM is tested using multimode fiber input and near IR semiconductor laser sources. The crosstalk level is measured to be less than -40dB. The system insertion losses are -23dB, -21dB, -20dB, -22dB respectively for 750 nm, 780 nm, 810 nm and 840 nm. The wavelength adjustability, integrated packaging and multimode fiber compatibility features make it ideal for expanding local and wide area networks communication system bandwidth.

This work is sponsored by Army SSDC, DARPA, ONR, BMDO and the ATP program of the State of Texas.

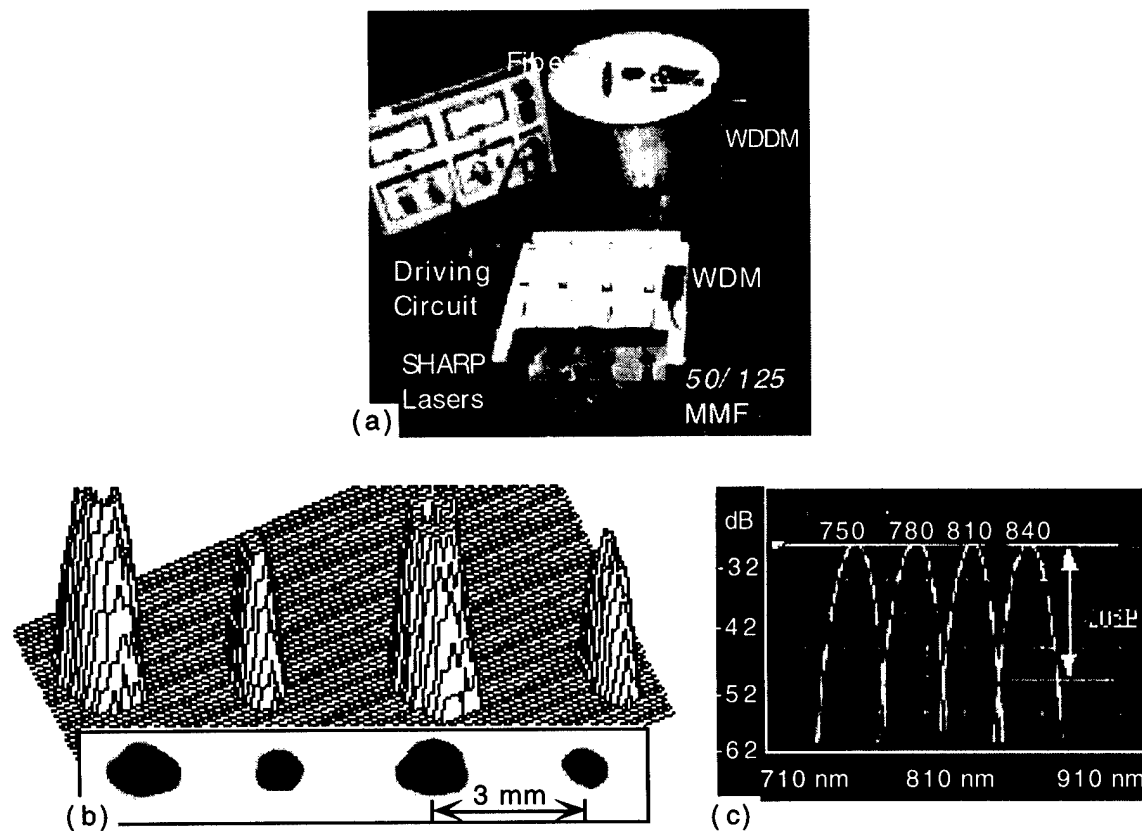


Fig.2 (a) The four channel WDM/WDDM light transmitting and receiving module picture,  
 (b) The four output spots of the four channel WDDM,  
 (c) The optical spectrum of the four wavelengths used in the WDM/WDDM system.

#### Reference

1. G. Georgiou, and A. Boucouvalas, "High-isolation single-mode wavelength-division multiplexer/demultiplexer," *Electronics Letters*, Vol. 22, No. 2, P. 62, 1986.
2. E. Acosta and K. Iga, "Design of a wavelength multiplexer-demultiplexer by the use of planar microlenses," *Applied Optics*, Vol., No. 16, P. 3415, 1994.
3. K. Okamoto, K. Syuto, H. Takahashi and Y. Ohmori, "Fabrication of 128-channel arrayed waveguide grating multiplexer with 25GHz channel spacing," *Electronics Letters*, Vol.32, No. 16, P. 1474, 1996.
4. E. J. Lerner, "Multiple wavelengths exploit fiber capacity," *Laser Focus World*, Vol. 33, No. 7, P. 119, 1997.
5. Y. Huang, D. Su and Y. Tsai, "Wavelength-division-multiplexing and -demultiplexing by using a substrate-mode grating pair," *Optics Letters*, Vol. 17, No. 22, P.1629, 1992.
6. M.R. Wang, G. J. Sonek, R. T. Chen and T. Jannson, "Large fanout optical interconnects using thick holographic gratings and substrate wave propagation," *Applied Optics*, Vol. 31, No. 2, p.236, 1992.
7. M. M. Li and R. T. Chen, "Two-channel surface-normal wavelength division demultiplexer using substrate guided waves in conjunction with multiplexed waveguide holograms," *Applied Physics Letters*, Vol. 66, No. 3, p.262, 1995.
8. M. M. Li, and R. T. Chen, "Five-channel surface-normal wavelength-division demultiplexer substrate guided waves in conjunction with a polymer-based Littrow hologram," *Optics Letters*, Vol. 20, No. 7, P.797, 1995.

# A Planarized Two-Dimensional Multi-Wavelength Routing Network with 1-to-many Cascaded Fanouts

Jian Liu and Ray T. Chen

Microelectronics Research Center  
Department of Electrical and Computer Engineering  
University of Texas at Austin  
Austin, Texas 78758

Tel: (512) 471-2003 Fax: (512) 471-8575

E-Mail: JLIU3@ECE.UTEXAS.EDU

Wavelength-division (de)multiplexer (WD(D)M) is a pivotal bandwidth enhancement component in optical fiber communications and optical sensor systems. Various types of optical WD(D)M have been proposed and demonstrated.<sup>1-13</sup> When the WDDMs are applied to the fiber-to-home network<sup>14</sup> or multi-sensors system<sup>15</sup>, it is necessary for them to be able to route separate wavelength channels and to distribute each channel to many users. Photopolymer-based substrate guided wave optical interconnects, using photopolymer

volume holograms combined with total internal reflection (TIR) in waveguiding substrates, have been demonstrated as efficient approaches for intra- and inter-module interconnections, optical clock distributions, optical backplane buses, and optical networks<sup>16-18</sup>. In this paper, a planarized two-dimensional (2-D) WDDM serving the functions of wavelength separation and 1-to-many fanouts is demonstrated. In our design, stacked volume holograms are employed as the input couplers to steer input optical signals with different wavelengths to their desired directions, and then coupled-out by output HOE arrays. This two-dimensional network configuration having both the input and output HOEs integrated on one waveguiding plate fulfills simultaneously wavelength separation, routing, and optical signal distribution. Experimental results of routing and distributing three optical channels at wavelengths of 760 nm, 790 nm, and 820 nm are presented.

Figure 1 shows a schematic diagram for a planarized two-dimensional WDDM network. The input and the output volume holograms are integrated on the same waveguiding substrate at their designated positions. Three stacked volume holograms are used as the optical wavelength routing filters to couple three input optical signals  $\lambda_1$ ,  $\lambda_2$ , and  $\lambda_3$  into their designed routing directions with an angle of  $45^\circ$  between

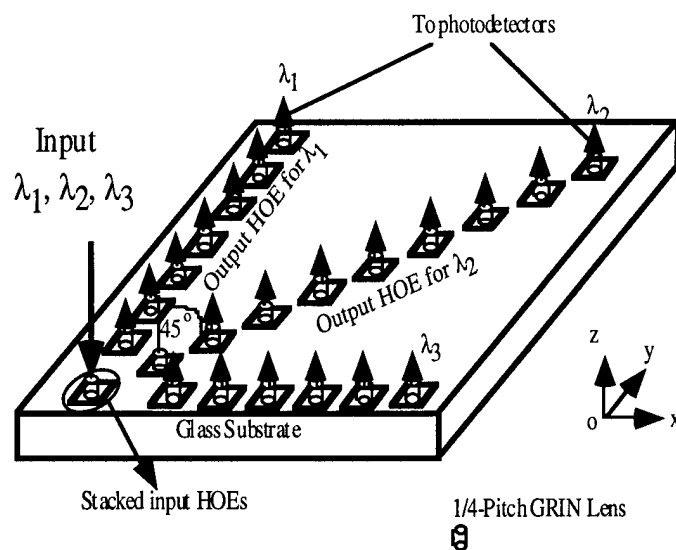


Fig. 1 Schematic diagram of a two-dimensional WDDM distributing network.

them in XY plane as indicated in Figure 1. The bouncing angle within the waveguiding substrate is  $48^\circ$ , greater than the critical angle of the substrate. The separated optical signals propagate within the waveguiding substrate with total internal reflection and are distributed to their respective destinations, and then coupled out surface-normally by the three arrays of cascaded volume holograms at the surface-normal direction. Many users may share the same source with this distributed 2-D WDDM.

For this substrate guided wave optical interconnect with the surface-normal configuration, the diffraction angle of the volume hologram is designed to be  $48^\circ$  in a quartz substrate while optical signal is incident from the surface-normal direction with  $\theta = 0$ . The deviation of operating wavelengths and the incident angle  $\theta$  are evaluated using coupled wave theory<sup>19</sup>. The simulation results of diffraction efficiencies versus the wavelength deviation from central wavelength 760 nm, 790 nm, and 820 nm of an s-wave were done for DuPont photopolymer films HRF 600x001-20 with refractive index  $n = 1.52$ . The film thickness is 20  $\mu\text{m}$ . The refractive index modulation is  $\Delta n = \sim 0.0166$  for the three wavelengths. These results show that it is feasible to separate optical signals of wavelength spacing of 30 nm with 20  $\mu\text{m}$  DuPont photopolymer films.

In our experiment, An Argon ion laser operating at 514 nm is used to record volume hologram. A Ti: Sapphire tunable laser is employed to carry out the measurement. We employ DuPont photopolymer film HRF 600 with a 20  $\mu\text{m}$  film thickness. To demonstrate the conceptual two-dimensional WDDM network shown in Figure 1, three stacked holographic films are sequentially laminated and are recorded on a quartz plate. The thickness of the substrate is  $d' = \sim 1.6$  mm. The bouncing angle within the substrate is  $48^\circ$ . The angle between the adjacent routing directions is designed to be  $45^\circ$ . Three arrays of output holographic grating couplers are fabricated along the desired

routing direction for reconstruction wavelength at 760 nm, 790 nm and 820 nm, respectively. By taking advantage of the fact that the collimated laser beam is with a Gaussian intensity profile during hologram recording, we are able to record the output couplers with relatively uniform fanout distribution for both arrays.

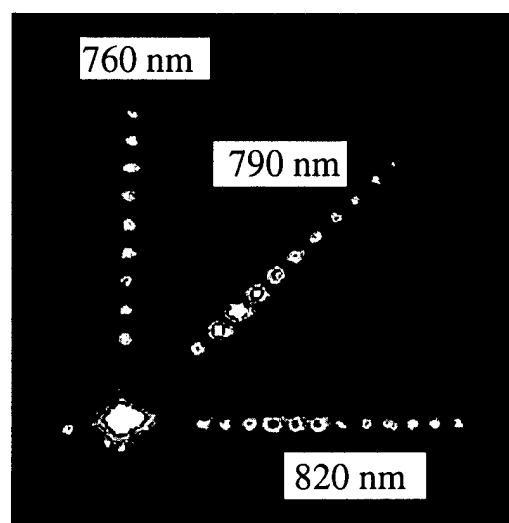


Figure 2 Experimental results of the two-dimensional WDDM device while operating at 760 nm 790 nm, and 820 nm.

Figure 2 shows the experimental results for device operates at 760 nm, 790 nm, and 820 nm. The three wavelengths are successfully separated and directed to their designed directions by the three stacked input holographic grating coupler. The crosstalks between two channels are measured to be smaller than -20dB. It is obvious that this two-dimensional network configuration provides a robust, reliable, surface-mountable, and cost-efficient device with combined functions of wavelength demultiplexing and distributing.

In conclusion, we demonstrated a cost-efficient and user-sharing two-dimensional wavelength demultiplexing and distributing optical network, with which optical signals at 760 nm, 790 nm, and 820 nm are separated and diffracted into the waveguiding plate in three different routing directions by three stacked DuPont holographic gratings,

distributed within the glass substrate with total internal reflection, and coupled out of the substrate to each user by output holographic grating. The crosstalks are measured to be  $< -20\text{dB}$ . The relatively uniform fanout energy distribution is pivotal to the integration with photodetector arrays for practical system designs. The monolithic integration of the input and output couplers on a waveguiding substrate provides a robust architecture against environmental and mechanical perturbations. Furthermore, it is possible to realize multi-wavelength channels routing and distribution involving  $0.8\text{ }\mu\text{m}$ ,  $1.3\text{ }\mu\text{m}$  and  $1.55\text{ }\mu\text{m}$  wavelengths. by stacking holographic gratings as input wavelength separating and routing couplers and by integrating arrays of output couplers at desired wavelengths.

**Acknowledgments:** This research is supported by Ballistic Missile Defence Organization, Army SSDC, the Center of Optoelectronics Science and Technology (COST), Office of Naval Research, Cray Research, DuPont, and the Advanced Technology Program (ATP) of the state of Texas.

#### References:

1. M. Seki, K. Kobayashi, Y. Odagiri, M. Shikada, T. Tanigawa, and R. Ishikawa, *Electron. Lett.* **18**, 257-258 (1982).
2. K. Nosu, H. Ishio, and K. Hashimoto, *Electron. Lett.* **15**, 414-415 (1979).
3. C. M. Lawson, P. M. Kopera, T. Y. Hsu, and V. J. Tekippe, *Electron. Lett.* **20**, 963-964 (1984).
4. B. H. Verbeek, C. H. Henry, N. A. Olsson, K. J. Orlowsky, R. F. Kazarinov, and B. H. Johnson, *IEEE J. Lightwave Technol.* **6**, 1011-1013 (1988).
5. C. Dragone, *IEEE Photon. Technol. Lett.* **3**, 812-814 (1991).
6. W. S. Whalen, M. D. Divino, and R. C. Alferness, *Electron. Lett.* **22**, 681-682 (1986).
7. K. H. Hirabayashi, H. Tuda, and T. Kurokawa, *IEEE Photon. Technol. Lett.* **3**, 213-215 (1991).
8. A. L. Dmitriev and A. V. Ivanov, *Opt. Spectrosc.* **62**, 91-93 (1987).
9. J. L. Horner and J. E. Ludman, *Appl. Opt.* **20**, 1845-1847 (1981).
10. M. M. Li and R. T. Chen, *Opt. Lett.* **20**, 797-799 (1995).
11. C. Wu, C-M Wu, D. G. Knight, C. Blaauw, N. Puetz, F. Shepherd, G. Rabikovs, and K. D. Chik, *Electron. Lett.* **31**, 231-232 (1995).
12. X. Fu and J. M. Xu, *IEEE Photon. Technol. Lett.* **9**, 779-781 (1997).
13. A. N. Starodumov, L. A. Zenteno, D. Monzon, and A. R. Boyain, *Opt. Comm.* **138**, 31-34 (1997).
14. I. P. Kaminow and T. L. Koch, *Optical Fiber Telecommunications IIIA*, Academic Press, New York (1997).
15. R. T. Chen, D. Robinson, H. Lu, M. R. Wang, T. Jansson, and R. Baumbick, *Opt. Eng.* **31**, 1098-1105 (1992).
16. R. T. Chen, C. Zhou, C. Zhao, and R. Lee, *Critical Rev. Optical Sci. Technol.* **CR-63**, 46-64 (1996).
17. Jian Liu, Chunhe Zhao, R. Lee, and Ray T. Chen, *Opt. Lett.* **22**, 1024-1026 (1997).
18. Jian Liu, Chunhe Zhao, and Ray T. Chen, *IEEE Photon. Technol. Lett.* **9**, 946-948 (1997).
19. H. Kogelnik, *The Bell Sys. Tech. J.* **13**, 2909-2947 (1969).

# Key to Authors and Presiders

- Abraham, Patrick ■ IMF1  
 Ahland, Andreas ■ ITuJ2  
 Ahn, Joo-Heon ■ IMG1  
 Aitchison, J. S. ■ IWA6  
 Aldariz, J. M. ■ IWA6  
 Anthony, Philip J. ■ IMA3  
 Aronson, Lewis B. ■ ITuL, IWD, IWD2  
 Baets, Roel ■ IMH18, IWB2  
 Bagley, B. G. ■ IMH4  
 Bakker, A. F. ■ ITuB3  
 Bava, G. P. ■ ITuD5  
 Becker, Ch. ■ ITuI3  
 Benson, T. M. ■ IMB3, IMH1  
 Berglund, William ■ IMC2  
 Bihari, Bipin ■ ITuH1  
 Bishop, S. G. ■ IMC5  
 Bjarklev, Anders ■ IMH11  
 Black, Alexis ■ IMF1  
 Bludszweit, M. ■ IME4  
 Bond, Aaron E. ■ IWB1  
 Boons, S. ■ IWB2  
 Bowers, John E. ■ IMF1, IWA2  
 Bräuer, A. ■ ITuL1  
 Bruce, A. J. ■ IMG5  
 Bryce, A. C. ■ ITuB2  
 Buckman, L. ■ IWD2  
 Burkhard, H. ■ ITuF5  
 Byun, Young Tae ■ IMF2  
 Cada, Michael ■ IMH16  
 Caekebeke, K. ■ IWB2  
 Camacho, F. ■ ITuB2  
 Cardinal, T. ■ IMC4  
 Carencio, A. ■ ITuE1  
 Caspar, C. ■ IMH14  
 Chan, K. S. ■ IMH5, IMH6  
 Chan, L. Y. ■ IWB4  
 Chan, Michael C. Y. ■ IMH5  
 Chandrasehkar, S. ■ ITuE  
 Chang, Hung-Chun ■ IMB4  
 Chang, W. S. C. ■ ITuE2  
 Charbonneau, S. ■ IMH19  
 Chaudhuri, S. K. ■ IMB1  
 Chaudhuri, Sujeet K. ■ IWA4  
 Chen, Ray T. ■ ITuH1, IWD4, IWD5  
 Chen, W. X. ■ IMF3  
 Chi, Jacques W. D. ■ IWC2  
 Chiou, Yih-Peng ■ IMB4  
 Cho, WoonJo ■ ITuJ3  
 Chu, S. T. ■ IMD3  
 Chuang, S. L. ■ ITuG, ITuJ4, IWC1  
 Chun, Young Yun ■ ITuK4  
 Chung, P. S. ■ IMH6  
 Chung, Youngchul ■ IMH3, IWA1  
 Cocorullo, G. ■ ITuH5, ITuK2  
 Coldren, Larry A. ■ IMD5, ITuE4  
 Colet, P. ■ IMH9  
 Conradi, O. ■ IMB2  
 Cross, Jeffrey ■ ITuF4  
 Crouse, D. ■ IMF4  
 Cucinotta, A. ■ IME3, IMH2  
 D'Urso, B. ■ ITuA4  
 Dagli, Nadir ■ IMF2, ITuI4  
 Dapkus, P. Daniel ■ IWB1  
 De Rosa, R. ■ ITuH5  
 DeLaRue, R. M. ■ IWB, IWB3  
 DeMarco, J. ■ IMG4, IMG5  
 Debernardi, P. ■ ITuD5  
 Deck, R. T. ■ IMH4  
 Delage, A. ■ IMH19  
 Della Corte, Francesco G. ■ ITuH5, ITuK2  
 Dellunde, J. ■ IWC4  
 Delprat, D. ■ IMD4  
 Demeester, P. ■ ITuE3  
 Dempewolf, Paul ■ IWD4  
 De Minicis, M. ■ IMB2  
 DenBaars, Steven P. ■ IMD5, ITuE4  
 Deri, Robert J. ■ IMA, ITuF, IWD3  
 Devaux, F. ■ ITuE1  
 Dhoedt, B. ■ IWB2  
 Dijaili, S. ■ IMH17  
 Doerr, C. R. ■ ITuB5  
 Dolfi, D. ■ IWD2  
 Donnelly, Joseph P. ■ ITuJ  
 Drake, John ■ ITuH4  
 Dridi, Kim ■ IMH11  
 Dries, J. C. ■ ITuB6  
 Ellerbusch, Ben ■ IMC2  
 Esquivias, I. ■ ITuG2  
 Fang, W. ■ IWC1  
 Farjady, F. ■ IMH23  
 Fedorov, V. A. ■ IMC3, ITuI1  
 Feit, M. D. ■ IMH17  
 Feng, Y. ■ IMH19  
 Fish, Greg A. ■ IMD5, ITuE4  
 Foisel, H.-M. ■ IMH14  
 Ford, Carol ■ IMC2  
 Forrest, S. R. ■ ITuB6  
 Frankena, H. J. ■ ITuE5  
 Fujita, Juni ■ ITuF3  
 Gan, F. Y. ■ IMH8  
 Gan, Jianhua ■ ITuH1  
 Garrett, H. E. ■ IWD3  
 Gavrilov, S. A. ■ IMC3  
 Gemelos, S. ■ IWD3  
 Giboney, K. ■ IWD2  
 Gini, Emilio ■ ITuB1  
 Glingener, C. ■ IME4  
 Goeman, S. ■ IWB2  
 Gokhale, M. R. ■ ITuB6  
 Goossen, K. W. ■ IMH20  
 Gopinath, Anand ■ IMC2, ITuJ3, IWC  
 Goward, W. ■ IMH17  
 Grand, G. ■ ITuC4  
 Grattan, K. T. V. ■ IME6  
 Gravert, M. ■ IMB2  
 Greiner, A. ■ ITuI3, ITuI5  
 Greus, Ch. ■ ITuF5  
 Gross, T. ■ ITuK3  
 Groen, F. H. ■ ITuB3, ITuE5  
 Grupen, Matt ■ ITuG1  
 Hadley, G. Ronald ■ IMB, IWC3  
 Hagness, S. C. ■ ITuD4  
 Haigh, R. E. ■ IWD3  
 Hamamoto, Kiichi ■ ITuB1  
 Hamilton, C. J. ■ ITuB2  
 Han, Seon-Gyu ■ IMG1  
 Haritos, D. ■ IWD2  
 Hatakeyama, H. ■ ITuC3  
 Hawkins, Aaron ■ IMF1  
 Haysom, J. E. ■ IMH19  
 He, J. J. ■ IMH19  
 Helfert, Stefan ■ IWA5  
 Henderer, B. D. ■ IWD3  
 Hennig, T. ■ ITuL1  
 Henry, C. H. ■ IMG5  
 Herben, C. G. P. ■ ITuE3, ITuE5  
 Hess, Karl ■ ITuG1  
 Ho, A. H. P. ■ IMH6  
 Ho., S. T. ■ ITuD4  
 Hodiak, J. H. ■ ITuE2  
 Hoekstra, H. J. W. M. ■ IMB2  
 Hoffmann, M. ■ ITuK3  
 Holtmann, Christoph ■ ITuB1  
 Hopkinson, Mark ■ ITuJ3  
 Hou, H. ■ IMF4  
 Hsu, A. ■ IWC1  
 Hu, Evelyn ■ IMF1  
 Huang, J. Z. ■ IMH7  
 Huang, Wei-Ping ■ IMB1, IMB5, IME, IME5  
 Hübner, B. ■ ITuF5  
 Hunter, Boyd V. ■ IWD4  
 Hunziker, Guido ■ ITuG4  
 Iodice, Mario ■ ITuK2  
 Itoh, M. ■ ITuC3  
 Jackel, Janet Lehr ■ IMG  
 Jalali, B. ■ ITuH2  
 Jeon, Heonsu ■ ITuB4  
 Jeong, Hyung Gon ■ ITuK4  
 Jiang, Ching-Long ■ ITuF1  
 Joannopoulos, J. D. ■ ITuA1  
 Johnson, Klein L. ■ IMC2  
 Jokerst, Nan Marie ■ ITuC, ITuF4  
 Kallman, J. S. ■ IMH17  
 Kaneko, Yawara ■ ITuF2  
 Karavanskii, V. V. ■ IMC3  
 Karthe, W. ■ ITuL1  
 Kato, Masaki ■ ITuJ1  
 Kato, T. ■ IMD3, ITuC3  
 Kawachi, Masao ■ IMA1  
 Kawakami, Shojiro ■ ITuA3  
 Keil, Norbert ■ ITuL2  
 Kendall, P. C. ■ IMB3, IMH1  
 Kim, Boo-Gyoun ■ IWA2  
 Kim, Byoung-Sung ■ IMH3  
 Kim, J.-Y. ■ ITuC1  
 Kim, Namhoon ■ IWA1  
 Kim, Sangin ■ ITuJ3

- Kim, Sun-Ho ■ IMH3  
 Kitamura, M. ■ ITuC3  
 Kitamura, N. ■ ITuC3  
 Kitamura, S. ■ ITuC3  
 Ko, Jack ■ IMF2  
 Kokubun, Y. ■ IMD3, IMG2  
 Kondoh, You ■ ITuF2  
 Kopka, P. ■ ITuK3  
 Koren, Uzi ■ ITuG4  
 Korkishko, Yuri N. ■ IMC3, ITuI1, ITuI2  
 Kostritskii, S. M. ■ ITuI1  
 Koteles, Emil S. ■ IMH19  
 Koyama, F. ■ IMH22  
 Krauss, Thomas F. ■ IWB3  
 Krijnen, G. J. M. ■ IMB2
- Laskowski, E. J. ■ IMG4  
 Lau, S. S. ■ IMF3  
 Lavrova, Olga A. ■ IMD5  
 Le Bihan, Jean ■ IWC2  
 Le Foulgoc, K. ■ IMC4  
 Lebby, Michael S. ■ IWD1  
 Lee, Hyung Jong ■ ITuK4  
 Lee, Hyung-Jong ■ IMG1  
 Lee, Myung-Hyun ■ IMG1  
 Lee, R. ■ ITuD2  
 Lee, Yong Tae ■ ITuK4  
 Legay, P ■ IMD4  
 Leibenguth, R. ■ IMH20  
 Leijtens, X. J. M. ■ ITuE3  
 Lemoff, B. ■ IWD2  
 Levi, A. F. J. ■ ITuD1  
 Levine, B. F. ■ ITuH3  
 Levy, M. ■ ITuF3  
 Li, G. L. ■ IMF3  
 Li, Kang ■ IMB1, IMB5  
 Li, N. Y. ■ IMF3  
 Little, B. ■ IMD3, ITuA, ITuD  
 Liu, Bin ■ IMF1, IWA2  
 Liu, Jian ■ IWD5  
 Liu, Q. Z. ■ IMF3  
 Livescu, Gabriela ■ IMD2  
 Lo, Y.-H. ■ IMF4  
 Loi, K. K. ■ ITuE2  
 Lowry, M. ■ IMH17, IWD3  
 Lui, Wayne W. ■ IMB5, IME5
- Ma, Byongjin ■ IMH21  
 Maat, D. H. P. ■ ITuE3, ITuE5  
 Madsen, C. K. ■ IMG4, IMG5  
 Maeda, T. ■ IMD3  
 Magel, Gregory A. ■ ITuK
- Makino, Toshihiko ■ IMH16  
 Margalit, Near ■ IMF1  
 Maring, David B. ■ ITuI2  
 Marsh, J. H. ■ IMH6, ITuB2  
 Mason, Beck ■ IMD5  
 Massit, Cl. ■ ITuC4  
 Mathur, Atul ■ ITuB4  
 Matsubara, Kenji ■ IME2  
 Matsuura, Shinnosuke ■ IMG2  
 Mei, X. B. ■ ITuE2  
 Melchior, Hans ■ IMA2, ITuB1  
 Meyer, J. R. ■ ITuJ5  
 Milbrodt, M. A. ■ IMG4, IMG5  
 Minford, William ■ ITuI  
 Mirasso, C. R. ■ IMH9  
 Mirkov, M. G. ■ IMH4  
 Moerman, I. ■ ITuB3, ITuE5  
 Moon, Jong Ha ■ ITuK4  
 Mori, S. ■ IMH22  
 Morohashi, Naofumi ■ IME1  
 Morvan, M. ■ IMD4  
 Mottier, P. L. ■ ITuC4  
 Mustafa, N. ■ ITuG2
- Nakagawa, Shigeru ■ ITuF2  
 Nakano, Hisamatsu ■ IME1, IME2  
 Nakano, Yoshiaki ■ IMH21, ITuJ1  
 Nishii, Junji ■ IMC1  
 Nolting, H.-P. ■ IMB2  
 Noutios, P. ■ IMH8
- O'Brien, J. ■ ITuD2  
 Oei, Y. S. ■ ITuE3  
 Oesselke, Th. ■ ITuI3  
 Oh, Min Cheol ■ IMG1  
 Ohmori, Yutaka ■ ITuL3  
 Ortega, D. ■ IWA6  
 Osgood, Jr., R. M. ■ IMH7, ITuF3  
 Ougazzaden, A. ■ IMD4  
 Ozturk, Cem ■ IMF2
- Paiella, Roberto ■ ITuG4  
 Painter, O. ■ ITuA4, ITuD2  
 Pan, W. ■ IMD3  
 Pape, A. ■ ITuI3  
 Parat, G. ■ ITuC4  
 Park, Kyoung-Hyun ■ IMH3  
 Park, Seoung-Hwan ■ ITuJ4
- Parker, M. C. ■ IMH23  
 Peng, G. ■ IMH8  
 Pesquera, Luis ■ ITuG2, IWC4  
 Poole, P. J. ■ IMH19  
 Pregla, R. ■ IMB2, IMH12  
 Pun, E. Y. B. ■ IMH6
- Qiu, W. ■ ITuI5
- Rafizadeh, D. ■ ITuD4  
 Rahman, B. M. A. ■ IME6  
 Rajarajan, M. ■ IME6  
 Ram-Mohan, L. R. ■ ITuJ5  
 Ramachandran, S. ■ IMC5  
 Ramaswamy, Ramu V. ■ ITuI2  
 Ramberg, Randy ■ IMC2  
 Ramdane, A. ■ IMD4  
 Ratowsky, R. P. ■ IMH17  
 Rendina, I. ■ ITuH5  
 Rendina, Ivo ■ ITuK2  
 Richardson, K. ■ IMC4  
 Roberts, John S. ■ IWB3  
 Rolland, Claude ■ IMF  
 Ronneberg, E. ■ ITuF5  
 Rosenberg, P. ■ IWD2  
 Rubino, A. ■ ITuH5
- Safavi-Naeini, S. ■ IMH13  
 Sakamoto, Steven R. ■ IMF2  
 Sarro, Pasqualina M. ■ ITuK2  
 Sasaki, J. ■ ITuC3  
 Sato, S. ■ IMD3  
 Scarmozzino, R. ■ IMH7  
 Scherer, A. ■ ITuA4, ITuD2  
 Scherer, Axel ■ IWB3  
 Schmidt, Frank ■ IWC5  
 Schulz, D. ■ IME4, ITuJ2  
 Schwartz, Ira B. ■ ITuD3  
 Seino, Minoru ■ IMG3  
 Seki, Shunji ■ ITuG3  
 Sekiguchi, Minoru ■ IME2  
 Selleri, S. ■ IME3, IMH2  
 Sewell, P. ■ IMB3, IMH1  
 Shakouri, Ali ■ IMF1, IWA2  
 Shibayama, Jun ■ IME2  
 Shimoda, T. ■ ITuC3  
 Shooshtari, A. ■ IMH13  
 Shore, K. A. ■ IMH9, IWA3, IWA, IWC2, IWC4  
 Shu, C. ■ IWB4  
 Sibilia, C. ■ IMB2  
 Smit, M. K. ■ ITuB3, ITuE3, ITuE5  
 Sohler, W. ■ ITuI3, ITuI5
- Soole, Julian B. ■ IMD  
 Soref, Richard A. ■ ITuH  
 Sorel, Y. ■ IMD4  
 Spencer, P. S. ■ IMH9  
 Stoffer, R. ■ IMB2  
 Strasser, T. A. ■ IMG4, IMG5  
 Straznicki, J. ■ IWD2  
 Strebel, B. ■ IMH14  
 Studenkov, P. V. ■ ITuB6  
 Stulemeijer, J. ■ ITuB3  
 Suche, H. ■ ITuI3, ITuI5  
 Sujecki, S. ■ IMB3  
 Sutton, Sean ■ IWD4
- Tada, Kunio ■ IMH21, ITuJ1  
 Taflove, A. ■ ITuD4  
 Tamanuki, T. ■ ITuC3  
 Tang, J. M. ■ IWA3  
 Tang, Suning ■ ITuH1  
 Tavlykaev, Robert F. ■ ITuI2  
 Terzini, E. ■ ITuH5  
 Thomas, Mikkell A. ■ ITuF4  
 Thomas, S. ■ ITuH2  
 Tidmarsh, Jolyon ■ ITuH4  
 Tohge, Noboru ■ IMC1  
 Triandaf, Ioana ■ ITuD3  
 Tsang, H. K. ■ IWB4  
 Tu, C. W. ■ IMF3, ITuE2
- van Brug, H. ■ ITuE5  
 van der Tol, J. J. G. M. ■ ITuE3  
 Vahala, Kerry J. ■ ITuG4  
 Valle, A. ■ IWC4  
 Van, Vien ■ IWA4  
 Van Caenegem, Tom ■ IMH18  
 Van Daele, P. ■ IWB2  
 Van Thourhout, Dries ■ IMH18  
 Veron, Ch. ■ ITuL1  
 Viens, J.-F. ■ IMC4  
 Villeneuve, A. ■ IMC4  
 Vincetti, L. ■ IME3, IMH2  
 Vinchant, Jean Francois ■ ITuB  
 Voges, E. ■ IME4, ITuJ2, ITuK3  
 Vollrath, G. ■ ITuF5  
 Vreeburg, C. G. M. ■ ITuE3  
 Vreze, Lance ■ IMC2
- Wächter, Ch. ■ ITuL1  
 Wagener, J. ■ IMG4  
 Walker, J. D. ■ IMH17, IWD3

- Walker, S. D. ■ IMH23  
Wang, Jing-Yi ■ IMH16  
Wang, Kang L. ■ ITuH2,  
ITuK1  
Wang, Tzyy-Jiann ■ ITuI6  
Wang, Way-Seen ■ ITuI6  
Watanabe, Satoshi ■ ITuF2  
Wei, Pei-Kuen ■ ITuI6  
Weidman, David L. ■ IMC  
Weinert, Carl M. ■ IMH14  
Weitzman, Peter S. ■ IMH10  
Wessel, R. ■ ITuI5  
Wickman, Randy ■ ITuH1  
Wolter, H. ■ ITuL1
- Wong, Y. H. ■ IMH6  
Wu, K. ■ IWD2  
Wu, Linghui ■ ITuH1  
Wu, Ming C. ■ ITuC2
- Xing, Q. J. ■ IMF3  
Xu, Chenglin ■ IMB1,  
IMB5, IME5
- Yam, S. P. ■ IWB4  
Yamada, Norihide ■ ITuF2  
Yamaguchi, M. ■ ITuC3  
Yamauchi, Junji ■ IME1,  
IME2
- Yao, Huihai ■ ITuL2  
Yariv, A. ■ ITuA4, ITuD2  
Yip, G. L. ■ IMH8  
Yokoyama, Kiyoyuki ■  
IMB5, IME5, ITuG3  
Yoneda, Shigeru ■ IMG2  
Yoo, S. J. B. ■ IWB5  
Yoshikuni, Y. ■ IMD1  
Yoshimoto, T. ■ ITuH2  
Yoshino, Katsumi ■ ITuL3  
Yu, L. S. ■ IMF3  
Yu, P. K. L. ■ IMF3  
Yuen, A. ■ IWD2
- Zappe, H. P. ■ IMF3  
Zavada, John M. ■ ITuI2  
Zawadzki, Crispin ■ ITuL2  
Zhang, Xiaobo ■ ITuJ3  
Zhao, Gaoyang ■ IMC1  
Zhou, Charles C. ■ IWD4  
Zhu, J. T. ■ IMF3  
Zhu, Z. H. ■ IMF4  
Ziari, Mehrdad ■ ITuB4  
Ziolkowski, R. W. ■ ITuA2,  
ITuA, ITuD

# Integrated Photonics Research

## IPR ADVISORY COMMITTEE

**David Yevick**, Chair, *Queen's University, Canada*  
**Anand Gopinath**, *University of Minnesota, USA*  
**Steven Korotky**, *Lucent Technologies, USA*  
**Curtis Menyuk**, *University of Maryland, USA*  
**Meint Smit**, *Technical University of Delft, The Netherlands*  
**David A. Smith**, *Case Western Reserve University, USA*

## IPR '98 TECHNICAL PROGRAM COMMITTEE MEMBERS

### General Chair:

**Robert Deri**, *Lawrence Livermore National Lab., USA*

### Program Co-Chairs:

**Nadir Dagli**, *University of California Santa Barbara, USA*  
**Jane E. Zucker**, *Lucent Technologies, Bell Labs, USA*

### Asia/Pacific Liaison Committee:

**Shunji Seki**, Chair, *NTT, Japan*  
**Edwin Y.B. Pun**, *City University of Hong Kong*  
**Rodney S. Tucker**, *University of Melbourne, Australia*

### Europe Liaison Committee:

**K. Alan Shore**, Chair, *University of Wales, UK*  
**Meint Smit**, *Technical University of Delft, Netherlands*  
**K. Petermann**, *Technische University Berlin, Germany*

### OSA Technical Council Representative:

**Terry Smith**, *3M Company, USA*

## TECHNICAL PROGRAM SUBCOMMITTEES

### Category I. Compound semiconductor photonic devices

**Julian Soole**, Chair, *Tellium, USA*  
**Niraj Agrawal**, *Heinrich Hertz Institut, Germany*  
**Martin Amersfoort**, *BBV Design BV, The Netherlands*  
**Roel Baets**, *University of Gent, Belgium*  
**S. Chandrasekhar**, *Bell Labs, Lucent Technologies, USA*  
**Richard De La Rue**, *University of Glasgow, UK*  
**Gregory A. Magel**, *Texas Instruments, USA*  
**Kunishige Oe**, *NTT Opto-electronics Laboratories, Japan*  
**Claude Rolland**, *Nortel Technology, Canada*  
**Jean-Francois Vinchant**, *Alcatel Optronics, France*  
**Robert Walker**, *GEC-Marconi Materials Technology, UK*

### Category II. Dielectric waveguides and photonic devices

**Leon McCaughan**, Chair, *University of Wisconsin-Madison, USA*  
**Martin M. Fejer**, *Stanford University, USA*  
**Fred Heismann**, *Bell Labs, Lucent Technologies, USA*  
**Martin Hempstead**, *University of Southampton, UK*

**Janet Jackel**, *Bellcore, USA*

**Bahram Jalali**, *University of California Los Angeles, USA*

**Yasuo Kokubun**, *Yokohama National University, Japan*

**William J. Minford**, *Bell Labs, Lucent Technologies, USA*

**Ed J. Murphy**, *Bell Labs, Lucent Technologies, USA*  
**Yutaka Ohmori**, *Osaka University, Japan*

**Ramu Ramaswamy**, *University of Florida, USA*

**Wolfgang Sohler**, *Universitat-GH Paderborn, Germany*

**Richard A. Soref**, *Rome Laboratory, USA*

**David Weidman**, *Corning Inc., USA*

### Category III. Modeling, numerical simulation, and theory

**Sujeet Chaudhuri**, Chair, *University of Waterloo, Canada*

**Shunji Seki**, *NTT Multimedia Systems Department, Japan*

**K. Alan Shore**, *University of Wales, UK*

**S.L. Chuang**, *University of Illinois, USA*

**Joe Donnelly**, *MIT Lincoln Labs, USA*

**G.R. Hadley**, *Sandia National Labs., USA*

**Y. Nakano**, *University of Tokyo, Japan*

**Eoin O'Reilly**, *University of Surrey, UK*

**K. Petermann**, *Technische University Berlin, Germany*

**B. Tromborg**, *Tele Denmark Research, Denmark*

**C.M. Weinert**, *Heinrich Hertz Institute, Germany*

**John M. Zavada**, *US Army Research Office, USA*

**R.W. Ziolkowski**, *University of Arizona, USA*

### Category IV. Photonic manufacturing, packaging and prototyping

**Lewis Aronson**, Chair, *Hewlett Packard, USA*

**Philip J. Anthony**, *Bell Labs, Lucent Technologies, USA*

**Ian R. Croston**, *Integrated Optical Components, UK*

**Paul O. Haugsjaa**, *GTE Laboratories, USA*

**Mark Lowry**, *Lawrence Livermore National Lab., USA*

**Mary Hibbs-Brenner**, *Honeywell Technology Center, USA*

**Nan-Marie Jokerst**, *Georgia Institute of Technology, USA*

**Peter Krusius**, *Cornell University, USA*

**Chip Mueller**, *AMP Inc., USA*

**Hyun-Kuk Shin**, *Samsung Electronics Co., Ltd., Korea*

**Laura Ann Weller-Brophy**, *Corning, Inc., USA and Applications Contact*

**Norihide Yamada**, *Hewlett-Packard Laboratories, Japan*